New Statistical Analysis on Diatom Proxy Data for the Estimation of Past Southern Ocean Properties

By

Alexander John Ferry

(BSc, Honours)

A thesis in fulfilment of the requirements for the degree of

Doctor of Philosophy

Department of Biological Sciences,

Macquarie University,

North Ryde 2109, Australia

20 January 2016

MACQUARIE University

SYDNEY·AUSTRALIA

This page is intentionally left blank.

Statement of Sources Declaration

I declare that all of the work within this thesis is my own original work and has not been submitted in any other form for a higher degree to any other university or institution. Any additional help and contributions from my supervisors and co-authors has been indicated within the 'Statement of co-authorship section'. No approval from the Macquarie University ethics committee was sought for any of the research presented within this thesis.

Signature:…… *Date:*……

Statement of Co-authorship

Chapter 1

I independently researched and produced the initial draft of sections 1.1, 1.2, 1.7 and 1.8. Feedback from my supervisors Dr Helen Phillips (University of Tasmania), Dr Tania Prvan (Macquarie University) and Dr Leanne Armand (Macquarie University) was integrated when finalising each of these sections. Sections 1.3, 1.4, 1.5 and 1.6 were also initially researched and written by myself. However, these latter sections were originally written as subsections within a book chapter co-authored by myself, Dr Leanne Armand and Prof Amy Leventer (Colgate University, U.S.A) (Armand, L.K., Ferry, A.J., and Leventer, A., (submitted). Chapter 26: Advances in palaeo sea ice estimation. In *An Introduction to Sea Ice*. 3rd Edition. Editor. Tomas, D. N. Wiley-Blackwell). Therefore, sections 1.3, 1.4, 1.5 and 1.6 of this thesis have received contributions from both Dr Leanne Armand and Prof Amy Leventer. In summary, I am responsible for producing 75% of this chapter.

As this thesis has been prepared in accordance with the standards for a thesis by publication, each of the data chapters (Chapters 2 through to 5) have separate introductions outlining the scientific background to each Chapter. Hence, there is some redundancy between these chapters when compiled together as a thesis by publication.

Chapter 2

I completed 90% of this chapter's statistical analysis by myself. I also completed 100% of this chapters write up, with feedback from my co-supervisors Dr Tania Prvan, Dr Brian Jersky (Cal

Poly Pomona, U.S.A), Dr Xavier Crosta (University of Bordeaux 1, France) and Dr Leanne Armand. I carried out 100% of the analysis for the hold out validation of each statistical model, application of statistical tests to assess model assumptions, computation of model performance statistics, species response modelling, and variance partitioning. Assistance from Dr David Nipperess (Macquarie University) was sought for the application of principal co-ordinate analysis of neighbour matrices. Dr David Nipperess also provided constructive feedback on a draft of this chapter, and assisted with reviewing my R scripts. Dr Drew Allen (Macquarie University) provided assistance with the use of the R packges 'maps' and 'mapproj' for the production of the maps presented within this Chapter. Dr Alex Fraser (University of Tasmania) provided extensive assistance with the extraction of winter sea-ice data from the bootstrapped sea-ice data product provided by the National Snow and Ice Data Centre.

I have presented this Chapter at two international conferences during 2012 and 2013.

1. PAGES sea-ice proxies working group meeting at Montreal, Canada, March 7-9. Oral presentation titled "New statistical analysis on diatom proxy data for the estimation of Past Southern Ocean sea ice extent".

2. PAGES sea-ice proxies working group meeting at Cambridge, United Kingdom, July 22-24. Oral presentation titled "Estimating winter sea ice based on diatoms: Comparing statistical methods".

Chapter 3

I produced 80% of this chapter by myself. My statistical contributions included the application of generalised additive models to estimate paleo winter sea-ice for marine sediment cores E27-23 and SO136-111, as well as the application of all reconstruction diagnostics. I was responsible for the write up of all sections of this chapter, with the exception of section 2.5, which was written by Dr Leanne Armand and Dr Xavier Crosta. Both Dr Armand and Dr Crosta carried out all of the analysis described in section 2.5. Assistance from Dr Rob Hyndman (Monash University) was sought for the application of the time series analysis using the 'forecast' package for R. I applied all of the time series analysis described in sections 2.2 and 3.1. Extensive feedback was received from my co-authors, Prof. Patrick Quilty (University if Tasmania), Dr William Howard (University of Melbourne), Dr. David Fink (ANSTO) and Dr Xavier Crosta during the write up of this chapter. Extensive feedback and advice from my principal supervisor, Dr Leanne Armand, was also integrated into this chapter.

Chapter 4

I carried out all of the research and the initial write up of this chapter. I also completed all of the statistical analysis presented within this chapter. Feedback on early drafts of this chapter were provided by Dr Andrés Rigual-Hernández (Macquarie University) and my co-supervisors, Dr Tania Prvan and Dr Helen Phillips. My principal supervisor, Dr Leanne Armand, provided extensive feedback for the final write up of this chapter and established the age models for cores MD88-787 and MD88-784 using the "Linage" subroutine of Analyseries 2.0.8. Consequently, with the input from my supervisors and colleagues, I produced 90% of this chapter.

Chapter 5

I wrote 95% of Chapter 5 and carried out all of the statistical analysis described, with the exception of section 2.1.3. The data analysis detailed in section 2.1.3, the extraction of the SSH contours, was carried out by my co-supervisor, Dr Helen Phillips. Dr Leanne Armand provided the Abbott diatom database used within this chapter, and clarified the diatom taxonomy used within this database. I applied all of the remaining analysis detailed in section 2.2 and section 3. The chapter was reviewed by my supervisors Dr Leanne Armand and Dr Helen Phillips, both of whom provided extensive feedback, which I integrated into this chapter. I therefore wrote 95% of Chapter 5.

Chapter 6

Chapter 6 was written by myself, with feedback from my supervisors Dr Leanne Armand, Dr Helen Phillips and Dr Tania Prvan.

Signature:…… *Date:*……

Acknowledgments

I want to send a very big thank you to my supervisors. In particular, I wish to send a special thanks to my principal supervisor, Dr Leanne Armand, for her guidance, encouragement and extreme patience as I progressed through my PhD. I am very grateful to my co-supervisors, Dr Helen Phillips and Dr Tania Prvan, for their encouragement and continued efforts to support my research. I am particularly grateful to Dr Tania Prvan and Dr Brian Jersky for offering support as I tackled many of the statistical hurdles I faced during the write up of this thesis. I also need to express my gratitude to Dr David Nipperes and Dr Drew Allen for their continued assistance with writing scripts for R. I am particularly grateful for the opportunity to participate in the Department of Science and Engineering's 'Genes to Geosciences' program, and the R training I received whilst participating in this program.

I thank the co-authors on many of my data chapters for their generous assistance and constructive input. In particular, I am grateful for the input I have received from Dr Xavier Crosta for both paleoceanographic and statistical discussions relevant to Chapters 2 and 3 of this thesis. Dr Xaiver Crosta was also kind enough to permit me access to his Southern Ocean diatom database, without which this thesis would not have been possible. I thank Dr Alex Fraser who donated a considerable amount of his time to assist me with the extraction of satellite sea-ice records throughout the Southern Ocean. The input from Prof Patrick Quilty, Dr William Howard and Dr David Fink on Chapter 3 of this thesis is gratefully acknowledged.

I am grateful to Macquarie University for awarding me with an Australian post graduate award. My continued casual employment within the Departments of Biological Sciences, Environment and Geography, and Statistics over these last 3.5 years is gratefully acknowledged. I have gained

some extensive and valuable teaching experience which I hope to utilize in the future. I have also really appreciated the company and support of my fellow tutors and all of the unit convenors whom I have worked with. I have had a thoroughly enjoyable time teaching at Macquarie University.

I am appreciative of the time I have been able to spend with my fellow 'lab mates', Dr Linda Armbrecht, Dr Penny Ajani and Dr Andrés Rigual-Hernández, all of whom have provided me with support and some fun times. Of course my good friends and dear family have been hugely supportive. Like most, I would not have accomplished all that I have up to this date without their love, support and wise words.

Abstract

The annual sea-ice cycle of formation and retreat influences atmospheric and oceanic processes on a global scale. An understanding of the paleo environmental occurrence of sea ice is therefore necessary when studying past and future climatic change. Currently, diatom abundances provide the most robust proxy for Southern Ocean paleo sea-ice cover and extent. Therefore, this thesis evaluated the performance of four statistical models on a southern hemisphere diatom relative abundance and winter sea-ice concentration (wSIC) training dataset. A Generalised Additive Model (GAM) provided the most robust estimates of wSIC when compared with the Modern Analog Technique, the Imbrie and Kipp transfer function, and Weighted Averaging Partial Least Squares. The GAM derived wSIC estimates were comparable with previously published paleo sea-ice data. The application of GAM was then focused on estimating a new wSIC record throughout the southwest Pacific sector of the Southern Ocean during the Last Glacial Maximum, the ensuing deglaciation, and the Holocene. A diatom proxy for February sea-surface temperature and the sea-surface height signature of the Polar Front's southern branch were developed to complement the paleo wSIC estimates. The GAM derived estimates provided the first indication that wSIC increased during the Antarctic Cold Reversal and early Holocene. Paleo wSIC and February sea-surface temperature data suggested that the Last Glacial Maximum lasted for ~11 kyr BP throughout the southwest Pacific, similar to the well documented extended Last Glacial Maximum of New Zealand. Notably, the Last Glacial Maximum was distinguished by two cold phases separated by a period of climatic amelioration, known as Antarctic Isotopic Maxima 2. The proposed diatom proxy for the sea-surface height signature of the Polar Front's southern branch indicated a northern migration of this Polar Front jet, prior to the expansion of wSIC, during the Last Glacial Maximum and the Antarctic Cold Reversal. A northern migration of the

Polar Front's southern jet, and resulting expansion of wSIC, resulted from a northern migration of the westerly winds and the subsequent northern migration of the Antarctic Circumpolar Current.

This page is intentionally left blank.

Table of Contents

Statement of Sources Declaration…….…… iii

Statement of Co-authorship……...……. iv

Acknowledgments…… viii

Abstract…… x

Table of Contents……..... 1

List of Figures…….. 5

List of Table……...… 10

List of Abbreviations……. 12

Chapter 1 – General Introduction…….. 17

Chapter 2 – Statistical modelling of Southern Ocean marine diatom proxy and winter sea ice data: Model comparison and developments……... 99

Chapter 3 – First records of winter sea-ice concentration in the southwest Pacific sector of the Southern Ocean……..115

Chapter 4 – New southwest Pacific winter sea ice and February sea-surface temperature records over the extended Last Glacial Maximum…… 165

Chapter 5 – Marine diatoms as a proxy for the sea-surface height signature of the Antarctic Polar Front southern branch: a feasibility study within the southeast Indian Ocean…..... 209

Chapter 6 – General Discussion and Conclusions……... 247

List of Appendices…….. 281

Appendix 2.1……...… 281

Appendix 2.2……... 282

Appendix 2.3……... 287

Appendix 2.4……... 290

Appendix 2.5……...… 295

Appendix 2.6……... 299

Appendix 2.7……... 303

Appendix 2.8……... 310

Appendix 2.9……... 311

Appendix 2.10…… 316

Appendix 3.1……... 320

Appendix 3.2……... 322

Appendix 3.3……... 323

Appendix 3.4……... 325

Appendix 3.5……... 326

Appendix 3.6……... 329

Appendix 4.1……... 331

Appendix 4.2……... 333

Appendix 4.3……... 335

Appendix 4.4……... 337

Appendix 4.5……... 347

Appendix 4.6……... 348

Appendix 4.7……... 349

Appendix 4.8……... 356

Appendix 4.9……... 358

Appendix 4.10…… 360

Appendix 4.11…… 365

Appendix 4.12…… 368

Appendix 5.1……... 372

Appendix 5.2……... 373

Appendix 5.3……... 375

Appendix 5.4……... 378

Appendix 5.5……... 379

Appendix 5.6……... 380

Appendix 5.7……... 382

Appendix 5.8……... 384

Appendix 5.9……... 385

Appendix 5.10…… 387

Appendix 5.11…… 390

List of Figures

Chapter 1

Figure 1. A record of atmospheric CO_2 over the last 800,000 years……. 23

Figure 2. A map of Antarctica and the Southern Ocean with all of the key regions labelled….. 25

Figure 3. The record of sea-salt aerosol (ssNa) flux from EPICA Dome C over the last 800 kyr BP……... 26

Figure 4. A map of the Antarctic and surrounding Southern Ocean illustrating the major formation sources of dense waters along the fringes of Antarctica before spreading out northwards into the abyssal layer of the world's oceans…….. 34

Figure 5. A schematic highlighting the circulation through the Arctic Oceans and the northern Atlantic……... 36

Figure 6. A generalized cross section of the Drake Passage between the Southern Ocean and north Atlantic…….. 37

Figure 7. A schematic illustrating the production of DMS by sea-ice algae, the oxidisation of DMS within the atmosphere, and the subsequent deposition of MSA over Antarctic ice sheets……. 39

Figure 8. The average amount of bromine and iodine in atmospheric columns over Antarctica…… 41

Figure 9. Micrograph images of the various diatom species……. 44

Figure 10. A schematic illustrating the premise for using diatom relative abundances as a proxy for winter sea-ice cover…….. 47

Figure 11. Key Southern Ocean diatom species associated with sea-ice concentrations and/or extent……..…… 48

Figure 12. Current estimated paleo positioning of the winter sea-ice edge throughout the Southern Ocean during the Last Glacial Maximum and/or time slices that correspond with the LGM from various sources……. 53

Figure 13. A map of the mean location for each of the Southern Ocean fronts, as defined by Sokolov and Rintoul (2009a,b) using sea-surface height data……... 56

Figure 14. Paleo climate records for the ACR……... 61

Figure 15. The location for each of the Crosta et al. (2004) samples used within this thesis….. 67

Figure 16. The locations of the six marine sediment cores that are used to produce estimates of paleo winter sea-ice concentrations during the LGM, LGM termination, and early Holocene within Chapters 3 and 4 of this thesis……. 69

Chapter 2

Figure 1. A map of the 163 samples we used for our analysis…… 102

Figure 2. A graphical display of the final HOF model (fitted to untransformed data) describing the response of each diatom taxa used within GAM along the winter sea ice gradient……. 104

Figure 3. A graphical display of the final HOF models (fitted to the logarithmically transformed data) describing the response of each diatom taxa used within GAM along the winter sea ice gradient……. 105

Figure 4. The observed data from our training data set plotted against the fitted values from IKTF, MAT, WA PLS and GAM……. 105

Figure 5. A biplot for the CCA applied to our training data base, and constrained by summer SST and winter sea ice concentration……... 106

Figure 6. The relative abundances of each diatom are plotted as a function of summer sea surface temperature and winter sea ice concentration……... 107

Figure 7. The paleo winter sea ice concentrations (wSIC) estimated by GAM, WA PLS, IKTF and untransformed MAT for core SO136-111……. 108

Figure 8. The wSIC record from GAM is plotted against the aeolian sediment content of Petherick et al. (2008) and the percentage of grass pollen recorded by Newnham et al. (2007)…… 110

Chapter 3

Figure 1. The locations of the 163 samples used in our training data base (red circles) with the winter sea-ice edge (dark blue shaded area) and summer sea-ice edge (light blue shaded area)…….. 122

Figure 2. Age calibrated $\delta^{18}O$ isotope curve comparison between the $\delta^{18}O$ (*Neogloboquadrina pachyderma* sinistral (planktic)) from E27-23 and SO136-111, and the global benthic $\delta^{18}O$ stack (LR04; Lisiecki and Raymo, 2005a,b)…… 130

Figure 3. Derivation of the E27-23 depth-age model…….. 131

Figure 4. Paleo wSIC estimates determined for core SO136-111……... 136

Figure 5. GAM/WSI/ETS model estimates of paleo winter sea-ice concentration from core site E27-23……... 136

Figure 6. A comparison between the wSIC records from SO136-111 and E27-23 with the paleo records discussed in text……... 140

Figure 7. The paleo monthly sea ice cover from Crosta et al (2004) (a) is compared with the winter sea-ice concentration records for core SO136-111 (b) and E27-23 (c) (solid blue lines)…….. 145

Chapter 4

Figure 1. All 243 surface sediment samples from Crosta et al. (2004) are plotted……. 172

Figure 2. Age calibrated $\delta^{18}O$ isotope curve comparison between the $\delta^{18}O$ (*Neogloboquadrina pachyderma* sinistral (planktic)) from cores MD88-787 and MD88-784, with core E27-23……... 173

Figure 3. The paleo wSIC records for: a) MD88-784, b) SO136-111, c) MS88-787, d) E27-23, e) PS1768-8 and f) PS58/271-1…… 182

Figure 4. The paleo fSST estimates for; a) MD88-784, b) SO136-111, c) MD88-787, d) E27-23, e) PS1768-8 and f) PS58/271-1…… 186

Figure 5: A comparison between the estimated winter sea-ice edge from Gersonde et al. (2005) (defined as the maximum extent of winter sea ice >15% concentration, solid light green line) and our estimated winter sea-ice edge (also defined as the maximum extent of >15% winter sea-ice concentration) throughout the southwest Pacific and Atlantic……. 190

Figure 6. The eLGM paleoclimatic records from New Zealand, Australia, the Scotia Sea and the EPICA EDML ice core record for the south Atlantic sector of the Southern Ocean…… 192

Chapter 5

Figure 1. A map of the mean Southern Ocean SSH…….215

Figure 2. Each of the sea-surface sediment samples from the Abbott database are plotted (red dots) against the position of the Polar Fronts southern (PF-S), middle (PF-M) and northern (PF-N) branches……. 218

Figure 3. A map illustrating the position of each Southern Ocean front as defined by Sokolov and Rintoul (2009a,b)…….. 221

Figure 4. The fitted species response (HOF) models used to model the association between diatom relative percentage abundances and the average monthly presence per annum (mpa) of the Antarctic Polar Front's southern branch (PF-S)…….. 226

Figure 5. The MAT estimates for the paleo presence of the PF-S, PF-M and PF-N mpa for marine sediment cores MD88-784 and MD88-787…….. 229

Figure 6. The estimated PF-S mpa at cores MD88-784 and MD88-787……. 233

Chapter 6

Figure 1. A schematic summarizing past oceanic and atmospheric changes, relative to the modern ocean conditions, the ACR, eLGM cold phases, and the pre-eLGM……... 266

List of Tables

Chapter 1

Table 1. The key studies that have used diatoms to estimate past Southern Ocean sea ice since 2010…… 50

Table 2. A summary of the published papers that have used the diatom sea-floor databases which were not accessible for this thesis……... 66

Chapter 2

Table 1. Output from all of the regression models fitted between the estimates sea ice from IKTF, MAT, WA PLS and GAM (i.e. fitted values) and observed sea ice data……. 105

Table 2. The average RMSEP of each model from 10-fold hold out validation and the two spatially independent hold out validations...…..……... 107

Chapter 3

Table 1. Final age model tie points used to determine the age model for E27-23…….. 128

Table 2. A summary of the final regression models with ARIMA errors for each sector of the Southern Ocean.……... 133

Table 3. A summary of the GAMs used to estimate paleo wSIC…… 137

Chapter 4

Table 1. Location, modern average February sea-surface temperature from Reynolds et al. (2002), age model, and previous reference source details for each of the six marine sediment cores covered in this study…… 171

Chapter 5

Table 1. Sea surface height labels associated with each branch of the ACC fronts (mean +/- 1 standard deviation) relative to 2500 dbar from Sokolov and Rintoul (2009b), and the total number of samples from the Abbott database that were sampled from regions influenced by Southern Ocean fronts……... 224

Chapter 6

Table 1. The average RMSEP computed for each of the models compared within Chapter 2... 249

List of Abbreviations

AABW = Antarctic Bottom Water

AAIW = Antarctic Intermediate Water

AAO = Antarctic Oscillation

ACC = Antarctic Circumpolar Current

ACR = Antarctic Cold Reversal

AESOPS = Antarctic Environment and Southern Ocean Process Study program

AIM = Antarctic isotopic maxima

AIM 2 = Antarctic Isotope Maxima 2

AMOC = Atlantic Meridional Overturing Circulation

ANSTO = Australian Nuclear Science and Technology Organization

AMS = Accelerator Mass Spectrometry

AMSR-E = advanced microwave scanning radiometer for EOS

ARIMA = Auto Regressive Integrated Moving Average

BA = Bølling-Allerød

CCA = Canonical Correspondence Analysis

CDW = Circumpolar Deep Water

CO_2 = carbon dioxide

DC = Dissimilarity coefficients

DEACON = deacon circulation cell

DML = EPICA Dronning Maud Land

DMS = dimethylsulphide

DMSP = Dimethylsulphoniopropionate

DSW = Dense Shelf Water

e = emissivity

EDC = EPICA Dome C

eLGM = extended Last Glacial Maximum

EM = electromagnetic radiation

EMSR = electrically scanning microwave radiometer

fSST = February sea-surface temperature

GAM = generalized additive model

GCMs = global climate models

GCV = Generalized Cross-validation criterion

HBI = highly branched isoprenoid

HOF = Huisman– Olff–Fresco model

IKTF = Imbrie and Kipp transfer function

IPCC = Intergovernmental Panel on Climate Change

IRD = ice rafted debris

k-NN = k-nearest neighbours

LDM = laminated diatom mat deposit

LGM = Last Glacial Maximum

LOTI = southern hemisphere Land-Ocean Temperature Index

MAT = modern analogue technique

MEI = multivariate El Niño Southern Oscillation Index

MIS = marine isotope stage

MPA = average monthly presence per annum

MSA = methanesulphonic acid

MWP = 19 kyr melt water pulse

MWP-1A = melt water pulse-1A

NADW = North Atlantic deep water

NOAA = National Oceanic and Atmospheric Administrations

NOSAMS = National Ocean Sciences Accelerator Mass Spectroscopy facility

NSIDC = National Snow and Ice Data Centre

NZ = New Zealand

NZI-CES = New Zealand INTIMATE Climate Event Stratigraphy

PCA = principal components analysis

PC = principal component

PCNM = principal coordinates analysis of neighbour matrices

pCO_2 = atmospheric partial pressure of CO_2

PF = Polar Front

PF-M = Polar Front middle branch

PF-N = Polar Front northern branch

PF-S = Polar Front southern branch

PFZ = Polar Front Zone

RMSE = Root mean squared error

RMSEP = Root mean square error of prediction

SACCF-N = ACC front northern branch

SACCF-S = ACC front southern branch

SAF = Sub-Antarctic Front

SAF-M = Sub-Antarctic Front middle branch

SAF-N = Sub-Antarctic Front northern branch

SAF-S = Sub-Antarctic southern branch

SAM = Southern Annular Mode

SB = Southern Boundary Front

SSH = sea surface height

SSM/I = special sensor microwave/imager

ssNa = sea-salt aerosol flux

SST = sea surface temperature

STC = Subtropical Convergence

STF = Subtropical Front

Tb = brightness temperature

TIR = thermal infrared

Ts = physical temperature

TSI = Total Solar Irradiance Index at Earth distance in W/m^2

VHOC = volatile halogenated organic compounds

VNIR = visible/near infrared

VPDB = Vienna Peedee Belemnite

WA = Weighted Averaging

WA PLS = weighted averaging partial least squares

wSIC = winter sea-ice concentration

Chapter 1

General Introduction

1.1 Introduction

Sea ice is one of the most seasonal and expansive geophysical parameters of the Earth's surface. Annual sea-ice growth and decay influences key oceanic and atmospheric processes, as well as the global climate (Comiso, 2010; Brandon et al., 2010). Sea ice exerts a significant influence on the radiative balance and ocean-atmosphere heat flux of the polar regions (Comiso, 2010). The paleo sea-ice record for the world's oceans is therefore an important aspect of any effort focusing on the study of past (and future) climate change (Dieckmann and Hellmer, 2010; Vaughan et al., 2013), mechanisms driving ice-age climates, and for testing paleo-climate models (Gersonde et al., 2003; Gersonde et al., 2005). Since the 1970s, oceanographers have worked towards reconstructing past oceanographic conditions (CLIMAP Project Members, 1976; CLIMAP Project Members, 1981), including paleo sea ice, with the field employing increasingly sophisticated methods, more highly resolved records, and a wider suite of proxies through time (de Vernal et al., 2013).

The paleoceanography of the Southern Ocean, in particular paleo sea-ice cover, is of considerable interest to a broad range of researchers, including climate modellers, paleo-climatologists, paleo-oceanographers and paleo-biologists (Armand and Leventer, 2010). Efforts to find new rapidly processed and analysed chemical proxies have embraced, to varying degrees, solutions involving the utility of ice-core records, such as sea-salt flux, methanesulphonic acid (MSA) (Abram et al., 2013), or the highly branched isoprenoid (HBI) lipid biomarker (Brown et al., 2014a).

Nonetheless, the traditional means of using sea ice associated diatoms has continued to supply the most frequently referred records of sea-ice cover for the last 220,000 years during the Holocene and Late Quaternary (de Vernal et al., 2013; Esper and Gersonde, 2014). The most recent IPCC report emphasizes the lack of modern sea-ice paleo records from all sectors of the Southern Ocean. The lack of Southern Ocean paleo sea-ice records hinders modelling efforts (Vaughan et al., 2013), hence major international initiatives are underway to pursue targeted research addressing this issue (e.g. PAGES Sea Ice Proxy Working Group; SCAR Six Priorities for Antarctic Science; Kennicutt et al., 2014).

The study of past climatic states that differ to the modern day climate provides an important tool for understanding the functioning of the climate system under differing boundary conditions. It also enables us to understand the climatic processes that were important drivers of past climatic change, but are not of importance in the modern day climate. The Last Glacial Maximum (LGM) and the transition into the modem day interglacial period, known as the Holocene, represent an important time slice that has been the subject of targeted research (Mix et al., 2001; Kucera et al., 2005; Gersonde et al., 2005; Fraser et al., 2009; Vandergoes et al., 2013).

The LGM is broadly defined as that most recent time interval during which global ice sheets reached their maximum integrated volume (Mix et al., 2001), and is thought to be an analogue for the Quaternary ice ages (Kucera et al., 2005). Hypotheses for the deglaciations associated with the transition between glacial (cold) and interglacial (warm) climates during the Quaternary rely on mechanisms associated with the circulation of the Southern Ocean, Southern Ocean sea-ice expansion and Antarctic ice-sheet formation (Ronge et al., 2015; Paillard, 2015). However, these mechanisms are still poorly documented (Paillard, 2015). Termination of the LGM and the transition into the Holocene represents a large natural global climate change. Study of the LGM

and its termination is valuable for a number of reasons. We can improve our understanding of how the global climate system responds to radiative perturbations (Jansen et al., 2007), assess the sensitivity of the global climate system (Kucera et al., 2005), and test important hypotheses for the functioning of the global climate system (Kucera et al., 2005; Jansen et al., 2007; Vandergoes et al., 2013).

Whilst Southern Ocean sea-ice played a significant role in both responding to, and influencing, changes in the climate system (Comiso, 2010), it is also important to consider the important role played by the fronts of the Southern Ocean in past climate changes (Graham et al., 2012). Oceanic fronts represent regions that separate two distinct water masses, hence ocean fronts can be identified by sea-surface temperature or with hydrographic measurements of sub-surface properties (Graham et al., 2012). The latitudinal position of Southern Ocean fronts can restrict surface water connectivity between ocean basins and reduce oceanic latitudinal heat re-distribution (Bard and Rickaby, 2009; McKay et al., 2012; Graham et al., 2012; Romero et al., 2015). The position of Southern Ocean fronts during glacial stages may result in a greater cooling of the climate system, driving the onset of cold glaciations during periods of stable atmospheric partial pressure of CO_2 (pCO_2) concentration (Bard and Rickaby, 2009). Under modern climatic conditions it is known that the fronts of the Southern Ocean, in particular those fronts within the Antarctic Circumpolar Current (ACC), are constricted by the bathymetry of the Southern Ocean (Neil et al., 2004; Kohfeld et al., 2013). As the ACC is driven by the westerly wind field, it is thought that an estimate for the paleo position of the Southern Ocean fronts could reflect the position of the westerly wind field. However, current paleo estimates for the latitudinal migration of the Southern Ocean fronts during past climates, such as the LGM, has failed to shed any light on the relative importance of the westerly winds or Southern Ocean bathymetry in defining the

position of the oceanic fronts (Kohfeld et al., 2013). Therefore, the nature and role of the Southern Ocean fronts in past climates, such as the LGM, still remains poorly understood (Kohfeld et al., 2013).

This introductory chapter will commence with a general description of the Quaternary climate, with a particular focus on what is currently know about the Quaternary, and why it is important to understand paleo climate during the Quaternary period in context of modern climate change. As global climate models are used to compliment paleo-proxy data, a brief examination for why (and how) paleo sea-ice data is required for the development and testing of global climate models follows. The second section of this chapter will then focus on Southern Ocean sea-ice cover. A description of Southern Ocean sea ice formation and coverage is provided, along with an outline of sea-ice monitoring via satellite remote sensing. Sections 3, 4 and 5 of this chapter will focus on the proxies that have been used to estimate paleo sea-ice cover throughout the Southern Ocean. Specifically, section 3 focuses on ice core sea-ice proxies, section 4 details the highly branched isoprenoid marine sediment core proxy, whilst section 5 focuses on the use of diatoms as a proxy for paleo winter sea-ice. Section 6 summarises the current body of knowledge regarding Southern Ocean paleoceanography over the Last Glacial Maximum and the transition into the Holocene period. Finally, sections 7 and 8 summarise the aims and structure of this thesis, respectively.

1.1.1 The Quaternary (last ~2 million years)

The Quaternary period of Earth's history commenced 2.4 million years (Ma) before the present day, during a period of pronounced climate change occurring between 2.8 and 2.4 Ma (Head et

al., 2008). The Quaternary period is characterised by frequent and rapid changes in Earth's climate (Paillard, 2015), with cold glacial periods distinguished by global cooling and the growth of land-based ice sheets (Williams et al., 1998; Head et al., 2008). The interglacial periods, such as the present day climate, were warmer stages that had restricted/less land ice coverage compared with the glacial stages (Williams et al., 1998). Present day anthropogenic climate change will strongly interfere with future ice-ages, and has placed Earth's climate close to a super-deglaciation (Paillard, 2015). In the context of anthropogenic climate change, knowledge of, and related to, past climate change may provide a valuable resource to aid our understanding of future climate change (Williams et al., 1998). Specifically, we need to understand the hydrological (and biological) events of the past and how they responded to past climatic fluctuation (Williams et al., 1998).

Milankovitch theory links the changes in the Earth's orbit, and the subsequent changes in the amount of solar radiation that reaches the Earth's surface (insolation), with the cyclical development and termination of Quaternary glacial/interglacial periods. Milankovitch theory suggests northern hemisphere ice sheets grew under orbitally-induced changes to insolation, raising Earth's albedo, and thus driving the onset of Quaternary glacial stages (ice ages) (Paillard, 2015). However, Earth's climate system does not respond in a linear manner to astronomically paced insolation variation. Nor is there a simple relationship between the amplitudes of insolation maxima and minima with any corresponding ice-volume maxima or minima. Furthermore, the largest climatic variations occurred every ~100,000 years (Wolff et al., 2006), despite the insignificant amplitude of the insolation changes that occur every 100,000 years (Parrenin and Paillard, 2004; Cheng et al., 2009). The predictions of Milankovitch theory do not match observations of the Quaternary climate, and nor does the theory account for the variation in

atmospheric carbon dioxide (CO_2). Hence, Milankovitch theory does not provide a sufficient explanation for Quaternary ice-age dynamics (Paillard, 2015). Rather, geochemical theories provide a better account for the relative timing between atmospheric CO_2 changes and Quaternary ice ages (Hillenbrand and Cortese, 2006; Wolff et al., 2009). Antarctic sea-ice growth, brine rejection and the formation of very dense and salty bottom waters stores carbon in the deep ocean, providing the link between ice-sheet growth (glacials) and atmospheric CO_2 (Hillenbrand and Cortese, 2006; Fischer et al., 2010; Paillard, 2015).

For the last 800,000 years, the natural variation in atmospheric CO_2 was bounded between 170 and 300 parts per million by volume (ppmv) (Fischer et al., 2010; Figure 1). The variation in CO_2 correlates with climate changes within the Southern Ocean, hinting that the Southern Ocean had a significant influence on atmospheric CO_2 concentrations. The correlation between atmospheric CO_2 and Antarctic temperatures on orbital and millennial scales can be explained by changes in the Southern Ocean surface buoyancy flux (Fischer et al., 2010). Surface buoyancy fluxes are fluxes of potential energy that reflect the changes in ocean water density due to heat and/or freshwater fluxes (Oberhuber, 1988). The topography of the ocean isobaric surfaces are altered by differential surface buoyancy fluxes, which induce horizontal pressure gradients and ocean surface circulation (Prasad, 1997). Southern Ocean surface buoyancy flux is primarily controlled by the growth and retreat of sea ice (Fischer et al., 2010). Sea-ice formation and the resultant brine rejection during cold glacials formed salty and dense bottom water along the Antarctic continental margin (Paillard, 2015). As the deep ocean contains ~90% of the combined oceanic, atmospheric and terrestrial carbon, any rearrangement to the formation of deep water masses could have a significant impact on the atmospheric carbon budget (Ferrari et al., 2014; Ronge et al., 2015). These dense waters reach the bottom of the ocean by overspilling the continental shelf

and then flowing as gravity currents, storing carbon within the deep ocean. As the Antarctic ice sheet grows, a significant portion of the Antarctic continental shelf is covered, breaking down the sea-ice brine rejection mechanism (Paillard, 2015). However, the breakdown of brine rejection by sea-ice whilst the Antarctic continental shelf is covered by ice sheets is debatable (DeConto et al., 2007).

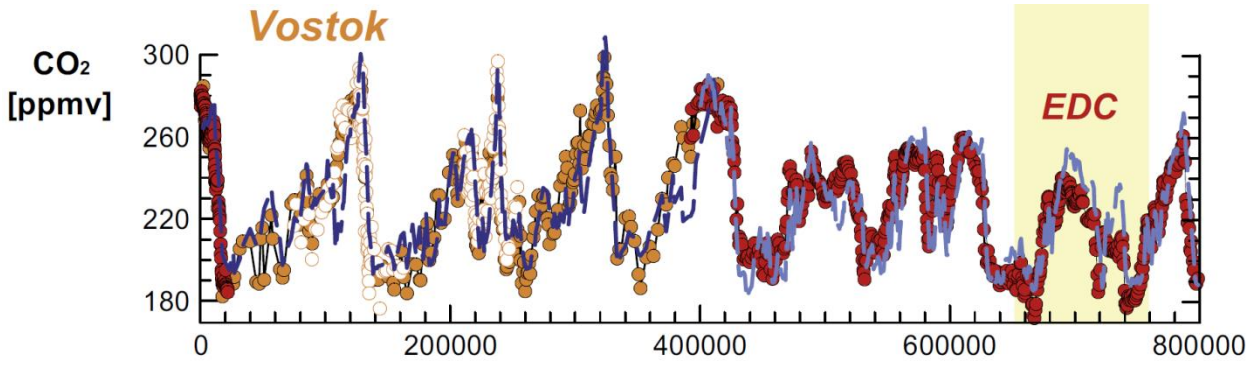

Figure 1. A record of atmospheric CO_2 over the last 800,000 years. The atmospheric CO_2 record for the last 800,000 years was derived from CO_2 concentrations measured from the EPICA Dome C (EDC) ice core (represented by red dots) and the VOSTOK ice core (represented by yellow dots) are shown. *(This figure appears in Fischer et al. (2010) as Figure 1, on page 195.)*

1.1.2 Paleo estimates of Southern Ocean sea ice during the late Quaternary (last 800ka)

The concentration of sea-salt aerosol flux (ssNa) within the Dome C ice core (Figure 2) provides a proxy for sea-ice extent throughout the Ross Sea and Indian sector of the Southern Ocean (Wolff et al., 2003; Wolff et al., 2006; Wolff et al., 2010; Röthlisberger et al., 2010). The ssNa flux record for the last 800,000 years before the present day (800 kyr BP, Figure 3) suggests that lower sea-ice extent during the warmer interglacial periods acted as an amplifier of climate warming (Wolff et al., 2010). Throughout the Indian Sector of the Southern Ocean, winter sea-ice

extent was tied with Antarctic temperature for the last 740 kyr BP. Increased ice core ssNa flux occurs during glacials, and is believed to be an indication of expanded winter sea-ice extent. Conversely, the measured flux of ice core ssNa was at a minimum during interglacials. The interglacial winter sea-ice extents have been hypothesised to be less than the modern-day winter sea-ice extent, with winter sea-ice extent considered to be placed at an intermediate position between the sea-ice extent of the recent glacial and the weaker interglacial periods of the last 440 kyr BP (Wolff et al., 2006). The ssNa flux proxy for sea-ice extent over the last 240 kyr BP was correlated with precessional variability every 23,000 years. The correlation was most prominent during cold glacial phases, illustrating the effect of insolation on sea ice around Antarctica, whereby an increase in spring insolation reduced sea-ice extent, which in turn reduced albedo and lead to further warming (Röthlisberger et al., 2010).

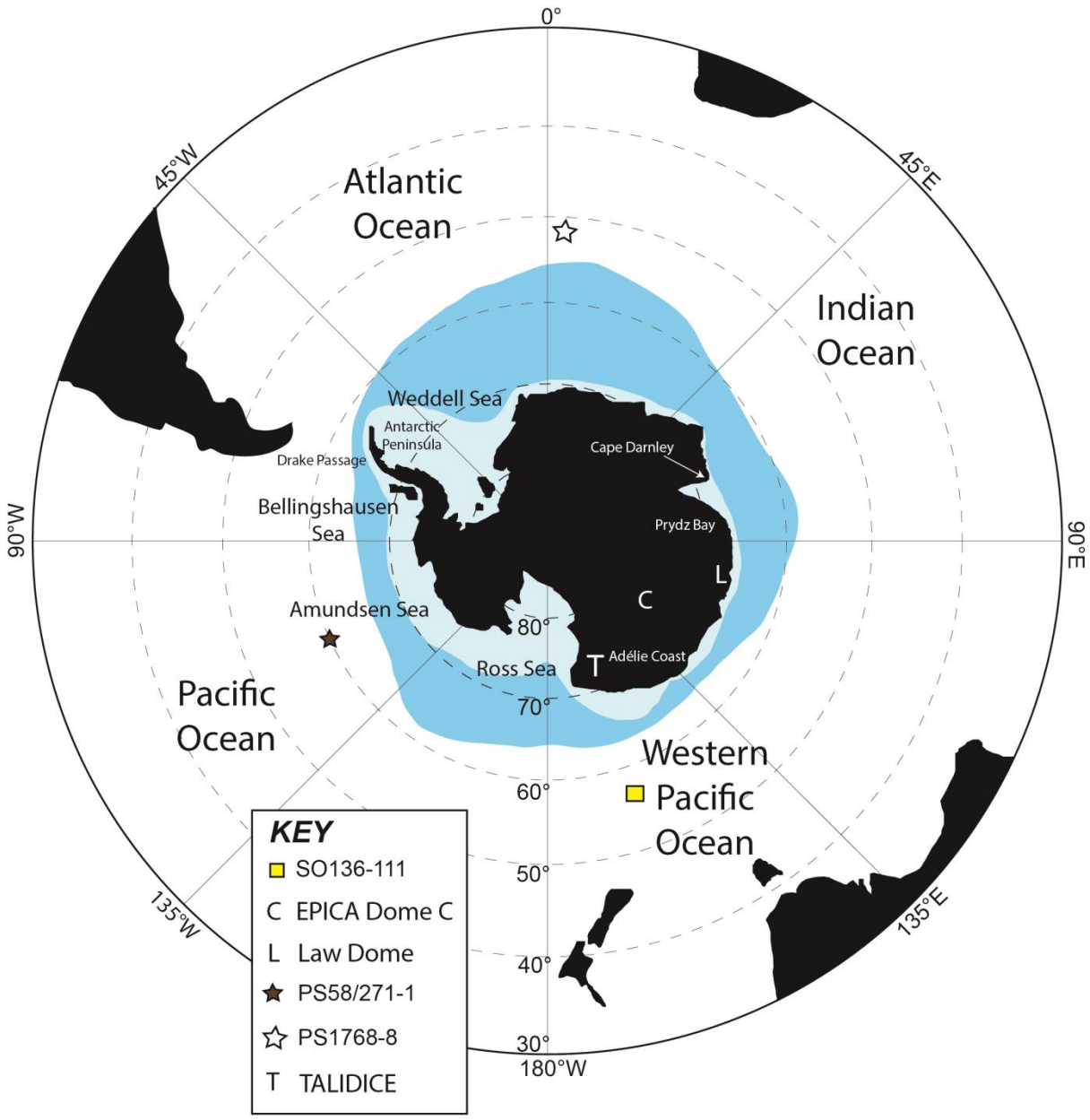

Figure 2. A map of Antarctica and the Southern Ocean with all of the key regions labelled. The locations of Antarctic ice cores and Southern Ocean marine sediment cores used to estimate the paleo sea-ice history of the Southern Ocean over the last 800,000 years are shown. The mid-blue shading corresponds to the average winter sea-ice area from 1979 to 2000, whilst the light blue shading highlights the average summer sea-ice area from 1979 to 2000 *(sea-ice data was sourced from the National Snow and Ice Data Centre (NSIDC)/Comiso, (2000))*.

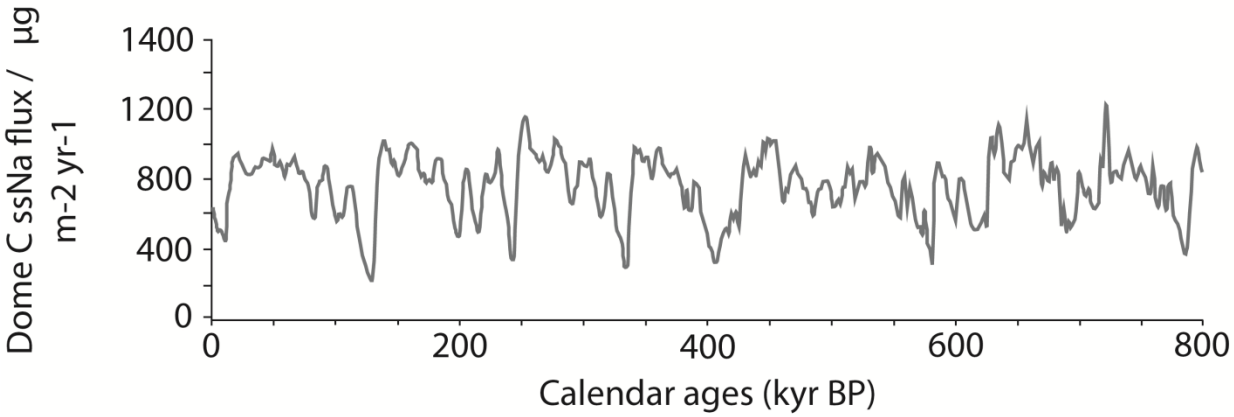

Figure 3. The record of sea-salt aerosol (ssNa) flux from EPICA Dome C over the last 800 kyr BP. The flux of sea-salt aerosol increases during glacial stages and then decreases during interglacial stages, with ssNA flux during glacial stages approximately twice that of the interglacial ssNa flux. *(This figure has been adapted from Wolff et al. (2010), figure 1, page 287).*

A record of bromine and iodine speciation measurements over the last 215 kyr BP from the TALDICE ice core (Figure 2) showed an increase in sea-ice extent during the glacial periods (Wolff et al. 2010). The glacial summer sea-ice edge extended 500 kilometres north of the Antarctic, with a maximum extension during the periods 205 to 134 and 80 to 16 kyr BP. The LGM winter sea-ice extent was approximately double that of the penultimate glacial period (Gersonde et al., 2005). Marine diatom paleo sea-ice records from marine sediment core SO136-111 (within the southwest Pacific, Figure 2) over the last 220 kyr BP documented increased sea-ice cover, represented by monthly average sea-ice coverage per year, during glacials, in which maximum sea-ice extent was observed at the end of each glacial stage (Crosta et al., 2004). Similarly, sea-ice records resolved from a diatom species index spanning the last 150 kyr BP within the Atlantic (core PS1768-8) and Pacific (core PS58/271-1) sectors of the Southern Ocean

(Figure 2) document increased winter sea-ice coverage during glacials (Esper and Gersonde, 2014).

The EPICA Dome C ssNa flux indicates an increase in winter sea-ice production throughout the Indian and Atlantic sectors of the Southern Ocean during the LGM. Indeed, the ssNA flux during the LGM was double that of the Holocene (Wolff et al., 2003). During the Holocene, a 30% increase in ssNa flux over the last 5 kyr BP implies that winter sea-ice extent had also increased (Wolff et al., 2003). For the last 7 kyr BP, Etourneau et al. (2013) estimated an increase in sea-ice cover based on a HBI proxy, which they attributed to a reduction in mean annual and spring insolation. Similarly, throughout Adélie Land (140°E) and Prydz Bay (77°E) (Figure 2), winter sea ice has increased since 7 kyr BP within both regions, with a pronounced winter sea-ice expansion between 4.5 and 3.5 kyr BP (Denis et al., 2010). Finally, the most recent sea-ice proxy record was derived from concentrations of methane sulphonic acid (MSA) concentrations within the Law Dome ice core (Figure 2). The MSA sea-ice proxy indicated that sea-ice extent, between 80°E and 140°E (the Indian sector of the Southern Ocean), was consistent for the time period between 1841 and 1950, but subsequently declined by 20% after 1950 (Curran et al., 2003).

1.1.3 Importance of paleo sea-ice estimates for the evaluation and development of Global climate models

Paleoclimatic data plays an important role in the evaluation of global climate models (GCMs). The data from a GCM is quantitatively compared with paleo proxy data (Goosse et al., 2006; Goosse et al., 2013; Flato et al., 2014) to evaluate the capacity of a climate model to successfully simulate past climate, and to assess the physics of a model (Lohmann et al., 2012; Goosse et al.,

2013). Such modelled paleo-proxy data comparisons are most successful when there is an abundance of paleo-proxy data for model assimilation (Gersonde et al., 2014). One of the first steps in the evaluation of a model involves a comparison between model data and satellite observations of sea-ice. However, satellite-based sea-ice records commenced in the 1970's (e.g. Parkinson et al., 1999; Parkinson and Cavalieri, 2012), such a short time-series of sea-ice data does not accommodate the estimation of the internal variation of sea-ice over a wide range of timescales, or an assessment for the influence of various forcing mechanisms that are important for sea-ice formation, distribution and melt. Therefore, models need to be compared with proxy records over greater time periods, such as, for example, the LGM (Goosse et al., 2013).

The comparison of model paleo data with paleoclimatic data facilitates the study of climatic mechanisms that were important for sea-ice development during past climates, but which are currently not playing an important role in sea-ice formation under modern climatic conditions. Paleo-oceanographers can also study centennial scale changes under a wider range of climatic conditions, the change in oceanic (and atmospheric) circulation in response to a modified surface-temperature gradient, and the impact of fresh water discharge at higher latitudes (Goose et al., 2013). Finally, paleo-climate data is used for model data assimilation, whereby an optimal combination of model results and proxy records is used to provide additional information for those processes responsible for past climate change and on the paste state(s) of the climate system (Goosse et al., 2013).

Therefore, the application of modelled to paleo-climate data comparisons helps to reduce the uncertainty surrounding model simulations, and estimates, of past climate. In turn, the modelled-paleo proxy data comparison helps to provide a test for the reliability of modelled projections for future climate change (Lohmann et al., 2012). A model that is in agreement with both the modern

day observational record and proxy-records of past climate suggests the physics, and the utility, of a given model is robust (Goosse et al., 2013).

1.2 Southern Ocean sea ice

1.2.1 The nature and formation of Southern Ocean sea ice

Sea ice possesses an uneven coverage over the surface area of the world's oceans due to cause and effect interactions with the surrounding physical environment. As such, sea ice is an irregular medium. Sea ice formation initially occurs at temperatures of ~ -1.8°C with the development of fine, suspended ice crystals during frazil freezing (Hanna, 1996). Upon freezing, the water molecules are arranged tetrahedrally around each other with a packaging density that is lower than liquid seawater. Hence, the material density of ice is lower than that of liquid water. The major ions present within sea-water cannot be incorporated into the ice-crystal lattice. Therefore, the ions are rejected at the ice-water interface as the ice crystals grow. The growth of frazil ice is responsible for the northward expansion of Antarctic sea ice throughout the Southern Ocean. The accretion of frazil ice crystals creates centimetre-sized ice floes. These ice floes then accrete into deci-centimetre-sized pans of ice. Wind and swell grinds the pans together to produce a semi-consolidated sea-ice cover comprised of a series of 2 to 10 centimetre thick discs with raised edges, known as pancakes. As these pancakes congeal, they form meta-pancakes. Ice-core evidence suggests Antarctic sea ice is comprised of individual pancakes that are tilted and stacked together. The interstices between each pancake are then consolidated with frazil ice growth and the freezing of congelation ice. Snow cover can sink sea ice below the ocean surface, where lateral and/or vertical percolation of sea-water and brine through the ice cover results in ice

growth between the snow and sea ice. The occurrence of surface flooding is important for some regions of the Southern Ocean, with up to 50% of the Southern Ocean sea ice being flooded (Eicken, 2010).

1.2.2 The development of Southern Ocean sea-ice remote sensing via satellite measurements

There are some basic premises on which passive microwave remote sensing is based. Given the typical temperatures of the Earth's surface and the microwave wave-length range, remote sensing uses the Rayleigh-Jean approximation to Plank's law of thermal radiative emission. Radiative power (which is expressed as a brightness temperature, (Tb) is proportional to physical temperature (Ts). Real world objects only emit a fraction of the energy that would be emitted from a perfect emitter, at the same temperature. This fraction is referred to as emissivity (e). Tb is then given by e×Ts. For a particular frequency and polarization, the variations in emissivity are predominantly due to surface variation (Gloersen et al., 1992).

Observations of the Earth's surface based on remote sensing techniques use electromagnetic radiation (EM) in the visible/near infrared (VNIR), thermal infrared (TIR) or microwave bands of the electromagnetic spectrum. Visual and near infrared EM bands are used to measure albedo, whilst the thermal infrared and passive microwave bands measure the thermal radiation emitted from the surface of the Earth. The VIS and IR channels use EM intervals of 0.4-2.5 μm, 3.5-4 μm and 10-13 μm, which have the highest atmospheric transmission. However, these channels do not penetrate cloud, as such microwaves with wavelengths of greater than 0.3 cm are necessary for the remote sensing of sea ice under cloud cover (Sandven and Johannessen, 2006).

Sea-ice remote sensing by satellites with microwaves uses two instruments. A radiometer, which is a receiver measuring the intensity of noise-like radiation emitted by a target, and a radar, which has both a transmitter and a receiver. The radar senses the reflection and backscatter of its own radiation, from which measurement of sea-ice (and Antarctic continental ice) properties can be obtained (Carsey, 1992). The use of passive microwave sensors on satellites for the purposes of monitoring sea-ice concentrations has been in place since 1972. The first set of passive microwave satellite sea-ice data was provided by the electrically scanning microwave radiometer (EMSR) sensor. Use of the special sensor microwave/imager (SSM/I) commenced in 1987. The availability and use of 85 GHz channels of the SSM/I in 1992 improved the spatial resolution of remotely sensed sea ice. Then, in 2002, the advanced microwave scanning radiometer for EOS (AMSR-E) was launched. Data from AMSR-E provided an improved spatial resolution, with a footprint area of 6 × 4 km (reduced from the 15 × 13 km, as provided by SSM/I) (Spreen et al., 2008). One weakness of satellite passive microwave instruments is that they are not able to detect the diffuse, saturated ice edge conditions typical of the summer season (Mayewski et al., 2009).

1.2.3 The role of sea-ice in the global climate system

Sea ice exerts a significant influence on the radiation energy balance of the Earth's surface. Sea ice is a strong mediator of ocean-to-atmosphere heat flux within the polar maritime environment due to its efficient insulating effect (DeConto et al., 2007; Kay et al., 2014; Simmonds, 2015). On inter-annual (and longer) time scales, the sea-ice albedo positive feedback mechanism will increase cooling (or warming) as a response to initial climatic cooling (warming). A cooler climate subsequently increases sea ice and albedo, reduces the absorption of solar radiation, in

turn leading to further cooling and sea-ice growth (DeConto et al., 2007). Solar radiation is the major source of heat input to sea ice during the polar winter. In winter, radiation balances are negative, leading to a strong cooling of the polar climates. The absorption and emission of radiant energy by sea ice, and the role of sea ice for the poleward flux of heat, means that sea ice has an important role to play in key large scale processes of Earth's climate system (Carsey, 1992; Dieckmann and Hellmer, 2010).

Sea ice may also be a mediator of glacial- interglacial oscillations under seasonally and orbitally varying solar forcing (Paillard, 2015). Models have suggested that the timing (phasing) and duration of 100 kyr land-ice volume oscillations is controlled by sea ice (Gildor and Tziperman, 2000). Atmospheric fluxes of moisture (i.e. precipitation) are moderated by the high albedo and insulating effect of sea ice. The sea ice's influence on atmospheric moisture fluxes and regional hydrological cycles may control the growth of land-based ice sheets. Therefore, sea ice induced changes in isolation acted as a driver for the timing and duration of land and ice-sheet growth periods (i.e. glacial events) (Gildor and Tziperman, 2000).

As well as being important in the mediation of surface heat fluxes, sea ice is also an important moderator of surface brine fluxes. Fully developed sea-ice cover is an effective insulator between the cold atmosphere and warmer ocean. Areas with open water and sporadic thin sea ice rapidly lose heat during the cool seasons, resulting in sea-ice growth and the injection of brine during sea-ice growth into the upper ocean. These fluxes of heat and brine form the most important source of dense water for the world's oceans (Carsey, 1992; Ohshima et al., 2013). For example, the growth of sea ice results in brine rejection and an increase in the salinity of waters off the Antarctic continental margin, forming Dense Shelf Water (DSW). The DSW, with sufficient negative buoyancy and an export pathway across the continental shelf, will mix with ambient

water masses down the continental shelf to produce Antarctic Bottom Water (AABW) (Saenko and Weaver, 2001; Ohshima et al., 2013; Ferrari et al., 2014; Paillard, 2015). The cold and dense AABW within the abyssal layer accounts for 30 to 40% of the global ocean mass (Ohshima et al., 2013). Total production of AABW is estimated at ~8 Sv (where 1 Sv = 10^6 m^3 s^{-1}), with 50% formed in the Weddell Sea, 25% in the Ross Sea and the remainder developing on the Adélie Land coast, Prydz Bay and Cape Darnley (Figure 4) (Meredith, 2013; Ohshima et al., 2013). AABW ventilates the deep ocean, drives the oceanic uptake of CO_2 and redistributes fresh water and heat across the globe (Saenko and Weaver, 2001). Variations in the formation and export rates of AABW are therefore of global significance (Hanna, 1996; Ferrari et al., 2014).

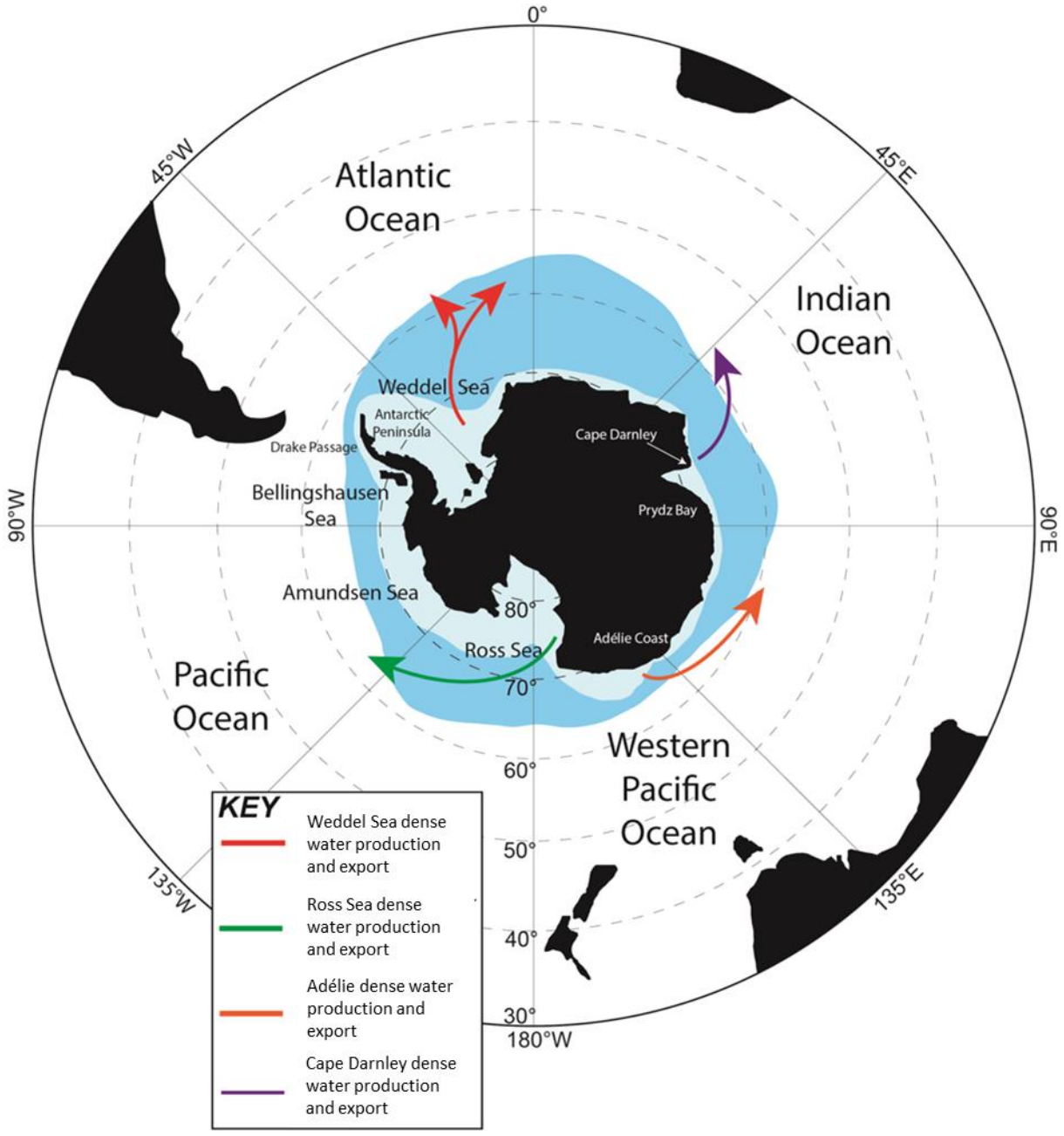

Figure 4. A map of the Antarctic and surrounding Southern Ocean illustrating the major formation sources of dense waters along the fringes of Antarctica before spreading out northwards into the abyssal layer of the world's oceans. This figure has been adopted from Meredith (2013). Modern average summer (light blue) and winter (mid-blue) sea-ice extents from 1979 to 2000 are shown surrounding Antarctica *(sea-ice data was sourced from the National Snow and Ice Data Centre (NSIDC)/Comiso, (2000))*.

Antarctic sea-ice growth is also important for the formation of Antarctic Intermediate Water (AAIW), via wind driven northern sea-ice transport and subsequent melt. Large scale wind patterns drive a northern transport and divergence of sea-ice. The divergence of sea-ice exposes open water to the cold atmosphere, triggering the growth of new ice, brine release into the ocean and a subsequent increase in salinity (Saenko and Weaver, 2001). The AAIW is an important contributor to the Atlantic Meridional Overturing Circulation (AMOC). Within the north Atlantic, the production of cool dense North Atlantic Deep Water (NADW), which flows south into the Southern Ocean (Huang et al., 2014), is partially off-set by northern return flow of AAIW in shallower waters, and the cold salty AABW at depth (Huang et al., 2014; Xie et al., 2014). The return surface currents of the AMOC include the Benguela Current off South Africa (via the Gulf Stream) and the North Atlantic Current, which flows into the Nordic Seas off Scandinavia (Figures 5 and 6) (Rahmstorf, 2006). Thus, sea ice and its northern transport via wind stress, facilitates a connection between large-scale high latitude atmospheric circulation within the southern hemisphere and the ventilation of the world ocean (Saenko and Weaver, 2001).

The AMOC is responsible for large scale redistributions of heat, salt, and carbon, and therefore plays an important role in global climate (Huang et al., 2014). The synchronisation between millennial scale climate events, of opposite phases, between Greenland and Antarctica has produced a bipolar record of climatic changes. When the Antarctic experiences widespread warming Greenland is characterised by a cooler climate. The opposite phases of millennial climate change between Antarctica and Greenland is referred to as the bipolar see-saw hypothesis. A leading hypothesis for the bipolar see-saw suggests a reduction in the strength of

the AMOC will decrease northern heat transport, cooling the north Atlantic, whilst the south Atlantic warms (Crowley, 1992; Barker et al., 2009; De Deckker et al., 2012).

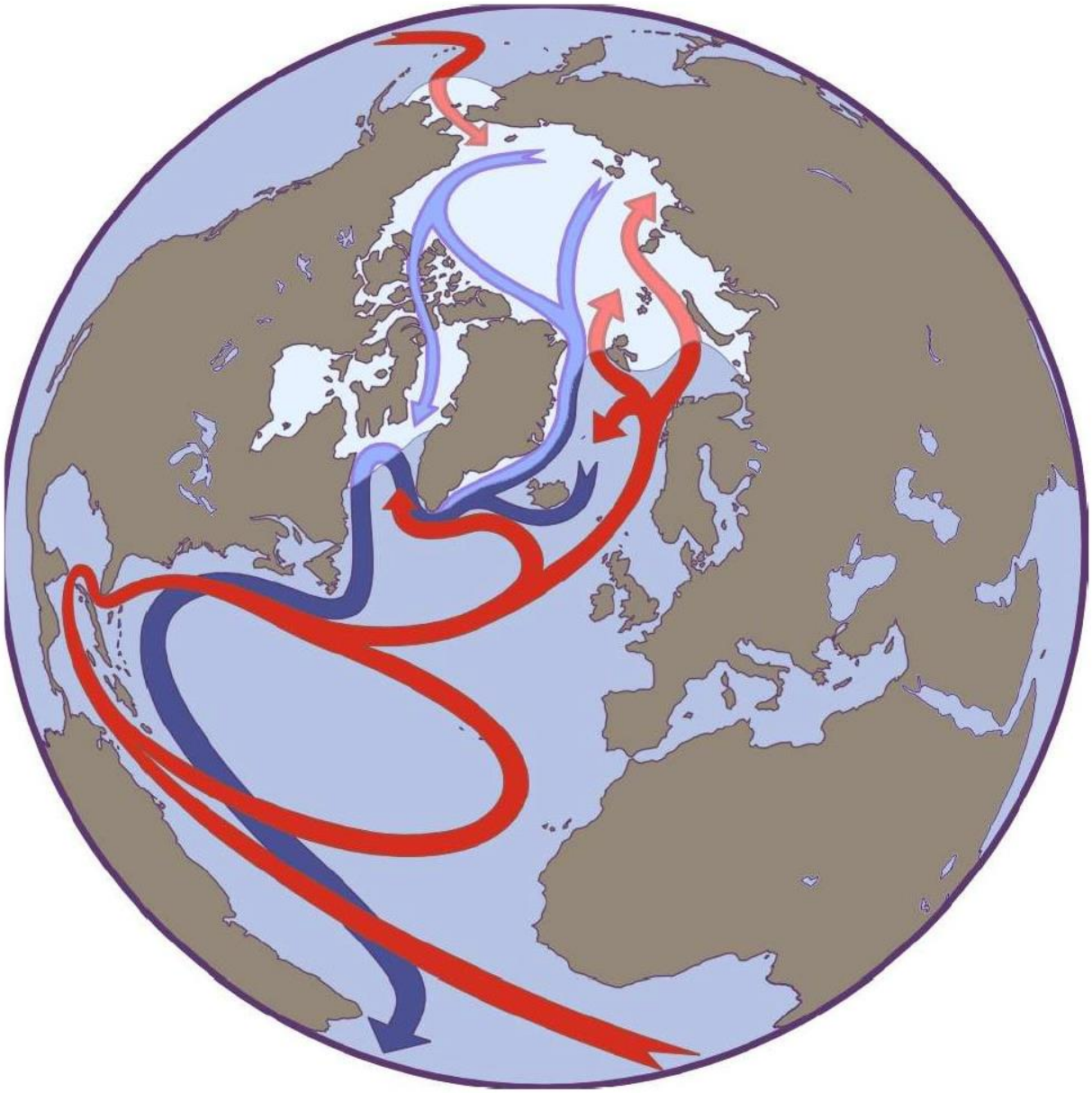

Figure 5. A schematic highlighting the circulation through the Arctic Oceans and the northern Atlantic. The surface currents are shown in red, whilst the deep, cool NADW flow is shown in blue. *(This schematic was adopted from Rahmstorf (2006), Figure 3 on page 3).*

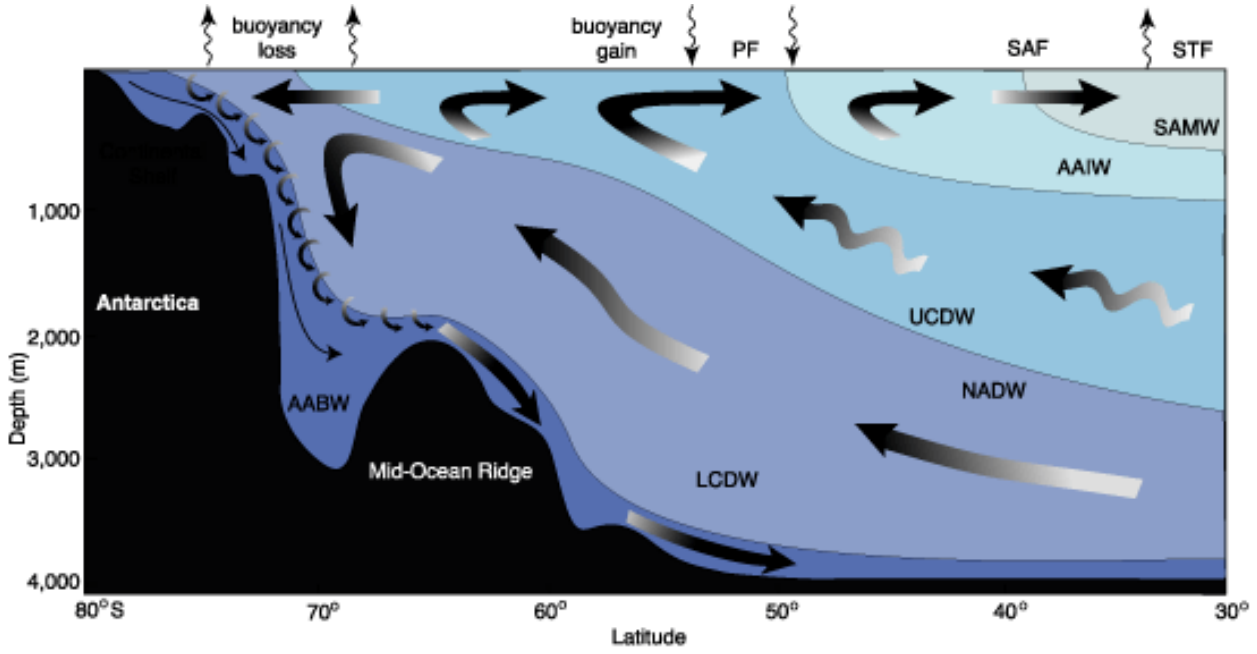

Figure 6. A generalized cross section of the overturning circulation within the Southern Ocean. The general flow paths of the cool, dense, deep waters (NADW and AABW) are shown. The south flowing deep waters from the North Atlantic are converted into intermediate and upper mode waters, whilst the deep bottom waters formed within the Southern Ocean flow northwards. For reference, the positions of the Southern Ocean fronts (PF- Polar Front, SAF- sub-Antarctic Front, and the STF- the Subtropical front) are also shown. (Image has been modified from Speer et al. (2000), Figure 8 on page 3221, and sourced from the Scientific Committee on Antarctic Research, http://acce.scar.org/wiki/The_role_of_the_Antarctic_in_the_global_climate_system, cited 13/11/2015).

1.3 The physical basis and development of Southern Ocean sea-ice proxies derived from ice-core records.

A significant effort has been made over the last decade to develop a series of sea-ice proxies based on the measured fluxes of atmospheric aerosols within Antarctic ice cores (Wolff et al., 2010; Abram et al., 2010; Spolaor et al., 2013; Abram et al., 2013). Each of these new ice-core proxies will be discussed, with a focus on their physical basis and limitations.

1.3.1 Sea-salt aerosol flux

It has been hypothesised that sea-salt flux is positively related to features of the sea-ice surface (Röthlisberger et al., 2008; Russell and McGregor, 2010; Wolff et al., 2010), with marine sea-salt flux increasing as the sea-ice area increases (Röthlisberger et al., 2010). However, interpreting the sea-salt flux recorded within Antarctic ice cores remains unclear. Currently, it is unknown if the sea-salt aerosol flux originates from frost flowers or the flooding and wicking of brine on the sea-ice surface (Wolff et al., 2010). It is also difficult to distinguish between sea-spray and sea-ice surface derived sea-salt fluxes (Spolaor et al., 2013). Furthermore, as atmospheric sea-salt aerosol concentrations decline during aeolian transport, only a small percentage of the sea-salt flux will remain after transportation over hundreds of kilometres inland. Therefore, the sea-salt flux proxy does not appear to be registered during colder climates when sea-ice areas are extensive (Fischer et al., 2007; Röthlisberger et al., 2008; Röthlisberger et al., 2010). Fischer et al. (2007) casted doubt on the utility of sea-salt flux as a sea-ice proxy after their sea-salt flux record failed to reflect any expression of the Antarctic Isotope Maxima events during marine isotopic stage three.

1.3.2 Methanesulphonic acid

The methanesulphonic acid (MSA) signature within Antarctic ice cores is derived from the oxidisation of dimethylsulphide (DMS), which is produced almost exclusively by marine algae (Hezel et al., 2011; Abram et al., 2013**)**. Dimethylsulphoniopropionate (DMSP), which is produced by certain phytoplankton species, is then converted to DMS, which is then exchanged to the atmosphere where oxidisation of DMS produces MSA (Abram et al., 2013) (Figure 7).

Therefore, as sea-ice coverage influences biological activity, sea ice may also influence MSA production. Increases in MSA deposition occur during summer in association with decreased sea-ice cover and increased biological activity. During winter, the MSA flux decreases as sea-ice expands and biological activity is reduced. To date, MSA has only provided a useful proxy for Antarctic sea ice between 80°E and 140°E (Curran et al., 2003).

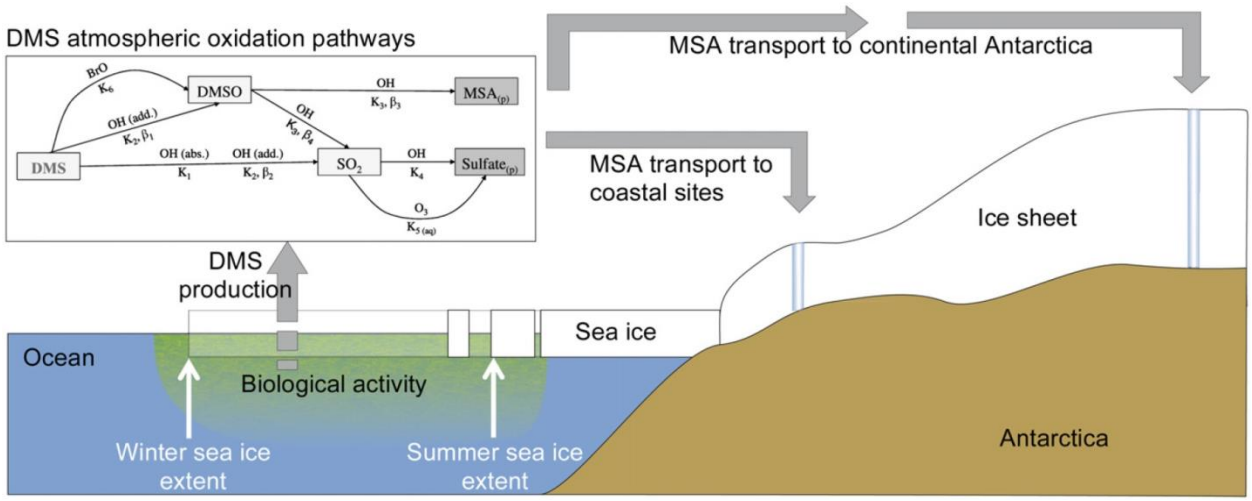

Figure 7. A schematic illustrating the production of DMS by sea-ice algae, the oxidisation of DMS within the atmosphere, and the subsequent deposition of MSA over Antarctic ice sheets. *(The schematic originally appeared in Abram et al. (2013) as Figure 7 on page 175).*

Ultimately, MSA is difficult to interpret as a proxy for Antarctic sea ice. Wind speed and direction are the primary factors controlling the concentration of MSA deposition over certain regions of the Antarctic (e.g. Hezel et al., 2011). Under modern conditions, areas with low snowfall accumulation rates experience a loss in methanesulphide concentration due to the slow evaporative loss of MSA (Spolaor et al., 2013). Similarly, MSA may be present as a non-volatile neutral salt rather than a volatile acid (Wolff et al., 2006). In light of the later complications

surrounding the MSA sea-ice proxy, recent ice core studies have chosen to focus on alternative ice core proxies (Wolff et al., 2010; Spolaor et al., 2013).

1.3.3 Halogens

Marine phytoplankton and sea-ice algae produce volatile halogenated organic compounds (VHOC) during photosynthesis via enzymatic removal of hydrogen peroxide by haloperoxides (Granfors et al., 2013). Recent work within the Amundsen and Ross Seas suggest halocarbon production/concentration is principally influenced by sea ice (Mattson et al., 2012; Granfors et al., 2013). Recorded fluxes of the halogens bromine and iodine are of particular interest as a proxy for Antarctic sea ice with enriched bromide concentrations used as an indicator for the presence of multi-year ice, whilst decreases in iodine indicate an extension of the sea-ice extent (Spolaor et al., 2013; Spolaor et al., 2014). Sea-ice algae produce organo-iodine, which in conjunction with bromine production at the sea-ice margin, results in the sea-ice margin becoming an area of active bromine and iodine chemistry (Figure 8). Recent *in-situ* measurements confirmed the Weddell Sea sea-ice environment as an iodine emission hotspot (Atkinson et al., 2012). Satellite measurements have shown a decrease in bromine oxide and iodine oxide concentration with increasing distance from the sea-ice margin (Spolaor et al., 2013). Recently Spolaor et al. (2014) illustrated how halogen production captured by satellite observations (Figure 8) was related to the preservation of a seasonal cycle of both halogens within century-old Antarctic ice cores. Therefore, sea-ice dynamics appear to act as the primary driver for bromine and iodine fluxes over glacial to interglacial cycles (Spolaor et al., 2013; 2014).

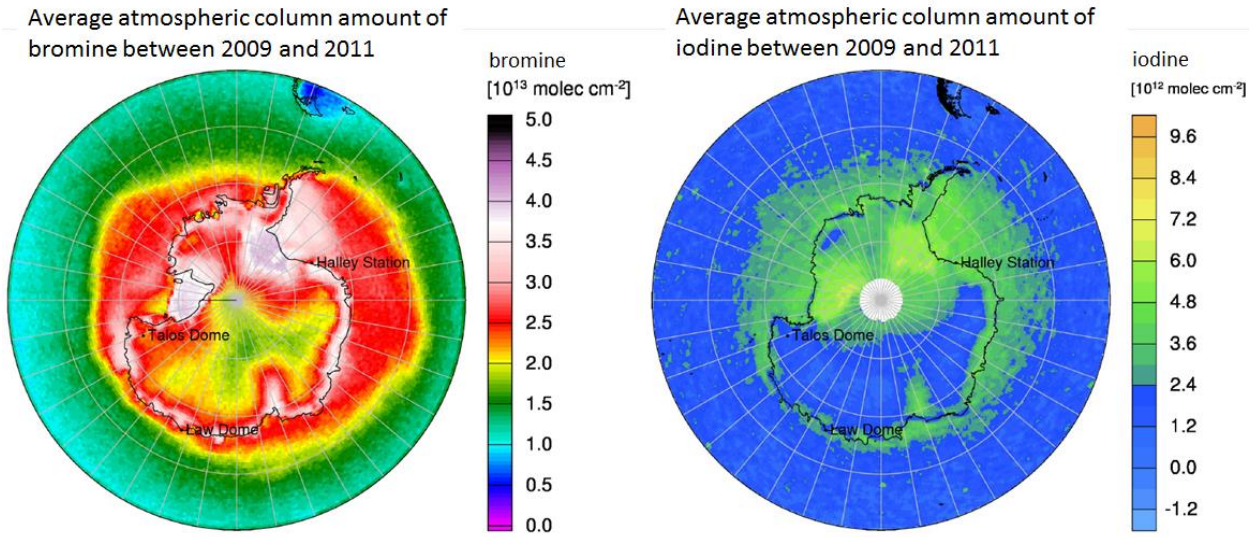

Figure 8. The average amount of bromine and iodine in atmospheric columns over Antarctica. The greatest concentrations of bromine and iodine occur along the Antarctic coast line and above the Antarctic ice shelves, whilst Southern Ocean sea-ice is clearly indicated as an area of active bromine and iodine chemistry. The three regions indicated on each map are Halley station, Talos Dome and Law Dome. *(This figure original appears within Spolaor et al. (2014), as Figure 1 on page 8203).*

1.4 The physical basis and development of Southern Ocean sea-ice proxies derived from marine sediment core records

1.4.1 Highly branched isoprenoids

Highly branched isoprenoids (HBI) diene and HBI triene have received recent attention as a potential proxy for Antarctic sea ice (Denis et al., 2010; Massé et al., 2011; Etourneau et al., 2013; Barbara et al., 2013). The di-unsaturated isomer (diene) is believed to be synthesised by diatoms living within the sea-ice matrix during the spring months (Collins et al., 2013), whilst tri-unsaturated (triene) may be biosynthesized within the open ocean areas of the marginal ice zone, near the sea-ice edge (Denis et al., 2010; Etourneau et al., 2013; Collins et al., 2013). Therefore,

the ratio of diene to triene has been used as a proxy for the ratio of sea ice to open ocean surrounding the west Antarctic Peninsula (Etourneau et al., 2013) and the Scotia Sea (Collins et al., 2013). Together, the HBIs diene and triene may provide a proxy for the duration of the sea-ice season, rather than a strictly sea ice versus open ocean proxy. Diene II is biosynthesized by diatoms in the bottom few centimetres of spring sea-ice whilst triene III is generated in the waters of the marginal sea-ice zone with minimal production in the open ocean zone. Therefore, the coeval absence of both HBIs may provide an important Antarctic summer sea-ice proxy (Collins et al., 2013). Similarly, the isotopically enriched ^{13}C HBI diene may provide a proxy for the contribution of organic matter, derived from sea-ice diatoms, to the sediments of the Adélie Land continental shelf (Massé et al., 2011; Campagne et al., 2015). The HBI proxy does, however, have shortcomings. The specific diatoms responsible for the biosynthesis of diene are currently unknown, although the sea-ice diatoms *Fragilariopsis curta* and *Fragilariopsis cylindrus* have been discounted as the source of diene (Collins et al., 2013). HBI preservation is altered by bacterial degradation and, whilst HBIs are resistant to degradation, a rapid sulfurization of HBIs under highly anoxic conditions does occur (Etourneau et al., 2013). An effort to improve our understanding of the HBI proxy is required, with a focus on comparing HBI records with other down core proxies between differing environments (Collins et al., 2013). The use of HBIs has also opened the door for trophic cascade determination related to the sea-ice environment (Brown et al., 2014b) but this approach has yet to be applied to the Antarctic. New Antarctic HBI research by a collaborative U.K., Australian and U.S. team is currently underway in an effort to understand the diatom sources, transport and entrainment of HBI's in the sediments.

1.5 Diatoms as a proxy for Antarctic sea-ice

1.5.1 Marine diatoms and their global importance

Diatoms are a eukaryotic unicellular microalgae within the Heterokontophyta (also known as Stramenopiles) division (Falciatore and Bowler, 2002; Hervé et al., 2012), which first appeared within the fossil record ~150 Ma (Levitan et al., 2014) and arose to ecological prominence with the opening of the Drake Passage ~34 Ma (Levitan et al., 2014). The two major diatom groups are distinguished on the basis of their cell wall structure. These two groups include the Pennates, which are elongated and bilaterally symmetrical in valve view, and the Centrics, which are radially symmetrical (Scala and Bowler, 2001) (Figure 9). Diatoms assimilate silicic acid to form their siliceous skeletons, known as frustules (Hervé et al., 2012; Levitan et al., 2014). The deposition of silica within diatoms occurs within silica deposition vesicles, which are specialized intracellular compartments responsible for selective release and polymerisation of silicic acid (Yi et al., 2012). The frustule is encased in an organic matrix, rich in proteins and sugars that prevent the silica from dissolving in sea water (Armbrust, 2009).

Diatoms colonise the oceans to the depth at which photosynthetically available radiation can penetrate (Falciatore and Bowler, 2002). Diatoms are dominant in well mixed coastal regions, areas of upwelling, and at the sea-ice edge where sufficient light, inorganic nitrogen, phosphorus, silica and trace elements are available for diatom growth (Armbrust, 2009; Lazarus et al., 2014). Diatoms are also the predominant algae associated with Antarctic sea ice (Falciatore and Bowler, 2002). It has been estimated that diatoms are responsible for roughly 40% of global marine primary productivity (Falkowski et al., 1998; Field et al., 1998; Hervé et al., 2012; Gao and Campbell, 2014), with annual diatom photosynthesis estimated to generate the same amount of

organic carbon as all of the terrestrial rainforest combined (Armbrust, 2009). Diatoms may be responsible for 20 to 25% of the globally fixed carbon and atmospheric oxygen (Vanormelingen et al., 2008; Gao and Campbell, 2014), and therefore play an important role in the global carbon cycle (Lazarus et al., 2014). The organic carbon generated by diatoms serves as a base for marine food webs (Hildebrand, 2008; Armbrust, 2009; Tew et al., 2014), whilst larger diatom cells, which have a lower dissolution and sink relatively rapidly, are a key component of the ocean carbon pump via the rapid sinking of large cells and aggregates (Litchman et al., 2009; Lazarus et al., 2014).

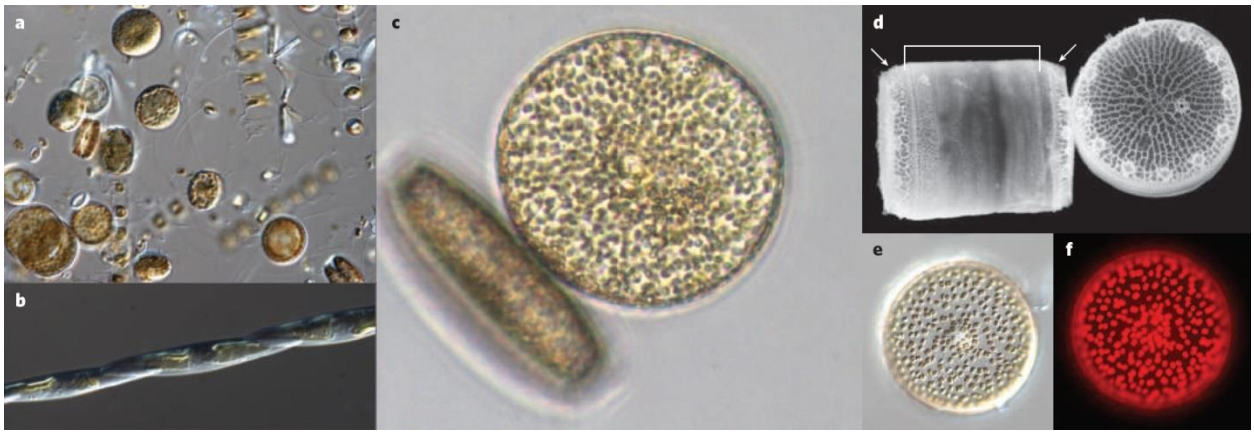

Figure 9. **Micrograph images of the various diatom species.** Diatoms can exist either as an individual cell or within a chain of cells (a). Diatoms are classed into two broad morphological categories, the pennates (b) and the centrics (c). The diatom cell wall is divided into two halves, known as theca, which join together in a similar manner to that of a petri dish. Each theca appears as a rounded (or oval) shape in valve view and rectangle in girdle view (c). Photosynthetic activity takes place within the membrane-bound plastids which appear as small discs within the diatom cell (e). The membrane-bound plastids contain chlorophyll *a* which, when illuminated with blue light, fluoresce with red light (f). *(This figure originally appears in Armbrust, 2009, Figure 1, page 186).*

1.5.2 Microfossil diatom distributions with respect to sea ice

The Southern Ocean's physical, chemical and biological conditions vary on seasonal and inter-annual time scales. The latter variability influences the biomass and composition of marine phytoplankton throughout the Southern Ocean **(**Garibotti et al., 2005; Iida and Odate 2014). Thus, the distribution of diatom assemblages throughout the Southern Ocean is related to the prevailing surface water conditions. For some key diatom species, the presence of sea ice is a key physical variable for their biogeography (Taylor et al., 1997; Cunningham and Leventer, 1998; Armand et al., 2005; Esper et al., 2010; Olguín and Alder, 2011; Esper and Gersonde, 2014). For example, large diatom blooms have been reported in association with the retreat of Southern Ocean sea ice (e.g. Smith and Nelson, 1986; Sullivan et al., 1988; Grigorov et al., 2014; Saba et al., 2014). The vertical stability of the water column and nutrient input that results from sea-ice melt enhances diatom productivity at the sea-ice edge and throughout the marginal sea-ice zone of the Southern Ocean (Buffen et al., 2007). Given the abundance of diatoms throughout the Southern Ocean, and the preservation of diatom opaline silica skeletons within Antarctic sediments, the distribution of diatom assemblages recorded within Southern Ocean sediments provides a proxy for paleoceanographic reconstructions of sea-ice distribution (Gersonde and Zielinski, 2000; Schneider-Mor et al., 2005; Buffen et al., 2007; Esper et al., 2010) (Figure 10).

Investigations into the biogeographical distribution of diatoms within the sediments of the Southern Ocean have revealed a distinct suite of diatom species that are closely linked to the sea-ice environment. These diatom species with a distribution linked to the sea-ice environment include *Actinocyclus actinochilus*, *Fragilariopsis cylindrus*, *Fragilariopsis curta*, *Porosira glacialis* and the *Thalassiosira antarctica* group (Figure 11). Each of these latter diatoms are restricted to the winter sea-ice zone, and tend to have a lower abundance at more northerly

locations (Taylor et al., 1997; Cunningham and Leventer, 1998; Armand et al., 2005; Buffen et al., 2007; Esper et al., 2010; Olguín and Alder, 2011; Esper and Gersonde, 2014). The diatoms *Porosira glacialis*, *Porosira pseudodenticulata*, *Stellarima microtrias* and *Thalassiosira tumida* are, generally, limited to the summer sea-ice zone (Armand et al., 2005).

The deployment of sediment traps within the seasonal sea-ice zone has helped to improve our understanding of the relationship between sea-ice cover and the transfer of sea ice related diatoms to the seafloor. The AESOPS longitudinal time series program recorded the biogeographic diatom flux in relation to sea-ice cover, providing the most detailed outline of the relationship between diatom flux and sea-ice cover (Grigorov et al., 2014). It was found that sea-ice cover was a clear determinant for the increased relative abundance of *Actinocyclus actinochilus*, *Fragilariopsis curta*, *F. cylindrus*, *F. obliquecostata*, *Stellarima microtrias* and *Eucampia antarctica* v. *recta*. Flux of the diatoms *Thalassiosira lentiginosa* and the *Thalassiosira antarctica/scotia* group were tied to the winter sea-ice edge, whereby the relative abundances of both species increased north of the winter sea-ice edge (Grigorov et al., 2014).

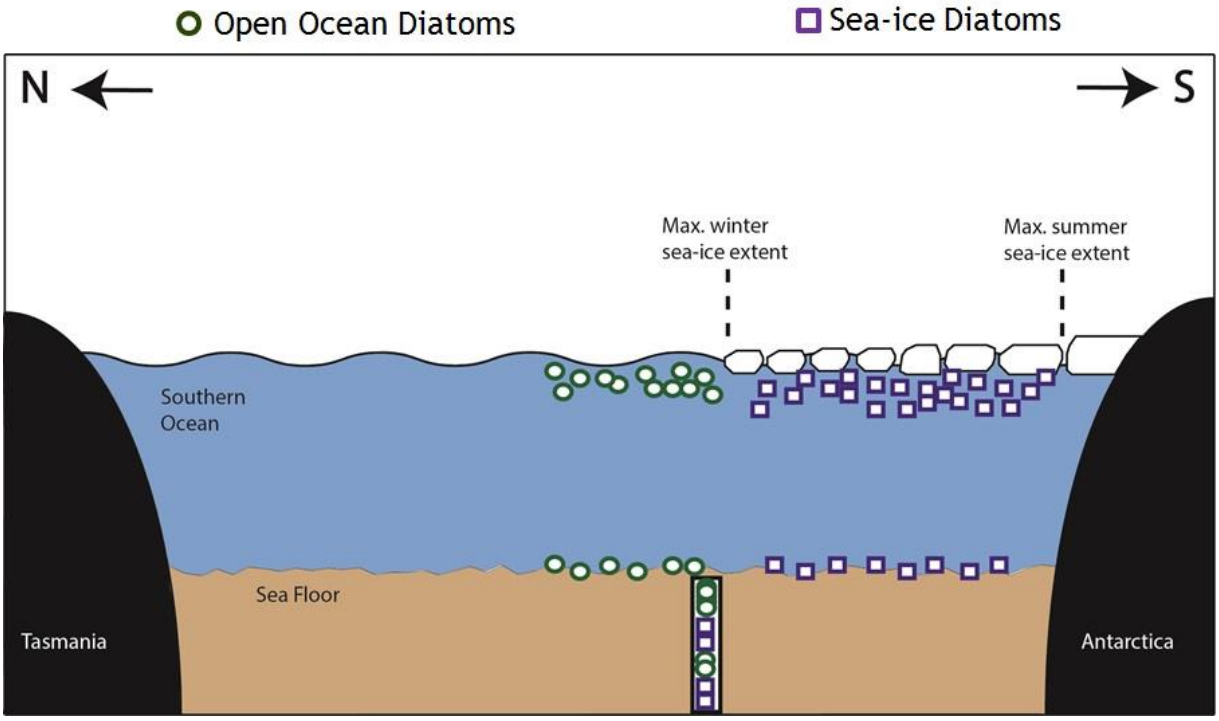

Figure 10. A schematic illustrating the premise for using diatom relative abundances as a proxy for winter sea-ice cover. Specific sea ice related diatoms live within the sea-ice zone, whilst the open ocean is characterised by another distinct assemblage of open ocean diatom species. The living assemblages are preserved on the Southern Ocean sea floor. Hence, marine sediment cores, and the fossilised diatoms therein, provide a record (i.e. proxy) for past sea-ice coverage. *(Figure adapted from Armand, 2000, Figure 1).*

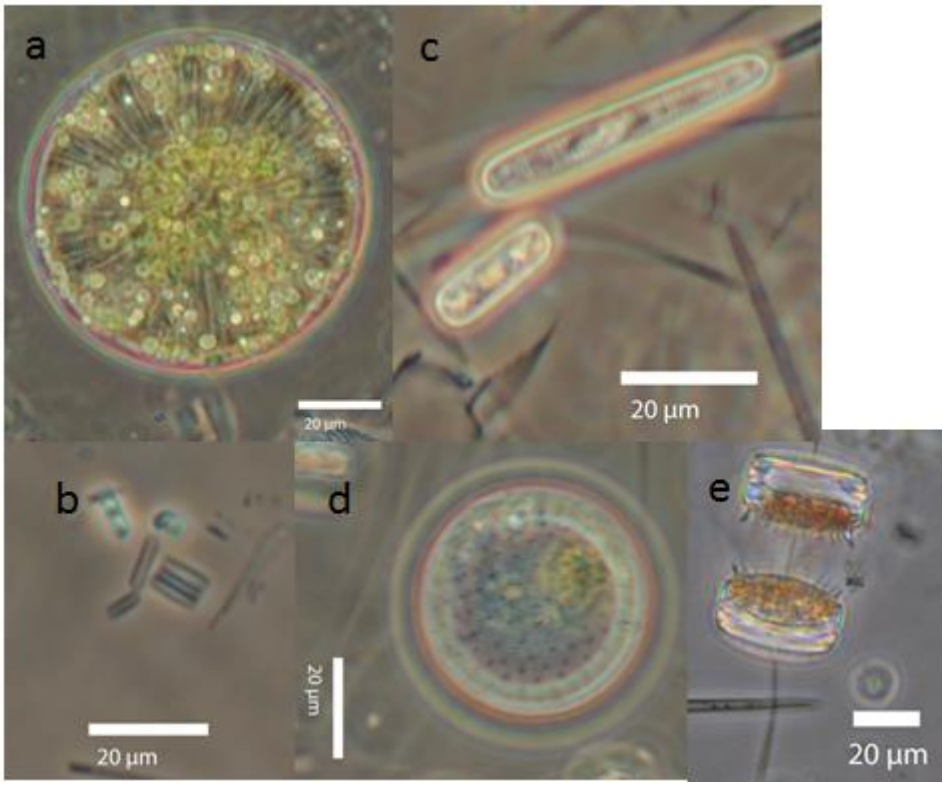

Figure 11. Key Southern Ocean diatom species associated with sea-ice concentrations and/or extent. The live species shown are a) *Actinocyclus actinochilus*, b) *Fragilariopsis cylindrus*, c) *Fragilariopsis curta*, d) *Porosira glacialis* and e) *Thalassiosira antarctica* group (with resting spores). Each of these species have a biogeography related to sea ice and can therefore be used as a proxy for past sea-ice concentration and extent. Scale bar is 20 µm in all images. *(Photographs used with permission from L. Armand, 2014, Sabrina Coast, East Antarctica).*

1.5.3 Diatom microfossils as a proxy for Southern Ocean sea ice

The estimation of Southern Ocean paleo sea-ice cover, based on diatom microfossil assemblages, has relied on the modern analogue technique (MAT) (Hutson, 1980; Crosta et al., 1998; Armand and Leventer, 2010) and a form of principal component regression, known as the Imbrie and Kipp transfer function (IKTF) (Imbrie and Kipp, 1971; Armand and Leventer, 2010). Since 2010, a small number of studies have utilised various statistical approaches to produce diatom-based sea-ice estimates from cores covering the Holocene to the last 220 kyr BP (Table 1). There is a

growing body of research that suggests the application of IKTF and MAT for the estimation of paleoceanographic variables is inappropriate (Telford and Birks, 2005; Juggins and Birks, 2012). Generally, the computation of principal components (as is done when applying IKTF) for the purpose of making subsequent predictions is inefficient (Juggins and Birks, 2012) and may provide inappropriate ecological answers when species assemblage data contains many zero values (i.e. diatom species are absent at certain sample sites, Legendre and Birks, 2012). Recent alternative approaches undertaken on the diatom database from the Alfred Wegener Institute has recommended the application of MAT (Esper and Gersonde, 2014), but their approach has yet to account for spatial structures within their database to ensure this approach remains valid using their database.

Table 1. **The key studies that have used diatoms to estimate past Southern Ocean sea ice since 2010.**

Reference/ Year	Region	Method	Time Period (BP)
Allen et al. (2010)	Neny Fjord, Antarctic Peninsula	Principal components analysis (PCA), to describe principal stratigraphic zones within the diatom data	Holocene (9 to 0.2 kyr)
Barbara et al. (2010)	Eastern Prydz Bay, East Antarctica	C25 ratio of HBI diene and triene in cores and fossil diatom assemblage analysis	11 to 9 kyr
Denis et al. (2010)	Adélie Land, East Antarctica	C25 ratio of HBI diene and triene in cores and fossil diatom assemblage analysis	7 kyr to present day
Röthlisberger et al. (2010)	Indian Ocean sector	MAT	Last 240 kyr
Allen et al. (2011)	Scotia Sea and Antarctic Peninsula	Calibration of Gersonde and Zielinski (2000)	LGM to Holocene
Collins et al. (2012)	Southwest Atlantic, Scotia Sea	Calibration of Gersonde and Zielinski (2000)	35 to 15 kyr
Maddison et al. (2012)	East Antarctic	Laminated diatom rich sediments	1136 to 3122 cal yr
Barbara et al. (2013)	Northwestern and Northeastern Antarctic Peninsula	Q-mode PCA	1935 to 1950 AD
Collins et al. (2013)	Southwest Atlantic, Scotia Sea	Diatom indicator species used as proxy for Antarctic sea ice (Gersonde and Zielinski, 2000). HBI diene and triene in cores.	60 to 0 kyr
Etourneau et al. (2013)	West Antarctic Peninsula, Palmer Deep Basin	Diatom indicator species used as proxy for Antarctic sea ice (Gersonde and Zielinski, 2000).	Holocene (last 9 kyr)
Tolotti et al. (2013)	Western Ross Sea	Diatom assemblage analysis in cores of the Ross continental shelf and continental slope.	Last 40 kyr
Esper and Gersonde (2014)	Atlantic and Pacific Oceans	MAT and IKTF	150 kyr

1.6 Southern Ocean paleo-oceanography and paleo sea-ice cover

1.6.1 The Last Glacial Maximum: timing, extent and climatic variability.

The Last Glacial Maximum (LGM) is defined as the most recent time interval in Earth's history when the global ice sheets reached their maximum integrated volume (Mix et al., 2001). The LGM period is of interest to paleo-climatologists as it is believed to represent a period which is analogous to the Quaternary ice ages (Kucera et al., 2005). The climatic drivers associated with Quaternary deglaciations rely on mechanisms that involve deep water formation and carbon

storage, which in turn rely on physical changes to the Antarctic ice sheet and Southern Ocean circulation. However, our current understanding of the climatic drivers that were important for driving Quaternary deglaciations remains poorly understood (Paillard, 2015).

The timing of the Last Glacial Maximum (LGM) has been previously placed between 23 to 19 kyr BP (Mix et al., 2001) and more recently as between ~26.5 to 19 kyr BP (Clark et al., 2009). Evidence suggests the LGM throughout eastern Australia, New Zealand and the South Pacific may have commenced earlier, at ~30 kyr BP, with a duration of 10,000 years (Petherick et al., 2008; Stephens et al., 2012; Vandergoes et al., 2013). Records of early glacial cooling have also been documented within New Guinea, the northeast Indian Ocean, as well as within western and southern Australia (Reeves et al., 2013). The climatic cooling between 29 and 19 kyr BP is known as the extended LGM (eLGM, Newnham et al., 2007).

It is believed the LGM winter sea-ice extent may have reached between 5° and 10° north of the modern winter sea-ice extent (e.g. Crosta et al., 2004; Gersonde et al., 2005; Allen et al., 2011). The study of southern bull kelp population genetics suggests sea-ice coverage during the LGM may have reached the Falkland Islands in the western Atlantic sector, and Macquarie Island in the east Pacific sector (Fraser et al., 2009) (Figure 12). The recent application of a MAT sea-ice estimation model on cores from the Pacific Polar Frontal Zone (60°S) and the Antarctic Zone (52°S) of the eastern Atlantic (Esper and Gersonde, 2014) (Figure 12) both indicated that maximum winter sea-ice extended out over the core sites. Sea-ice concentrations of up to ~60% (representative of consolidated sea-ice cover) were estimated during marine isotope stage (MIS) 2 (Esper and Gersonde, 2014). The timing for MIS 2 has been placed from 29 kyr BP to 14 kyr BP (Lisiecki and Raymo, 2005a), which generally corresponds with the timing for the eLGM period. Thus, the LGM winter sea-ice area has been estimated at 39×10^6 km^2, which represents a

100% increase in winter sea-ice coverage from the modern day winter sea-ice area of 19×10^6 km^2 (Gersonde et al. 2005; Allen et al. 2011).

Paleoclimate estimates over the eLGM period from New Zealand and southern Australia suggest the eLGM was a period of climatic variability. Both the commencement and termination of the eLGM was marked by a period of distinct cooling. A consensus around the timing of each cold period is beginning to appear, whereby the first cold phase occurred between ~30 to 26 kyr BP, whilst the second followed around ~23 to 18 kyr BP (Petherick et al., 2008; Zink et al., 2010; Stephens et al., 2012; Vandergoes et al., 2013; Reeves et al., 2013). The two eLGM cold phases were separated by a warm event known as the eLGM interstadial/Antarctic Isotope Maxima 2 (AIM 2) (Petherick et al., 2008; Williams et al., 2010; Stephens et al., 2012; Newnham et al., 2012). The variable eLGM climate of New Zealand and eastern Australia is consistent with the marine paleo sea-ice record of Crosta et al. (2004) and the EPICA Dronning Maud Land (DML) Antarctic ice core from West Antarctica (Vandergoes et al., 2013).

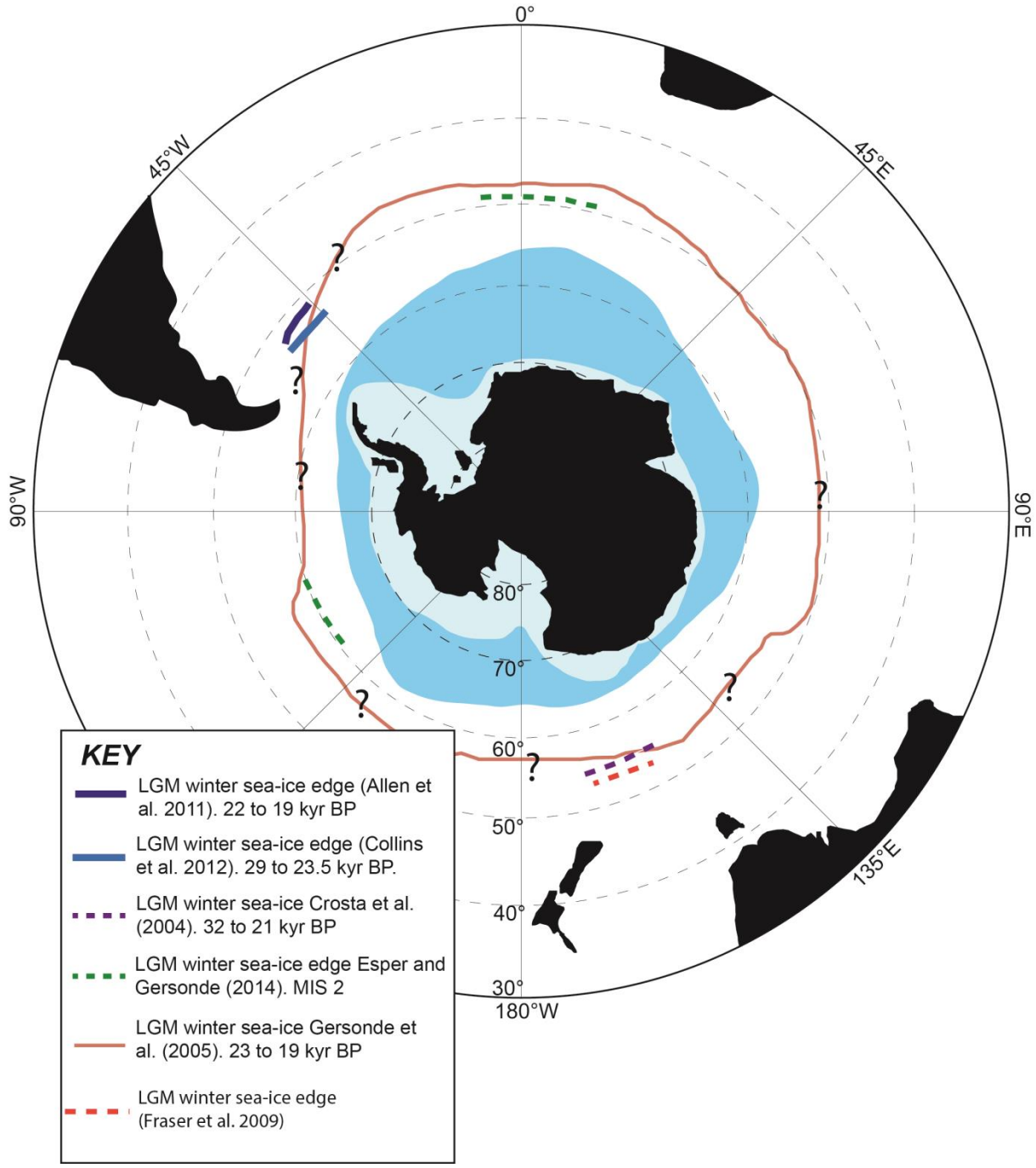

Figure 12. Current estimated paleo positioning of the winter sea-ice edge throughout the Southern Ocean during the Last Glacial Maximum and/or time slices that correspond with the LGM from various sources. Question marks represent those areas where no information for the LGM winter sea-ice edge currently exists. The maximum average extent of modern winter sea ice from 1979 to 2000 is indicated by the mid-blue shading whilst the maximum extent of modern summer sea ice is indicated by the light blue shading.

Our current understanding of eLGM sea-ice coverage throughout the southern hemisphere remains incomplete (Fraser et al., 2009). Unresolved debate regarding the forcing mechanisms and hemispheric teleconnections that established the southern hemispheres LGM climate remains. The hypotheses proposed for the southern hemisphere LGM climate are difficult to test where the available paleoclimatic data records lack any replication (Turney et al., 2006). Whilst recent research is underway (Esper and Gersonde, 2014), an accurate reconstruction of the Southern Ocean's eLGM climate requires additional marine sediment core, and associated paleo sea-ice data, from the Pacific (Gersonde et al., 2005). The anatomy, and future assessment of marine proxy inferred LGM climate events throughout New Zealand and the Pacific sector of the Southern Ocean (e.g. Crosta et al., 2004), need to be assessed once the age models for such records have been updated (Vandergoes et al., 2013).

The nature of southern hemisphere LGM climatic variation, in particular, the amount of climatic cooling, and the spatial extent of each LGM cold phase, also remains uncertain (Petherick et al., 2008; Verleye and Louwye, 2010). In particular, the oceanic changes, considered drivers for the onset of the cold phases that occurred at the commencement and termination of the LGM, are poorly understood (Verleye and Louwye, 2010). Additional marine paleoclimatic data, across latitudinal gradients, is required to provide a test of those hypotheses for the eLGM climatic variability estimated throughout New Zealand (Newnham et al., 2012).

1.6.2 The fronts of the Southern Ocean

The fronts of the Southern Ocean correspond with regions where two distinct water masses meet. Therefore, ocean fronts are areas with strong horizontal gradients in water mass properties, in

particular salinity and sea surface temperature (SST), as well as sea surface height (SSH). Hence the fronts of the southern ocean can be identified by hydrographic measurements, in particular by a specific gradient in SST and/or SSH (Graham et al., 2012, Figure 13). The fronts of the Southern Ocean play an important role in the global climate system (Graham et al., 2012). The latitudinal position of Southern Ocean fronts changes the connectivity between surface water and deep ocean currents. Thus, Southern Ocean fronts affect the transport of heat between ocean basins (Bard and Rickaby, 2009; Graham et al., 2012; McKay et al., 2012; Romero et al., 2015).

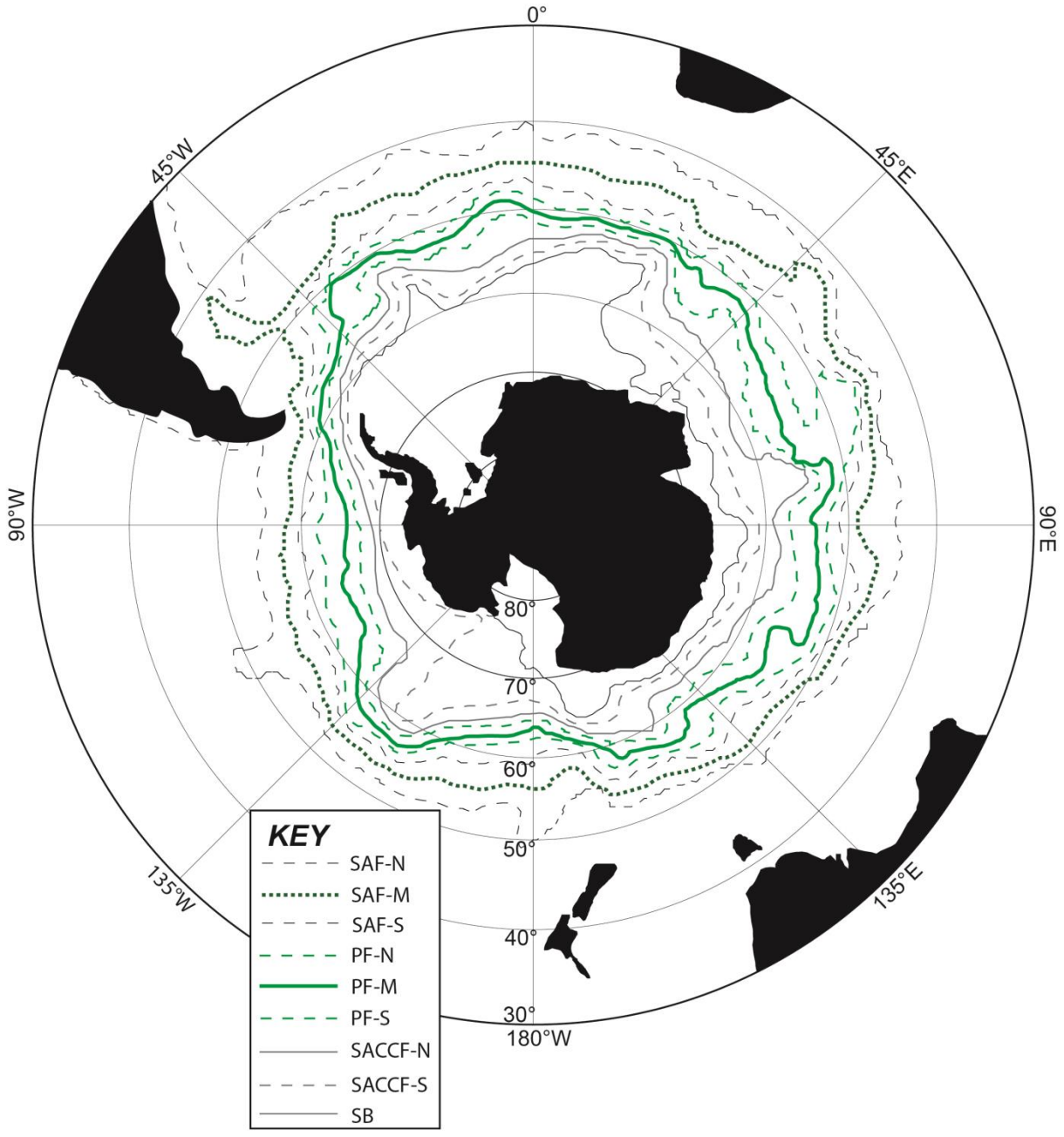

Figure 13. A map of the mean location for each of the Southern Ocean fronts, as defined by Sokolov and Rintoul (2009a,b) using sea-surface height data. The Southern Ocean fronts illustrated within this figure are as follows: the Sub-Antarctic Front northern branch (SAF-N), Sub-Antarctic Front middle branch (SAF-M) Sub-Antarctic southern branch (SAF-S), Polar Front northern branch (PF-N), Polar Front middle branch (PF-M), Polar Front southern branch (PF-S), southern ACC front northern branch (SACCF-N), southern ACC front southern branch (SACCFF-S) and the Southern Boundary Front (SB). *(All data was sourced from Sokolov and Rintoul (2009a,b)).*

The role played by the fronts of the Southern Ocean, and how the position of each front may have varied during past climatic events, such as the LGM, remains a point of controversy (Kemp et al., 2010; Kohfeld et al., 2013). Based on the assumption that the SST signature of a given front remained unchanged during past glaciations, previous research has attempted to infer the position of the Southern Ocean fronts based on paleo proxy based estimates of SST (e.g. De Deckker et al., 2012; Romero et al., 2015). Proxy based paleoclimatic data suggests that the Southern Ocean fronts were north of their modern day position during the eLGM (Ling Ho et al., 2012; Shetye et al., 2014; Gottschalk et al., 2015; Manoj and Thamban, 2015). However, potential atmospheric and oceanographic responses, notably the absence of any change in Southern Ocean stratification or the latitudinal position of the southern westerly winds and/or ACC, suggest that the position of eLGM Polar Front was not different to its present day position (Matsumoto et al., 2001; Shulmeister et al., 2004; MARGO project members, 2009). Other issues include the lack of any specific correspondence between the position of a Southern Ocean front and given surface isotherm based on modern satellite observations (Kohfeld et al., 2013). The fronts of the Southern Ocean do not have a homogenous circumpolar SST signature (Kostianoy et al., 2004; Kohfeld et al., 2013), hence it may not be valid to assume a constant SST signature for each front during the eLGM, and use this SST signature to track the paleo position of Southern Ocean fronts. If the role and importance of Southern Ocean fronts during the eLGM is to be better understood, a new, more robust proxy for the presence of each front is required.

1.6.3 The interglacial and transition into the Holocene

The termination of the LGM and shift to the present day Holocene interglacial represents a large natural change in global climate. Improving our knowledge regarding the timing and duration of the shift from the LGM climate into the Holocene provides paleo climatologists with an opportunity to examine important hypotheses for the functioning of the global climate system (Kucera et al., 2005; Jansen et al., 2007; Vandergoes et al., 2013). In particular, post glacial periods provide an opportunity to assess the sensitivity of the global climate system (Kucera et al., 2005) and evaluate how the Earth's climate system responds to radiative perturbations (Jansen et al., 2007).

1.6.4 LGM termination and onset of the Antarctic Cold Reversal

The Antarctic Cold Reversal (ACR) was a ~1000 year period of climatic cooling between 14.5 and 12.5 kyr BP, interrupting the transition from the Last Glacial Maximum into full deglacial conditions (Stenni et al., 2001; Divine et al., 2010). The full geographical extent of the ACR throughout the Southern Ocean remains unclear. Evidence for a cooler climate during the ACR has been recorded within the central Southern Alps of New Zealand (at 44°S), in paleo SST records from the south of Australia (at 36°S), to ~41°S within the southeast Pacific Ocean (near Chile), 41°S within the South Atlantic and at 75°S within the east Antarctic Plateau (Putnam et al., 2010, Figure 14). The paleo climate records described by Putnam et al., (2010) and Jomelli et al. (2014) indicate that the cooler climate of the ACR extended into the southern mid-latitudes of the southwestern Pacific and tropical Andes, respectively.

During the ACR, Carter et al. (2008) found southern hemisphere oceanic and atmospheric changes established climatic conditions conducive to sea-ice expansion. Between ~14 to 12.4 kyr BP, moderate increases in windiness and sea-ice cover may have increased deep-water production, in turn invigorating the thermohaline Pacific Deep Western Boundary Current off eastern New Zealand (NZ). Also, against a background of increased NADW input, there may have been a reduction in Southern Ocean upwelling and atmospheric CO_2 concentrations, which cooled the ocean surface (Putnam et al., 2010, Figure 14). The atmospheric changes, dated between 13.5 and 11.5 kyr BP, included increased windiness, along with a drier and cooler climate. Carter et al. (2008) argue that such atmospheric changes, notably the cooling of the atmosphere in conjunction with a drier climate, were driven from Antarctica. Cooling during the ACR may have forced the northerly expansion of the cold atmosphere and oceanic temperatures, effectively producing a scaled down LGM (Carter et al., 2008). Warming over Greenland during the Bølling-Allerød (BA), a period of climatic warming documented throughout the northern hemisphere, occurred during the ACR in the Southern Hemisphere. The co-occurrence of the BA and ACR suggests that the ACR is an expression of the bipolar see-saw (refer to section 1.2.3) (Putnam et al., 2010, Figure 14). ACR-like conditions then prevailed between 13.5 to 11.5 kyr BP, characterized by a cooler, windier and less seasonal climate (Carter et al., 2008).

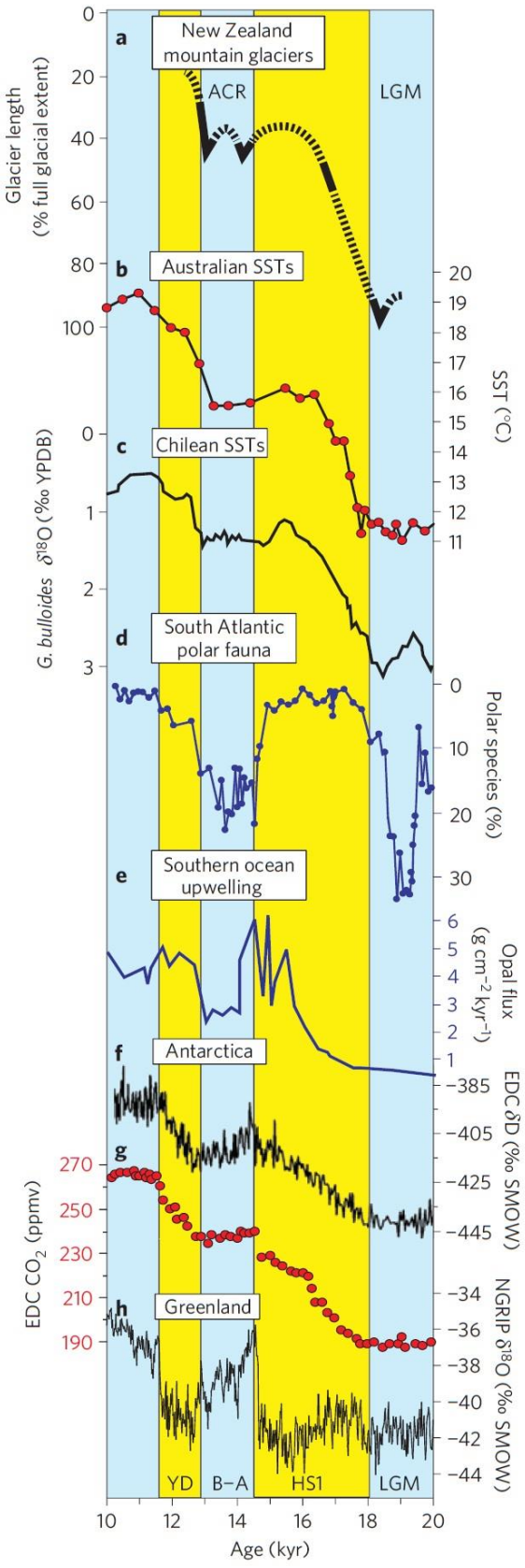
a
New Zealand mountain glaciers
ACR
LGM
Glacier length (% full glacial extent)
b
Australian SSTs
SST (°C)
c
Chilean SSTs
G. bulloides δ18O (‰ YPDB)
d
South Atlantic polar fauna
Polar species (%)
e
Southern ocean upwelling
Opal flux (g cm−2 kyr−1)
f
Antarctica
EDC δD (‰ SMOW)
g
EDC CO2 (ppmv)
h
Greenland
NGRIP δ18O (‰ SMOW)
YD
B–A
HS1
LGM
Age (kyr)

Figure 14. Paleo climate records for the ACR. Panel a) illustrates the New Zealand moraines and ^{10}Be surface exposure chronology from Putnam et al. (2010). b) illustrates the paleo SST estimates from Calvo et al. (2007), from the south of Australia, c) is the record of SST of Lamy et al. (2004) (derived from $\delta^{18}O$) from Chile, d) illustrates south Atlantic cryophilic foraminifera described by Barker et al. (2009), e) is the biogenic opal flux of Anderson et al. (2009), f) shows Antarctic air temperature records derived from ice core deuterium records (Monnin et al. 2001)), whilst g) plots atmospheric CO_2 on the NGRIP methane-synchronised timescale of Lemieux-Dudon et al. (2010). The NGRIP ice core $\delta^{18}O$ (NGRIP members, 2004; Rasmussen et al. 2006) is plotted in h). *(This figure was adopted from Putnam et al. (2010), Figure 3, on page 703).*

Diatom paleo sea-ice estimates from the Atlantic sector of the Southern Ocean document a general expansion of sea ice during the ACR (Bianchi and Gersonde, 2004; Divine et al., 2010), whilst there was no indication of sea ice expansion during the ACR from several locations across the southwest Pacific, in part due to the low sedimentation rates there (Crosta et al., 1998; Crosta et al., 2004). Additional paleoclimatic data will allow us to improve our understanding for the ACR's timing and geographic extent. Paleoclimatologists could then use what is known about the ACR climate to further our understanding of the interhemispheric linkages that have driven Earth's climate between glacial and interglacial climates (Putnam et al., 2010).

1.6.5 The southern hemisphere Holocene climate.

The Holocene period, which encompasses the present day, commenced 10 kyr BP (Williams et al., 1998). The climate of the southern hemisphere during the Holocene period remains poorly understood, as does our understanding of the various forcing mechanisms that have driven Holocene climatic variation (Divine et al., 2010). Holocene climatic changes, on millennial time-scales, have been recorded within paleoclimate records to the south of Australia (Moros et al., 2009), the west Antarctic Peninsula (Shevenell et al., 2011; Etourneau et al., 2013), Palmer Deep

(Shevenell and Kennett, 2002), as well as within both coastal and inland Antarctic ice cores (Masson et al., 2000). By examining these records to develop our knowledge of Antarctic climatic variations during the Holocene, we can improve our understanding of recent global warming, ice-sheet mass balance and sea-level changes (Masson et al., 2000).

There is some controversy around the expansion or otherwise of Southern Ocean sea-ice cover during the Holocene period. The records of paleo sea-ice cover throughout the southwest Pacific suggest sea-ice did not expand during the Holocene period (Crosta et al., 2004; Röthlisberger et al., 2010). However, paleo sea-ice records from the Atlantic sector suggest that sea-ice expanded during both the Holocene and ACR, with the expansion of sea-ice during the Holocene appearing to be similar to the record of ACR sea-ice expansion (Bianchi and Gersonde, 2004; Divine et al., 2010; Esper and Gersonde, 2014). It is important to note that unlike the locations of the Atlantic paleo sea-ice records, the southwest Pacific paleo sea-ice record is derived from just a single a location that is situated north of the modern winter sea-ice edge. Hence, the nature of Holocene paleo sea-ice extent and variability across the southwest Pacific remains largely unknown.

1.7 Key research directions

Ever since the publication of the IKTF method in 1971 by Imbrie and Kipp (1971), there has been very little research that focused on assessing the statistical methods used to estimate paleo sea-ice and sea surface temperature. The first application of MAT by Crosta et al. (1998) offered the only advance in the estimation of paleo sea-ice for the Southern Hemisphere. However, no rigorous assessment of the statistical methods used in paleoceanography has yet been provided.

Hence, this thesis will examine all of the current statistical models used, and propose the use of alternative statistical methods for estimating paleo sea-ice throughout the Southern Ocean.

The paleoceanography for the Pacific Sector of the Southern Ocean remains largely unknown. The current paleo sea-ice and sea surface temperature data available for the Southwest Pacific is restricted to a four marine sediment cores (Crosta et al. 1998; Crosta et al. 2004; Gersonde et al. 2005). Thus, this thesis will provide an analysis from a new marine sediment core record (core E27-23) within the Southwest Pacific. In particular, the new paleo data from core E27-23 will be used to compliment the paleo records from core SO136-111 (Crosta et al. 1998; Crosta et al. 2004), and provide an independent paleo record with which the record from core SO136-111 can be compared. Given the currently limited understanding of the southwest Pacific paleoceanography, a focus will be made on the paleo sea-ice records from 45 kyr BP, over the Last Glacial Maximum, the interglacial, and the early Holocene.

Southern Ocean fronts are believed to have played an important role during past climate changes (Romero et al., 2015), hence tracking the paleo position of the Southern Ocean fronts using paleo SST data has been an area of active research (Marino et al., 2009; Findlay and Flores, 2000; Romero et al., 2015). Given the uncertainties of the SST method for estimating the position of Southern Ocean fronts, a novel diatom proxy for the SSH signature of the Southern Ocean Polar Front will be developed and applied within this thesis. The first record for the paleo position of the Southern Ocean Polar Front based on SSH data will then be presented for the Southwest Pacific sector of the Southern Ocean.

1.8 Aims and Objectives

This thesis will focus on four key aims to address knowledge gaps and develop methodological advances to improve paleo sea-ice records and paleoceanographic interpretations specifically within the southwest Pacific Sector of the Southern Ocean. The four key aims for this thesis are:

1. To assess the applicability of statistical models that are used for the estimation of Southern Ocean paleo sea-ice cover based on a diatom proxy. In particular, we consider the capacity for each statistical model to provide robust and unbiased estimates of paleo sea-ice cover when applied to a validation (or test) database that is spatially autocorrelated. The outcome of the aim will be to propose a statistical method that permits the estimation of confidence intervals for all paleo sea-ice estimates and the evaluation of statistically significant associations between specific diatom proxy species (Chapter 2).

   To apply the most robust statistical model and produce a new paleo winter sea-ice concentration data set for the southwest Pacific, with a focus on the Antarctic Cold Reversal and the late to mid-Holocene. The new winter sea-ice concentration record will be compared with the paleo sea-ice records from the Atlantic sector of the Southern Ocean (Chapter 3).

2. To provide a modernised account of winter sea-ice concentration and February sea-surface temperature (fSST) records over the Last Glacial Maximum (LGM), throughout the southwest and southeast Pacific, with a focus on cold and warm phases of the extended LGM (eLGM). To complement the new paleo winter sea-ice records, we will briefly compare the statistical models used to estimate February sea-surface temperature (fSST). The most robust model will be used to

provide revised LGM fSST estimates. Our regional paleo sea-ice data will be compared with previously published Antarctic ice core records, terrestrial records, as well as southeast Pacific and southeast Atlantic sector marine sediment cores (Chapter 4).

3. To examine the utility of diatom abundances as a proxy for the specific sea-surface height (SSH) signature associated with each of the Southern Ocean fronts. In particular, a diatom proxy and statistical procedure for estimating the paleo presence of the Southern Ocean Polar Front will be investigated and tested (Chapter 5).

The following section provides a detailed summary of each chapter within this thesis, and elaborates on the methodologies followed to address each of the key aims for this thesis.

1.9 Thesis outline by chapter.

Chapter 2 of this thesis aims to evaluate the applicability of the current statistical models (referred to as transfer functions within the paleoceanography literature) to the only publically available diatom surface sediment training database compiled and originally described by Crosta et al. (2004) (Figure 15). I acknowledge here that access to the published diatom seafloor datasets represented under the following papers of Zielinski and Gersonde (1997); Zielinski et al. (1998); Gersonde and Zielinski (2000); Gersonde et al. (2005); Esper et al. (2010) and Esper and Gersonde (2014), and archived through PANGEA (Table 2), was deliberately denied by Prof. Rainer Gersonde (Alfred-Wegener Institute) (pers. comm, 2012 and 2013). Therefore a full investigation incorporating all published data was impossible for this thesis.

Table 2. A summary of the published papers that have used the diatom sea-floor databases which were not accessible for this thesis. Each of the specific references are listed and, where applicable, a link to the password protected data record stored at PANGAEA (http://www.pangaea.de/) is provided.

Reference	PANGAEA Data link
Zielinski and Gersonde (1997)	
Zielinski et al. (1998)	http://doi.pangaea.de/10.1594/PANGAEA.54632
Gersonde and Zielinski (2000)	
Gersonde et al. (2005)	
Esper et al. (2010)	http://doi.pangaea.de/10.1594/PANGAEA.681699
Esper and Gersonde (2014)	http://doi.pangaea.de/10.1594/PANGAEA.828674

Both MAT and IKTF are the main statistical techniques applied to estimate paleo sea ice throughout the Southern Ocean (Crosta et al., 1998; Crosta et al., 2004; Esper and Gersonde 2014). MAT and IKTF will be compared with the application of weighted averaging partial least squares (WA PLS) and a generalized additive model (GAM). A 10-fold hold out validation of each model will be applied to test relevant statistical assumptions and compare the fit of each model to the training database of Crosta et al. (2004). A hold out validation, with a partitioning of the training database, into training and test subsets, will ensure a geographic separation between each subset. Therefore, we investigate the importance of spatial autocorrelation within the training database of Crosta et al. (2004), and the bias that spatial autocorrelation may have in estimating the predicative success under hold out validation for each of the statistical methods compared. To complement the hold out validation of each model, variance partitioning and principal co-ordinates analysis will be applied in an attempt to reveal the relative importance of winter sea-ice concentrations, and the spatial patterns within the Crosta et al. (2004) training database, in explaining the variation within diatom relative abundances. Investigation into the nature of each diatom's species-response relationship with winter sea-ice concentration will be

introduced and considered when evaluating each statistical model. In this chapter the aim will be to identify which statistical model provides the most statistically, and biologically, robust method for estimating past winter sea-ice cover.

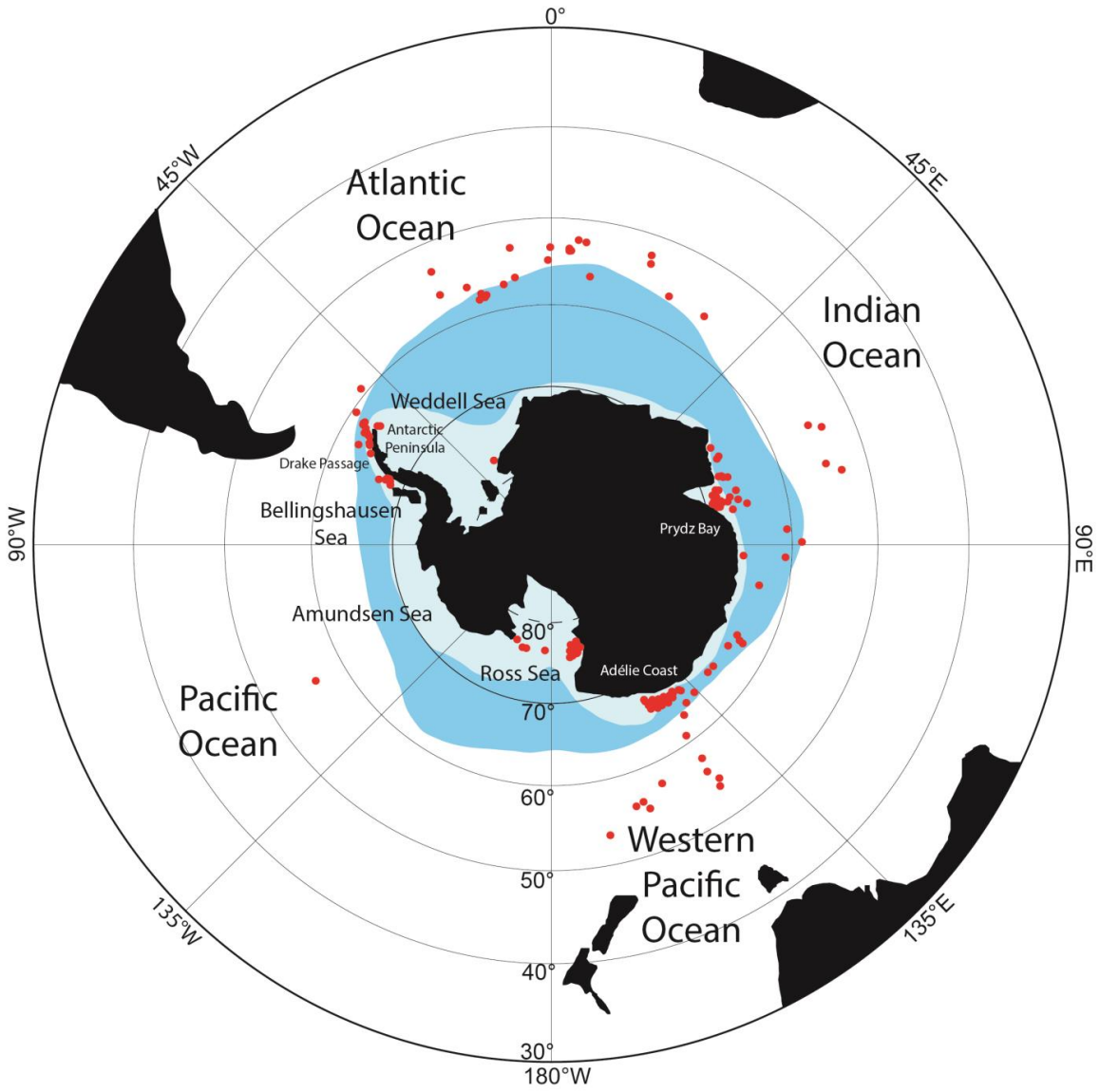

Figure 15. The location for each of the Crosta et al. (2004) samples used within this thesis. The red dots represent a subset of the surface sediment database compiled by Crosta et al. (2004), which will be used within this thesis for estimating paleo winter sea-ice concentrations. Also shown are the key regions and locations through the Southern Ocean and Antarctica. Modern average summer (light blue) and winter (mid-blue) sea-ice extents from 1979 to 2000 are shown surrounding Antarctica *(sea-ice data was sourced from the National Snow and Ice Data Centre (NSIDC)/Comiso, (2000)).*

Chapter 3 builds upon Chapter 2 by examining the application of the most robust statistical model for diatom-based winter sea-ice paleo estimation on two marine sediment cores (SO136-111 and E27-23, Figure 16) situated within the southwest Pacific sector of the Southern Ocean. Specifically, the model, and its paleo winter sea-ice estimates, will be compared with the previously published MAT-based paleo sea-ice estimates from Crosta et al. (2004) to highlight the general consistency between both techniques. Importantly, this chapter will focus on the first seasonal (winter) paleo sea-ice record for SO136-111, and examine the first paleo sea-ice record from a new marine sediment core, E27-23. Core E27-23 is located further south than the only currently published marine sediment core with a paleo sea-ice record within the southwest Pacific, core SO136-111. Therefore, core E27-23 will provide an additional paleo winter sea-ice record from the southwest Pacific that can be compared with the current Atlantic paleo sea-ice records (Divine et al., 2010; Esper and Gersonde, 2014). Here a comparison between the paleo sea-ice record from the south Atlantic (Divine et al., 2010; Esper and Gersonde, 2014) with the records for the southwest Pacific over the last 15 kyr BP are presented. The aim of the chapter is to expand the paleo sea-ice record for the southwest Pacific, and focus on these first paleo estimates of winter sea-ice concentration during the LGM termination and Holocene.

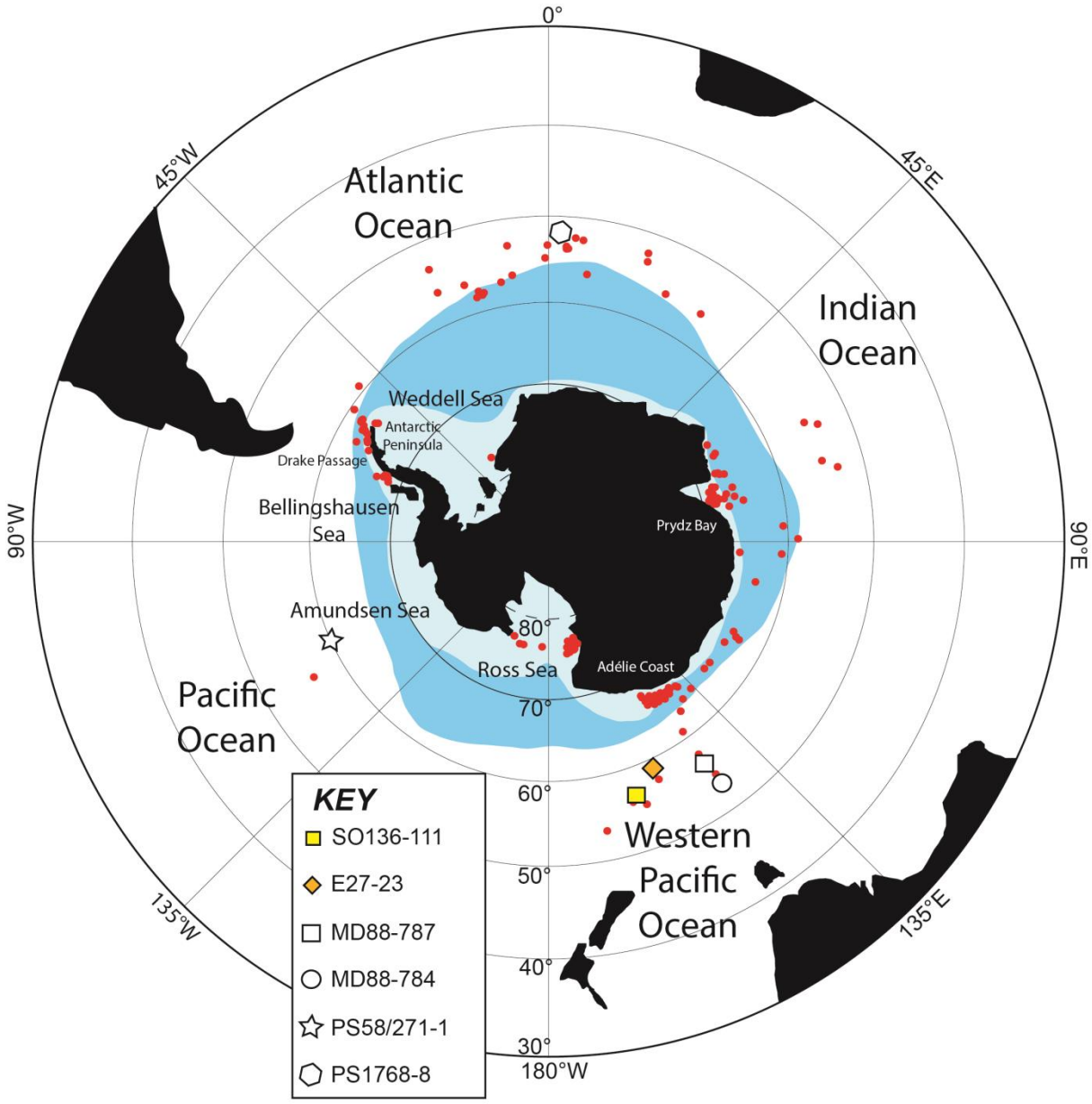

Figure 16. The locations of the six marine sediment cores that are used to produce estimates of paleo winter sea-ice concentrations during the LGM, LGM termination, and early Holocene within Chapters 3 and 4 of this thesis. The small red dots show the locations for the samples within the Crosta et al. (2004) database used within this thesis. Modern average summer (light blue) and winter (mid-blue) sea-ice extents from 1979 to 2000 are shown surrounding Antarctica *(sea-ice data was sourced from the National Snow and Ice Data Centre (NSIDC)/Comiso, (2000)).*

Chapter 4 will focus on the paleo winter sea-ice records for the southwest Pacific, southeast Pacific and east Atlantic during the LGM. The LGM paleo winter sea-ice estimates are derived from the most robust model that was evaluated and described in Chapter 2 of this thesis. This chapter includes results from two additional marine sediment cores, MD88-787 and MD88-784, to broaden the regional interpretations (Figure 16). Our synthesis of LGM paleo winter sea-ice conditions will be compared with paleo-climate records from New Zealand, southeast Australia and East Antarctica to build a picture of southern hemisphere climatic conditions over the extended LGM period. This chapter will focus on the new paleo winter sea-ice record from all of the cores located within the southwest Pacific. Paleo sea-ice data from the southwest Pacific will be used to test hypotheses for the onset of the southern hemisphere LGM, and the nature of the LGM climate, specifically, the duration of the LGM and LGM climatic variability.

Chapter 5 will examine the potential for marine diatoms to be used as a proxy for the sea-surface height signature of Southern Ocean fronts (Figure 13). In particular, we aim to establish a proxy for the SSH signature of ocean fronts to overcome the confounding nature of the SST signature proxy that has been previously used to infer frontal movement. An evaluation of significant species-response relationships between diatom relative abundances and the mean annual monthly presence of the Polar Front SSH signature will be investigated. Appropriate statistical models for estimating the paleo presence of the Polar Front's SSH signature will be a focus of the chapter, with the model deemed to be the most appropriate applied to two southwest Pacific Ocean sediment cores (MD88-787 and MD88-784, Figure 16). The paleoclimatic significance of the Polar Front's latitudinal migration throughout the southwest Pacific during the LGM will be discussed.

In Chapter 6, this thesis will conclude with a summary of key conclusions drawn from Chapters 2, 3, 4 and 5. A brief overview of the statistical developments will be provided, followed by a synthesis of the key paleoceanographic, and atmospheric, changes that drive the expansion of winter sea-ice cover and SST throughout the southwest Pacific LGM, ACR and Holocene. The latter summary will also focus on our interpretation of the role played by the fronts of the Southern Ocean in driving the LGM paleoceanographic changes and paleo sea-ice record. Finally, a summary for future research directions will be provided.

References

Abram, N. J., Thomas, E.R., McConnell, J.R., Mulvaney, R., Bracegirdle, T.J., Sime, L.C., and Aristarain, A.J., (2010), Ice core evidence for a 20th century decline of sea ice in the Bellingshausen Sea, Antarctica, *Journal of Geophysical Research*, 115, DOI:10.1029/2010JD014644.

Abram, N. J., Wolff, E.W., and Curran, M.J., (2013), A review of sea ice proxy information from polar ice cores, *Quaternary Science Reviews*, 79, 168-183.

Allen, C. S., Oakes-Fretwell, L., Anderson, J.B., and Hodgson, D.A., (2010), A record of Holocene glacial and oceanographic variability in Neny Fjord, Antarctic Peninsula, *The Holocene*, 20, 551–564.

Allen, C. S., Pike, J., and Pudsey, C.J., (2011), Last glacial-interglacial sea-ice cover in the SW Atlantic and its potential role in global deglaciation, *Quaternary Science Reviews*, 30, 2446-2458.

Anderson, R. F., Ali, S., Bradtmiller, L.I., Nielsen, S.H.H., Fleisher, M.Q., Anderson, B.E., and Burckle, L.H., (2009), Wind-Driven Upwelling in the Southern Ocean and the Deglacial Rise in Atmospheric CO2, *Science*, 323, 1443-1448.

Armand, L. K. (2000), An Ocean of Ice - Advances in the Estimation of Past Sea Ice in the Southern Ocean, *GSA Today*, 10, 1-7.

Armand, L.K., and Leventer, A., (2010), Palaeo sea ice distribution and reconstruction derived from the geological record. In: Thomas, D.N., G.S., Dieckmann, (Eds.), Sea Ice, Second Ed. pp.469- 529, Wiley-Blackwell, Oxford, UK. ch13.

Armand, L. K., Crosta, X., Romeroc, O., and Pichon, J.J., (2005), The biogeography of major diatom taxa in Southern Ocean sediments: 1. Sea ice related species, *Palaeogeography, Palaeoclimatology, Palaeoecology*, 223, 93– 126.

Armbrust, V. E., (2009), The life of diatoms in the world's oceans, *Nature*, 459, DOI:10.1038/nature08057.

Atkinson, H. M., Huang, R.-J., Chance, R., Roscoe, H.K., Hughes, C., Davidson, B., Schönhardt, A., Mahajan, A.S., Saiz-Lopez, A., Hoffman, T., and Lizz, P.S., (2012), Iodine emissions from the sea ice of the Weddell Sea, *Atmospheric Chemistry and Physics Discussions*, 12, 11229-11244.

Barbara, L., Crosta, X., Massé, G. and Ther, O., (2010) Deglacial environments during the Holocene in East Antarctica, *Quaternary Science Reviews*, 29, 2731-2740.

Barbara, L., Crosta, X., Schmidt, S., and Massé, G., (2013), Diatoms and biomarkers evidence for major changes in sea ice conditions prior the instrumental period in Antarctic Peninsula, *Quaternary Science Reviews*, 79, 99-110.

Bard, E., and Rickaby, E.M., (2009), Migration of the subtropical front as a modulator of glacial climate, *Nature*, 460, DOI:10.1038/nature08189.

Barker, S., Diz, P., Vautravers, M.J., Pike, J., Knorr, G., Hall, I.R., and Broecker, W.S., (2009), Interhemispheric Atlantic seesaw response during the last deglaciation, *Nature*, 457, DOI:10.1038/nature07770.

Bianchi, C., and Gersonde, R., (2004), Climate evolution at the last deglaciation: the role of the Southern Ocean, *Earth and Planetary Science Letters*, 228, 407– 424.

Brandon, M. A., Cottier, F.R., and Nilsen, F., (2010), Sea Ice and Oceanography. In: Thomas, D.N., G.S., Dieckmann, (Eds.), Sea Ice, Second Ed. pp.469- 529, Wiley-Blackwell, Oxford, UK. ch3.

Brown, T. A., Belt, S.T., Tatarekm, A., and Mundy, C.J., (2014a), Source identification of the Arctic sea ice proxy IP25, *Nature Communications*, 5, DOI:10.1038/ncomms5197.

Brown , T. A., Yurkowski, D.J., Ferguson, S.H., Alexander, C., and Belt, S.T., (2014b), H-Print: a new chemical fingerprinting approach for distinguishing primary production sources in Arctic ecosystems, *Environmental Chemistry Letters*, 12, 387-392.

Buffen, A., Leventer, A., Rubin, A., and Hutchins, T., (2007), Diatom assemblages in surface sediments of the northwestern Weddell Sea, Antarctic Peninsula, *Marine Micropaleontology*, 62, 7–30.

Calvo, E., Pelejero, C., De Deckker, P., and Logan, A., (2007), Antarctic deglacial pattern in a 30 kyr record of sea surface temperature offshore South Australia, *Geophysical Research Letters*, 34, DOI:10.1029/2007GL029937.

Campagne, P., Crosta, X., Houssais, M.N., Swingedouw, D., Schmidt, S., Martin, A., Devred, E., Capo, S., Marieu, V., Closset, I., and Massé, G., (2015), Glacial ice and atmospheric forcing on the Mertz Glacier Polynya over the past 250 years, *Nature Communications*, 6, DOI:10.1038/ncomms7642.

Carsey, F. D., (1992), Microwave remote sensing of sea ice, American Geophysical Union, Geophysical monograph no:68 0065-8448, Washington, DC, 462pp.

Carter, L., Manighetti, B., Ganssen, G., and Northcote, L., (2008), Southwest Pacific modulation of abrupt climate change during the Antarctic Cold Reversal–Younger Dryas, *Palaeogeography, Palaeoclimatology, Palaeoecology*, 260, 284–298.

Cheng, H., Edwards, L.R., Broecker, W.S., Denton, G.H., Kong, X., Wang, Y., Zhang, R., and Wang, X., (2009), Ice Age Terminations, *Science*, 326, DOI:10.1126/science.1177840.

Clark, P. U., Dyke, A.S., Shakun, J.D., Carlson, A.E., Clark, J., Wohlfarth, B., Mitrovica, J.X., Hostetler, S.W., and McCabe, A.M., (2009), The Last Glacial Maximum, *Science*, 325, 710-714.

CLIMAP Project Members, (1976), The surface of the ice-age Earth, *Science*, 191, 1131-1137.

CLIMAP Project Members, (1981), Seasonal reconstruction of the Earth's surface at the last glacial maximum, *Geological Society of America, Map and Chart Series*, C36.

Collins, L. G., Allen, C.S., Pike, J., Hodgson, D.A., Weckström, K., and Massé, G., (2013), Evaluating highly branched isoprenoid (HBI) biomarkers as a novel Antarctic sea-ice proxy in deep ocean glacial age sediments, *Quaternary Science Reviews*, 79, 87–98.

Collins, L. G., Pike, J., Allen, C.S. and Hodgson, D.A., (2012), High-resolution reconstruction of southwest Atlantic sea-ice and its role in the carbon cycle during marine isotope stages 3 and 2. *Palaeoceanography*, 27, DOI:10.1029/2011PA002264.

Comiso, J.C., (2010), Large-scale characteristics and variability of the global sea ice cover. In: Thomas, D.N., G.S., Dieckmann, (Eds.), Sea Ice. pp.112- 142, Wiley-Blackwell, Oxford, UK. Ch4.

Comiso, J. C., (2000), updated 2015, *Bootstrap Sea Ice Concentrations from Nimbus-7 SMMR and DMSP SSM/I-SSMIS*, Version 2, Boulder, Colorado USA: NASA National Snow and Ice Data Centre Distributed Active Archive Centre. http://dx.doi.org/10.5067/J6JQLS9EJ5HU.

Comiso, J.C., (2010), Variability and Trends of the Global Sea Ice Cover, in Sea Ice, edited by D. N. Thomas, and Dieckmann, G.S., pp. 247- 282, Blackwell Publishing LtD. ch6.

Crosta, X., Pichon, J-J., and Burckle, L.H., (1998), Application of modern analog technique to marine Antarctic diatoms: Reconstruction of maximum sea-ice extent at the Last Glacial Maximum, *Palaeoceanography*, 13, 284-297.

Crosta, X., Sturm, A., Armand, L., and Pichon, J.-J., (2004), Late Quaternary sea ice history in the Indian sector of the Southern Ocean as recorded by diatom assemblages, *Marine Micropaleontology*, 50, 209-223.

Crowley, T. J., (1992), North Atlantic deep water cools the southern hemisphere *Palaeoceanography*, 7, 489-497.

Cunningham, W. L., and Leventer, A., (1998), Diatom assemblages in surface sediments of the Ross Sea: relationship to present oceanographic conditions, *Antarctic Science*, 10, 134-146.

Curran, M. A. J., van Ommen, T.D., Morgan, V., Phillips, K.L., and Palmer, A.S., (2003), Ice Core Evidence for Antarctic Sea Ice Decline Since the 1950s, *Science*, 302, 1203-1206.

De Deckker, P., Moros, M., Perner, K., and Jansen, E., (2012), Influence of the tropics and southern westerlies on glacial interhemispheric asymmetry, *Nature Geoscience*, 5, DOI: 10.1038/NGEO1431.

de Vernal, A., Gersonde, R., Goosse, H., Seidenkrantz, M.S., and Wolff, E.W., (2013), Sea ice in the paleoclimate system: the challenge of reconstructing sea ice from proxies- an introduction, *Quaternary Science Reviews*, 79, 1-8.

DeConto, R., Pollard, D., and Harwood, D., (2007), Sea ice feedback and Cenozoic evolution of Antarctic climate and ice sheets, *Paleoceanography*, 22, DOI:10.1029/2006PA001350.

Denis, D., Crosta, X., Barbara, L., Massé, G., Renssen, H., Ther, O., and Giraudeau, J., (2010), Sea ice and wind variability during the Holocene in East Antarctica: insight on middleehigh latitude coupling, *Quaternary Science Reviews*, 29, 3709-3719.

Dieckmann, G. S., and Hellmer, H.H., (2010), The Importance of sea ice: An overview, in Sea Ice, edited by D. N. Thomas, and Dieckmann, G.S., pp. 1-22, Blackwell Publishing LtD. ch1.

Divine, D. V., Koç, N., Isaksson, E., Nielsen, S., Crosta, x., and Godtliebsen, F., (2010), Holocene Antarctic climate variability from ice and marine sediment cores: Insights on ocean–atmosphere interaction, *Quaternary Science Reviews*, 29, 303–312.

Eicken, H., (2010), From the Microscopic, to the Macroscopic, to the regional scale: Growth, microstructure and properties of sea ice., in Sea ice: an introduction to its physics, chemistry, biology and geology, edited by D. N. Thomas, and Dieckmann, G.S., pp. 22-81, Blackwell Publishing LtD, Oxford. Ch 2.

Esper, O., and Gersonde, R., (2014), New tools for the reconstruction of Pleistocene Antarctic sea ice, *Palaeogeography, Palaeoclimatology, Palaeoecology*, 399, 260–283.

Esper, O., Gersonde, R., Kadagies, N., (2010), Diatom distribution in southeastern Pacific surface sediments and their relationship to modern environmental variables, *Palaeogeography, Palaeoclimatology, Palaeoecology*, 27, 1-27.

Etourneau, J., Collins, L.G., Willmott, V., Kim, J.H., Barbara, L., Leventer, A., Schouten, S., Sinninghe Damsté, J.S., Bianchini, A., Klein, V., Crosta, X., and Massé, G., (2013), Holocene climate variations in the western Antarctic Peninsula: evidence for sea ice extent predominantly controlled by changes in insolation and ENSO variability, *Climate of the Past*, 9, 1431–1446.

Falciatore, A., and Bowler, C., (2002), Revealing the molecular secrets of marine diatoms, *Annual Review of Plant Biology*, 53, DOI:10.1146/annurev.arplant.1153.091701.153921.

Falkowski, P. G., Barber, R.T., and Smetacek, V., (1998), Biogeochemical Controls and Feedbacks on Ocean Primary Production, *Science*, 281, 200-206.

Ferrari, R., Jansen, M.F., Adkins, J.F., Burke, A., Stewart, A.L., and Thompson, A.F., (2014), Antarctic sea ice control on ocean circulation in present and glacial climates, *PNAS*, 111, 8753–8758.

Field, C. B., Behrenfeld, M.J., Randerson, J.T., and Falkowski, P., (1998), Primary Production of the Biosphere: Integrating Terrestrial and Oceanic Components, *Science*, 281, 237-240.

Fischer, H., Fundel, F., Ruth, U., Twarloh, B., Wegner, A., Udisti, R., Becagli, S., Castellano, E., Morganti, A., Severi, M., Wolff, E., Littot, G., Röthlisberger, R., Mulvaney, R., Hutterli, M.A., Kaufmann, P., Federer, U., Lambert, F., Bigler, M., Hansson, M., Jonsell, U., de Angelis, M., Boutron, C., Siggaard-Andersen, M.L., Steffensen, J.P., Barbante, C., Gaspari, V., Gabrielli, P., and Wagenbach, D., (2007), Reconstruction of millennial changes in dust emission, transport and regional sea ice coverage using the deep EPICA ice cores from the Atlantic and Indian Ocean sector of Antarctica, *Earth and Planetary Science Letters*, 260, 340–354.

Fischer, H., Schmitt, J., Lüthi, D., Stocker, T.F., Tschumi, T., Parekh, P., Joos, F., Köhler, P., Völker, C., Gersonde, R., Barbante, C., Floch, M.L., Raynaud, D., and Wolff, E., (2010), The role of Southern Ocean processes in orbital and millennial CO2 variations – A synthesis, *Quaternary Science Reviews*, 29, 193–205.

Flato, G., Marotzke, J., Abiodun, B., Braconnot, P., Chou, S.C., Collins, W., Cox, P., Driouech, F., Emori, S., Eyring, V., Forest, C., Gleckler, P., Guilyardi, E., Jakob, C., Kattsov, V., Reason, C., and Rummukainen, M., (2014), Evaluation of Climate Models, in Climate Change 2013: The Physical Science Basis. Contribution of Working Group I to the Fifth Assessment Report of the Intergovernmental Panel on Climate Change, edited by T. F. Stocker, Qin, D., Plattner, G.-K., Tignor, M., Allen, S.K., Boschung, J., Nauels, A., Xia, Y., Bex, V., and Midgley, P.M., Cambridge University Press, Cambridge, United Kingdom and New York, NY, USA.

Fraser, C. I., Nikula, R., Spencer, H.G., and Waters, J.M., (2009), Kelp genes reveal effects of subantarctic sea ice during the Last Glacial Maximum, *PNAS*, 106, 3249-3253.

Gao, K., and Campbell, D.A., (2014), Photophysiological responses of marine diatoms to elevated CO2 and decreased pH: a review, *Functional Plant Biology*, 41, 449-459.

Garibotti, I. A., Vernet, M., and Ferrario, M.E., (2005), Annually recurrent phytoplanktonic assemblages during summer in the seasonal ice zone west of the Antarctic Peninsula (Southern Ocean), *Deep-Sea Research I*, 52, 1823–1841.

Gersonde, R., Crosta, X., Abelmann, A., and Armand, L., (2005), Sea-surface temperature and sea ice distribution of the Southern Ocean at the EPILOG Last Glacial Maximum- a circum-Antarctic view based on siliceous microfossil records, *Quaternary Science Reviews*, 24, 869–896.

Gersonde, R., de Vernal, A., and Wolff, E.W., (2014), Past sea ice reconstruction - proxy data and modeling, *PAGES Magazine*, 22, 97.

Gersonde, R., and Zielinski, U., (2000), The reconstruction of late Quaternary Antarctic sea-ice distribution—the use of diatoms as a proxy for sea-ice, *Palaeogeography, Palaeoclimatology, Palaeoecology*, 162, 263–286.

Gildor, H., and Tziperman, E., (2000), Sea ice as the glacial cycles climate switch: role of seasonal and orbital forcing, *Palaeoceanography*, 15, 605-615.

Gloersen, P., W.J., Campbell, D.J., Cavalieri, J.C., Comiso, C.L., Parkinson, and H.J., Zwally (1992), *Arctic and Antarctic Sea Ice, 1978- 1987, Satellite Passive-Microwave Observations and Analysis*. NASA Special Publication, 511, 289 pp, National Aeronautics and Space Administration, Washington, D.C.

Goosse, H., Renssen, H., Timmermann, A., Bradley, R.S., and Mann, M.E., (2006), Using paleoclimate proxy-data to select optimal realisations in an ensemble of simulations of the climate of the past millennium, *Climate Dynamics*, 27, DOI:10.1007/s00382-00006-00128-00386.

Goosse, H., Roche, D.M., Mairesse, A., Berger, M., (2013), Modelling past sea ice changes, *Quaternary Science Reviews*, 79, 191-206.

Gottschalk, J., Skinner, L.C., and Waelbroeck, C., (2015), Contribution of seasonal sub-Antarctic surface water variability to millennial-scale changes in atmospheric CO2over the last deglaciation and Marine Isotope Stage 3, *Earth and Planetary Science Letters*, 411, 87-99.

Graham, R. M., de Boer, A.M., Heywood, K.J., Chapman, M.R., and Stevens, D.P., (2012), Southern Ocean fronts: Controlled by wind or topography?, *Journal of Geophysical Research*, 117, DOI:10.1029/2012JC007887

Granfors, A., Karlsson, A., Mattsson, E., Smith, W.O., and Abrahamsson, K., (2013), Contribution of sea ice in the Southern Ocean to the cycling of volatile halogenated organic compounds, *Geophysical Research Letters*, 40, DOI:10.1002/grl.50777.

Grigorov, I., Rigual-Hernandez, A.S., Honjo, S., Kemp, A.E.S., and Armand, L.K., (2014), Settling fluxes of diatoms to the interior of the Antarctic circumpolar current along 170°W, *Deep-Sea Research Part I: Oceanographic Research Papers*, 93, 1-13.

Hanna, E., (1996), The role of Antarctic sea ice in global climate change, *Progress in Physical Oceanography*, 20, 371-401.

Head, M., Gibbard, P., and Salvador, A., (2008), The Quaternary: its character and definition, *Episodes*, 31, 234-238.

Hervé, V., Derr, J., Douady, S., Quinet, M., Moisan, L., and Lopez, P.J., (2012), Multiparametric Analyses Reveal the pH-Dependence of Silicon Biomineralization in Diatoms, *PLOS one*, 7, e46722.

Hezel, P. J., Alexander, B., Bitz, C.M., Steig, E.J., Holmes, C.D., Yang, X., and Sciare, J., (2011), Modeled methanesulfonic acid (MSA) deposition in Antarctica and its relationship to sea ice, *Journal of Geophysical Research*, 116, DOI:10.1029/2011JD016383.

Hildebrand, M., (2008), Diatoms, Biomineralization Processes, and Genomics, *Chemical Reviews*, 108, 4855–4874.

Hillenbrand, C. D., and Cortese, G., (2006), Polar stratification: A critical view from the Southern Ocean, *Palaeogeography, Palaeoclimatology, Palaeoecology*, 242, 240–252.

Huang, K. F., Oppo, D.W., and Curry, W.B., (2014), Decreased influence of Antarctic intermediate water in the tropical Atlantic during North Atlantic cold events, *Earth and Planetary Science Letters*, 389, 200–208.

Hutson, W. H., (1980), The Agulhas Current during the Late Pleistocene: Analysis of Modern Faunal Analogs, *Science*, 207, 64-66.

Iida, T., and Odate, T., (2014), Seasonal variability of phytoplankton biomass and composition in the major water masses of the Indian Ocean sector of the Southern Ocean, *Polar Science*, 8, 283-297.

Imbrie, J., and Kipp, N.G., (1971), A New Micropaleontological Method for Quantitative Paleoclimatology: Application to a late Pleistocene Caribbean Core. In The Late Cenozoic Glacial Ages, edited by K. K. Turekian, pp. 71-147, Yale University Press, London.

Jansen, E. J., Overpeck, K.R., Briffa, J.-C., Duplessy, F., Joos, V., Masson-Delmotte, D., Olago, B., Otto-Bliesner, W.R., Peltier, S., Rahmstorf, R., Ramesh, D., Raynaud, D., Rind, O., Solomina, R., Villalba, and D. Zhang., (2007), Palaeoclimate. In: Climate Change 2007: The Physical Science Basis. Contribution of Working Group I to the Fourth Assessment Report of the Intergovernmental Panel on Climate Change, Cambridge University Press, Cambridge, United Kingdom and New York, NY, USA.

Jomelli, V., Favier, V., Vuille, M., Braucher, R., Martin, L., Blard, P.H., Colose, C., Brunstein, D., He, F., Khodri, M., Bourlés, D.L., Leanni, L., Rinterknecht, V., Grancher, D., Francou, B., Ceballos, J.L., Fonseca, H., Liu, Z., and Otto-Bliesner, B.L., (2014), A major advance of tropical Andean glaciers during the Antarctic cold reversal, *Nature*, 513, DOI:10.1038/nature13546.

Juggins, S., and Birks, J.B., (2012), Quantitative Environmental Reconstructions from Biological Data, in Tracking Environmental Change Using Lake Sediments, edited by H. J. B. Birks, Lotter, A.F., Jugins, S., and Smol, J.P., pp. 431-494, Springer Science and Business Media.

Kay, J. E., Medeiros, B., Hwang, Y.T., Gettelman, A., Perket, J., and Flanner, M.G., (2014), Processes controlling Southern Ocean shortwave climate feedbacks in CESM, *Geophysical Research Letters*, 41, DOI:10.1002/2013GL058315.

Kemp, A. E. S., Grigorov, I., Pearce, R.B., and Naveira Garabato, A.C., (2010), Migration of the Antarctic Polar Front through the mid-Pleistocene transition: evidence and climatic implications, *Quaternary Science Reviews*, 29, 1993-2009.

Kennicutt, M. C., Chown, S.L., Cassano, J.J., Liggett, D., Massom, R., Peck, L.S., Rintoul, S.R., Storey, J.W.V., Vaughan, D.G., Wilson, T.J., and Sutherland, W.J., (2014), Polar research: Six priorities for Antarctic science, *Nature*, 512, 23-25.

Kohfeld, K. E., Graham, R.M., de Boer, A.M., Sime, L.C., Wolff, E.W., Le Quéré, C., and Bopp, L., (2013), Southern Hemisphere Westerly Wind Changes during the Last Glacial Maximum: Paleo-data Synthesis, *Quaternary Science Reviews*, 68, 76-95.

Kostianoy, A. G., Ginzburg, A.I., Frankignoulle, M., and Delille, B., (2004), Fronts in the Southern Indian Ocean as inferred from satellite sea surface temperature data, *Journal of Marine Systems*, 45, 55– 73.

Kucera, M., Weinelt, M., Kiefer, T., Pflaumann, U., Hayes, A., Weinelt, M., Chen, M.-T., Mix, A.C., Barrows, T.T., Cortijo, E., Duprat, J., Juggins, S., and Waelbroeck, C., (2005), Reconstruction of sea-surface temperatures from assemblages of planktonic foraminifera: multi-technique approach based on geographically constrained calibration data sets and its application to glacial Atlantic and Pacific Oceans, *Quaternary Science Reviews*, 24, 951–998.

Lamy, F., Kaiser, J., Ninnemann, U., Hebbeln, D., Arz, H.W., and Stoner, J., (2004), Antarctic timing of surface water changes off Chile and Patagonian ice sheet response, *Science*, 304, 1959-1962.

Lazarus, D., Barron, J., Renaudie, J., Diver, P., Türke, A., (2014), Cenozoic Planktonic Marine Diatom Diversity and Correlation to Climate Change, *PLoS one*, 9, e84857.

Legendre, P., and Birks, H.J.B., (2012), From Classical to Canonical Ordination, in Tracking Environmental Change Using Lake Sediments, edited by H. J. B. Birks, Lotter, A.F., Jugins, S., and Smol, J.P., pp. 201-248, Springer Science and Business Media.

Lemieux-Dudon, B., Blayo, E., Petit, J.R., Waelbroeck, C., Svensson, A., Ritz, C., Barnola, J.M., Narcisi, B.M., and Parrenin, F., (2010), Consistent dating for Antarctic and Greenland ice cores, *Quaternary Science Reviews*, 29, 8–20.

Levitan, O., Dinamarca, J., Hochman, G., Falkowski, P.G., (2014), Diatoms: a fossil fuel of the future, *Trends in Biotechnology*, 32, 117-124.

Ling Ho, S., Mollenhauer, G., Lamy, F., Martínez-Garcia, A., Mohtadi, M., Gersonde, R., Hebbeln, D., Nunez-Ricardo, S., Rosell-Melé, A., and Tiedemann, R., (2012), Sea surface temperature variability in the Pacific sector of the Southern Ocean over the past 700 kyr, *Palaeoceanography*, 27, DOI:10.1029/2012PA002317.

Lisiecki, L. E., and Raymo, M.E., (2005a), A Pliocene-Pleistocene stack of 57 globally distributed benthic $\delta^{18}O$ records, *Paleoceanography*, 20, DOI:10.1029/2004PA001071.

Litchman, E., Klausmeier, C.A., and Yoshiyama, K., (2009), Contrasting size evolution in marine and freshwater diatoms, *PNAS*, 106, 2665–2670.

Lohmann, G., Pfeiffer, M., Laepple, T., Leduc, G., Kim, J.H., (2012), A model–data comparison of the Holocene global sea surface temperature evolution, *Climate of the Past*, 9, 1807–1839.

Maddison, E. J., Pike, J., and Dunbar, R., (2012), Seasonally laminated diatom-rich sediments from Dumont d'Urville Trough, East Antarctic Margin: Late-Holocene Neoglacial sea-ice conditions, *The Holocene*, 22, DOI: 10.1177/0959683611434223.

Manoj, M. C., and Thamban, M., (2015), Shifting frontal regimes and its influence on bioproductivity variations during the Late Quaternary in the Indian sector of Southern Ocean, *Deep Sea Research Part II: Topical Studies in Oceanography*, http://dx.DOI.org/10.1016/j.dsr1012.2015.1003.1011i.

MARGO project members., (2009), Constraints on the magnitude and patterns of ocean cooling at the Last Glacial Maximum, *Nature Geoscience*, 2, DOI: 10.1038/NGEO1411.

Massé, G., Belt, S., Crosta, X., Schmidt, S., Snape, I., Thomas, D.N., and Rowland, S.J., (2011), Highly branched isoprenoids as proxies for variable sea ice conditions in the Southern Ocean, *Antarctic Science*, 23, 487-498.

Masson, V., Vimeux, F., Jouzel, J., Morgan, V., Delmotte, M., Ciais, P., Hammer, C., Johnsen, S., Lipenkov, V.Y., Thompson, E.M., Petit, J.R., Steig, E.J., Stievenard, M., Vaikmae, R., (2000), Holocene Climate Variability in Antarctica Based on 11 Ice-Core Isotopic Records, *Quaternary Research*, 54, 348–358.

Matsumoto, K., Lynch-Stieglitz, J., and Anderson, R.F., (2001), Similar glacial and Holocene Southern Ocean hydrography, *Palaeoceanography*, 16, 445-454.

Mattson, E., Karlsson, A., Smith, W.O., and Abrahamsson, K., (2012), The relationship between biophysical variables and halocarbon distributions in the waters of the Amundsen and Ross Seas, Antarctica, *Marine Chemistry*, 140-141, 1-9.

Mayewski, P. A., Meredith, M.P., Summerhayes, C.P., Turner, J., Worby, A., Barrett, P.J., Casassa, G., Bertler, N.A.N., Bracegirdle, T., Naveira Garabato, A.C., Bromwich, D., Campbell, H., Hamilton, G.S., Lyons, W.B., Maasch, K.A., Aoki, S., Xiao, C., and Tas van Ommen., (2009), State of the Antarctic and Southern Ocean Climate System, *Reviews of Geophysics*, 47, RG1003.

McKay, R., Naish, T., Carter, L., Riesselman, C., Dunbarc, R., Sjunneskog, C., Winter, D., Sangiorgi, F., Warren, C., Pagani, M., Schouten, S., Willmott, V., Levy, R., DeConto, R., and Powell, R.D., (2012), Antarctic and Southern Ocean influences on Late Pliocene global cooling, *PNAS*, 109, 6423–6428.

Meredith, M. P. (2013), Replenishing the abyss, *Nature Geoscience*, 6, 166-167.

Mix, A. C., Bard, E., and Schneider, R., (2001), Environmental processes of the ice age: land, oceans, glaciers (EPILOG), *Quaternary Science Reviews*, 20, 627-657.

Monnin, E., Indermühle, A., Dällenbach, A., Flückiger, J., Stauffer, B., Stocker, D.F., Raynaud, D., and Barnola, J.M., (2001), Atmospheric CO2 concentrations over the last glacial termination, *Science*, 291, 112-114.

Moros, M., De Deckker, P., Jansen, E., Perner, K., Telford, R.J., (2009), Holocene climate variability in the Southern Ocean recorded in a deep-sea sediment core off South Australia, *Quaternary Science Reviews*, 28, 1932–1940.

Neil, H. L., and Carter, L., (2004), Thermal isolation of Campbell Plateau, New Zealand, by the Antarctic Circumpolar Current over the past 130 kyr, *Palaeoceanography*, 19, DOI:10.1029/2003PA000975.

Newnham, R. M., Lowe, D.J., Giles, T., and Alloway, B.V., (2007), Vegetation and climate of Auckland, New Zealand, since ca. 32 000 cal. yr ago: support for an extended LGM, *Journal of Quaternary Science*, 22, 517–534.

Newnham, R. M., Vandergoes, M.J., Sikes, E., Carter, L., Wilmshurst, J.M., Lowe, D.J., McGlone, M.S., and Sandiford, A., (2012), Does the bipolar seesaw extend to the terrestrial southern mid-latitudes?, *Quaternary Science Reviews*, 36, 214-222.

NGRIP Members., (2004), High-resolution record of Northern Hemisphere climate extending into the last interglacial period, *Nature*, 431, 141-151.

Oberhuber, J. M., (1988), An atlas based on the 'COADS' data set: The budgets of heat, buoyancy and turbulent kinetic energy at the surface of the global ocean, Max-Planck-Institute for Meteorology, Hamburg.

Ohshima, K. I., Fukamachi, Y., Williams, G.D., Nihashi, S., Roquet, F., Kitade, Y., Tamura, T., Hirano, D., Herraiz-Borreguero, L., Field, I., Hindell, M., Aoki, S., and Wakatsuchi, M., (2013), Antarctic Bottom Water production by intense sea-ice formation in the Cape Darnley polynya, *Nature Geoscience*, 6, DOI: 10.1038/NGEO1738.

Olguín, H. F., and Alder, V.A., (2011), Species composition and biogeography of diatoms in antarctic and subantarctic (Argentine shelf) waters (37–76°S), *Deep-Sea Research II*, 58, 139–152.

Paillard, D., (2015), Quaternary glaciations: from observations to theories, *Quaternary Science Reviews*, 107, 11-24.

Paillard, M., Weinelt, M., Kiefer, T., Pflaumann, U., Hayes, A., Weinelt, M., Chen, M.-T., Mix, A.C., Barrows, T.T., Cortijo, E., Duprat, J., Juggins, S., and Waelbroeck, C., (2005), Reconstruction of sea-surface temperatures from assemblages of planktonic foraminifera: multi-technique approach based on geographically constrained calibration data sets and its application to glacial Atlantic and Pacific Oceans, *Quaternary Science Reviews*, 24, 951–998.

Parkinson, C. L., and Cavalieri, D.J., (2012), Antarctic sea ice variability and trends, 1979–2010, *The Cryosphere*, 6, 871–880.

Parkinson, C. L., Cavalieri, D.J., Gloersen, P., Zwally, H.J., Comiso, J.C., (1999), Arctic sea ice extents, areas and trends, 1978-1996, *Journal of Geophysical Research*, 97, 17715-17728.

Parrenin, F., and Paillard, D., (2004), Amplitude and phase of glacial cycles from a conceptual model, *Earth and Planetary Science Letters*, 214, 243-250.

Petherick, L., McGowan, H., and Moss, P., (2008), Climate variability during the Last Glacial Maximum in eastern Australia: evidence of two stadials?, *Journal of Quaternary Science*, 23, 787–802.

Prasad, T. G. (1997), Annual and seasonal mean buoyancy fluxes for the tropical Indian Ocean Current, *Science*, 73, 667-674.

Putnam, A. E., Denton, G.H., Schaefer, J.M., Barrell, D.J.A., Andersen, B.G., Finkel, R.C., Schwartz, R., Doughty, A.M., Kaplan, M.R., and Schlüchter, C., (2010), Glacier advance in southern middle-latitudes during the Antarctic Cold Reversal, *Nature Geoscience*, 3, 700-704.

Rahmstorf, S., (2006), Thermohaline Ocean Circulation, in Encyclopaedia of Quaternary Sciences, edited by S. A. Elias, Elsevier, Amsterdam.

Rasmussen., O., S., Andersen, K.K., Svensson, A.M., Steffensen, J.P., Vinther, B.M., Clause, H.B., Siggaard-Andersen, M.L., Johnsen, S.J., Larsen, L.B., Dahl-Jensen, D., Bigler, M., Röthlisberger, R., Fischer, H., Goto-Azuma, K., Hansson, M.E., and Ruth, U., (2006), A new Greenland ice core chronology for the last glacial termination, *Journal of Geophysical Research: Atmospheres*, 111, D06102.

Reeves, J. M., Barrows, T.T., Cohen, T.J., Kiem, A.S., Bostock, H.C., Fitzsimmons, K.E., Jansen, J.D., Kemp, J., Krause, C., Petherick, L., Phipps, S.J., and OZ-INTIMATE Members, (2013), Climate variability over the last 35,000 years recorded in marine and terrestrial archives in the Australian region: an OZ-INTIMATE compilation, *Quaternary Science Reviews*, 74, 21-34.

Romero, O. E., Kim, J.H., Bárcena, M.A., Hall, I.R., Zahn, R., and Schneider, R., (2015), High-latitude forcing of diatom productivity in the southern Agulhas Plateau during the past 350kyr, *Paleoceanography*, 30, DOI:10.1002/2014PA002636.

Ronge, T. A., Steph, S., Tiedemann, R., Prange, M., Merkel, U., Nürnberg, D., and Kuhn, G., (2015), Pushing the boundaries: Glacial/interglacial variability of intermediate and deep waters in the southwest Pacific over the last 350,000 years, *Paleoceanography*, 30, DOI:10.1002/2014PA002727.

Röthlisberger, R., Crosta, X., Abram, N.J., Armand, L., and Wolff, E.W., (2010), Potential and limitations of marine and ice core sea ice proxies: an example from the Indian Ocean sector, *Quaternary Science Reviews*, 29, 296–302.

Röthlisberger, R., Mudelsee, M., Bigler, M., de Angelis, M., Fischer, H., Hansson, M., Lambert, F., Masson-Delmotte, V., Sime, L., Udisti, R., Wolff, E.W., (2008), The Southern Hemisphere at glacial terminations: insights from the Dome C ice core, *Climate of the Past*, 4, 345–356.

Russell, A., and McGregor, G.R., (2010), Southern hemisphere atmospheric circulation: impacts on Antarctic climate and reconstructions from Antarctic ice core data, *Climatic Change*, 99, 155–192.

Saba, G. K., Fraser, W.R., Saba, V.S., Iannuzzi, R.A., Coleman, K.E., Doney, S.C., Ducklow, H.W., Martinson, D.G., Miles, T.N., Patterson-Fraser, D.L., Stammerjohn, S.E., Steinberg, D.K., and Schofield, O.M., (2014), Winter and spring controls on the summer food web of the coastal West Antarctic Peninsula, *Nature Communications*, 5, DOI:10.1038/ncomms5318.

Saenko, O. A., and Weaver, A.J., (2001), Importance of wind-driven sea ice motion for the formation of Antarctic Intermediate Water in a global climate model, *Geophysical Research Letters*, 28, 4147-4150.

Sandven, S., and Johannessen, O.M., (2006), Sea ice monitoring by remote sensing. In Gower, J.F.R., eds, Manual of remote sensing, Vol. 6, Remote sensing of the marine environment. Third edition. Bethesda, MA, American Society for Photogrammetry and Remote Sensing, 241–283.

Scala, S., and Bowler, C., (2001), Molecular insights into the novel aspects of diatom biology, *Cellular and Molecular Life Sciences*, 58, 1666–1673.

Schneider-Mor, A., Yam, R., Bianchi, C., Kunz-Pirrung, M., Gersonde, R., and Shemesh, A., (2005), Diatom stable isotopes, sea ice presence and sea surface temperature records of the past 640 ka in the Atlantic sector of the Southern Ocean, *Geophysical Research Letters*, 32, DOI:10.1029/2005GL022543.

Shetye, S. S., Mohan, R., and Nair, A., (2014), Latitudinal shifts in the Polar Front in Indian sector of the Southern Ocean: evidences from silicoflagellate assemblage, *Geosciences Journal*, 18, 241−246.

Speer, K., S.R., Rintoul, and B., Sloyan (2000), The Diabatic Deacon Cell, *Journal of Physical Oceanography*, 30, 3212-3222.

Shevenell, A. E., Ingalls, A.E., Domack, E.W., and Kelly, C., (2011), Holocene Southern Ocean surface temperature variability west of the Antarctic Peninsula, *Nature*, 470, 250-254.

Shevenell, A. E., and Kennett, J.P., (2002), Antarctic Holocene climate change: A benthic foraminiferal stable isotope record from Palmer Deep, *Paleoceanography*, 17, DOI: 10.1029/2000PA000596.

Shulmeister, J., Goodwin, I., Renwick, J., Harle, K., Armand, L., McGlone, M.S., Cook, E., Dodson, J., Hesse, P.P., Mayewski, P., and Curran, M., (2004), The Southern Hemisphere westerlies in the Australasian sector over the last glacial cycle: a synthesis, *Quaternary International*, 118–119, 23–53.

Simmonds, I., (2015), Comparing and contrasting the behaviour of Arctic and Antarctic sea ice over the 35 year period 1979–2013, *Annals of Glaciology*, 56, DOI:10.3189/2015AoG3169A3909.

Smith, W. O., and Nelson, D.M., (1986), Importance of Ice Edge Phytoplankton Production in the Southern Ocean, *BioScience*, 36, 251-257.

Sokolov, S., and Rintoul, S.R., (2009a), Circumpolar structure and distribution of the Antarctic Circumpolar Current fronts: 2. Variability and relationship to sea surface height, *Journal of Geophysical Research*, 114, DOI:10.1029/2008JC005248.

Sokolov, S., and Rintoul, S.R., (2009b), Circumpolar structure and distribution of the Antarctic Circumpolar Current fronts: 1. Mean circumpolar paths, *Journal of Geophysical Research*, 114, DOI:10.1029/2008JC005108.

Spolaor, A., Vallelonga, P., Gabrieli, J., Kehrwald, N., Turetta, C., Cozzi, G., Poto, L., Plane, J.M.C., Boutron, C., and Barbante, C., (2013), Speciation analysis of iodine and bromine at picogram-per-gram levels in polar ice, Analytical and Bioanalytical Chemistry, 405, 647-654.

Spolaor, A., Vallelonga, P., Gabrieli, J., Martma, T., Björkman, M.P., Isaksson, E., Cozzi, G., Turetta, C., Kjær, H.A., Curran, M.A.J., Moy, A.D., Schönhardt, A., Blechschmidt, A.M., Burrows, J.P., Plane, J.M.C., and Barbante, C., (2014), Seasonality of halogen deposition in polar snow and ice, *Atmospheric Chemistry and Physics Discussions*, 14, 8185–8207.

Spreen, G., Kaleschke, L., and Heygster, G., (2008), Sea ice remote sensing using AMSR-E 89-GHz channels, *Journal of Geophysical Research: Oceans*, 113, DOI:10.1029/2005JC003384.

Stenni, B., Masson-Delmotte, V., Johnsen, S., Jouzel, J., Longinelli, A., Monnin, E., Röthlisberger, R., and Selmo, E., (2001), An Oceanic Cold Reversal During the Last Deglaciation, *Science*, 293, 2074-2077.

Stephens, T., Atkin, D., Augustinus, P., Shane, P., Lorrey, A., Street-Perrott, A., Nilsson, A., and Snowball, I., (2012), A late glacial Antarctic climate teleconnection and variable Holocene seasonality at Lake Pupuke, Auckland, New Zealand, *Journal of Paleolimnology*, 48, 785–800.

Sullivan, C. W., McClain, C.R., Comiso, J.C., and Smith, W.O., (1988), Phytoplankton standing crops within an Antarctic ice edge assessed by satellite remote sensing, *Journal of Geophysical Research*, 93, 12487-12498.

Taylor, F., McMinn, A., and Franklin, D., (1997), Distribution of diatoms in surface sediments of Prydz Bay, Antarctica, *Marine Micropaleontology*, 32, 209-229.

Telford, R. J., and Birks, H.J.B., (2005), The secret assumption of transfer functions: problems with spatial autocorrelation in evaluating model performance, *Quaternary Science Reviews*, 24, 2173–2179.

Tew, K. S., Kao, Y.C., Ko, F.C., Kuo, J., Meng, P.J., Liu, P.J., and Glover, D.C., (2014), Effects of elevated CO_2 and temperature on the growth, elemental composition, and cell size of two marine diatoms: potential implications of global climate change, *Hydrobiologia*, 741, 79–87.

Tolotti, R., Salvi, C., Salvi, G., and Bonci, M.C., (2013), Late Quaternary climate variability as recorded by micropalaeontological diatom data and geochemical data in the western Ross Sea, Antarctica, *Antarctic Science*, 25, 804–820.

Turney, C. S. M., Haberle, S., Fink, D., Kershaw, A.P., Barbetti, M., Barrows, T.T., Black, M., Cohen, T.J., Corrège, T., Hesse, P.P., Hua, Q., Johnston, R., Morgan, V., Moss, P., Nanson, G., Van Ommen, T., Rule, S., Williams, N.J., Zhao, J.X., D'costa, D., Feng,

Y.X., Gagan, M., Mooney, S., and Xia, Q., (2006), Integration of ice-core, marine and terrestrial records for the Australian Last Glacial Maximum and Termination: a contribution from the OZ INTIMATE group, *Journal of Quaternary Science*, 21, 751–761.

Vandergoes, M. J., Newnham, R.M., Denton, G.H., Blaauw, M., Barrell, D.J.A., (2013), The anatomy of Last Glacial Maximum climate variations in south Westland, New Zealand, derived from pollen records, *Quaternary Science Reviews*, 74, 215-229.

Vanormelingen, P., Verleyen, E., and Vyverman, W., (2008), The diversity and distribution of diatoms: from cosmopolitanism to narrow endemism, *Biodiversity and Conservation*, 17, 393–405.

Vaughan, D. G., Comiso, J.C., Allison, I., Carrasco, J., Kaser, G., Kwok, R., Mote, P., Murray, T., Paul, F., Ren, J., Rignot, E., Solomina, O., Steffen, K., and Zhang, T., (2013), Observations: Cryosphere, in Climate Change 2013: The Physical Science Basis. Contribution of Working Group I to the Fifth Assessment Report of the Intergovernmental Panel on Climate Change, edited by T. F. Stocker, Qin, D., Plattner, G.K., Tignor, M., Allen, S.K., Boschung, J., Nauels, A., Xia, Y., Bex, V., and Midgley, P.M.,, Cambridge University Press, Cambridge, United Kingdom and New York, NY, USA.

Verleye, T. J., and Louwye, S., (2010), Recent geographical distribution of organic-walled dinoflagellate cysts in the southeast Pacific (25–53°S) and their relation to the prevailing hydrographical conditions, *Palaeogeography, Palaeoclimatology, Palaeoecology*, 298, 319–340.

Williams, M., Dunkerley, D., De Dekker, P., Kershaw, P., and Chappell, J., (1998), Quaternary Environments, Arnold, 329, pages.

Williams, P. W., Neil, H.L., and ZhaoJ.-X., (2010), Age frequency distribution and revised stable isotope curves for New Zealand speleothems: palaeoclimatic implications, *International Journal of Speleology*, 39, 99-112.

Wolff, E. W., Barbante, C., Becagli, S., Bigler, M., Boutron, C.F., Castellano, E., de Angelis, M., Federer, U., Fischer, H., Fundel, F., Hansson, M., Hutterli, M., Jonsell, U., Karlin, T., Kaufmann, P., Lambert, F., Littot, G.C., Mulvaney, R., Röthlisberger, R., Ruth, U., Severi, M., Siggaard-Andersen, M.L., Sime, L.C., Steffensen, J.P., Stocker, T.F., Traversi, R., Twarloh, B., Udisti, R., Wagenbach, D., and Wegner, A., (2010), Changes in environment over the last 800,000 years from chemical analysis of the EPICA Dome C ice core, *Quaternary Science Reviews*, 29, 285–295.

Wolff, E. W., Fischer, H., Fundel, F., Ruth, U., Twarloh, B., Littot, G.C., Mulvaney, R., Röthlisberger, R., de Angelis, M., Boutron, C.F., Hansson, M., Jonsell, U., Hutterli, M.A., Lambert, F., Kaufmann, P., Stauffer, B., Stocker, T.F., Steffensen, J.P., Bigler, M., Siggaard-Andersen, M.L., Udisti, R., Becagli, S., Castellano, E., Severi, M., Wagenbach, D., Barbante, C., Gabrielli, P., and Gaspari, V., (2006), Southern Ocean sea-ice extent, productivity and iron flux over the past eight glacial cycles, *Nature*, 440, DOI:10.1038/nature04614.

Wolff, E. W., Fischer, H., and Röthlisberger, R., (2009), Glacial terminations as southern warmings without northern control, *Nature Geoscience*, 2, DOI:10.1038/NGEO1442.

Wolff, E. W., Rankin, M., and Röthlisberger, R., (2003), An ice core indicator of Antarctic sea ice production?, *Geophysical Research Letters*, 30, DOI:10.1029/2003GL018454.

Xie, R. C., Marcantonio, F., and Schmidt, M.W., (2014), Reconstruction of intermediate water circulation in the tropical North Atlantic during the past 22,000 years, *Geochimica et Cosmochimica Acta*, 140, 455–467.

Xie, K. F., Oppo, D.W., and Curry, W.B., (2014), Decreased influence of Antarctic intermediate water in the tropical Atlantic during North Atlantic cold events, *Earth and Planetary Science Letters*, 389, 200–208.

Yi, J., Jang, H.S., Lee, J.S., and Park, W.L., (2012), Bioinspired Morphogenesis of Highly Intricate and Symmetric Silica Nanostructures, *Nano Letters*, 12, 3743−3748.

Zielinski, U., and Gersonde, R., (1997), Diatom distribution in Southern Ocean surface sediments (Atlantic sector): Implications for paleoenvironmental reconstructions, *Palaeogeography, Palaeoclimatology, Palaeoecology*, 129, 213-250.

Zielinski, U., Gersonde, R., Seiger, R., and Fütterer, D., (1998), Quaternary surface water temperature estimations: Calibration of a diatom transfer function for the Southern Ocean, *Palaeoceanography*, 13, 365-383.

Zink, K. G., Vandergoes, M.J., Mangelsdorf, K., Dieffenbacher-Krall, A.C., and Schwark, L., (2010), Application of bacterial glycerol dialkyl glycerol tetraethers (GDGTs) to develop modern and past temperature estimates from New Zealand lakes, *Organic Geochemistry*, 41, 1060–1066.

Chapter 2

Statistical modelling of Southern Ocean marine diatom proxy and winter sea ice data: Model comparison and developments

Authors:

Alexander J. Ferry, Tania Prvan, Brian Jersky, Xavier Crosta, Leanne K. Armand.

Journal:

Progress in Oceanography

Available online 10 December 2014

http://www.sciencedirect.com/science/article/pii/S0079661114002031

Printed in Volume 131 (2015), pages 100-112.

I have made two edits to Chapter 2 based on my examiners comments. Firstly, the term "hold out cross-validation" has been changed to "hold out validation" throughout the document. Secondly, I have clarified throughout the Chapter that linear regression between model fitted values and observed data used the observed data as the response variable, and the model fitted values as the predictor. The text within Chapter 2 where these edits have been applied has been coloured red for clarity.

Progress in Oceanography 131 (2015) 100–112

Contents lists available at ScienceDirect

Progress in Oceanography

journal homepage: www.elsevier.com/locate/pocean

Statistical modeling of Southern Ocean marine diatom proxy and winter sea ice data: Model comparison and developments

Alexander J. Ferry [a,⇑], Tania Prvan [b], Brian Jersky [c], Xavier Crosta [d], Leanne K. Armand [a]

[a] Department of Biological Sciences, Faculty of Science and Engineering, Macquarie University, New South Wales 2109, Australia
[b] Department of Statistics, Faculty of Science and Engineering, Macquarie University, New South Wales 2109, Australia
[c] College of Science, Dean's Office, Cal Poly Pomona, CA 91768, USA
[d] DGO, UMR-CNRS 5805 EPOC, Université de Bordeaux 1, Avenue des Facultés, 33405 Talence Cedex, France

article info

Article history:
Received 7 April 2014
Received in revised form 27 November 2014
Accepted 1 December 2014
Available online 10 December 2014

abstract

We compare the performance of the modern analog technique (MAT), the Imbrie and Kipp transfer function (IKTF), the generalized additive model (GAM) and weighted averaging partial least squares (WA PLS) on a southern hemisphere diatom relative abundance and winter sea ice concentration training data set. All relevant model assumptions are tested with a random 10-fold hold out validation, whilst a hold out validation tested the explanatory power of each model on spatially independent validation data. We used auto correlograms on model residuals, variance partitioning, and principal coordinates analysis of neighbor matrices (PCNM) to investigate the importance of the spatial structure of our training database. A set of hierarchical logistic regression models (or Huisman–Olff–Fresco models) are used to infer the response of each diatom species along the winter sea ice gradient. Our analyses suggest that IKTF is an inappropriate sea ice estimation approach as its underlying statistical assumptions do not hold and the fit of IKTF to our data under hold out validation was poor. We conclude that MAT may be biased by spatial autocorrelation, and together with IKTF fails to provide unbiased estimates of winter sea ice. We find GAM and WA PLS are more appropriate than IKTF and MAT for the estimation of paleo winter sea ice cover throughout the Southern Ocean. However, as WA PLS is based on a unimodal species response, which is rarely exhibited by diatoms along the winter sea ice gradient, we ultimately advocate the appli- cation of GAM. GAM only uses diatoms with a statistically significant association, and ecologically based link, with sea ice. GAM outperformed all other models under hold out validation in terms of performance statistics, the fit of GAM to the training dataset and diagnostic tests for model assumptions. We also dem- onstrate that GAM provides a more detailed and potentially more accurate (based on a comparison with New Zealand and southeast Australian paleo climatic records) paleo winter sea ice record for the south- western Pacific Ocean in comparison with IKTF, MAT and WA PLS.

Introduction

A range of statistical models are used to estimate the relationships between marine microorganism assemblages and sea ice cover. The chosen models are then used to estimate past sea ice cover from marine microfossil assemblages recorded within a sediment core. The adopted statistical models are referred to as transfer functions within the paleoceanographic community (Justwan and Koç, 2008). Use of these statistical models is specific to certain regions due to the fossil taxa preserved in the sediments. The results of such applications are used either as a location specific record of sea ice cover over time or as wider hemispheric time slice reconstructions (Armand and Leventer, 2010).

A key and timely goal of this paper is to extend the current statistical models used by the paleoceanographic community to associate diatom assemblages with sea ice. The Intergovernmental Panel on Climate Change (IPCC) made an active call for more paleo sea ice data from the Southern Hemisphere. The IPCC Working Group I (Jansen et al., 2007, Chapter 6) found the paleoceanographic study of climate change lagged modern observational and modeling efforts. The IPCC authors noted the need for updated data and modern analyses relevant for placing into context the changes faced in Earth's future. A specific reference was made regarding the limited body of knowledge surrounding southern hemisphere climatic variability over the last one to two thousand years. Robust

⇑ Corresponding author. Tel.: +61 2 9850 8205.
E-mail addresses: alexander.ferry@mq.edu.au (A.J. Ferry), tania.prvan@mq.edu.au (T. Prvan), bjersky@csupomona.edu (B. Jersky), x.crosta@epoc.u-bordeaux1.fr (X. Crosta).

http://dx.doi.org/10.1016/j.pocean.2014.12.001
0079-6611/

paleo sea ice estimates are also of particular use for the sea ice modeling community who utilize paleo sea ice data to verify climate model data.

We focus our analysis on four inverse statistical models, the modern analog technique (MAT), the Imbrie and Kipp transfer function (IKTF), the generalized additive model (GAM) and weighted averaging partial least squares (WA PLS). The classical approach computes the function $Y = f(X)$ + error, where Y is the matrix of biological assemblages and X is the environmental variable of interest.

The function is then inverted via a maximum likelihood estimation or some other optimization procedure. The models we compare are inverse in the sense that Y and X are modelled with an 'inverse' regression, $X = g(Y)$ + error, fitted directly to the data (Birks, 2012). It is these inverse techniques that are used by the paleoceanographic community for paleo sea ice estimation.

Our paper has four main objectives. Firstly, we aim to evaluate the applicability of each model to our training data set. To do so we apply 10-fold hold out validation to assess the fit of each model to our data and ensure all statistical assumptions hold. Our second major aim is to investigate the presence (and importance) of spatial auto- correlation within our training set. Hold out validation is used to assess the explanatory power of each model on spatially independent data. We therefore illustrate which of the models may be least biased by spatial autocorrelation and thus potentially provide the most robust paleo sea ice records based on fossilized diatom assemblages. We use variance partitioning and principal coordinates analysis of neighbor matrices to understand the relative importance of winter sea ice concentration and the spatial patterns of our data in explaining the total variation in our diatom relative abundance data. Some of the statistical models applied assume a specific species response along a given environmental gradient. Therefore, our third aim is to assess the type of response each diatom species has along the winter sea ice gradient and to discuss the implications of this for the application of each model. Finally, we compare the paleo winter sea ice estimates from each model derived from sediment core SO136-111 (Crosta et al., 2004), located in the southwestern Pacific Ocean (56°40^{0}S, 160°14^{0}E). We highlight the key paleo climatic events present within the paleo sea ice record and compare our results with independent New Zealand and east Australian-based paleo climate reconstructions.

Methods

Databases used

We used the Crosta et al. (1998) surface sediment diatom database documenting the relative abundance of 32 diatom species across 243 sea-floor sediment samples. Details regarding the depth of each sample, diatom counts, age of the surface samples and the methods used to extract each sample are described by Pichon et al. (1992), Crosta et al. (1998) and Crosta et al. (2004). Appendix A lists the 32 diatom species recorded within the surface sediment diatom database used within our training dataset. Our analysis used 163 of the 243 samples available (Fig. 1). Sample exclusion attempted to establish a more even sampling of the environmental gradient (Telford and Birks, 2011) and accounted for the spatial structure of our data. Samples from a broad range of longitudinal and latitudinal bands were removed in order to preserve the spatial diversity among the samples. We felt the inclusion of open ocean samples intended for sea-surface temperature estimation was redundant for our purposes. These latter open ocean samples were excluded as no sea ice cover is recorded at these sample sites and diatoms with a biogeography that is closely tied with sea ice cover are absent from these samples. We compare the down core winter sea ice concentration (wSIC) estimates from each model on marine sediment core SO136-111, focusing on wSIC estimates over the last 130 kyr BP, with a particular focus on the extended Last Glacial Maximum (eLGM). The stratigraphy and age model of core SO136-111 is provided by Crosta et al. (2004).

For each sample we extracted a time series of satellite recorded winter (September) average sea ice concentration data from November 1977 to December 1991, keeping the time series of satellite data we use consistent with the published accounts by Crosta et al. (2004) and Röthlisberger et al. (2011). The satellite data was sourced from the sea ice data product of Comiso (2000) provided by the National Snow and Ice Data Center (NSIDC). We also use the sea surface temperature (SST) data compiled and previously analyzed by Crosta et al. (2004) when analyzing our training data set with canonical correspondence analysis (CCA). The CCA is used to explore the importance of both winter sea ice and SST in explaining diatom relative abundances. In order to satisfy the statistical assumptions for some of the methods, to improve the fit of each model to the data, and to deal with the bounded nature of the winter sea ice response variable, we used appropriate logarithmic transformations of both the diatom relative percentage abundance (X) and wSIC (Y) in all the models we considered. However, since MAT can accommodate the untransformed data, we applied it to both transformed and untransformed data, to assist in comparing our results with previously published research. The specific transformations used were $\ln(10X + 1)$ and $\ln[(Y + 0.5)/(100.5 - Y)]$.

Reconstruction diagnostics

A series of diagnostics are used to assess the applicability of the models developed on our training set to the fossilized assemblages of core SO136-111. We compare the maximum abundances of each diatom species recorded in our training set and core SO136-111 to identify the presence of diatoms with higher abundances within core SO136-111 and a lower abundance in our training set. We used the Hills N2 diversity index (Hill, 1973; Gadagkar, 1989) to identify those species which may have a poorly defined optima. Analogue quality, and the presence of non-analogue samples for core SO136-111, is explored with a squared chord distance and the five closest analogues. A redundancy analysis ordination, constrained by wSIC, is used to compute a squared residual length for the taxonomic distances between the winter sea ice axis and the samples of both the training set and core SO136-111 (Birks et al., 1990; Birks, 2003).

Statistical methods

Species response modelling via Hierarchical Logistic regression

Five hierarchical logistic regression models, also known as Huisman–Olff–Fresco (HOF) models (Huisman et al., 1993) and two bimodal species response models (Jansen and Oksanen, 2013) were used to infer the response of all 32 diatom species along the winter sea ice environmental gradient. Each species response model is connected with an ecological theory for species-response along an environmental gradient. The simplest of the seven response models that sufficiently explained the observed diatom responses to winter sea ice were chosen via statistical inference (Jansen and Oksanen, 2013). Response models were fitted to untransformed data for each of the 32 diatom species, with the final model selected via bootstrapping and Akaike's information criterion (Jansen and Oksanen, 2013). The same analysis was applied to our logarithmically transformed data to investigate the type of species response that exist on the log scale.

Imbrie and Kipp transfer function (IKTF)

The Imbrie and Kipp transfer function (IKTF) (Imbrie and Kipp, 1971) is an application of principal component regression. A

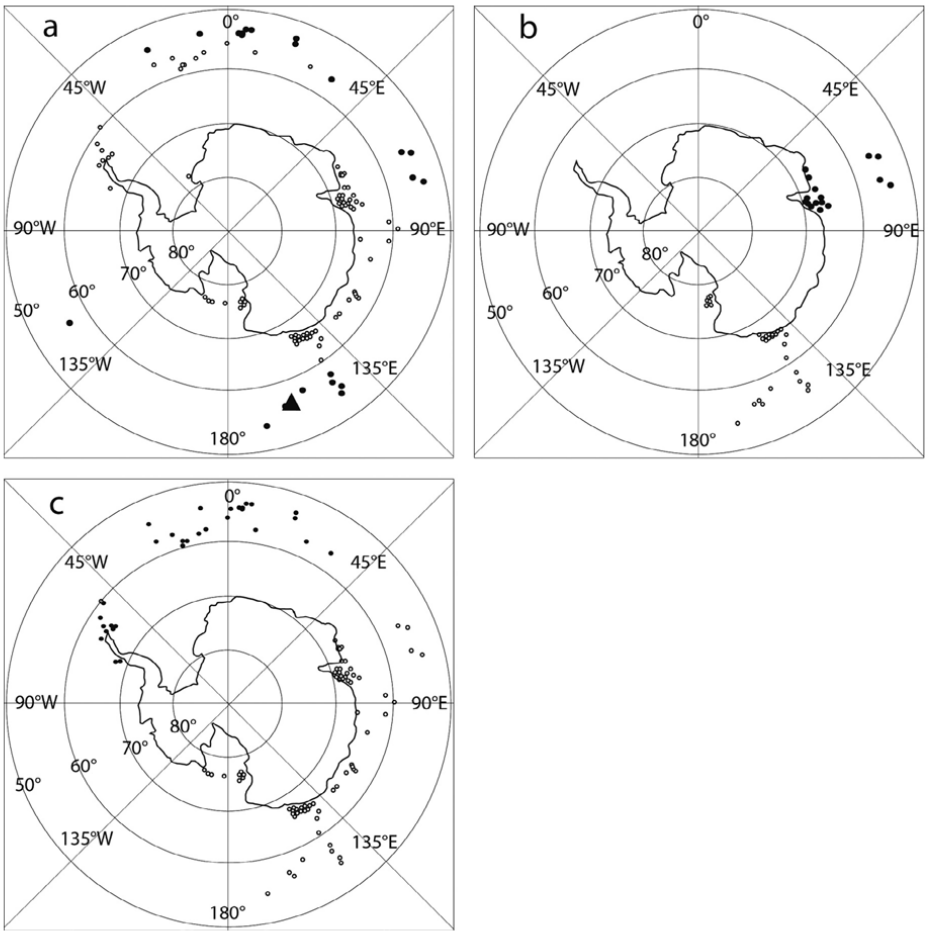

Fig. 1. (a) A map of the 163 samples we used for our analysis. Solid black dots are those samples for which no winter sea ice cover is recorded whilst the open circles are for those samples where winter sea ice cover is recorded. The location of core SO136-111 is indicated by the black triangle in panel a. Panels b and c map the samples used in our training (open circles) and validation (black circles) data sets under the two hold out validations for the South Indian Ocean (b) and South Atlantic Ocean (c).

principal components analysis (PCA) is applied to the matrix of 32 log transformed diatom relative abundance values. Climate variables are regressed onto the PC scores using a multiple linear regression model with quadratic terms (Dowsett and Poore, 1990; Guiot and de Vernal, 2007). Fossil assemblages are projected onto the selected PCs and then entered into the previously calculated regression equations to estimate paleoclimate variables (Guiot and de Vernal, 2007).

Our choice of PCs to use as predictors was guided by a visual inspection of a scree plot (Jackson, 1993). Significance of the selected PCs as predictors for winter sea ice was evaluated during the regression step using the alpha level of 0.05. Any non-significant PCs were excluded from the final model.

Modern analogue technique

The modern analogue technique (MAT) compares dissimilarity coefficients (DC) calculated between modern and fossilized species assemblages (Gavin et al., 2003). DCs measure the similarity between calibration and fossil samples making MAT a k-nearest neighbors (k-NN) technique (ter Braak, 1995). Values for each selected analogue, which are assumed to represent oceanographic properties at the locality of a core, are averaged to provide an estimate. We trained MAT on 163 core top samples, using 32 diatom species, a square chord distance and the five closest analogues.

Weighted averaging partial least squares (WAPLS)

A full description of WAPLS is provided by ter Braak and Juggins (1993). In summary, the first component is a two-way weighted average for the original environmental property, with all subsequent components being two-way weighted averages for the residual of this environmental property. The estimates of the environmental property are obtained via a linear combination of components from the WA PLS, with each component being a weighted average of species scores (ter Braak and Juggins, 1993). Our application of WA PLS selected the number of components to extract based on a randomization *t*-test, which assessed the

statistical significance of each component at the 5% significance level (van der Voet, 1994). Only statistically significant components were used.

Generalized additive model

GAM is a generalized linear model replacing the linear predictor with a sum of smooth functions for each predictor (Wood, 2006). Our application of GAM used a Gaussian (identity) link function and penalized regression splines, with estimation of the smoothing parameter using a generalized cross-validation (GCV) criterion. A more detailed discussion of GAM is provided by Hastie and Tibshirani (1987) and Wood (2006).

Our application of GAM uses diatom abundances as our predictors and wSIC as our response variable. Therefore, we apply GAM as an 'inverse' model (Birks, 2012). The application of GAM as an inverse model is not appropriate where diatoms have a unimodal response along the winter sea ice gradient, as GAM will fit a linear relationship with a slope that is dependent on the density of the winter sea ice data. Therefore, we examine all fitted functions from GAM fitted firstly as a 'classical' model (using winter sea ice as a predictor variable), and then secondly as an inverse model, to ensure GAM has successfully fitted an appropriate function to the data. The visual inspection of GAM functions is complimented by statistical tests on GAM residuals to assess the assumptions made for GAM errors (refer to Section 'Hold out validation' for further detail).

When fitting GAM to our data, we first evaluated the significance of all 32 diatom species, individually. Our choice for the final species to use as our sea ice proxy within GAM was guided by *a priori* biological knowledge (Armand et al., 2005; Crosta et al., 2005, Armand pers obs. 2014), previous quantitative research on diatom biogeography (Zielinski and Gersonde, 1997; Buffen et al., 2007; Esper et al., 2010; Olguín and Alder, 2011) and statistical tests to ensure that the assumptions of GAM were satisfied. The papers cited above represent the most detailed study of Southern Ocean diatom ecology, and therefore provided us with a reference to ensure that the diatom species we used within GAM had an ecology that is closely linked with the sea ice environment.

Hold out validation

We used a 10-fold hold out validation procedure to verify the fit of each model to our training data set and ensured that the statistical assumptions relevant for each model were satisfied. It has been suggested that 10-fold hold out validation provides the minimum bias in estimating model parameters (Kohavi, 1995) and has been widely used in the statistical literature (e.g. Bouckaert and Frank, 2004). To test the assumption for normality of model errors (relevant for GAM and IKTF) we applied the Shapiro–Wilk and Lilliefors tests. Bartels test and a runs test for randomness were applied to the residuals of all models. To discriminate objectively between the performance of each model we computed the root mean square error of prediction (RMSEP) and applied a linear regression with observed data as the response and model fitted values as the predictor. Using regression as a diagnostic for model performance in this way, would reveal an unbiased model as having a slope of one with a zero intercept (Bennett et al., 2013). We used a 95% confidence interval to infer if the slopes of the regression lines were significantly different from one.

As spatial autocorrelation is a known feature of marine proxy data it is important to validate each model on a spatially independent validation set (Telford and Birks, 2005; Juggins and Birks, 2012). It is important to establish diversified training and validation subsets whilst maintaining the spatial independence of these subsets. Therefore, we subjectively identified two divisions of our training dataset that maintained a diverse enough range of samples for training each model, whilst establishing an appropriate geographical separation between the training and validation data subsets to achieve two spatially independent hold out validation (Fig. 1b and c). We compared model performance, using average RMSEP between 10-fold and spatially independent hold out validation, to identify the bias that may arise due to spatial autocorrelation. After training each model on all 163 samples, autocorrelograms of model residuals were used to infer a non-independence of model errors. As other unmeasured environmental variables, which are important for diatom biogeography are excluded from our models, we expect that the residuals from each model will be autocorrelated. Any model with uncorrelated residuals may have inappropriately exploited the spatial structure of our training set, and may therefore be biased by spatial autocorrelation (Telford and Birks, 2005).

Principal coordinate analysis of neighbor matrices (PCNM)

We investigated the spatial patterns within our data via principal coordinate analysis of neighbor matrices (PCNM) and variance partitioning. PCNM computes a set of spatial explanatory variables that account for spatial variation over all of the spatial scales within a data matrix (Borcard et al., 2004; Legendre et al., 2005). These spatial explanatory variables are then used as predictors within statistical models (Borcard and Legendre, 2002; Dray et al., 2006). We applied PCNM on a matrix of great circle distances between each of our 163 samples. A backward selection procedure with sea ice as the response and the PCNM spatial eigenvectors as predictors within a GAM defined the subset of PCNM spatial predictors to use within further analyses.

Variance partitioning

Variance partitioning separated the total variance of our untransformed diatom relative abundance matrix into components explained by winter sea ice (which also remained untransformed), the spatial structures of our data (PCNM spatial variables) and the co-variation between winter sea ice and space (PCNM spatial variables) (Borcard et al., 1992). We used variance partitioning for the entire diatom relative abundance matrix (all 32 species) and again only on those diatom species used as predictors within our application of GAM.

Software

We used the freely available package 'PAST' of Hammer et al. (2001) to apply MAT and CCA. The IKTF model was fitted using the 'princomp' and 'lm' functions of R. The following R packages were used for the remaining analysis. We used mgcv (Wood, 2013, for GAM), eHOF (Jansen and Oksanen, 2013, for HOF modelling), rioja (Juggins, 2012, for WA PLS and reconstruction diagnostics), vegan (Oksanen et al., 2013, for Variance partitioning), spacemakeR (Dray, 2013, for PCNM), fields (Furrer et al., 2013, for computing a great circle distance matrix), fBasics (Wuertz, 2013, for normality tests), lawstat (Gastwirth et al., 2013, for Bartels test of randomness and the runs test) and finally, the packages maps (Becker and Wilks, 2013) and mapproj (McIlroy, 2013) to map our database samples. All graphs were produced using R (version 3.0.0) and Adobe Illustrator™.

Results

Species response modelling via Hierarchical Logistic regression

Huisman–Olff–Fresco (HOF) models (Huisman et al., 1993; Jansen and Oksanen, 2013) were successfully fitted to 24 of the diatom species recorded within our training database. The remaining diatom species constituted rarer species with low abundance

and were not modelled. HOF analysis on untransformed diatom abundance and sea ice data suggests a diverse response of diatoms along the winter sea ice gradient exists. There were 10 monotonic, 4 unimodal, 6 bimodal, 1 unidirectional and 3 non-response models that provided an optimal fit. HOF analysis on log transformed data revealed 6 monotonic, 4 unimodal, 11 bimodal, and 3 unidirectional response models.

HOF analysis of untransformed data (Fig. 2) suggests the response of both *Actinocyclus actinochilus* and *Fragilariopsis cylindrus* along the winter sea ice gradient was best approximated by model type 4, a unimodal symmetrical distribution with a single optimum. Model type 3, a unidirectional plateau model with a decreasing response provided the better approximation of the relationship between *Fragilariopsis curta* and winter sea ice. A bimodal response model with 2 optima (model type 7) provided the best summary for the response of *Thalassiosira lentiginosa* to winter sea ice (Fig. 2). Fitting HOF models to logarithmically transformed data (Fig. 3) provided the same species response for *T. lentiginosa* and *F. cylindrus*. The response of *F. curta* was best approximated by model 5 (a unimodal response) whilst model 2 (a monotonic response) best described the response of *A. actinochilus* (Fig. 3).

Imbrie and Kipp transfer function

Generally, coefficients for the first and second PC's, along with a coefficient for the quadratic term for the first PC, were significant. The Bartels test provides a non-parametric test for randomness. Applying Bartels test to the residuals from IKTF allows us to infer that the errors of the IKTF model may be random. A linear regression using observed data as the response and each model's fitted values as the predictor had slopes that were equal to one with an intercept of zero (Table 1). A plot of IKTF fitted values and observed data for the training database is pro- vided in Fig. 4. IKTF residuals were significantly autocorrelated only over the shortest distance class and do not follow a normal distribution.

Only the first two principal components (PCs) were statistically significant within the regression step of IKTF. These first two PCs explained 67.72% of the variance within our diatom assemblage matrix. Examination of loadings for each PC reveals a grouping of distinctly sea ice related diatom species. Large loadings for the first PC were identified for the diatoms *Chaetoceros* resting spores, *F. curta*, *F. cylindrus*, *Fragilariopsis obliquecostata*, *Fragilariopsis sublinearis*, *S. microtrias*, and *Thalassiosira antarctica* group, all of which have been previously recognized as sea ice related species (Armand et al., 2005; Esper and Gersonde, 2014). Examination of loadings suggests the second PC represents a grouping of sea ice and open ocean species. Those species with higher loadings for the second PC included *F. curta*, *F. obliquecostata*, *Fragilariopsis rhombica*, *Fragilariopsis separanda*, *F. sublinearis* (all sea ice related species, Armand et al., 2005), *Fragilariopsis kerguelensis*, *Thalassiosira gracilis* group, *T. lentiginosa* and *Thalassiothrix* spp. group (open ocean related diatoms, as identified by Crosta et al., 2005).

Modern analogue technique

MAT residuals were significantly autocorrelated only over the shortest distance class. Linear regression between MAT fitted values and observed data had slopes that were significantly less than 1 and an intercept that was greater than zero (Table 1). Fig. 4 illustrates the fitted values from MAT with observed data for the training database.

Weighted averaging partial least squares

Randomization *t*-tests defined the number of components retained in each WA PLS model during 10-fold hold out validation. Generally, only the first two components were significant predictors for wSIC. WA PLS residuals were significantly autocorrelated over all distance classes. The linear regression between WA PLS fitted values and observed data revealed a 1:1 slope with an intercept that was greater than zero (Table 1). The observed data from our training database, along with the fitted values from WA PLS, are plotted in Fig. 4.

GAM

The residuals of GAM were significantly autocorrelated over all distance classes. Regression between GAM fitted values and observed data had a slope of one and an intercept of zero (Table 1). GAM fitted values are plotted against observed data for the training database in Fig. 4. The assumptions, in which GAM errors are normally distributed with a constant variance, appear to be satisfied. When adding PCNM spatial variables as additional predictor

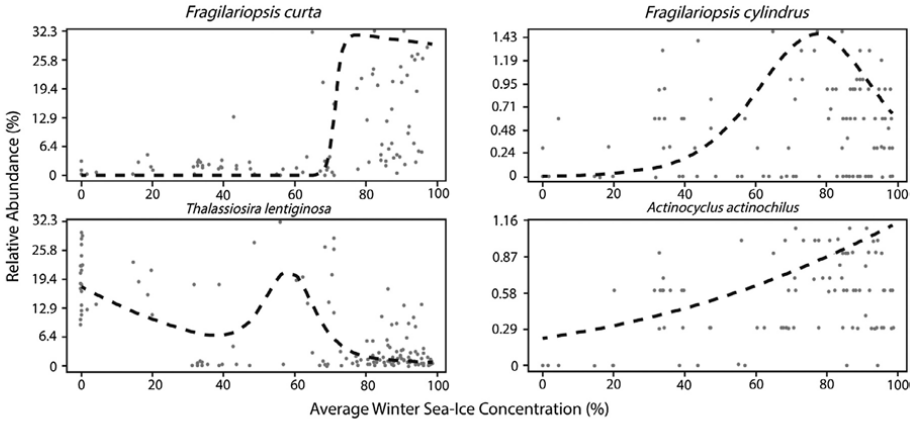

Fig. 2. A graphical display of the final HOF model (fitted to untransformed data) describing the response of each diatom taxa used within GAM along the winter sea ice gradient.

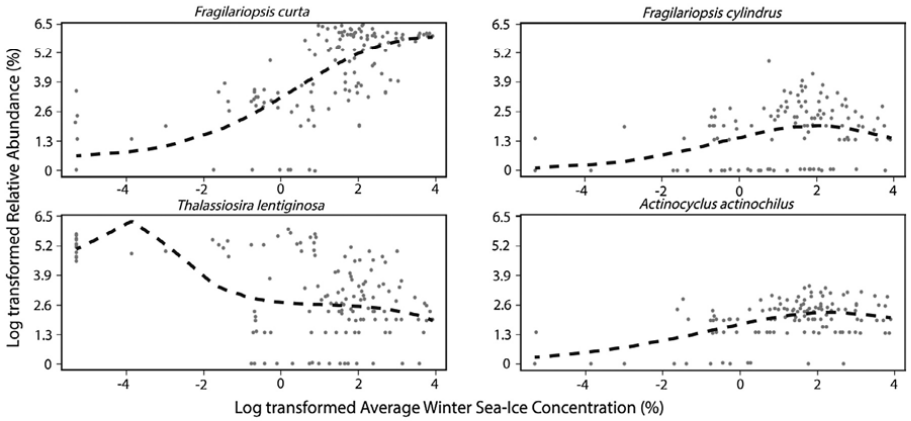

Fig. 3. A graphical display of the final HOF models (fitted to the logarithmically transformed data) describing the response of each diatom taxa used within GAM along the winter sea ice gradient.

Table 1
Output from all of the regression models fitted between the estimates sea ice from IKTF, MAT, WA PLS and GAM (i.e. fitted values) and observed sea ice data. The values shown are the slope (m), intercept (b), lower (LCL) and upper (UCL) 95% confidences limits for the slope (m) for all of the random 10-fold hold out validations on our training data base.

	IKTF				MAT				WA PLS				GAM			
	m	b	LCL (m)	UCL (m)	m	b	LCL (m)	UCL (m)	m	b	LCL (m)	UCL (m)	m	b	LCL (m)	UCL (m)
1	1.00	0.00	0.9	1.10	0.86	0.11	0.77	0.96	1.00	−0.13	0.89	1.11	1.01	−0.00	0.92	1.10
2	1.00	0.00	0.89	1.11	0.87	0.05	0.78	0.96	1.00	−0.13	0.89	1.10	1.01	−0.00	0.92	1.11
3	1.00	0.00	0.89	1.11	0.85	0.11	0.76	0.94	1.00	−0.13	0.89	1.11	1.01	−0.01	0.92	1.11
4	1.00	0.00	0.89	1.11	0.85	0.09	0.76	0.95	1.00	−0.11	0.89	1.11	1.02	−0.00	0.93	1.11
5	1.00	0.00	0.89	1.11	0.88	0.07	0.79	0.96	1.00	−0.11	0.89	1.10	1.01	0.00	0.92	1.11
6	1.00	0.00	0.88	1.12	0.86	0.10	0.76	0.96	1.00	−0.12	0.89	1.12	1.02	−0.01	0.91	1.12
7	1.00	0.00	0.88	1.12	0.89	0.05	0.80	0.98	1.00	−0.10	0.89	1.11	1.02	−0.00	0.92	1.11
8	1.00	0.00	0.88	1.12	0.85	0.07	0.75	0.95	0.99	−0.19	0.85	1.12	1.01	−0.00	0.91	1.11
9	1.00	0.00	0.89	1.11	0.85	0.17	0.77	0.94	1.00	−0.19	0.87	1.12	1.02	−0.01	0.92	1.11
10	1.00	0.00	0.89	1.11	0.86	0.10	0.76	0.96	1.02	−0.02	0.91	1.12	1.01	−0.00	0.92	1.11

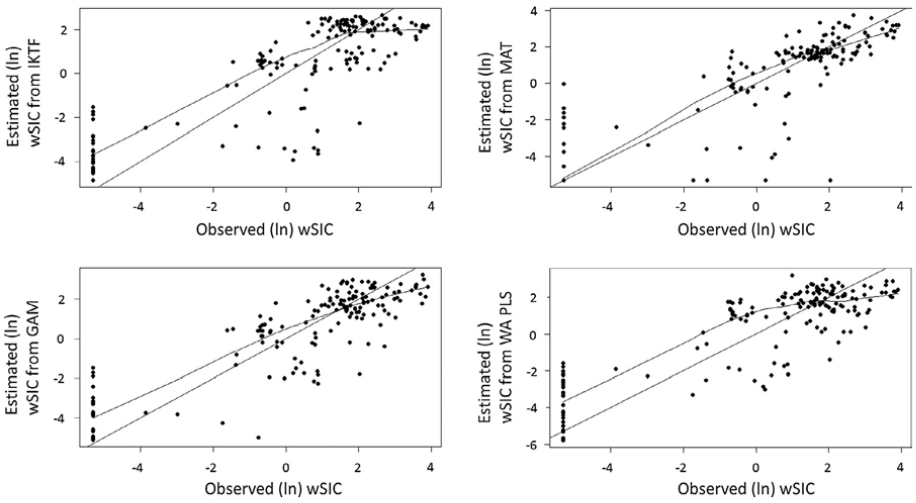

Fig. 4. The observed data from the our training data set plotted against the fitted values from IKTF, MAT, WA PLS and GAM. Also plotted are a 1:1 line and a lowness smoother fitted to the data based on a locally-weighted polynomial regression.

variables within GAM, the smooth functions fitted for each of our diatom species remained statistically significant.

Of the 32 diatom species within our training data set, 19 have a statistically significant relationship with wSIC. From these 19 diatom species, we chose *A. actinochilus*, *F. curta*, *F. cylindrus* and *T. lentiginosa* as the predictors (proxy species) within our final GAM. The four separate GAMs using *A. actinochilus*, *F. curta*, *F. cylindrus* and *T. lentiginosa* as response variables (and wSIC as the predictor) did indeed fit an appropriate function to the data, and did not approximate a simple linear relationship due to GAMs inability to handle a unimodal response. The diatom taxa chosen in our GAM also had to pass the tests applied to GAM residuals to infer that the assumptions regarding the errors of GAM were satisfied (i.e. normality of model errors and that the errors were independent). The use of additional diatom species as fifth predictors within GAM, using a forward selection procedure, revealed that many were not significant. Furthermore, the use of a significant fifth diatom did not improve the performance of GAM. Based on the principle of parsimony (Juggins and Birks, 2012), we chose to use GAM with only four diatoms (*A. actinochilus*, *F. curta*, *F. cylindrus* and *T. lentiginosa*) as predictors for wSIC.

A biplot of the extracted components from a canonical correspondence analysis (CCA) (Justwan and Koç, 2008) (Fig. 5) illustrates the ordination of the diatom species with respected to winter sea ice and summer sea surface temperature (SST). The CCA indicates that SST and winter sea ice concentration are strongly negatively correlated with each other, and that the variation in our diatom samples is primarily driven by both sea ice and sea surface temperature (SST). Fig. 6 summarizes the relative abundance of each diatom species used within our GAM with respect to winter sea ice concentration and SST. The figure illustrates that it would be difficult to determine on statistical grounds if either winter sea ice concentration or summer SST were more important in explaining the relative abundances of diatoms. The CCA biplot and Fig. 6 both suggest the effect of winter sea ice concentration and summer SST cannot be separated, with both variables effectively acting as surrogates for each other. However, we feel our analysis supports previous research that suggests the species specific ecology, and the habitat linkages identified, provide a Southern Ocean surface water hydrology signature for these species. Therefore diatom assemblages can provide robust paleo environmental reconstructions both sea ice concentrations and SST (Armand et al., 2005; Crosta et al., 2005; Buffen et al., 2007; Esper et al., 2010).

Hold out validation

Under random 10-fold hold out validation the average RMSEP of GAM was higher than that of IKTF and MAT applied to (transformed-MAT) and untransformed (Untransformed-MAT) data. WAPLS had the highest RMSEP under 10-fold hold out validation. The RMSEP's of all the methods increased under our spatially independent hold out validations. GAM provided the lowest average RMSEP when tested on the two spatially independent hold out validation data sets, whilst untransformed-MAT had the greatest increase in RMSEP (Table 2).

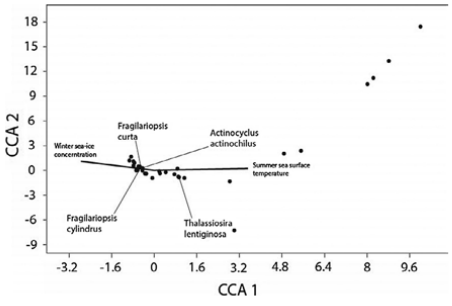

Fig. 5. A biplot for the CCA applied to our training data base, and constrained by summer SST and winter sea ice concentration.

Variance partitioning

We applied variance partitioning (redundancy analysis ordination) on untransformed data to explore the relative importance of sea ice and the spatial structures of our data set in explaining diatom relative abundance. The eight PCNM spatial explanatory variables selected via a backward selection procedure (refer to Section 'Principal coordinate analysis of neighbor matrices (PCNM)') were used to describe the spatial structure of our data set. Variance partitioning on the entire diatom relative abundance matrix revealed that 11.55% of the variation in diatom abundances was explained by winter sea ice, 19.57% was explained by the spatial explanatory variables, whilst the co-variation between spatial explanatory variables and wSIC explained 12.29% of the variation in diatom abundances. Redundancy analysis ordination on the four diatom species used as predictors within our GAM revealed that 24.86% of their variation was explained by wSIC, with spatial structures (PCNM eigenvectors) explaining 13.88% of their variation, and co-variation between wSIC and the spatial explanatory variables explaining 13.59% of their variation.

Reconstruction diagnostics

Only two diatom species have a higher maximum abundance in core SO136-111 compared to their maximum abundances within our training set. No species with poorly defined optima were abundant within core SO136-111. Regarding analogue quality, of the 164 samples within core SO136-111, only one sample had no analogue whilst another 15 samples had poor analogues. The remaining samples within core SO136-111 had good analogues. The redundancy analysis ordination with winter sea ice suggests that 31 samples from core SO136-111 had a squared residual length that exceeded the 90th percentile for the squared residuals lengths computed on the training set.

Comparing the paleo winter sea ice records for core SO136-111

The application of the four estimation models on the diatom fossil record from the 130 kyr BP core SO136-111 produced a clear fluctuation in winter sea ice cover between Marine Isotopic Stages (MIS) 1 through to 5. The estimated wSIC paleo data is divided into values less than 15% (indicating no sea ice cover), 15–40% (unconsolidated sea ice) and over 40% sea ice (consolidated sea ice), as defined and described by Armand et al. (2005). GAM indicates winter sea ice cover last occurred around 13.8 thousand years before present (kyr BP) during the Antarctic Cold Reversal (ACR), after which no winter sea ice was estimated for the last 11 kyr BP (the Holocene). GAM suggests winter sea ice reached the site of core SO136-111 from 20 to 35 kyr BP over the extended last glacial maximum (eLGM) time slice, with clear increases in winter sea ice during the eLGM cold phases, separated by a decrease in winter sea ice during the eLGM interstadial/Antarctic isotopic maxima (AIM) 2. The variability in wSIC during the eLGM climatic events and between marine isotopic stages is greatest for the GAM. GAM provides the paleoceanographer is the provision of a readily computed and interpreted 95% confidence interval for the estimates of paleo sea ice cover. Similarly, confidence intervals for MAT, IKTF and WA PLS can be computed through a bootstrapping

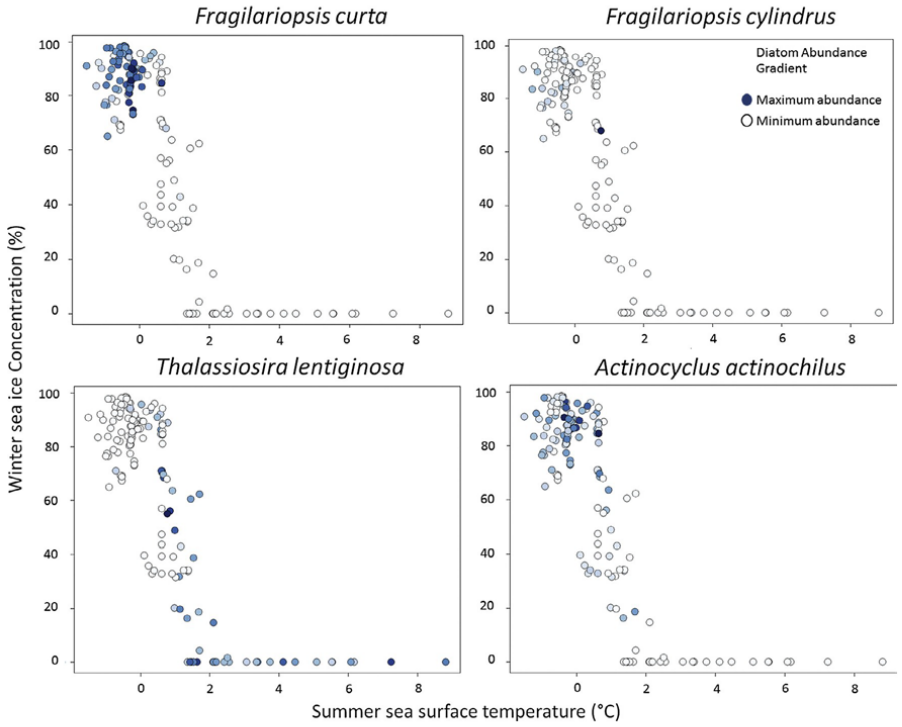

Fig. 6. The relative abundances of each diatom are plotted as a function of summer sea surface temperature and winter sea ice concentration. Dark blue points correspond to those samples in which each respective diatom is recorded in its highest abundance value, whilst the open circle indicates those sample where a diatom is not recorded. (For interpretation of the references to color in this figure legend, the reader is referred to the web version of this article.)

Table 2
The average RMSEP of each model from 10-fold hold out validation and the two spatially independent hold out validations.

Model	Mean RMSEP under random 10-fold hold out validation	Mean RMSEP from spatially independent hold out validation
GAM	21.21	23.73
WA PLS	23.78	25.91
Transformed-MAT	17.24	26
Untransformed-MAT	14.71	28.04
IKTF	21.08	26.59

procedure (Efron, 1979). A measure of confidence around an estimated value for a paleo climatic variable better facilitates the comparison of data derived from differing proxy records and climate model data. MAT documents an absence of sea ice during theHolocene, an increase in winter sea ice during the ACR, with sea ice reaching the site of core SO136-111 from 20 to 35 kyr BP over the eLGM time slice. MAT also documents clear increases in winter sea ice during the eLGM cold phases, separated by a decrease in winter sea ice during the eLGM interstadial/AIM 2. The paleo winter sea ice records for WA PLS and IKTF were consistent. No winter sea ice was estimated throughout the Holocene. During early MIS 3 winter sea ice was absent from the site of core SO136-111. During later MIS 3 and early MIS 2 (over the eLGM) wSIC increased to ~25%. Both WA PLS and IKTF document increases and decreases in winter sea ice between MIS 1–5 (Fig. 7).

Discussion

Diatom response along the winter sea ice gradient

The shape of a diatom species response along a given environmental gradient has important implications when establishing a particular statistical model for paleoceanographic purposes. For instance, quadratic functions are not suitable for skewed species responses (Austin, 2007). Huisman–Olff–Fresco (HOF) models evaluate a species response along an environmental gradient (Oksanen and Minchin, 2002) and provide an effective tool for univariate species response modelling (Jansen and Oksanen, 2013). The diatom species used as a proxy for winter sea ice within our GAM, *F. curta*, *T. lentiginosa*, *F. cylindrus* and *A. actinochilus* had unimodal, bimodal, unimodal and monotonic species responses on logarithmically transformed data, respectively.

As IKTF uses linear combinations of the diatom relative abundance data (i.e. principal components) this particular technique assumes an underlying linear response exists between diatom assemblages and winter sea ice cover, whilst WA PLS is based on an underlying unimodal species response model (Juggins and Birks, 2012). Application of HOF models to assess the response curve between diatom and winter sea ice revealed that only five diatom species possessed a unimodal response. The dominance of bimodal and monotonic (and to a lesser extent, unidirectional) response curves for diatom species is an issue for both IKTF and WA PLS, hindering the utility of these particular methods.

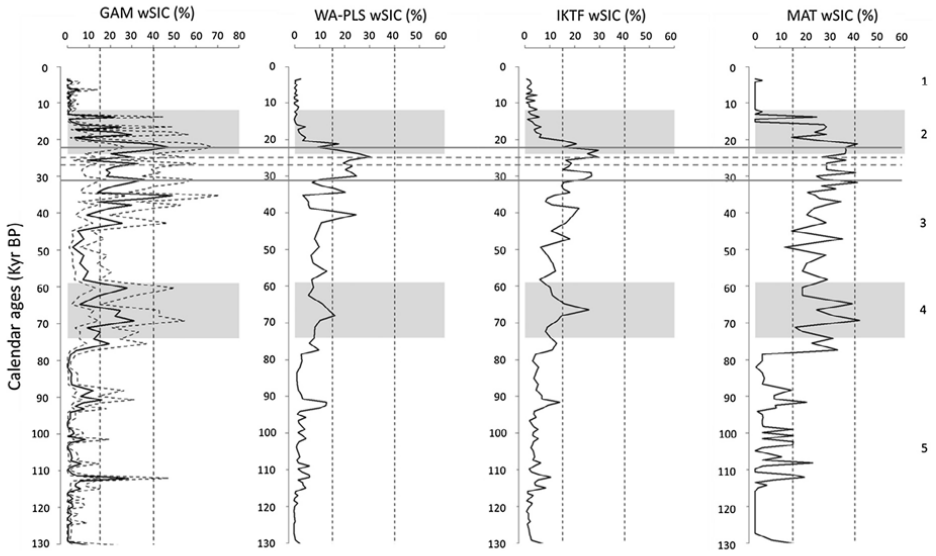

Fig. 7. The paleo winter sea ice concentrations (wSIC) estimated by GAM, WA PLS, IKTF and untransformed MAT for core SO136-111. The solid black lines correspond to the estimate for wSIC by each method, whilst the dashed black line corresponds to the 95% confidence interval for the paleo wSIC estimates of GAM. All models were trained on 163 samples, with MAT using 32 diatom species and the 5 closest analogues. Marine Isotopic Stages (MIS) 1 through to 5 are labelled on the right hand side of the figure, with the glacial MIS shaded gray. The solid gray lines correspond to each of the LGM cold phases, whereas the area bounded by the dashed gray lines highlights the AIM2/eLGM interstadial. The vertical dashed lines correspond to 15% and 40% wSIC, with <15% wSIC indicating an absence of wSIC, 15–40% corresponding to unconsolidated wSIC, and >40% indicating consolidated wSIC.

Comparing the performance of IKTF, MAT and WAPLS

We suggest IKTF is not the most appropriate model for the estimation of paleo wSIC. One key assumption for regression, namely normality of model errors (Bennett et al., 2013), is not satisfied. Additionally, PCA may not be an appropriate ordination method for the diatom relative abundance data of Crosta et al. (1998). PCA preserves Euclidean distances between species abundances, so those species with many zero values will have a small Euclidean distance value, which can produce inappropriate ecological answers (Legendre and Birks, 2012). As our diatom abundance data contains many zero values, application of PCA on our diatom data is doubtful. Furthermore, as Juggins and Birks (2012) note, extraction of PCs is an inefficient method for prediction. Any model used to produce paleoclimate estimates based on biological proxy data benefits from transparency. Use of PCs as predictors in a model hinders the interpretability of the model and how important given variables (i.e. diatom species) are within it (Dürrenmatt and Gujer, 2012). We, therefore, conclude that MAT and IKTF may not provide robust estimates of wSIC.

Whilst MAT does, upon investigation of analogue samples, provide limited information on which species contribute to given estimates (Malmgren et al., 2001), it is still far from clear which particular diatom species are providing the 'sea ice signal'. Additionally, we found MAT performance statistics (RMSEP) were optimistic in the presence of spatial autocorrelation (refer to Section 'Variance partitioning and hold out validation' for more detail).

WA PLS is a more appropriate alternative to MAT for the estimation of wSIC. Evaluating WA PLS with linear regression between fitted values and observed data indicated WA PLS was never consistently over-estimating or under-estimating wSIC.

Variance partitioning and hold out validation

The spatial structure of our training database accounts for a substantial portion of the variance in both the full diatom matrix and the four diatom species used within GAM. However, winter sea ice explained a larger portion of the variance in the four diatom sea ice species used within our GAM compared to the entire diatom matrix. Indeed, for the four diatoms used within our GAM, wSIC explained more of their variation in comparison to the PCNM spatial eigenvectors. This latter result is perhaps due to the diatoms we selected for our GAM having a biogeography throughout the Southern Ocean primarily regulated by sea ice coverage (Armand et al., 2005). Therefore, we believe those species used within our GAM, and their Southern Ocean surface water hydrological 'signature', are appropriate for paleo-sea ice reconstructions.

Variance partitioning, nonetheless, indicates that the spatial structure of our training dataset is important given the large portion of the total variance within the diatom abundance matrix explainable by the PCNM spatial eigenvectors. It is likely that these spatial structures are in part a product of other ecologically important, and spatially autocorrelated, environmental variables. As these unmeasured environmental variables are obviously not included within MAT, GAM, IKTF or WA PLS, we expected to find a significant autocorrelation amongst model residuals (Telford and Birks, 2005). Indeed, the residuals of IKTF and MAT had the lowest autocorrelation. The lower autocorrelation amongst model residuals suggests MAT and IKTF have exploited the spatial structures of the training data set to a greater degree than GAM or WA PLS. In contrast, WA PLS and GAM had a higher, and statistically significant, autocorrelation amongst residuals. This suggests

that GAM and WA PLS do not inappropriately exploit the spatial structures of our training database (and subsequently provide overly optimistic performance statistics) to the same extent as MAT and IKTF.

MAT produces a lower average RMSEP than GAM under 10-fold hold out validation (on autocorrelated data), and a higher RMSEP on our spatially independent data. We suggest this is due to MAT over fitting our training dataset by exploiting the autocorrelation struc- ture of the data. Given that MAT can exploit spatial auto correla- tion to improve its performance, we feel that whilst MAT appears to fit the entire training data set well (as shown in Fig. 4), it is under spatially independent hold out validation that we can truly begin to understand how MAT really performs when producing paleo sea-ice estimated on core data. Our spatially independent hold out validation suggests that MAT is biased by spatial autocorrelation. Hence we feel that MAT may be performing well on the training data set due to its capacity to be biased by spatial autocorrelation, and that the per- formance reduction of MAT under spatially independent hold out validation (which is indicative of MATs performance when producing paleo sea ice estimates on core data) is due to the poorer capacity of MAT to produce paleo sea ice estimates on new, independent (i.e. core) data sets.

Our results are comparable with those of Telford and Birks (2005), who suggested MAT improved its estimates of SST through an exploitation of the spatial structures within their training data set. As down-core assemblages are temporally independent from our training set, MAT's explanatory power on core data (substituting space for time) will be lower than the model's explanatory power on an autocorrelated training database. In contrast, we find the explanatory power of GAM, WA PLS and IKTF on independent validation data remains unchanged. As such, these models may provide paleo winter sea ice estimates with a degree of precision

GAM

Our analysis suggests that both GAM and WA PLS are statistically robust procedures, whilst MAT and IKTF are not. Performance statistics indicate that the loss of explanatory power for GAM, when applied to independent data, may be less than that of MAT. Use of linear regression between the fitted values of GAM (as the predictor variable) and observed data suggests GAM is unbiased. Based on these latter linear regressions, GAM appears to be the better choice of model for the estimation of paleo winter sea ice when compared with MAT.

Our application of GAM used only four diatoms as predictors for winter sea ice, *A. actinochilus*, *F. curta*, *F. cylindrus* and *T. lentiginosa*. This is in contrast to MAT, IKTF and WA PLS where the entire diatom relative abundance matrix is used (all 32 species). Use of only four species provides GAM with a greater transparency and interpretability in biological/ecological terms. Our current knowledge of diatom ecology suggests the use of these four diatoms to estimate winter sea ice provides a biologically meaningful method to derive paleo sea ice estimates (Armand et al., 2005; Crosta et al., 2005).

Previous research on the ecology and biogeography of diatoms within the Southern Ocean supports the use of *F. cylindrus*, *F. curta*, *A. actinochilus* and *T. lentiginosa* as sea ice proxies within our application of GAM. The use of multivariate analysis has suggested *F. cylindrus*, *F. curta*, and *A. actinochilus* each possess an affinity for the sea ice environment (Taylor et al., 1997; Cunningham and Leventer, 1998; Armand et al., 2005; Buffen et al., 2007; Esper et al., 2010; Olguín and Alder, 2011; Esper and Gersonde, 2014). *T. lentiginosa* has a negative association with winter sea ice cover, hence the utility of *T. lentiginosa* as a sea ice proxy within our GAM. Abundances of *T. lentiginosa* have been shown to be higher in open ocean regions (Taylor et al., 1997) adjacent to the winter sea ice edge, with the abundances of *T. lentiginosa* observed between a SST of 1–8 °C, displaying an inverse relationship with sea ice (Crosta et al., 2005). Indeed, Buffen et al. (2007) identified *T. lentiginosa* as a dominant diatom within their 'open coastal ocean assemblage', an assemblage that was highly correlated with sea ice. Modern water column observations from Antarctic coastal locations clearly indicate small and persistent abundances of *T. lentiginosa* in amongst the sea ice diatom community (Armand and Leventer (Totten and Mertz regions) pers. obs. 2014) clearly indicating that the species is not completely inhibited by sea ice conditions. Therefore, we feel the diatoms used within our GAM as a sea ice proxy are well justified by current knowledge and observations.

The work of Armand et al. (2005) suggests *F. cylindrus*, *F. curta* and *A. actinochilus* possess a threshold response to sea ice cover, with abundances being more responsive to higher sea ice concentration. In contrast, *T. lentiginosa* may be more responsive to lower sea ice concentration (Crosta et al., 2005). In conclusion, we feel our transformation of the winter sea ice variable, which places an increased weighting on the importance of changes to both lower and higher sea ice concentrations, can be justified on ecological and observational grounds. The log transformation of the winter sea ice variable also overcomes the bounded nature of the variable.

Comparing the paleo winter sea ice records for GAM, WA PLS, IKTF and MAT

The GAM based paleo winter sea ice concentration (wSIC) record for core SO136-111 suggests winter sea ice expansion may have occurred within the southwestern Pacific Ocean during the Antarctic Cold Reversal (ACR) (also known as the New Zealand late glacial reversal, Williams et al., 2010) (Fig. 8). The GAM sea ice record also reveals an updated eLGM climatology that broadly agrees with New Zealand pollen (Newnham et al., 2007) and east Australian aeolian sediment-based climatic reconstructions (Petherick et al., 2008), as shown in Fig. 8. GAM estimates winter sea ice was present at the site of core SO136-111 throughout the extended LGM (eLGM), dated between 18 and 30 kyr BP (Petherick et al., 2008; Newnham et al., 2007; Williams et al., 2010).

During the eLGM time-slice, GAM winter sea ice estimates declined during the eLGM interstadial/Antarctic Isotope maxima 2 (AIM 2) (Petherick et al., 2008; Vandergoes et al., 2013) and increased during the two eLGM cold phases dated from rv30.8 to 27.6 and rv24 to 19 kyr BP (Stephens et al., 2012; Petherick et al., 2008). The eLGM cold phases and interstadial, as well as the duration of the eLGM itself, are hypothesized to have been widely registered/expressed throughout the Southern Ocean (Newnham et al., 2007; Vandergoes et al., 2013). Our GAM derived paleo winter sea ice records provide the first indication of a southwestern Pacific Ocean sea ice response to the eLGM cold phases and interstadial. Therefore, our paleo sea ice record can be used to test hypotheses for eLGM climatic variability that imply a wider expression of the eLGM climatic variation throughout the Southern Ocean.

The paleo winter sea ice records provided by WA PLS and IKTF failed to indicate a change in southwestern Pacific Ocean winter sea ice climatology, particularly in identifying an expression of the LGM interstadial/AIM 2 and the ACR (Fig. 7). Similarly, no significant increase in winter sea ice was estimated to reflect the potential expression of the LGM cold phases by these two methods. Both WA PLS and IKTF fail to agree with GAM on the timing of the LGM. Similarly, whilst MAT provided an LGM paleo winter sea ice record that generally agreed with GAM, the variation in MAT based estimates of winter sea ice between the climatic events of the LGM

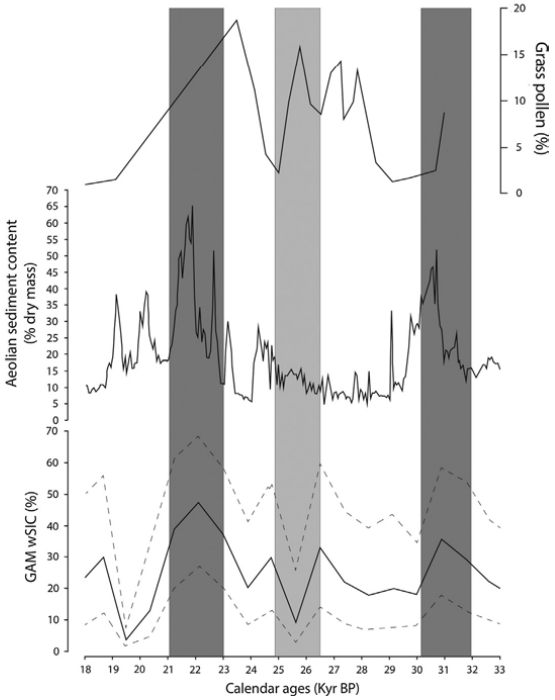

Fig. 8. The wSIC record from GAM is plotted against the aeolian sediment content of Petherick et al. (2008) and the percentage of grass pollen recorded by Newnham et al. (2007). Each of the proxy records are plotted with solid black lines. The 95% confidence intervals for our wSIC estimates are illustrated by the dashed black lines. An increase in the grass pollen percentage generally indicates a cooler climate (Newnham et al., 2007) whilst increases in aeolian sediment content are indicative of elevated dust transport, increased aridity and (possibly) a cooler climate (Petherick et al., 2008). The eLGM cold phases are shaded dark gray whilst AIM 2 is shaded in light gray.

was small. MAT estimates highlighted a timing interval for the LGM that was in broad agreement with our GAM estimates, furthermore MAT estimates also resolved winter sea ice was present at the site of core SO136-111 during the ACR.

GAM appears to provide the most detailed paleo winter sea ice record for the site of SO136-111 and appears to agree with previous New Zealand and east Australian based studies. As such the GAM sea ice record supports hypotheses suggesting the paleo climate of New Zealand may have been influenced by broader scale changes, which should have produced a similar climatic amelioration throughout the Southern Ocean (Newnham et al., 2007 and Vandergoes et al., 2013).

Conclusions

Robust and reliable estimates of paleo sea ice require that the relevant assumptions of the statistical methods applied are not violated. Similarly, as some methods (i.e. IKTF and WA PLS) have an assumed biological species-response model, their applicability to biological datasets that do not conform to these *a priori* assumptions could be limited. The IKTF method makes strict assumptions on model errors (namely normality of model errors and an underlying linear relationship between diatom taxa and winter sea ice), which are not satisfied. We, therefore, conclude that IKTF is not an appropriate model for estimating Southern Ocean paleo sea ice based on diatoms. We also discussed the inappropriateness of applying PCA to diatom relative abundance data, suggesting again that the IKTF model is not appropriate. A hold out validation on spatially independent data suggests that GAM, WA PLS and IKTF, when compared with MAT, are the least biased by spatial autocorrelation. Our analysis does suggest that MAT utilizes spatial structures within our data to achieve an apparently lower RMSEP. We applied a statistical test to evaluate the success, or failure, of each model to capture the key associations between diatom assemblages and wSIC under 10-fold hold out validation. The latter statistical test involved fitting a linear regression between model estimates (fitted values) and observed data, and then assessing if the slopes were significantly different from one, with a zero intercept. Evaluating MAT, IKTF, GAM and WAPLS in this way revealed that MAT possessed the poorest fit to our data, whilst IKTF, WA PLS and GAM fitted the data better.

We demonstrated the underlying species response models that best define the association between sea ice diatoms and winter sea ice cover is generally not unimodal. As WA PLS assumes an underlying unimodal species-response function (ter Braak et al., 1993) the model will fail when applied to non-unimodal species response curves. The presence of monotonic, bimodal and unidirectional species-response curves poses an issue for the application of WA PLS to our database. Additionally, a comparison of HOF modelling on untransformed (suggesting three diatoms had no response to sea ice) and log transformed data (with a response for all species) suggests log transforms may enhance the influence of rare taxa (i.e. noise) that have no significant relationship with sea ice. Whilst GAM uses only diatoms with a significant response to sea ice regardless of the data transform applied, WA PLS, IKTF and MAT incorporate diatoms with no statistically significant relation to

sea ice when estimating paleo sea ice cover. Application of such models in earlier literature have failed to address such relationships, having often assumed methods used for the estimation of sea-surface temperatures from diatoms would be applicable wholesale to the estimation of winter sea ice cover/concentrations. We have demonstrated that either GAM or WA PLS are the more appropriate models for estimating southern hemisphere wSIC based on a relevant diatom proxy. However, we believe GAM provides the most robust method for estimating paleo wSIC. The GAM model is more readily interpreted through a graphical summary of the relationship's GAM uses and the evaluation, and thus significance, of an individual diatom species as a proxy for wSIC is straight forward. GAM also has a stronger biological basis, using only those species that have a clear ecological relationship with winter sea ice cover. Finally, the underlying species response curves between diatom abundance and winter sea ice is variable, and often not unimodal, which poses an issue for WA PLS, whilst GAM can better deal with an array of species response curves. Analysts could therefore 'train' their GAM to use only biologically relevant proxy species, with the benefit of ignoring other species that may be spatially autocorrelated due to other unmeasured environmental variables. In turn, GAM may have a smaller tendency to be biased by autocorrelation within the predictor (species assemblage) matrix.

We argue that GAM provides the most detailed paleo sea ice data for core SO136-111, indicating that the ACR, eLGM, AIM 2 and eLGM cold periods were important for the southwestern Pacific. Additionally, GAM winter sea ice paleo data complements New Zealand based studies that suggest the LGM may have started at ~30 kyr BP and ended by 18 kyr BP, an interval referred to as the eLGM. Paleo sea ice reconstructions from WA PLS and IKTF do not suggest winter sea ice coverage was altered during the ACR or eLGM interstadial/AIM 2. The paleo winter sea ice records derived from MAT were in a broader agreement with GAM and clearly document sea ice coverage during the ACR. Ultimately, one could argue that GAM is better placed to test the hypotheses recently proposed by New Zealand paleo climatic studies, which have suggested mechanisms for climate change that should have produced similar changes throughout the Southern Ocean (Newnham et al., 2007; Vandergoes et al., 2013).

Acknowledgments

This research was funded by the Australian Government through the provision of an Australian Postgraduate Award granted to Alexander Ferry. We also wish to gratefully acknowledge funding from PAGES for the authors to attend the recent PAGES Sea ice Proxies working group workshops held in Montreal, Canada and Cambridge, UK. The provision of data from Petherick et al. (2008), by Lynda Petherick, for the comparison of paleo data presented within our paper is gratefully acknowledged. We appreciate the constructive comments provided by the reviewers, which greatly improved our work.

Appendix A

A list of the diatom species included within our training database.

Actinocyclus actinochilus
Alveus marinus
Azpeitia tabularis var. *tabularis*
Chaetoceros resting spores
Fragilariopsis curta
Fragilariopsis cylindrus
Fragilariopsis doliolus
Fragilariopsis kerguelensis
Fragilariopsis obliquecostata
Fragilariopsis rhombica
Fragilariopsis ritscheri
Fragilariopsis separanda
Fragilariopsis sublinearis
Hemidiscus cuneiformis
Porosira glacialis
Porosira pseudodenticulata
Rhizosolenia antennata group sensu Crosta et al. (2004)
Rhizosolenia styliformis group sensu Crosta et al. (2004)
Roperia tesselata
Stellarima microtrias
Thalassionema nitzschioides var. *lanceolata* group
T. nitzschioides var. *parva*
Thalassionema nitzschioides
Thalassiosira antarctica group
Thalassiosira symmetrica Fryxell and *Hasle* and morphologically related species
Thalassiosira gracilis group
Thalassiosira lentiginosa
Thalassiosira oestrupii var. *oestrupii*
Thalassiosira oliverana
Thalassiosira tumida
Thalassiothrix spp. group
Trichotoxon reinboldii

References

Armand, L.K., Leventer, A., 2010. Palaeo sea ice distribution and reconstruction derived from the geological record. In: Thomas, D.N., Dieckmann, G.S. (Eds.), Sea Ice, second ed. Wiley-Blackwell, Oxford, UK. http://dx.doi.org/10.1002/9781444317145.ch13.

Armand, L.K., Crosta, X., Romero, O., Pichon, J.J., 2005. The biogeography of major diatom taxa in Southern Ocean sediments: 1. Sea ice related species. Palaeogeography, Palaeoclimatology, Palaeoecology 223, 93–126.

Austin, M., 2007. Species distribution models and ecological theory: a critical assessment and some possible new approaches. Ecological Modelling 200, 1–19.

Becker, R.A., Wilks, A.R., 2013 (Original S code). R Version by Ray Brownrigg. Enhancements by Thomas P. Minka <tpminka@media.mit.edu>. Maps: Draw Geographical Maps. R Package Version 2.3-2. <http://CRAN.R-project.org/package=maps>.

Bennett, N.D., Croke, B.F.W., Guariso, G., Guillaume, J.H.A., Hamilton, S.H., Jakeman, A.J., Marsili-Libelli, S., Newham, L.T.H., Norton, J.P., Perrin, C., Pierce, S.A., Robson, B., Seppelt, R., Voinov, A.A., Fath, B.D., Andreassian, V., 2013. Characterising performance of environmental models. Environmental Modelling and Software 40, 1–20.

Birks, H.J.B., 2003. Quantitative palaeoenvironmental reconstructions from Holocene biological data. In: Mackay, A., Battarbee, R.W., Birks, H.J.B., Oldfield, F. (Eds.), Global Change in the Holocene, London, pp. 107–123.

Birks, H.J.B., 2012. Overview of numerical methods in palaeolimnology. In: Birks, J.H.B., Andrè, F.L., Juggins, S., Smol, J.P. (Eds.), Tracking Environmental Change Using Lake Sediments. Springer, Netherlands, pp. 19–92.

Birks, H.J.B., Line, J.M., Juggins, S., Stevenson, A.C., Ter Braak, C.J.F., 1990. Diatoms and pH reconstruction. Philosophical Transactions of the Royal Society of London. Series B, Biological Sciences 327, 263–278.

Borcard, D., Legendre, P., 2002. All-scale spatial analysis of ecological data by means of principal coordinates of neighbour matrices. Ecological Modelling 153, 51–68.

Borcard, D., Legendre, P., Drapeau, P., 1992. Partialling out the spatial component of ecological variation. Ecology 73, 1045–1055.

Borcard, D., Legendre, P., Avois-Jacquet, C., Tuomisto, H., 2004. Dissecting the spatial structure of ecological data at multiple scales. Ecology 85, 1826–1832.

Bouckaert, R.R., Frank, E., 2004. Evaluating the replicability of significance tests for comparing learning algorithms. Advances in Knowledge Discovery and Data Mining 3056, 3–12.

Buffen, A., Leventer, A., Rubin, A., Hutchins, T., 2007. Diatom assemblages in surface sediments of the northwestern Weddell Sea, Antarctic Peninsula. Marine Micropaleontology 62, 7–30.

Comiso, J., 2000. Bootstrap Sea Ice Concentrations from Nimbus-7 SMMR and DMSP SSM/I-SSMIS. Version 2. National Snow and Ice Data Center, Boulder, Colorado, USA.

Crosta, X., Pichon, J.-J., Burckle, L.H., 1998. Application of modern analog technique to marine Antarctic diatoms: reconstruction of maximum sea-ice extent at the Last Glacial Maximum. Palaeoceanography 13, 284–297.

Crosta, X., Sturm, A., Armand, L., Pichon, J.-J., 2004. Late Quaternary sea ice history in the Indian sector of the Southern Ocean as recorded by diatom assemblages. Marine Micropaleontology 50, 209–223.

Crosta, X., Romero, O., Armand, L.K., Pichon, J.J., 2005. The biogeography of major diatom taxa in Southern Ocean sediments: 2. Open ocean related species. Palaeogeography, Palaeoclimatology, Palaeoecology 223, 66–92.

Cunningham, W.L., Leventer, A., 1998. Diatom assemblages in surface sediments of the Ross Sea: relationship to present oceanographic conditions. Antarctic Science 10, 134–146.

Dowsett, H.J., Poore, R.Z., 1990. A new planktic foraminifer transfer function for estimating Pliocene–Holocene paleoceanographic conditions in the North Atlantic. Marine Micropaleontology 16, 1–23.

Dray, S., 2013. spacemakeR: Spatial Modelling. R Package Version 0.0-5/r113. <http://R-Forge.R-project.org/projects/sedar/>.

Dray, S., Legendre, P., Peres-Neto, P.R., 2006. Spatial modelling: a comprehensive framework for principal coordinate analysis of neighbour matrices (PCNM). Ecological Modelling 196, 483–493.

Dürrenmatt, D.J., Gujer, W., 2012. Data-driven modeling approaches to support wastewater treatment plant operation. Environmental Modelling & Software 30, 47–56.

Efron, B., 1979. Bootstrap methods: another Look at the Jackknife. The Annals of Statistics 7, 1–26.

Esper, O., Gersonde, R., 2014. New tools for the reconstruction of Pleistocene Antarctic sea ice. Palaeogeography, Palaeoclimatology, Palaeoecology 399, 260–283.

Esper, O., Gersonde, R., Kadagies, N., 2010. Diatom distribution in southeastern Pacific surface sediments and their relationship to modern environmental variables. Palaeogeography, Palaeoclimatology, Palaeoecology 27, 1–27.

Furrer R., Nychka, D., Sain, S., 2013. Fields: Tools for Spatial Data. R Package Version 6.7.6. <http://CRAN.R project.org/package=fields>.

Gadagkar, R., 1989. An undesirable property of Hill's diversity index N_2. Oecologia 80, 140–141.

Gastwirth, J.L., Gel, Y.R., Hu, W.L.W., Lyubchich, V., Miao, W., Noguchi, K., 2013. An R Package for Biostatistics, Public Policy, and law. <http://cran.r-project.org/web/packages/lawstat/index.html>.

Gavin, D.G., Oswald, W.W., Wahl, E.R., Williams, J.W., 2003. A statistical approach to evaluating distance metrics and analog assignments for pollen records. Quaternary Research 60, 356–367.

Guiot, J., de Vernal, A., 2007. Transfer function: methods for quantitative paleoceanography based on microfossils. In: Hillaire-Marcel, C., De Vernal, A. (Eds.), Proxies in Late Cenozoic Paleoceanography. Elsevier, Amsterdam, pp. 523–557.

Hammer, Ø., Harper, D.A.T., Ryan, P.D., 2001. PAST: Paleontological Statistics Software Package for Education and Data Analysis. Palaeontologia Electronica, vol. 4, 9pp.

Hastie, T., Tibshirani, R., 1987. Generalized additive models: some applications. Journal of the American Statistical Association 82, 371–386.

Hill, M.O., 1973. Diversity and evenness: a unifying notation and its consequences. Ecology 54, 427–432.

Huisman, J., Olff, H., Fresco, L.F.M., 1993. A hierarchical set of models for species response analysis. Journal of Vegetation Science 4, 37–46.

Imbrie, J., Kipp, N.G., 1971. A new micropaleontological method for quantitative paleoclimatology: application to a late Pleistocene Caribbean core. In: Turekian, K.K. (Ed.), The Late Cenozoic Glacial Ages. Yale University Press, London, pp. 71–147.

Jackson, D.A., 1993. Stopping rules in principal components analysis: a comparison of heuristical and statistical approaches. Ecology 74, 2204–2214.

Jansen, F., Oksanen, J., 2013. How tomodel species responses along ecological gradients – Huisman–Olff–Fresco models revisited. Journal of Vegetation Science 24, 1108–1117.

Jansen, E., Overpeck, J., Briffa, K.R., Duplessy, J.-C., Joos, F., Masson-Delmotte, V., Olago, D., Otto-Bliesner, B., Peltier, W.R., Rahmstorf, S., Ramesh, R., Raynaud, D., Rind, D., Solomina, O., Villalba, R., Zhang, D., 2007. Palaeoclimate. In: Solomon, S., Qin, D., Manning, M., Chen, Z., Marquis, M., Averyt, K.B., Tignor, M., Miller, H.L. (Eds.), Climate Change 2007: The PhysicalScience Basis. Contribution of Working Group I to the Fourth Assessment Report of the Intergovernmental Panel on Climate Change. Cambridge University Press, Cambridge, United Kingdom and New York, NY, USA.

Juggins, S., 2012. rioja: Analysis of Quaternary Science Data, R Package Version (0.8-4). <http://cran.r-project.org/package=rioja>.

Juggins, S., Birks, J.B., 2012. Quantitative environmental reconstructions from biological data. In: Birks, H.J.B., Lotter, A.F., Jugins, S., Smol, J.P. (Eds.), Tracking Environmental Change Using Lake Sediments. Springer Science and Business Media, pp. 431–494.

Justwan, A., Koç, N., 2008. A diatom based transfer function for reconstructing sea ice concentrations in the North Atlantic. Marine Micropaleontology 66, 264–278.

Kohavi, R., 1995. A study of cross-validation and bootstrap for accuracy estimation and model selection. In: International Joint Conference on Artificial Intelligence, vol. 2, pp. 1137–1143.

Legendre, P., Birks, H.J.B., 2012. From classical to canonical ordination. In: Birks, H.J.B., Lotter, A.F., Jugins, S., Smol, J.P. (Eds.), Tracking Environmental Change Using Lake Sediments. Springer Science and Business Media, pp. 201–248.

Legendre, P., Borcard, D., Peres-Neto, P., 2005. Analyzing beta diversity: partitioning the spatial variation of community composition data. Ecological Monographs 75, 435–450.

Malmgren, B.A., Kucera, M., Nyberg, J., Waelbroeck, C., 2001. Comparison of statistical and artificial neural network techniques for estimating past sea surface temperatures from planktonic foraminifer census data. Palaeoceanography 16, 1–11.

McIlroy, D., Packaged for R by Ray Brownrigg, Thomas P. Minka and transition to Plan 9 codebase by Roger Bivand. 2013. mapproj: Map Projections. R Package Version 1.2-1. <http://CRAN.R-project.org/package=mapproj>.

Newnham, R.M., Lowe, D.J., Giles, T., Alloway, B.V., 2007. Vegetation and climate of Auckland, New Zealand, since ca. 32,000 cal. yr ago: support for an extended LGM. Journal of Quaternary Science 22, 517–534.

Oksanen, J., Minchin, P.R., 2002. Continuum theory revisited: what shape are species responses along ecological gradients? Ecological Modelling 157, 119–129.

Oksanen, J., Blanchet, F.G., Kindt, R., Legendre, P., Minchin, P.R., O'Hara, R.B., Simpson, G.L., Solymos, P., Henry, M., Stevens, H., Wagner, H., 2013. vegan: Community Ecology Package. R Package Version 2.0-7. <http://CRAN.R-project.org/package=vegan>.

Olguín, H.F., Alder, V.A., 2011. Species composition and biogeography of diatoms in antarctic and subantarctic (Argentine shelf) waters (37–76°S). Deep-Sea Research II 58, 139–152.

Petherick, L., McGowan, H., Moss, P., 2008. Climate variability during the Last Glacial Maximum in eastern Australia: evidence of two stadials? Journal of Quaternary Science 23, 787–802.

Pichon, J.J., Labeyrie, L.D., Gilles, B., Labracherir, M., Duprat, J., Jouzel, J., 1992. Surface water temperature changes in the high latitudes of the Southern Hemisphere over the last glacial–interglacial cycle. Palaeoceanography 7, 289–318.

Röthlisberger, R., Crosta, X., Abram, N.J., Armand, L., Wolff, E.W., 2011. Potential and limitations of marine and ice core sea ice proxies: an example from the Indian Ocean sector. Quaternary Science Reviews 29, 296–302.

Stephens, T., Atkin, D., Augustinus, P., Shane, P., Lorrey, A., Street-Perrott, A., Nilsson, A., Snowball, I., 2012. A late glacial Antarctic climate teleconnection and variable Holocene seasonality at Lake Pupuke, Auckland, New Zealand. Journal of Paleolimnology 48, 785–800.

Taylor, F., McMinn, A., Franklin, D., 1997. Distribution of diatoms in surface sediments of Prydz Bay, Antarctica. Marine Micropaleontology 32, 209–229.

Telford, R.J., Birks, H.J.B., 2005. The secret assumption of transfer functions: problems with spatial autocorrelation in evaluating model performance. Quaternary Science Reviews 24, 2173–2179.

Telford, R.J., Birks, H.J.B., 2011. Effect of uneven sampling along an environmental gradient on transfer-function performance. Journal of Paleolimnology 46, 99–106.

ter Braak, C.J.F., 1995. Non-linear methods for multivariate statistical calibration and their use in palaeoecology: a comparison of inverse (k-nearest neighbours, partial least squares and weighted averaging partial least squares) and classical approaches. Chemometrics and Intelligent Laboratory Systems 28, 165–180.

ter Braak, C.J.F., Juggins, S., 1993. Weighted averaging partial least squares regression (WA-PLS): an improved method for reconstructing environmental variables from species assemblages. Hydrobiologia 269 (270), 485–502.

Ter Braak, C.J.F., Juggins, S., Birks, H.J.B., van der Voet, H., 1993. Weighted averaging partial least squares regression (WA-PLS): definition and comparison with other methods for species-environment calibration. In: Patil, G.P., Rao, C.R. (Eds.), Multivariate Environmental Statistics. Elsevier Science Publishers B.V. (North-Holland), Amsterdam, pp. 525–560 (Chapter 25).

van der Voet, H., 1994. Comparing the predictive accuracy of models using a simple randomization test. Chemometrics and Intelligent Laboratory Systems 25, 313–323.

Vandergoes, M.J., Newnham, R.M., Denton, G.H., Blaauw, M., Barrell, D.J.A., 2013. The anatomy of Last Glacial Maximum climate variations in south Westland, New Zealand, derived from pollen records. Quaternary Science Reviews 74, 215–229.

Williams, P.W., Neil, H.L., Zhao, J.-X., 2010. Age frequency distribution and revised stable isotope curves for New Zealand speleothems: palaeoclimatic implications. International Journal of Speleology 39, 99–112.

Wood, S.N., 2006. Generalized Additive Models: An Introduction with R. Chapman and Hall/CRC Press, Boca Raton, Fl.

Wood, S.N., 2013. mgcv: Mixed GAM Computation Vehicle with GCV/AIC/REML Smoothness Estimation. R Package Version 1.7-26. <http://cran.r-project.org/web/packages/mgcv/index.html>.

Wuertz, D., 2013. Rmetrics core team members, uses code built in from the following R contributed packages: gmm from Pierre Chauss, gld from Robert King, gss from Chong Gu, nortest from Juergen Gross, HyperbolicDist from David Scott, sandwich from Thomas Lumley, Achim Zeileis, fortran/C code from Kersti Aas and akima from Albrecht Gebhardt.fBasics: Rmetrics – Markets and Basic Statistics. R Package Version 3010.86. <http://CRAN.R-project.org/package=fBasics>.

Zielinski, U., Gersonde, R., 1997. Diatom distribution in Southern Ocean surface sediments (Atlantic sector): implications for paleoenvironmental reconstructions. Palaeogeography, Palaeoclimatology, Palaeoecology 129, 213–250.

List of Appendices for Chapter 2

Appendices 2.1 through to 2.10 provide R scripts, output and data that was used within Chapter 2, but were not included in any published supplementary material, tables or figures within Chapter 2. The contents of each appendix have been ordered to match the content of Chapter 2. Appendix 2.1 provides the R scripts and output from the HOF models fitted to untransformed diatom abundances and the winter sea-ice concentration data. The contents of Appendix 2.1 are described on pages 103 to 104 in Chapter 2, under the subsection entitled 'Species response modelling via Hierarchical logistic regression'. Appendices 2.2, 2.4, 2.5 and 2.6 list the R scripts used for the 10 fold hold out validation of IKTF, MAT, WA PLS and GAM, respectively. We also list the R scripts used for the application of tests for all statistical assumptions, and the computation of RMSE and RMSEP for each model. The analysis presented in Appendices 2.2, 2.4, 2.5 and 2.6 are described on pages 103 to 106 of Chapter 2. Appendix 2.3 provides output from the PCA used in the application of the IKTF model to our training database, as detailed on page 104, in the sub-section entitled 'Imbrie and Kipp transfer function'. In Appendix 2.7 the use of a classical GAM, to assess the ability of our GAM to deal with unimodal species response relationships, is detailed. The analysis presented in Appendix 2.6 is described on page 103 Chapter 2. Appendix 2.8 lists the R output, and scripts, from the variance partitioning outlined on page 103 in the sub-section entitled 'Variance partitioning' in Chapter 2. Finally, in Appendix 2.10 the data plotted in Figure 7 of Chapter 2 is provided.

Data from the study are available from the Australian Oceans Data Network (AODN; http://catalogue.aodn.org.au/geonetwork/srv/en/metadata.show?uuid=5fed5a0c-3419-429a-a05c-c3e536913f1f).

This page is intentionally left blank.

Chapter 3

First records of winter sea-ice concentration in the southwest Pacific sector of the Southern Ocean.

Authors:

Alexander J. Ferry[1], Xavier Crosta[2], Patrick G. Quilty[3], David Fink[4], William Howard[5] and Leanne K. Armand[1]

1. Department of Biological Sciences, Climate Futures at Macquarie University, North Ryde, 2109, New South Wales, Australia. alexander.ferry@mq.edu.au, leanne.armand@mq.edu.au

2. DGO, UMR-CNRS 5805 EPOC, Université de Bordeaux I, Avenue des Facultés, 33405 Talence Cedex, France. x.crosta@epoc.u-bordeaux1.fr

3. School of Earth Sciences, University of Tasmania, Private Bag 79, Hobart, 7001, Tasmania, Australia. P.Quilty@utas.edu.au

4. Institute for Environmental Research, Australian Nuclear Science and Technology Organization, PMB 1, Menai, 2234, New South Wales, Australia. fink@ansto.gov.au

5. School of Earth Sciences, University of Melbourne, Melbourne, 3010, Victoria, Australia. whoward@unimelb.edu.au

Anticipated Journal:

Paleoceanography

Keywords: MWP-1A, Antarctic Cold Reversal, Holocene, diatoms, sea ice, Generalized Additive Model, Modern Analogue Technique

Abstract

Using a Generalized Additive Model (GAM) we provide a winter sea-ice concentration record from two cores located within the southwest Pacific sector of the Southern Ocean. We use a time series analysis on satellite records of sea-ice concentration data to extend the standard 13.25 year time series used for paleoceanography. It is shown that the paleo sea-ice record from GAM is consistent with previously published records. We expand the paleo winter sea-ice record for the southwest Pacific sector of the Southern Ocean with the inclusion of new paleo winter sea-ice estimates for marine sediment core E27-23 (59°37.1´S, 155°14.3´E). Core E27-23 allows us to provide a more comprehensive view of winter sea-ice dynamics for the southwest Pacific Ocean over the last 15 kyr BP. Our paleo winter sea-ice concentration estimates provide the first suggestion that winter sea-ice within the southwestern Pacific may have expanded during the Antarctic Cold Reversal. Throughout the Holocene, core E27-23 documents millennial scale variability in paleo winter sea-ice coverage within the southwest Pacific. The Antarctic Cold Reversal may have been the product of melt water pulse -1A. Holocene winter sea-ice expansion may have resulted from the Laurentide Ice Sheet deglaciation, increased intensity of the westerly winds, as well as a northern migration of the Subtropical and/or Sub-Antarctic Fronts. Brief consideration is given to the development of a paleo summer sea-ice proxy. There is no evidence that summer sea ice ever existed at core sites SO136-111 and E27-23 over the last 220 and 52 thousand years, respectively.

1 Introduction

Sea ice is the most obvious expansive and seasonal geophysical parameter on the Earth's surface (Comiso, 2010). The annual sea-ice cycle of formation and retreat influences atmospheric and oceanic processes, therefore modulating the global climate (Dieckmann and Hellmer, 2010; Comiso, 2010; Brandon et al., 2010). Sea ice exerts a significant influence on the radiative balance of the polar regions and acts as an insulator limiting ocean-atmosphere heat and gas fluxes (Comiso, 2010). Reconstructing the historical and paleo environmental occurrence of sea ice is a key component of any effort attempting to understand past and future climatic change (Dieckmann and Hellmer, 2010).

Diatom abundances are a well-established proxy for Southern Ocean sea ice, providing a means to obtain qualitative (Gersonde and Zielinski, 2000; Schneider-Mor et al., 2005) and quantitative estimates for winter (September) sea-ice concentrations, as well as monthly sea-ice cover (Crosta et al., 1998; Gersonde et al., 2005; Armand and Leventer, 2010, Chapter 2). Core SO136-111 (~56°S, 160°E) permitted the first quantitative reconstruction of paleo sea ice over the previous two climatic cycles, documenting glacial to interglacial sea-ice advance and retreat during marine isotopic stages 6, 4, and 2 (Crosta et al., 2004).

The paleo sea-ice record derived from core SO136-111 has served as a benchmark for the establishment of new Southern Ocean sea-ice proxies such as sea-salt flux (Röthlisberger et al., 2010), and iodide and iodate speciation deposited within an Antarctic ice core (Spolaor et al., 2013). The signals recorded within proxy data can constrain hypotheses to be tested by climate models, whilst climate models can be evaluated by comparison of their output with proxy records. Comparisons between models and proxies provide an opportunity to study mechanisms

that may have been important for past sea-ice variability, but may be of less significance in the modern day climate (Goosse et al., 2013). Our paleo sea-ice records at the locations of cores SO136-111 and E27-23 (59°S, 155°E) provide paleo data against which new proxies and climate models can be validated.

This paper applies a Generalized Additive Model (GAM; Chapter 2) to revise paleo sea-ice estimates for core SO136-111. Chapter 2 concluded that GAM was the most robust method for estimating paleo sea-ice as it had the lowest prediction error, was the least biased by spatial autocorrelation, and provided the most unbiased paleo sea-ice estimates. In applying GAM to core SO136-111 we aim to compare GAM with the Modern Analogue Technique (MAT) of Crosta et al. (2004), illustrating the broad consistency between the two methods, as well as the improvement GAM provides the paleo-oceanographer.

As the diatom core top samples represent, on average, 1 kyr of sedimentation, it is important that the sea-ice training data set excludes the effects of recent decadal climate change. Previous work used the 13.25 year satellite record of Schweitzer (1995), which ends in December 1991, to exclude the effects of recent decadal climatic change. However, Armand and Leventer (2010) questioned whether the use of a 13.25 year satellite record of sea-ice concentration data may be too short for computing an average sea-ice concentration value that is representative of the sea-ice climatology. We apply a time series analysis on sea-ice concentration data to identify residual trends, defined as statistically significant increases or decreases in sea-ice concentration over time that cannot be explained by climatic variables (for example, the El Niño Southern Oscillation) or seasonal (and decadal) variations in sea-ice concentrations. Excluding that portion of the satellite sea-ice concentration record in which such trends can be identified may assist in the estimation of climatologically representative sea-ice concentrations for our training data set.

We then provide the first paleo winter sea-ice records for cores SO136-111 and E27-23, expanding the paleo sea-ice record of the southwest Pacific sector of the Southern Ocean to include seasonality. We compare our sea-ice records for the southwest Pacific sector with paleo sea-ice records from the south Atlantic sector of the Southern Ocean (Bianchi and Gersonde, 2004; Divine et al., 2010). Core E27-23, compared to core SO136-111, is located closer to the modern winter sea-ice edge in a position that is more analogous to the Atlantic cores. Therefore, core E27-23 allows us to provide a more robust comparison between the paleo sea-ice record from southwest Pacific and Atlantic sectors of the Southern Ocean over the last 15 kyr BP. Our focus then shifts to the southwest Pacific over last 15 kyr BP, focusing on the Antarctic Cold Reversal (ACR) and Holocene millennial scale climatic changes.

2 Methods

2.1 Training and core data sets

We use 163 sea-floor samples from the 243 samples present within the training database of Crosta et al. (2004) to estimate winter paleo sea-ice concentrations (Figure 1). Each of the sea-floor samples documents the relative abundance of 32 diatom species. The original training data set included many open ocean samples used to estimate sea-surface temperature; the inclusion of which, for the purposes of sea-ice estimation, would have been redundant. We chose to exclude some samples to establish a more even sampling of the environmental gradient within our training data set (Telford and Birks, 2011). Exclusion of samples was also carried out with respect to the spatial structure of our data, so that no single geographic locality was over- or under-represented within our training set. Thus, our objective was to remove samples from a broad range of longitudinal and latitudinal bands in order to preserve spatial diversity. All marine isotope stages (MIS) are defined according to Lisiecki and Raymo (2005a). We define the extended Last Glacial Maximum (eLGM) as that period between 35 and 18 kyr BP (Newnham et al. 2007), whilst the timing for the Antarctic Cold Reversal (ACR) is 14.2 to 12.5 kyr BP (Weber et al. 2014).

Core SO136-111 (Crosta et al., 2004) was collected from 56°40´S, 160°14´E within the Emerald Basin and Polar Frontal Zone (southwest Pacific sector of the Southern Ocean) (Figure 1). The core preserves a record of the last 200 kyr BP. However, as the core top is missing, the record of paleo sea-ice cover ends during the late Holocene at ~3 kyr BP. Sediment core E27-23 was extracted from 59°37.1´S, 155°14.3´E from a water depth of 3182 meters (Cassidy et al., 1977) in the Permanent Open Ocean Zone. The core chronology is presented hereafter for the first time.

Both cores are situated south of the Sub-Antarctic Front within the Antarctic Circumpolar Current (ACC), with E27-23 located closer to the modern winter sea-ice edge than core SO136-111 (Figure 1).

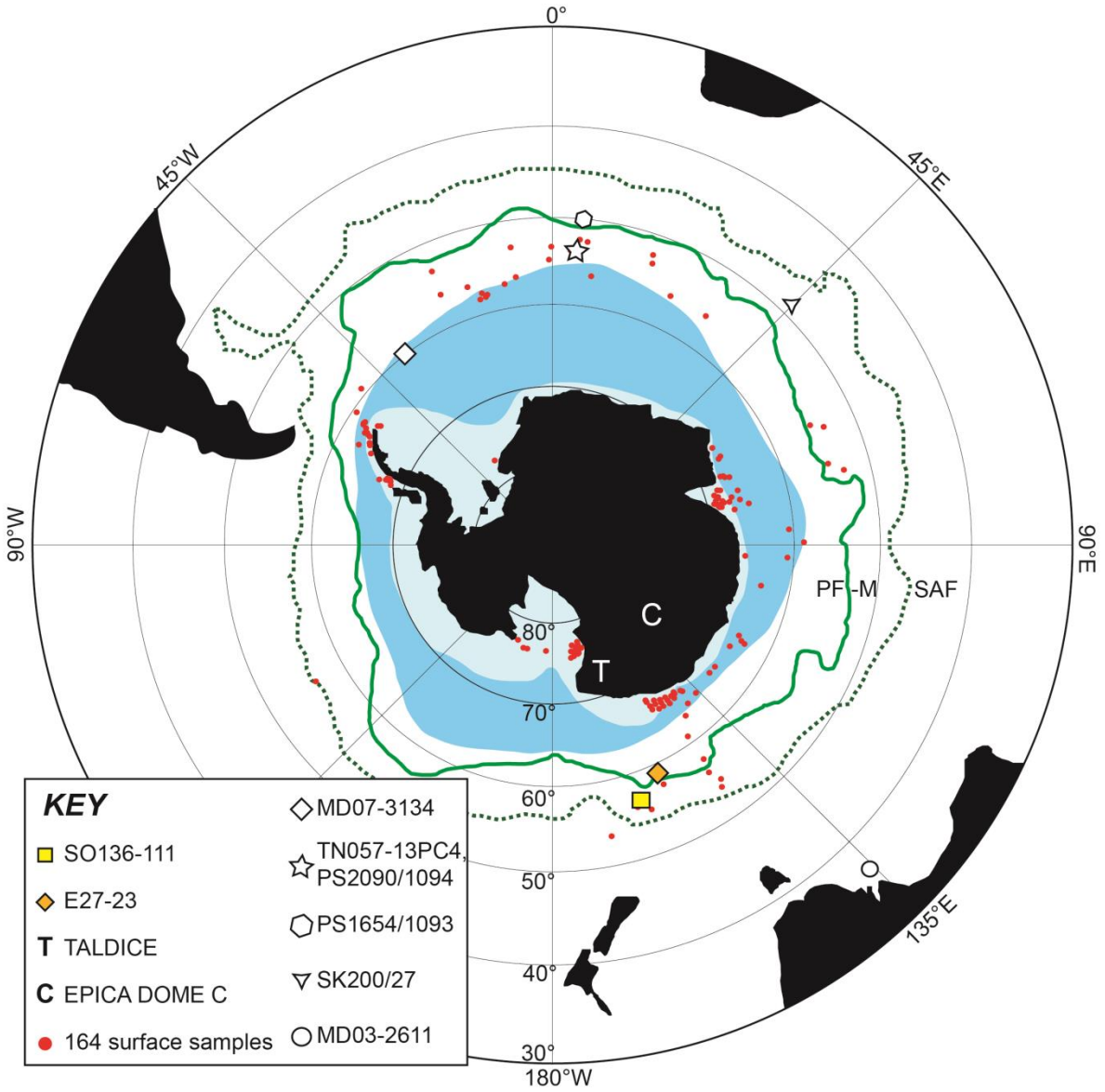

Figure 1. **The locations of the 163 samples used in our training data base (red circles) with the average winter sea-ice edge (dark blue shaded area) and summer sea-ice edge (light blue shaded area) from 1979 to 2000.** Also shown for context are the mean locations for the Polar Front (PF-M; green line) and the Sub-Antarctic Front (SAF; dashed green line) (Sokolov and Rintoul, 2009). Locations for the TALDICE and EPICA Dome C ice cores and marine sediment cores SO136-111, E27-23 (from the southwest Pacific), TN057-13PC4, PS2090/1094 and PS1654/1093 (from the Atlantic) are also indicated. *(Cores SK200/27 (Manoj et al., 2013) and MD07-3134 (Weber et al., 2014) used to examine iceberg-rafted debris records are identified).*

2.2 Analysis of the sea-ice data time series

Whilst Antarctic sea-ice extent as a whole has been increasing over the last 35 years, it is still important to investigate sea-ice behaviour on a regional scale (Stammerjohn et al. 2012; Parkinson and Cavalieri, 2012; Massom et al. 2013; Simmonds, 2015). As seasonality is present within the monthly winter sea-ice concentration time series (wSIC), we applied a regression with Auto Regressive Integrated Moving Average (ARIMA) errors (Bianco et al., 2001) and a time trend to the sea-ice satellite record. Regression with ARIMA errors describes the wSIC time series as a function of its past values and significant climatic variables. The regression with ARIMA errors includes autoregressive parameters, moving average parameters, and the number of differencing passes to describe seasonally recurring patterns in the wSIC time series. Sea-ice concentration data were derived from the bootstrapped algorithm of Comiso (2000), from November 1978 to December 2010, and supplied by the National Snow and Ice Data Centre. Winter sea-ice concentration (wSIC) was defined as the September average sea-ice concentration (Gersonde et al., 2005). Sea-ice concentration is defined as that fraction, or percentage, of ocean area that is covered by sea ice (Cavalieri et al. 1996). The regression model was fitted using the forecast package for R, version 4.01 (Hyndman, 2014). The input series (covariates) included within our regression included the following: the multivariate El Niño Southern Oscillation Index (MEI), the Southern Annular Mode (SAM), the Antarctic Oscillation (AAO), the average monthly CO_2 concentrations for Mauna Loa, the Total Solar Irradiance Index at Earth distance in W/m^2 (TSI), average monthly maximum temperatures, and the southern hemisphere Land-Ocean Temperature Index (LOTI). The significance of the time trend included within the regression model was used to determine the appropriate end point of the sea-ice time series to use for this study.

AAO data were sourced from the National Oceanic and Atmospheric Administrations (NOAA) national weather service, climate prediction centre. MEI is provided by the NOAA physical sciences division. TSI data are published by the University of Colorado, Boulder SORCE experiment. SAM data were compiled by the British Antarctic Survey and month/yr average CO_2 was sourced from NOAA ESRI data.

We focused our analysis on two sea-ice concentration data sets. The first represents a winter average sea-ice concentration calculated from 13.25 years of satellite data, consistent with the methodology of Crosta et al. (2004). The second sea-ice concentration data set uses average sea-ice concentrations calculated from an extended time series of satellite data. The exact temporal extent of the satellite data used is unique to each sector of the Southern Ocean and defined by our regression model with ARIMA errors.

2.3 Reconstruction diagnostics

We compare the maximum recorded diatom abundances between our training set and the fossilized assemblages of marine sediment cores SO136-111 and E27-23. Hills N2 diversity Index (Hill, 1973) was used to identify the effective number of occurrences for each diatom species within the training data set, and therefore to identify species that may have poorly defined optima. Analogue quality, and the presence of non-analogue samples for cores SO136-111 and E27-23, was explored with a squared chord distance and the five closest analogues. Regarding analogue quality, those samples considered to have no analogue had a distance greater than the 5^{th} percentile of all distances computed between the training and core data sets, whilst samples with poor analogues had a distance between the 10^{th} and 5^{th} percentiles of all distances.

Examination of analogue quality, and the presence of no analogue samples, is relevant not only for MAT, but is important to consider when applying all methods for the reconstruction of paleo sea ice. Sea-ice estimations derived from all reconstruction methods on core samples with poor analogues need to be treated with caution. A canonical correspondence analysis constrained by wSIC was used to compute a squared residual length for the taxonomic distances between the winter sea-ice axis and the samples within our training data set and the cores SO136-111 and E27-23. A core sample, with a squared residual length exceeding the 90th percentile for the squared residual lengths computed on the training set, is regarded as poorly fitted by winter sea-ice concentrations (Hill, 1973; Birks et al., 1990).

2.4 The statistical models used

Our paleo winter sea-ice data were estimated with a new application of GAM (Chapter 2). The absence of diatom flux to the sea-floor is considered to provide a proxy for permanent sea-ice cover and, by extension, the presence of summer sea ice (Gersonde et al., 2005). We therefore examined the presence of diatoms recorded in each core to infer the potential presence of summer sea-ice cover at the sites of core SO136-111 and E27-23. We used the statistical software PAST (Hammer et al., 2001) to apply MAT. We used the package mgcv (Wood, 2014) to apply GAM and rioja (Juggins, 2014) to apply the reconstruction diagnostics. Following Gloersen et al. (1992) and Gersonde et al. (2005), we consider wSIC less than 15% to indicate no sea-ice cover, 15 to 40% represents unconsolidated sea-ice, and concentrations above 40% to represent consolidated winter sea-ice. MAT estimates equal to or above an average of one month of sea-ice coverage per year are regarded as an indicator for the presence of sea-ice.

2.5 Material and stratigraphy

2.5.1 E27-23 chronology

A chronostratigraphy for piston core E27-23 (59°37.1'S, 155°14.3'E, water depth 3182 m) was established principally from Accelerator Mass Spectrometry (AMS) radiocarbon dating. Samples of the planktonic foraminifer *Neogloboquadrina pachyderma* sinistral were ultrasonically cleaned in methanol and oven-dried at 60°C prior to analysis. Twenty-six AMS ^{14}C measurements were made at the Australian Nuclear Science and Technology Organization (ANSTO) using the ANTARES accelerator facility (Fink et al., 2004). The conversion of foraminiferal calcite to CO_2 at ANSTO used a reaction with 85% phosphoric acid. H2/Fe catalytic reduction then converted the gas to graphite (Hua et al., 2001). A Micromass IsoPrime EA/IRMS at ANSTO measured $\delta^{13}C$ from the graphite of each sample, with a range of -0.5 to -3‰. When sample sizes were too small to allow $\delta^{13}C$ measurement to be made on the graphite, a value of 0% was assigned for the purposes of radiocarbon age calculation, consistent with the $\delta^{13}C$ of foraminiferal calcite being close to that of seawater $\delta^{13}C$-DIC. Six AMS ^{14}C measurements, following a similar method at the National Ocean Sciences Accelerator Mass Spectroscopy (NOSAMS) facility (Woods Hole, Massachusetts, USA), were added to the ANSTO AMS ^{14}C measurements (Burckle pers.comm.; Anderson et al., 2009; Appendix 3.1) to construct an age model.

Ten AMS ^{14}C measurements were discarded because they were outliers or presented age reversals (Appendix 3.1). All remaining AMS dates were converted to calendar ages using the linear-based CALIB07 (Stuiver and Reimer, 1993) with calibration to the Marine13 dataset (Reimer et al., 2013) at 95.4% confidence (2 sigma) and included a correction for the surface water reservoir age of ~752 years at the site of core E27-23 resolved from the marine radiocarbon

reservoir correction database and software available from http://radiocarbon.LDEO.columbia.edu/ (Butzin et al., 2005). For comparison, we also used OXCAL 4.2 (Bronk Ramsey 2009; Blaauw 2010), to calibrate the dates with the same curve and surface reservoir age and found <5 years difference between the calibrated ages for ages younger than 30 kyr BP. The greatest calibration offset was 40 years at our only sample older than 35 kyr BP (Appendix 3.2). For the sake of consistency with other palaeoceanographic records in this region, we have retained the CALIB07 calibrated AMS ages for the construction of our chronostratigraphy. Due to the nearly identical AMS dates obtained at 579 and 599 cm (13,020 and 13,029 Cal yr BP, respectively) we have averaged the depths and ages to provide a single tie point (589 cm, 13,024.5 Cal yr BP) (Table 1).

Table 1. Final age model tie points used to determine the age model for E27-23. Calibrated ages principally represent calibrated ages from ^{14}C AMS dates using CALIB07. Alternate methods were used to determine ages where ^{14}C AMS dates were not obtained. Three tie points (between 849-949 cm) were determined by calibrating the $\delta^{18}O_{Nps}$ to the Lisiecki and Raymo benthic $\delta^{18}O$ stack (Lisiecki and Raymo, 2005a,b) ($\delta^{18}O$ tuning LR04) applying Analyseries 2.0.8 (Paillard et al., 1996). Core top ages (0-4 cm), were determined from a linear extrapolation of the estimated sedimentation rate at the top of the core. Additional information is provided in Appendix 3.1.

Mid point Depth (cm)	Tie Point Method used	Final Age Model Tie Point (Cal yr BP)
1	Sed. rate CALIB07 +LR04	1472
3	Sed. rate CALIB07 +LR04	1541
4.0	^{14}C AMS CALIB07	1576
26.5	^{14}C AMS CALIB07	2132
32.5	^{14}C AMS CALIB07	2167
103.0	^{14}C AMS CALIB07	5136
199.0	^{14}C AMS CALIB07	6030
299.0	^{14}C AMS CALIB07	6786
379.0	^{14}C AMS CALIB07	7510
439.0	^{14}C AMS CALIB07	8073
509.0	^{14}C AMS CALIB07	10201
529.0	^{14}C AMS CALIB07	10946
589.0	^{14}C AMS CALIB07: Av. 579 and 599 cm	13025
600.5	^{14}C AMS CALIB07	13268
619.0	^{14}C AMS CALIB07	13584
629.0	^{14}C AMS CALIB07	14596
639.0	^{14}C AMS CALIB07	15586
719.0	^{14}C AMS CALIB07	16785
760.5	^{14}C AMS CALIB07	17138
779.0	^{14}C AMS CALIB07	17337
780.5	^{14}C AMS CALIB07	21136
799.0	^{14}C AMS CALIB07	27759
849.0	^{14}C AMS CALIB07	35271
879.1	$\delta^{18}O$ tuning LR04-Linage	45126
899.0	$\delta^{18}O$ tuning LR04-Linage	48969
948.8	$\delta^{18}O$ tuning LR04-Linage	51905

To supplement the 21 AMS calibrated ages we also measured the oxygen isotopes (expressed as $\delta^{18}O$) on planktonic foraminifera *N. pachyderma* (sinistral; >150 µm). The foraminiferal samples were cleaned as described for the radiocarbon analysis above.

Measurements of $\delta^{18}O$ were made on a Finnigan MAT 251 isotope ratio mass spectrometer with an automated individual carbonate reaction ('Kiel') device at the Australian National University. The samples, weighing between 59 and 221 µg, were reacted with 105% phosphoric acid for 13 minutes at 90°C. Isotope values are reported as per mil (%) deviations relative to the Vienna Peedee Belemnite (VPDB) (Appendix 3.3) and calibrated via the National Bureau of Standards

carbonate standard NBS-19. Analytical precision (2 sigma) for NBS-19 standards, run with these samples, was ±0.07 ‰ for $\delta^{18}O$ and ±0.03 ‰ for $\delta^{13}C$ (n=39).

Three tie points for the deepest section of the core (849-949 cm) were used to correlate our $\delta^{18}O$ record to the global composite benthic $\delta^{18}O$ record LR04 (Lisiecki and Raymo, 2005a,b) (Table 1, Figure 2) applying the "Linage" subroutine of Analyseries 2.0.8 (Paillard et al., 1996). Although a recent benthic $\delta^{18}O$ global overview was compiled by Stern and Lisiecki, (2014), data coverage throughout the south Pacific sector of the Southern Ocean was absent, hindering their ability to evaluate the variability in the timing of the $\delta^{18}O$ response (Stern and Lisiecki, 2014). Therefore, our chronology used the $\delta^{18}O$ record of Lisiecki and Raymo (2005a,b). Our accepted calibrated AMS ages were used as additional tie points during this process. In contrast, to determine the core top ages (0-4 cm), we used a linear extrapolation of the estimated sedimentation rate (34.8 cm/kyr) near the top of the core. Our final age model for core E27-23 is based on 26 tie points, of which 21 are calibrated ^{14}C dates (Table 1, Figure 3).

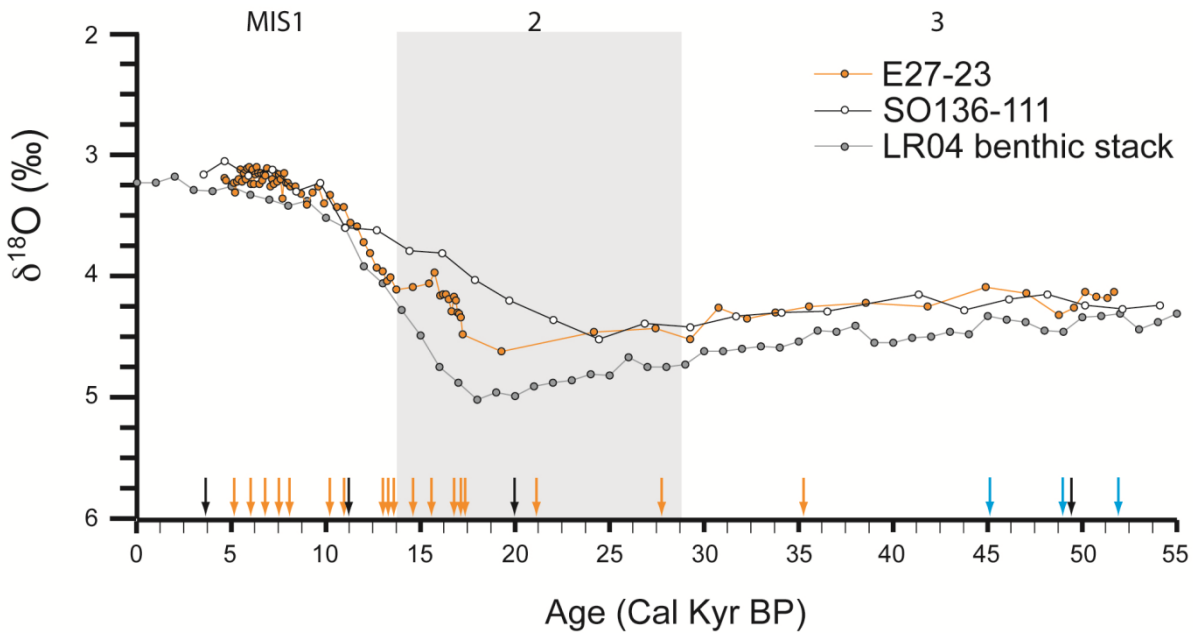

Figure 2. Age calibrated $\delta^{18}O$ isotope curve comparison between the $\delta^{18}O$ (*Neogloboquadrina pachyderma* sinistral (planktic)) from E27-23 and SO136-111, and the global benthic $\delta^{18}O$ stack (LR04; Lisiecki and Raymo, 2005a,b). Arrows indicate the calibrated ^{14}C AMS age pointers from E27-23 (orange) and SO136-111 (black) used to correlate to the global benthic stack. Three additional correlation tie points (Table 1, blue arrows) for the core E27-23 are based on a direct correlation between E27-23 and the LR04 benthic stack.

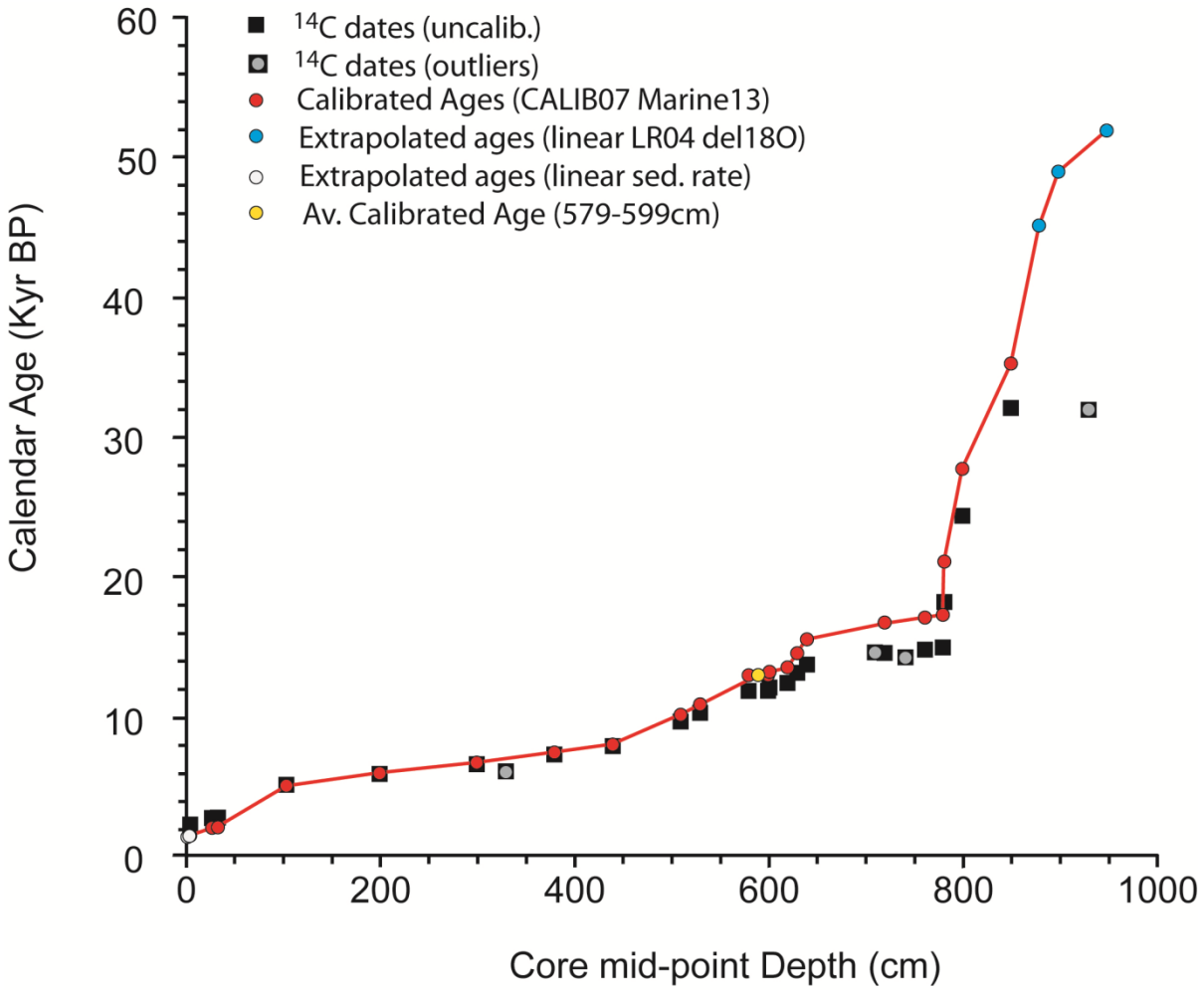

Figure 3. **Derivation of the E27-23 depth-age model.** Included within the figure are the raw ^{14}C AMS dates (black squares) including outliers (black squares with grey dots); CALIB07 Calibrated Ages from non-outlier dates (red dots and line); with superimposed averaged calibrated age at 589 cm (yellow dot) and additional ages based on correlation to the LR04 benthic $\delta^{18}O$ stack (blue dots) and extrapolated linear sedimentation rates (white dots).

2.5.2 SO136-111 chronology

Details regarding the original age model of gravity core SO136-111 (56°40′S, 160°14′E, water depth 3912 m) have been provided elsewhere (Crosta et al., 2002; 2004; 2005). In this paper, we have revised the age model to duplicate the same chronostratigraphic process applied to E27-23. We have recalibrated the original ^{14}C dates (Crosta et al., 2004) using the CALIB07 software and Marine13 dataset (Stuiver and Reimer, 1993; Reimer et al., 2013) at 95.4% confidence. Due to the more northerly location of SO136-111, a slightly lower surface water reservoir age of ~623 years was derived from the marine radiocarbon reservoir correction database and applied to the calibration model (http://radiocarbon.LDEO.columbia.edu/, Butzin et al., (2005)). The $\delta^{18}O$ planktonic foraminifera record was tuned to the LR04 stack (Lisiecki and Raymo, 2005a,b) using Analyseries 2.0.8, to provide additional tie points beyond the radiocarbon time frame. Thus, both calibrated ^{14}C and $\delta^{18}O$ tie points (Appendix 3.4) serve to provide a refined and comparable age model for SO136-111 (Figure 2).

3 Results

3.1 Sea-ice time series analysis

The regression models with ARIMA errors included a time trend, the significance of which was used to determine an appropriate end point for the satellite sea-ice time series. The surface sediment data used to estimate "modern" diatom assemblages represent an average diatom abundance over the last ~1000 years. It is therefore not possible to have a coupling between the timing represented by the sediments and the satellite sea-ice concentration record. We therefore make an assumption that the modern day satellite sea-ice records are representative of the average sea-ice concentrations over the last ~1000 years. Hence, a regression model with ARIMA errors was used to identify any trend in sea-ice concentration that could be representative of modern day climate change, and hence produce sea-ice conditions (and satellite records) that do not represent the sea-ice condition of the last ~1000 years. We found that the full satellite record (32 years) can be used when computing average winter sea-ice concentrations for the sea-floor diatom assemblage samples located within the Indian Ocean, west Pacific Ocean, and the Weddell Sea sectors of the Southern Ocean. The calculations of winter sea-ice averages were restricted to the year 1995 for the samples located within the Ross Sea (17 years), and to 2005 for samples within the Bellingshausen/Amundsen Sea sector (27 years) (Table 2). The resultant winter sea-ice data we use within our training data set accounts for the sector specific changes in sea ice cover, and is therefore more representative than the data set previously used (Crosta et al., 2004).

Table 2. **A summary of the final regression models with ARIMA errors for each sector of the Southern Ocean.** All significant climatic indices (southern annular mode (SAM) and El Niño Southern Oscillation Index (MEI)) and identified sector trends in sea-ice cover are provided. The final sector specific time series, where no trend in sea-ice concentrations could be identified are listed.

Sector (Gloersen et al., 1992)	Significant Climate Indices	Trend Identified	Time series with no significant Trend
Weddell Sea	SAM, CO_2	None	November 1978 to December 2010
West Pacific Ocean	Monthly average maximum temperature, CO_2	None	November 1978 to December 2010
Indian Ocean	MEI, Monthly average maximum temperature	None	November 1978 to December 2010
Ross Sea	MEI	Positive	November 1978 to December 1996
Bellingshausen Amundsen Sea	MEI	Negative	November 1978 to December 2006

3.2 Reconstruction diagnostics

Two diatom species had higher maximum abundances in core SO136-111 (*Thalassionema nitzschioides* and *Thalassiothrix* spp. group) than within our training set, whilst six species (*Thalassiothrix* spp. Group, *Fragilariopsis ritscheri*, *Trichotoxon reinboldii*, *Actinocyclus actinochilus*, *Thalassionema nitzschioides* and *Thalassiosira tumida*) had higher abundances within core E27-23 than in the training set. No species with poorly defined optima were abundant within either core. Of the 164 samples within core SO136-111, only one sample had no analogue (at ~201 kyr BP) whilst another eight samples had poor analogues (Appendix 3.5, Figure 4a). Core E27-23 had 16 samples with no analogue and 39 samples with poor analogues (Appendix 3.6, Figure 5). A canonical correspondence analysis, constrained by winter sea ice, suggests that 31 samples (at ~123-124, 115-121, 7 and 4 kyr BP) from core SO136-111 had a squared residual length that exceeded the 90th percentile for the squared residual lengths computed on the training set. Core E27-23 had 17 samples (at ~10, 9.2, 7.5 and 4.6 kyr BP) exceeding the 90th percentile for the squared residual lengths computed on the training set.

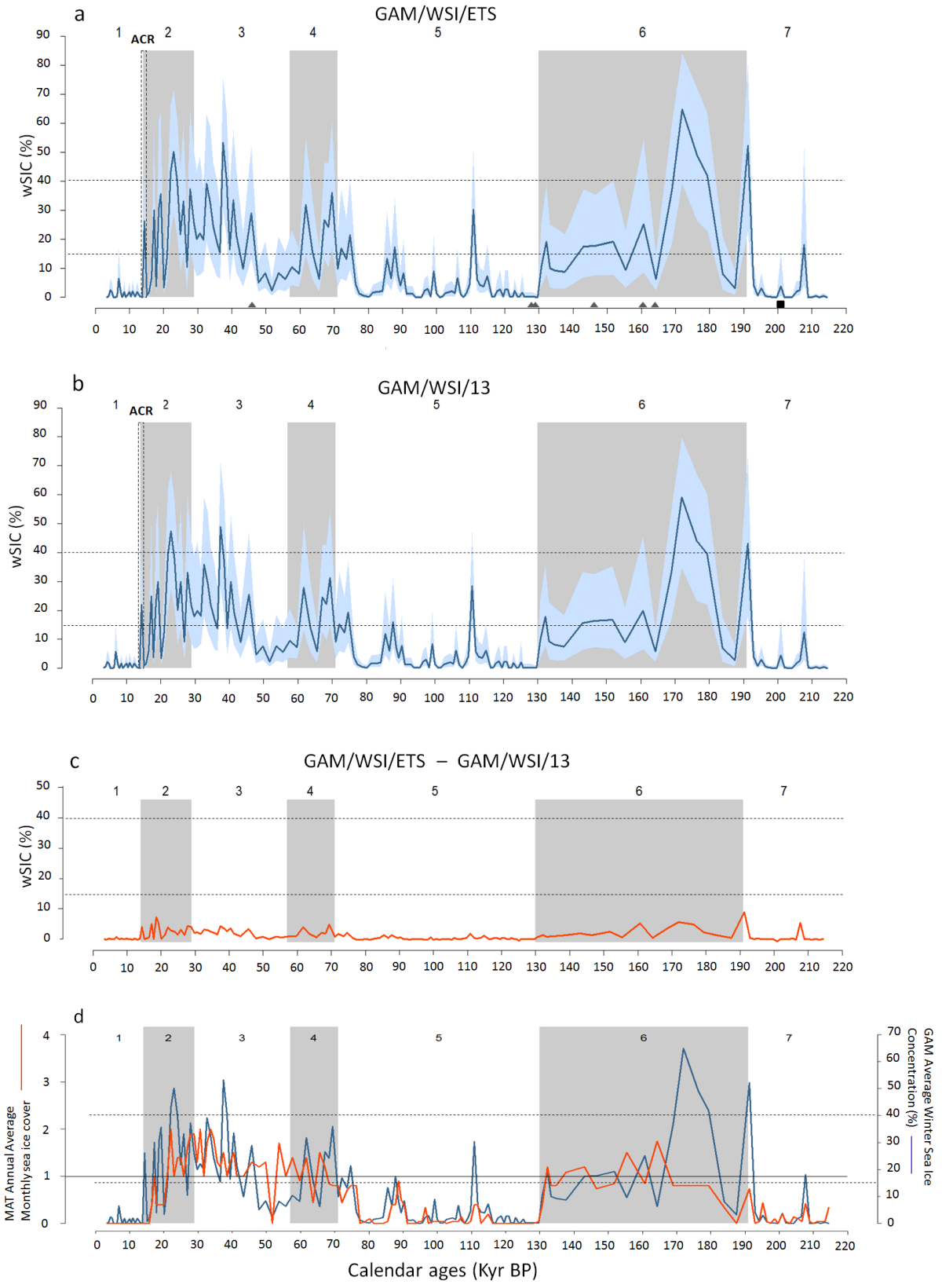
a
GAM/WSI/ETS
ACR
wSIC (%)
b
GAM/WSI/13
ACR
wSIC (%)
c
GAM/WSI/ETS – GAM/WSI/13
wSIC (%)
d
MAT Annual Average
Monthly sea ice cover
GAM Average Winter Sea Ice
Concentration (%)
Calendar ages (Kyr BP)

Figure 4. **Paleo wSIC estimates determined for core SO136-111.** Shown are the estimates from (a) GAM/WSI/ETS and (b) GAM/WSI/13. Panel (c) plots the difference in wSIC estimates between GAM/WSI/ETS and GAM/WSI/13. The solid blue line indicates the paleo wSIC % concentration estimate whilst the light blue shading corresponds to a 95% confidence interval. The dashed box in panels a and b highlights the Antarctic Cold Reversal, whilst in panel a, the solid black square inside the x-axis highlights no analogue samples whilst the grey triangles highlight samples with poor analogues. All of the marine isotopic stages (1 to 7) are labelled with the glacial marine isotope stages shaded grey. MAT paleo month/yr sea-ice cover estimates from Crosta et al. (2004) (solid orange line) for SO136-111, contrasted against the wSIC estimates from GAM/WSI/ETS (solid blue line) (d). Estimates of wSIC less than 15% to indicate no sea-ice cover, 15 to 40% represent unconsolidated sea-ice, whilst concentrations above 40% represent consolidated winter sea-ice (all shown with dashed black horizontal lines) (Gloersen et al., 1992). MAT estimates equal to or above an average of one month of sea-ice coverage (shown by a solid grey horizontal line) per year are regarded as an indicator for the presence of sea ice.

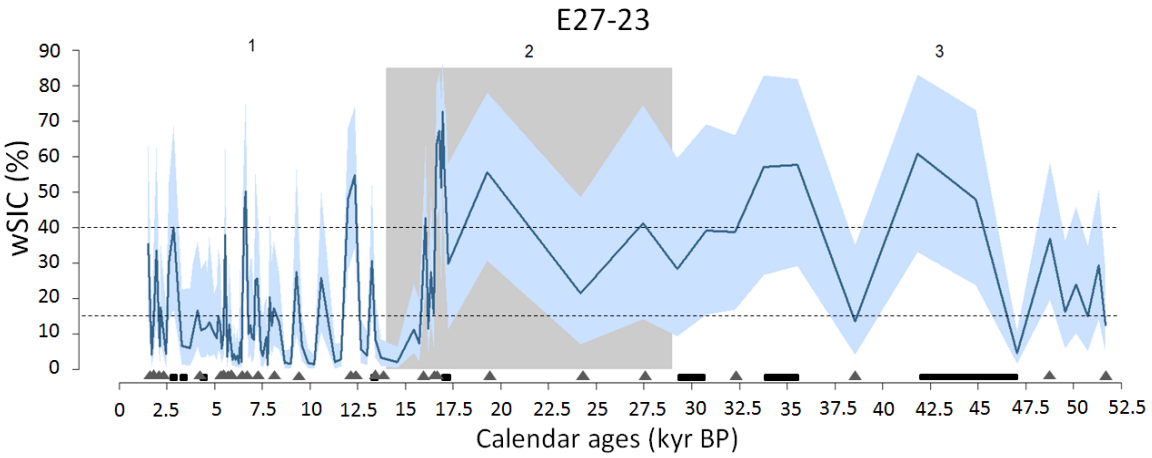

Figure 5. **GAM/WSI/ETS model estimates of paleo winter sea-ice concentration from core site E27-23.** The blue line indicates the paleo wSIC% estimate whilst the light blue shading corresponds to a 95% confidence interval. The solid black rectangles on the x-axis highlight those core samples for which there were no analogues, whilst the grey triangles highlight those samples with poor analogues. All marine isotopic stages are labelled, with the glacial marine isotope stage 2, shaded grey.

3.3 The attributes of the wSIC Generalized Additive Model's

We herein refer to the GAM used to estimate winter sea-ice concentration (wSIC) calculated from 13.25 years of satellite sea-ice concentration data as GAM/WSI/13. We found *Actinocyclus actinochilus*, *Fragilariopsis curta*, *Fragilariopsis cylindrus* and *Thalassiosira lentiginosa* to be statistically significant proxies for average wSIC computed from 13.25 years of data (Chapter 2). The GAM fitted to the wSIC averages calculated from our Extended Time Series satellite record (herein referred to as GAM/WSI/ETS) used the same diatom proxies as GAM/WSI/13. Table 3 summarizes both of the GAM's fitted to our wSIC training data sets.

Table 3. **A summary of the GAMs used to estimate paleo wSIC.** Each applied GAM differs according to the satellite sea-ice database used to compute average sea-ice concentrations for our 163 diatom relative abundance samples. The diatoms used in each of the final models as predictors for a given sea-ice cover are listed along with the p-values used to indicate the significance of each diatom as a predictor for winter sea-ice concentration.

Model	Adjusted R^2	Diatom Proxies	p-value
GAM/WSI/13	0.73	*Actinocyclus actinochilus*	0.002
		Fragilariopsis curta	< 0.001
		Thalassiosira lentiginosa	0.002
		Fragilariopsis cylindrus	0.009
GAM/WSI/ETS	0.716	*Actinocyclus actinochilus*	0.003
		Fragilariopsis curta	< 0.001
		Thalassiosira lentiginosa	0.002
		Fragilariopsis cylindrus	0.015

3.4 GAM versus MAT paleo sea-ice records

The paleo wSIC estimates provided by GAM/WSI/ETS (Figure 4a) and GAM/WSI/13 (Figure 4b) are both consistent with each other, revealing an average estimate difference of 1.06% and never >10% concentration over the last 220 kyr BP (Figure 4c). However, as GAM/WSI/ETS is likely to be more climatologically representative given the longer satellite record used to compute an average wSIC, we focus our discussion on the paleo wSIC estimates of GAM/WSI/ETS.

GAM/WSI/ETS estimated consolidated winter sea-ice at 191, 179, 176, and 171 Kyr BP, whilst MAT estimated an absence of sea-ice (Figure 4d). At 38, 37.5, 23 and 22 kyr BP, over the eLGM, GAM/WSI/ETS suggests unconsolidated winter sea-ice was present over SO136-111 whilst, in contrast, MAT does not record any parallel peak sea-ice cover. During early MIS 3 (59 to 47 kyr BP) GAM/WSI/ETS suggests winter sea-ice was absent whilst MAT estimates the presence of sea-ice cover. Both MAT and GAM/WSI/ETS indicate sea-ice coverage over the eLGM period, with GAM/WSI/ETS estimating occasional consolidated winter sea-ice coverage. During the ACR, only GAM/WSI/ETS suggests the winter sea-ice edge was present over core SO136-111. Throughout the Holocene, GAM/WSI/ETS and MAT-based estimates indicated no sea-ice cover. Henceforth, we interpret our results using GAM derived estimates primarily because the method is less biased by spatial autocorrelation, provided a better fit to our training data set, and has a stronger biological basis (Chapter 2).

3.5 The paleo sea-ice record

3.5.1 Paleo sea ice record for core SO136-111

The site of core SO136-111 generally records wSIC during glacial stages and an absence of winter sea-ice during interglacials (Figure 4 and Appendix 3.5). Consolidated winter sea ice seems to have been present between about 180 and 170 kyr BP during MIS6, and may have been sporadically present in the later stages of MIS3 and in MIS 2. Unconsolidated winter sea ice may have been briefly present for some intervals during MIS 5 at the site of core SO136-111 at 110, 87, 74 and 72 kyr BP. From 59 to 47.7 kyr BP, during the end of MIS 4 and early MIS 3, there was no winter sea-ice coverage at the site of core SO136-111. Unconsolidated winter sea-ice was

estimated during the eLGM from 35 to 27 kyr BP, and from 25.8 to 21 kyr BP. An isolated increase in wSIC at 14.5 kyr BP corresponds with the ACR, after which (during the Holocene) no winter sea-ice cover is estimated for the remainder of the core record. We acknowledge that the 95% confidence intervals for all estimates of unconsolidated and consolidated winter sea-ice are large (Figure 4a, b) which hinders our ability to confidently discriminate between consolidated and unconsolidated winter sea-ice cover. The samples of core SO136-111 provided a continuous down core record of diatom fossils, suggesting the site of core SO136-111 was not covered by consolidated summer sea-ice.

3.5.2 Paleo sea-ice record for core E27-23

During MIS 3 the site of E27-23 was covered by consolidated winter sea-ice at 45, 42, 35.5 and 33.7 kyr BP, whilst unconsolidated winter sea-ice was estimated at 51.3 to 48.7 kyr BP (Figure 6). Over MIS 2 and the eLGM, consolidated winter sea-ice may have been present at 27.4, 19.3, 17 to 16.5, and 16 kyr BP. Unconsolidated winter sea-ice coverage was documented at 39 to 28.3, 24.1 and 17.3 kyr BP. Consolidated Holocene winter sea-ice may have reached the core site at 12.3 to 11.9 and 6.8 to 6.5 kyr BP. Unconsolidated winter sea-ice was estimated at 13.2, 10.5, 9.3, 7.8, 6.5, 2.8 to 2.6, 1.9 and 1.5 kyr BP (Figure 5, Appendix 3.6). Again, the 95% confidence intervals for all estimates of unconsolidated and consolidated winter sea-ice are large (Figure 5), hence we tentatively discriminate between consolidated and unconsolidated winter sea-ice cover. As all of the samples from core E27-23 documented the presence of diatoms we conclude the core was never covered by consolidated summer sea-ice.

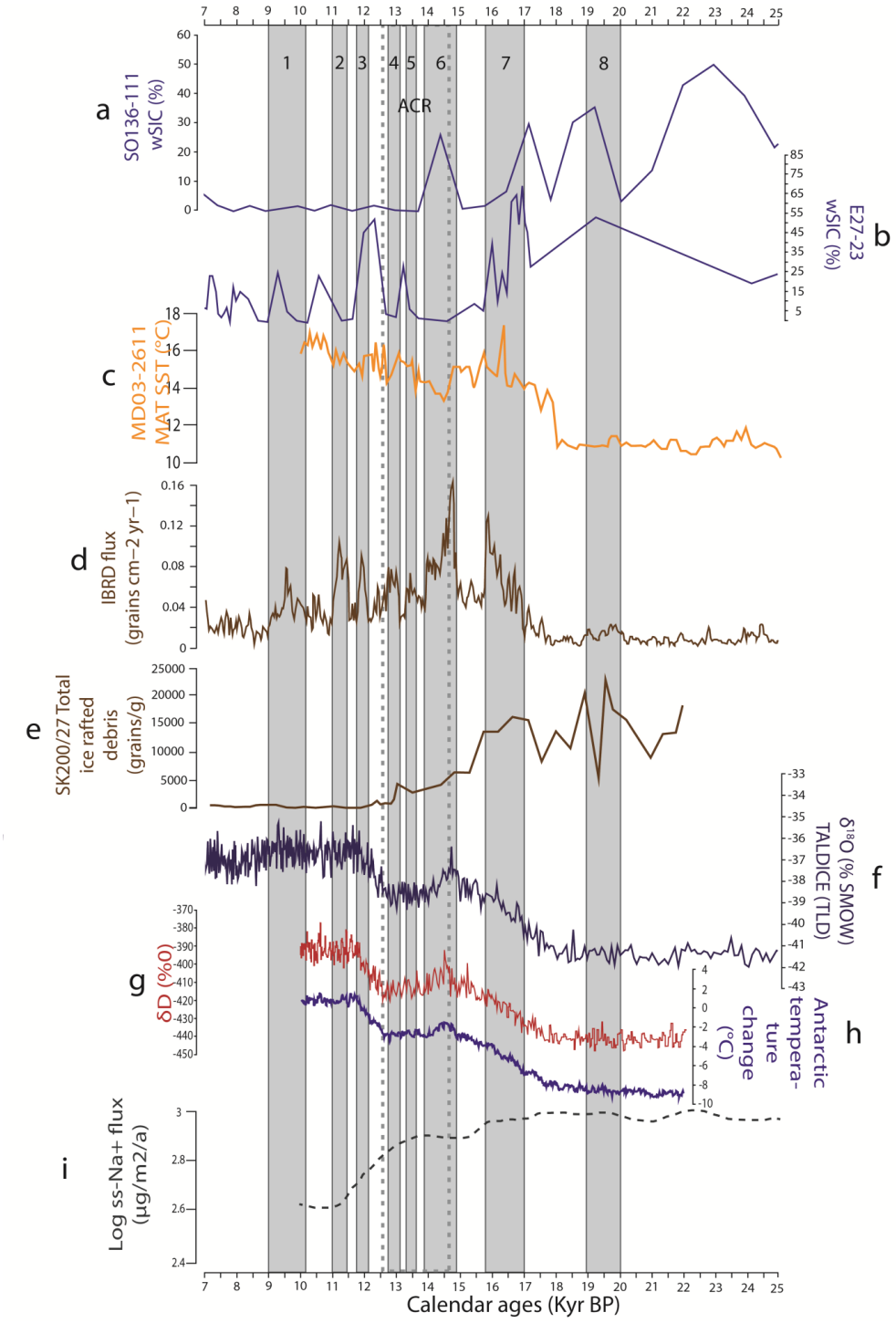

Figure 6. A comparison between the wSIC records from SO136-111 and E27-23 with the paleo records discussed in text. The paleo winter sea-ice estimates for cores SO136-111 (a) and E27-23 (b) (solid blue lines) are plotted against the sea-surface temperature record from De Deckker et al., (2012) (c). The Scotia Sea sediment flux reported by Weber et al. (2014) is shown in panel d and the Indian Ocean IRD record of Manoj et al., (2013) is shown in panel e (brown lines). The TALDICE $\delta^{18}O$ record from Stenni et al., (2010) is shown in panel f (purple

line). Panel's g and h provide the record of δD from the EPICA Dome C ice core and Antarctic temperature change (Parrenin et al. 2013). Also shown is the EPICA Dome C log sea-salt sodium (ssNa) flux proxy for sea-ice extent throughout the Indian Ocean sector (Röthlisberger et al., 2010) (i). The Antarctic Ice Sheet Discharges (AID) first identified and described by Weber et al., (2014) are highlighted in light grey and labelled 1 through to 8. The Antarctic Cold Reversal, again as defined by Weber et al., (2014), is labelled and outlined with a dashed grey rectangle.

4 Discussion

4.1 The paleo winter sea-ice records from cores SO136-111 and E27-23

Here we commence our discussion focused on the glacial and deglacial winter sea-ice record from the southwest Pacific sector of the Southern Ocean, outlining the differences in reported sea-ice advances from previous records originating in the Atlantic sector (Bianchi and Gersonde, 2004; Divine et al., 2010). The remainder of our discussion is directed towards developing a regional synthesis for the southwest Pacific paleo winter sea-ice record over the last 15 kyr BP, covering sea-ice advance during the ACR and specifically through the Holocene with the higher resolution record provided from core E27-23. We link our paleo winter sea-ice data with additional oceanographic, ice core and terrestrial paleo proxy records to place our regional sea-ice synthesis in context to hemispheric scale climate change.

4.1.1 Glacial/ interglacial variation in winter sea-ice cover

The increase and associated decrease in wSIC between glacial and interglacial climates may be driven by oceanic and atmospheric changes. For instance, the intensity of the Antarctic Circumpolar Current (ACC) and westerly wind field may increase, whilst migrating to northern latitudes, during glacial stages (Shulmeister et al., 2004; Mazaud et al., 2010; Kohfeld et al., 2013), which effectively expands the atmospheric polar cell, cools the ocean surface and facilitates sea-ice expansion in the Southern Ocean (Putnam et al., 2010).

Although the Campbell Plateau provides a bathymetric control on the ACC's position within the southwest Pacific (Neil et al., 2004), it has been argued that the northern extension of paleo sea

ice implies a release of the ACC from bathymetric control (Martinson, 2012). Similarly, it has been suggested that the westerly winds migrated north during glacials (Neil et al, 2004; Putnam et al., 2010) however, the discrepancy between model and paleo data based inferences of past westerly wind intensity and latitudinal positioning remains unexplained (Kohfeld et al., 2013). Our paleo estimates represent an expansion of unconsolidated winter sea-ice to 56°S, south of the Tasman Sea, during glacial stages. Others have inferred that the expansion of winter sea-ice was a factor in the oceanic fronts of the ACC and the STF migrating north (Neil et al. 2004; Martinson, 2012), our work now provides the latitudinal evidence for increased winter sea-ice coverage at the sites of E27-23 and SO136-111. However, as the summer sea-ice extent could not be shown as an influence over these sites, whether the fronts of the AAC could be, or were, mobile seasonally is far from being resolved.

4.1.2 The deglacial and Antarctic Cold Reversal (ACR)

The Antarctic Cold Reversal (ACR) refers to a period of climatic cooling between 14.5 to 12.5 kyr BP, which interrupted the transition from the Last Glacial Maximum into deglacial conditions (Stenni et al., 2001; Divine et al., 2010). The ACR has been previously identified from variations to ice rafted debris (Manoj et al., 2013; Weber et al., 2014) (Figure 6e and d), $\delta^{18}O$ data from the TALDICE ice core (Stenni et al., 2010) (Figure 6f), opal flux records within the south Atlantic (Anderson et al. 2009) and from diatom assemblages within lake sediments of southern South America (Recasens et al. 2015). Opal flux records from E27-23 and, in particular, the south Atlantic, declined during the ACR, corresponding with a plateau in atmospheric CO_2, reduced upwelling and reduced sea-surface temperatures (Anderson et al. 2009). Our paleo estimates

suggest winter sea-ice cover increased within the southwest Pacific sector of the Southern Ocean over the sites of cores E27-23 and SO136-111 at 14.4 and 13.23 kyr BP, respectively. A robust feature is the higher sea-ice concentration estimated in the southern core (50% at 12.3 kyr BP, for E27-23) compared with the northern core (25% at 14.4 kyr BP for SO136-111). Yet, the assumption of a constant radiocarbon reservoir age over time introduces a source of error into age models (Hendy et al. 2011; Cook and Keigwin, 2015) and therefore contributes to the chronological uncertainties of our age models. Hence, resolving the ACR signal within both core records appears difficult given the uncertainties surrounding the independent age models for each core. Due to chronological uncertainties, we suggest that both cores appear to indicate an expression of the ACR where estimates of wSIC increase between 14.4 and 13.23 kyr BP (Figure 6a and b).

Interestingly, our paleo wSIC records for the southwest Pacific (cores SO136-111 and E27-23) contrast to those derived from the Atlantic sector of the Southern Ocean (Bianchi and Gersonde, 2004; Divine et al. 2010) (Figure 7d, e, and f). Whilst our sea-ice records at the site of SO136-111 suggest sea-ice cover during the ACR was greater than any time during the Holocene, ACR sea-ice expansion within the Atlantic sector was no greater than estimated monthly sea-ice cover during the early Holocene (Bianchi and Gersonde, 2004; Divine et al. 2010). Such regional differences are perhaps not surprising since Holocene sea-ice expansion within the south Atlantic may have resulted from a northern expansion and intensification of the Weddell Sea gyre circulation (Bianchi and Gersonde, 2004), which subsequently increased the northward transport of sea ice (Divine et al. 2010). The southwest Pacific is not under the direct influence of such a gyre system, with sea-ice extent within this region having the least interannual variation (Ackley 1981, Parkinson 1992).

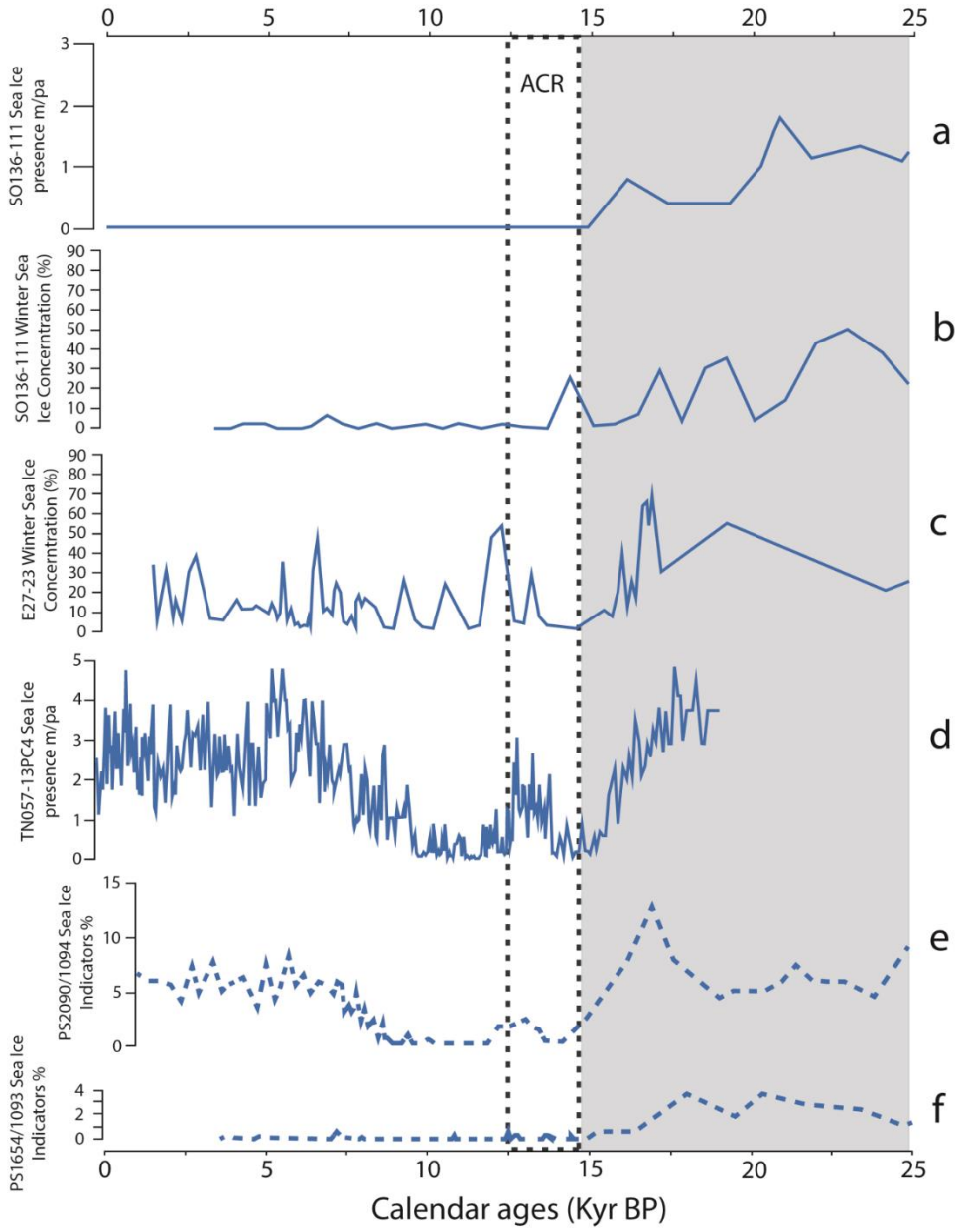

Figure 7. **The paleo monthly sea ice cover from Crosta et al (2004) (a) is compared with the winter sea-ice concentration records for core SO136-111 (b) and E27-23 (c) (solid blue lines).** The average monthly sea ice presence of Divine et al., (2010) (solid blue lines, d) and the diatom sea ice indicator species of Bianchi and Gersonde (2004) (dashed blue lines, e and f) from the South Atlantic sector are shown for comparison.

The onset of the ACR has been attributed to melt water pulse-1A (MWP- 1A) and the (likely) concomitant Bølling-Allerød warming throughout the north Atlantic region. Both events have

been dated between 14.65 and 14.32 kyr BP (Weaver et al., 2003; Stenni et al., 2010; Deschamps et al., 2012; Kopp, 2012; Weber et al., 2014; Golledge et al., 2014; Williams, 2014) and are thought to have potentially been a consequence of the Antarctic ice sheet collapse (Kopp, 2012; Weber et al., 2014; Golledge et al., 2014). Although any contribution of the Antarctic ice sheet to MWP-1A is thought to be small, direct evidence for the source of collapse from either the West or East Antarctic ice sheet, has yet to be determined (Denton, 2011; Williams, 2014).

The record of Antarctic temperature and deuterium (δD) from EPICA Dome C (Parrenin et al. 2013) suggest temperatures declined during the ACR, whilst the sea salt flux from Dome C suggests the decline in sea-ice extent throughout the Indian Ocean after the LGM halted during the ACR period (Röthlisberger et al. 2010) (Figure 6i). As the ACR cooling may have extended throughout the southwest Pacific and Indian sectors of the Southern Ocean, a climatic mechanism, such as MWP-1A, which can account for the broader changes of the Southern Ocean, provides a favourable explanation for the climatic changes documented during the ACR. Similarly, a recent modelling study demonstrated that a freshwater flux of +100 mSv from the West Antarctic during the Holocene (specifically, 10 to 8 kyr BP) produced oceanic cooling of 0.7°C and a strengthening of southern hemisphere westerly winds (+6 %) (Mathiot et al., 2013). It is plausible that the modelling by Mathiot et al. (2013) is analogous to the oceanic and atmospheric changes that drove the ACR winter sea-ice expansion at the locations of cores E27-23 and SO136-111.

Indeed, Earth system models of intermediate complexity suggest that a discharge of freshwater from the Antarctic ice sheet results in considerable Southern Ocean cooling and sea-ice expansion during the ACR (Weber et al. 2014). Three ice rafted debris (IRD) discharge events from the Scotia Sea (Weber et al. 2014) (Figure 6d) may also be present within the record of IRD

within the Indian Ocean sector (Manoj et al. 2013) (Figure 6e). Increased Indian Ocean IRD at ~15 kyr BP (Figure 6e) has been attributed to a northern migration of the SAF and Polar Front (PF) (Manoj et al. 2013). Around 15 kyr BP sea-surface temperatures south of Australia suggest the influence of the warm Leeuwin Current decreased at 14.5 and 11.8 kyr BP due to a more northerly positioning of the STF and the westerly winds (De Deckker et al. 2012) (Figure 6c). Our paleo winter sea-ice estimates show that the sites of E27-23 and SO136-111 were both covered by unconsolidated winter sea-ice during the ACR. In conjunction with the broader implications of MWP-1A, our winter sea-ice data indicates a northern migration of the oceanic fronts and a reduction in the influence of the Leeuwin Current to the south of Australia.

4.1.3 The Holocene winter sea ice increases estimated from core E27-23

Millennial-scale Holocene paleoclimatic changes have been identified south of Australia at 9.2, 7.3 and 5.3 kyr BP (Moros et al., 2009), the west Antarctic Peninsula (Shevenell et al., 2011; Etourneau et al., 2013), Palmer Deep (Shevenell and Kennett, 2002), within both coastal and inland Antarctic ice cores (Masson et al. 2000) and from global paleoclimatic records (Mayewski et al., 2004). The Holocene millennial scale cooling identified by Shevenell and Kennett (2002), Mayewski et al. (2004), Shevenell et al. (2011) and Etourneau et al. (2013) were attributed to short (and longer) term variation in the intensity and/or latitudinal positioning of the westerly winds. For example, more southern, and stronger, westerly winds over the west Antarctic Peninsula bring more Circumpolar Deep Water (CDW) onto the shelf, warming sea-surface temperatures and melting sea-ice (Shevenell et al., 2011). We acknowledge that our wSIC record for E27-23 does not have the necessary resolution to adequately discuss millennial winter sea-ice

variation. However, we feel it is possible that our Holocene paleo wSIC record, which documents unconsolidated (i.e. wSIC >15%) wSIC roughly every 1 kyr, (Figure 6b) could suggest southwestern Pacific sea-ice cover may have increased during periods of climatic cooling identified by Masson et al. (2000), Shevenell and Kennett (2002) and Shevenell et al. (2011).

During the mid to early Holocene (9 to 5.7 kyr BP) New Zealand experienced increased winter frosts, cooler summers, and forest-scale destruction from windstorms and/or droughts (Stephens et al., 2012), whilst the Antarctic cooled (Moros et al. 2009). Antarctic cooling had been attributed to a strengthening of the westerly winds and a northern displacement of the Southern Ocean's STF (Moros et al. 2009), both of which support the idea of Holocene sea-ice expansion, which we observe within the southwest Pacific sector of the Southern Ocean.

Modelling studies have indicated that the Southern Ocean may have cooled in response to the Laurentide Ice Sheet melting during the early Holocene (Renssen et al., 2010). Melt water flux from the Laurentide Ice Sheet deglaciation cooled the surface of the North Atlantic, subsequently cooling the source waters for North Atlantic Deep Water (NADW) formation. In turn, the deep North Atlantic cooled at depths from 1500 to 3500 metres. Northern heat transport by the North Atlantic was also reduced by 28% due to the absence of deep convection within the Labrador Sea in association with Laurentide Ice Sheet meltwater flux. Therefore, melting of the Laurentide Ice Sheet produced cooler NADW, which upwelled within the Southern Ocean, cooling surface temperatures and overwhelming the bipolar see-saw in regions south of the Polar Frontal Zone (Renssen et al. 2010). Such alterations in oceanic circulation provide a plausible explanation for the cold conditions reconstructed by proxies in high southern hemisphere latitudes from 9 to 7 kyr BP (Renssen et al., 2010). Renssen et al. (2010) found cooler conditions in the Southern Ocean during the early Holocene (resulting from the melting of the Laurentide Ice Sheet)

increased sea-ice cover within their models; a result supported by our proxy-based estimates of increased wSIC at 9.3, 7.9, and 7.3 to 7.1 kyr BP. Subsurface ocean temperatures from the East Antarctic coast (Dumont d'Urville Trough) increased at roughly 6 kyr BP, possibly owing to a complete recession of the Laurentide Ice Sheet and the resulting re-establishment of deep convection within the Labrador Sea. In turn, NADW flux and temperature increased, warming the Southern Ocean waters from below (Kim et al., 2012), all of which is consistent with the low wSIC values between 6 to 3 kyr BP within the paleo wSIC record of E27-23.

5 Conclusions

We provide the first quantitative paleo winter sea-ice estimates for marine sediment cores E27-23 and SO136-111, extending our paleoceanographic knowledge of the southwest Pacific sector of the Southern Ocean. To complement our refinement of the paleo sea-ice record, we proposed and applied an extension of the available satellite record of sea-ice concentration according to a time series analysis on 30 years of sea-ice concentration data for each sector of the Southern Ocean.

During glacial stages unconsolidated winter sea-ice was present at 54°S within the southwest Pacific sector of the Southern Ocean. The glacial winter sea-ice expansion was concomitant with a northern migration of the ACC, PF, SAF and/or STF. GAM-based paleo wSIC estimates indicate an expression of recent paleoclimatic events, notably winter sea-ice expansion during the ACR and the Holocene within the paleo sea-ice record for the (currently) open ocean region of the southwest Pacific sector of the Southern Ocean. The sea-ice concentration increases documented during the ACR are consistent with a northern migration of regional oceanic fronts (PF, SAF, STF), a northern migration of the ACC, and reduced influence of the Leeuwin Current to the south of Australia. An important driver for the ACR cooling may have been MWP-1A. The wSIC increases documented during the ACR and the Holocene are consistent with theories suggesting a latitudinal shift and/or increase in the westerly wind field were the causal mechanisms for documented climatic changes. However, we cannot contribute any clarification regarding the controversial role potentially played by shifts in the positioning or intensity of the westerly wind field during past climatic shifts. At no stage did our cores record the existence of summer sea-ice cover up to 56°S, and thus a strong seasonal sea-ice growth and retreat cycle has been maintained over cooling expansions for the last 15 kyr BP. The influence on oceanic and

atmospheric fronts as a result of such large seasonal differences cannot be determined here but should be considered in paleo modelling scenarios.

Acknowledgements

All of the data provided within Appendices 3.1 through to 3.6 are available via the Australian Antarctic Division metadata records (DOI http://dx.doi.org/10.4225/15/546C10AD26A7D) This research was funded by the Australian Government through the provision of an Australian Postgraduate Award granted to Alexander Ferry. We are also grateful for the input and assistance from Dr R. Hyndman in the application of regression models with ARIMA errors, using the R package 'forecast'.

The work on core E27-23 was originally undertaken through the Antarctic Cooperative Research Centre's Palaeoenvironments Program and was completed via support from ASAC Grant No. 2534 to PQ and LA, AINSE Grant 2572 to PQ and WH, and additional support from the University of Tasmania's School of Earth Sciences and the Australian Government's Cooperative Research Centres Program through the Antarctic Climate and Ecosystems Cooperative Research Centre (ACE CRC). Technical support from Ms L. Robertson and Dr D. Roberts at the University of Tasmania is acknowledged. Dr Lloyd Burckle (LDEO) originally provided radiocarbon dates for three intervals in the core through the laboratory of Dr J. Lynch-Stieglitz (LDEO). Drs T. Janecek, M. Curran and S. Nielsen (former curators of the Florida State University Antarctic Core Repository) assisted us with sampling requests for E27-23. We thank Dr M. Gagan, Ms H. Scott-Gagan, and Mr J. Cali for use of the mass spectrometer at ANU. We are thankful for the assistance of Drs S. Rintoul and S. Sokolov of CSIRO Marine and Atmospheric Research with oceanography, Dr R. Massom of ACE CRC with sea-ice cover, and Prof. R. Anderson of Lamont Doherty Earth Observatory for palaeoceanographic discussions.

References

Ackley, S.F. (1981), A review of sea-ice weather relationships in the Southern Hemisphere. In *Sea level, Ice and Climate change*. (Editor Allison, I.) IAHS publication, 131 pp 127-159.

Anderson, R. F., S., Ali, L.I., Bradtmiller, S.H.H., Nielsen, M.Q., Fleisher, B.E., Anderson, and L.H., Burckle (2009), Wind-driven upwelling in the Southern Ocean and the deglacial rise in atmospheric CO_2, *Science*, 323, 1443-1448.

Armand, L.K., and A., Leventer (2010), Palaeo sea ice distribution and reconstruction derived from the geological record. In: Thomas, D.N., G.S., Dieckmann, (Eds.), Sea Ice, Second Ed. pp.469- 529, Wiley-Blackwell, Oxford, UK. ch13.

Bianchi, C., and R., Gersonde (2004), Climate evolution at the last deglaciation: the role of the Southern Ocean, *Earth Planet. Sci. Lett.*, 228, 407– 424.

Bianco, A.M., M. García Ben, E.J. Martínez and V.J. Yohai (2001), Outlier Detection in Regression Models with ARIMA Errors using Robust Estimates, *J. Forecast*., 20, 565-579.

Birks, H. J. B., J.M., Line, S., Juggins, A.C., Stevenson, and C.J.F., ter Braak (1990), Diatoms and pH reconstruction, *Philos. Trans. R. Soc. Lond., B, Biol. Sci.*, 327, 263-278.

Blaauw, M. (2010), Methods and code for 'classical' age-modelling of radiocarbon sequences, *Quat. Geochronol.*, 5, 512–518.

Brandon, M. A., R.R., Cottier, and F., Nilsen (2010), Sea Ice and Oceanography. In: Thomas, D.N., G.S., Dieckmann, (Eds.), Sea Ice, Second Ed. pp. 79-111, Wiley-Blackwell, Oxford, UK.

Bronk Ramsey, C. (2009), Bayesian analysis of radiocarbon dates, *Radiocarbon.*, 51, 337-360.

Butzin, M., M., Prange, and G., Lohmann (2005), Radiocarbon simulations for the glacial ocean: The effects of wind stress, Southern Ocean sea ice and Heinrich events, *Earth Planet. Sci. Lett.,* 235, 45– 61.

Cassidy, D.S., F.A., Kaharoeddin, I., Zemmels, M.B., Knapp (1977), USNS ELTANIN. An inventory of core location data with core location maps and cruise 55 core descriptions. Antarctic Research Facility, Tallahassee. No. 44.

Comiso, J. (2000), Bootstrap sea ice concentrations from Nimbus-7 SMMR and DMSP SSM/I-SSMIS, Version 2, National Snow and Ice Data Center, Boulder, Colorado, USA.

Comiso, J.C., (2010), Large-scale characteristics and variability of the global sea ice cover. In: Thomas, D.N., G.S., Dieckmann, (Eds.), Sea Ice. pp.112- 142, Wiley-Blackwell, Oxford, UK. Ch4.

Cook, M. S., and L.D., Keigwin (2014, in press), Radiocarbon profiles of the NW Pacific from the LGM and deglaciation: evaluating ventilation metrics and the effect of uncertain surface reservoir ages, *Paleoceanography*, DOI: 10.1002/2014PA002649.

Crosta, X., J-J., Pichon, and L.H., Burckle (1998), Application of modern analog technique to marine Antarctic diatoms: Reconstruction of maximum sea-ice extent at the Last Glacial Maximum, *Palaeoceanography*, 13, 284-297.

Crosta, X., A., Shemesh, J., Etourneau, R., Yam, I., Billy, and J-J., Pichon (2005), Nutrient cycling in the Indian sector of the Southern Ocean over the last 50,000 years, *Global Biogeochem. Cycles*, 19, DOI:10.1029/2004GB002344.

Crosta, X., A., Shemesh, M-.E., Salvignac, H., Gildor, and R., Yam (2002), Late Quaternary variations of elemental ratios (C/Si and N/Si) in diatom-bound organic matter from the Southern Ocean, *Deep Sea Res., Part II,* 49, 1939–1952.

Crosta, X., A., Sturm, L., Armand, and J-J., Pichon (2004), Late Quaternary sea ice history in the Indian sector of the Southern Ocean as recorded by diatom assemblages, *Mar. Micropaleontol*, 50, 209-223.

De Deckker, P., M., Moros, K., Perner, and E., Jansen (2012), Influence of the tropics and southern westerlies on glacial interhemispheric asymmetry, *Nat. Geosci.*, 5, 266-269.

Denton, G. H. (2011), East Antarctic retreat, *Nat. Geosci*, 4, 135- 136.

Deschamps, P. N., N., Durand, E., Bard, B., Hamelin, G., Camoin, A.L., Thomas, G.M., Henderson, J., Okuno, and Y., Yokoyama (2012), Ice-sheet collapse and sea-level rise at the Bølling warming 14,600 years ago, *Nature,* 483, 559–564.

Dieckmann, G. S., and H.H., Hellmer (2010), The importance of sea ice: an overview. In: Thomas, D.N., G.S., Dieckmann, (Eds.), Sea Ice, Second Ed. pp. 1-22, Wiley-Blackwell, Oxford, U.K.

Divine, D. V., N., Koç, E., Isaksson, S., Nielsen, X., Crosta, and F., Godtliebsen (2010), Holocene Antarctic climate variability from ice and marine sediment cores: insights on ocean–atmosphere interaction, *Quat. Sci. Rev.,* 29, 303–312.

Etourneau, J., L.G., Collins, V., Willmott, J.H., Kim, L., Barbara, A., Leventer, S., Schouten, J.S., Sinninghe Damsté, A., Bianchini, V., Klein, X., Crosta and G., Massé (2013), Holocene climate variations in the western Antarctic Peninsula: evidence for sea ice extent predominantly controlled by changes in insolation and ENSO variability, *Clim. Past*, 9, 1431–1446.

Ferry, A.J., T., Prvan., B., Jersky., X., Crosta., and L.K., Armand (2015), Statistical modeling of Southern Ocean marine diatom proxy and winter sea ice data: model comparison and developments, *Progr. Oceanogr.*,131, 100-112.

Fink, D., M., Hotchkis, Q., Hua, G., Jacobsen, A.M., Smith, S.U., Zoppi, D., Child, C., Mifsud, H., van der Gaast, A., Williams, and M., Williams (2004), The ANTARES AMS facility at ANSTO, *Nucl. Instrum. Methods Phys. Res., Sect. B,* 223–224, 109–115.

Gersonde, R., and U., Zielinski (2000), The reconstruction of late Quaternary Antarctic sea-ice distribution—the use of diatoms as a proxy for sea-ice, *Palaeogeogr., Palaeoclimatol., Palaeoecol.*, 162, 263–286.

Gersonde, R., X., Crosta, A., Abelmann, and L., Armand (2005), Sea-surface temperature and sea ice distribution of the Southern Ocean at the EPILOG Last Glacial Maximum—a circum-Antarctic view based on siliceous microfossil records, *Quat. Sci. Rev.*, 24, 869–896.

Gloersen, P., W.J., Campbell, D.J., Cavalieri, J.C., Comiso, C.L., Parkinson, and H.J., Zwally (1992), *Arctic and Antarctic Sea Ice, 1978- 1987, Satellite Passive-Microwave Observations and Analysis*. NASA Special Publication, 511, 289 pp, National Aeronautics and Space Administration, Washington, D.C.

Golledge, N. R., L., Menviel, L., Carter, C.J., Fogwill, M.H., England, G., Cortese and R.H., Levy (2014), Antarctic contribution to meltwater pulse 1A from reduced Southern Ocean overturning, *Nat. Commun.*, 5, DOI: 10.1038/ncomms6107.

Goosse, H., D.M., Roche, A., Mairesse, and M., Berger (2013), Modelling past sea ice changes, *Quat. Sci. Rev.*, 79, 191-206.

Hammer, Ø., D.A.T., Harper, and P.D., Ryan (2001), PAST: Paleontological statistics software package for education and data Analysis, *Palaeontologia Electronica,* 4, 9 pp.

Hendy, I. L., L., Dunn, A., Schimmelmann and D.K., Pak (2011), Millennial-scale surface water mass radiocarbon reservoir age changes recorded on the California Margin, American Geophysical Union, Fall Meeting abstract #PP52A-04.

Hill, M. O. (1973), Diversity and evenness: A unifying notation and its consequences, *Ecology*, 54, 427-432.

Hua, Q., G.E., Jacobsen, U., Zoppi, E.M., Lawson, A.A., Williams, A.M., Smith, and M.J., McGann (2001), Progress in radiocarbon target preparation at the ANTARES AMS centre, *Radiocarbon,* 43, 275–282.

Hyndman, R. (2014), Forecast. R package version 5.4. http://cran.r-project.org/web/packages/forecast/index.html

Juggins, S. (2014), rioja: Analysis of Quaternary Science Data, R oackage version 0.9-3, http://cran.r-project.org/web/packages/rioja/index.html

Kim, J. H., X., Crosta, V., Willmott, H., Renssen, J., Bonnin, P., Helmke, S., Schouten, and J.S.S., Damsté (2012), Holocene subsurface temperature variability in the eastern Antarctic continental margin, *Geophys. Res. Lett.,* 39, DOI:10.1029/2012GL051157.

Kohfeld, K. E., R.M., Graham, A.M., de Boer, L.C., Sime, E.W., Wolff, C., Le Quéré, and L., Bopp (2013), Southern hemisphere westerly wind changes during the Last Glacial Maximum: paleo-data synthesis, *Quat. Sci. Rev.*, 68, 76-95.

Kopp, R. E. (2012), Tahitian record suggests Antarctic collapse. *Nature,* 483, 549-550.

Lisiecki, L. E., and M.E., Raymo (2005a), A Pliocene-Pleistocene stack of 57 globally distributed benthic $\delta^{18}O$ records, *Paleoceanography*, 20, DOI:10.1029/2004PA001071.

Lisiecki, L.E., and M.E., Raymo (2005b), LR04 Global Pliocene-Pleistocene Benthic $\delta^{18}O$ stack, IGBP PAGES/world data center for paleoclimatology data contribution series #2005-008, NOAA/NGDC Paleoclimatology Program, Boulder CO, USA.

Manoj, M. C., M., Thamban, A., Sahana, R., Mohan and K., Mahender (2013), Provenance and temporal variability of ice rafted debris in the Indian sector of the Southern Ocean during the last 22,000 years, *J. Earth Syst. Sci.*, 122, 491–501.

Martinson, D. G. (2012), Antarctic circumpolar current's role in the Antarctic ice system: an overview, *Palaeogeogr. Palaeoclimatol. Palaeoecol.*, 335-336, 71–74.

Massom, R., P., Reid, S., Stammerjohn, B., Raymond, A., Fraser, S., and Ushio (2013), Change and variability in East Antarctic sea ice seasonality, 1979/80–2009/10, *PLoS One,* 8, DOI: 10.1371/journal.pone.0064756.

Masson, V., F., Vimeux, J., Jouzel, V., Morgan, M., Delmotte, P., Ciais, C., Hammer, S., Johnsen, V.Y., Lipenkov, E.M., Thompson, J.R., Petit, E.J., Steig, M., Stievenard, and R., Vaikmae (2000), Holocene climate variability in Antarctica based on 11 ice-core isotopic records, *Quat. Res.*, 54, 348–358.

Mathiot, P., H., Goosse, X., Crosta, B., Stenni, M., Braida, H., Renssen, C.J., Van Meerbeeck, V., Masson-Delmotte, A., Mairesse, and S., Dubinkina (2013), Using data assimilation to investigate the causes of Southern Hemisphere high latitude cooling from 10 to 8 ka BP, *Clim. Past*, 9, 887–901.

Mayewski, P. A., E.E., Rohling, J.C., Stager, W., Karlén, K.A., Maasch, L.D., Meeker, E.A., Meyerson, F., Gasse, S., van Kreveld, K., Holmgren, J., Lee-Thorp, G., Rosqvist, F., Rack, M., Staubwasser, R.R., Schneider and E.J., Steig (2004), Holocene climate variability, *Quat. Res.*, 62, 243– 255.

Mazaud, A., E., Michel, F., Dewilde, and J.L., Turon (2010), Variations of the Antarctic Circumpolar Current intensity during the past 500 ka, *Geochem., Geophys., Geosyst.*, 11, DOI:10.1029/2010GC003033.

Moros, M., P., De Deckker, E., Jansen, K., Perner, and R.J., Telford (2009), Holocene climate variability in the Southern Ocean recorded in a deep-sea sediment core off South Australia, *Quat. Sci. Rev.*, 28, 1932–1940.

Neil, H. L., and L., Carter (2004), Thermal isolation of Campbell Plateau, New Zealand, by the Antarctic Circumpolar Current over the past 130 kyr, *Palaeoceanography*, 19, DOI:10.1029/2003PA000975.

Newnham, R. M., D.J., Lowe, T., Giles, and B.V., Alloway (2007), Vegetation and climate of Auckland, New Zealand, since ca. 32 000 cal. yr ago: support for an extended LGM, *J. Quaternary Sci.*, 22, 517–534.

Paillard, D., L., Labeyrie and P., Yiou (1996), Macintosh program performs time-series analysis, *Eos Trans. AGU*, 77: 379.

Parkinson, C. L., and D.J., Cavalieri (2012), Antarctic sea ice variability and trends, 1979–2010, *The Cryosphere*, 6, 871–880.

Parkinson, C.L. (1992), Interannual variability of monthly Southern Ocean sea ice distributions, *J. Geophys. Res.*, 97, 5349-5363.

Parrenin, F., V., Masson-Delmotte, P., Köhler, D., Raynaud, D., Paillard, J., Schwander, C., Barbante, A., Landais, A., Wegner and J., Jouzel (2013), Synchronous change of atmospheric CO_2 and Antarctic temperature during the last Deglacial warming, *Science*, 339, 1060-1063.

Putnam, A. E., G.H., Denton, J.M., Schaefer, D.J.A., Barrell, B.G., Andersen, R.C., Finkel, R., Schwartz, A.M., Doughty, M.R., Kaplan, and C., Schlüchter (2010), Glacier advance in southern middle-latitudes during the Antarctic Cold Reversal, *Nat. Geosci.,* 3, 700-704.

Recasens, C., Ariztegui, D., Maidana, N.I., Zolitschka, B., and the PASADO Science Team (2015), Diatoms as indicators of hydrological and climatic changes in Laguna Potrok Aike (Patagonia) since the Late Pleistocene, *Palaeogeogr., Palaeoclimatol., Palaeoecol.*, 417, 309–319.

Reimer, P.J., E. Bard, A. Bayliss, J.W., Beck, P.G., Blackwell, C., Bronk Ramsey, C.E., Buck, H. Cheng, R.L., Edwards, M., Friedrich, P.M., Grootes, T.P., Guilderson, H., Haflidason, I., Hajdas, C., Hatté, T.J., Heaton, D.L., Hoffmann, A.G., Hogg, K.A., Hughen, K.F., Kaiser, B., Kromer, S.W., Manning, M., Niu, R.W., Reimer, D.A., Richards, E.M., Scott, J.R., Southon, R.A., Staff, C.S.M., Turney, and J., van der Plicht (2013), IntCal13 and Marine13 radiocarbon age calibration curves 0–50,000 years cal BP, *Radiocarbon*, 55, 1869–1887.

Renssen, H., H., Goosse, X., Crosta, and D.M., Roche (2010), Early Holocene Laurentide Ice Sheet deglaciation causes cooling in the high-latitude Southern Hemisphere through oceanic teleconnection, *Paleoceanography*, 25, DOI:10.1029/2009PA001854.

Röthlisberger, R., X., Crosta, N.J., Abram, L., Armand, and E.W., Wolff (2010), Potential and limitations of marine and ice core sea ice proxies: an example from the Indian Ocean sector, *Quat. Sci. Rev.,* 29, 296–302.

Schneider-Mor, A., R., Yam, C., Bianchi, M., Kunz-Pirrung, R., Gersonde, and A., Shemesh (2005), Diatom stable isotopes, sea ice presence and sea surface temperature records of

the past 640 ka in the Atlantic sector of the Southern Ocean, *Geophys. Res. Lett.,* 32, DOI:10.1029/2005GL022543.

Schweitzer, P. N. (1995), Monthly average polar sea-ice concentration: U.S. Geological Survey digital data series DDS-27. U.S. Geological Survey, Reston, Virginia, http://pubs.usgs.gov/dds/dds27/

Shevenell, A. E., and J.P., Kennett (2002), Antarctic Holocene climate change: A benthic foraminiferal stable isotope record from Palmer Deep, *Paleoceanography*, 17, DOI: 10.1029/2000PA000596.

Shevenell, A. E., A.E., Ingalls, E.W., Domack and C., Kelly (2011), Holocene Southern Ocean surface temperature variability west of the Antarctic Peninsula, *Nature*, 470, 250-254.

Shulmeister, J., I., Goodwin, J., Renwick, K., Harle, L., Armand, M.S., McGlone, E., Cook, J., Dodson, P.P., Hesse, P., Mayewski, and M., Curran (2004), The Southern Hemisphere westerlies in the Australasian sector over the last glacial cycle: a synthesis, *Quaternary Int.*, 118–119, 23–53.

Simmonds, I. (2015), Comparing and contrasting the behavior of Arctic and Antarctic sea ice over the 35 year period 1979–2013, *Ann. Glaciol.*, 56, DOI: 10.3189/2015AoG3169A3909.

Spolaor, A., P., Vallelonga, J., Gabrieli, N., Kehrwald, V., Turetta, G., Cozzi, L., Poto, J.M.C., Plane, C., Boutron, and C., Barbante (2013), Speciation analysis of iodine and bromine at picogram-per-gram levels in polar ice, *Anal. Bioanal. Chem.*, 405, 647-654.

Stammerjohn, S., R., Massom, D., Rind, and D., Martinson (2012), Regions of rapid sea ice change: An inter-hemispheric seasonal comparison, *Geophys. Res. Lett.,* 39, DOI:10.1029/2012GL050874.

Stenni, B., D., Buiron, M., Frezzotti, S., Albani, C., Barbante, E., Bard, J.M., Barnola, M., Baroni, M., Baumgartner, M., Bonazza, E., Capron, E., Castellano, J., Chappellaz, B., Delmonte, S., Falourd, L., Genoni, P., Iacumin, J., Jouzel, S., Kipfstuhl, A., Landais, B., Lemieux-Dudon, V., Maggi, V., Masson-Delmotte, C., Mazzola, B., Minster, M., Montagnat, R., Mulvaney, B., Narcisi, H., Oerter, F., Parrenin, J.R., Petit, C., Ritz, C., Scarchilli, A., Schilt, S., Schüpbach, J., Schwander, E., Selmo, M., Severi, T.F., Stocker, and R., Udisti (2010), Expression of the bipolar see-saw in Antarctic climate records during the last deglaciation, *Nat. Geosci.*, 4, DOI: 10.1038/NGEO1026.

Stenni, B., V., Masson-Delmotte, S., Johnsen, J., Jouzel, A., Longinelli, E., Monnin, R., Röthlisberger, and E., Selmo (2001), An oceanic cold reversal during the last deglaciation, *Science*, 293, 2074-2077.

Stern, J., and E., Lisiecki (2014), Termination 1 timing in radiocarbon-dated regional benthic $\delta^{18}O$ stacks, *Palaeoceanography*, 29, DOI:10.1002/2014PA002700.

Stephens, T., D., Atkin, P., Augustinus, P., Shane, A., Lorrey, A., Street-Perrott, A., Nilsson, and I., Snowball (2012), A late glacial Antarctic climate teleconnection and variable Holocene seasonality at Lake Pupuke, Auckland, New Zealand, *J. Paleolim.*, 48, 785–800.

Stuiver, M., and P.J. Reimer (1993), Extended ^{14}C database and revised CALIB radiocarbon calibration program, *Radiocarbon*, 35: 215-230.

Telford, R. J., and H.J.B., Birks (2011), Effect of uneven sampling along an environmental gradient on transfer-function performance, *J. Paleolim.*, 46, 99–106.

Weaver, A. J., O.A., Saenko, P.U., Clark, and J.X., Mitrovica (2003), Meltwater pulse 1A from Antarctica as a trigger of the Bølling-Allerød warm interval, *Science*, 299, DOI: 10.1126/science.1081002

Weber, M. E., P.U., Clark, G., Kuhn, A., Timmermann, D., Sprenk, R., Gladstone, X., Zhang, G., Lohmann, L., Menviel, M.O., Chikamoto, T., Friedrich, and C., Ohlwein (2014), Millennial-scale variability in Antarctic ice-sheet discharge during the last deglaciation, *Nature*, 510, DOI:10.1038/nature13397.

Williams, T. (2014), How Antarctic ice retreats, *Nature*, 510, 39-40.

Wood, S. (2014), mgcv: Mixed GAM Computation Vehicle with GCV/AIC/REML Smoothness Estimation, R package version 1.8-5, http://cran.r-project.org/web/packages/mgcv/index.html

This page is intentionally left blank.

Chapter 4

New southwest Pacific winter sea ice and February sea-surface temperature records over the extended Last Glacial Maximum.

Authors:

Alexander J. Ferry[1], Leanne K. Armand[1], (authors to be included upon submission to Quaternary Science Reviews) Elisabeth Michel[2] and Xavier Crosta[3]

1. Department of Biological Sciences, Climate Futures at Macquarie University, North Ryde, 2109, New South Wales, Australia. alexander.ferry@mq.edu.au, leanne.armand@mq.edu.au

2. Laboratoire des Sciences du Climate et de l'Environment (LSCE), IPSL, CEA, UVSQ, CNRS, Gif sur Yvette, France. elisabeth.michel@lsce.ipsl.fr

3. DGO, UMR-CNRS 5805 EPOC, Université de Bordeaux I, Avenue des Facultés, 33405 Talence Cedex, France. x.crosta@epoc.u-bordeaux1.fr

Anticipated Journal:
Climate of the Past

Key Words: extended Last Glacial Maximum, Antarctic Isotope Maxima, Generalized Additive Model, sea ice, sea-surface temperature, Southern Ocean.

Abstract

Unanswered questions exist regarding the climatic mechanisms that were important for instigating cooling during the Last Glacial Maximum climate and its eventual termination. To assess the potential climatic mechanisms, we analysed six marine sediment cores in the Southern Ocean; four from the southwest Pacific, one from the southeast Pacific and one from southeast Atlantic sector of the Southern Ocean. For each core we estimate February sea-surface temperature using weighted averaging partial least squares, and winter sea-ice concentration using a generalized additive model. Our data provides the first indication that the extended Last Glacial Maximum of the southwest Pacific was characterized by two cold phases from ~36 to 28 kyr BP and 23 to 19 kyr BP, separated by a period of climatic amelioration known as Antarctic Isotopic Maxima 2. Our paleo winter sea-ice estimates provide the first record of a winter sea ice reduction during Antarctic Isotopic Maxima 2 within the southwest Pacific. Our new extended Last Glacial Maximum winter sea-ice record may be explainable by atmospheric cooling and stratification of the Southern Ocean, which allowed for increased winter duration and sea-ice formation. Such southern hemisphere cooling responses have been explained by a northern hemisphere insolation forcing, which cooled North Atlantic Deep Water, and subsequently increased the salinity of Antarctic Bottom Water formed within the Weddell Sea. The bipolar see-saw hypothesis provides a plausible explanation for the two cold phases either side of Antarctic Isotopic Maxima 2 during the extended Last Glacial Maximum. Finally, our data is consistent with a termination of the extended Last Glacial Maximum that resulted from a breakdown of Southern Ocean stratification and/or the northern hemisphere sourced 19 kyr BP melt water pulse.

1 Introduction

The Last Glacial Maximum (LGM) is defined as that most recent time interval at which global ice sheets reached their maximum integrated volume (Mix et al., 2001). It has been suggested the LGM period could be representative of Quaternary ice ages (Kucera et al., 2005). Climate change scenarios associated with Quaternary deglaciations are reliant on mechanisms, such as deep water formation and carbon storage, which involve physical changes to the Antarctic ice sheet and circulation of the Southern Ocean. However, such mechanisms are poorly documented (Paillard, 2015). The transition from the LGM climate to the present Holocene interglacial represents a natural global climatic shift. Developing a detailed understanding for the timing and duration of the transition from the LGM into the Holocene provides an opportunity to examine important hypotheses concerning the functioning of the global climate system (Kucera et al., 2005; Jansen et al., 2007; Vandergoes et al., 2013). The periods that follow glaciation can provide an opportunity to evaluate how Earth's climate system may respond to radiative perturbations (Jansen et al., 2007) and to assess the sensitivity of the global climate system (Kucera et al., 2005).

Aeolian sedimentation rates from eastern Australia (Petherick et al., 2008), along with paleolimnological and pollen records from New Zealand (Stephens et al., 2012; Vandergoes et al., 2013) suggest the extended LGM may have commenced at ~29 kyr BP and lasted for ~10 kyr. The climatic cooling between 29 and 19 kyr BP has been referred to as the extended LGM (eLGM, Newnham et al., 2007). The eLGM throughout eastern Australia and New Zealand has been characterised by two distinct periods of climatic cooling at its inception and termination, separated by a period of climatic warming known as the eLGM interstadial or Antarctic Isotope Maxima 2 (Petherick et al., 2008; Stephens et al., 2012; Newnham et al., 2012) (herein referred to

as AIM 2). The eLGM climatic variability documented within New Zealand and eastern Australia is consistent with Southern Ocean marine records from the southwest Pacific and EPICA Dronning Maud Land (DML) Antarctic ice core from West Antarctica, used to understand the sea-ice feedbacks on atmospheric circulation (Vandergoes et al., 2013).

Our current body of knowledge regarding eLGM sea-ice coverage throughout the southern hemisphere remains incomplete (Fraser et al., 2009). Although efforts are under way (Esper and Gersonde, 2014a,b), there remains a need for additional marine sediment core data, and associated paleo sea-ice data, from the Pacific sector of the Southern Ocean. The current lack of eLGM marine sediment core data throughout the Pacific is a specific hindrance for the accurate reconstruction of eLGM paleoclimate throughout the Southern Ocean (Gersonde et al., 2005).

Therefore, our paper has two main aims. Firstly, we seek to provide new paleo winter sea ice and February sea-surface temperature (fSST) records from four marine sediment cores within the southwestern Pacific. Two of the cores from the southwest Pacific, E27-23 and SO136-111, have been previously reported (Crosta et al., 2004; Chapter 3), whilst estimates of winter sea-ice concentrations from an additional two cores (MD88-787 and MD88-784) are used to complement existing paleo sea-ice records. Paleo winter sea-ice data is derived from a recently described statistical approach based on a diatom proxy (Chapter 2). In elucidating a regional eLGM paleo sea-ice synthesis for the southwest Pacific sector of the Southern Ocean from these cores, we then compare our synthesis against revised winter sea-ice estimate records from the southeast Pacific (core PS58/271-1) and east Atlantic (core PS1768-8). Secondly, we compare our paleo winter sea-ice data with paleo climate records from New Zealand, eastern Australia, and east Antarctica to infer the nature of the eLGM climate throughout the Pacific sector of the Southern Ocean. We test current hypotheses that suggest the onset of the eLGM was attributable to

stratification of the Southern Ocean (Putnam et al., 2013) and/or northern hemisphere insolation forcing (Adkins, 2013), and that the eLGM cold phases, in conjunction with AIM 2, are explainable via a bipolar see-saw (Dürkop et al., 2008).

2 Data and Methods

2.1 Winter sea ice, February sea-surface temperature and marine sediment core data sets

Our analysis used the core top training database compiled by Crosta et al. (2004), which documents the relative abundance of 32 diatom species across 243 Southern Ocean sample locations. Our analysis follows the methodology developed within Chapter 2, using just 163 of the samples compiled by Crosta et al. (2004). Sea-ice concentration data was derived from the bootstrapped algorithm of Comiso (2000). We therefore provide paleo estimates of winter sea-ice concentrations (wSIC), defined as a September average sea-ice concentration (Gersonde et al., 2005), using the generalized additive model (GAM) described within Chapter 2.

The February sea-surface temperature (fSST) records used and estimated in this study were originally compiled by Crosta et al. (2004), using the World Ocean Atlas program and the paleo toolbox software, all available through the PANGAEA portal. All 243 samples of the Crosta et al. (2004) database were retained as part of our fSST training set (Figure 1). Modern fSST values at each of the marine cores used in this study were derived from Reynolds et al. (2002).

Our paper examines the paleoceanographic record from six marine sediment cores. Four sediment cores, MD88-787, SO136-111, MD88-784 and E27-23, were sampled from the southwestern Pacific sector of the Southern Ocean (Table 1). We also included sediment core PS58/271-1 from the east Pacific Sector and core PS1768-8 from the eastern Atlantic (Table 1). Cores MD88-787, SO136-111, MD88-784, and PS58/271-1 are located south of the Sub-Antarctic Front (SAF) and to the north of the Polar Front (PF) in the Sub-Antarctic Zone. PS1768-8 and E27-23 are both situated south of the PF. All of the cores are north of the modern winter sea-ice edge (Figure 1).

Table 1. **Location, modern average February sea-surface temperature from Reynolds et al. (2002), age model, and previous reference source details for each of the six marine sediment cores covered in this study.**

Core	Latitude	Longitude	Depth (meters)	Modern average February fSST (°C)	Reference for Core Age Models	Reference for previous Paleo sea-ice record	Data Archive Source
southwest Pacific							
E27-23	-59.61	155.24	3182	3.51	Chapter 3		Australian Antarctic Division (DOI http://dx.doi.org/10.4225/15/546C10AD26A7)
MD88-787	-56.38	145.3	3020	4.21	This paper	Armand, 1998 (GAM)	AODN/Blue Link: ISO19115/19139 (http://bluenet.aodn.org.au/geonetwork/srv/en/metadata.show?id=726&currTab=simple)
SO136-111	-56.67	160.23	3912	5.78	Crosta et al. (2004); Chapter 3	Crosta et al. (2004) (Modern analogue technique); GAM (Chapter 2)	Xavier Crosta (pers. comm. 2011)
MD88-784	-54.19	144.79	2800	5.52	This paper	Armand, 1998 (GAM)	AODN/Blue Link: ISO19115/19139. (http://bluenet.aodn.org.au/geonetwork/srv/en/metadata.show?id=728&currTab=simple)
southeast Pacific							
PS58/271-1	-60.24	-116.05	5139	4.43	No age model (Esper, pers comm. 2014)	Esper and Gersonde, (2014b) (Modern analogue technique , Imbrie and Kipp Transfer Function)	PANGAEA: doi:10.1594/PANGAEA.693745
southeast Atlantic							
PS1768-8	-52.59	4.48	3270	2.71	No age model (Esper, pers comm. 2014)	Esper and Gersonde (2014b) (Modern analogue technique , Imbrie and Kipp Transfer Function)	PANGAEA: doi:10.1594/PANGAEA.693743

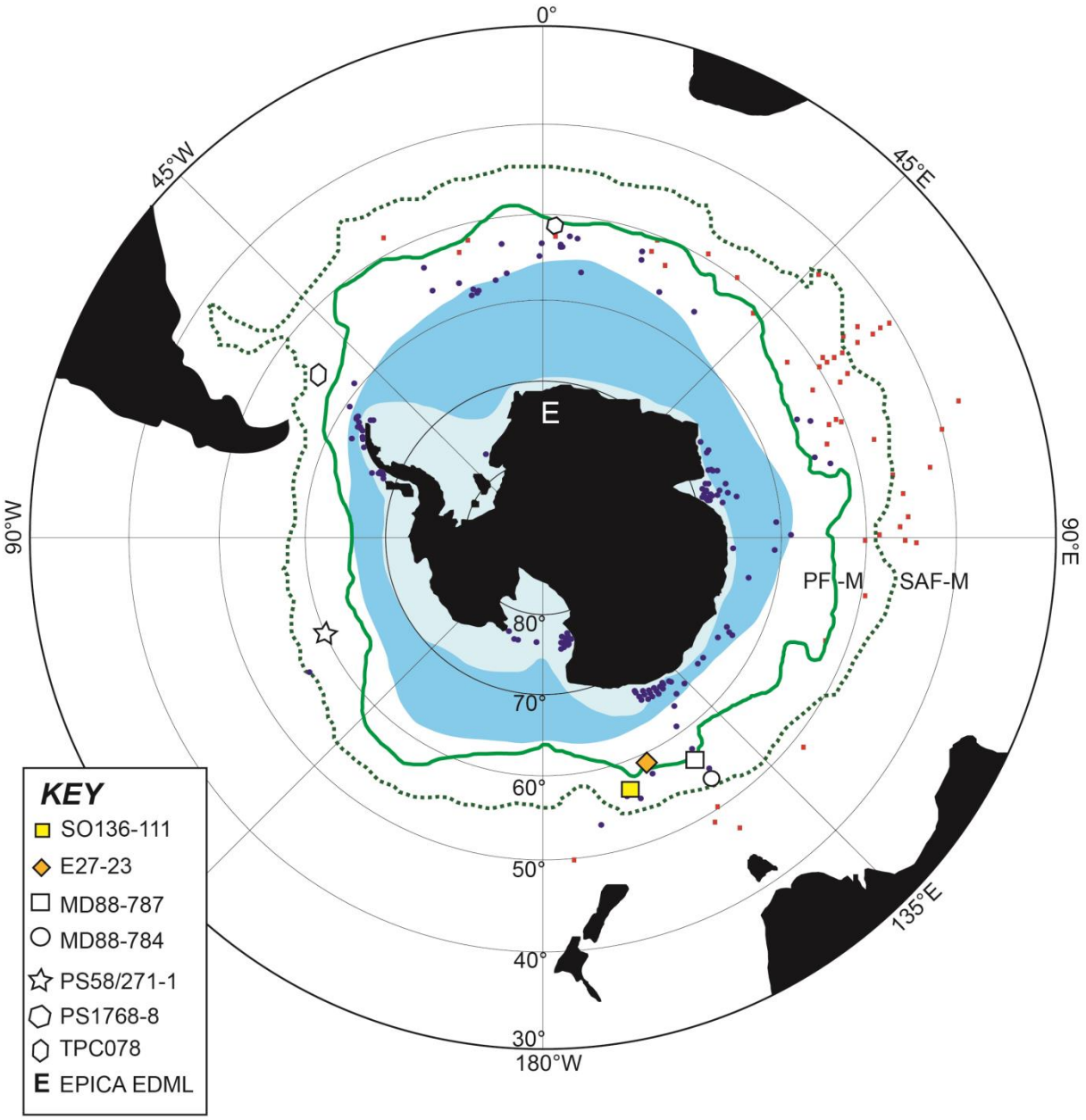

Figure 1. **All 243 surface sediment samples from Crosta et al. (2004) are plotted.** Blue dots indicate samples used within our sea-ice training set whilst the red squares/dots correspond with those additional samples used within the fSST training set. The locations of sediment cores SO136-111, E27-23, MD88-784, MD88-787, PS1768-8, PS58/271-1 and TPC078 are identified. Refer to Table 1 for core locations and references. The modern average winter sea-ice extent from 1979 to 2000 is shaded mid-blue, whilst light blue shading indicates the maximum summer sea-ice extent. For context the mean position for both the Polar Front middle branch (PF-M) and Sub-Antarctic Front's middle branch (SAF-M) are shown (Sokolov and Rintoul, 2009).

2.2 Material and stratigraphy

The age models for cores MD88-787 and MD88-784 are based on $\delta^{18}O$ isotope records derived from *Neogloboquadrina pachyderma* sinistral (200-250µm fraction, versus PDB) (pers. comm. E. Michel LSCE-IPSL-CNRS, 2014). The isotopic records from MD88-787 and MD88-784 were tuned over the last 50 kyr to the $\delta^{18}O$ isotope record of E27-23 (Figure 2), as this latter record presents the best regionally-resolved age model backed by ^{14}C dating (Chapter 3). Independent tuning of both $\delta^{18}O$ isotope records used the "Linage" subroutine of Analyseries 2.0.8 (Paillard et al., 1996). As in Chapter 3, the chronology used for MD88-787 and MD88-784 did not use the recent benthic $\delta^{18}O$ global overview compiled by Stern and Lisiecki (2014), due to the lack of data coverage throughout the south Pacific sector of the Southern Ocean. Age model formulation for MD88-787 and MD88-784 and associated data are presented in Appendices 4.1 and 4.2, respectively.

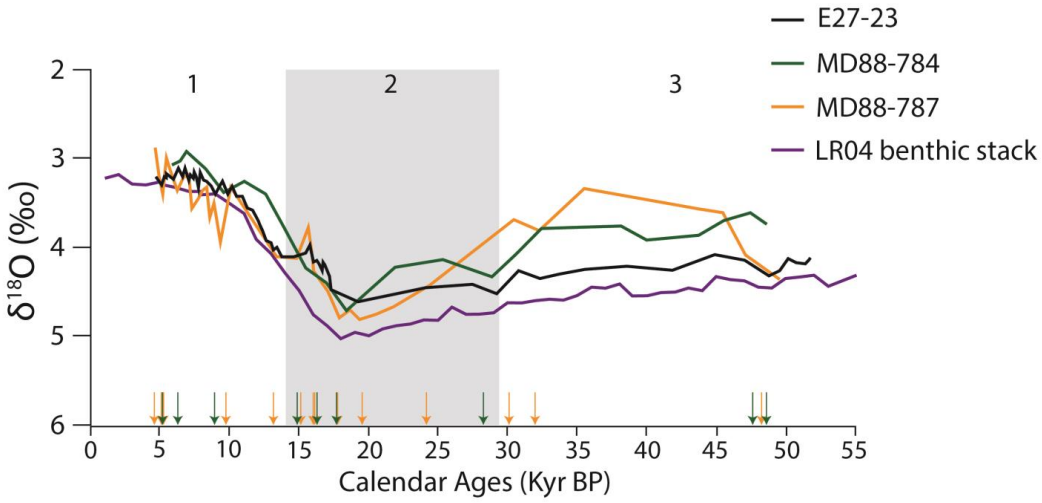

Figure 2. Age calibrated $\delta^{18}O$ isotope curve comparison between the $\delta^{18}O$ (*Neogloboquadrina pachyderma* sinistral (planktic)) from cores MD88-787 and MD88-784, with core E27-23. Arrows indicate the calibrated ^{14}C AMS age pointers from MD88-787 (orange) and MD88-784 (green) used to correlate to the age calibrated $\delta^{18}O$ isotope curve from E27-23. The LR04 global benthic $\delta^{18}O$ stack (Lisiecki and Raymo, 2005a,b)) is also shown in purple.

2.3 Reconstruction diagnostics

A comparison was made between the maximum recorded abundance for each diatom species documented within our training set and the maximum recorded fossilized assemblage within each marine sediment core. In addition, we used the diversity measure, Hills N2, to identify those species that may have a poorly defined optima (Hill, 1973). Analogue quality, and the presence of non-analogue samples for each core, was assessed with a squared chord distance and the five closest analogues. Those core samples with a distance greater than the 5^{th} percentile of all distances were classed as having no analogue. Core samples with distances between the 10^{th} and 5^{th} percentiles of all distances are considered to have poor analogues (Birks et al., 1990; Birks, 2003).

2.4 Statistical methods used to estimate paleo sea-ice cover

The GAM developed within Chapter 2 was applied to estimate paleo wSIC from all six of the marine sediment cores used in this study. Gersonde et al. (2005) suggested that diatom-based estimates of paleo summer sea ice are uncertain, as diatom assemblages are predominantly produced in open-ocean conditions, whilst areas with longer term sea-ice coverage preserve fewer diatoms. The absence of diatom remains within a marine sediment core was interpreted as an indicator for the presence of permanent sea-ice cover. We made no attempt to provide a quantitative estimate of summer sea-ice concentrations based on fossilized diatom assemblages. We have discriminated between the type of sea ice following Gloersen et al. (1992), whereby wSIC less than 15% was considered to indicate no sea-ice cover, 15 to 40% represented unconsolidated sea ice, whilst concentrations above 40% represented consolidated winter sea ice.

2.5 Statistical methods used to estimate paleo February sea-surface temperature

We compared the performance of three statistical methods applied to the Crosta et al. (2004) fSST and diatom relative abundance training set. The methods compared included the Imbrie and Kipp transfer function (IKTF), modern analogue technique (MAT), and weighted averaging partial least squares (WA PLS). When applying statistical models to our training dataset we considered both log transformed diatom abundance values, using ln(abundance*10+1) (Zielinski et al., 1998; Esper and Gersonde, 2014; Chapter 2), and untransformed data. The application of IKTF, MAT and WA PLS used all of the 32 diatom species recorded within the Crosta et al. (2004) diatom training database.

The fit of each model to our training set was evaluated by applying a linear regression between each model's fitted values and the observed values within our training set. Use of regression in this way would reveal a perfect model as having a slope of one with a zero intercept. We used a 95% confidence interval to determine whether a fitted regression slope was significantly different from one (Bennett et al., 2013). Statistical assumptions were assessed with Shapiro-Wilk's and Lilliefors tests for the normality of residuals (for IKTF), whilst (for IKTF and WA PLS) a runs test and Bartels test were used to determine whether model errors were random and centered on a mean value of zero. All of the above model diagnostic tests were applied when evaluating each statistical model under a random tenfold hold out validation, and when fitting each model to the complete fSST training set.

Previous work has demonstrated the bias that arises from spatial autocorrelation within oceanographic training sets when evaluating the predictive success of a model (Telford and Birks, 2005). Therefore, we applied two hold out validations on our data, using spatially

independent training and validation data subsets, to assess the performance of each model on independent data (Appendix 4.3). Doing so allowed us to infer the predictive capacity of each model on independent (for example, marine sediment core) data and to overcome the undue bias arising from autocorrelation within our training set when computing a root mean squared error of prediction (RMSEP).

2.6 Software

We used the package 'PAST' of Hammer et al. (2001) for MAT. All remaining analyses were applied with R, version 3.0.2. IKTF was trained on our data using the R functions 'princomp' and 'lm'. We used mgcv (Wood, 2014) to apply GAM, rioja (Juggins, 2014) for WA PLS and broken stick models, fBasics (Wuertz et al., 2013) for normality tests on model residuals, and finally car (Fox et al., 2015) for the Beuch Pagan test. All graphics were produced using R and Adobe Illustrator™.

3 Results

3.1 Comparison of the statistical models used for paleoceanographic estimation

3.1.1 February sea-surface temperatures

The statistical assumptions of relevance to the IKTF method, namely normality and constant variance of model errors (as inferred from tests on model residuals), were not satisfied when fitting the model to the full fSST training data set. The non-linear relationship between diatom abundances and fSST cannot be modelled with the IKTF method (Appendix 4.4). Hence IKTF was not considered for further application. Based on our random 10-fold hold out validation, MAT applied to both log transformed and untransformed data had the lowest average RMSEP (1.13). Use of a hold out validation helped to assess the performance of each model on spatially independent data. Under hold out validation, WA PLS, when applied to log transformed data, provided the lowest average RMSEP (1.08). Similarly, the lowest RMSEP for MAT (1.52) was computed on log transformed data (Appendix 4.5). Finally, a linear regression between model fitted values and observed data for both WA PLS and MAT provided fitted slopes that were not significantly different from one (Appendix 4.6). As the application of WA PLS on log transformed data provided the lowest RMSEP under our spatially independent hold out validation (Appendix 4.5), all estimates of fSST are derived from the application of WA PLS on log transformed data. As previous work has already tested and verified the utility of WA PLS for estimating SST (Telford and Birks, 2005), we did not consider developing a new GAM to estimate fSST.

3.2 Reconstruction diagnostics

Of the diatom species within our training dataset that had poorly defined optima, none were highly abundant within any of the cores we analysed within this study (Appendix 4.7). Similarly, none of the diatom species were considerably more abundant within the core samples in comparison with the surface sediment samples of our training data set (Appendix 4.7). Marine sediment core MD88-784 had no samples for which there were no analogues (Appendix 4.8), whilst core MD88-787 had seven samples with no modern analogue. None of the remaining samples of core MD88-787 had poor analogues (Appendix 4.9). Core PS58/271-1 had 86 samples with no modern analogue, and 117 samples with poor analogues (Appendix 4.10). Core PS1768-8 had 50 samples with no modern analogue and 26 samples with poor analogues (Appendix 4.11). The reconstruction diagnostics for marine sediment cores SO136-111 and E27-23 are provided within Chapter 3 and are therefore not repeated here.

3.3 Paleo winter sea-ice concentrations

Results from the application of GAM to estimate past wSIC over the last 50 kyr BP for the four cores located within the southwest Pacific are plotted in Figure 3 (a to d). At the northern most core, MD88-784, unconsolidated wSIC was present over the core site between ~44.2 and 40.5 kyr BP, whilst the core site remained sea ice free through to the start of the eLGM. Unconsolidated wSIC was sporadically present at ~31, 28, 21 and 17 kyr BP, over the eLGM period (Appendix 4.8). The increase in wSIC recorded at 28 and 21 kyr BP matches the timing of the first and second eLGM cold phases, respectively. A distinct decline in wSIC (<15%), between 26.5 and 23 kyr BP (during the eLGM), may be attributable to AIM 2 (Figure 3a). Since

the end of the eLGM, and through marine isotope stage (MIS) 1, no sea ice is estimated at the location of MD88-784.

Over the last 50 kyr BP unconsolidated winter sea ice predominately influenced the location of SO136-111 (Figure 3b, Chapter 3, appendix 3.5). More substantial cover, representative of consolidated wSIC, was estimated only at ~36 kyr BP and 24 kyr BP. Due to the consistently prolonged consolidated sea-ice conditions across MIS 3 and into the eLGM, differentiating the first cold phase and warm AIM 2 are difficult. However, the benthic isotope record (Chapter 3, Figure 2) reveals a slight maxima at 26 kyr BP that could be interpreted as the AIM 2 maxima. The benthic isotopic maximum for SO136-111 is in alignment with the estimated decline of wSIC at 26 kyr BP (Figure 3b). We place the first cold phase of the eLGM where sea ice increases from ~29 kyr BP, whilst we consider the second phase may occur at ~24 kyr BP. The compact sea-ice edge was therefore present at the site of SO136-111 during both eLGM cold phases, whilst no sea ice was present during AIM 2 (Figure 3b). Not unlike the MD88-784 record to the west of SO136-111, MIS 1 reveals no influence of winter sea-ice cover over the location of the core site.

Contrary to the estimates of the more northerly SO136-111 core, wSIC cover was not consistent throughout MIS 3 at the site of MD88-787 (Figure 3c). From ~24 to 17 kyr BP winter sea-ice estimates were representative of unconsolidated to consolidated cover. Consolidated winter sea ice covered the core site at 20.5, 17.9 and 14.5 kyr BP (Fig. 2c; Appendix 4.9). The eLGM shows no period attributable to AIM 2, which the isotope record would otherwise suggest might be expressed at 19 kyr BP (Figure 2). Equally, only a single phase of distinct major cooling at 20.5 kyr BP is likely to be representative of one of the two main cooling phases. Consistent with the

preceding cores, the site of core MD88-787 has no record of winter sea-ice estimates through MIS 1.

The site of the southernmost southwest Pacific core, E27-23, was covered by consolidated sea ice from ~45 to 40 and 35 to 32 kyr BP, just prior to the eLGM (Figure 3d). Unconsolidated winter sea-ice cover was present at the core site from 31 to 21 kyr BP over the LGM period. Consolidated winter sea-ice cover was then estimated at ~21 to 17 and ~12.5 kyr BP. The estimates of unconsolidated winter sea ice from 29 to 26 kyr BP, and consolidated winter sea ice from 21 to 17 kyr BP, may be a sea-ice expression of the eLGM cold phases (Figure 3d). The benthic isotope record for E27-23 (Figure 2) reveals a slight maxima at 26 kyr BP. The decline in wSIC at the site of E27-23 from ~27 to 24 kyr BP are roughly consistent with the E27-23 isotope maxima, and may be an expression of AIM 2 (Figure 3d). During MIS 1 many northward excursions of the winter sea ice are estimated indicative predominately of the outer sea-ice edge and unconsolidated sea-ice cover at 13.2, 12.3, 11.9, 10.5, 9.2, 7.2, 6.5, 5.5, 2.8, 1.9 and 1.5 kyr BP, most significantly at 12.6, 12.2, and 6.3 kyr BP (Chapter 3, appendix 3.6).

In contrast, the revised south Atlantic wSIC estimates from core PS1768-8, located south of the PF, suggests consolidated sea-ice cover throughout MIS 2 and 3, whereas from 160cm depth in the core, at the close of MIS 2, winter sea-ice cover retreated abruptly from the site to only return at unconsolidated levels toward the top of the core (Figure 3e; Appendix 4.11). No clear interpretation of eLGM features of cold phases interrupted by AIM 2 can be readily diagnosed from the relatively constant high levels of wSIC resolved down core, although any one of the three minor decreases in sea-ice cover at 250, 210 and 160 cm core depth may be reflective of AIM 2. There are no age models to assist with the placement of the paleo wSIC record for this or

the following core (Esper, pers. comm. 2014). Therefore, the boundaries for MIS 2 and 3 within cores PS1768-8 and PS58/271-1 are repeated from the published figures (Esper and Gersonde, 2014a,b).

The southeast Pacific core located between the SAF and PF, PS58/271-1, was sporadically covered by unconsolidated winter sea ice during MIS 3 (Fig. 2f, Appendix 4.10). At the end of MIS 3 there was no winter sea-ice cover at the site of PS58/271-1. During MIS 2 unconsolidated winter sea-ice cover was again intermittently recorded at the core site, whilst no significant wSIC is estimated throughout MIS 1 (Appendix 4.10). Although there is no age model for the core PS58/271-1 (Esper, pers. comm. 2014), there were estimates indicative of a warming phase at 422 to 392 cm depth, at the end of MIS 3.

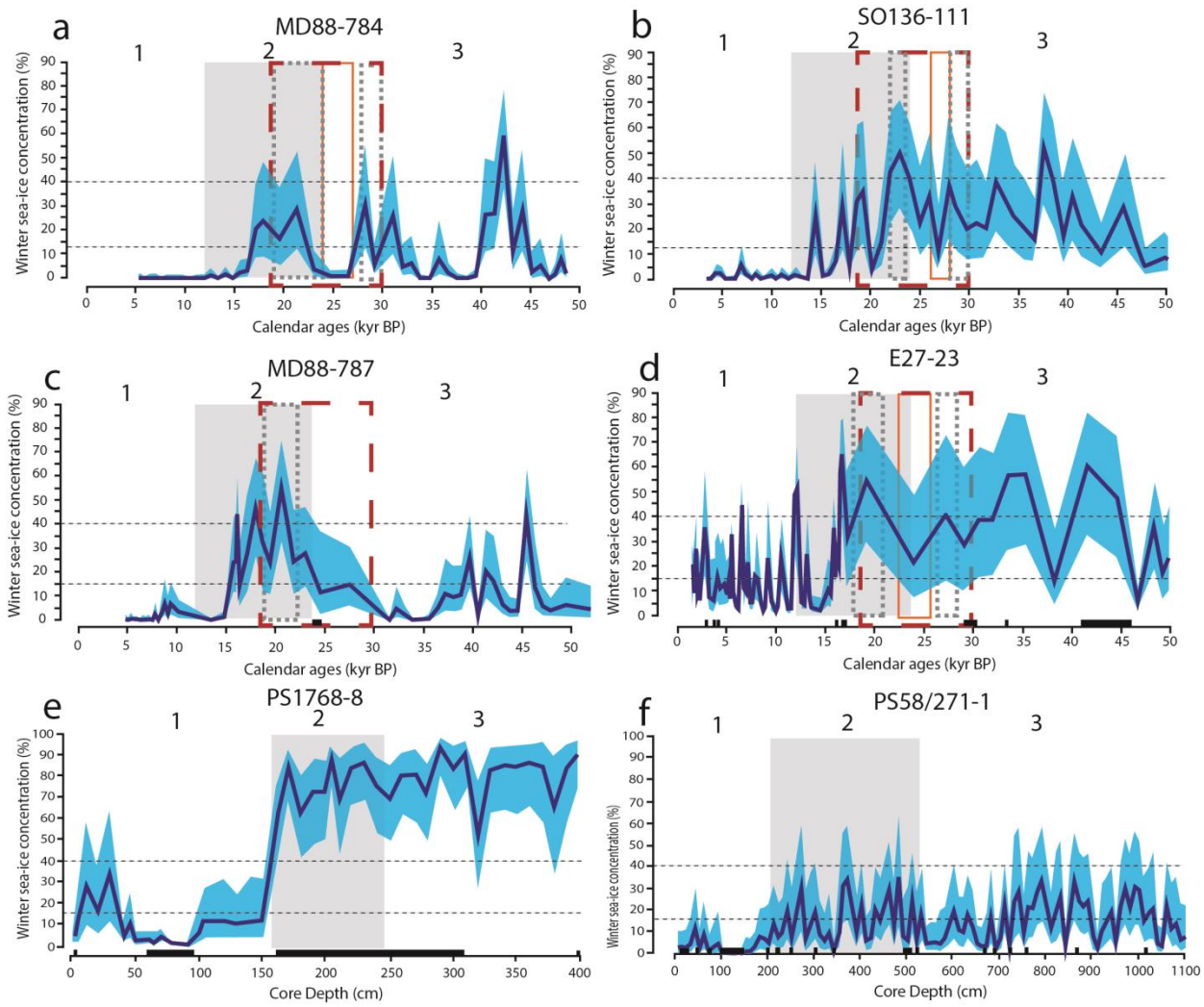

Figure 3. **The paleo wSIC records for: a) MD88-784, b) SO136-111, c) MS88-787, d) E27-23, e) PS1768-8 and f) PS58/271-1.** The solid blue line indicates the paleo wSIC estimate whilst the light blue shading corresponds to a 95% confidence interval. The dashed grey boxes highlight the eLGM cold phases whilst the solid orange box highlights AIM 2. Glacial MIS 2 is shaded in light grey. The eLGM period is highlighted with the dashed red rectangle. Horizontal grey dashed lines represent winter sea-ice concentrations of 15% and 40%, each delineating the sea-ice outer edge and the compacted sea-ice edge, respectively (Gloersen et al., 1992). The black boxes along the x-axis highlight the core samples for which there were no modern analogues. MIS = Marine Isotope Stages, with grey shading representing glacial periods.

3.4 Paleo February sea-surface temperature records

The estimated paleo fSST over the last 50 kyr BP from the southwest Pacific cores are plotted in Figure 4a-d. The complete paleo fSST record for the most northerly core, MD88-784, was approximately two to three degrees lower than the modern average fSST at the core location (Figure 4a, Table 1). The lowest fSSTs for the last 50 kyr of the core record were estimated during the eLGM, where fSST was 1.5°C and 1.6°C at 32 and 21.3 kyr BP, respectively (Figure 4a, Appendix 4.8). The decline of fSST at 29.2 kyr BP, to 1.93°C, occurs during the first eLGM cold phase. An increase in fSST from 1.9°C at 29.2 kyr BP to 3°C at 26 kyr BP occurs in concert with the small isotopic maxima in MD88-784 (Figure 2), and may be a fSST expression of AIM 2 (Figure 4a). The lowest paleo fSST (1.6°C) estimate appears within our hypothesized second eLGM cold phase between 23 and 19 kyr BP.

The paleo fSST record at the site of core SO136-111 (Appendix 4.12) was also lower than the modern fSST values currently observed over the core site (Figure 4b, Table 1). A fSST decline from 3°C at 22 kyr BP to 1.45°C at 31.6 kyr BP occurs just before the eLGM. No decline in fSST appears to correspond with the first eLGM cold phase. The fSST estimates at the site of core SO136-111 are the lowest from 27 kyr BP to 24 kyr BP, at ~ 1.5°C. From 25 kyr BP to 16 kyr BP the paleo fSST record increases from 1.3°C to 4.5°C. The paleo fSST record does not record any notable increase in fSST at 26 kyr BP that coincides with the 26 kyr BP maxima in the benthic isotope record for SO136-111 (Chapter 3, Figure 2) and AIM 2. Similarly, the paleo fSST record at the site of SO136-111 does not indicate a clear fSST decline at the end of the eLGM period that could be considered an expression of the second eLGM cold phase (Figure 4b).

Like the more northerly SO136-111, the paleo record of fSST at the site of core MD88-787 is lower than the modern fSST value of 4.21°C (Figure 4c). The highest fSST temperature during MIS 3 (3.1°C) is estimated at 32.25 kyr BP. A steady fSST decline then occurs from 30.45 kyr BP (2.7°C fSST) to the lowest recorded fSST value (1°C) for the core record at 19.3 kyr BP. A fSST decline at the site of MD88-787 is estimated between ~20.5 (1.9°C) and 19.3 (1°C) kyr BP, consistent with the timing for the second eLGM cold phase. The isotopic record for MD88-787 has maxima at ~20 kyr BP. However, the paleo fSST record at the site of MD88-787 decreases between 23 and 19.3 kyr BP. Therefore, the paleo fSST record at the site of core MD88-787 does not reflect an expression of AIM 2 (Figure 4c) (Appendix 4.9).

Estimated fSST at the site of core E27-23 (Appendix 4.12) during MIS 3 and 2 is lower than the modern 3.51°C fSST at the site of E27-23. The fSST record from E27-23 during MIS 3 records two distinct paleo fSST declines. The first occurs between 47 kyr BP and 41 kyr BP, with fSST declining from 2.3°C to 0.6°C. The second decrease then occurs from 38.5 kyr BP (1.87°C fSST) and 35.5 kyr BP (0.27°C fSST). The transition into the eLGM period is marked by a fSST reduction from 1.6°C at 30 kyr BP to the lowest recorded fSST value for the eLGM, -0.08°C at 24.1 kyr BP. The latter reduction in fSST marks the first eLGM cold phase. The benthic isotope record from E27-23 has a maxima at 26 kyr BP (Figure 2) which occurs just prior to a distinct increase in fSST at the core site at 24.1 to 19.3 kyr BP. The increase in paleo fSST from 24.1 kyr BP (-0.08°C fSST) to 19.3 kyr BP (1.08°C fSST) occurs just after AIM 2 (Figure 4d). There is no decline in the fSST record for E27-23 that corresponds with the second eLGM cold phase. During MIS 1, fSST increased above the modern value to 4.7°C at 11.6 kyr BP and 4.1°C at 5.6 kyr BP.

Throughout MIS 3 and 2, the paleo fSST record at the site of core PS1768-8 is lower than the modern fSST value of 2.71°C. The fSST estimates during MIS 2 are the lowest throughout the core record. The MIS 2 fSST varies between 0.9°C to 0.02°C, between the core depths of 290 and 150 cm (Figure 4e, Appendix 4.11). During MIS 1, paleo fSST were higher than the modern day fSST. The fSST during MIS 1 were 5.45, 3.87, 3.85, 3.32, 2.95 and 3.34°C, at core depths of 80, 60, 50, 46, 40, and 30 cm, respectively. Estimates of fSST estimates at the site of core PS58/271-1, throughout MIS 3, 2 and 1, are all lower than the modern day fSST value of 4.43°C. The record of fSST for core PS58/271-1 declines at the end of MIS 3, possibly marking the start of the eLGM, and is lowest during MIS 2. As cores PS1768-8 and PS58/271-1 do not have age models (Esper, pers comm. 2014) we are unable to place the paleo fSST record for PS58/271-1 in context of the eLGM cold phases and AIM 2 (Figure 4f, Appendix 4.10).

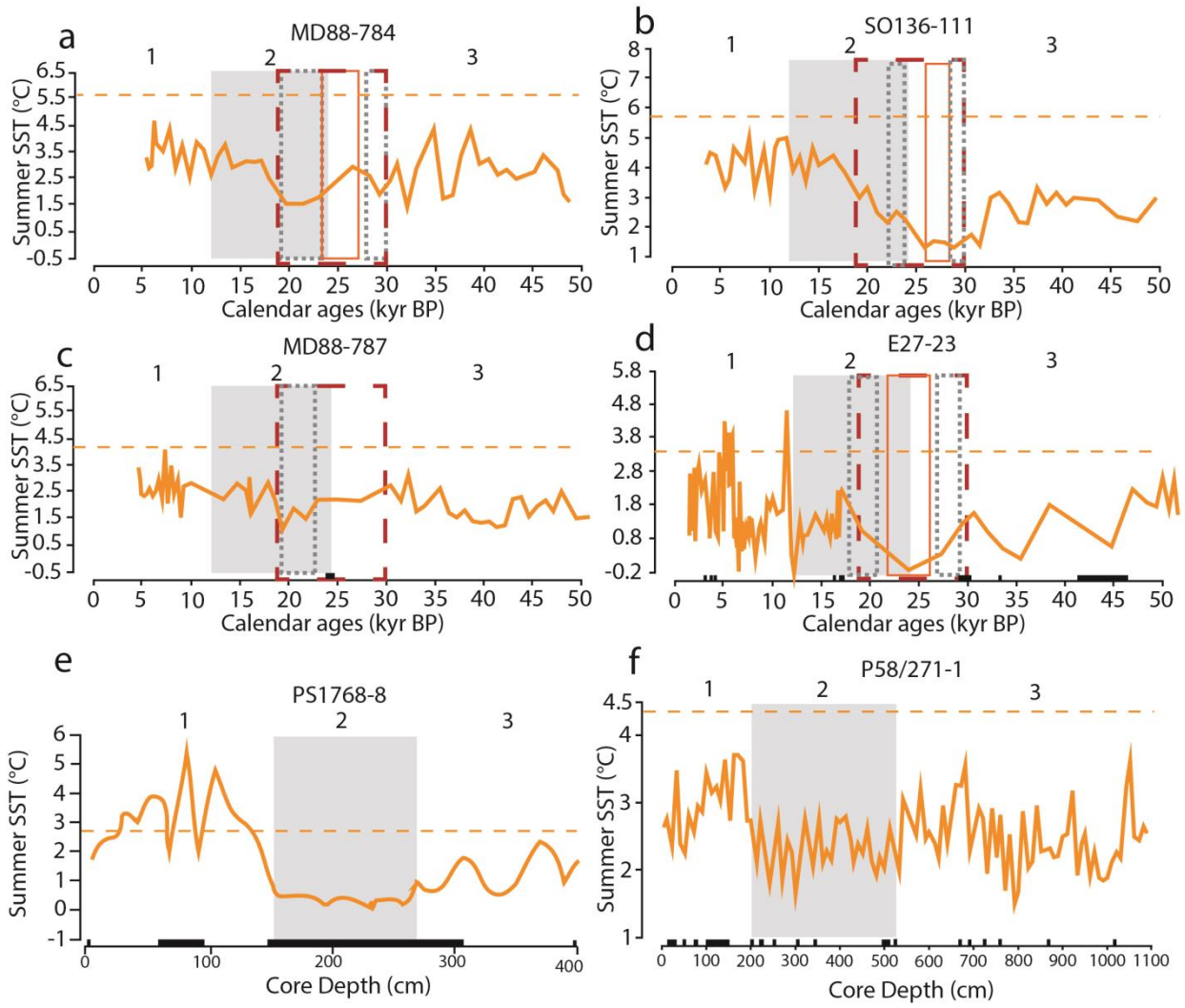

Figure 4. The paleo fSST estimates for; a) MD88-784, b) SO136-111, c) MD88-787, d) E27-23, e) PS1768-8 and f) PS58/271-1. The solid orange line corresponds to the paleo fSST estimates, whilst the horizontal dashed orange line represents the modern fSST value at each core location (Table 1).. The RMSEP under our hold out validation was 1.05°C. The glacial MIS 2 is shaded in light grey. The eLGM period is highlighted with the dashed red rectangle. The dashed grey boxes highlight the eLGM cold phases whilst the solid orange box highlights AIM 2. The black boxes along the x-axis highlight the core samples for which there were no modern analogues.

4 Discussion

4.1 Onset of the eLGM

Previous knowledge of the circumpolar LGM winter sea-ice extent (23 to 19 kyr BP) was confined largely to the re-analysis study of Gersonde et al. (2005) whose work replaced the early CLIMAP efforts (CLIMAP 1976; CLIMAP, 1981). Marine sediment cores from the Scotia Sea, south Atlantic, suggested an earlier maximum expansion of winter sea-ice from 25 to 23.5 kyr BP, which extended out to 53°S (Collins et al. 2012) (Figure 5). Evidence suggests sea-ice scour affected Macquarie Island (54°37'S, 158°54'E) during the LGM, therefore indicating an LGM expansion of sea ice to 54°S within the southwest Pacific (Fraser et al. 2009) (Figure 5). However, the LGM expansion of sea ice around Macquarie Island could not be robustly dated (Fraser et al. 2009). Our new continuous wSIC estimates from cores within the southwest Pacific, south Atlantic and southeast Pacific allow for a further refinement of the paleo maximum winter sea-ice history in the southwest and southeast Pacific sectors of the Southern Ocean.

Regional cooling throughout the southwest Pacific appears to have had its beginnings in mid MIS 3 (~47kyr BP), as revealed by the estimates of increasing wSIC and decreasing fSST at our most southerly placed core, E27-23 (Fig. 3d, 4d). Northeast of core E27-23, cores MD88-787 and MD88-784 both indicate a reduction in fSST and wSIC expansion from ~ 30 kyr BP. One possible explanation for the increased winter sea-ice cover at the sites of SO136-111 and E27-23 at ~35 kyr BP (Figure 3b, d) is the stratification of the Southern Ocean (at ~36 kyr BP), which has been attributed to orbital forcing and atmospheric cooling (Putnam et al., 2013). The stratification hypothesis is based on the observation that Southern Ocean buoyancy driven stratification occurs as the density of sea water is more sensitive to changes in salinity rather than

to changes in temperature. Winter time cooling, sea-ice growth, and subsequent wind driven sea-ice export can stratify the open ocean (Putnam et al. 2013). The cooler surface waters inhibit the upwelling of relatively warmer deep waters (Gordon, 1981), increasing winter sea-ice growth (Putnam et al. 2013). Recent evidence suggests that during the eLGM, the south Atlantic had a salinity driven density stratification of the upper water column (Gottschalk et al. 2015), whilst Antarctic Bottom Waters (AABW) within the Pacific had a greater salinity driven density stratification (Insua et al., 2014). During the LGM, sea-ice melt within the southwest Pacific increased the freshwater input into Antarctic Intermediate Water (AAIW). Increased freshwater input hindered the downward expansion of AAIW and raised the interface between AAIW and Upper Circumpolar Deep Water. Subsequently, deep ocean glacial carbon storage increased (Ronge et al. 2015). Hence, the pre-LGM wSIC expansion we estimate within the southwest Pacific may have been a driver for the onset of the LGM climate.

Alteration of the global thermohaline circulation, resulting from northern hemisphere insolation forcing, provides one other possible explanation for the early onset of the southwest Pacific eLGM (Figure 3b,d) and increase in eLGM sea-ice cover within the Atlantic (Figure 3e). Insolation forcing cooled north Atlantic Deep Water (NADW), subsequently, the cooler NADW fails to melt the Antarctic ice shelves when it upwells. As a result, cold and salty water is formed along the edge of the Weddell Sea continental shelf, which then increased the salinity of AABW (Adkins, 2013). Therefore, AABW salinity exceeded its NADW counterpart, which decreased the density of NADW relative to AABW, stratified the deep ocean, allowing the deep ocean to become a more effective carbon trap, lowering atmospheric CO_2 (Adkins, 2013). Indeed, models indicate that the LGM south Atlantic Ocean was stratified, owing to the presence of a saltier AABW which prevented NADW from sinking (Marson et al., 2014).

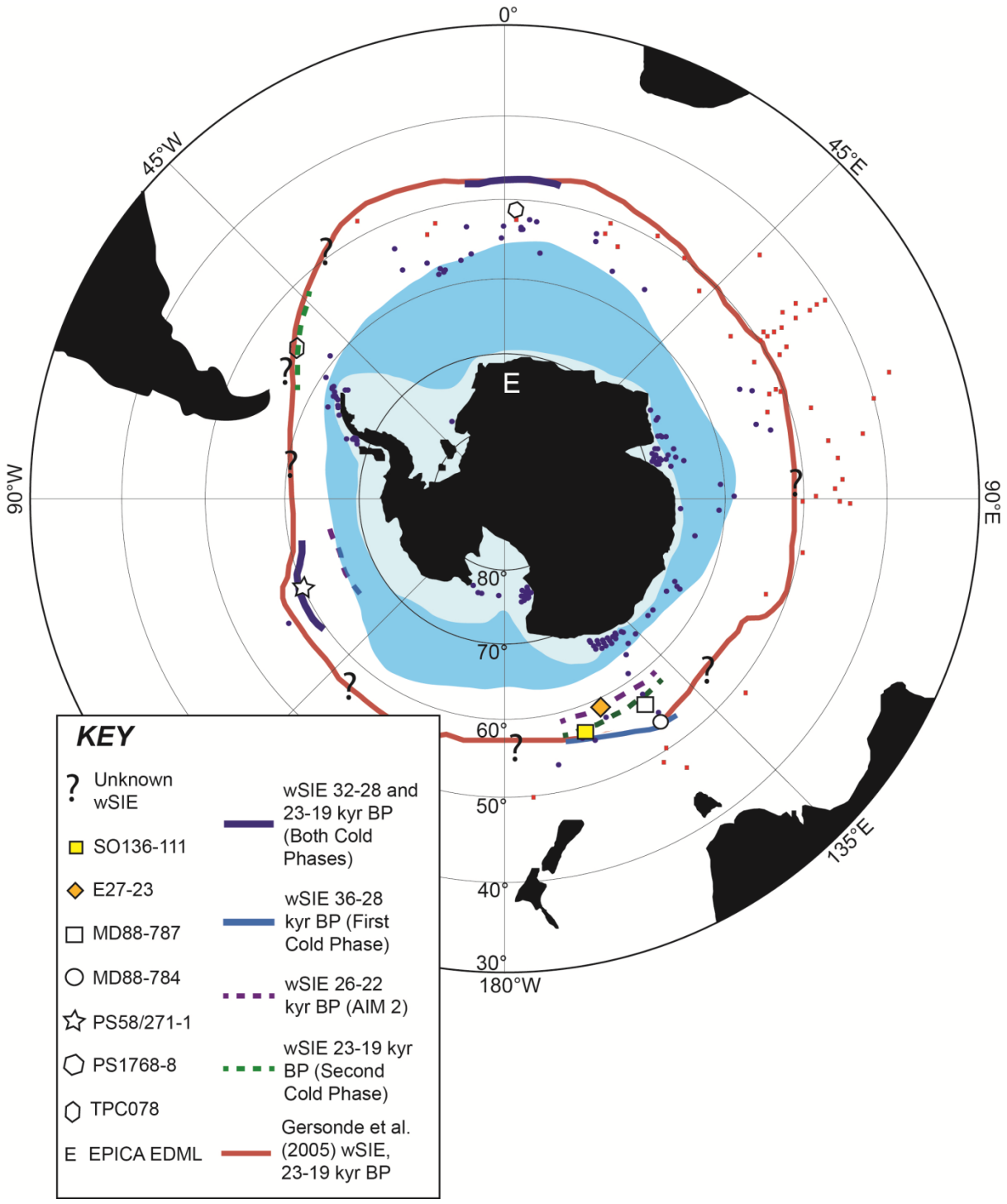
0°
45°W
45°E
90°W
90°E
135°E
180°W
80°
70°
60°
50°
40°
30°
E
?
KEY
Unknown wSIE
SO136-111
E27-23
MD88-787
MD88-784
PS58/271-1
PS1768-8
TPC078
E EPICA EDML
wSIE 32-28 and 23-19 kyr BP (Both Cold Phases)
wSIE 36-28 kyr BP (First Cold Phase)
wSIE 26-22 kyr BP (AIM 2)
wSIE 23-19 kyr BP (Second Cold Phase)
Gersonde et al. (2005) wSIE, 23-19 kyr BP

Figure 5. **A comparison between the estimated winter sea-ice edge from Gersonde et al. (2005) (defined as the maximum extent of winter sea ice >15% concentration, solid light green line) and our estimated winter sea-ice edge (also defined as the maximum extent of >15% winter sea-ice concentration) throughout the southwest Pacific and Atlantic.** We plot the winter sea-ice edge during the first eLGM cold phase (~36 to 28 kyr BP, light blue line), AIM 2 (~26 to 22 kyr BP, dashed purple line) and the second eLGM cold phase (~23 to 19 kyr BP, dashed green line). The solid blue line indicates the estimated winter sea-ice edge during both eLGM cold phases within the southeast Pacific and southeast Atlantic. The estimate for the position of the Scotia Sea winter sea-ice edge (at the site of core TPC078) during the second eLGM cold phase is based on the work from Collins et al. (2013). All of the cores used and/or referred to within this study, along with the average modern summer and winter sea-ice extents from 1979 to 2000, are also plotted for reference. The winter sea-ice edges for cores PS58/271-1 and PS1768-8 are derived from the paleo wSIC data from Figure 2e and 2f. As there are no cores immediately north of PS58/271-1 and PS1768-8, we are unable to confidently constrain the northern eLGM winter sea-ice extent at sites of each core. Thus the estimated winter sea-ice edges presented within this figure are conservative.

4.2 eLGM climatic variation throughout the southwestern Pacific

4.2.1 eLGM cold phases

Two distinct periods of climatic cooling at both the inception and termination of the eLGM have been documented within New Zealand (from 27.6 to 26 kyr BP and 21 to 19 kyr BP) (Zink et al., 2010; Stephens et al., 2012), east Australia (Petherick et al., 2008), the central Scotia Sea (Collins et al., 2013) (Figure 6) and within the southeast Pacific (Verleye and Louwye, 2010). Early glacial cooling has also been documented in New Guinea, western and southern Australia, and the northeast Indian Ocean (Reeves et al., 2013).

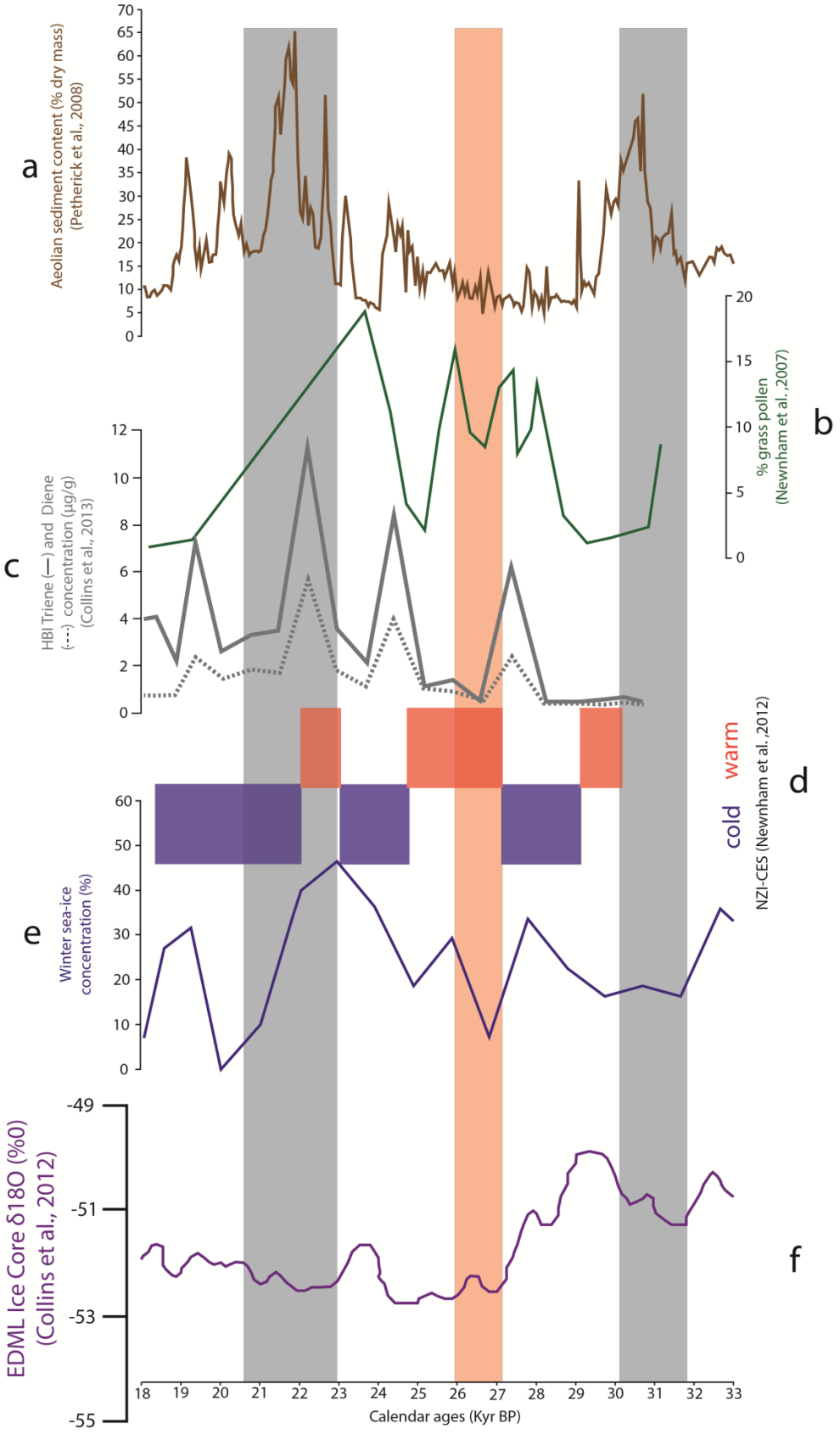
a
Aeolian sediment content (% dry mass)
(Petherick et al., 2008)
b
% grass pollen
(Newnham et al.,2007)
c
HBI Triene (—) and Diene
(----) concentration (µg/g)
(Collins et al., 2013)
d
cold
warm
NZI-CES (Newnham et al.,2012)
e
Winter sea-ice
concentration (%)
f
EDML Ice Core δ18O (‰)
(Collins et al., 2012)
Calendar ages (Kyr BP)

Figure 6. The eLGM paleoclimatic records from New Zealand, Australia, the Scotia Sea and the EPICA EDML ice core record for the south Atlantic sector of the Southern Ocean. The paleo records from eastern Australia (Petherick et al. 2008) (a), New Zealand (Newnham et al., 2007) (b), core TPC078 from the central Scotia Sea (Collins et al., 2013) (c) are plotted with the New Zealand Intimate Climate Event Stratigraphy (NZI-CES) (adapted from Newnham et al., 2012) (d), our wSIC estimates from marine sediment core SO136-111 (e) and the EPICA EDML ice core $\delta^{18}O$ record (Collins et al., 2012). The eLGM cold phases are highlighted with the grey bars, whist AIM 2 is highlighted by the orange bar. The timing for the eLGM cold phases, as shown within this figure, represent an estimate based on our paleo wSIC records (Figure 3) and the paleo records shown within this figure. As there is no clear consensus for the timing of the eLGM cold phases within the literature, our estimated timing represents our best effort to combine all available proxy data into a single consensus estimation for the timing of the eLGM cold phases.

Our paleo wSIC data provides the first record of winter sea-ice expansion throughout the southwest Pacific during the eLGM cold phases. We identified two periods of increased winter sea-ice coverage from ~30 to 26 kyr BP and ~24 to 19 kyr BP, separated by AIM 2 (Figure 6). The synchronicity of cooling and our estimated winter sea-ice expansion throughout the southwest and southeast Pacific suggests a common regional driver for eLGM cooling. A decline in atmospheric CO_2 prior to 25 kyr BP precludes greenhouse gas forcing as a driver of the southern hemisphere early eLGM cold phase (Zech et al., 2011; Reeves et al., 2013). Rather, the expansion of paleo winter sea ice provides evidence that is consistent with, and directly supportive of, a northern migration of the Sub-Antarctic and/or Sub-Tropical Front (Verleye and Louwye, 2010; Reeves et al., 2013), which increased the influence of cool Sub-Antarctic Water (Reeves et al., 2013) whilst reducing the influence of the warm Leeuwin current to the south of Australia (De Deckker et al., 2012).

4.2.2 Antarctic Isotopic Maxima 2

A brief period of climatic amelioration during the eLGM, commonly referred to as Antarctic Isotopic Maxima (AIM) 2, has been widely documented within New Zealand (Newnham et al., 2007; Newnham et al., 2012), the EPICA EDML ice core (Collins et al., 2012) (Figure 6), dust flux records from the east Antarctic Plateau (Lambert et al., 2012) and the tropical east Indian Ocean (Dürkop et al., 2008; Lambert et al., 2012). Currently, to the best of our knowledge, there is not yet an overall authoritative reference that defines the ages for each AIM event (Robert Anderson, pers. Comm. 2013). Nonetheless, our paleo winter sea-ice records provide the first record of winter sea ice reduction during AIM 2 (between 27 and 22 kyr BP) within the southwest Pacific (Figures 3 and 5).

Rapid climatic changes, such as AIM 2, have been attributed to the bipolar see-saw (EPICA community members, 2006; Jouzel et al., 2007; Dürkop et al., 2008; Böhm et al., 2015). However, an underlying explanation for the warming over New Zealand during AIM 2 remains elusive and requires further explanation. In particular, Newnham et al. (2012) called for additional marine paleoclimatic records, across latitudinal gradients, to robustly test the bipolar see-saw hypothesis as an explanation for eLGM climatic variation. Our updated paleo fSST records for the eastern Pacific sector of the Southern Ocean also indicates that the site of core MD88-787 experienced an increase in fSST within the upper surface of the Southern Ocean during AIM 2. We do stress however that the age model for core MD88-787 was difficult to constrain between 27 and 40 kyr BP (refer to section 2.2). Hence we interpret the AIM 2 signal at the site of MD88-787 with caution until additional 14C dating is made available. Importantly, recent work suggests the Atlantic Meridional Overturning Circulation (AMOC) is only prone to destabilization during periods with fully developed ice sheets, with dimensions close to those of

glacial maxima (Böhm et al., 2015). Therefore, the bipolar see-saw hypothesis provides a plausible explanation (as advocated by Dürkop et al., 2008; Newnham et al., 2012; Böhm et al., 2015) for the fSST warming in the east Pacific and wSIC declines within the southwest Pacific estimated during AIM 2.

4.3 eLGM termination

Our paleo fSST records suggest ocean temperatures increased at the site of each core during the eLGM at ~20 kyr BP, leading the subsequent declines in wSIC. Our data is consistent with a hypothesized termination of the eLGM throughout the southwest Pacific that resulted from a breakdown of Southern Ocean stratification. The breakdown of Southern Ocean stratification produced temperature rises of ~3.6°C between the New Zealand eLGM and Antarctic Cold Reversal (dated between 14 and 12.5 kyr BP), a net poleward migration of the Subtropical Front (potentially in conjunction with the bipolar see-saw mechanism), increased atmospheric CO_2 and upwelling south of the PF (Putnam et al., 2013).

A northern hemisphere sourced freshwater perturbation at 19 kyr BP, known as the 19 kyr BP melt water pulse (MWP), that reduced NADW formation and weakened the AMOC (Clark et al., 2004; Clark et al., 2009) was concomitant with Southern Ocean de-stratification. As the AMOC transports heat into the Atlantic basin, any reduction in AMOC produces a compensatory warming of the tropical Atlantic and Southern Ocean via the bipolar see-saw (Clark et al., 2004; Roche et al., 2012). Important associated climatic feedbacks involved Southern Ocean sea-surface temperature increases and subsequent sea-ice retreat, which increased warming of the Southern Ocean via the ice-albedo feedback, and exposure of the atmosphere to the underlying

ocean (Clark et al., 2004; Clark et al., 2009). We suggest that de-stratification and a weakening of the AMOC provide two reasonable explanations for the reduction in paleo wSIC, and increased fSST, that occurred during the eLGM termination throughout the southwest Pacific.

5 Conclusions

We demonstrated that WA PLS provides the most statistically robust means for estimating fSST when compared with IKTF and MAT. Thus, our application of WA PLS for estimating fSST and GAM to estimate wSIC allowed us to provide new eLGM paleoceanographic data based on the most appropriate statistical models currently available.

Our paleoceanographic data indicates that winter sea-ice expansion throughout the southwest Pacific and Atlantic occurred earlier than previously suggested (Gersonde et al., 2005), at ~36 kyr BP. Our paleo winter sea ice and fSST data document eLGM climatic variability throughout the southwest Pacific. Specifically, we identify two eLGM cold phases, characterized by an expansion of winter sea-ice, separated by AIM 2, during which winter sea-ice cover declined. Whilst eLGM climatic variability has been previously documented throughout New Zealand (Williams et al., 2010, Stephens et al., 2012; Newnham et al., 2012), Antarctic ice cores (EPICA community members, 2006; Jouzel et al., 2007; Lambert et al., 2012), and within Southwest Atlantic paleo records (Collins et al., 2012), our paleo reconstructions provide the first paleoceanographic evidence for widespread eLGM climatic variability throughout the southwestern Pacific.

Our data is consistent with previous work suggesting that stratification of the Southern Ocean was important for driving the onset of the eLGM. Atmospheric cooling stratified the Southern Ocean, which in turn increased sea-ice formation and winter time duration (Putnam et al., 2013). The southern hemisphere's eLGM onset, in contrast to the northern hemisphere records, is consistent with a cooling of NADW in response to 65°N insolation forcing. Cooling of NADW is thought to have resulted in the formation of colder and more saline AABW within the Weddell

Sea. Therefore, AABW density increased relative to the density of NADW, establishing cold and salty bottom waters throughout the Southern Ocean. By implication, Antarctica cooled as a result of northern hemisphere insolation forcing (Adkins, 2013).

Our data shows an expansion of winter sea-ice cover and decreased fSST throughout the southwest Pacific during the eLGM cold phases, separated by a decline in winter sea-ice extent and a concomitant fSST increase during AIM 2. The bipolar see-saw hypothesis provides a possible explanation for the two cold phases and warmer AIM 2 event during the eLGM. Similarly, the eventual termination of the eLGM at 19 kyr BP is explainable by two hypotheses, the de-stratification of the Southern Ocean (Putnam et al., 2013) and the fresh water perturbation of the 19 kyr BP MWP (Clark et al., 2004).

Acknowledgements

This research was funded by the Australian Government through the provision of an Australian Postgraduate Award granted to Alexander Ferry at Macquarie University.

References

Adkins, J. F., (2013), The role of deep ocean circulation in setting glacial climates, *Palaeoceanography*, 28, 539-561.

Bennett, N. D., Croke, B.F.W., Guariso, G., Guillaume, J.H.A., Hamilton, S.H., Jakeman, A.J., Marsili-Libelli, S., Newham, L.T.H., Norton, J.P., Perrin, C., Pierce, S.A., Robson, B., Seppelt. R., Voinov, A.A., Fath, B.D., Andreassian, V., (2013), Characterising performance of environmental models, *Environmental Modelling and Software*, 40, 1-20.

Birks, H. J. B., (2003), Quantitative palaeoenvironmental reconstructions from Holocene biological data, in Global Change in the Holocene, edited by A. Mackay, Battarbee, R.W., Birks, H.J.B., and Oldfield, F., pp. 107-123, London.

Birks, H. J. B., Line, J.M., Juggins, S., Stevenson, A.C., and Ter Braak, C.J.F., (1990), Diatoms and pH Reconstruction, *Philosophical Transactions of the Royal Society of London. Series B, Biological Sciences*, 327, 263-278.

Böhm, E., Lippold, J., Gutjahr, M., Frank, M., Blaser, P., Antz, B., Fohlmeister, J., Frank, N., Andersen, M.B., and Deininger, M., (2015), Strong and deep Atlantic meridional overturning circulation during the last glacial cycle, *Nature*, 74, DOI:10.1038/nature14059.

Clark, P. U., Dyke, A.S., Shakun, J.D., Carlson, A.E., Clark, J., Wohlfarth, B., Mitrovica, J.X., Hostetler, S.W., and McCabe, A.M., (2009), The Last Glacial Maximum, *Science*, 325, 710-714.

Clark, P. U., McCabe, A.M., Mix, A.C., and Weaver, A.J., (2004), Rapid Rise of Sea Level 19,000 Years Ago and Its Global Implications, *Science*, 304, DOI:10.1126/science.1094449.

Climate: Long-Range Investigation, Mapping, and Prediction (CLIMAP) Project Members, (1976), The surface of the Ice Age Earth, *Science*, 191, 1131–1137.

Climate: Long-Range Investigation, Mapping, and Prediction (CLIMAP) Project Members (1981), Seasonal reconstructions of the Earth's surface at the Last Glacial Maximum, *Geological Society of American Map Chart Series*, MC-36, 1–18.

Collins, L. G., Allen, C.S., Pike, J., Hodgson, D.A., Weckström, K., and Massé, G., (2013), Evaluating highly branched isoprenoid (HBI) biomarkers as a novel Antarctic sea-ice proxy in deep ocean glacial age sediments, *Quaternary Science Reviews*, 79, 87–98.

Collins, L. G., Pike, J., Allen, C.S., and Hodgson, D.A., (2012), High-resolution reconstruction of southwest Atlantic sea-ice and its role in the carbon cycle during marine isotope stages 3 and 2, *Paleoceanography*, 27, DOI:10.1029/2011PA002264.

Comiso, J. (2000), Bootstrap Sea Ice Concentrations from Nimbus-7 SMMR and DMSP SSM/I-SSMIS.

Crosta, X., Sturm, A., Armand, L., and Pichon, J.-J., (2004), Late Quaternary sea ice history in the Indian sector of the Southern Ocean as recorded by diatom assemblages, *Marine Micropaleontology*, 50, 209-223.

De Deckker, P., Moros, M., Perner, K., and Jansen, E., (2012), Influence of the tropics and southern westerlies on glacial interhemispheric asymmetry, *Nature Geoscience*, 5, DOI: 10.1038/NGEO1431.

Dürkop, A., Holbourn, A., Kuhnt, W., Zuraida, R., Andersen, N., and Grootes, P.M., (2008), Centennial-scale climate variability in the Timor Sea during Marine Isotope Stage 3, *Marine Micropaleontology*, 66, 208–221.

EPICA community members, (2006), One-to-one coupling of glacial climate variability in Greenland and Antarctica, *Nature*, 444, 195-198.

Esper, O., and Gersonde, R., (2014a), Quaternary surface water temperature estimations: New diatom transfer functions for the Southern Ocean, *Palaeogeography, Palaeoclimatology, Palaeoecology*, 414, 1-19.

Esper, O., and Gersonde, R., (2014b), New tools for the reconstruction of Pleistocene Antarctic sea ice, *Palaeogeography, Palaeoclimatology, Palaeoecology*, 399, 260–283.

Ferry, A. J., Prvan, T., Jersky, B., Crosta, X., and Armand, L.K., (2015), Statistical modeling of Southern Ocean marine diatom proxy and winter sea ice data: Model comparison and developments, *Progress in Oceanography*, 131, 100–112.

Fox, J., Weisberg, S., Bates, D., Ellison, S., Firth, D., Friendly, M., Gorjanc, G., Graves, S., Heiberger, R., Laboissiere, R., Monette, D., Nilsson, H., Ogle, D., Ripley, B., and Zeileis, A., (2015), Companion to Applied Regression, R package version 2.14.0, https://r-forge.r-project.org/projects/car/

Fraser, C. I., Nikula, R., Spencer, H.G., and Waters, J.M., (2009), Kelp genes reveal effects of subantarctic sea ice during the Last Glacial Maximum, *PNAS*, 106, 3249-3253.

Gersonde, R., Crosta, X., Abelmann, A., and Armand, L., (2005), Sea-surface temperature and sea ice distribution of the Southern Ocean at the EPILOG Last Glacial Maximum—a circum-Antarctic view based on siliceous microfossil records, *Quaternary Science Reviews*, 24, 869–896.

Gloersen, P., Campbell, W.J., Cavalieri, D.J., Comiso, J.C., Parkinson, C.L., and Zwally, H.J., (1992), Arctic and Antarctic Sea Ice, 1978- 1987, Satellite Passive- Microwave Observations and Analysis, Scientific and Technical Information Program, Washington, D.C.

Gordon, A.L., (1981), Seasonality of Southern Ocean sea ice, *Journal of Geophysical Research*, 86, 4193-4197.

Gottschalk, J., Skinner, L.C., and Waelbroeck, C., (2015), Contribution of seasonal sub-Antarctic surface water variability to millennial-scale changes in atmospheric CO2over the last deglaciation and Marine Isotope Stage 3, Earth and Planetary Science Letters, 411, 87-99.

Hammer, Ø., Harper, D.A.T., and Ryan, P.D., (2001), PAST: Paleontological Statistics Software Package for Education and Data Analysis, *Palaeontologia Electronica*, 4, 1-9.

Hill, M. O., (1973), Diversity and Evenness: A Unifying Notation and Its Consequences, *Ecology*, 54, 427-432.

Insua, T. L., Spivack, A.J., Graham, D., D'Hondt, S., and Moran, K., (2014), Reconstruction of Pacific Ocean bottom water salinity during the Last Glacial Maximum, *Geophysical Research Letters*, 41, DOI:10.1002/2014GL059575.

Jansen, E. J., Overpeck, K.R., Briffa, J.-C., Duplessy, F., Joos, V., Masson-Delmotte, D., Olago, B., Otto-Bliesner, W.R., Peltier, S., Rahmstorf, R., Ramesh, D., Raynaud, D., Rind, O., Solomina, R., Villalba, and D. Zhang., (2007), Palaeoclimate. In: Climate Change 2007: The Physical Science Basis. Contribution of Working Group I to the Fourth Assessment Report of the Intergovernmental Panel on Climate Change, Cambridge University Press, Cambridge, United Kingdom and New York, NY, USA.

Jouzel, J., Masson-Delmotte, V., Cattani, O., Dreyfus, G., Falourd, S., Hoffmann, G., Minster, B., Nouet, J., Barnola, J.M., Chappellaz, J., Fischer, H., Gallet, J.C., Johnsen, S., Leuenberger, M., Loulergue, L., Luethi, D., Oerter, H., Parrenin, F., Raisbeck, G., Raynaud, D., Schilt, A., Schwander, J., Selmo, E., Souchez, R., Spahni, R., Stauffer, B., Steffensen, J.P., Stenni, B., Stocker, T.F., Tison, J.L., Werner, M., and Wolff, E.W., (2007), Orbital and Millennial Antarctic Climate Variability over the Past 800,000 Years, *Science*, 317, 793-796.

Juggins, S., (2014), rioja: Analysis of Quaternary Science Data, R package version 0.9-3, http://cran.r-project.org/web/packages/rioja/index.html.

Kucera, M., Weinelt, M., Kiefer, T., Pflaumann, U., Hayes, A., Weinelt, M., Chen, M.-T., Mix, A.C., Barrows, T.T., Cortijo, E., Duprat, J., Juggins, S., and Waelbroeck, C., (2005), Reconstruction of sea-surface temperatures from assemblages of planktonic foraminifera: multi-technique approach based on geographically constrained calibration data sets and its application to glacial Atlantic and Pacific Oceans, *Quaternary Science Reviews*, 24, 951–998.

Lambert, F., Bigler, M., Steffensen, J.P., Hutterli, M., and Fischer, H., (2012), Centennial mineral dust variability in high-resolution ice core data from Dome C, Antarctica, *Climate of the Past*, 8, 609–623.

Lisiecki, L. E., and M.E., Raymo (2005a), A Pliocene-Pleistocene stack of 57 globally distributed benthic $\delta^{18}O$ records, *Paleoceanography*, 20, DOI:10.1029/2004PA001071.

Lisiecki, L.E., and M.E., Raymo (2005b), LR04 Global Pliocene-Pleistocene Benthic $\delta^{18}O$ stack, IGBP PAGES/world data center for paleoclimatology data contribution series #2005-008, NOAA/NGDC Paleoclimatology Program, Boulder CO, USA.

Marson, J. M., Wainer, I., Mata, M.M., and Liu, Z., (2014), The impacts of deglacial meltwater forcing on the South Atlantic Ocean deep circulation since the Last Glacial Maximum, *Climate of the Past*, 10, 1723–1734.

McCave, I. N., Crowhurst, S.J., Kuhn, G., Hillenbrand, C.-D., and Meredith, M.P., (2014), Minimal change in Antarctic Circumpolar Current flow speed between the last glacial and Holocene, *Nature Geoscience*, 7, DOI: 10.1038/NGEO2037.

Mix, A. C., Bard, E., and Schneider, R., (2001), Environmental processes of the ice age: land, oceans, glaciers (EPILOG), *Quaternary Science Reviews*, 20, 627-657.

Newnham, R. M., Lowe, D.J., Giles, T., and Alloway, B.V., (2007), Vegetation and climate of Auckland, New Zealand, since ca. 32 000 cal. yr ago: support for an extended LGM, *Journal of Quaternary Science*, 22, 517–534.

Newnham, R. M., Vandergoes, M.J., Sikes, E., Carter, L., Wilmshurst, J.M., Lowe, D.J., McGlone, M.S., and Sandiford, A., (2012), Does the bipolar seesaw extend to the terrestrial southern mid-latitudes?, *Quaternary Science Reviews*, 36, 214-222.

Paillard, D., Labeyrie, L., and Yiou, P., (1996), Macintosh program performs time-series analysis, *Eos Transactions. AGU*, 77: 379.

Paillard, D., (2015), Quaternary glaciations: from observations to theories, *Quaternary Science Reviews*, 107, 11-24.

Petherick, L., McGowan, H., and Moss, P., (2008), Climate variability during the Last Glacial Maximum in eastern Australia: evidence of two stadials?, *Journal of Quaternary Science*, 23, 787–802.

Putnam, A. E., Schaefer, J.M., Denton, G.H., Barrell, D.J.A., Birkel, S.D., Andersen, B.G., Kaplan, M.R., Finkel, R.C., Schwartz, R., and Doughty, A.M., (2013), The Last Glacial Maximum at 44°S documented by a 10Be moraine chronology at Lake Ohau, Southern Alps of New Zealand, *Quaternary Science Reviews*, 62, 114-141.

Reeves, J. M., Barrows, T.T., Cohen, T.J., Kiem, A.S., Bostock, H.C., Fitzsimmons, K.E., Jansen, J.D., Kemp, J., Krause, C., Petherick, L., Phipps, S.J., and OZ-INTIMATE Members, (2013), Climate variability over the last 35,000 years recorded in marine and terrestrial archives in the Australian region: an OZ-INTIMATE compilation, *Quaternary Science Reviews*, 74, 21-34.

Reynolds, R.W., Rayner N.A., Smith, T.M., Stokes, D.C., and Wang, W., (2002), An Improved In Situ and Satellite SST Analysis for Climate, *Journal of Climate*, 15, 1609-1625.

Roche, D. M., Crosta, X., and Renssen, H., (2012), Evaluating Southern Ocean sea-ice for the Last Glacial Maximum and pre-industrial climates: PMIP-2 models and data evidence, *Quaternary Science Reviews*, 56, 99-106.

Ronge, T. A., Steph, S., Tiedemann, R., Prange, M., Merkel, U., Nürnberg, D., and Kuhn, G., (2015), Pushing the boundaries: Glacial/interglacial variability of intermediate and deep waters in the southwest Pacific over the last 350,000 years, Paleoceanography, 30, DOI:10.1002/2014PA002727.

Sokolov, S., and Rintoul, S.R., (2009), Circumpolar structure and distribution of the Antarctic Circumpolar Current fronts: 2. Variability and relationship to sea surface height, *Journal of Geophysical Research*, 114, DOI:10.1029/2008JC005248.

Stephens, T., Atkin, D., Augustinus, P., Shane, P., Lorrey, A., Street-Perrott, A., Nilsson, A., and Snowball, I., (2012), A late glacial Antarctic climate teleconnection and variable Holocene seasonality at Lake Pupuke, Auckland, New Zealand, *Journal of Paleolimnology*, 48, 785–800.

Stern, J., and Lisiecki, E., (2014), Termination 1 timing in radiocarbon-dated regional benthic $\delta^{18}O$ stacks, *Palaeoceanography*, 29, DOI:10.1002/2014PA002700.

Telford, R. J., and Birks, H.J.B., (2005), The secret assumption of transfer functions: problems with spatial autocorrelation in evaluating model performance, *Quaternary Science Reviews*, 24, 2173–2179.

Vandergoes, M. J., Newnham, R.M., Denton, G.H., Blaauw, M., Barrell, D.J.A., (2013), The anatomy of Last Glacial Maximum climate variations in south Westland, New Zealand, derived from pollen records, *Quaternary Science Reviews*, 74, 215-229.

Verleye, T. J., and Louwye, S., (2010), Recent geographical distribution of organic-walled dinoflagellate cysts in the southeast Pacific (25–53°S) and their relation to the prevailing hydrographical conditions, *Palaeogeography, Palaeoclimatology, Palaeoecology*, 298, 319–340.

Williams, P. W., Neil, H.L., and ZhaoJ.-X., (2010), Age frequency distribution and revised stable isotope curves for New Zealand speleothems: palaeoclimatic implications, *International Journal of Speleology*, 39, 99-112.

Wood, S., (2014), mgcv: Mixed GAM Computation Vehicle with GCV/AIC/REML Smoothness Estimation, R package version 1.8-5, http://cran.r-project.org/web/packages/mgcv/index.html

Wuertz, D., Setz, T., and Chalabi, Y., (2013), fBasics: Rmetrics - Markets and Basic Statistics, R package version 3010.86, http://CRAN.R-project.org/package=fBasics.

Zielinski, U., Gersonde, R., Seiger, R., and Fütterer, D., (1998), Quaternary surface water temperature estimations: Calibration of a diatom transfer function for the Southern Ocean, *Palaeoceanography*, 13, 365-383.

Zech, R., Zech, J., Kull, C., Kubik, P.W., and Veit, H., (2011), Early last glacial maximum in the southern Central Andes reveals northward shift of the westerlies at ~39 ka, *Climate of the Past*, 7, 41–46.

Zink, K. G., Vandergoes, M.J., Mangelsdorf, K., Dieffenbacher-Krall, A.C., and Schwark, L., (2010), Application of bacterial glycerol dialkyl glycerol tetraethers (GDGTs) to develop modern and past temperature estimates from New Zealand lakes, *Organic Geochemistry*, 41, 1060–1066.

This page is intentionally left blank.

Chapter 5

Marine diatoms as a proxy for the sea-surface height signature of the Antarctic Polar Front southern branch: a feasibility study within the southeast Indian Ocean.

Authors:

Alexander J. Ferry[1], Helen E. Phillips[2], and Leanne Armand[1]

1. Department of Biological Sciences, Climate Futures at Macquarie University, North Ryde, 2109, New South Wales, Australia. alexander.ferry@mq.edu.au, leanne.armand@mq.edu.au

2. Institute for Marine and Antarctic Studies, University of Tasmania, Hobart, 7005, Tasmania, Australia. h.e.phillips@utas.edu.au.

Anticipated Journal:

Geophysical Research Letters

Keywords: Diatom, extended Last Glacial Maximum, Modern Analogue Technique, Polar Front, Polar Front branch, Sea Ice, Sea-surface height, Southern Ocean.

Abstract

Estimating the paleo positioning of Southern Ocean fronts has been largely based on sea-surface temperature (SST) reconstructions and the associated modern SST signature of a given oceanic front. However, modern satellite data does not reveal any specific correspondence between Southern Ocean fronts and a given surface isotherm, whilst the modern SST signature associated with Southern Ocean fronts varies both zonally and seasonally. Therefore, the SST signature associated with a given oceanic front in the past (e.g. during the Last Glacial Maximum) may differ from the SST signature observed under modern conditions. As such, tying frontal presence and/or positioning to a given isotherm or SST signature may be misleading. Use of sea-surface height (SSH) data, as opposed to hydrographic data, provides a greater resolution for studying the structure and variability of Southern Ocean fronts. Key fronts of the Antarctic Circumpolar Current, in particular the Polar Front, are assumed to reflect the position of the Antarctic Circumpolar Current and westerly wind belt. Hence, inferring the paleo position of the Polar Front is an important topic in paleoceanography. We hypothesize that fossil diatoms may provide a proxy for the SSH signature associated with the Polar Front southern (PF-S), middle (PF-M), and northern (PF-N) branches. To test this hypothesis, we used a surface sediment training set from the southeast Indian Ocean and two marine sediment cores along a transect, situated north of the modern PF-S, to establish a record for the paleo position of the PF-S. Our pilot study suggests the PF-S was situated north of its modern position during glacial periods, the extended Last Glacial Maximum and the Antarctic Cold Reversal. The expansion of the winter sea-ice area occurred after the PF-S migrated to more northerly latitudes. We stress the important limitations associated with our small, and spatially limited, training database. Our preliminary results need to be revised and validated once additional surface sediment reference samples from the modern

Antarctic Polar Front Zone become available to increase the robustness of our proposed sea-surface height proxy.

1. Introduction

Oceanic fronts are regions of strong horizontal gradients in water mass properties and sea-surface height (SSH). Southern Ocean fronts can be identified using sea-surface signatures, such as SSH, sea-surface temperature (SST) or with hydrographic measurements of subsurface properties (Rintoul et al., 2001; Graham et al., 2012). The fronts of the Southern Ocean play an important role within the global climate system (Graham et al., 2012). For example, it has been hypothesized that a northern migration of Southern Ocean fronts may restrict surface water connectivity between ocean basins, subsequently reducing the transport of heat into the higher latitudes of the north Atlantic Ocean (Bard and Rickaby, 2009; McKay et al., 2012; Graham et al., 2012; Romero et al., 2015).

The modern fronts of the Southern Ocean are characterised by various physical parameters and are often identified by a SST signature. For example, the Polar Front has a sea-surface temperature (SST) expression of 1° to 6°C (Dong et al., 2006). Paleo SST data has been used to track the latitudinal movement of a front's SST signature based on the assumption that the modern SST signature of oceanic fronts has remained constant over time. Previous research has utilised planktonic foraminiferal fauna to track the Polar Front (Howard and Prell, 1992; Wells and Okada, 1997), Subtropical front (STF) (Bostock et al., 2015), Subtropical Convergence (STC) and the Tasman Front (Martínez, 1994; Kawagata, 2001). Radiolarian assemblages have been used as a proxy for distinct water masses south of the Polar Front, between the STC and Polar Front, and north of the STC (Morley, 1989). Others have used distinct assemblages of calcareous nanoplankton to track the movement of the Tropical Convergence, STC, Tasman Front (Hiramatsu and De Dekker, 1997) and the Sub-Antarctic Front (SAF) (Marino et al., 2009; Findlay and Flores, 2000). Recently, Romero et al. (2015) inferred paleo migrations of the STF

using diatom-based SST estimates for the south Agulhas Plateau. Ultimately, establishing a temperature gradient along a transect is required to ascertain any potential frontal movement. The use of a single core should be regarded as insufficient in reconstructing the temperature gradients necessary to infer paleo frontal migration (Kohfeld et al., 2013).

The inference of frontal paleo-positions based on SST reconstructions assumes that (i) SST changes provide direct indications of paleo frontal positioning, and (ii), that fronts are sufficiently well defined by a given SST 'signature' with which a specific front's paleo-position can be inferred (Graham et al., 2012; Kohfeld et al., 2013). However, modern satellite observations have revealed a lack of any specific correspondence between Southern Ocean fronts and any given surface isotherm. Therefore, tying frontal presence and positioning to a given isotherm may be erroneous (Kohfeld et al., 2013). The SST of modern fronts varies zonally and seasonally in the southern Indian Ocean (Kostianoy et al., 2004; Kohfeld et al., 2013), hence the mean SST for any given front during the extended Last Glacial Maximum (eLGM) may have differed to the modern expression or condition. Whilst satellite observations of sea-surface dynamic heights indicate there are numerous fronts throughout the Pacific sector of the Southern Ocean, the SST gradients associated with those fronts are weak. Frontal shifts may, therefore, only produce a small change in SST, hampering any attempt to track the paleo position of fronts based on paleo SST estimates. It may therefore be unreasonable to assume a zonally symmetric response of SST to frontal migration during the eLGM (Kohfeld et al., 2013), thus use of the SST gradient method to identify Southern Ocean fronts may be misleading (Graham et al., 2012). The current paleoclimatic inferences regarding the paleo-migration of Southern Ocean fronts, particularly the Polar Front, SAF and STF, remain controversial (Kemp et al., 2010; Kohfeld et al., 2013). Paleo-oceanographers and atmospheric scientists face an issue where fossil (proxy) evidence suggests

the Polar Front migrated north during the eLGM (Manoj and Thamban, 2015), whilst potential atmospheric and oceanographic responses suggest a northern migration of the Polar Front may not have occurred (Shulmeister et al., 2004; MARGO project members, 2009; Gottschalk et al., 2015). Clearly, an alternative proxy for Southern Ocean fronts, aside from SST gradients, may offer paleo-oceanographers a valuable tool to ascertain the true nature of oceanic fronts during paleoclimatic events/periods.

Fronts of the Antarctic Circumpolar Current (ACC) are associated with strong, deep reaching geostrophic currents, and are therefore clearly seen in maps of SSH gradients (delta SSH). The structure of ACC fronts are complex (with several branches), yet they possess consistent spatial and temporal features. The multiple branches of the ACC fronts have been shown to be associated with particular SSH values (Sokolov and Rintoul, 2007, 2009a, 2009b, Figure 1). Such associations are robust, remaining despite interactions between mean flow, eddy field and topography. Use of SSH as a proxy for ACC fronts revealed the structure and variability of the fronts with a temporal resolution of a few weeks and spatial resolution of 50-100km (Sokolov and Rintoul, 2007). The association between fronts and stream lines (local maxima in SSH gradients) holds for the entire Southern Ocean, allowing the circumpolar structure and distribution of ACC fronts to be determined in detail from maps of absolute SSH (Sokolov and Rintoul, 2009b).

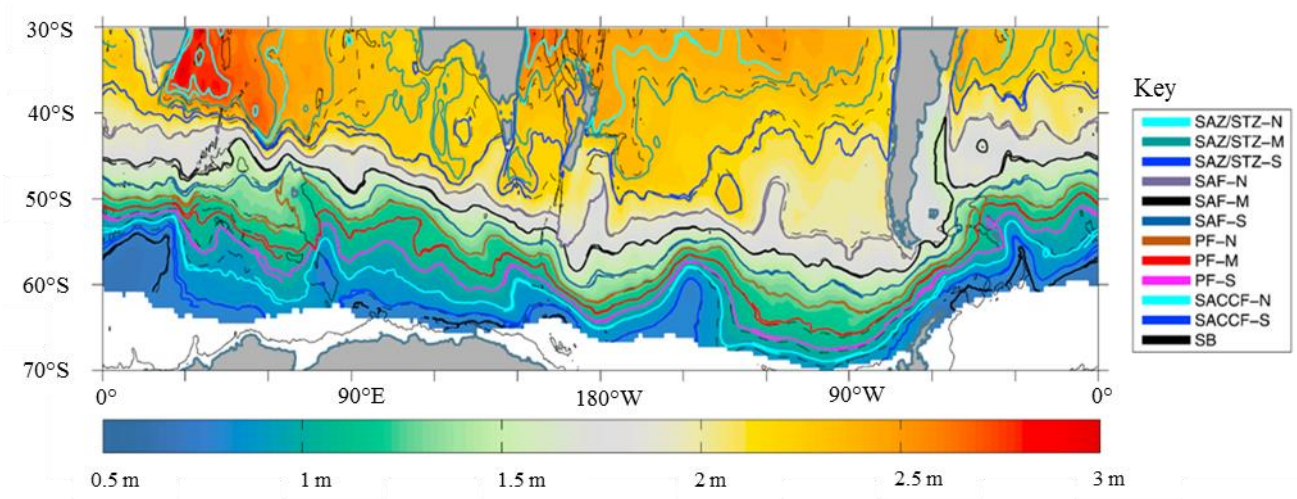

Figure 1. A map of the mean Southern Ocean sea-surface height (SSH). The mean position for the ACC fronts are also shown based on local (solid lines) and circumpolar (dashed lines) SSH labels. This figure originally appeared as Figure 1 within Sokolov and Rintoul (2009 a). Abbreviations are as follows: The Sub-Antarctic zone north (SAZ/STZ-N), middle (SAZ/STZ-M) and south (SAZ/STZ-S). Sub-Antarctic Front northern (SAF-N), middle (SAF-M) and southern (SAF-S) branches. The Polar Front northern (PF-N), middle (PF-M) and southern (PF-S) branches. The Southern ACC front northern (SACCF-N) and southern (SACCF-S) branches. The southern boundary of the ACC (SB).

Previous work suggests diatoms may possess some utility for reconstructing the paleo-position of the Polar Front (Cervato and Burckle, 2003; Kemp et al., 2010). The Polar Front is an important biogeochemical divider within the Southern Ocean, with higher silicate and nitrate south of the Polar Front, whilst only nitrate is significantly present north of the Polar Front (Kemp et al., 2010). Therefore, north of the Polar Front where silicate is limited, diatoms have a lower abundance whilst south of the Polar Front diatoms are highly abundant (Kemp et al., 2010; Rigual-Hernández et al., in review). Therefore, it stands to reason that one could establish a diatom proxy for the specific SSH contours of the Polar Fronts southern (PF-S), middle (PF-M) or northern (PF-N) branches. Given that the Polar Front itself has an impact on diatom distribution, we aim to define a statistical link between the presence of the Polar Front and diatom abundances. In doing so, we will be able determine if the Polar Front is present at the location of a marine sediment core. Estimating the paleo position of the Polar Front using our

proposed methodology is based on the observation that the Polar Front is an important biogeochemical divider (Kemp et al., 2010), marked by higher diatom abundances south of the front (Kemp et al., 2010; Rigual-Hernández et al., in review, Manoj and Thamban, 2015). Linking diatoms with a dynamic oceanographic 'signature' of the Polar Front (i.e. SSH) would thus circumvent the issues that arise when using the confounding physical SST gradient signature for estimating the paleo position of an oceanic front.

Our paper has four main aims. Firstly, we identify significant species response relationships between fossil diatom relative abundance and the average monthly presence per annum (mpa) of the PF-S, PF-M and PF-N SSH signature. Secondly, given the outcome from our first aim, we then consider the appropriate statistical techniques to produce paleo estimates of the PF-S, PF-M and PF-N. Thirdly, we will present the first attempt to derive paleo estimates for the PF-S, PF-M and PF-N SSH signatures based on a diatom proxy. Finally, we will consider the first paleo estimates for the SSH signatures of the PF-S, PF-M, and/or PF-N from two marine sediment cores along a transect within the southeast Indian Ocean.

2 Methods

2.1 Databases used

2.1.1 Training data base

We used the surface sediment diatom database complied by Abbott (1973), herein referred to as the Abbott database. The Abbott database is comprised of 60 core top samples from the southeast Indian Ocean sector (Figure 2), which document the relative abundance of 55 diatom species (Abbott, 1973; Armand, 1997). For the site of each surface sediment sample within the Abbott database we extracted 20 years of SSH contour data to compute the average annual monthly presence of each Southern Ocean front (refer to section 2.1.3 below).

There are some intrinsic limitations with the Abbott database that need to be acknowledged. The Abbott database only represents samples from the southeast Indian Ocean, hence the Abbott database is spatially biased. Given that the samples of the Abbott database integrated 2 centimetres of sediment, which is not considered to be part of the sediment surface (Armand, 1997), the samples are also temporally unrepresentative. Many common diatom species were not documented by Abbott, whilst some of the species identified by him were not counted into any further category species and were therefore grouped together with other similar species or generic taxa. Other more common species had been categorised into (presumably) sub-species that are not currently recognised (Armand, 1997).

We had access to a more modern diatom database compiled by Crosta et al. (2004) to consider using in this pilot study. However, very few samples in the Crosta database were located within regions of the Southern Ocean where the fronts of the Southern Ocean are currently present (Appendix 5.1). We, therefore, did not use the modern diatom database of Crosta et al. (2004)

within this study due to the lack of samples located at the fronts of the Southern Ocean and its incompatibility with the Abbott database.

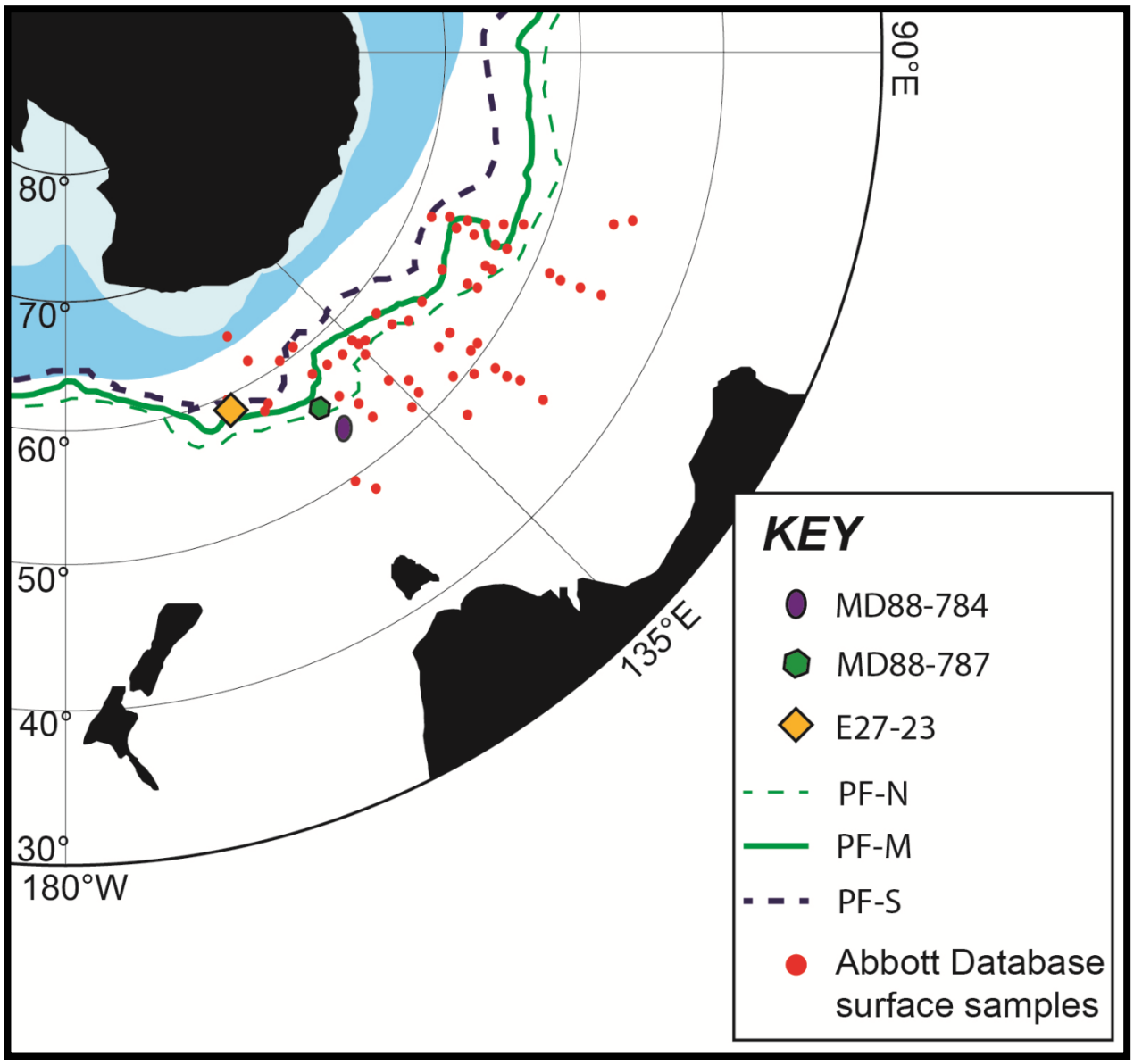

Figure 2. Each of the sea-surface sediment samples from the Abbott database are plotted (red dots) against the position of the Polar Fronts southern (PF-S), middle (PF-M) and northern (PF-N) branches. The locations of marine sediment cores MD88-787, MD88-784 and E27-23 (refer to section 4.4) are also shown. The average maximum winter sea-ice extent from 1979 to 2000 is indicated by the dark blue shading, whilst the maximum extent of summer sea-ice is indicated by light blue shading.

2.1.2 Marine sediment cores

Core MD88-784 was taken within the southeast Indian sector of the Southern Ocean at 54°11.4'S**,** 144°47.4'E and preserves a diatom record for the last 48 kyr BP (Appendix 5.2). Marine sediment core MD88-787 was extracted from 56°22.8'S, 145°18'E and has a diatom record over the last 191 kyr BP (Appendix 5.3). Both cores are located north of the modern day PF-M and the PF-S (Figure 2). The age models for cores MD88-787 and MD88-784 are based on $\delta^{18}O$ isotope records derived from *Neogloboquadrina pachyderma* sinistral (Chapter 4).

2.1.3 Extraction of SSH contours

Monthly gridded SSH anomalies for the period January 1992 to December 2012 were downloaded from AVISO (Archiving, Validation and Interpretation of Satellite Oceanographic Data). We used the delayed time, merged version with a 1/3° grid, referenced to the mean of the period 1993-1999. We constructed the full SSH field by adding the SSH anomalies to a mean sea surface dynamic height field (referenced to 2500 dbar) calculated from the WOCE hydrographic climatology (Gouretski and Koltermann, 2004), as used by Sokolov and Rintoul (2009a,b). Through this 20 year time series, we identified the positions of nine ACC fronts based on the SSH labels of Sokolov and Rintoul (2009a,b). We list their mean and standard deviation of SSH for each front (over the 15 year period 1992-2007) in Table 1.

The inference of frontal positions based on SSH maps was validated with Argo float data and high resolution hydrographic sections by Sokolov and Rintoul (2009a,b). There was significant consistency in the inference of frontal positions based on SSH contours, SSH gradients, and

traditional water mass features from Argo data and hydrographic sections (Sokolov and Rintoul, 2009a,b).

For each of the sample sites within the Abbott database and the marine sediment cores, we extracted a 20-year monthly time series of SSH. We tested for the average monthly presence per annum (mpa) of nine fronts. The fronts included the Sub-Antarctic Front northern, middle and southern branches (SAF-N, SAF-M and SAF-S); the Polar Front northern, middle and southern branches (PF-N, PF-M and PF-S); the Southern ACC Front northern and southern branches (SACCF-N, SACCF-S); and the southern boundary of the ACC (SB, Figure 3). A front was determined to be present if the value of SSH at the site was within +/- one standard deviation of the mean SSH value associated with each front (Table 1). We computed the average monthly presence per annum (mpa) for each of the ACC fronts over the 20 year time series.

The range of possible values for a front's mpa is 0 to 12, with values of 0 mpa representing the year round absence of a front, whilst values of 12 mpa are equivalent to a front being permanently over the site (potentially tied topographically).

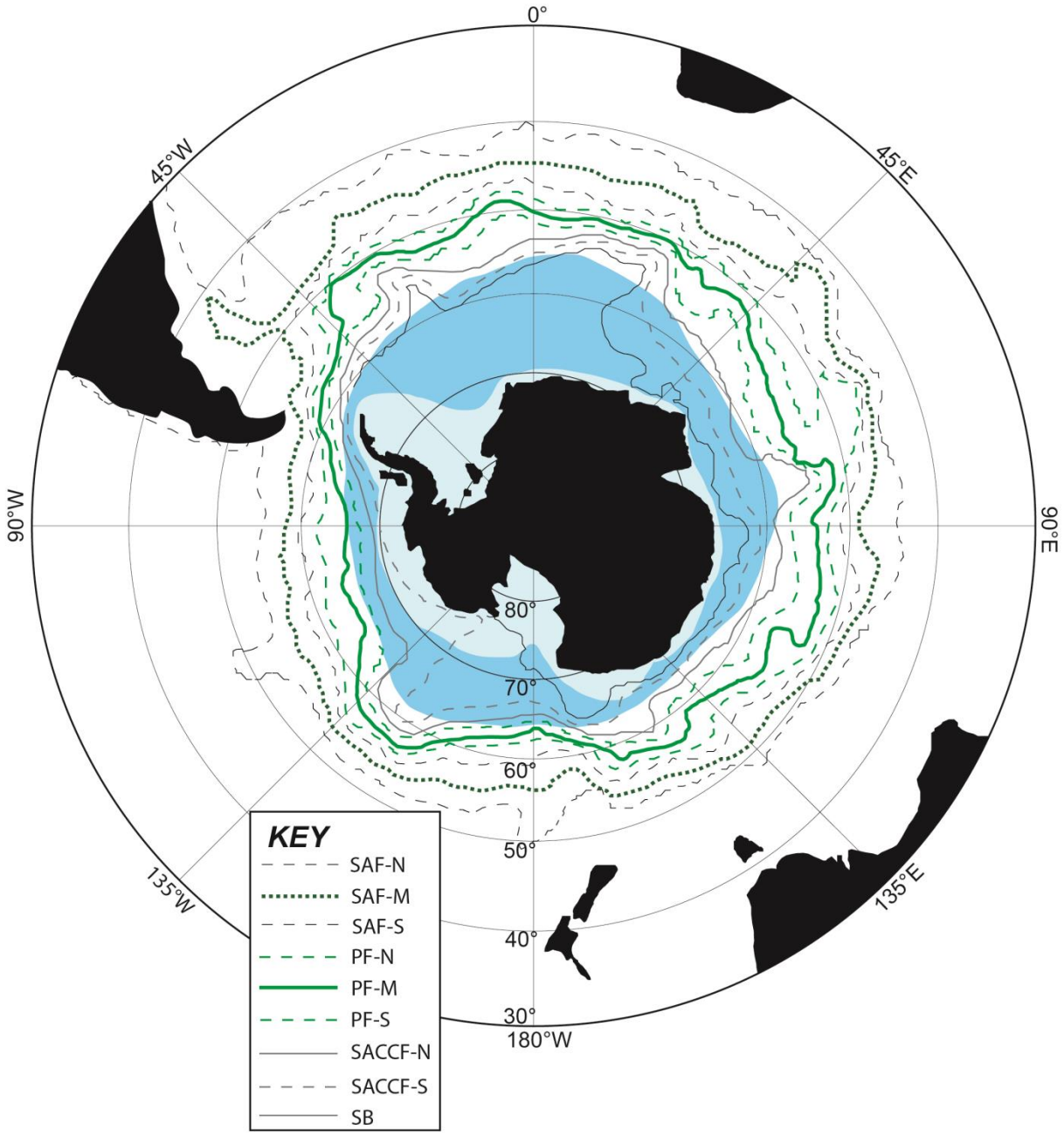

Figure 3. A map illustrating the position of each Southern Ocean front as defined by Sokolov and Rintoul (2009a,b); Abbreviations: Sub-Antarctic Front northern branch (SAF-N), Sub-Antarctic Front middle branch (SAF-M) Sub-Antarctic southern branch (SAF-S), Polar Front northern branch (PF-N), the Polar Front middle branch (PF-M), the Polar Front southern branch (PF-S), the southern ACC front, northern branch (SACCF-N), southern ACC front southern branch (SACCF-S) and the Southern Boundary Front (SB). The modern day average maximum extents for winter and summer sea-ice from 1979 to 2000 are shown by the dark and light blue shading, respectively.

2.2 Statistical analyses and paleoceanographic estimation

2.2.1 Species response (Huisman-Olff-Fresco) models

The nature of a diatom's species-response along an environmental gradient must be considered when identifying the most appropriate statistical model for paleoceanographic research. For example, weighted averaging (WA) and Weighted Averaging Partial Least Squares (WA PLS) assume that diatoms have a unimodal species-response function along an environmental gradient (ter Braak and Juggins, 1993). In contrast, a Generalised Additive Model (GAM) may not handle unimodal functions, whilst the Modern Analogue Technique (MAT) has no underlying assumption regarding species-response functions. A suite of Huisman-Olff-Fresco (HOF) models can be used to identify a particular species response function along an environmental gradient (Oksanen and Minchin, 2002). We applied five HOF models (Huisman et al., 1993) and two bimodal species response models, each of which were compared with a GAM model (Jansen and Oksanen, 2013). The suite of HOF models were applied to untransformed data, using average annual presence of a front as the predictor variable, to identify significant associations between diatom abundances and the average monthly presence per annum (mpa) of the Southern Ocean fronts. The simplest of the eight response functions (or models) that sufficiently explained the observed diatom responses to changes in frontal positioning (as inferred from SSH data) were chosen via bootstrapping and Akaike's information criterion (Jansen and Oksanen, 2013).

2.2.2 Paleoceanographic estimation: Modern Analogue Technique

The MAT computes and then compares dissimilarity coefficients between those samples from the training data set and a marine sediment core (ter Braak, 1995). A sample from the training data

set with a dissimilarity coefficient below a certain threshold value is considered to be a modern analogue for the fossil sample within the marine sediment core. The selected analogue samples are assumed to represent oceanographic properties at the locality of a core. We applied MAT using only those diatom species that had a significant association with the presence of the branches of the Southern Oceans fronts (see section 3.2), a square chord distance and the five closest analogues. Section 3.3 outlines our justification for applying MAT to the Abbott database when estimating the paleo position of Southern Ocean fronts.

2.3 Software

We used the freely available software R (version 3.0.0) and PAST (Hammer et al., 2001) for all statistical analysis. We used the R package eHOF (Jansen and Oksanen, 2015) for HOF modelling, whilst the packages maps (Becker and Wilks, 2014) and mapproj (McLlory, 2014) were used to map our database samples. MAT was applied using PAST. All graphs were produced using R (version 3.0.0) and Adobe Illustrator™.

3 Results

3.1 Sea-surface height contours

Table 1 summarises the total number of samples from the Abbott database that were sampled from regions of the Southern Ocean where oceanic fronts are present. Those samples from the Abbott database that were found to be associated with the PF-S, PF-M and PF-N are listed in Appendix 5.4, whilst those samples with the SAF (S, M and N), SACCF (S and N) are listed in Appendix 5.5.

Table 1. Sea surface height labels associated with each branch of the ACC fronts (mean +/- 1 standard deviation) relative to 2500 dbar from Sokolov and Rintoul (2009b), and the total number of samples from the Abbott database that were sampled from regions influenced by Southern Ocean fronts.

Frontal Branch	SSH (m)	Abbott database # samples
SAF-N	1.97 ± 0.02	15
SAF-M	1.71 ± 0.02	10
SAF-S	1.47 ± 0.02	6
PF-N	1.29 ± 0.01	28
PF-M	1.15 ± 0.01	33
PF-S	1.04 ± 0.02	24
SACCF-N	0.94 ± 0.02	10
SACCF-S	0.84 ± 0.01	2
SB	0.75 ± 0.01	0

3.2 HOF models

There were insufficient samples in those regions where the SAF (S, M and N), SACCF- (S and N) and SB are present, preventing a statistical analysis of the association between diatom

abundances and the presence of each of these fronts. Therefore we only considered a diatom proxy for the PF-S, and PF-M and PF-N. The suite of HOF models fitted to our training database show that *Thalassionema nitzschioides*, *Thalassiosira lentiginosa*, *Fragilariopsis kerguelensis*, and *Thalassiothrix antarctica* had a statistically significant relationship with the average annual monthly presence of the PF-S. The diatoms *Fragilariopsis kerguelensis*, *Thalassiothrix antarctica* and *Thalassiosira lentiginosa* had a significant response to the presence of the PF-M. *Fragilariopsis kerguelensis, Thalassiothrix Antarctica, Thalassiosira lentiginosa, Fragilariopsis separanda, Thalassionema nitzschioides*, and *Azpeitia tabularis* were significantly associated with the PF-N (Appendix 5.6). The relative percentage abundance of the diatoms within the Abbott database that had a significant species response relationship with the PF-S, PF-M and PF-N mpa are listed in Appendix 5.7. All of the remaining diatom species identified within the Abbott database did not have a statistically significant association with the average annual presence of the PF-S, PF-M or PF-N.

The species response relationship between the monthly presence of the PF-S and the abundances of both *Fragilariopsis kerguelensis* and *Thalassiothrix antarctica* were best explained by a GAM. The non-parametric GAM model fitted a cubic regression spline to model the association between *Fragilariopsis kerguelensis* and *Thalassiothrix antarctica*, and PF-S mpa. The response model that best explained the relationship between *Thalassionema nitzschioides, Thalassiosira lentiginosa* and *Fragilariopsis separanda* and the PF-S mpa, was a bimodal species response model with two optima. Therefore, the maximum abundances of *Thalassionema nitzschioides, Thalassiosira lentiginosa* and *Fragilariopsis separanda* are recorded at two different values of PF-S mpa (Figure 4).

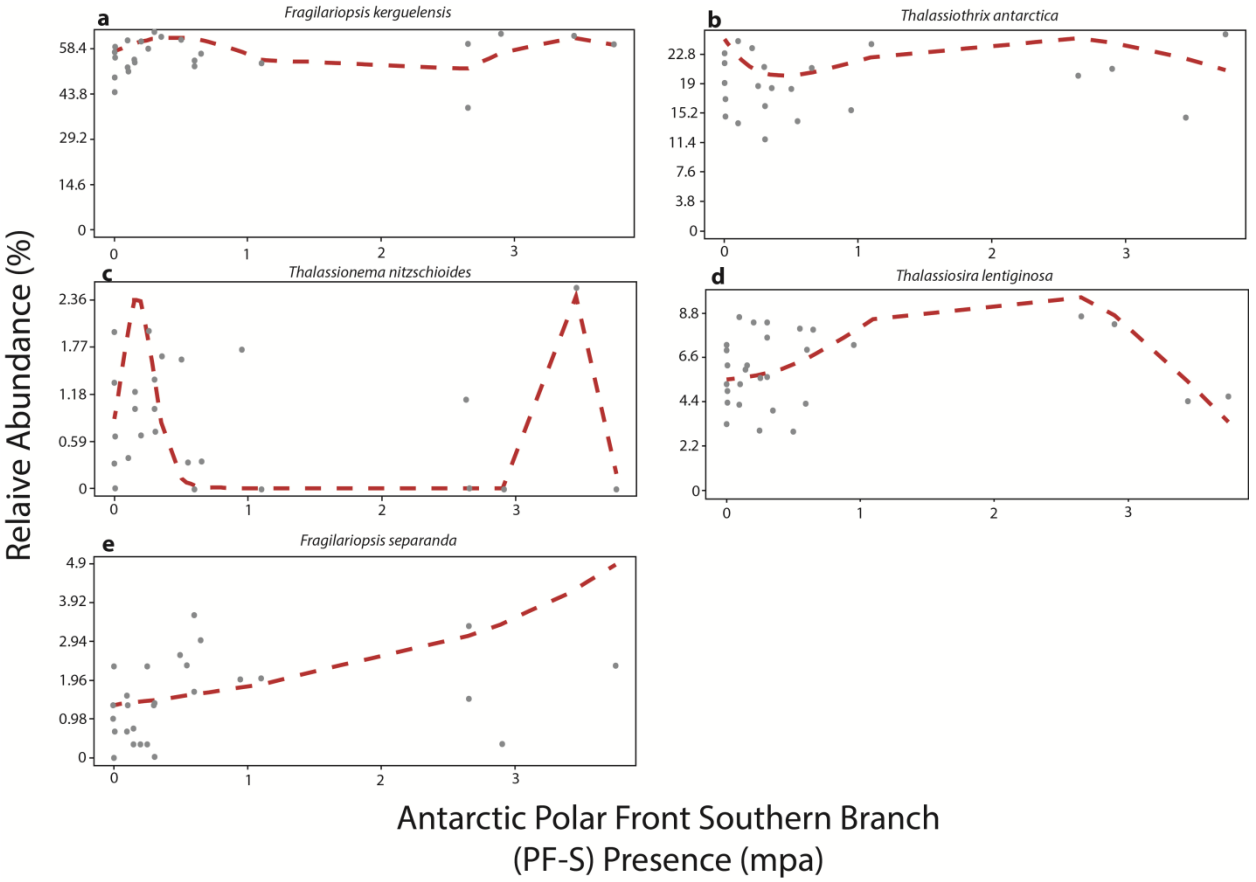

Figure 4. The fitted species response (HOF) models used to model the association between diatom relative percentage abundances and the average monthly presence per annum (mpa) of the Antarctic Polar Front's southern branch (PF-S). Shown are the fitted GAM functions for *Fragilariopsis kerguelensis* (a) and *Thalassiothrix antarctica* (b). The bimodal species response models for *Thalassionema nitzschioides*, *Thalassiosira lentiginosa* and *Fragilariopsis separanda* are shown in panel's c, d and e, respectively.

3.3 Choosing the statistical model

WA and WA-PLS both assume an underlying unimodal species response model. As our HOF analysis indicated, unimodal species response relationships may not exist between diatom assemblages and the presence of the PF-S. Hence, we did not continue on with the application of WA or WA-PLS. The Imbrie and Kipp transfer function (IKTF) uses Principal Components Analysis, which is an inefficient method for prediction (Juggins and Birks, 2012) and hinders

model interpretability (Dürrenmatt and Gujer, 2012). Using a forward selection procedure, we applied GAM as an inverse model, treating the diatom assemblages as the predictor variable and PF-S mpa as the response (Birks, 2012). Inverse models are applied by the paleoceanographic community for estimating paleoceanographic properties, such as sea-ice cover and sea-surface temperatures (Chapter 2). When applying GAM as an inverse model, *Fragilariopsis separanda* was the only significant predictor for the PF-S mpa. GAM fitted statistically significant functions to describe the association between abundances of *Fragilariopsis separanda, Azpeitia tabularis, Thalassiosira lentiginosa,* and the annual presence of the PF-N, whilst no diatoms were significant predictors for the PF-M (Appendix 5.10). We believe the use of only a single diatom proxy species and non-significant functions within GAM may not produce accurate paleo estimates of PF-S, PF-M and PF-N mpa. GAMs unreliability when extrapolated and the inability to accommodate the bounded nature of the response variable (presence of the PF-S) also hindered the application of this model. Therefore, for the Abbott database used in this pilot study, we believe the Modern Analogue Technique currently provides the most appropriate approach for estimating PF-S mpa.

3.4 Modern Analogue Technique paleo PF-S mpa estimates

For the period January 1992 to December 2012 the PF-S, PF-M and PF-N are present for 0, 1.95, and 0 mpa, respectively, at the site of core MD88-787. The PF-S, PF-M and PF-N were present for 0.6, 0 and 0.45 mpa, respectively, at the site of core MD88-784 (Figure 5, dashed horizontal lines). Therefore, we have interpreted values of >1 mpa to represent a seasonal occurrence for the SSH signature of the PF-S and PF-N. The seasonal occurrence of the PF-M at the site of core

MD88-784 (54°S) is considered to occur with PF-M mpa values >1. Whilst for core MD88-787 (56°S), occurrences of >3 mpa were considered to indicate the presence of the PF-M.

The application of MAT to core MD88-784 indicated that the PF-N and PF-M were not located over the core site (Figure 5, Appendix 5.8). Throughout the core record, the maximal estimated value for average monthly PF-N and PF-M presence per annum (mpa) was 1.3. PF-S coverage over the site of core MD88-784 was interpreted to have occurred between 29 to 17 kyr BP during the eLGM (35 to 18 kyr BP) and Antarctic Cold Reversal (ACR). The remainder of the core record, except for the period between 38 and 41 kyr BP, indicates that the PF-S was not present at the core site (Figure 5, Appendix 5.8). The paleo record for core MD88-787 suggests the PF-N and PF-M were absent over the core's location. The presence of the PF-S was estimated at the site of core MD88-787 from 19.3 to 27.5 kyr BP (the eLGM) and at 17 kyr BP during the ACR. Paleo estimates suggest the PF-S was present at the site of MD88-787 during MIS 6 and the transition from MIS 6 to MIS 5. During MIS 5 the PF-S was present at 109.5 and 95 kyr BP (Figure 5, Appendix 5.9).

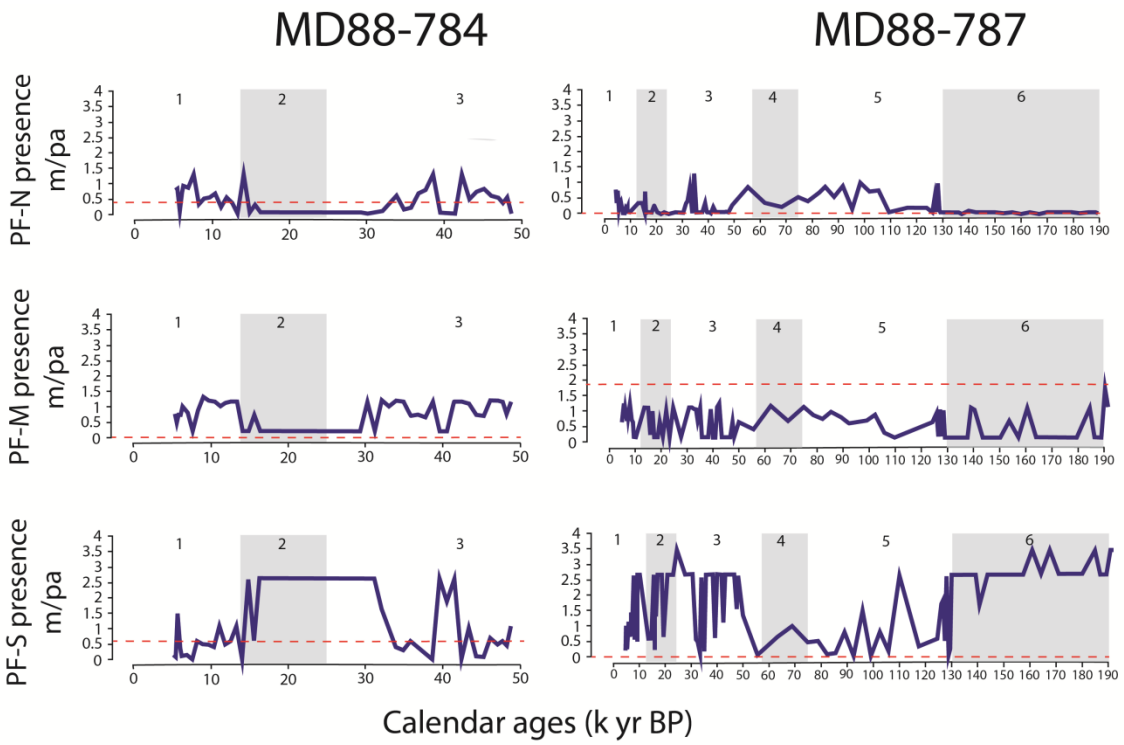

Figure 5. The MAT estimates for the paleo presence of the PF-S, PF-M and PF-N mpa for marine sediment cores MD88-784 and MD88-787. The paleo estimates are indicated with the blue line whilst the glacial marine isotopic stages (MIS) are shaded in grey. The horizontal dashed red line represents the modern day presence (mpa) of each frontal branch. Values >1 mpa are interpreted as a seasonal occurrence of the PF-S and PF-N for both cores. Front presence >1mpa indicate the seasonal occurrence of the PF-M at the site of core MD88-784, whilst for core MD88-787 values >3 mpa are considered to indicate the presence of the PF-M.

4 Discussion

4.1 Diatoms as a proxy for the sea-surface height signature of the Southern Ocean Polar Front

The biogeography of marine diatoms throughout the Southern Ocean reveals a general circumpolar distribution of diatom species that are associated with the presence of the Polar Front and the Polar Frontal Zone (PFZ). Two such species include *Fragilariopsis kerguelensis* and *Thalassiosira lentiginosa*, with abundance patterns suggesting these two diatoms provide a marker for the Polar Front/PFZ within the southeast Pacific (Esper et al., 2010), Pacific (Wolf et al., 2014; Grigorov et al., 2014), Indian (Crosta et al., 2005; Mohan et al., 2006), Atlantic (Crosta et al., 2005), south Atlantic (Kemp et al., 2010; Romero et al., 2015) and east Atlantic (Fischer et al., 2002) sectors of the Southern Ocean. Other diatoms that have elevated abundances in/at the PFZ/Polar Front include *Fragilariopsis separanda*, *Thalassiothrix antarctica* and *Thalassionema nitzschioides* (Crosta et al., 2005; Esper et al., 2010), all of which may maintain a circumpolar association with the Polar Front/PFZ (Esper et al., 2010). Within the east Atlantic and Pacific sectors of the Southern Ocean, recorded abundances of *Azpeitia tabularis* increased within the PFZ (Fischer et al., 2002; Grigorov et al., 2014).

Our preliminary analysis has provided the first statistically significant associations between specific diatom species and the presence of the dynamic PF-S SSH signature throughout the southeast Indian Ocean. Specifically, abundances of *Fragilariopsis kerguelensis*, *Thalassionema nitzschioides*, *Thalassiosira lentiginosa*, *Thalassiothrix antarctica* and *Fragilariopsis separanda* were all significantly associated with the PF-S, a result that is in good agreement with the literature (Fischer et al., 2002; Crosta et al., 2005; Mohan et al., 2006; Esper et al., 2010; Wolf et al., 2014; Grigorov et al., 2014). The association between the relative percentage abundance of

marine diatoms and the presence of the dynamic PF-S appears to be consistent throughout the Southern Ocean. Therefore, our proposed diatom proxy for the PF-S may have a broader utility throughout the Southern Ocean.

4.2 Paleoclimatic significance

It has been suggested that the Polar Front shifted to more northerly latitudes within the Indian, Pacific and Atlantic sectors of the Southern Ocean during the eLGM (Ling Ho et al., 2012; Shetye et al., 2014; Gottschalk et al., 2015; Manoj and Thamban, 2015). Our paleo record for the position of the PF-S at the sites of cores MD88-784 and MD88-787 also suggests the Polar Front was further north during glacial stages and the eLGM. The northern migration of the PF-S is concomitant with an expansion of paleo winter sea-ice (Chapter 4) (Figure 6, Appendix 5.11) and, by extension, the ACC (Martinson, 2012). Interestingly, the paleo wSIC and PF-S mpa records for MD88-784 and MD88-787 show that winter sea-ice expansion occurs after a northern migration of the PF-S. For example, the record for MD88-784 shows that PF-S mpa increases from 0.3 mpa at 34 kyr BP, to 2.65 mpa between 32 and 21kyr BP. The increase in paleo wSIC at the site of MD88-784 increased to 25% at 31.1 kyr BP (from 0.3% at 33.9 kyr BP), after the PF-S had migrated north. Similarly, PF-S mpa at core MD88-787 increased from 0.6 mpa at 31.5 kyr BP, to 2.65 mpa at 30.45 kyr BP, whilst wSIC increased from 0% at 31.5 kyr BP to 17% and 30% at 27.5 and 23 kyr BP, respectively (Figure 6, Appendices H, I and K).

The ACC is a wind-driven current, it has therefore been assumed that the position of the ACC oceanic fronts reflects the position of the westerly wind field (Kohfeld et al., 2013). However, assuming any change in the position of the ACC fronts is a direct reflection for the position of the

westerly wind field may not be valid. Currently, it is known that the Southern Ocean bathymetry steers and constricts the ACC and fronts of the Southern Ocean (Neil et al., 2004, Kohfeld et al., 2013), however, the relative importance of the westerly winds and bathymetry in dictating the positions of the ACC fronts is still unknown (Kohfeld et al., 2013). High resolution models have suggested that, between 120° and 160°E, the ACC southern boundary may shift south in response to a southern position of the westerly winds under a warming climate. Whilst throughout the remainder of the Southern Ocean there was no discernible shift of the Polar Front in association with a southern shift of the westerly wind field (Graham et al., 2012). Nonetheless, Graham et al. (2012) did note a small (1.3°) southerly shift of the westerly winds within their model, which may account for the lack of any corresponding meridional shift in the Polar Front. The possibility remains that larger shifts in the westerly wind field, as is thought to have occurred during the LGM (Bostock et al., 2015), might have an influence on frontal positions (Graham et al., 2012). Our paleo estimates for the PF-S northern migration at the sites of core MD88-784 and MD88-787 during the eLGM could be the result of a more significant equatorward migration of the westerly wind field. The northern migration of the westerly winds could, in turn, drive the northern migration of the ACC and Polar Front (Graham et al., 2012), resulting in a northern expansion of the winter sea-ice field during the eLGM period.

Our paleo record suggests the PF-S migrated to southerly latitudes at the termination of the eLGM. We suggest the southern migration of the PF-S may have been concomitant with a southern migration of the STF, increased atmospheric CO_2, and the subsequent breakdown of Southern Ocean stratification, which combined drove the eLGMs termination (Putnam et al., 2010).

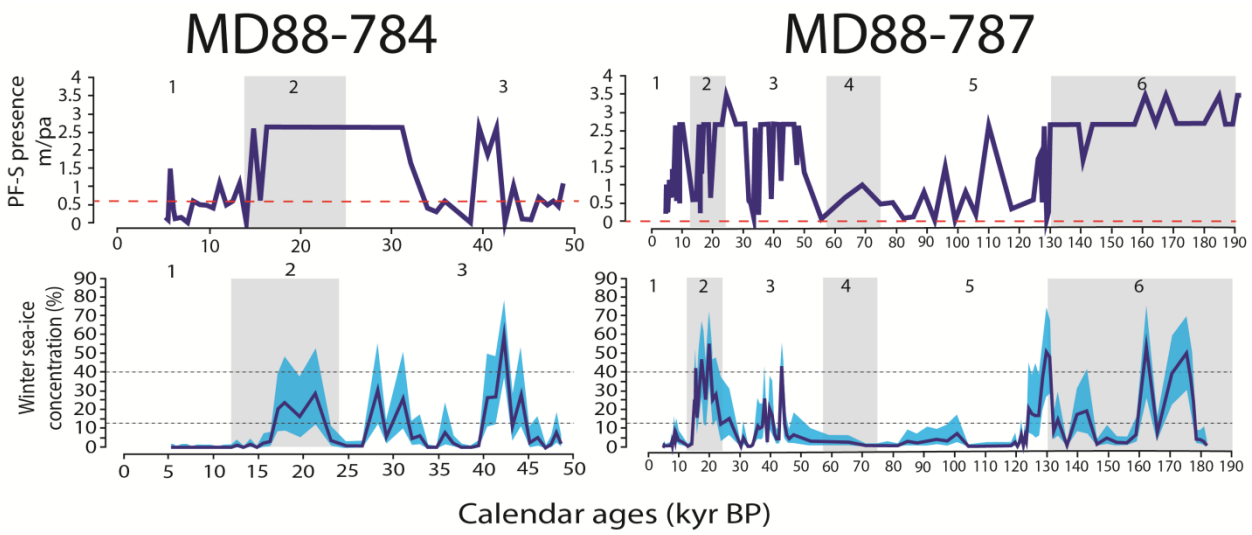

Figure 6. **The estimated PF-S mpa at cores MD88-784 (a) and MD88-787 (b) (solid purple line).** Also plotted are the paleo winter sea-ice reconstructions (solid blue line), and associated 95% confidence intervals (light blue shading) from Chapter 4 for MD88-784 (c) and MD88-787 (d). The horizontal dashed red line represents the modern day presence (mpa) of each frontal branch. Horizontal black lines mark sea-ice concentrations of 15% and 40%, indication the sea-ice outer edge and the compacted sea-ice edge, respectively (Gloersen et al., 1992).

4.3 Limitations

In section 2.1.1 we outlined some important limitations with the Abbott database. One important limitation was the different diatom classification and identification schemes used between the Abbott database and the database of Crosta et al. (2004). One such species that was not consistently classified and identified was *Thalassiothrix*, a diatom that had been identified within the preliminary analysis we present within this paper as a potential proxy species for the PF-S SSH signature. A substantial Southern Ocean diatom abundance database compiled by Zielinski et al. (1998), and recently published by Esper and Gersonde (2014), was not provided upon request for access to the data and was therefore unable to be included within our analysis. Hence our preliminary results need to be interpreted with caution until additional Southern Ocean

diatom surface sediment samples can be included within our SSH training dataset. In particular, our application of MAT to estimate the paleo presence of the PF-S for a more southerly core, core E27-23 (Figure 2), did not yield any estimates for the presence of the PF-S. Whilst this may be due to the PF-S never migrating over the site of core E27-23, we suggest it is more likely that the absence of any southerly samples within the Abbott database means there are no analogues for the samples within core E27-23. Therefore, additional samples are essential to improve the robustness of the diatom SSH proxy we propose here, and to provide a more meaningful paleoceanographic interpretation when applying our diatom SSH proxy to marine sediment cores.

5 Conclusions

Any change in the position of the Southern Ocean fronts during past climate changes remains controversial (Kemp et al., 2010). Previous work has focused on reconstructing the presence of the Southern Ocean fronts via a reconstruction of SST gradients (e.g. Howard and Prell, 1992; De Deckker et al., 2012; Romero et al., 2015). However, the assumption that a latitudinal migration of Southern Ocean fronts produces a zonally symmetric response in SST, an essential assumption for inferring the paleo position of an oceanic front via paleo SST data, may be unreasonable (Graham et al., 2012; Kohfeld et al., 2013). Therefore, we examined the potential for marine diatoms to provide a proxy for the SSH signature of the Southern Ocean's dynamic fronts. Using the Abbott database, our analysis suggested that six diatom species could be used as proxy for the southern branch of the dynamic Polar Front (PF-S). Our analysis showed that *Fragilariopsis kerguelensis*, *Fragilariopsis separanda*, *Thalassiothrix antarctica*, *Thalassionema nitzchioides* and *Thalassiosira lentiginosa* had statistically significant associations with the SSH signature of the PF-S. Current literature on the biogeography of marine diatoms throughout the Southern Ocean supports our findings and suggests that our proposed diatom proxy for the SSH signature of the PF-S has a sound ecological basis.

Our estimates for the PF-S's paleo positioning at the sites of cores MD88-784 and MD88-787 were based on the MAT, which we deemed to be the most suitable choice for the Abbott database. However, access to all published data and/or new samples from the Southern Ocean will be required to validate our proxy and properly evaluate the statistical models used to estimate the paleo position of the PF-S. Currently, we are limited by the small Abbott database that cannot accommodate a meaningful model cross-validation or investigation into the importance of spatial autocorrelation. The Abbott database is restricted to the southwest Indian Ocean. Therefore our

capacity to robustly evaluate the extent to which the statistical associations between diatoms and SSH data hold for the entire Southern Ocean is limited. Despite the above limitations, we believe the consistency between our proposed diatom proxy for the PF-S and those diatoms previously identified as having a biogeography linked with the PFZ (Crosta et al., 2005; Esper et al., 2010) suggests our proposed proxy may have a utility within the Atlantic and Pacific Sectors of the Southern Ocean.

Despite the limitations of our data set, we feel it is interesting to note our estimation of the PF-S's northern migration at 145°E, to ~54°S, during glacial stages, over the eLGM and perhaps during the ACR. The northern migration of the PF-S appears to occur just prior to an estimated northern expansion of winter sea-ice to 54°S (Chapter 4) as well as the northern migrations of the SAF and STF during glacial stages and the eLGM (Neil et al., 2004; De Deckker et al., 2012). Our attempt to provide a more robust proxy for Southern Ocean fronts may help to resolve those climatic changes that are related to latitudinal shifts of the ACC and/or westerly wind field on glacial to interglacial, and shorter term, climatic changes (e.g. the ACR).

Acknowledgements

This research was funded by the Australian Government through the provision of an Australian Postgraduate Award granted to Alexander Ferry. HEP acknowledges support from the ARC Centre of Excellence in Climate Systems Science (CE110001028) and ARC Discovery Projects DP0877098 and DP130102088.

References

Abbott, W., (1973), Vertical and lateral patterns of diatomaceous ooze found between Australia and Antarctica, University of South Carolina, Columbia, PhD thesis.

Armand, L.K., (1997), The use of diatom transfer functions in estimating sea-surface temperature and sea-ice in cores from the southeast Indian Ocean, Australian National University, Canberra, PhD thesis.

Bard, E., and Rickaby, E.M., (2009), Migration of the subtropical front as a modulator of glacial climate, *Nature*, 460, DOI:10.1038/nature08189.

Becker, R.A., and Wilks, A.R., (2014) maps: Draw Geographical Maps, R package version 2.3-9, http://cran.r-project.org/web/packages/maps/index.html.

Birks, H.J.B., (2012), Overview of numerical methods in palaeolimnology. In: Birks, J.H.B., André, F.L., Juggins, S., Smol, J.P. (Eds.), Tracking Environmental Change Using Lake Sediments. Springer, Netherlands, pp. 19–92.

Bostock, H., Hayward, B.W., Neil, H., Sabaa, A.T., and Scott, G.H., (2015, in press), Changes in the position of the Subtropical Front south of New Zealand since the last glacial period, *Palaeoceanography*, doi: 10.1002/2014PA002652.

Cervato, C., and Burckle, L., (2003), Pattern of first and last appearance in diatoms: Oceanic circulation and the position of polar fronts during the Cenozoic, *Paleoceanography*, 18, DOI:10.1029/2002PA000805.

Crosta, X., Romero, O., Armand, L.K., and Pichon, J.J., (2005), The biogeography of major diatom taxa in Southern Ocean sediments: 2. Open ocean related species, *Palaeogeography, Palaeoclimatology, Palaeoecology*, 223, 66– 92.

Crosta, X., Sturm, A., Armand, L., and Pichon, J.-J., (2004), Late Quaternary sea ice history in the Indian sector of the Southern Ocean as recorded by diatom assemblages, *Marine Micropaleontology*, 50, 209-223.

Cunningham, W. L., and Leventer, A., (1998), Diatom assemblages in surface sediments of the Ross Sea: relationship to present oceanographic conditions, *Antarctic Science*, 10, 134-146.

De Deckker, P., Moros, M., Perner, K., and Jansen, E., (2012), Influence of the tropics and southern westerlies on glacial interhemispheric asymmetry, *Nature Geoscience*, 5.

Dong, S., Sprintall, J., and Gille, S.T., (2006), Location of the Antarctic Polar Front from AMSR-E Satellite Sea Surface Temperature Measurements, *Journal of Physical Oceanography*, 36, 2075- 2089.

Dürrenmatt, D. J., and Gujer, W., (2012), Data-driven modelling approaches to support wastewater treatment plant operation, *Environmental Modelling and Software*, 30, 47-56.

Esper, O., and Gersonde, R., (2014), New tools for the reconstruction of Pleistocene Antarctic sea ice., *Palaeogeography, Palaeoclimatology, Palaeoecology*, 399, 260–283.

Esper, O., Gersonde, R., Kadagies, N., (2010), Diatom distribution in southeastern Pacific surface sediments and their relationship to modern environmental variables, *Palaeogeography, Palaeoclimatology, Palaeoecology*, 27, 1-27.

Ferry, A. J., Prvan, T., Jersky, B., Crosta, X., and Armand, L.K., (2015), Statistical modeling of Southern Ocean marine diatom proxy and winter sea ice data: Model comparison and developments, *Progress in Oceanography*, 131, 100–112.

Findlay, C. S., and Flores, J.A., (2000), Subtropical Front fluctuations south of Australia (45°09´S, 146°17´E) for the last 130 ka years based on calcareous nannoplankton, *Marine Micropaleontology*, 40, 403–416.

Fischer, G., Gersonde, R., and Wefer, G., (2002), Organic carbon, biogenic silica and diatom fluxes in the marginal winter sea-ice zone and in the Polar Front Region: interannual variations and differences in composition, *Deep-Sea Research II*, 49, 1721–1745.

Graham, R. M., de Boer, A.M., Heywood, K.J., Chapman, M.R., and Stevens, D.P., (2012), Southern Ocean fronts: Controlled by wind or topography?, *Journal of Geopgysical Research*, 117, DOI:10.1029/2012JC007887.

Gloersen, P., Campbell, W.J., Cavalieri, D.J., Comiso, J.C., Parkinson, C.L., and Zwally, H.J., (1992), Arctic and Antarctic Sea Ice, 1978- 1987, Satellite Passive- Microwave Observations and Analysis, NASA Special Publication, 511, 289 pp, National Aeronautics and Space Administration, Washington, D.C.

Gottschalk, J., Skinner, L.C., and Waelbroeck, C., (2015), Contribution of seasonal sub-Antarctic surface water variability to millennial-scale changes in atmospheric CO2over the last deglaciation and Marine Isotope Stage 3, *Earth and Planetary Science Letters*, 411, 87-99.

Gouretski, V. V., and Koltermann, K.P., (2004), WOCE global hydrographic climatology, Tech. Rep. 35/2004, 52 pp., Berichte des Bundesamtes fu¨r Seeschifffahrt und Hydrographie, Hamburg, Germany.

Grigorov, I., Rigual-Hernandez, A.S., Honjo, S., Kemp, A.E.S., and Armand, L.K., (2014), Settling fluxes of diatoms to the interior of the Antarctic circumpolar current along 170°W, *Deep-Sea Research* 1, 93, 1-13.

Hammer, Ø., Harper, D.A.T., and Ryan, P.D., (2001), PAST: Paleontological Statistics Software Package for Education and Data Analysis., *Palaeontologia Electronica*, 4, 9pp.

Hiramatsu, C., and De Deckker, P., (1997), The calcareous nannoplankton assemblages of surface sediments in the Tasman and Coral Seas, *Palaeogeography, Palaeoclimatology, Palaeoecology*, 131, 257–285.

Howard, W. R., and Prell, W.L., (1992), Late Quaternary surface circulation of the Southern Indian Ocean and its relationship to orbital variations, *Palaeoceanography*, 7, 79-117.

Huisman, J., Olff, H., and Fresco, L.F.M., (1993), A hierarchical set of models for species response analysis, *Journal of Vegetation Science*, 4, 37-46.

Jansen, F., and Oksanen, J., (2015), eHOF: Extended hierarchical logistic regression (Huisman-Olff-Fresco) models, R package version 1.5.7, http://cran.r-project.org/web/packages/eHOF/index.html

Jansen, F., and Oksanen, J., (2013), How to model species responses along ecological gradients – Huisman–Olff–Fresco models revisited, *Journal of Vegetation Science*, 24, 1108–1117

Juggins, S., and Birks, J.B., (2012), Quantitative Environmental Reconstructions from Biological Data, in Tracking Environmental Change Using Lake Sediments, edited by H. J. B. Birks, Lotter, A.F., Jugins, S., and Smol, J.P., pp. 431-494, Springer Science and Business Media.

Kawagata, S., (2001), Tasman Front shifts and associated paleoceanographic changes during the last 250,000 years: foraminiferal evidence from the Lord Howe Rise, *Marine Micropaleontology*, 41, 167-191.

Kemp, A. E. S., Grigorov, I., Pearce, R.B., and Naveira Garabato, A.C., (2010), Migration of the Antarctic Polar Front through the mid-Pleistocene transition: evidence and climatic implications, *Quaternary Science Reviews*, 29, 1993-2009.

Kohfeld, K. E., Graham, R.M., de Boer, A.M., Sime, L.C., Wolff, E.W., Le Quéré, C., and Bopp, L., (2013), Southern Hemisphere Westerly Wind Changes during the Last Glacial Maximum: Paleo-data Synthesis, *Quaternary Science Reviews*, 68, 76-95.

Kostianoy, A. G., Ginzburg, A.I., Frankignoulle, M., and Delille, B., (2004), Fronts in the Southern Indian Ocean as inferred from satellite sea surface temperature data, *Journal of Marine Systems*, 45, 55– 73.

Ling Ho, S., Mollenhauer, G., Lamy, F., Martínez-Garcia, A., Mohtadi, M., Gersonde, R., Hebbeln, D., Nunez-Ricardo, S., Rosell-Melé, A., and Tiedemann, R., (2012), Sea surface temperature variability in the Pacific sector of the Southern Ocean over the past 700 kyr, *Palaeoceanography*, 27, DOI:10.1029/2012PA002317.

MARGO project members, (2009), Constraints on the magnitude and patterns of ocean cooling at the Last Glacial Maximum, *Nature Geoscience*, 2, DOI: 10.1038/NGEO1411.

Manoj, M. C., and Thamban, M., (2015), Shifting frontal regimes and its influence on bioproductivity variations during the Late Quaternary in the Indian sector of Southern Ocean, *Deep Sea Research Part II: Topical Studies in Oceanography*, http://dx.doi.org/10.1016/j.dsr1012.2015.1003.1011i.

Marino, G., Rohling, E.J., Sangiorgi, F., Hayes, A., Casford, J.L., Lotter, A.F., Kucera, M., and Brinkhuis, H., (2009), Early and middle Holocene in the Aegean Sea: interplay between high and low latitude climate variability, *Quaternary Science Reviews*, 28, 3246–3262.

Martínez, J. I., (1994), Late Pleistocene palaeoceanography of the Tasman Sea: Implications for the dynamics of the warm pool in the western Pacific, *Palaeogeography, Palaeoclimatology, Palaeoecology*, 112, 19-62.

Martinson, D. G., (2012), Antarctic circumpolar current's role in the Antarctic ice system: An overview, *Palaeogeography, Palaeoclimatology, Palaeoecology*, 335-336, 71–74.

McKay, R., Naish, T., Carter, L., Riesselman, C., Dunbarc, R., Sjunneskog, C., Winter, D., Sangiorgi, F., Warren, C., Pagani, M., Schouten, S., Willmott, V., Levy, R., DeConto, R., and Powell, R.D., (2012), Antarctic and Southern Ocean influences on Late Pliocene global cooling, *PNAS*, 109, 6423–6428.

McLlory, D., (2014), maps. R package version 1.2-2, http://cran.r-project.org/web/packages/mapproj/index.html

Mohan, R., Shanvas, S., Thamban, M., and Sudhakar, M., (2006), Spatial distribution of diatoms in surface sediments from the Indian sector of Southern Ocean, *Current Science*, 91, 1495-1502.

Morley, J. J., (1989), Variation of high-latitude oceanographic fronts in the southern Indian Ocean: an estimation based on faunal changes, *Palaeoceanography*, 4, 547-554.

Neil, H. L., Carter, L., and Morris, Y., (2004), Thermal isolation of Campbell Plateau, New Zealand, by the Antarctic Circumpolar Current over the past 130 kyr, *Palaeoceanography*, 19, doi:10.1029/2003PA000975.

Oksanen, J., and Minchin, P.R., (2002), Continuum theory revisited: what shape are species responses along ecological gradients?, *Ecological Modelling*, 157, 119-129.

Olguín, H. F., and Alder, V.A., (2011), Species composition and biogeography of diatoms in antarctic and subantarctic (Argentine shelf) waters (37–76°S), *Deep-Sea Research II*, 58, 139–152.

Putnam, A. E., Denton, G.H., Schaefer, J.M., Barrell, D.J.A., Andersen, B.G., Finkel, R.C., Schwartz, R., Doughty, A.M., Kaplan, M.R., and Schlüchter, C., (2010), Glacier advance in southern middle-latitudes during the Antarctic Cold Reversal, *Nature Geoscience*, 3, DOI: 10.1038/NGEO962.

Rigual-Hernández, A.S., Trull, T.W., Bray, S.G., Cortina, A. and Armand, L.K., (in review), Latitudinal and temporal distributions of diatom populations in the main pelagic hydrological regions of the Southern Ocean and their role in the biological pump, *Biogeosciences*.

Rintoul, S. R., Hughes, C., and Olbers, D., (2001), The Antarctic Circumpolar Current System. In: Siedler, G., Church, J., and Gould, J., (Eds.). Ocean circulation and climate. Academic Press, London, pp., 271-302.

Romero, O. E., Kim, J.H., Bárcena, M.A., Hall, I.R., Zahn, R., and Schneider, R., (2015), High-latitude forcing of diatom productivity in the southern Agulhas Plateau during the past 350kyr, *Paleoceanography*, 30, DOI:10.1002/2014PA002636.

Shetye, S. S., Mohan, R., and Nair, A., (2014), Latitudinal shifts in the Polar Front in Indian sector of the Southern Ocean: evidences from silicoflagellate assemblage, *Geosciences Journal*, 18, 241−246.

Shulmeister, J., Goodwin, I., Renwick, J., Harle, K., Armand, L., McGlone, M.S., Cook, E., Dodson, J., Hesse, P.P., Mayewski, P., and Curran, M., (2004), The Southern Hemisphere

westerlies in the Australasian sector over the last glacial cycle: a synthesis, *Quaternary International*, 118–119, 23–53.

Sokolov, S., and Rintoul, S.R., (2007), Multiple Jets of the Antarctic Circumpolar Current South of Australia, *Journal of Physical Oceanography*, 37, 1394-1412.

Sokolov, S., and Rintoul, S.R., (2009a), Circumpolar structure and distribution of the Antarctic Circumpolar Current fronts: 1. Mean circumpolar paths, *Journal of Geophysical Research*, 114, DOI:10.1029/2008JC005108.

Sokolov, S., and Rintoul, S.R., (2009b), Circumpolar structure and distribution of the Antarctic Circumpolar Current fronts: 2. Variability and relationship to sea surface height, *Journal of Geophysical Research*, 114, DOI:10.1029/2008JC005248.

Taylor, F., McMinn, A., and Franklin, D., (1997), Distribution of diatoms in surface sediments of Prydz Bay, Antarctica, *Marine Micropaleontology*, 32, 209-229.

ter Braak, C. J. F., (1995), Non-linear methods for multivariate statistical calibration and their use in palaeoecology: a comparison of inverse (k-nearest neighbours, partial least squares and weighted averaging partial least squares) and classical approaches, *Chemometrics and Intelligent Laboratory Systems*, 28, 165-180.

ter Braak, C. J. F., and Juggins, S., (1993), Weighted averaging partial least squares regression (WA-PLS) : an improved method for reconstructing environmental variables from species assemblages, *Hydrobiologia*, 269/270, 485-502.

Wells, P., and Okada, H., (1997), Response of nannoplankton to major changes in sea-surface temperature and movements of hydrological fronts over Site DSDP 594 (south Chatham Rise, southeastern New Zealand), during the last 130 kyr, *Marine Micropaleontology*, 32, 341-363.

Wolf, C., Frickenhaus, S., Kilias, E.S., Peeken, I., and Metfies, K., (2014), Protist community composition in the Pacific sector of the Southern Ocean during austral summer 2010, *Polar Biology* 37, 375-389.

Zielinski, U., Gersonde, R., Seiger, R., and Fütterer, D., (1998), Quaternary surface water temperature estimations: Calibration of a diatom transfer function for the Southern Ocean, *Palaeoceanography*, 13, 365-383.

Chapter 6

General Discussion and Conclusions

This concluding chapter is organised into three main parts. Part 1 (sections 6.1.1 to 6.1.4) summarises the key findings from Chapters 2, 3, 4 and 5 to address aims 1, 2, 3 and 4, respectively. In part 2 (section 6.2) a final concluding paleoceanographic synthesis for the southwest Pacific, from the eLGM through to the Holocene, is provided. Finally, some key future research directions are briefly discussed within the third and final part of this concluding chapter (section 6.3).

6.1 Thesis aim evaluation

6.1.1 *AIM 1: To assess the statistical models that are used for the estimation of Southern Ocean paleo sea-ice cover based on a diatom proxy.*

Chapter 2 evaluated the applicability of the current statistical models (referred to as transfer functions within the paleoceanography literature) to the only publically available diatom surface sediment training database compiled and originally described by Crosta et al. (2004). Currently, the Modern Analogue Technique (MAT) and the Imbrie and Kipp Transfer Function (IKTF) are the main methods that have been used to estimate paleo sea ice throughout the Southern Ocean

(Crosta et al., 1998; Crosta et al., 2004; Esper and Gersonde 2014). Chapter 2 compared MAT and IKTF with the application of Weighted Averaging Partial Least Squares (WA PLS) and a Generalized Additive Model (GAM). A 10-fold hold out validation of each model was applied to test relevant statistical assumptions and compare the fit of each model to the training database of Crosta et al. (2004). A hold out validation, with a partitioning of the training database into training and test subsets, ensured a geographic separation between each subset. Therefore, this thesis investigated the importance of spatial autocorrelation within the training database of Crosta et al. (2004), and the bias that spatial autocorrelation may produce when estimating the predictive error of each statistical method under random 10-fold hold out validation. To complement the hold out validation of each model, variance partitioning and principal co-ordinates analysis revealed the relative importance of winter sea-ice concentrations (wSIC), and the spatial patterns within the Crosta et al. (2004) training database, in explaining the variation within diatom relative abundances. Investigation into the nature of each diatom's species-response relationship with wSIC was introduced and considered in the evaluation of each statistical model. Therefore, the primary aim for Chapter 2 was achieved, whereby the GAM provided the most statistically, and biologically, appropriate method for estimating past wSIC.

6.1.1.1 Comparison of all models under 10-fold and hold out validation

Hold out validation of each statistical model allowed for (1) an assessment of a model's predictive error (defined as the root mean squared error of prediction (RMSEP)), (2) evaluation of the accuracy of each model when fitted to the training dataset (by using linear regression between observed data and model estimates), and (3) for an assessment of each model's *a priori* statistical assumptions.

Evaluating each of the statistical models (GAM, WA PLS, MAT and IKTF) with a 10-fold hold out validation showed that GAM had a higher average RMSEP than IKTF and MAT, whilst the highest RMSEP was computed for WAPLS. When applying a spatially independent hold out validation, the RMSEP for all models increased. The RMSEP for GAM was the lowest, whilst MAT had the highest RMSEP (Table 1) (Chapter 2).

Table 1: The average RMSEP computed for each of the models compared within Chapter 2.

Model	Mean RMSEP under random 10-fold hold out validation	Mean RMSEP from spatially independent hold out validation
GAM	21.21	23.73
WA PLS	23.78	25.91
Transformed-MAT	17.24	26.0
Untransformed-MAT	14.71	28.04
IKTF	21.08	26.59

Chapter 2 suggested that IKTF, a form of principal component regression, is an inappropriate model for estimating paleo wSIC. As regression assumes the normality of model errors (Bennett et al., 2013), the violation of this assumption when applying IKTF suggested the application of IKTF was not appropriate (Chapter 2).

Importantly, principal components analysis (PCA) may not be an appropriate method for the ordination of the Crosta et al. (2004) diatom relative abundance database. PCA preserves Euclidean distances between species abundances, therefore those species with many zero values will have a small Euclidean distance value, providing incorrect ecological answers (Legendre and Birks, 2012). The Crosta et al. (2004) diatom abundance database contains many zero values, hence the utility of PCA for modelling the Crosta et al. (2004) database may be limited. Any statistical model that estimates paleoclimate data using a diatom proxy would ideally be

biologically transparent, and therefore interpretable. However, the use of principal components as predictors hinders a model's interpretability, as well as the relative importance of given variables (i.e. diatom species) within the model (Dürrenmatt and Gujer, 2012; Juggins and Birks, 2012).

MAT had a higher RMSEP under hold out validation compared with the 10-fold hold out validation, suggesting MAT exploited the spatial autocorrelation structure within the training database. Therefore, MAT would be less successful when used to predict wSIC on temporally independent (i.e. marine sediment core) data. Importantly, use of linear regression between observed data and the predicted values from MAT, under 10-fold hold out validation, revealed that MAT was not an unbiased predictor of wSIC, and failed to adequately model the association between marine diatom assemblages and the presence of wSIC.

Based on the analysis detailed in Chapter 2, it was concluded that both GAM and WA PLS were the most statistically appropriate procedures for estimating paleo wSIC when applied to spatially autocorrelated data. Importantly, both models provided an unbiased fit to the database of Crosta et al. (2004) under 10-fold hold out validation, as revealed by linear regression models between observed data and predicted values with slopes and intercepts that were close to 1 and 0, respectively.

6.1.1.2 Spatial analysis of the Crosta et al. (2004) database

The application of principal coordinate analysis of neighbour matrices (PCNM) and variance partitioning assessed the relative importance of wSIC and the spatial structures of the Crosta et al. (2004) database in explaining the variance of diatom relative abundance values. Variance

partitioning and PCNM indicated that the diatom database of Crosta et al. (2004) was significantly spatially autocorrelated (Chapter 2).

The significant spatial autocorrelation could be the product of other ecologically important, but unmeasured, spatially autocorrelated environmental variables. Based on the work of Telford and Birks (2005), one would have expected to find a significant autocorrelation amongst the residuals of IKTF, MAT, GAM and WA PLS since these unmeasured spatially autocorrelated environmental variables were not included within each of the models. Both GAM and WA PLS had significantly autocorrelated residuals, whilst IKTF and MAT did not. The latter result suggested that MAT and IKTF exploited the spatial structures (i.e. autocorrelation) of the Crosta et al. (2004) database, whilst GAM and WA PLS did not (Chapter 2).

The application of GAM only required four diatom species to estimate wSIC. Use of variance partitioning revealed that a greater portion of the variance in the abundances of the diatoms used within GAM was explained by wSIC compared with the PCNM spatial variables. In contrast, PCNM spatial variables explained more of the variance in the total diatom database than wSIC. The latter result can be attributed to the use of specific diatom species within GAM, in particular those with a biogeography that is clearly linked with the sea-ice environment (Armand et al., 2005; Esper et al., 2010). Hence, the four diatoms used within GAM, and their Southern Ocean surface water hydrological signature, provide the most reliable proxy for the estimation of wSIC.

6.1.1.3 Why the GAM provides the most reliable method for Southern Ocean sea-ice paleo estimates

The application of Huisman-Olff-Fresco (HOF) models identified the type of species-response curve that best approximated the relationship between diatom relative abundances and wSIC. Importantly, WA PLS assumes an underlying unimodal species-response relationship, however, the HOF models indicated that unimodal species-response curves are rare. Instead, monotonic, bimodal and unidirectional species-response curves represented the majority of the relationships between these latter two parameters. Whilst GAM can handle monotonic, bimodal and unidirectional species-response curves, WA PLS does not, hence GAM was preferred over WA PLS (Chapter 2).

The GAM model developed and proposed within Chapter 2 used *Actinocyclus actinochilus*, *Fragilariopsis curta*, *Fragilariopsis cylindrus* and *Thalassiosira lentiginosa* as proxies for wSIC. Use of just four diatom species provided GAM with a greater transparency, a stronger biological basis, and an improved interpretability compared with MAT, IKTF and WA PLS. Indeed, the current understanding of diatom biogeography throughout the Southern Ocean suggests that the diatoms used within GAM are clearly linked with the sea-ice environment (Armand et al., 2005; Crosta et al., 2005; Esper et al., 2010). The biogeographical distribution of the proxy species *Actinocyclus actinochilus*, *Fragilariopsis cylindrus*, and *Fragilariopsis curta*, has been shown to be limited to the winter sea-ice zone. Each of these three species have lower abundances at more northerly locations (Taylor et al., 1997; Cunningham and Leventer, 1998; Armand et al., 2005; Buffen et al., 2007; Esper et al., 2010; Olguín and Alder, 2011; Esper and Gersonde, 2014). In contrast, the relative abundance of the proxy species *Thalassiosira lentiginosa* is closely tied to the position of the winter sea-ice edge, with abundances of *Thalassiosira lentiginosa* increasing

north of the winter sea-ice edge (Grigorov et al., 2014). Importantly, application of GAM allows for the simple computation of confidence intervals for each estimate of paleo wSIC, and an evaluation for the statistical significance of each diatom species that is used as a proxy for wSIC. Therefore, GAM provided the most useful means for estimating paleo wSIC based on a marine diatom proxy.

6.1.2 *AIM 2: To apply the most robust statistical model and produce a new paleo wSIC data set for the southwest Pacific, focussing on the Antarctic Cold Reversal, late to mid-Holocene, and a comparison with the Atlantic sector.*

Chapter 3 focussed on an application of the GAM model proposed in Chapter 2 on two marine sediment cores within the southwest Pacific sector of the Southern Ocean. In doing so, Chapter 3 provided the first winter paleo sea-ice record for SO136-111, and examined the first paleo sea-ice record from a new marine sediment core within the southwest Pacific, E27-23. The GAM paleo wSIC estimates for core SO136-111 were compared with the MAT estimates of average annual monthly sea-ice cover (Crosta et al. 2004), highlighting the general consistency between both techniques. Core E27-23 is located in a position analogous to those cores extracted from the south Atlantic sector of the Southern Ocean. This thesis, therefore, provided a comparison between the paleo sea-ice record for the south Atlantic (Divine et al., 2010; Esper and Gersonde, 2014) with the record for the southwest Pacific over the last 15 kyr BP.

6.1.2.1 Holocene millennial wSIC variability within the southwest Pacific

Holocene paleo wSIC estimates presented within Chapter 3 are consistent with the predicted sea-ice conditions described from a number of proposed hypotheses.

One hypothesis is that millennial scale changes to the latitudinal position and/or intensity of the westerly wind field has driven Holocene climatic variation throughout the southern hemisphere (Shevenell and Kennett, 2002; Mayewski et al., 2004; Shevenell et al., 2011; Etourneau et al., 2013). Under such a scenario, the stronger and northerly displaced westerly winds, in conjunction with a northern displacement of the Subtropical Front (STF), cooled Antarctica between 9 and 6 kyr BP (Moros et al., 2009). The millennial scale variation in estimated wSIC at the site of core E27-23 is consistent with this hypothesis (Chapter 3).

A second hypothesis is focussed on the cooling of North Atlantic Deep Water (NADW) as a result of a fresh water flux from the melt of the Laurentide ice sheet. The upwelling of cooler NADW within the Southern Ocean is considered to have overwhelmed the bipolar see-saw, whereby regions south of the Polar Frontal Zone (PFZ) cooled between 9 and 7 kyr BP (Renssen et al., 2010). Paleo climate models have suggested that the melting of the Laurentide ice sheet would have increased southern hemisphere sea-ice cover and, hence, provided an additional driver for the increased Holocene wSIC estimated at the site of core E27-23 (Chapter 3).

6.1.2.2 wSIC during the Antarctic Cold Reversal

The GAM-derived paleo wSIC estimates from cores E27-23 and SO136-111 provided the first evidence for an increase in wSIC during the ACR period. Increased wSIC during the ACR is consistent with hypotheses that invoke (1) oceanic changes resulting from Melt Water Pulse-1A

and (2) a northern migration of the Polar Front (PF), Sub-Antarctic Front (SAF), STF and/or the westerly wind field (De Deckker et al., 2012; Manoj et al., 2013; Weber et al., 2014).

A fresh water perturbation from Melt Water Pulse 1A (MWP-1A), which may have been sourced from the Antarctic ice sheet, cooled the Southern Ocean, and increased wSIC (Weber et al., 2014). Ice-rafted debris from the southwest Pacific indicates that at 15 kyr BP the PF and SAF were situated north of their modern day positions (Manoj et al., 2013). In addition, an associated northern migration of the STF and westerly wind field reduced the influence of the warm Leeuwin current to the south of Australia between 14.5 and 11.8 kyr BP (De Deckker et al., 2012). Thus, the ACR wSIC records from cores SO136-111 and E27-23 support the hypothesized oceanic changes that are associated with MWP-1A, as well a northern migration of the ACC and its associated fronts (Chapter 5) and/or the westerly wind field (Chapter 3).

6.1.2.3 Comparison of the paleo winter sea-ice records between the Atlantic and southwest Pacific

The paleo wSIC records from the southwest Pacific contrast those from the Atlantic sector of the Southern Ocean (Chapter 3). Notably, the paleo wSIC estimates from core SO136-111 suggest the expansion of wSIC during the ACR was greater than any of the sea-ice advances that followed the ACR during the Holocene. The contrasting paleo sea-ice data from the Atlantic suggests the expansion of sea ice during the ACR was no greater than at any other time-frame during the Holocene (Bianchi and Gersonde, 2004; Divine et al., 2010). The increase in Holocene sea-ice cover throughout the south Atlantic has been attributed to an expansion and intensification of the Weddell Sea gyre, which subsequently increased the northward transport of

winter sea ice (Bianchi and Gersonde, 2004; Divine et al., 2010). However, the southwest Pacific sector is not influenced by any analogous gyre circulation system, and under modern conditions, the areal extent of Antarctic sea ice within the southwest Pacific also has the least inter-annual variation (Ackley 1981; Parkinson, 1992). Thus, the discrepancy between the southwest Pacific paleo wSIC estimates determined from this thesis and the paleo sea-ice estimates from the south Atlantic appear to be attributable to the regional oceanography of these two contrasting sectors of the Southern Ocean.

6.1.3 *AIM 3: To provide a modernised account of wSIC and February sea-surface temperature (fSST) records over the Last Glacial Maximum (LGM) throughout the southwest and southeast Pacific, with a focus on the cold and warm phases of the extended LGM (eLGM).*

Chapter 4 focused on the paleo wSIC records for the southwest Pacific, southeast Pacific and southeast Atlantic during the LGM. This chapter introduced the first record of paleo wSIC estimates over the extended LGM (eLGM) period from three marine sediment cores, MD88-784, MD88-787 and E27-23. The eLGM paleo wSIC estimates were derived from the GAM model that was evaluated and described in Chapter 2. The synthesis of eLGM paleo wSIC was then compared with terrestrial paleo climate records from New Zealand, southeast Australia, and east Antarctica. This chapter focused on testing hypotheses for the onset of the eLGM, as well as the presence of two eLGM cold phases and Antarctic Isotopic Maxima 2 (AIM 2).

6.1.3.1 An expansion of wSIC throughout the southwest Pacific during the eLGM

Maximum wSIC at the sites of cores SO136-111, MD88-784 and E27-23 all occurred around 35 kyr BP (Chapter 4). The increase in wSIC therefore occurred before the northern hemisphere LGM, dated between ~26.5 and 18 kyr BP (Clark et al., 2009; Negre et al., 2010).

The eLGM paleo wSIC data presented within this thesis is compared with the New Zealand terrestrial paleo data described by Putnam et al. (2013). Hence, the paleo wSIC data presented in Chapter 4 is consistent with the hypothesis of Putnam et al. (2013). Due to atmospheric cooling, driven primarily by orbital forcing, the Southern Ocean is thought to have stratified, increasing high latitude winter duration and sea-ice formation. The circum-Antarctic westerly wind field exported sea ice northward throughout the Southern Ocean, with subsequent brine rejection (associated with sea-ice formation) leading to a further stratification of the Southern Ocean. A stratified Southern Ocean hindered the upwelling of warm deep water, permitting the spread of winter sea ice (Putnam et al., 2013). Orbital forcing also influenced the cooling of NADW, resulting in the formation of very cold and salty water along the edge of the Weddell Sea continental shelf, which is believed to have increased the salinity of AABW. As a result, the density of NADW decreased relative to AABW, stratifying the deep ocean, leading to an efficient carbon trap and a lowering of atmospheric CO_2 (Adkins, 2013).

6.1.3.2 Winter sea-ice expansion during the LGM cold phases

The paleo wSIC and February sea-surface temperature (fSST) estimates described within Chapter 4 indicate that the eLGM was not only longer than previously thought, but had a variable climate oscillating between cold and warm phases on millennial time scales. The eLGM paleo wSIC estimates from E27-23 identified two periods of distinct wSIC increases, between 30 to 26 kyr

BP and 24 to 19 kyr BP, separated by the eLGM interstadial/AIM 2. The paleo wSIC reconstructions described within Chapter 4 extend our knowledge of the southern hemisphere eLGM, and provided a complimentary record with previous paleoclimatic records from New Zealand and East Australia (Petherick et al., 2008; Stephens et al., 2012). The two eLGM cold phases documented within the paleo wSIC data, presented in Chapter 4, are compatible with hypotheses that invoke a northern migration of the ACC (Verleye and Louwye, 2010; Martinson, 2012), the PFZ (Verleye and Louwye, 2010; Chapter 5) as well as the STF and SAF (Reeves et al., 2013). The more northerly position of the STF and SAF may have increased the influence of cool Sub-Antarctic waters within the southwest Pacific (Reeves et al., 2013) and reduce the influence of the warm Leeuwin Current to the south of Australia (De Deckker et al., 2012).

6.1.3.3 The wSIC decline during Antarctic Isotopic Maxima 2

Paleo fSST records indicated that the sites of cores SO136-111 and MD88-784 experienced an increase in fSST, concomitant with reduced wSIC, during a period of eLGM climatic amelioration. The eLGM climatic amelioration may be an expression of AIM 2, and/or the eLGM interstadial documented within speleothem and pollen records from New Zealand's North Island (Newnham et al., 2007; Williams et al., 2010, Stephens et al., 2012; Newnham et al., 2012).

Newnham et al. (2012) called for additional marine paleoclimatic records across latitudinal gradients to robustly test the bipolar see-saw hypothesis as an explanation for eLGM climatic variation. The paleo wSIC and fSST records detailed in Chapter 4 attest that the bipolar see-saw hypothesis provides a plausible explanation for the observed variability between New Zealand's late glacial climate records and those from southwest Pacific deep-sea cores (Chapter 4).

6.1.3.4 The termination of the eLGM

The revised paleo fSST record suggested that ocean temperatures increased prior to atmospheric CO_2 increases (Chapter 4), thus complementing previous work documenting de-glacial warming prior to atmospheric CO_2 forcing (Clark et al., 2004; Stott et al., 2007; Tachikawa et al., 2009). The paleo data discussed within Chapter 4 is consistent with two broad hypotheses for the termination of the eLGM throughout the Southern Ocean; (1) a de-stratification of the Southern Ocean, and (2) the injection of a fresh water perturbation from the 19 kyr melt water pulse (MWP).

Paleo fSST suggest ocean temperatures increased during the eLGM at ~20 kyr BP, leading the subsequent declines in wSIC (Chapter 4). Evidence from the southwestern Pacific sector of the Southern Ocean also suggests warming occurred prior to the termination of the eLGM due to a breakdown of Southern Ocean stratification (Putnam et al., 2013). Climate models based on the data from Putnam et al. (2013) suggest the de-stratification of the Southern Ocean lead to a temperature rise of ~3.6°C between the New Zealand LGM and the ACR (Chapter 3). A net poleward migration of the STF, as well as increased atmospheric CO_2 and upwelling south of the PF, also occurred between the LGM and ACR (Putnam et al., 2013).

The paleo fSST increases, which lead the subsequent wSIC declines (Chapter 4), are supportive of an eLGM termination that could also be attributable to the 19 kyr MWP. The 19 kyr MWP provided a fresh water perturbation that reduced NADW formation and AMOC circulation, leading to a compensatory warming of the tropical Atlantic and Southern Ocean via the bipolar see-saw (Putnam et al., 2013).

***6.1.4** AIM 4: To examine the utility of diatom abundances as a proxy for the specific sea-surface height (SSH) signature associated with each of the Southern Ocean fronts.*

Chapter 5 examined the potential of diatom relative abundances to provide a proxy for the physical SSH signature of Southern Ocean fronts. Estimation of the past migration of Southern Ocean fronts has been largely based on the use of paleo SST estimates to track the SST 'signature' of a given oceanic front (e.g. De Deckker et al., 2012; Romero et al., 2015). However, tying the presence of a front to a certain SST signature can be misleading (Graham et al., 2012; Kohfeld et al., 2013). The SST signatures of the Southern Ocean fronts varies both zonally and horizontally (Kostianoy et al., 2004; Kohfeld et al., 2013), hence assuming a constant SST signature for each front during the eLGM, and using this SST signature to track the paleo position of Southern Ocean fronts, may not be valid. Therefore, in Chapter 5 a proxy for the SSH signature of the Polar Fronts southern branch (PF-S) using the diatom database of Abbott (1973) was proposed and applied.

6.1.4.1 Use of diatoms as a proxy for the sea-surface height signature for the southern branch of the Polar Front

In Chapter 5 the application of HOF species-response models identified a significant association between the relative abundance of five diatom species (*Fragilariopsis kerguelensis*, *Thalassionema nitzschioides*, *Thalassiosira lentiginosa*, *Thalassiothrix antarctica* and *Fragilariopsis separanda)* and the mean annual monthly presence of the PF-S determined from SSH data. Previous research had already established that the abundance pattern of these diatoms

is associated with the presence of the PF/PFZ in various sectors of the Southern Ocean in the modern era: within the southeast Pacific (Esper et al., 2010), Pacific (Wolf et al., 2014; Grigorov et al., 2014) Indian (Crosta et al., 2005; Mohan et al., 2006), Atlantic (Crosta et al., 2005), south Atlantic (Kemp et al., 2010; Romero et al., 2015) and east Atlantic (Fischer et al., 2002). Importantly, Esper et al. (2010) suggested that the association between *Fragilariopsis separanda*, *Thalassiothrix antarctica* and *Thalassionema nitzschioides* and PF/PFZ may extend beyond certain sectors of the Southern Ocean. Thus, the proposed diatom proxy for the presence of the PF-S may be applicable within other sectors of the Southern Ocean.

6.1.4.2 Summary of the MAT technique used to estimate the paleo position of the PF-S SSH signature

Analysis on the Abbott (1973) database examined the utility of MAT and GAM for estimating the paleo presence of the PF-S SSH signature based on a diatom proxy. The HOF analysis applied on the Abbott (1973) database suggests there was not a unimodal species-response relationship between diatom relative abundances and the average annual monthly presence of the PF-S SSH. Therefore, methods that assume a unimodal species-response relationship, namely WA PLS, were not applied. The issues surrounding the IKTF model, such as the inefficiency of PCA as a method for prediction, as well as the difficulties associated with interpreting a model that is based on PCA (Juggins and Birks, 2012; Dürrenmatt and Gujer, 2012; Chapter 2), prevented an application of the IKTF model.

Application of GAM was deemed unsuitable for the Abbott (1973) database. Application of a GAM as an inverse model, using diatom relative abundance as the predictor variable, revealed

that only *Fragilariopsis separanda* had a statistically significant association with the PF-S. Additionally, as GAMs are unreliable when extrapolated and cannot handle the bounded nature of the response variable (average annual monthly presence of the PF-S SSH signature), the application of a GAM was deemed inappropriate.

Therefore, the use of MAT was proposed for estimating the paleo presence of the PF-S SSH signature. The MAT model was applied to only those diatom species that had a significant species-response relationship with the PF-S SSH signature, using a squared chord distance to select the five closest analogues (Chapter 5).

6.1.4.3 A summary of the paleo estimates for the PF-S SSH signature during the LGM

Recent research suggested the eLGM PF was further north of its modern day position in all sectors of the Southern Ocean (Ling Ho et al., 2012; Shetye et al., 2014; Gottschalk et al., 2015). However, there remains considerable uncertainty within the literature regarding the potential migration of the Southern Ocean fronts and/or westerly wind field (Shulmeister et al., 2004; MARGO project members, 2009; Kohfeld et al., 2013). Analysis of the Abbott database, along with the development and application of MAT, has helped to resolve the eLGM climatic changes that may be associated with the latitudinal migration of the ACC and/or westerly wind field (Chapter 5). The results presented within Chapter 5 suggest the PF-S migrated north to 54°S, along a transect at 145°E, during the eLGM and (potentially) during the ACR. The northern migration of the PF-S was accompanied by an expansion of wSIC (Chapter 4), as well as a northern migration of the SAF and STF during the eLGM period (Neil et al., 2004; De Deckker et al., 2012).

The northern migration of the PF-S also indicates a northern migration of the westerly wind field, which in turn drove the northern migration of the ACC and PF (Graham et al., 2012). The equatorward migration of the westerly winds, PF and ACC occurred prior to a northern expansion of the winter sea-ice field during the eLGM (Chapter 5). During the termination of the eLGM, the PF-S migrated south to its modern day position. It was suggested that, concomitant with a southern migration of the PF-S, the STF migrated south, increasing atmospheric CO_2, breaking down the stratification of the Southern Ocean, and thus driving the termination of the southern hemisphere eLGM (Putnam et al., 2010).

6.2 Conclusions: Paleoceanography of the southwest Pacific sector of the Southern Ocean from the eLGM through to the Holocene

The expansion of wSIC throughout the southwest Pacific occurred at ~35 kyr BP (Chapter 4), before the northern hemisphere LGM, dated between 26.5 and 18 kyr BP (Clark et al., 2009; Negre et al., 2010). Southwest Pacific wSIC reached a latitude of 54°S (Chapter 4), corroborating independent data that suggested that eLGM sea ice had extended to Macquarie Island, also situated at 54°S (Fraser et al. 2009) (Figure 1c). Stratification of the Southern Ocean occurred in response to atmospheric cooling under orbital forcing. In turn, wSIC and the duration of the winter season at high latitudes increased. The northward export of sea ice, and the subsequent sea-ice melt, further increased stratification of the Southern Ocean (Putnam et al., 2010).

Modifications to the global thermohaline circulation were also import for driving the onset of the eLGM climate. NADW cooled due, in part, to insolation forcing, which lead to the development of saltier AABW and a salinity-driven stratification of the deep ocean (Adkins, 2013; Insua et al.,

2014). A stratified deep ocean hindered the upwelling of warmer deep waters (Putnam et al., 2010) and acted as an efficient trap for atmospheric CO_2 (Adkins, 2013; Ronge et al. 2015) (Figure 1d). During the eLGM, fresh water input into AAIW from the melting of sea ice hampered the downward expansion of AAIW. The interface between AAIW and upper circumpolar deep water (UCDW) was displaced toward the ocean surface within the southwest Pacific, subsequently increasing the glacial carbon pool (Ronge et al. 2015) (Figure 1d).

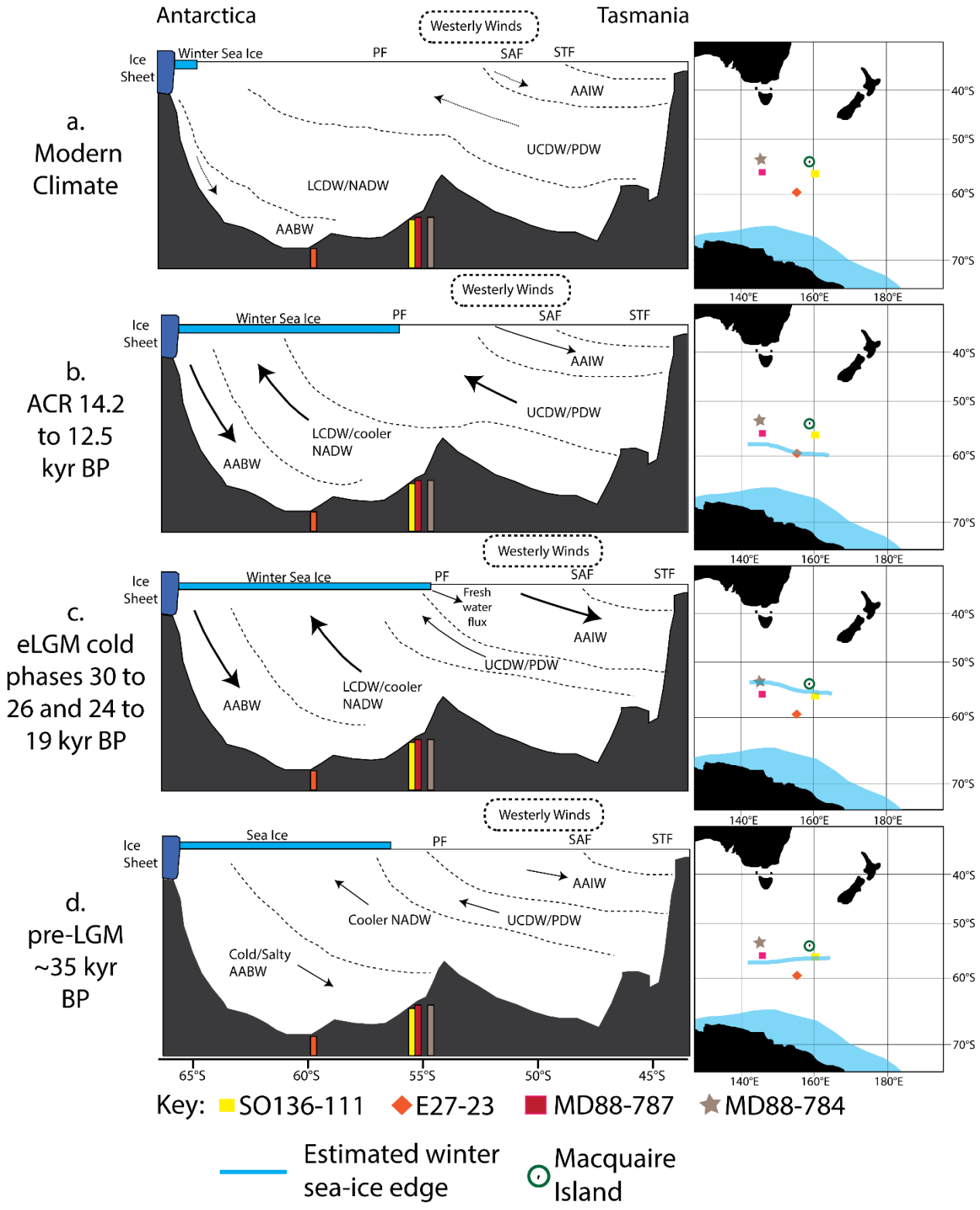
Antarctica
Tasmania
Westerly Winds
Ice Sheet
Winter Sea Ice
PF
SAF
STF
AAIW
UCDW/PDW
LCDW/NADW
AABW
a. Modern Climate
LCDW/cooler NADW
b. ACR 14.2 to 12.5 kyr BP
Fresh water flux
c. eLGM cold phases 30 to 26 and 24 to 19 kyr BP
Sea Ice
Cooler NADW
Cold/Salty AABW
d. pre-LGM ~35 kyr BP
65°S
60°S
55°S
50°S
45°S
40°S
50°S
60°S
70°S
140°E
160°E
180°E
Key: SO136-111 E27-23 MD88-787 MD88-784
Estimated winter sea-ice edge
Macquaire Island

Figure 1. A schematic summarizing past oceanic and atmospheric changes, relative to the (a) modern ocean conditions, (b) the ACR, (c) eLGM cold phases, and (d) the pre-eLGM. The modern state of the ocean shown in panel a is based on the World Ocean Circulation Experiment repeat section SR3 transect (Rintoul and Bullister, 1999). All panels have been adapted from Bostock et al. (2013) and Ronge et al. (2015). The average modern winter sea-ice area from 1979 to 2000 is indicated by the light blue shading (sea-ice data was sourced from the National Snow and Ice Data Centre (NSIDC)/Comiso, (2000)). The position of the modern day westerly wind field is based on Varma et al. (2012).The inferred winter sea-ice edge during the eLGM cold phases and the ACR are highlighted by the dashed blue line. The direction of flow for each water mass is indicated by the black arrows. Thicker arrows indicate the increased influence (defined as an increase in water transport and/or a reduction in water temperature) of given water masses relative to the modern day. The positions of the marine sediment cores used within this thesis are identified *viz.* SO136-111 (56°S), E27-23 (59°S), MD88-787 (56°S), MD88-784 (54°S). Panel d outlines the key oceanic changes that may have occurred prior to the LGM (following Adkins, 2013).

At the commencement and termination of the eLGM there were two distinct periods of wSIC expansion and fSST reduction (Chapter 4). The eLGM expansion of wSIC resulted from a northern migration of the ACC and PF (Verleye and Louwye, 2010; Martinson, 2012; Chapter 5) (Figure 1c). The climate then warmed during the mid eLGM, which was expressed as AIM 2. The wSIC reduction and fSST increase, identified here during AIM 2, can be considered an expression of the bipolar see-saw (Dürkop et al., 2008; Newnham et al., 2012).

The fSST increase and wSIC decline pre-dated the rise in atmospheric CO_2, precluding CO_2 forcing as the main driver for the eLGM termination. Rather, eLGM termination occurred in response to a breakdown of Southern Ocean stratification, a poleward shift of the westerly wind field and increased upwelling south of the PF (Putnam et al., 2013). The data from Chapter 4 also suggests that the termination of the eLGM may have resulted from the 19 kyr melt water pulse (MWP). The 19 kyr MWP reduced NADW formation, and slowed the AMOC, producing a compensatory warming of the Southern Ocean. As fSST increased, sea ice retreated and exposed

more open ocean, in turn increasing the absorption of solar radiation, subsequently increasing fSST (Putnam et al., 2013).

The transition from the eLGM into the Holocene interglacial period was briefly slowed by a period of climatic cooling, known as the ACR (Stenni et al., 2001; Divine et al., 2010; Chapter 3; Chapter 5). The ACR has been documented throughout the southern hemisphere (Stenni et al., 2001; Weber et al., 2014; Recasens et al. 2015; Chapter 3), hence the data presented within Chapter 3 is most consistent with hypotheses that explain hemisphere-scale cooling during the ACR. The ACR wSIC increase, and fSST decline (Chapter 4), resulted from MWP-1A, which has been shown to increase Southern Ocean sea-ice cover within models (Weber et al., 2014), and/or from a northern migration of the ACC and PF (Manoj et al., 2013, Chapter 5) (Figure 1b).

Finally, Chapter 3 detailed the first paleo wSIC data revealing an increase in wSIC during the early and mid-Holocene throughout the southwest Pacific. The expansion of Holocene winter sea ice was the product of a more northerly positioning of the westerly wind belt (Shevenell and Kennett, 2002; Mayewski et al., 2004; Shevenell et al., 2011; Etourneau et al., 2013). The stronger and more northerly westerly winds isolated and cooled Antarctica (Moros et al., 2009), driving the expansion of Holocene winter sea-ice extent to ~59°S (Chapter 3).

The Holocene sea-ice records between the Atlantic and Pacific sectors of the Southern Ocean were not consistent. ACR sea-ice expansion throughout the Atlantic was no greater than estimated Holocene sea-ice expansion. The southwest Pacific, however, had a greater expansion of sea ice during the ACR compared with the Holocene (Figure 1a and b). The contrasting oceanography between these two regions provides the most likely explanation for the contrasting paleo sea-ice records between the Atlantic and southwest Pacific. An intensified and expanded

Weddell Sea gyre transports Atlantic sea ice north (Bianchi and Gersonde, 2004; Divine et al., 2010), whilst the Pacific sector is not under the influence of any similar gyre system (Ackley 1981, Parkinson, 1992).

6.3 Recommendations for future research

The utility of diatoms as a proxy for wSIC, fSST and Southern Ocean fronts, as well as the future study of Southern Ocean paleoceanography based on diatom records, requires a merger between the databases currently in independent use by Crosta et al. (2004) and Esper and Gersonde (2014). The merged database should then be analyzed using model boosting that incorporates spatial autocorrelation and non-stationarity (Hothorn et al., 2011) between diatom and winter sea-ice correlations between the differing sectors of the Southern Ocean. A merged database will also improve our understanding of the southern circumpolar distribution of diatoms. Importantly, a merged database would also have an improved spatial representativeness of the Southern Ocean, an essential criteria for the development of diatom-based sea-ice proxies for estimating circum-Antarctic paleo sea ice. The database of Esper and Gersonde (2014) was not availiable for this thesis, hance all analysis was restricted to the database used by Crosta et al. (2004).

Whist the distribution of marine diatoms throughout the Southern Ocean has been largely established (Armand et al., 2005; Esper et al., 2010), a thorough understanding of the southern circumpolar distribution is currently hindered by a lack of data from the Pacific sector of the Southern Ocean (Esper et al., 2010). To fully elucidate the circumpolar distribution and environmental preferences of marine diatoms, and to better understand the utility of diatoms as a proxy for past climate, further sampling of the Pacific sector of the Southern Ocean is required.

In particular, additional sea floor surface samples are required from the summer and marginal sea-ice zones to establish a diatom training set that is more representative of the sea-ice environment. Wider and increased sample coverage may reduce the predictive error of the statistical models that are used to study the associations between diatom abundances and sea-ice concentrations. Elucidating paleo summer sea-ice concentrations remains difficult, and is unlikely to be resolved with a fossil diatom proxy (Gersonde et al., 2005). The study of paleo summer sea-ice concentrations needs to focus on the development of alternative proxies, such as halogens and highly branched isoprenoids.

Regarding the utility of diatoms as a proxy for the SSH signature of Southern Ocean fronts, in particular the PF, utilization of a larger diatom database will clearly improve upon the analysis, methodology and preliminary findings presented within Chapter 5. It is essential that additional samples from all sectors of the Southern Ocean are utilized as part of any future effort aimed at establishing a reliable diatom proxy for the SSH signature of Southern Ocean fronts. In particular, additional samples need to be obtained from the PFZ. Once additional samples have been collected there is a need to re-evaluate MAT and identify the most appropriate statistical model to use when estimating the paleo presence of the PF-S SSH signature.

Estimating the paleo position of the PF-S, as well as the PF-M and PF-N, SSH signatures requires additional marine sediment cores situated along a transect extending both north and south of the modern day PFZ. The extra cores would allow paleoceanographers to better constrain the latitudinal migration of the PFZ over glacial to interglacial stages.

References

Abbott, W., (1973), Vertical and lateral patterns of diatomaceous ooze found between Australia and Antarctica, 136 pp, University of South Carolina, Columbia.

Ackley, S.F., (1981), A review of sea-ice weather relationships in the Southern Hemisphere. In *Sea level, Ice and Climate change*, (Editor Allison, I.) IAHS publication, 131 pp 127-159.

Adkins, J. F., (2013), The role of deep ocean circulation in setting glacial climates, *Palaeoceanography*, 28, 539-561.

Armand, L. K., Crosta, X., Romero, O., Pichon, J.J., (2005), The biogeography of major diatom taxa in Southern Ocean sediments: 1. Sea ice related species, *Palaeogeography, Palaeoclimatology, Palaeoecology*, 223, 93– 126.

Bennett, N. D., Croke, B.F.W., Guariso, G., Guillaume, J.H.A., Hamilton, S.H., Jakeman, A.J., Marsili-Libelli, S., Newham, L.T.H., Norton, J.P., Perrin, C., Pierce, S.A., Robson, B., Seppelt. R., Voinov, A.A., Fath, B.D., Andreassian, V., (2013), Characterising performance of environmental models, *Environmental Modelling and Software*, 40, 1-20.

Bianchi, C., and Gersonde, R., (2004), Climate evolution at the last deglaciation: the role of the Southern Ocean, *Earth and Planetary Science Letters*, 228, 407– 424.

Bostock, H., Hayward, B.W., Neil, H., Sabaa, A.T., and Scott, G.H., (2015), Changes in the position of the Subtropical Front south of New Zealand since the last glacial period, *Palaeoceanography*, DOI: 10.1002/2014PA002652.

Bostock, H. C., Barrows, T.T., Carter, L., Chase, Z., Cortese, G., Dunbar, G.B., Ellwood, M., Hayward, B., Howard, W., Neil, H.L., Noble, T.L., Mackintosh, A., Moss, P.T., Moy, A.D., White, D., Williams, M.J.M., and Armand, L.K., (2013), A review of the Australia and New Zealand sector of the Southern Ocean over the last 30 ka (Aus-INTIMATE project), *Quaternary Science Reviews*, http://dx.doi.org/10.1016/j.quascirev.2012.1007.1018.

Clark, P. U., Dyke, A.S., Shakun, J.D., Carlson, A.E., Clark, J., Wohlfarth, B., Mitrovica, J.X., Hostetler, S.W., and McCabe, A.M., (2009), The Last Glacial Maximum, *Science*, 325, 710-714.

Clark, P. U., McCabe, A.M., Mix, A.C., and Weaver, A.J., (2004), Rapid Rise of Sea Level 19,000 Years Ago and Its Global Implications, *Science*, 304, DOI:10.1126/science.1094449.

Comiso, J., (2000), Bootstrap Sea Ice Concentrations from Nimbus-7 SMMR and DMSP SSM/I-SSMIS.

Crosta, X., Pichon, J-J., and Burckle, L.H., (1998), Application of modern analog technique to marine Antarctic diatoms: Reconstruction of maximum sea-ice extent at the Last Glacial Maximum, *Palaeoceanography*, 13, 284-297.

Crosta, X., Romero, O., Armand, L.K., and Pichon, J.J., (2005), The biogeography of major diatom taxa in Southern Ocean sediments: 2. Open ocean related species, *Palaeogeography, Palaeoclimatology, Palaeoecology*, 223, 66– 92.

Crosta, X., Sturm, A., Armand, L., and Pichon, J.-J., (2004), Late Quaternary sea ice history in the Indian sector of the Southern Ocean as recorded by diatom assemblages, *Marine Micropaleontology*, 50, 209-223.

Cunningham, W. L., and Leventer, A., (1998), Diatom assemblages in surface sediments of the Ross Sea: relationship to present oceanographic conditions, *Antarctic Science*, 10, 134-146.

De Deckker, P., Moros, M., Perner, K., and Jansen, E., (2012), Influence of the tropics and southern westerlies on glacial interhemispheric asymmetry, *Nature Geoscience*, 5.

Divine, D. V., Koç, N., Isaksson, E., Nielsen, S., Crosta, x., and Godtliebsen, F., (2010), Holocene Antarctic climate variability from ice and marine sediment cores: Insights on ocean–atmosphere interaction, *Quaternary Science Reviews*, 29, 303–312.

Dürkop, A., Holbourn, A., Kuhnt, W., Zuraida, R., Andersen, N., and Grootes, P.M., (2008), Centennial-scale climate variability in the Timor Sea during Marine Isotope Stage 3, *Marine Micropaleontology*, 66, 208–221.

Dürrenmatt, D. J., and Gujer, W., (2012), Data-driven modelling approaches to support wastewater treatment plant operation, *Environmental Modelling and Software*, 30, 47-56.

Esper, O., and Gersonde, R., (2014), New tools for the reconstruction of Pleistocene Antarctic sea ice., *Palaeogeography, Palaeoclimatology, Palaeoecology*, 399, 260–283.

Esper, O., Gersonde, R., Kadagies, N., (2010), Diatom distribution in southeastern Pacific surface sediments and their relationship to modern environmental variables, *Palaeogeography, Palaeoclimatology, Palaeoecology*, 27, 1-27.

Etourneau, J., Collins, L.G., Willmott, V., Kim, J.H., Barbara, L., Leventer, A., Schouten, S., Sinninghe Damsté, J.S., Bianchini, A., Klein, V., Crosta, X., and Massé, G., (2013), Holocene climate variations in the western Antarctic Peninsula: evidence for sea ice extent predominantly controlled by changes in insolation and ENSO variability, *Climate of the Past*, 9, 1431–1446.

Fischer, G., Gersonde, R., and Wefer, G., (2002), Organic carbon, biogenic silica and diatom fluxes in the marginal winter sea-ice zone and in the Polar Front Region: interannual variations and differences in composition, *Deep-Sea Research II*, 49, 1721–1745.

Fraser, C. I., Nikula, R., Spencer, H.G., and Waters, J.M., (2009), Kelp genes reveal effects of subantarctic sea ice during the Last Glacial Maximum, *PNAS*, 106, 3249-3253.

Gottschalk, J., Skinner, L.C., and Waelbroeck, C., (2015), Contribution of seasonal sub-Antarctic surface water variability to millennial-scale changes in atmospheric CO_2 over the last deglaciation and Marine Isotope Stage 3, *Earth and Planetary Science Letters*, 411, 87-99.

Graham, R. M., de Boer, A.M., Heywood, K.J., Chapman, M.R., and Stevens, D.P., (2012), Southern Ocean fronts: Controlled by wind or topography?, *Journal of Geophysical Research*, 117, DOI:10.1029/2012JC007887.

Grigorov, I., Rigual-Hernandez, A.S., Honjo, S., Kemp, A.E.S., and Armand, L.K., (2014), Settling fluxes of diatoms to the interior of the Antarctic circumpolar current along 170°W, *Deep-Sea Research 1*, 93, 1-13.

Hothorn, T., Müller, J., Schröder, B., Kneib, T., and Brandl, R., (2011), Decomposing environmental, spatial, and spatiotemporal components of species distribution. *Ecological Monographs*, 81, 329- 347.

Insua, T. L., Spivack, A.J., Graham, D., D'Hondt, S., and Moran, K., (2014), Reconstruction of Pacific Ocean bottom water salinity during the Last Glacial Maximum, *Geophysical Research Letters*, 41, DOI:10.1002/2014GL059575.

Juggins, S., and Birks, J.B., (2012), Quantitative Environmental Reconstructions from Biological Data, in Tracking Environmental Change Using Lake Sediments, edited by H. J. B. Birks, Lotter, A.F., Jugins, S., and Smol, J.P., pp. 431-494, Springer Science and Business Media.

Kemp, A. E. S., Grigorov, I., Pearce, R.B., and Naveira Garabato, A.C., (2010), Migration of the Antarctic Polar Front through the mid-Pleistocene transition: evidence and climatic implications, *Quaternary Science Reviews*, 29, 1993-2009.

Kohfeld, K. E., Graham, R.M., de Boer, A.M., Sime, L.C., Wolff, E.W., Le Quéré, C., and Bopp, L., (2013), Southern Hemisphere Westerly Wind Changes during the Last Glacial Maximum: Paleo-data Synthesis, *Quaternary Science Reviews*, 68, 76-95.

Kostianoy, A. G., Ginzburg, A.I., Frankignoulle, M., and Delille, B., (2004), Fronts in the Southern Indian Ocean as inferred from satellite sea surface temperature data, *Journal of Marine Systems*, 45, 55– 73.

Legendre, P., and Birks, H.J.B., (2012), From Classical to Canonical Ordination, in Tracking Environmental Change Using Lake Sediments, edited by H. J. B. Birks, Lotter, A.F., Jugins, S., and Smol, J.P., pp. 201-248, Springer Science and Business Media.

Ling Ho, S., Mollenhauer, G., Lamy, F., Martínez-Garcia, A., Mohtadi, M., Gersonde, R., Hebbeln, D., Nunez-Ricardo, S., Rosell-Melé, A., and Tiedemann, R., (2012), Sea surface temperature variability in the Pacific sector of the Southern Ocean over the past 700 kyr, *Palaeoceanography*, 27, DOI:10.1029/2012PA002317.

Manoj, M. C., Thamban, M., Sahana, A., Mohan, R., and Mahender, K., (2013), Provenance and temporal variability of ice rafted debris in the Indian sector of the Southern Ocean during the last 22,000 years, *Journal of Earth System Science*, 122, 491–501.MARGO Project Members, (2009), Constraints on the magnitude and patterns of ocean cooling at the Last Glacial Maximum, *Nature Geoscience*, 2, DOI: 10.1038/NGEO1411.

Martinson, D. G. (2012), Antarctic circumpolar current's role in the Antarctic ice system: An overview, *Palaeogeography, Palaeoclimatology, Palaeoecology*, 335-336, 71–74.

Mayewski, P. A., Rohling, E.E., Stager, J.C., Karlén, W., Maasch, K.A., Meeker, L.D., Meyerson, E.A., Gasse, F., van Kreveld, S., Holmgren, K., Lee-Thorp, J., Rosqvist, G., Rack, F., Staubwasser, M., Schneider, R.R., and Steig, E.J., (2004), Holocene climate variability, *Quaternary Research*, 62, 243– 255.

McCave, I. N., Crowhurst, S.J., Kuhn, G., Hillenbrand, C.-D., and Meredith, M.P., (2014), Minimal change in Antarctic Circumpolar Current flow speed between the last glacial and Holocene, *Nature Geoscience*, 7, DOI: 10.1038/NGEO2037.

Mohan, R., Shanvas, S., Thamban, M., and Sudhakar, M., (2006), Spatial distribution of diatoms in surface sediments from the Indian sector of Southern Ocean, *Current Science*, 91, 1495-1502.

Moros, M., De Deckker, P., Jansen, E., Perner, K., Telford, R.J., (2009), Holocene climate variability in the Southern Ocean recorded in a deep-sea sediment core off South Australia, *Quaternary Science Reviews*, 28, 1932–1940.

Negre, C., Zahn, R., Thomas, A.L., Masqué, P., Henderson, G.M., Martínez-Méndez, G., Hall, I.R., and Mas, J.L., (2010), Reversed flow of Atlantic deepwater during the Last Glacial Maximum, *Nature*, 468, DOI:10.1038/nature09508.

Neil, H. L., Carter, L., and Morris, Y., (2004), Thermal isolation of Campbell Plateau, New Zealand, by the Antarctic Circumpolar Current over the past 130 kyr, *Palaeoceanography*, 19, DOI:10.1029/2003PA000975.

Newnham, R. M., Lowe, D.J., Giles, T., and Alloway, B.V., (2007), Vegetation and climate of Auckland, New Zealand, since ca. 32 000 cal. yr ago: support for an extended LGM, *Journal of Quaternary Science*, 22, 517–534.

Newnham, R. M., Vandergoes, M.J., Sikes, E., Carter, L., Wilmshurst, J.M., Lowe, D.J., McGlone, M.S., and Sandiford, A., (2012), Does the bipolar seesaw extend to the terrestrial southern mid-latitudes?, *Quaternary Science Reviews*, 36, 214-222.

Olguín, H. F., and Alder, V.A., (2011), Species composition and biogeography of diatoms in Antarctic and Subantarctic (Argentine shelf) waters (37–76°S), *Deep-Sea Research II*, 58, 139–152.

Parkinson, C.L., (1992), Interannual variability of monthly Southern Ocean sea ice distributions, *Journal of Geophysical Research*, 97, 5349-5363.

Petherick, L., McGowan, H., and Moss, P., (2008), Climate variability during the Last Glacial Maximum in eastern Australia: evidence of two stadials?, *Journal of Quaternary Science*, 23, 787–802.

Putnam, A. E., Denton, G.H., Schaefer, J.M., Barrell, D.J.A., Andersen, B.G., Finkel, R.C., Schwartz, R., Doughty, A.M., Kaplan, M.R., and Schlüchter, C., (2010), Glacier advance in southern middle-latitudes during the Antarctic Cold Reversal, *Nature Geoscience*, 3, DOI: 10.1038/NGEO962.

Putnam, A. E., Schaefer, J.M., Denton, G.H., Barrell, D.J.A., Birkel, S.D., Andersen, B.G., Kaplan, M.R., Finkel, R.C., Schwartz, R., and Doughty, A.M., (2013), The Last Glacial Maximum at 44°S documented by a 10Be moraine chronology at Lake Ohau, Southern Alps of New Zealand, *Quaternary Science Reviews*, 62, 114-141.

Recasens, C., Ariztegui, D., Maidana, N.I., Zolitschka, B., and the PASADO Science Team., (2015), Diatoms as indicators of hydrological and climatic changes in Laguna Potrok Aike (Patagonia) since the Late Pleistocene, *Palaeogeography, Palaeoclimatology, Palaeoecology*, 417, 309–319.

Reeves, J. M., Barrows, T.T., Cohen, T.J., Kiem, A.S., Bostock, H.C., Fitzsimmons, K.E., Jansen, J.D., Kemp, J., Krause, C., Petherick, L., Phipps, S.J., and OZ-INTIMATE Members (2013), Climate variability over the last 35,000 years recorded in marine and terrestrial archives in the Australian region: an OZ-INTIMATE compilation, *Quaternary Science Reviews*, 74, 21-34.

Renssen, H., Goosse, H., Crosta, X., and Roche, D.M., (2010), Early Holocene Laurentide Ice Sheet deglaciation causes cooling in the high-latitude Southern Hemisphere through oceanic teleconnection, *Paleoceanography*, 25, doi:10.1029/2009PA001854.

Rintoul, S. R., and Bullister, J.L., (1999), A late winter hydrographic section from Tasmania to Antarctica, *Deep-Sea Research I*, 46, 1417-1454.

Romero, O. E., Kim, J.H., Bárcena, M.A., Hall, I.R., Zahn, R., and Schneider, R., (2015), High-latitude forcing of diatom productivity in the southern Agulhas Plateau during the past 350kyr, *Paleoceanography*, 30, DOI:10.1002/2014PA002636.

Ronge, T. A., Steph, S., Tiedemann, R., Prange, M., Merkel, U., Nürnberg, D., and Kuhn, G., (2015), Pushing the boundaries: Glacial/interglacial variability of intermediate and deep waters in the southwest Pacific over the last 350,000 years, *Paleoceanography*, 30, DOI:10.1002/2014PA002727.

Shetye, S. S., Mohan, R., and Nair, A., (2014), Latitudinal shifts in the Polar Front in Indian sector of the Southern Ocean: evidences from silicoflagellate assemblage, *Geosciences Journal*, 18, 241−246.

Shevenell, A. E., and Kennett, J.P., (2002), Antarctic Holocene climate change: A benthic foraminiferal stable isotope record from Palmer Deep, *Paleoceanography*, 17, DOI: 10.1029/2000PA000596.

Shevenell, A. E., Ingalls, A.E., Domack, E.W., and Kelly, C., (2011), Holocene Southern Ocean surface temperature variability west of the Antarctic Peninsula, *Nature*, 470, 250-254.

Shulmeister, J., Goodwin, I., Renwick, J., Harle, K., Armand, L., McGlone, M.S., Cook, E., Dodson, J., Hesse, P.P., Mayewski, P., and Curran, M., (2004), The Southern Hemisphere westerlies in the Australasian sector over the last glacial cycle: a synthesis, *Quaternary International*, 118–119, 23–53.

Stenni, B., Masson-Delmotte, V., Johnsen, S., Jouzel, J., Longinelli, A., Monnin, E., Röthlisberger, R., and Selmo, E., (2001), An Oceanic Cold Reversal During the Last Deglaciation, *Science*, 293, 2074-2077.

Stephens, T., Atkin, D., Augustinus, P., Shane, P., Lorrey, A., Street-Perrott, A., Nilsson, A., and Snowball, I., (2012), A late glacial Antarctic climate teleconnection and variable Holocene seasonality at Lake Pupuke, Auckland, New Zealand, *Journal of Paleolimnology*, 48, 785–800.

Stott, L., Timmermann, A., and Thunell, R., (2007), Southern Hemisphere and Deep-Sea Warming Led Deglacial Atmospheric CO2 Rise and Tropical Warming, *Science*, 318, 435-438.

Tachikawa, K., Vidal, L., Sonzogni, C., and Bard, E., (2009), Glacial/interglacial sea surface temperature changes in the Southwest Pacific ocean over the past 360 ka, *Quaternary Science Reviews*, 28, 1160–1170.

Taylor, F., McMinn, A., and Franklin, D., (1997), Distribution of diatoms in surface sediments of Prydz Bay, Antarctica, *Marine Micropaleontology*, 32, 209-229.

Telford, R. J., and Birks, H.J.B., (2005), The secret assumption of transfer functions: problems with spatial autocorrelation in evaluating model performance, *Quaternary Science Reviews*, 24, 2173–2179.

Varma, V., Prange, M., Merkel, U., Kleinen, T., Lohmann, G., Pfeiffer, M., Renssen, H., Wagner, A., Wagner, S., and Schulz, M., (2012), Holocene evolution of the Southern Hemisphere westerly winds in transient simulations with global climate models, *Climate of the Past*, 8, 391–402.

Verleye, T. J., and Louwye, S., (2010), Recent geographical distribution of organic-walled dinoflagellate cysts in the southeast Pacific (25–53°S) and their relation to the prevailing hydrographical conditions, *Palaeogeography, Palaeoclimatology, Palaeoecology*, 298, 319–340.

Weber, M. E., Clark, P.U., Kuhn, G., Timmermann, A., Sprenk, D., Gladstone, R., Zhang, X., Lohmann, G., Menviel, L., Chikamoto, M.O., Friedrich, T., and Ohlwein, C., (2014), Millennial-scale variability in Antarctic ice-sheet discharge during the last deglaciation, *Nature*, 510, DOI:10.1038/nature13397.

Williams, P. W., Neil, H.L., and Zhao, J.-X., (2010), Age frequency distribution and revised stable isotope curves for New Zealand speleothems: palaeoclimatic implications, *International Journal of Speleology*, 39, 99-112.

Wolf, C., Frickenhaus, S., Kilias, E.S., Peeken, I., and Metfies, K., (2014), Protist community composition in the Pacific sector of the Southern Ocean during austral summer 2010, *Polar Biology*, 37, 375-389.

List of Appendices

Appendix 2.1

The R scripts and output from the application of HOF models on the untransformed diatom relative abundance and winter sea-ice concentration data sets. The diatoms that are not listed in the output (*Fragilariopsis doliolus*, *Hemidiscus cuneiformis*, *Rhizosolenia styliformis* group, *Roperia tesselata*, *Thalassionema nitzschioides*, as well as *Thalassiosira oestrupii* including the varieties *oestrupii* and v*enrickae*) have a low abundance within the training database used for this study. Therefore, no HOF models were fitted to explain the species response relationship between each of these later diatoms and winter sea-ice concentrations. The final HOF models were chosen via bootstrapping, with the most frequently fitted model selected. Additionally, models were compared using the Alike Information Criterion. As all models are compared with a model that has no optima (which, if selected, would imply that diatom species have no response to winter sea-ice concentration), allowing one to infer that a chosen HOF model, with a given response, is significant. Importantly, GAM's were also considered in the HOF modelling used for this thesis. By including GAM within the suite of HOF models fitted, it is possible to also identify linear relationships between diatoms and winter sea-ice concentration.

```
HOFmod <- HOF(AllSIsppActualabun, SIC, family=gaussian, lim=100, bootstrap=100, test='AIC')
pick.model(HOFmod, level=0.95, test=("AIC"), gam=T, selectMethod=('bootselect'))
```

```
> pick.model(HOFmod, level=0.95, test=("AIC"), gam=T, selectMethod=('bootselect'))
   Aactinochil        Aztabgp           ChRS         Fcurta     Fcylindrus     Fkerguelens
         "IV"           "II"          "VII"          "III"           "IV"          "VII"
   Fobliquecos      Frhombica    Fritscherii     Fseparanda   Fsublinearis     Poglacialis
         "III"          "IV"            "I"          "VII"          "III"           "IV"
  Popseudodent       Rantengp    Smicrotrias    Thnitzlance       Tantargp       Tgracilis
         "II"           "IV"           "II"           "II"           "VII"          "VII"
  Tlentiginosa        Toestgp     Toliverana        Ttumida Thalassiothrix     Trichotoxon
         "VII"            "I"           "II"           "II"           "II"            "I"
```

Appendix 2.2

The R scripts used to validate the IKTF model on our training database. Also included is the output from the hold out validation of the IKTF model on the first random partition of our training database. The shapiro-wilk and KS normality tests were used to test the assumption that model errors are normally distributed. This test was applied at the 5% significance level, with p-values below 0.05 indicating that the normality assumption does not hold. The normal probability plot (labelled as a normal Q-Q plot in R) provides a visual assessment of model residuals, allowing one to assess if model residuals (and thus model errors) are normal. Normally distributed residuals will fall along the 1:1 line. The Bartels test, NCV test and runs test can be used to assess the assumption that model errors have a constant variance. Similarly, a plot of residuals versus model fitted values should show a random scatter if the assumption of constant variance holds. One cannot properly assess the significance of each predictor within a model, nor can confidence intervals be computed, if the assumption that model errors are normal and have a constant variance, does not hold. The linear regression model using overserved data as the response and fitted values as the predictor (mod <- lm(min1SI$wSIC13yrTtran~fit)) would reveal an unbiased model as having a zero intercept and a 1:1 slope.

```
pca <- princomp(min1spp, score=T)
plot(pca)
lines(bstick(pca))
trainscore <- pca$score
regCOMPone <- trainscore[,1]
regCOMPtwo <- trainscore[,2]
regCOMPthree <- trainscore[,3]
regCOMPoneQD <- (trainscore[,1])^2
regCOMPtwoQD <- (trainscore[,2])^2
regCOMPthreeQD <- (trainscore[,3])^2
model <- lm(min1SI$wSIC13yrTtran ~ regCOMPone + regCOMPtwo + regCOMPoneQD)
ncvTest(model)
sqrt(vif(model)) > 2
plot(min1SI$wSIC13yrTtran, res, pch=16)
fit <- fitted(model)
res <- residuals(model)
RMSE <- sqrt(sum(res^2)/147)
RMSE
mean(res)
proj <- predict(pca, newdata=one)
regCOMPoneVAL <- proj[,1]
regCOMPtwoVAL <- proj[,2]
regCOMPthreeVAL <- proj[,3]
pred1QUAD <- regCOMPoneVAL^2
pred2QUAD <- regCOMPtwoVAL^2
pred3QUAD <- regCOMPthreeVAL^2
model <- lm(oneSI$wSIC13yrTtran ~ regCOMPoneVAL + regCOMPtwoVAL + regCOMPthreeVAL +
pred1QUAD)
res <- residuals(model)
```

```
RMSEP <- sqrt(sum(res^2)/16)
RMSPP
model <- lm(min1SI$wSIC13yrTtran ~ regCOMPone + regCOMPtwo + regCOMPoneQD)
> summary(model)
Call:
lm(formula = min1SI$wSIC13yrTtran ~ regCOMPone + regCOMPtwo +
    regCOMPoneQD)
Residuals:
    Min      1Q  Median      3Q     Max
-3.4575 -1.0004 -0.3181  0.9126  4.7356
Coefficients:
             Estimate Std. Error t value Pr(>|t|)
(Intercept)   0.973716   0.226641   4.296 3.19e-05 ***
regCOMPone   -0.341531   0.038796  -8.803 3.96e-15 ***
regCOMPtwo   -0.194810   0.043041  -4.526 1.25e-05 ***
regCOMPoneQD -0.032160   0.008132  -3.955  0.00012 ***
---
Signif. codes:  0 ‘***’ 0.001 ‘**’ 0.01 ‘*’ 0.05 ‘.’ 0.1 ‘ ’ 1
Residual standard error: 1.496 on 143 degrees of freedom
Multiple R-squared:  0.7138,        Adjusted R-squared:  0.7078
F-statistic: 118.9 on 3 and 143 DF,  p-value: < 2.2e-16
vif(model)
  regCOMPone   regCOMPtwo regCOMPoneQD
    2.312480     1.000205     2.312684
ncvTest(model)
Non-constant Variance Score Test
Variance formula: ~ fitted.values
Chisquare = 38.5276    Df = 1     p = 5.398487e-10
plot(min1SI$wSIC13yrTtran, res, pch=16)
ncvTest(model)
Non-constant Variance Score Test
Variance formula: ~ fitted.values
Chisquare = 38.5276    Df = 1     p = 5.398487e-10
> pca <- princomp(min1spp, score=T)
> trainscore <- pca$score
> regCOMPone <- trainscore[,1]
> regCOMPtwo <- trainscore[,2]
> regCOMPthree <- trainscore[,3]
> regCOMPoneQD <- (trainscore[,1])^2
> regCOMPtwoQD <- (trainscore[,2])^2
> regCOMPthreeQD <- (trainscore[,3])^2
> model <- lm(min1SI$wSIC13yrTtran ~ regCOMPone + regCOMPtwo + regCOMPoneQD)
> res<- residuals(model)
> runs.test(res, alternative="two.sided")
                Runs Test - Two sided
data:  res
Standardized Runs Statistic = -1.4065, p-value = 0.1596
> bartels.test(res, alternative="two.sided")
                Bartels Test - Two sided
data:  res
Standardized Bartels Statistic = -0.6302, RVN Ratio = 1.896,
p-value = 0.5285
```

A plot of the IKTF models residuals (‘res’) versus the models fitted vales (‘fit).

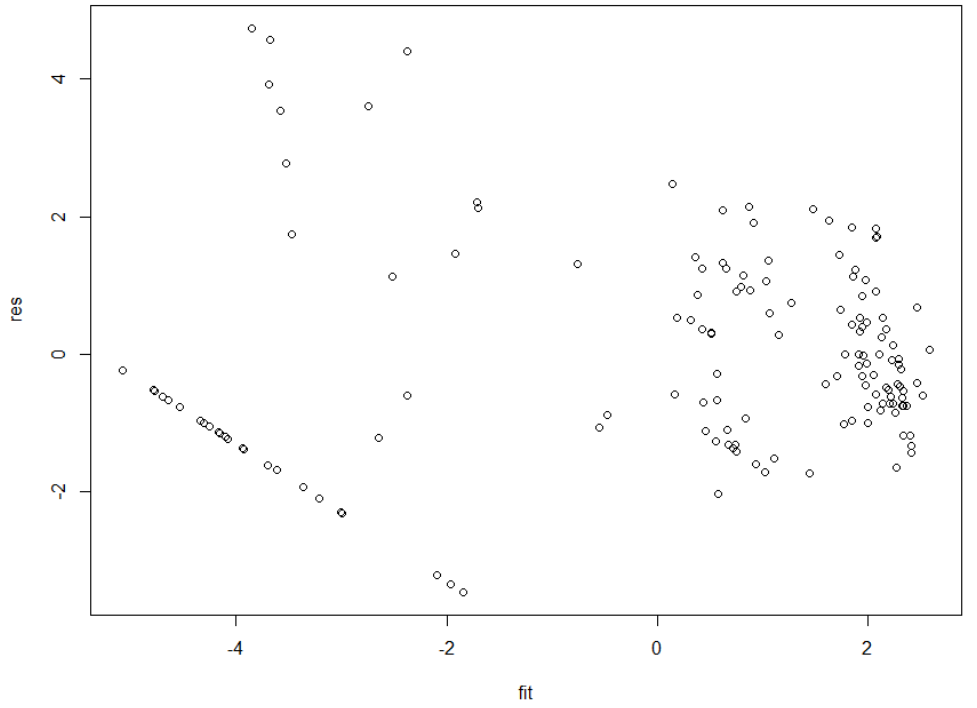

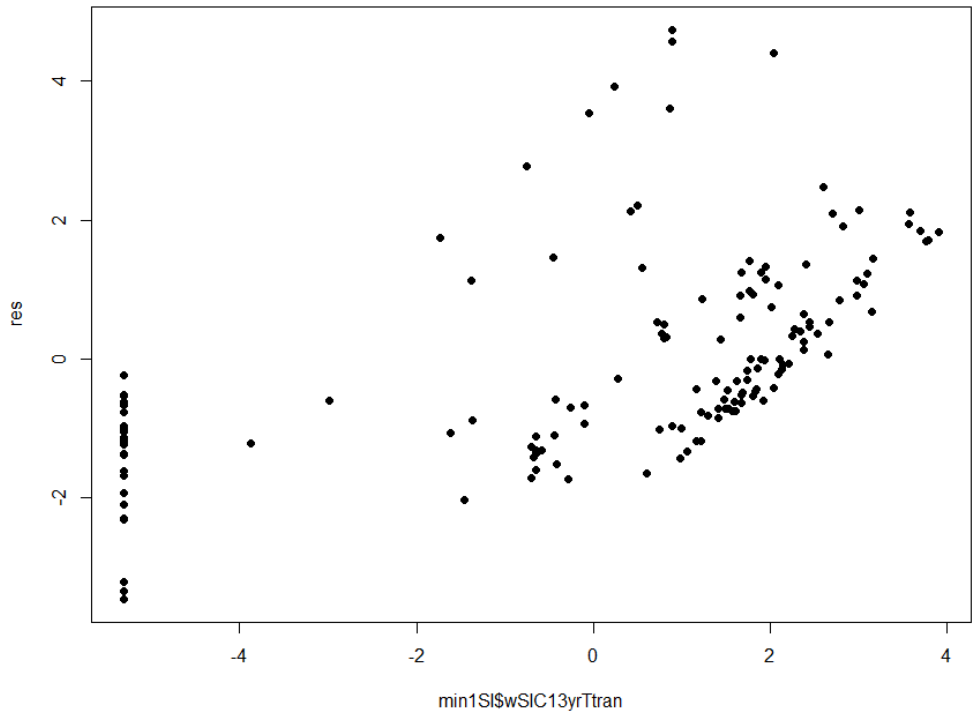

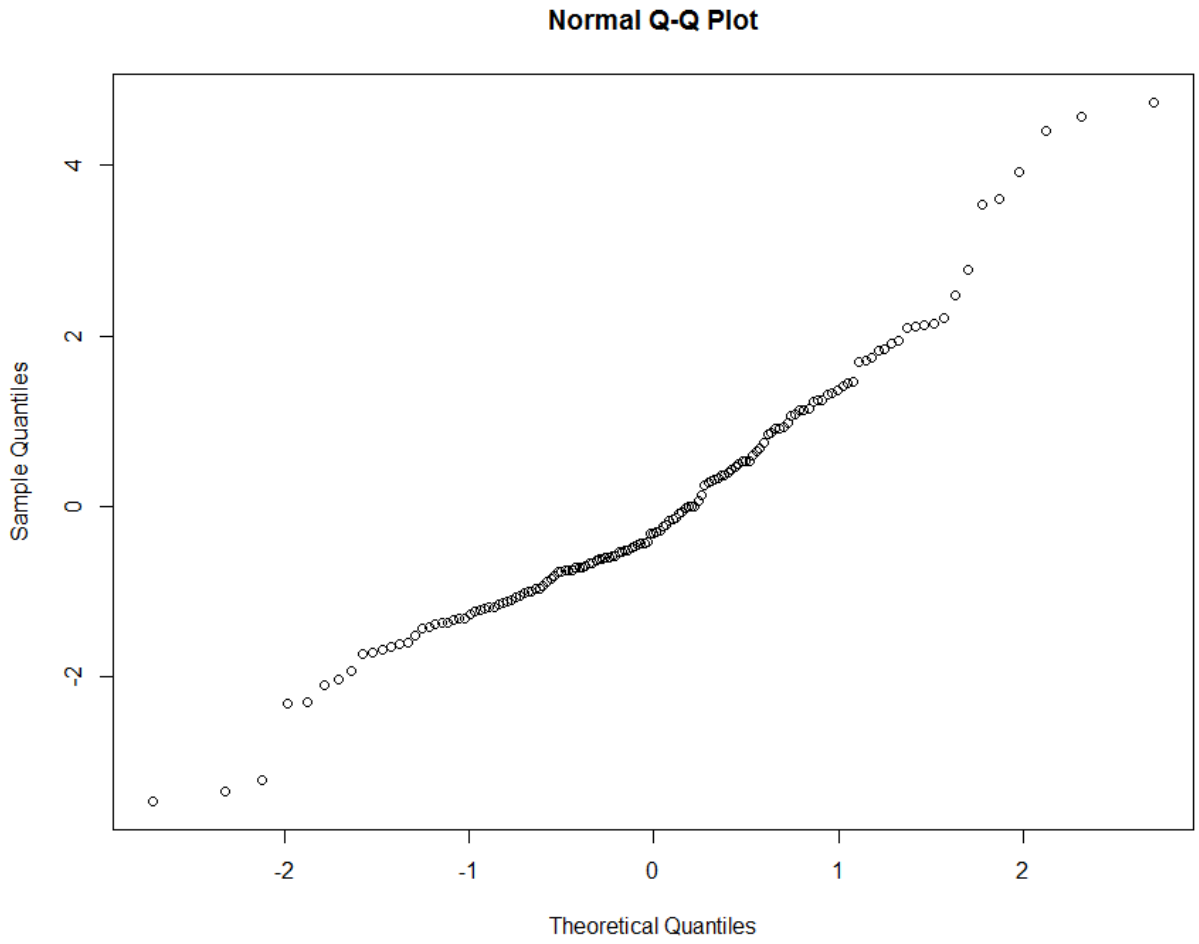


```
lillieTest(res)
Title:
 Lilliefors (KS) Normality Test
Test Results:
  STATISTIC:
    D: 0.102
  P VALUE:
    0.0007384
shapiroTest(res)
Title:
 Shapiro - Wilk Normality Test
Test Results:
  STATISTIC:
    W: 0.9564
  P VALUE:
    0.0001365
RMSE
[1] 1.47516
> mean(res)
[1] -1.186538e-17
RMSEP <- sqrt(sum(res^2)/16)
> RMSEP
[1] 1.516087
```

```
model <- lm(min1SI$wSIC13yrTtran ~ regCOMPone + regCOMPtwo + regCOMPoneQD)
fit <- fitted(model)
mod <- lm(min1SI$wSIC13yrTtran~fit)
summary(mod)
Call:
lm(formula = min1SI$wSIC13yrTtran ~ fit)

Residuals:
    Min      1Q  Median      3Q     Max
-3.4575 -1.0004 -0.3181  0.9126  4.7356

Coefficients:
             Estimate Std. Error t value Pr(>|t|)
(Intercept) -7.326e-17  1.231e-01    0.00        1
fit          1.000e+00  5.258e-02   19.02   <2e-16 ***
---
Signif. codes:  0 ‘***’ 0.001 ‘**’ 0.01 ‘*’ 0.05 ‘.’ 0.1 ‘ ’ 1

Residual standard error: 1.485 on 145 degrees of freedom
Multiple R-squared:  0.7138,        Adjusted R-squared:  0.7118
F-statistic: 361.7 on 1 and 145 DF,  p-value: < 2.2e-16
```

Appendix 2.3

The R scripts used to apply IKTF to our training database along with the scripts and results from the application of each statistical diagnostic test. The R output from the application of PCA on our training database is illustrated.

```
pca <- princomp(SO136trainAbuns, score=T)
> summary(pca)
> summary(pca)
Importance of components:
                          Comp.1    Comp.2     Comp.3     Comp.4     Comp.5     Comp.6
Standard deviation     4.8068505 2.8563423 1.71742014 1.33332576 1.09235545 0.98866984
Proportion of Variance 0.5004906 0.1767239 0.06388925 0.03850767 0.02584655 0.02117275
Cumulative Proportion  0.5004906 0.6772144 0.74110369 0.77961136 0.80545791 0.82663066
                          Comp.7    Comp.8     Comp.9    Comp.10    Comp.11   Comp.12
Standard deviation     0.94916856 0.9303019 0.83729037 0.80211215 0.74715426 0.7180396
Proportion of Variance 0.01951468 0.0187466 0.01518542 0.01393622 0.01209192 0.0111679
Cumulative Proportion  0.84614533 0.8648919 0.88007735 0.89401357 0.90610549 0.9172734
                          Comp.13   Comp.14    Comp.15    Comp.16     Comp.17
Standard deviation     0.70307838 0.6855931 0.63265063 0.60638311 0.577028993
Proportion of Variance 0.01070735 0.0101814 0.00866967 0.00796469 0.007212236
Cumulative Proportion  0.92798074 0.9381621 0.94683181 0.95479650 0.962008740
                          Comp.18     Comp.19     Comp.20     Comp.21     Comp.22
Standard deviation     0.562296951 0.502245876 0.489633538 0.462695159 0.448120458
Proportion of Variance 0.006848668 0.005463959 0.005192984 0.004637294 0.004349749
Cumulative Proportion  0.968857408 0.974321367 0.979514351 0.984151645 0.988501394
                          Comp.23     Comp.24     Comp.25     Comp.26      Comp.27
Standard deviation     0.407524302 0.377653286 0.316885047 0.260094291 0.1533715763
Proportion of Variance 0.003597342 0.003089308 0.002175095 0.001465333 0.0005095238
Cumulative Proportion  0.992098736 0.995188044 0.997363139 0.998828472 0.9993379954
                          Comp.28      Comp.29 Comp.30
Standard deviation     0.1455951741 0.0967696653       0
Proportion of Variance 0.0004591649 0.0002028398       0
Cumulative Proportion  0.9997971602 1.0000000000       1
> |
```

```
plot(pca)
```

A scree plot from the IKTF PCA step.

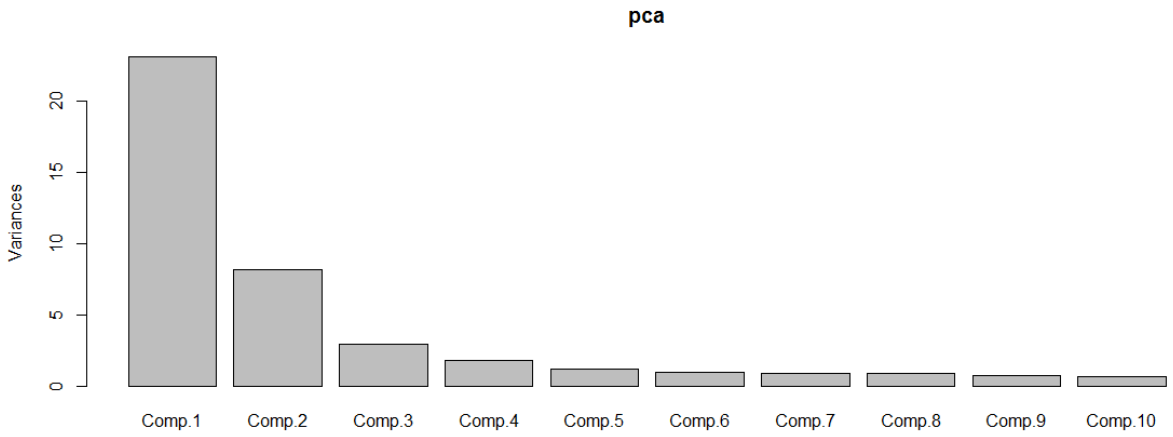

lines(bstick(pca))

A scree plot from the IKTF PCA step, with a broken stick model plotted.

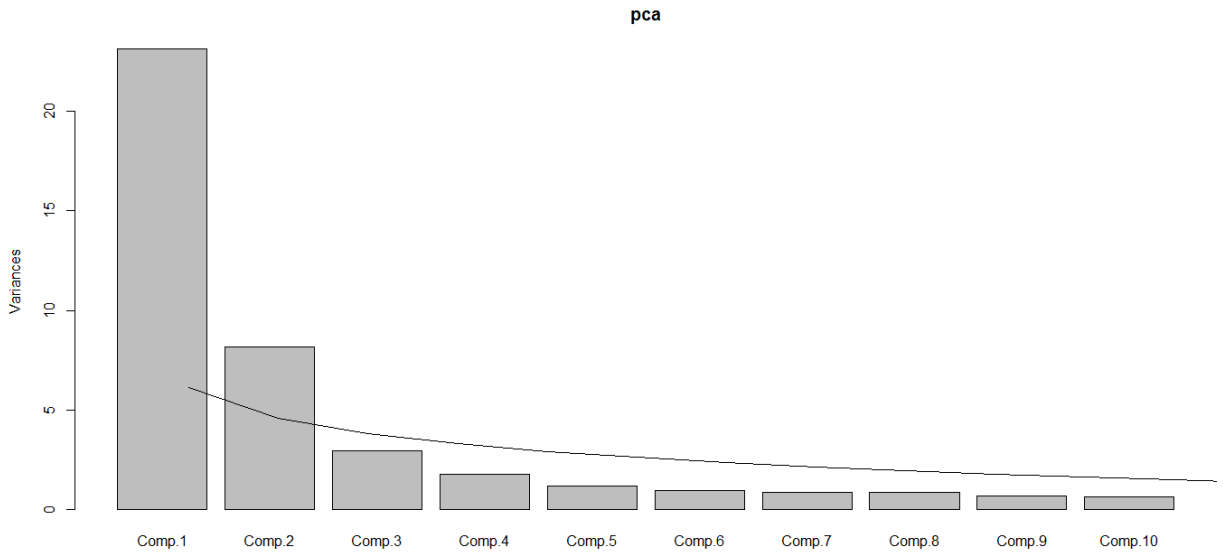

biplot(pca)

A biplot from the IKTF PCA step, using the first two principal components.

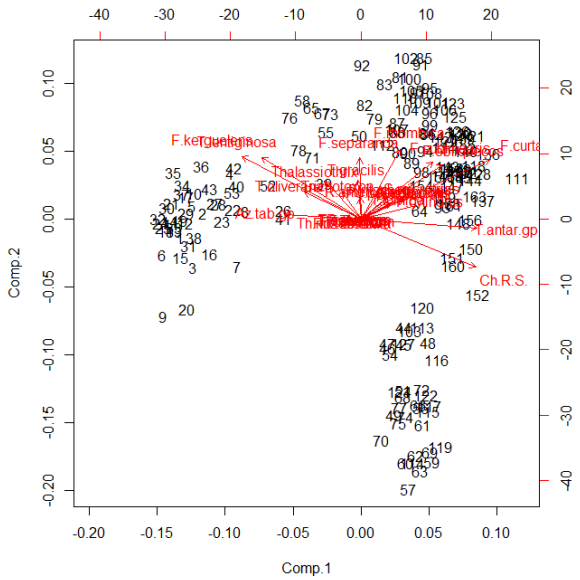

```
> loadings(pca)

Loadings:
               Comp.1 Comp.2 Comp.3 Comp.4 Comp.5 Comp.6
A.actinochil    0.127  0.119                0.196  0.111
Az.tab.gp      -0.240         0.112        -0.113
Ch.R.S.         0.357 -0.254 -0.343 -0.477 -0.160  0.130
F.curta         0.402  0.311        -0.127 -0.125
F.cylindrus     0.172        -0.306        -0.317 -0.403
F.doliolus
F.kerguelens   -0.372  0.329 -0.283 -0.270         0.284
F.obliquecos    0.254  0.285  0.149        -0.197
F.rhombica      0.122  0.365 -0.255  0.268 -0.176  0.275
F.ritscherii           0.126 -0.137         0.320 -0.485
F.separanda            0.320  0.224 -0.267        -0.109
F.sublinearis   0.225  0.299  0.142  0.160 -0.139
H.cuneiform
Po.glacialis    0.132  0.105 -0.186  0.543  0.229  0.130
Po.pseudodent          0.111  0.231  0.206  0.214
R.anten.gp             0.111 -0.466         0.338 -0.281
R.stylif.gp
Ro.tessalata
S.microtrias    0.152  0.129  0.188         0.131 -0.177
Th.nitz.lance                              -0.160
Th.nitz
T.antar.gp      0.362               -0.145  0.449  0.410
T.eccent.gp
T.gracilis             0.203        -0.203  0.137
T.lentiginosa  -0.309  0.323        -0.111         0.161
T.oest.gp
T.oliverana    -0.177  0.142  0.206 -0.231  0.184 -0.199
T.tumida                    0.268               -0.172
Thalassiothrix -0.114  0.201               -0.260
Trichotoxon            0.142 -0.208
```

Appendix 2.4

The R scripts used to validate the MAT model on our training database. Also included is the output from the hold out validation of the MAT model on the second random partition of our training database. It should be noted that the application of MAT to our training data base under hold out validation was applied using the program/software PAST version 2.13. The PAST output was then analysed within R. The shapiro-wilk and KS normality tests were used to test the assumption that model errors are normally distributed. This test was applied at the 5% significance level, with p-values below 0.05 indicating that the normality assumption does not hold. The normal probability plot (labelled as a normal Q-Q plot in R) provides a visual assessment of model residuals, allowing one to assess if model residuals (and thus model errors) are normal. Normally distributed residuals will fall along the 1:1 line. The Bartels test, NCV test and runs test can be used to assess the assumption that model errors have a constant variance. Similarly, a plot of residuals versus model fitted values should show a random scatter if the assumption of constant variance holds. One cannot properly assess the significance of each predictor within a model, nor can confidence intervals be computed, if the assumption that model errors are normal and have a constant variance, does not hold.

```
plot(min2$Reconstructed, min2$Residual, pch=16)
 lines(lowess(x=min2$Reconstructed, y=min2$Residual, f=0.2))
abline(lm(min2$Reconstructed ~ min2$Residual), lty=2)
abline(0,0)
```

A scatter plot of the MAT residuals (‘min2$Residual’) versus the fitted values from MAT (‘min2$Reconstructed’).

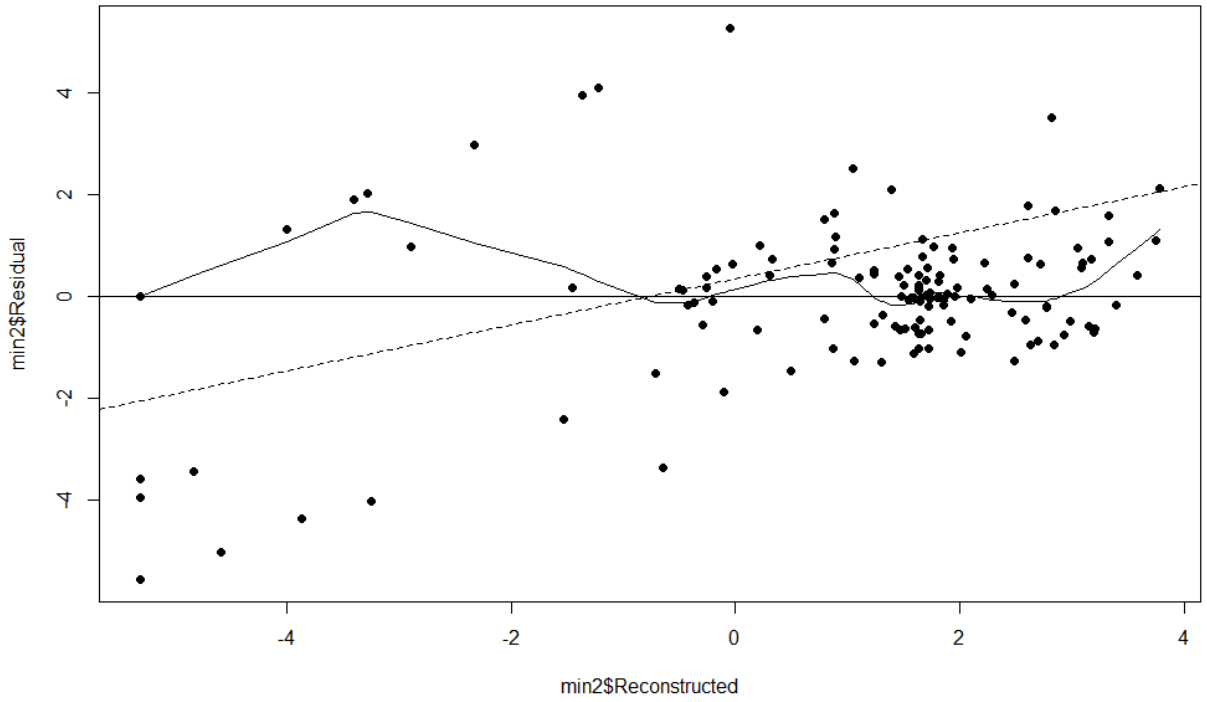


```
bartels.test(min2$Residual, alternative="two.sided")
Bartels Test - Two sided
data:  min2$Residual
Standardized Bartels Statistic = 0.4641, RVN Ratio = 2.077, p-value = 0.6425
runs.test(y=min2$Residual, plot.it=F)
                Runs Test - Two sided
data:  min2$Residual

Standardized Runs Statistic = -0.4133, p-value = 0.6794
```

A scatter plot of the MAT residuals (‘min2$Residual’) versus the observed data (‘min2$wSIC13yrTtran’).

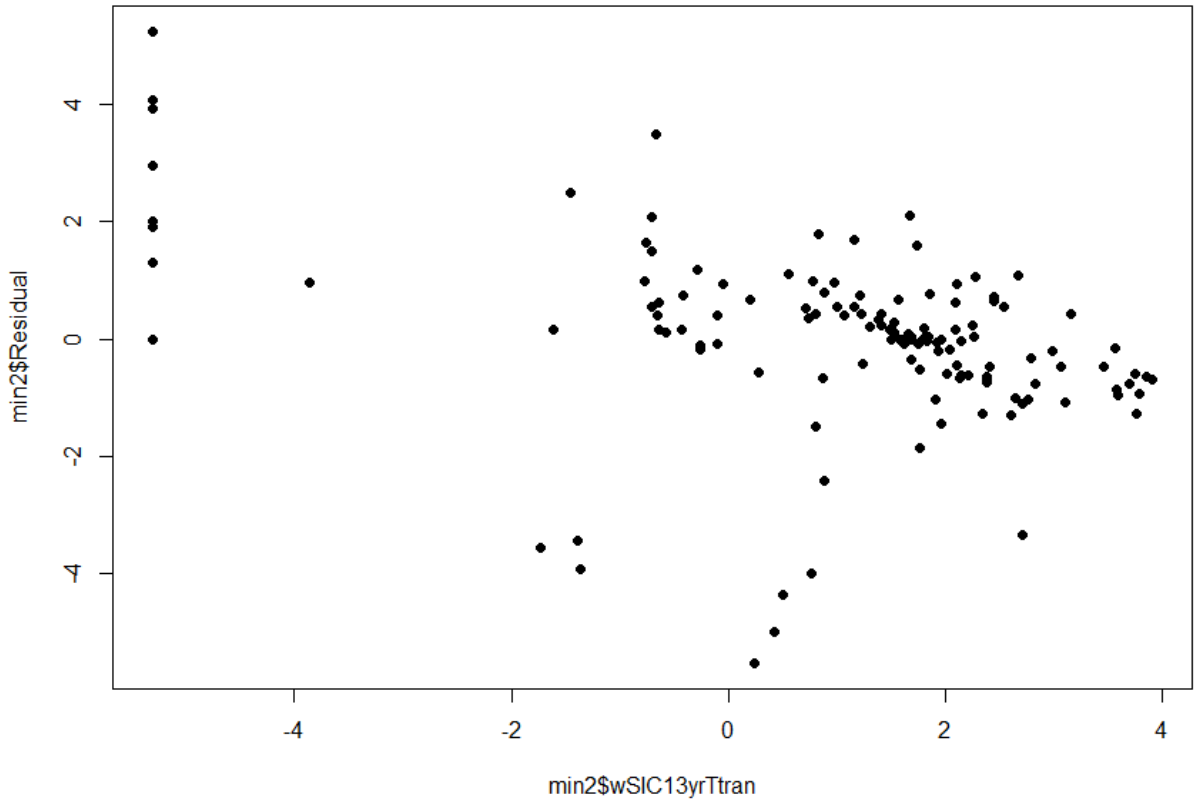


```
plot(min2$wSIC13yrTtran, min2$Reconstructed, pch=16)
> lines(lowess(x=min2$wSIC13yrTtran, y=min2$Reconstructed, f=0.2))
> abline(lm(min2$wSIC13yrTtran ~ min2$Reconstructed), lty=2)
> md <- lm(min2$wSIC13yrTtran ~ min2$Reconstructed)
> summary(md)
Call:
lm(formula = min2$wSIC13yrTtran ~ min2$Reconstructed)
Residuals:
    Min      1Q  Median      3Q     Max
-5.3149 -0.7449  0.0075  0.6998  4.7963
Coefficients:
                  Estimate Std. Error t value Pr(>|t|)
(Intercept)        0.05322    0.11883   0.448    0.655
min2$Reconstructed  0.86958    0.04336  20.056   <2e-16 ***
---
Signif. codes:  0 '***' 0.001 '**' 0.01 '*' 0.05 '.' 0.1 ' ' 1
Residual standard error: 1.429 on 145 degrees of freedom
Multiple R-squared:  0.735,         Adjusted R-squared:  0.7332
F-statistic: 402.2 on 1 and 145 DF,  p-value: < 2.2e-16
```

A scatter plot of the MAT fitted values ('min2$Reconstructed') versus the observed data ('min2$wSIC13yrTtran').

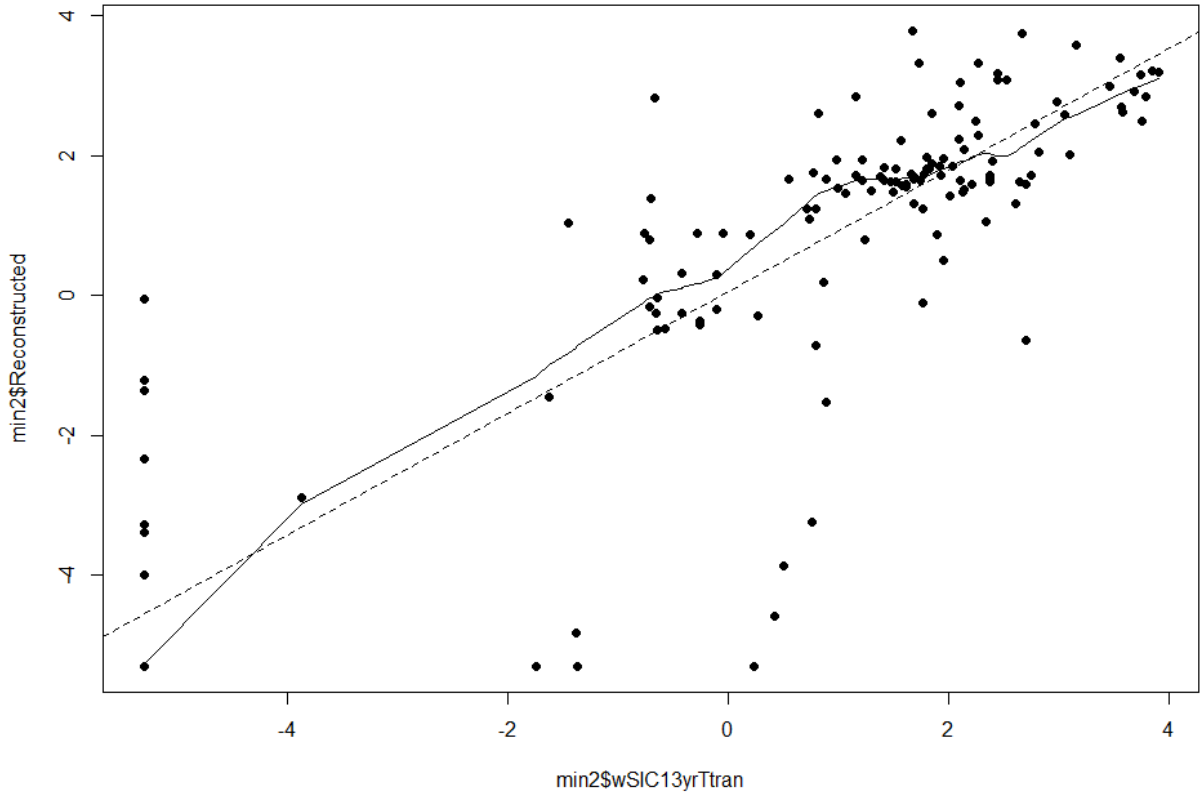


```
> res<- residuals(md)
> lillieTest(res)
Title:
 Lilliefors (KS) Normality Test
Test Results:
  STATISTIC:
    D: 0.1478
  P VALUE:
    2.387e-08
Description:
 Thu Sep 19 11:23:13 2013 by user: aferry
> shapiroTest(res)
Title:
 Shapiro - Wilk Normality Test
Test Results:
  STATISTIC:
    W: 0.9299
  P VALUE:1.22e-06
Description:
 Thu Sep 19 11:23:13 2013 by user: aferry
> ncvTest(md)
Non-constant Variance Score Test
Variance formula: ~ fitted.values
Chisquare = 38.45264    Df = 1     p = 5.609856e-10
```

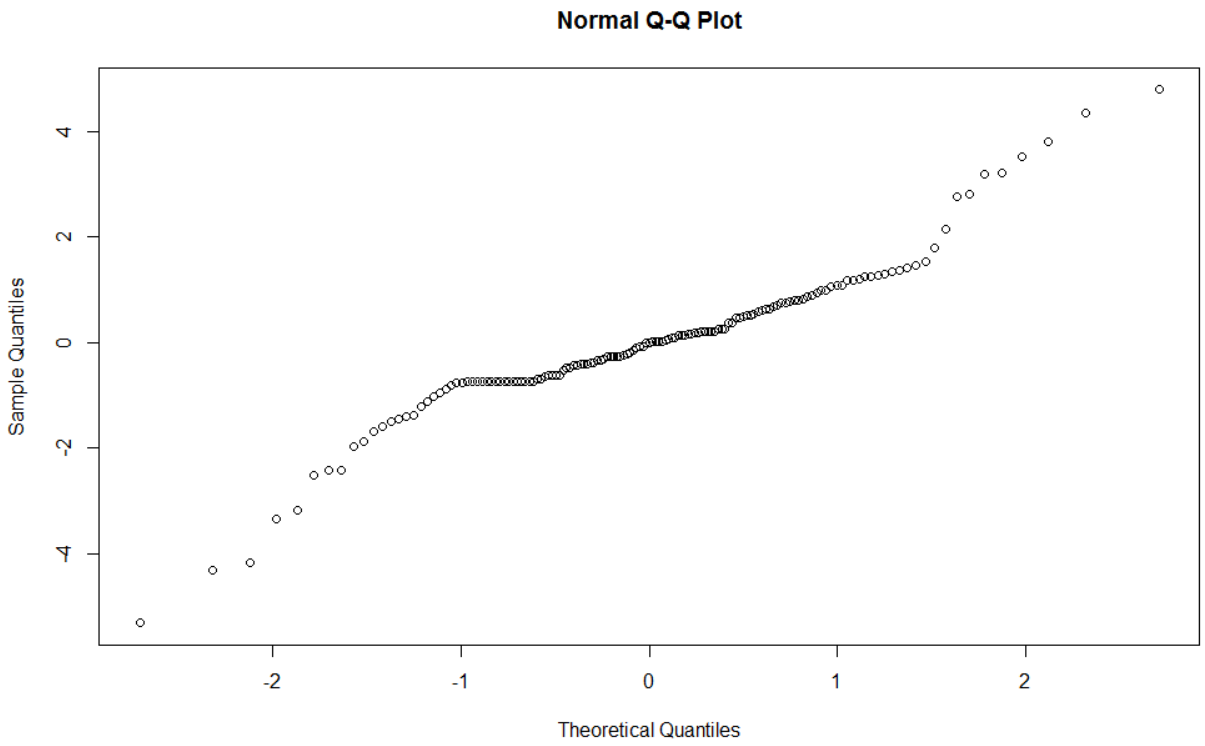
Normal Q-Q Plot
Sample Quantiles
Theoretical Quantiles
-4
-2
0
2
4
-2
-1
0
1
2

Appendix 2.5

The R scripts used to validate the WA PLS model on our training database. Also detailed is the output from the hold out validation of the WA PLS model on the first random partition of our training database. The shapiro-wilk and KS normality tests were used to test the assumption that model errors are normally distributed. This test was applied at the 5% significance level, with p-values below 0.05 indicating that the normality assumption does not hold. The normal probability plot (labelled as a normal Q-Q plot in R) provides a visual assessment of model residuals, allowing one to assess if model residuals (and thus model errors) are normal. Normally distributed residuals will fall along the 1:1 line. The Bartels test, NCV test and runs test can be used to assess the assumption that model errors have a constant variance. Similarly, a plot of residuals versus model fitted values should show a random scatter if the assumption of constant variance holds. One cannot properly assess the significance of each predictor within a model, nor can confidence intervals be computed, if the assumption that model errors are normal and have a constant variance, does not hold. The linear regression model using observed data as the response and fitted values as the predictor (reg <- lm(min1ice$wSIC13yrTtran ~ fit)) would reveal an unbiased model as having a zero intercept and a 1:1 slope.

```
model <- WAPLS(min1spp, min1ice, npls=5, iswapls=T)

fit.cv <- crossval(model, cv.method="loo")
rand.t.test(fit.cv)
model <- WAPLS(min1spp, min1ice, npls=2, iswapls=T)
res <- residuals(model)
 fit <- fitted(model)
 plot(fit, res, pch=16)
abline(0,0)
 RMSE <- sqrt(sum(res^2)/147)
 RMSE
2.218473
mean(res)
-0.1602462
```

A scatter plot of the WA PLS residuals (‘res’) versus the fitted values from MAT (‘fit’).

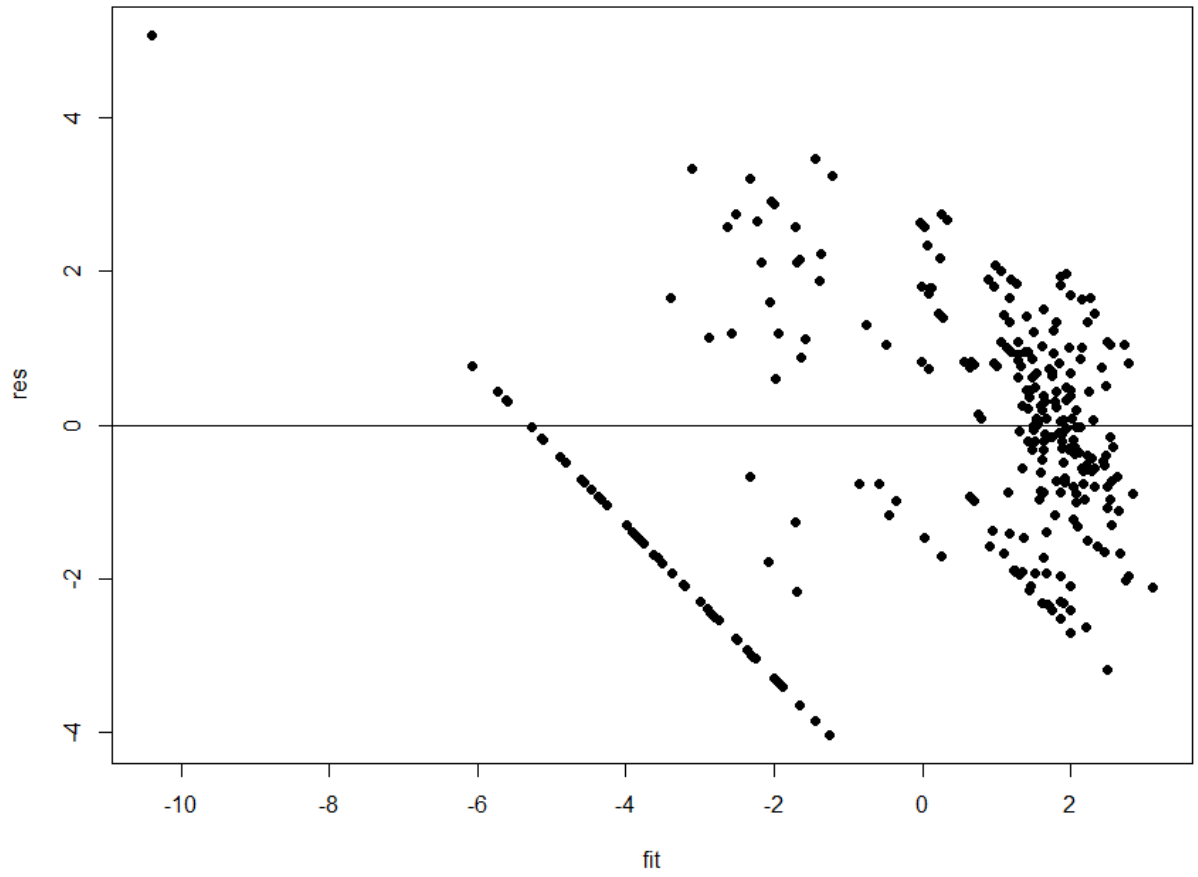


```
estTRAIN <- predict(model)
 fitestTRAIN <- estTRAIN[,2]
 plot(fitestTRAIN, min1ice$wSIC13yrTtran, pch=16)
est <- predict(model, spp1)
fitest <- est$fit[,2]
residual <- (SI1$wSIC13yrTtran-fitest)
RMSEP <- sqrt(sum(residual^2)/16)
RMSEP
[1] 2.033764
mean(residual)
[1] 0.4114493
```

```
model <- WAPLS(min1spp, min1ice, npls=5, iswapls=T)
> fit.cv <- crossval(model, cv.method="loo")
LOO sample 50
LOO sample 100
> rand.t.test(fit.cv)
         RMSE       R2    Avg.Bias Max.Bias    Skill   delta.RMSE     p
Comp01 1.693939 0.6284116 -0.20633921 2.226567 62.26292 -38.56948475 0.001
Comp02 1.616127 0.6617614 -0.11756940 1.873490 65.65025  -4.59356760 0.016
Comp03 1.599215 0.6675148 -0.02537951 2.513224 66.36539  -1.04644482 0.355
Comp04 1.599417 0.6699110 -0.02770171 2.505464 66.35690   0.01262142 0.492
Comp05 1.680088 0.6448741 -0.02054607 2.597952 62.87754   5.04378125 0.925
> model <- WAPLS(min1spp, min1ice, npls=2, iswapls=T)
```

```
> est <- fitted(model)
> fit <- est[,2]
> res <- (fit-min1ice$wSIC13yrTtran)
> RMSE <- sqrt(sum((res^2)/147))
> RMSE
[1] 1.483843
> plot(min1ice$wSIC13yrTtran, fit, pch=17)
> abline(lm(min1ice$wSIC13yrTtran ~ fit), lty=2)
> reg <- lm(min1ice$wSIC13yrTtran ~ fit)
> summary(reg)
Call:
lm(formula = min1ice$wSIC13yrTtran ~ fit)
Residuals:
    Min      1Q  Median      3Q     Max
-3.5260 -0.8921 -0.0573  0.9552  3.6084
Coefficients:
            Estimate Std. Error t value Pr(>|t|)
(Intercept) -0.12736    0.12415  -1.026    0.307
fit          1.00162    0.05283  18.959   <2e-16 ***
---
Signif. codes:  0 ‘***’ 0.001 ‘**’ 0.01 ‘*’ 0.05 ‘.’ 0.1 ‘ ’ 1
Residual standard error: 1.489 on 145 degrees of freedom
Multiple R-squared:  0.7125,        Adjusted R-squared:  0.7106
F-statistic: 359.4 on 1 and 145 DF,  p-value: < 2.2e-16
```

A scatter plot of the WA PLS fitted values ('fit') versus the observed data ('min1ice$wSIC13yrTtran').

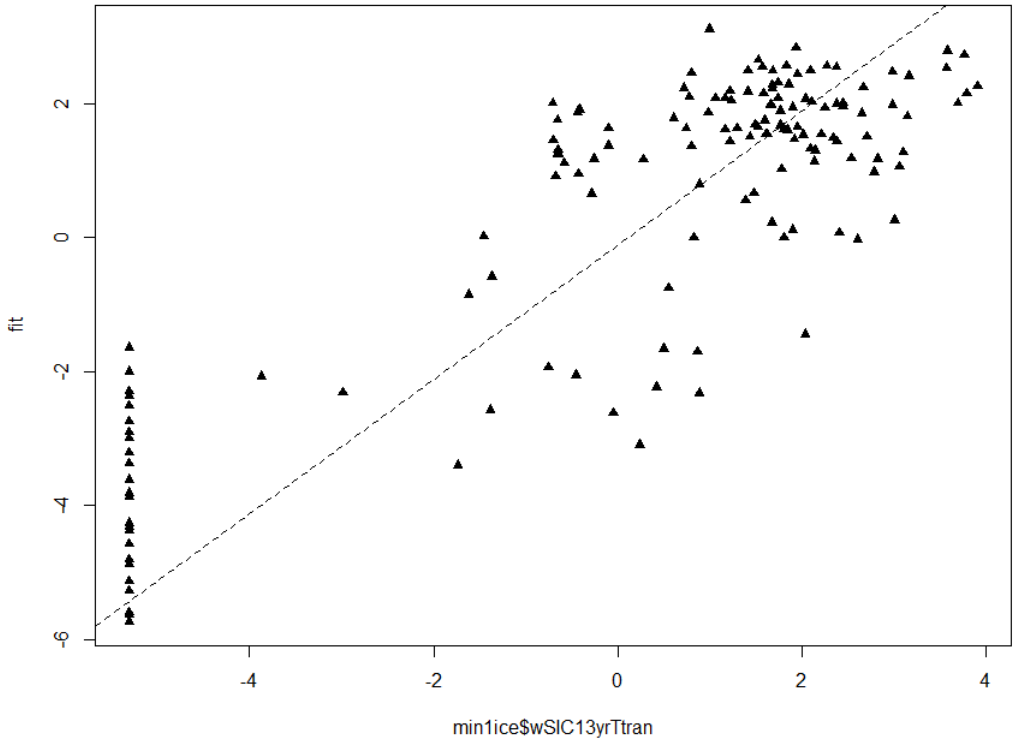


```
res<- residuals(reg)
> lillieTest(res)
Title:
 Lilliefors (KS) Normality Test
Test Results:
  STATISTIC:
    D: 0.0402
  P VALUE:
    0.8123
Description:
 Thu Sep 19 11:15:17 2013 by user: aferry
> shapiroTest(res)
Title:
 Shapiro - Wilk Normality Test
Test Results:
  STATISTIC:
    W: 0.9929
  P VALUE:
    0.6802
Description:
 Thu Sep 19 11:15:17 2013 by user: aferry
> ncvTest(reg)
Non-constant Variance Score Test
Variance formula: ~ fitted.values
Chisquare = 12.63338    Df = 1     p = 0.0003789192
```

Appendix 2.6

The R scripts used to validate the GAM model on our training database. Also included is the output from the hold out validation of the GAM model on the second random partition of our training database. The R scripts used to validate the WA PLS model on our training database. Also detailed is the output from the hold out validation of the WA PLS model on the first random partition of our training database. The shapiro-wilk and KS normality tests were used to test the assumption that model errors are normally distributed. This test was applied at the 5% significance level, with p-values below 0.05 indicating that the normality assumption does not hold. The normal probability plot (labelled as a normal Q-Q plot in R) provides a visual assessment of model residuals, allowing one to assess if model residuals (and thus model errors) are normal. Normally distributed residuals will fall along the 1:1 line. The Bartels test, NCV test and runs test can be used to assess the assumption that model errors have a constant variance. Similarly, a plot of residuals versus model fitted values should show a random scatter if the assumption of constant variance holds. One cannot properly assess the significance of each predictor within a model, nor can confidence intervals be computed, if the assumption that model errors are normal and have a constant variance, does not hold. The linear regression model using observed data as the response and fitted values as the predictor (md <- lm(min2$wSIC13yrTtran ~ fit)) would reveal an unbiased model as having a zero intercept and a 1:1 slope.

```
model <- gam(wSIC13yrTtran ~ s(A.actinochil) + s(F.curta) +s(F.cylindrus) + s(T.lentiginosa), data=min2)
> res <- residuals(model)
> fit <- fitted(model)
> plot(fit, res, pch=16)
> lillieTest(res)
Title:
 Lilliefors (KS) Normality Test
Test Results:
  STATISTIC:
    D: 0.0595
  P VALUE:
    0.2288
Description:
 Mon Aug 26 13:37:48 2013 by user: aferry
> shapiroTest(res)
Title:
 Shapiro - Wilk Normality Test
Test Results:
  STATISTIC:
    W: 0.9884
  P VALUE:
    0.2595
Description:
 Mon Aug 26 13:37:48 2013 by user: aferry
> qqnorm(res)
> plot(min2$wSIC13yrTtran, res, pch=16)
> RMSE <- sqrt(sum(res^2/147))
> RMSE
```

```
[1] 1.331106
> bias <- sum(res/147)
> bias
[1] -2.377845e-15
> est <- predict(model, two)
> RMSEP <- sqrt(sum((est-two$wSIC13yrTtran)^2)/16)
> RMSEP
[1] 1.815668
```

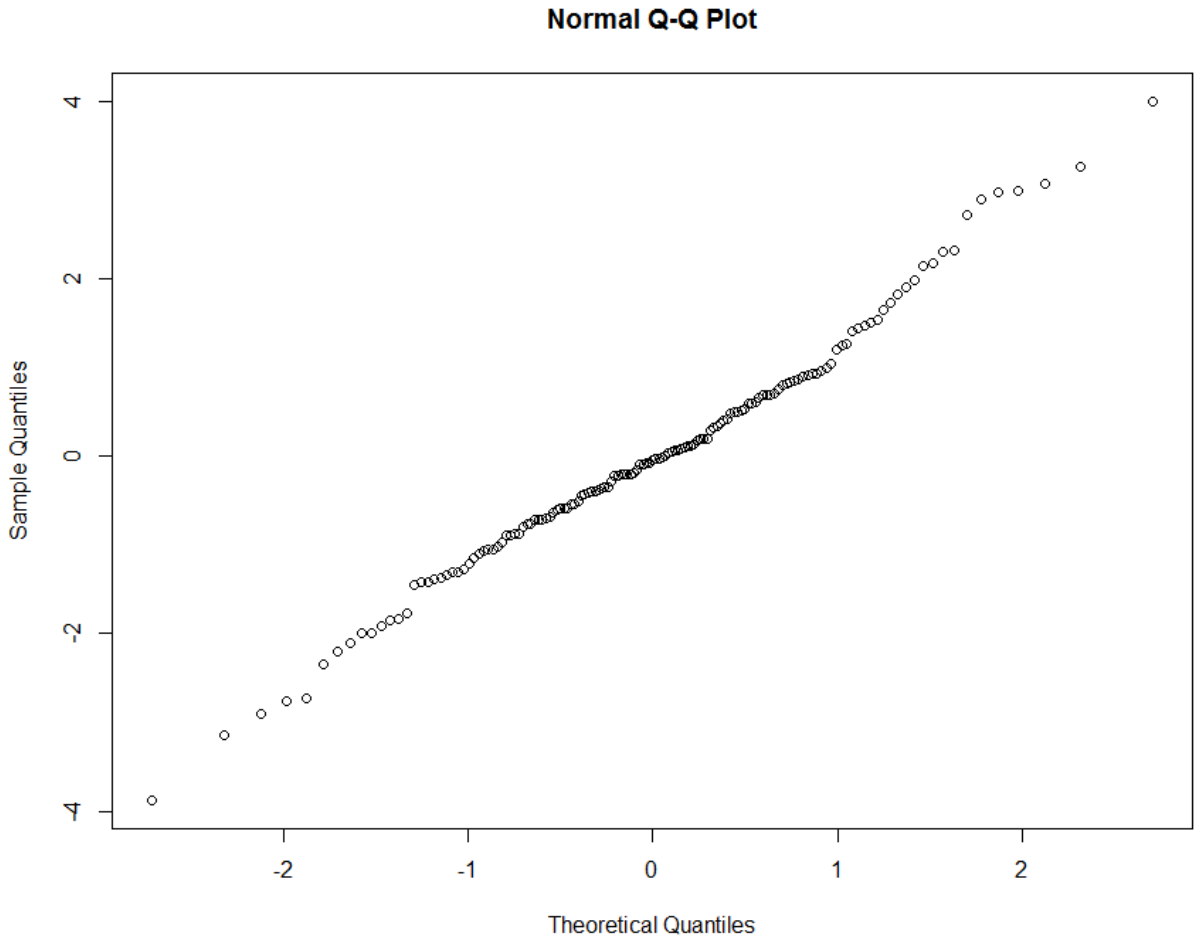


```
> model <- gam(wSIC13yrTtran ~ s(A.actinochil) + s(F.curta) +s(F.cylindrus) + s(T.lentiginosa), data=min2)
> res <- residuals(model)
> runs.test(res, alternative="two.sided")
        Runs Test - Two sided
data:  res
Standardized Runs Statistic = -1.2409, p-value = 0.2146
> bartels.test(res, alternative="two.sided")
        Bartels Test - Two sided
data:  res
Standardized Bartels Statistic = -1.1186, RVN Ratio = 1.815,
```

```
p-value = 0.2633

model <- gam(wSIC13yrTtran ~ s(A.actinochil) + s(F.curta) +s(F.cylindrus) + s(T.lentiginosa), data=min2)
> res <- residuals(model)
> fit <- fitted(model)
> plot(min2$wSIC13yrTtran, fit, pch=16)
> abline(lm(min2$wSIC13yrTtran ~ fit), lty=2)
> md <- lm(min2$wSIC13yrTtran ~ fit)
> summary(md)
Call:
lm(formula = min2$wSIC13yrTtran ~ fit)

Residuals:
    Min      1Q  Median      3Q     Max
-3.8503 -0.7895 -0.0670  0.6993  4.0725
Coefficients:
            Estimate Std. Error t value Pr(>|t|)
(Intercept) -0.005182   0.111718  -0.046    0.963
fit          1.014652   0.046422  21.857   <2e-16 ***
---
Signif. codes:  0 ‘***’ 0.001 ‘**’ 0.01 ‘*’ 0.05 ‘.’ 0.1 ‘ ’ 1
Residual standard error: 1.34 on 145 degrees of freedom
Multiple R-squared:  0.7672,        Adjusted R-squared:  0.7656
F-statistic: 477.7 on 1 and 145 DF,  p-value: < 2.2e-16
```

A scatter plot of the GAM fitted values (‘fit’) versus the observed data (‘min2$wSIC13yrTtran’).

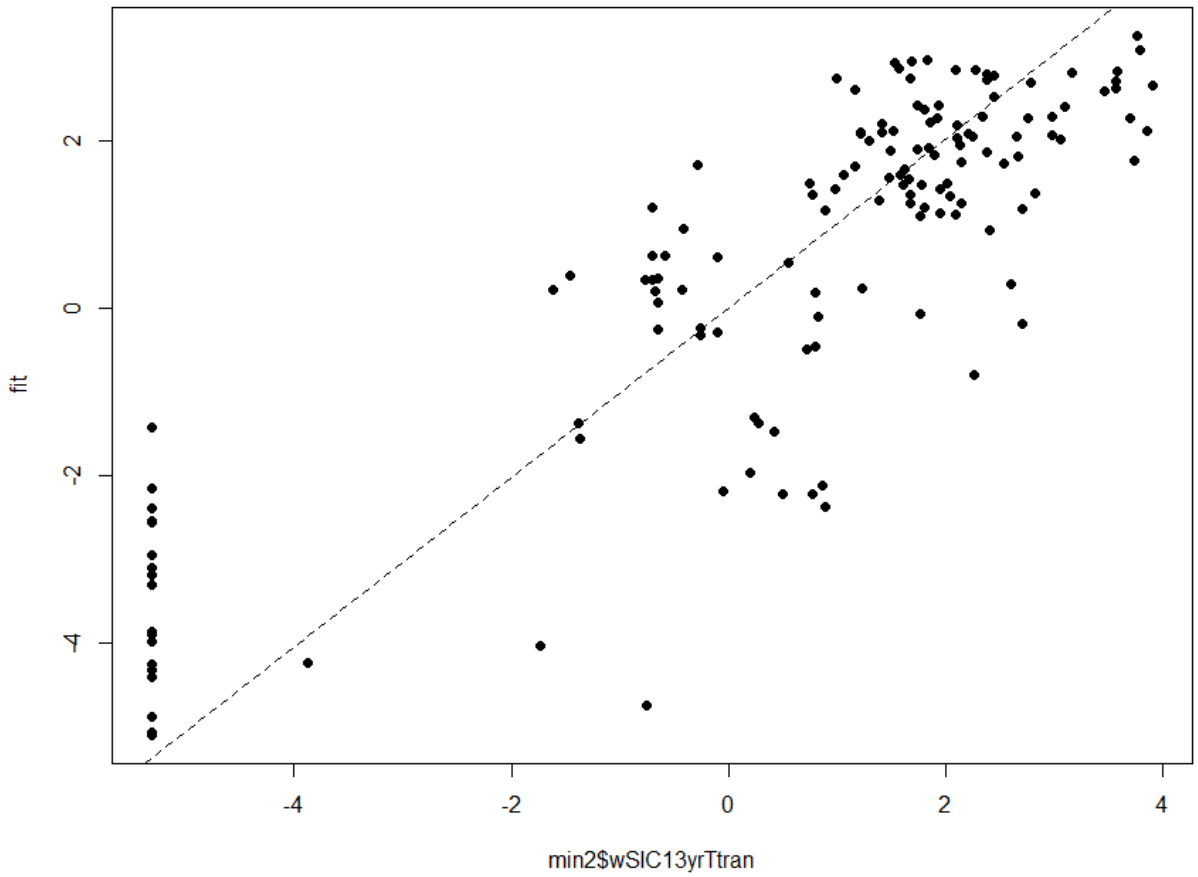


```
> res <- residuals(md)
> lillieTest(res)
Title:
 Lilliefors (KS) Normality Test
Test Results:
  STATISTIC:
    D: 0.0606
  P VALUE:
    0.2066
Description:
 Thu Sep 19 10:50:23 2013 by user: aferry
> shapiroTest(res)
Title:
 Shapiro - Wilk Normality Test
Test Results:
  STATISTIC:
    W: 0.9866
  P VALUE:
    0.1683
Description:
 Thu Sep 19 10:50:23 2013 by user: aferry
> ncvTest(md)
Non-constant Variance Score Test
Variance formula: ~ fitted.values
Chisquare = 26.964    Df = 1     p = 2.072806e-07
```

Appendix 2.7

The R output and scripts from our application of GAM as both an inverse and a classical model. The inverse model uses diatoms as the predictor variable. The classical model uses the diatom species as the response variable and winter sea-ice concentrations as the predictor variable. Where diatoms have a unimodal response to winter sea-ice concentration, a classical GAM may only fit a linear function. The fitted functions for the GAM applied as a classical model show, however, that the classical GAM has been able to successfully model the non-linear relationship between diatom abundance and winter sea-ice concentrations.

Fragilariopsis cylindrus

```
model <- gam(F.cylindrus ~ s(wSIC13yr), data=Lnabun163DataFTSand.13yrWsic)
summary(model)
Family: gaussian
Link function: identity
Formula:
F.cylindrus ~ s(wSIC13yr)
Parametric coefficients:
            Estimate Std. Error t value Pr(>|t|)
(Intercept)  1.44204    0.08665   16.64   <2e-16 ***
---
Signif. codes:  0 ‘***’ 0.001 ‘**’ 0.01 ‘*’ 0.05 ‘.’ 0.1 ‘ ’ 1
Approximate significance of smooth terms:
              edf Ref.df     F  p-value
s(wSIC13yr) 3.034  3.696 14.39 1.85e-09 ***
---
Signif. codes:  0 ‘***’ 0.001 ‘**’ 0.01 ‘*’ 0.05 ‘.’ 0.1 ‘ ’ 1
R-sq.(adj) =  0.241   Deviance explained = 25.5%
GCV score =  1.255  Scale est. = 1.224     n = 163
```

The smooth function fitted by GAM as a classical model.

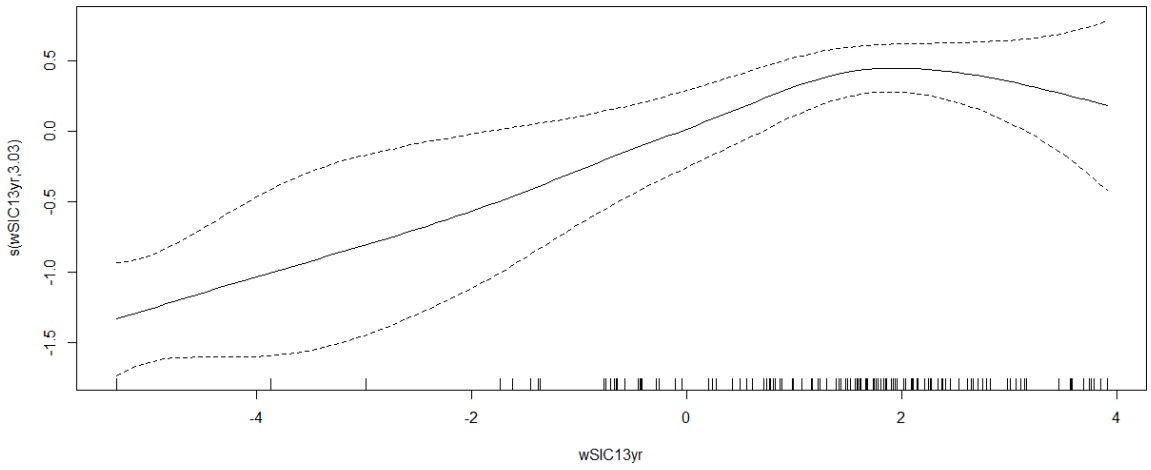

```
plot(Lnabun163DataFTSand.13yrWsic$wSIC13yr, Lnabun163DataFTSand.13yrWsic$F.cylindrus)

> model <- gam(wSIC13yr ~ s(F.cylindrus), data=Lnabun163DataFTSand.13yrWsic)
> summary(model)
Family: gaussian
Link function: identity
Formula:
wSIC13yr ~ s(F.cylindrus)
Parametric coefficients:
            Estimate Std. Error t value Pr(>|t|)
(Intercept)   0.3362     0.1880   1.788   0.0756 .
---
Signif. codes:  0 ‘***’ 0.001 ‘**’ 0.01 ‘*’ 0.05 ‘.’ 0.1 ‘ ’ 1
Approximate significance of smooth terms:
                edf Ref.df     F  p-value
s(F.cylindrus) 1.887  2.321 21.88 7.15e-10 ***
---
Signif. codes:  0 ‘***’ 0.001 ‘**’ 0.01 ‘*’ 0.05 ‘.’ 0.1 ‘ ’ 1
R-sq.(adj) =  0.236   Deviance explained = 24.5%
GCV score = 5.8648  Scale est. = 5.7609    n = 163
plot(model)
```

The smooth function fitted by GAM as an inverse model.

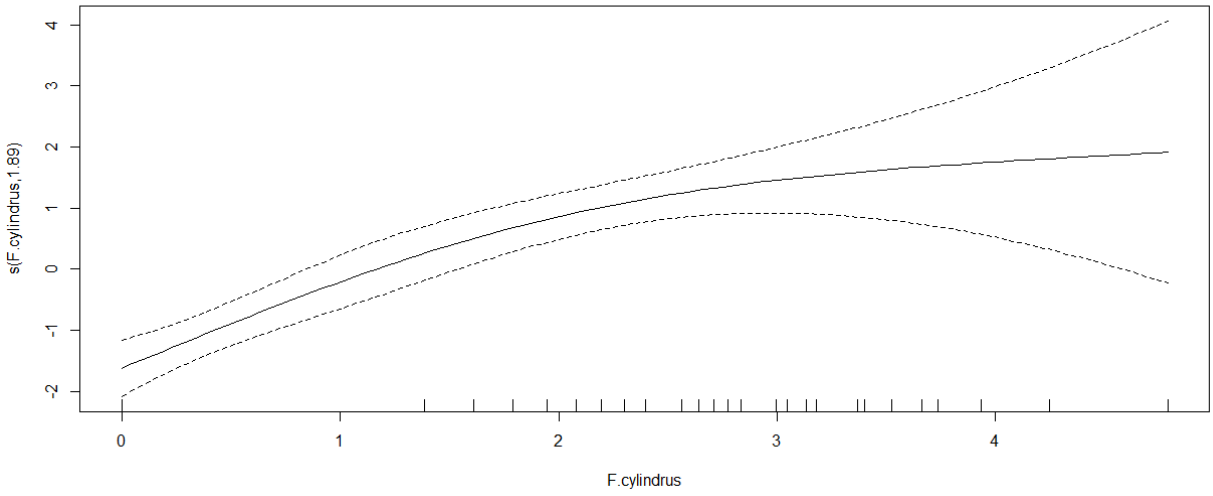


```
plot(Lnabun163DataFTSand.13yrWsic$F.cylindrus, Lnabun163DataFTSand.13yrWsic$wSIC13yr)
```

Actinocyclus actinochilus

```
> model <- gam(A.actinochil ~ s(wSIC13yr), data=Lnabun163DataFTSand.13yrWsic)
> summary(model)
Family: gaussian
Link function: identity
Formula:
A.actinochil ~ s(wSIC13yr)
Parametric coefficients:
            Estimate Std. Error t value Pr(>|t|)
(Intercept)  1.75043    0.05365   32.63   <2e-16 ***
---
Signif. codes:  0 ‘***’ 0.001 ‘**’ 0.01 ‘*’ 0.05 ‘.’ 0.1 ‘ ’ 1
Approximate significance of smooth terms:
              edf Ref.df    F p-value
s(wSIC13yr) 6.008  7.131 22.5  <2e-16 ***
---
Signif. codes:  0 ‘***’ 0.001 ‘**’ 0.01 ‘*’ 0.05 ‘.’ 0.1 ‘ ’ 1
R-sq.(adj) =  0.492   Deviance explained = 51.1%
GCV score = 0.49015  Scale est. = 0.46908   n = 163
plot(model)
```

The smooth function fitted by GAM as a classical model.

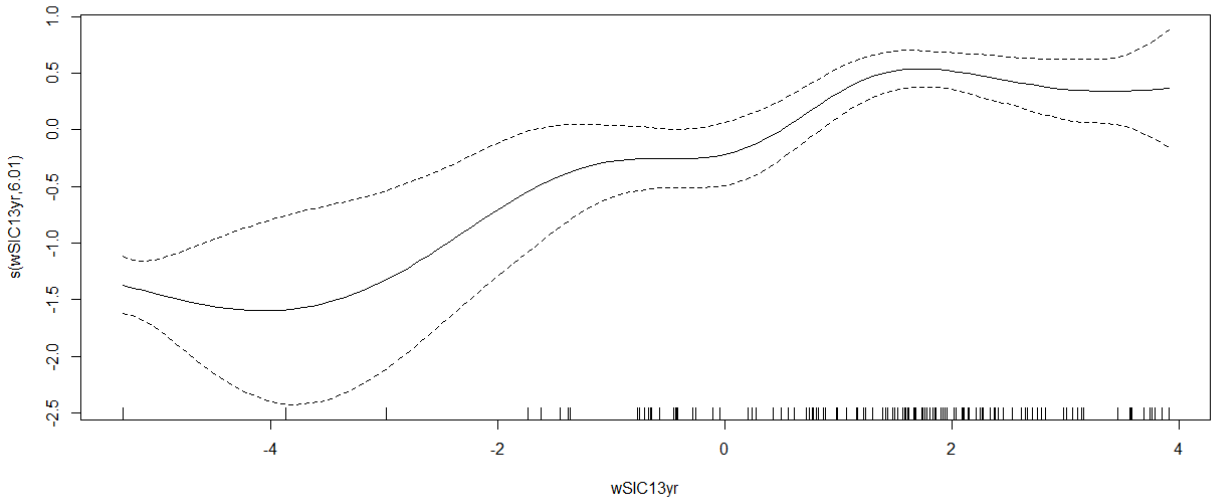


```
plot(Lnabun163DataFTSand.13yrWsic$wSIC13yr, Lnabun163DataFTSand.13yrWsic$A.actinochil)

model <- gam(wSIC13yr ~ s(A.actinochil), data=Lnabun163DataFTSand.13yrWsic)
> summary(model)
Family: gaussian
Link function: identity
Formula:
wSIC13yr ~ s(A.actinochil)
Parametric coefficients:
            Estimate Std. Error t value Pr(>|t|)
```

```
(Intercept)   0.3362     0.1556    2.16   0.0323 *
---
Signif. codes:  0 ‘***’ 0.001 ‘**’ 0.01 ‘*’ 0.05 ‘.’ 0.1 ‘ ’ 1
Approximate significance of smooth terms:
                edf Ref.df     F p-value
s(A.actinochil) 2.054  2.485 59.61  <2e-16 ***
---
Signif. codes:  0 ‘***’ 0.001 ‘**’ 0.01 ‘*’ 0.05 ‘.’ 0.1 ‘ ’ 1
R-sq.(adj) =  0.476   Deviance explained = 48.3%
GCV score = 4.0243  Scale est. = 3.9489    n = 163
plot(model)
```

The smooth function fitted by GAM as an inverse model.

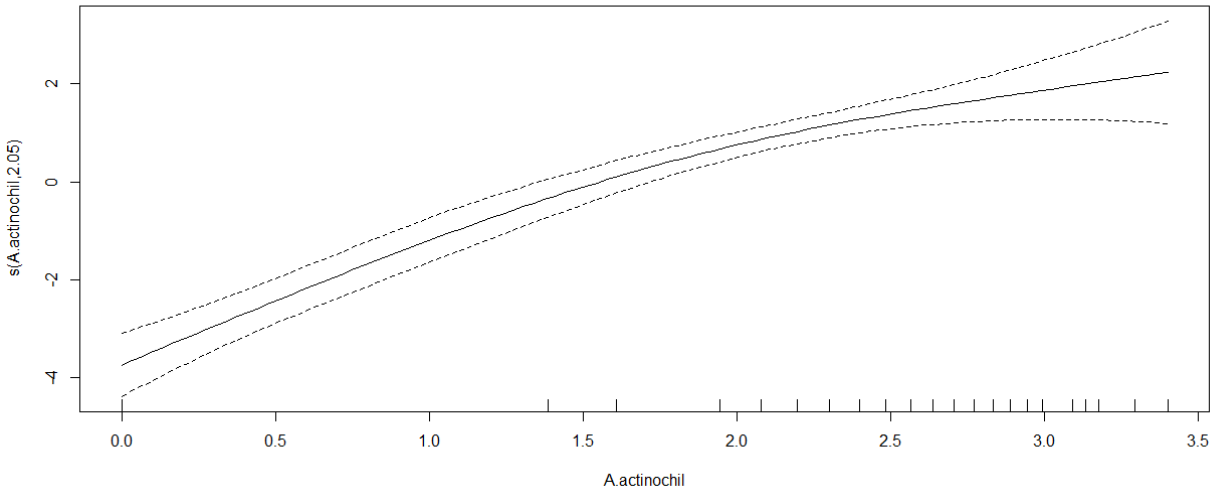


```
plot(Lnabun163DataFTSand.13yrWsic$wSIC13yr, Lnabun163DataFTSand.13yrWsic$A.actinochil)
lines(lowess(x= Lnabun163DataFTSand.13yrWsic$A.actinochil, y=Lnabun163DataFTSand.13yrWsic$wSIC13yr, f=0.2))
```

Fragilariopsis curta

```
model <- gam(F.curta ~ s(wSIC13yr), data=Lnabun163DataFTSand.13yrWsic)
> plot(model)
```

The smooth function fitted by GAM as a classical model.

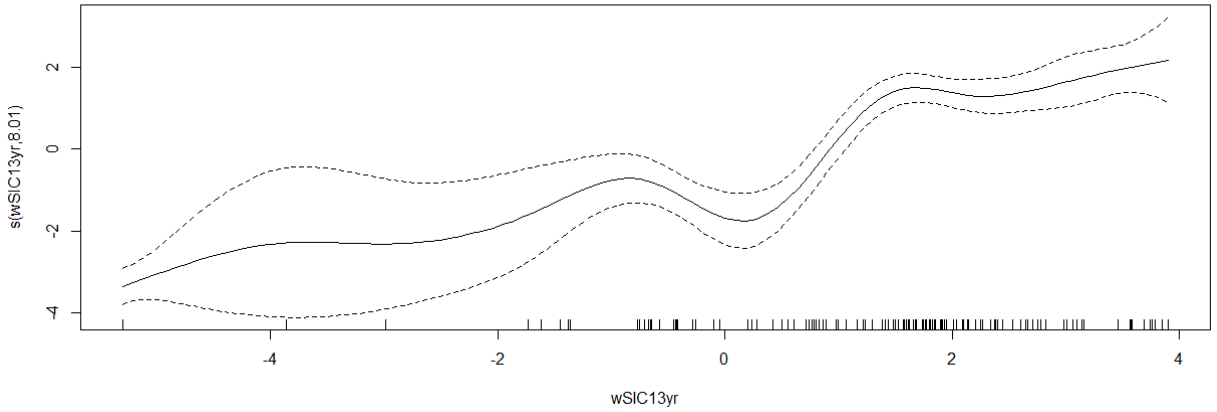


```
model <- gam(wSIC13yr ~ s(F.curta), data=Lnabun163DataFTSand.13yrWsic)
> plot(model)
```

The smooth function fitted by GAM as an inverse model.

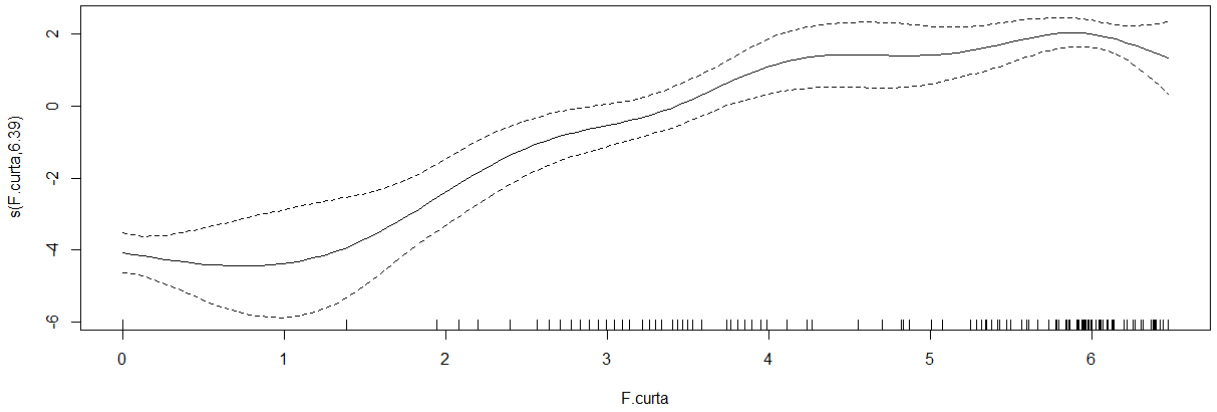

Thalassiosira lentiginosa

```
model <- gam(T.lentiginosa ~ s(wSIC13yr), data=Lnabun163DataFTSand.13yrWsic)
> plot(model)
```

The smooth function fitted by GAM as a classical model.

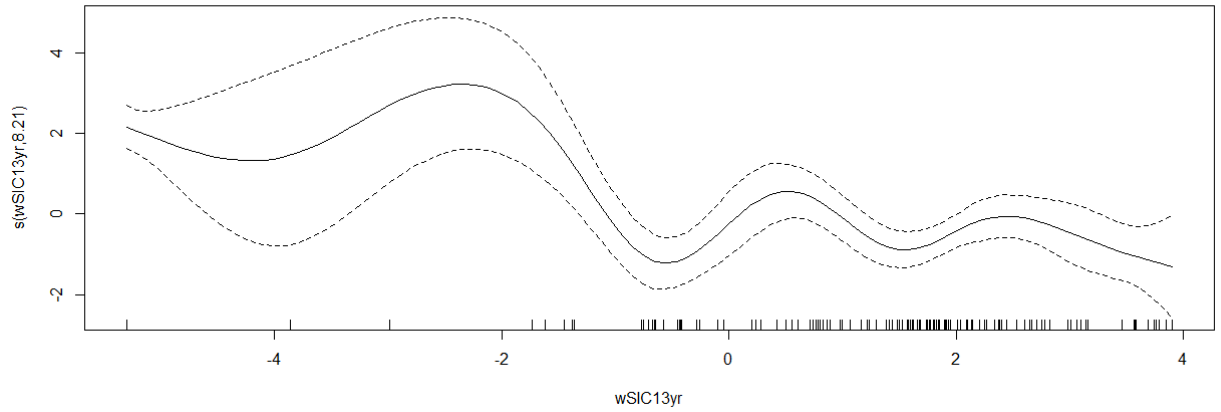


```
model <- gam(wSIC13yr ~ s(T.lentiginosa), data=Lnabun163DataFTSand.13yrWsic)
> plot(model)
```

The smooth function fitted by GAM as an inverse model.

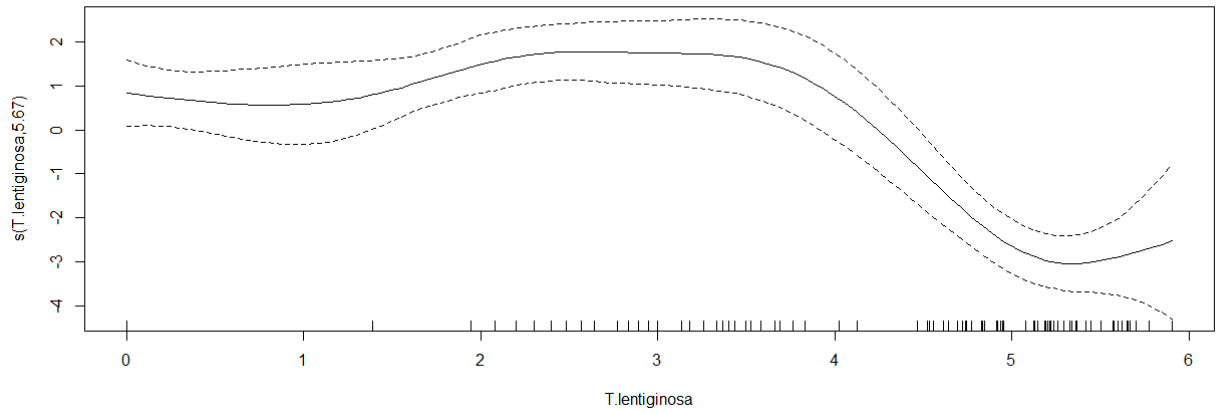

```
model <- gam(T.lentiginosa ~ s(wSIC13yr), data=Lnabun163DataFTSand.13yrWsic)
> plot(model)
```

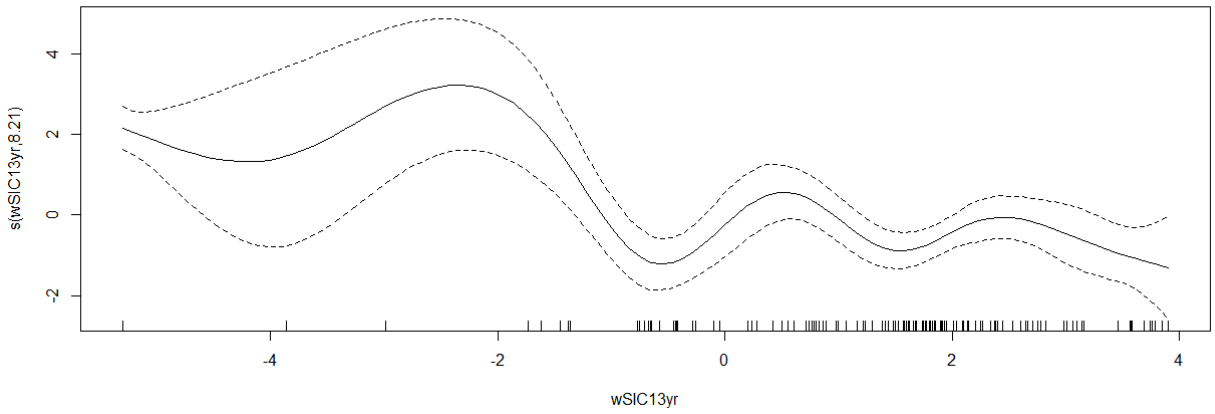


```
model <- gam(wSIC13yr ~ s(T.lentiginosa), data=Lnabun163DataFTSand.13yrWsic)
> plot(model)
```

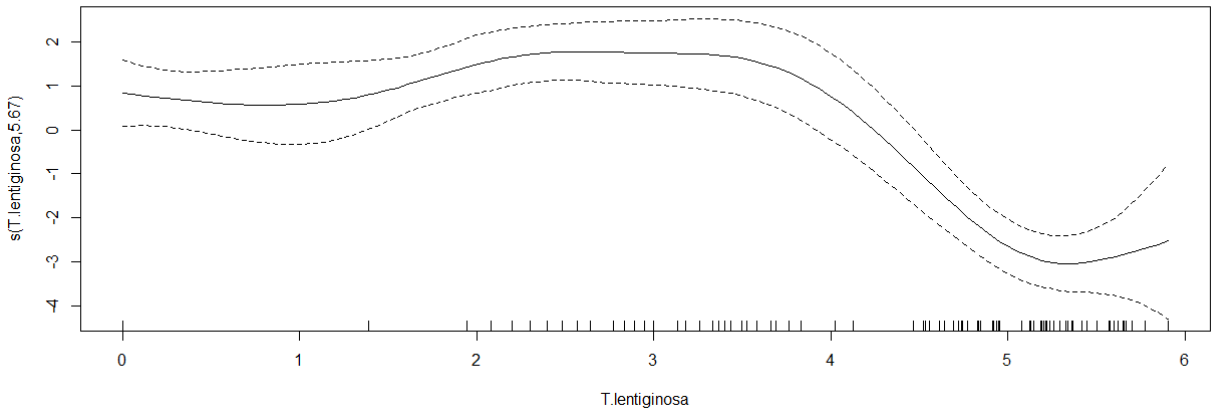

Appendix 2.8

The application of variance partitioning within R is illustrated. The R scripts and output from the variance partitioning on the entire diatom relative abundance matrix, and on the four diatoms used within the GAM from Chapter 2, are provided.

```
mod <- varpart(allDiaSppAbunsUntrans, PCNMselBYbackTRANS, wSIC13yr)
> mod
Partition of variation in RDA
Call: varpart(Y = allDiaSppAbunsUntrans, X = PCNMselBYbackTRANS, wSIC13yr)
Explanatory tables:
X1:  PCNMselBYbackTRANS
X2:  wSIC13yr
No. of explanatory tables: 2
Total variation (SS): 365143
          Variance: 2254
No. of observations: 163
Partition table:
                    Df R.squared Adj.R.squared Testable
[a+b] = X1           8   0.35214       0.31849     TRUE
[b+c] = X2           1   0.24300       0.23829     TRUE
[a+b+c] = X1+X2      9   0.46544       0.43399     TRUE
Individual fractions
[a] = X1|X2          8                 0.19570     TRUE
[b]                  0                 0.12279    FALSE
[c] = X2|X1          1                 0.11551     TRUE
[d] = Residuals                        0.56601    FALSE
---
Use function 'rda' to test significance of fractions of interest

> mod <- varpart(AactFcurtTlenFcylindUNtrans, PCNMselBYbackTRANS, wSIC13yr)
> mod
Partition of variation in RDA
Call: varpart(Y = AactFcurtTlenFcylindUNtrans, X = PCNMselBYbackTRANS, wSIC13yr)
Explanatory tables:
X1:  PCNMselBYbackTRANS
X2:  wSIC13yr
No. of explanatory tables: 2
Total variation (SS): 76535
          Variance: 472.44
No. of observations: 163
Partition table:
                    Df R.squared Adj.R.squared Testable
[a+b] = X1           8   0.31048       0.27466     TRUE
[b+c] = X2           1   0.38828       0.38449     TRUE
[a+b+c] = X1+X2      9   0.54974       0.52326     TRUE
Individual fractions
[a] = X1|X2          8                 0.13877     TRUE
[b]                  0                 0.13589    FALSE
[c] = X2|X1          1                 0.24859     TRUE
[d] = Residuals                        0.47674    FALSE
---
Use function 'rda' to test significance of fractions of interest
```

Appendix 2.9

The R scripts and output for the three reconstruction diagnostics applied to our training database and marine sediment core SO136-111. We wish to acknowledge the blog by Associate Professor Richard Telford and the R scripts outlined within Richard's blog (https://quantpalaeo.wordpress.com/2014/05/29/comparison-of-reconstruction-diagnostics/, cited May, 2014). All of the R scripts listed within this appendix were adopted from Richard Telford. A url link to Richards blog is provided for each of reconstruction diagnostic procedures. The Hills N2 diversity measure is used to identify diatom species that may have a poorly defined optima. In each plot, the maximum abundance of each diatom within a marine sediment core is plotted against the same diatoms maximum abundance within the winter sea-ice training data set. Taxa with a greater abundance within the core data, in comparison with the training data set, can introduce a source of error when used to produce paleo estimates. Any diatom species with a low Hills N2, which are therefore likely to have a poorly defined optima, are coloured red. All of the R scripts used to run the analyses are also included.

Transfer functions and species coverage

```
sppmax<-sapply(trainSET,max)
> fosmax<-sapply(core136,max)
> n2<-Hill.N2(trainSET)
> n2[is.infinite(n2)]<-0
> x11(4.5,4.5);par(mar=c(3,3,1,1), mgp=c(1.5,.5, 0))
> plot(sppmax,fosmax, xlab="Calibration set maximum", ylab="Fossil data maximum", col=ifelse(n2<=5, 2,1), pch=
ifelse(n2<=5, 16,1))
> abline(0,1, col=2)
> identify(sppmax,fosmax, labels=names(sppmax), cex=0.7)
```

A scatterplot of the maximum abundance values for each diatom species within core SO136-111 versus the training database of Crosata et al. (2004).

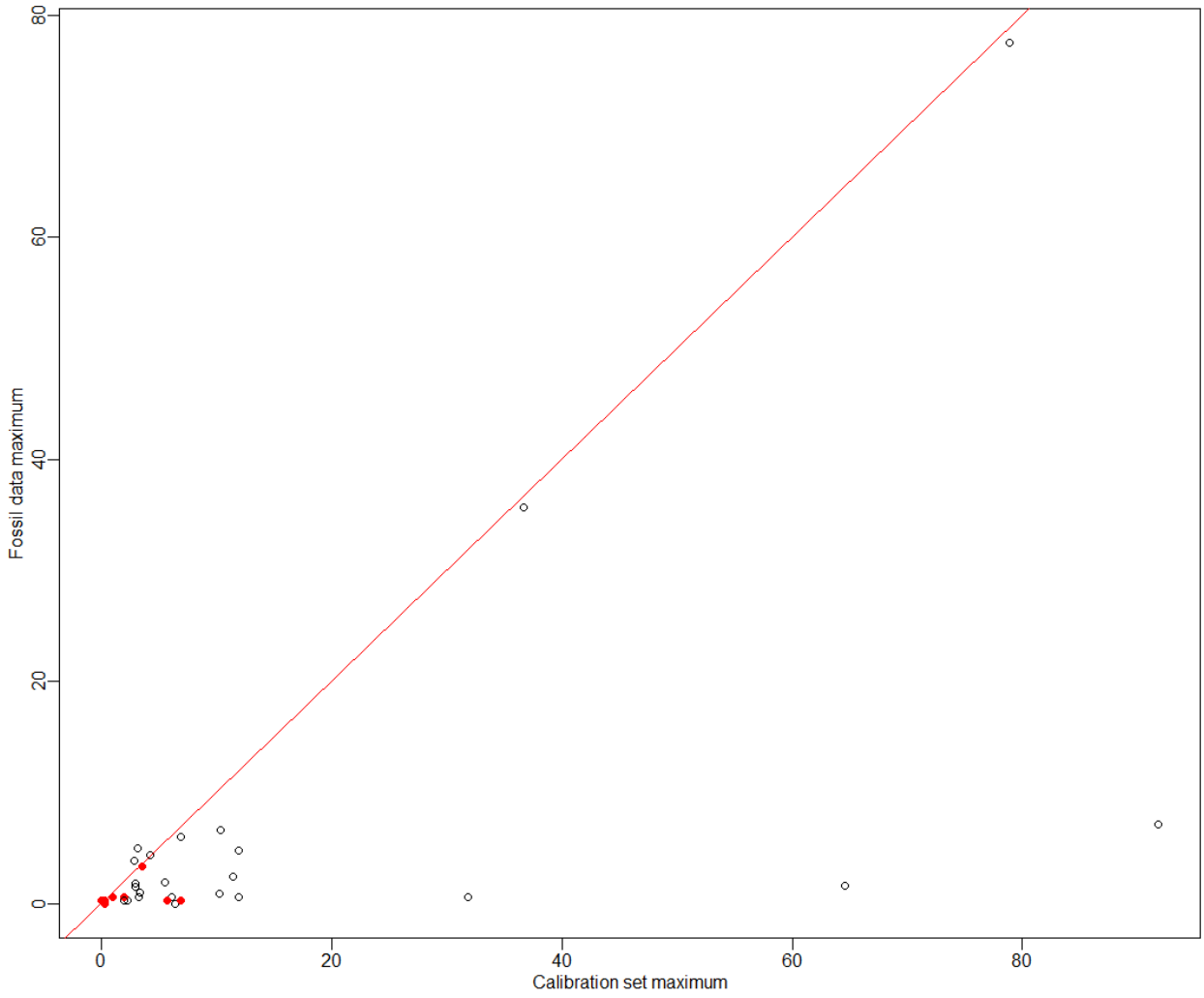

The maximum sum of taxa in the fossil data that are not present in the modern data is:

```
max(rowSums(core136[,n2==0 ,drop=F]))
[1] 0.3
```

Analogue quality, and reconstruction quality

From; http://quantpalaeo.wordpress.com/2014/05/11/analogue-quality-reconstruction-quality/

```
SI <- wSIC13yr$wSIC13yr
depths<-as.numeric(rownames(core136))
mod<-MAT(trainSET, SI)
pred<-predict(mod,core136)
> plot(depths, pred$dist.n[,1], ylab="Squared chord distance", xlab="Depth")
goodpoorbad<-quantile(paldist(trainSET), prob=c(0.05, 0.1))
> abline(h=goodpoorbad, col=c("orange", "red"))
```

The squared chord values for each of the samples within core SO136-111.

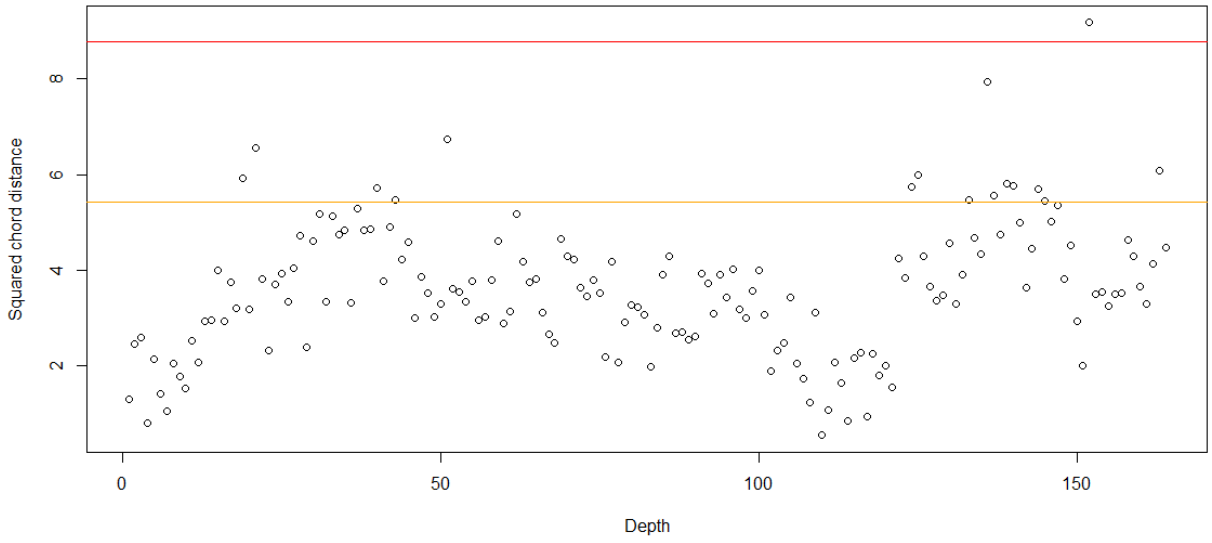

Constrained ordination

From: http://quantpalaeo.wordpress.com/2014/05/17/beyond-nearest-analogue-distance/

```
myspp <- trainSET
myfos <- core136
myenv <- wSIC13yr$wSIC13yr
plot(cca(myspp~myenv))
depths<-as.numeric(rownames(myfos))
```

A biplot of the first two axes from the CCA on the training database of Crosta et al. (2004), constrained by winter sea-ice concentration.

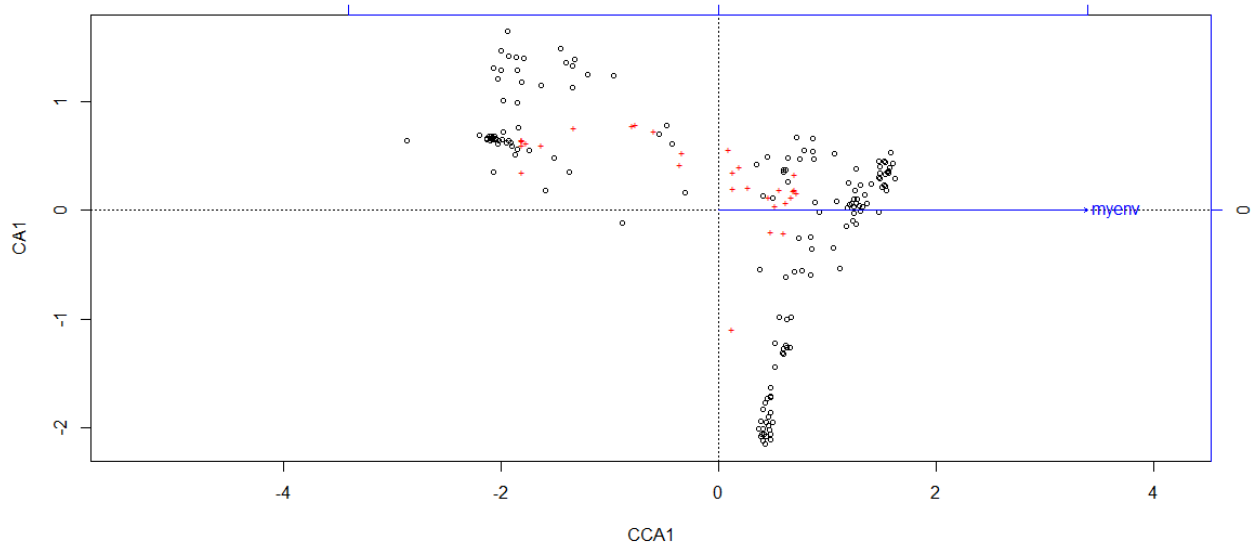


```
rlen<-residLen(myspp, myenv, myfos, method="rda")
plot(depths, rlen$passive, ylab="Squared residual length", xlab="Depth")
abline(h=quantile(rlen$train, probs = c(0.9,0.95)), col=c("orange", "red"))
```

The squared residual length for each of the samples within core SO136-111.

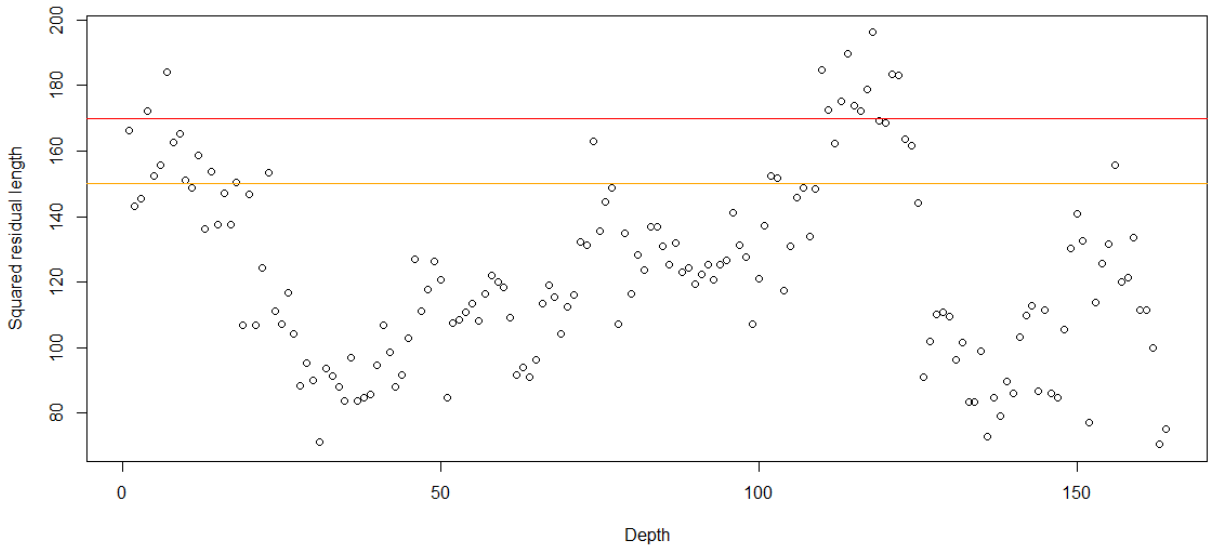


```
decorana(myspp)
Call:
decorana(veg = myspp)
Detrended correspondence analysis with 26 segments.
Rescaling of axes with 4 iterations.
                DCA1    DCA2    DCA3    DCA4
Eigenvalues     0.7151 0.27635 0.20692 0.21783
Decorana values 0.7379 0.08177 0.04161 0.03591
Axis lengths    3.8309 1.70519 1.48964 1.51463
```

Appendix 2.10

All of the paleo winter sea-ice estimates, along with the 95% confidence bounds from GAM, plotted in Figure 7 of Chapter 2.

GAM wSIC (%)	GAM wSIC (%) Lower 95% Confidence Interval	GAM wSIC (%) Upper 95% Confidence Interval	MAT wSIC (%)	WA-PLS wSIC (%)	IKTF wSIC (%)
0.15	-0.18	0.83	0.00	2.44	0.78
0.33	-0.08	1.14	2.92	0.17	2.01
2.34	0.69	6.11	0.00	0.34	2.32
1.66	0.41	4.54	0.00	0.11	2.45
0.09	-0.22	0.73	0.00	0.94	2.14
0.08	-0.22	0.73	0.00	0.22	1.14
0.22	-0.21	1.26	0.00	-0.16	0.95
5.71	2.02	14.00	0.00	0.70	2.55
1.66	0.41	4.53	0.00	0.48	2.58
0.08	-0.22	0.73	0.00	-0.05	0.65
1.67	0.41	4.59	0.00	1.21	4.95
0.12	-0.20	0.77	0.00	-0.09	0.81
0.71	0.11	1.87	0.00	-0.14	0.49
1.65	0.41	4.48	0.00	1.48	4.05
0.24	-0.13	0.98	0.00	-0.19	0.51
1.97	0.55	5.19	0.00	-0.14	1.72
0.28	-0.11	1.06	0.00	1.61	1.71
1.66	0.41	4.56	0.00	1.11	4.92
0.49	0.00	1.45	2.92	0.05	1.46
0.09	-0.23	0.78	0.00	0.82	2.32
22.03	8.88	44.55	24.77	0.17	5.75
0.78	0.15	2.00	0.00	-0.07	0.99
1.67	0.43	4.51	0.00	0.18	3.01
6.19	2.81	12.57	27.48	0.78	3.86
24.93	10.02	49.33	28.72	4.36	6.47
3.81	1.60	8.13	27.48	1.36	3.76
23.15	8.15	49.95	23.88	1.68	4.29
29.99	12.32	56.33	28.72	2.43	6.53
3.30	1.34	7.22	14.61	4.41	5.75
12.90	4.96	28.83	26.70	3.19	15.37
38.97	20.16	61.65	41.18	17.71	20.65
47.30	27.15	68.35	36.24	8.79	15.26
37.38	20.22	58.34	36.50	17.74	29.56
20.15	8.23	41.02	36.24	25.67	25.00
29.98	13.18	54.43	26.73	30.42	29.37
9.18	2.77	24.92	36.50	22.06	16.36
33.09	14.06	59.68	28.72	19.42	18.74
22.03	8.88	44.55	28.72	22.96	17.88
17.92	6.75	39.06	28.72	20.32	15.14

19.84	7.12	43.74	40.37	22.83	26.63
18.10	8.43	34.29	24.64	24.78	26.73
35.94	18.05	58.69	27.48	10.48	23.76
29.54	12.79	54.25	41.18	7.01	15.54
22.02	9.92	41.63	26.70	10.90	14.84
17.06	6.75	36.27	32.51	16.49	15.42
13.82	6.04	28.05	21.02	20.26	18.06
48.91	27.41	70.81	24.15	3.22	11.82
36.76	18.87	59.11	25.79	4.55	9.05
13.78	4.94	32.11	34.62	5.52	8.21
29.91	13.99	52.60	28.72	5.50	10.92
19.48	7.94	39.90	23.70	6.14	21.75
8.98	3.65	19.73	20.70	24.68	19.61
25.57	11.80	46.58	28.50	10.67	16.62
4.76	1.80	11.08	14.61	9.24	10.62
7.67	3.08	17.09	35.22	7.90	18.04
2.24	0.65	5.86	11.68	9.81	6.21
7.57	2.65	18.68	28.50	6.59	8.97
5.70	2.04	13.87	20.70	7.37	11.09
9.44	3.84	20.67	18.96	12.94	12.25
7.25	3.30	14.65	29.09	6.85	5.98
27.87	12.89	49.95	18.96	7.49	10.13
13.92	5.57	30.06	18.96	5.56	11.02
5.73	1.82	15.20	39.16	10.99	15.85
24.53	12.28	42.77	24.64	13.45	25.73
22.18	9.73	42.59	31.42	16.22	14.81
31.17	14.46	54.59	42.05	10.08	13.14
9.17	3.58	20.77	16.04	8.10	8.94
15.27	5.98	33.15	18.96	7.91	8.20
12.22	5.49	24.51	31.42	7.85	10.63
19.40	8.88	36.91	22.76	5.85	12.72
4.01	1.26	10.57	33.17	9.65	11.05
1.38	0.31	3.78	2.92	2.63	4.41
0.49	0.00	1.45	2.92	2.96	3.08
0.20	-0.21	1.19	0.31	2.10	5.50
1.79	0.54	4.49	2.92	0.87	4.56
1.68	0.43	4.53	3.79	0.86	3.57
1.80	0.44	5.01	2.92	1.04	5.41
11.99	4.76	26.36	14.61	1.39	4.46
5.99	2.19	14.34	7.74	2.78	6.83
15.99	7.28	31.14	7.74	3.21	6.86
7.23	2.89	16.21	20.70	12.73	14.11
3.50	1.30	8.15	8.05	12.56	9.31
7.86	3.02	18.10	8.61	10.16	7.18
1.25	0.24	3.60	0.87	2.21	3.82
1.26	0.25	3.61	2.92	0.99	3.61
1.37	0.31	3.76	3.24	4.51	4.42
0.21	-0.15	0.93	2.92	1.38	1.87
0.14	-0.19	0.80	2.92	1.77	2.68
0.16	-0.18	0.84	3.24	2.96	3.43
2.30	0.68	6.03	15.39	4.05	5.39

3.06	1.05	7.47	2.92	1.28	3.30
0.26	-0.12	1.01	15.39	3.22	3.13
8.41	3.25	19.23	2.92	4.44	5.39
1.53	0.40	4.02	15.39	1.70	3.48
0.15	-0.18	0.83	15.02	0.89	3.06
0.28	-0.11	1.06	2.92	0.69	2.52
1.33	0.24	3.94	0.00	1.09	3.31
2.01	0.57	5.31	10.66	2.00	3.91
1.51	0.39	3.99	2.92	0.88	3.13
6.19	2.28	14.72	23.13	1.41	6.36
1.27	0.25	3.62	3.24	5.97	3.85
0.08	-0.23	0.74	0.00	1.32	1.78
1.68	0.43	4.52	0.00	2.83	2.59
4.20	1.36	10.85	15.39	5.85	6.30
28.51	15.08	47.06	19.83	5.87	10.47
5.86	2.39	12.92	7.74	1.25	5.40
3.94	1.49	9.11	0.00	3.25	3.93
3.53	1.32	8.19	4.81	3.39	4.25
6.10	2.14	15.10	1.18	4.54	8.47
0.26	-0.22	1.53	0.00	0.44	1.18
0.14	-0.21	0.93	0.00	0.22	1.17
1.76	0.43	4.86	0.00	1.37	3.35
2.37	0.44	7.87	0.00	0.20	2.36
0.25	-0.21	1.45	0.00	-0.23	0.68
2.32	0.46	7.52	0.00	1.22	2.93
2.36	0.45	7.79	0.00	0.14	2.38
0.16	-0.21	0.99	0.00	-0.11	1.42
0.28	-0.22	1.67	0.00	-0.31	0.73
1.87	0.46	5.25	0.00	-0.09	1.43
0.23	-0.21	1.35	0.00	-0.12	1.49
0.22	-0.21	1.26	0.00	0.04	1.52
2.13	0.18	9.11	0.00	0.13	2.19
0.27	-0.22	1.61	0.00	-0.26	0.96
0.28	-0.22	1.69	0.00	-0.24	1.62
0.27	-0.22	1.61	0.00	-0.26	1.90
0.17	-0.17	0.86	6.87	0.30	2.67
9.67	3.37	23.65	18.96	2.72	8.63
17.83	7.61	35.86	23.78	9.58	14.86
9.26	3.20	22.86	20.15	20.99	15.40
8.29	2.75	21.17	35.22	19.66	23.61
7.51	2.64	18.47	37.65	8.79	7.97
15.65	6.30	33.24	36.24	9.86	22.32
16.41	7.26	32.53	39.16	4.21	12.29
16.72	6.74	35.25	22.76	8.86	11.60
8.89	3.25	21.14	36.24	14.52	13.82
19.92	6.63	45.79	37.54	12.00	21.18
5.85	2.20	13.71	38.46	10.79	17.26
33.10	16.55	55.08	23.78	22.87	17.70
59.15	34.64	79.89	22.76	8.65	22.65
44.13	23.27	67.24	31.42	8.01	19.22
39.60	21.93	60.40	32.30	14.89	26.02

6.86	2.26	17.72	15.39	6.06	6.48
2.86	0.76	8.15	3.79	12.11	10.57
43.15	17.78	72.60	7.31	2.17	6.98
3.89	1.25	10.05	0.00	0.46	2.30
0.71	0.11	1.87	2.92	-0.24	1.13
2.94	0.91	7.65	18.96	3.16	7.10
0.61	0.06	1.68	2.92	0.80	2.07
0.23	-0.14	0.96	0.31	1.84	2.01
0.12	-0.22	0.86	0.31	0.82	1.95
0.08	-0.23	0.74	0.00	0.69	2.02
4.43	0.80	16.46	0.78	2.82	5.18
0.16	-0.18	0.84	3.24	1.43	4.70
0.12	-0.20	0.77	0.00	1.13	1.60
0.09	-0.22	0.73	3.24	3.11	3.37
1.67	0.41	4.59	0.31	2.63	3.90
2.56	0.94	5.87	2.92	0.91	3.24
12.54	3.02	37.73	28.32	3.36	2.48
0.14	-0.18	0.81	2.92	0.22	1.87
0.10	-0.21	0.73	0.00	0.65	1.28
0.44	-0.02	1.36	3.24	1.02	3.11
0.13	-0.19	0.78	2.92	0.02	2.00
0.49	0.00	1.45	4.87	0.51	2.45
0.11	-0.20	0.76	19.33	2.60	4.01

Appendix 3.1

Complete list of AMS dating completed on E27-23 from various identified sources with original ^{14}CAge and reported error. Three dates identified as Burckle pers comm. here were provided by Dr Lloyd Burckle (LDEO) to Dr L. Armand for this work. Outlier attributions are identified; the term 'averaged' identifies the two samples where final calibrated dates were averaged in this work. All remaining AMS dates were converted to calendar ages using the linear-based CALIB07 (Stuiver and Reimer, 1993) with calibration to the Marine13 dataset (Reimer et al., 2013) at 95% confidence (sigma 2) and included a correction for the surface water reservoir age of ~752 years at the site of core E27-23 resolved from the marine radiocarbon reservoir correction database and software available from http://radiocarbon.LDEO.columbia.edu/ (Butzin et al., 2005). The percent Marine Carbon relative attribution is provided. The Median age (Cal Yr BP) used as the final age at each respective (mid) depth is provided.

Mid point Depth (cm)	Sample Code	Source	Raw ^{14}C age yr BP	Corrected raw age (RA=752)	Outlier Type	95.4 % (2s) cal age ranges	Relative area under distribution (Marine 13)	Median Age Cal Yr BP
4.0	OS34727	Burckle pers. comm.	2360±40	1608		cal BP 1329-1820	1	1576
26.5	OZJ414	This paper	2830±60	2078		cal BP 1838-2412	1	2132
32.5	OZJ415	This paper	2860±60	2108		cal BP 1868-2462	1	2167
103.0	OZ1872	This paper	5200±70	4448		cal BP 4836-5439	1	5136
199.0	OZ1873	This paper	5980±90	5228		cal BP 5713-6298	1	6030
279.0	OZ1784	This paper	8450±100	7698	Outlier			
299.0	OZK204	This paper	6670±90	5918		cal BP 6475-7131	1	6786
329.0	OZJ416	This paper	6160±70	5408	Reversal	cal BP 5929-6467	1	6216
379.0	OZJ417	This paper	7370±80	6618		cal BP 7269 -7744	1	7510
439.0	OZ1785	This paper	7960±70	7208		cal BP 7833-8328	1	8073
509.0	OZ1876	This paper	9720±90	8968		cal BP 9797-10551	1	10201
529.0	OZK205	This paper	10340±120	9588		cal BP 10551-11285	1	10946
539.0	OZK206	This paper	7810±70	7058	Outlier			
549.0	OZI877	This paper	14410±120	13658	Outlier			
579.0	OZJ418	This paper	11900±100	11148	Averaged	cal BP 12724-13296	1	13020
599.0	OZJ419	This paper	11910±100	11158	Averaged	cal BP 12731-13304	1	13029
600.5	OS51913	Anderson et al. 2009	12150±60	11398		cal BP 13013-13498	1	13268
619.0	OZK207	This paper	12470±140	11718		cal BP 13251-13955	1	13584
629.0	OZI878	This paper	40700±1700	39948	Outlier			

629.0	OZK208	This paper	13200±130	12448		cal BP 14046-15171	1	14596
639.0	OZK211	This paper	13780±120	13028		cal BP 15148-16049	1	15586
709.0	OZ1879	This paper	3890±70	3138	Outlier			
709.0	OZK209	This paper	14660±180	13908	Reversal	cal BP 16252-17448	1	16843
719.0	OZK359	This paper	14620±110	13868		cal BP 16300-17241	1	16785
740.5	OS51910	Anderson et al. 2009	14300±65	13548	Reversal	cal BP 15956-16721	1	16320
760.5	OS51914	Anderson et al. 2009	14850±65	14098		cal BP 16731-17503	1	17138
779.0	OZK210	This paper	15010±170	14258		cal BP 16762-17882	1	17337
780.5	OS51915	Anderson et al. 2009	18250±95	17498		cal BP 20727-21549	1	21136
799.0	OS29761	Burckle pers. comm.	24400±190	23648		cal BP 27417-28165	1	27759
849.0	OZK360	This paper	32100±560	31348		cal BP 34185-36347	1	35271
859.0	OZI880	This paper	9690±80	8938	Outlier			
929.0	OZI881	This paper	31970±690	31218	Reversal	cal BP 33871-36505	1	35171

Appendix 3.2

Comparison of calibration output from the input of accepted ^{14}C dates using OXCAL 4.2 (Bronk Ramsey 2009; Blaauw 2010), and CALIB07 (Stuiver and Reimer, 1993), both using the Marine13 calibration curve (Reimer et al., 2013) at 95.4% confidence (sigma 2) and including a correction for the surface water reservoir age of ~752 years at the site of core E27-23. The calibration output difference between the median Cal Yr BP, regardless of calibration method employed, was ≥40 Cal Yr BP. Calibration data from the output of CALIB07 has been used in this paper to determine chronostratigraphy.

			OXCAL 4.2 Marine13, Delta R352, 2 sigma.						CALIB07 Marine13, DeltaR352, 2 sigma				
Mid pt Depth (cm)	**Sample Code**	**Raw ^{14}C age yr BP**	**lower cal range BP**	**upper cal range BP**	**%**	**mu**	**sigma**	**median Cal Yr BP**	**corrected error #**	**lower cal range BP**	**upper cal range BP**	**median Cal Yr BP**	**Calibration Offset OXCAL-CALIB Cal Yr BP**
4.0	OS34727	2360±40	1330	1825	95.4	1579	127	1576	108	1329	1820	1576	0
26.5	OZJ414	2830±60	1840	2422	95.4	2134	146	2134	117	1838	2412	2132	2
32.5	OZJ415	2860±60	1870	2470	95.4	2170	149	2169	117	1868	2462	2167	2
103.0	OZ1872	5200±70	4837	5441	95.4	5136	160	5137	122	4836	5439	5136	1
199.0	OZ1873	5980±90	5714	6304	95.4	6028	149	6031	135	5713	6298	6030	1
299.0	OZK204	6670±90	6477	7135	95.4	6791	165	6788	135	6475	7131	6786	2
379.0	OZJ417	7370±80	7273	7751	95.4	7513	116	7511	128	7269	7744	7510	1
439.0	OZ1785	7960±70	7836	8331	95.4	8077	125	8074	122	7833	8328	8073	1
509.0	OZ1876	9720±90	9803	10557	95.4	10194	189	10204	135	9797	10551	10201	3
529.0	OZK205	10340±120	10553	11298	95.4	10947	194	10949	156	10551	11285	10946	3
579.0	OZJ418	11900±100	12726	13300	95.4	13019	148	13021	141	12724	13296	13020	1
599.0	OZJ419	11910±100	12733	13308	95.4	13028	149	13030	141	12731	13304	13029	1
600.5	OS51913	12150±60	13016	13504	95.4	13266	117	13269	117	13013	13498	13268	1
619.0	OZK207	12470±140	13256	13965	95.4	13596	180	13587	172	13251	13955	13584	3
629.0	OZK208	13200±130	14050	15177	95.4	14607	309	14600	164	14046	15171	14596	4
639.0	OZK211	13780±120	15154	16054	95.4	15592	235	15590	156	15148	16049	15586	4
719.0	OZK359	14620±110	16305	17251	95.4	16788	239	16789	149	16300	17241	16785	4
760.5	OS51914	14850±65	16737	17506	95.4	17134	194	17139	119	16731	17503	17138	1
779.0	OZK210	15010±170	16777	17890	95.4	17334	276	17342	197	16762	17882	17337	5
780.5	OS51915	18250±95	20732	21557	95.4	21144	207	21139	138	20727	21549	21136	3
799.0	OS29761	24400±190	27422	28188	95.4	27781	187	27764	215	27417	28165	27759	5
849.0	OZK360	32100±560	34196	36480	95.4	35353	588	35311	569	34185	36347	35271	40

Appendix 3.3

The foraminiferal stable isotope data from E27-23. Ratios of oxygen ($\delta^{18}O$) measured from the planktonic foraminifer *Neogloboquadrina pachyderma* sinistral (>150 µm). Isotope values are reported as per mil (%) deviations relative to the Vienna Peedee Belemnite (VPDB).

Mid pt Depth (cm)	Sample Weight (µg)	$\delta^{18}O$ (‰ VPDB)	$\delta^{13}C$ (‰ VPDB)
91	125	3.19	0.76
99	82	3.21	0.81
103	90	3.23	0.84
109	95	3.31	0.62
119	107	3.22	0.76
129	71	3.20	0.75
139	73	3.12	0.88
149	89	3.22	0.76
159	121	3.15	0.82
169	127	3.20	0.89
179	90	3.11	0.72
189	71	3.10	0.70
199	153	3.24	0.91
209	97	3.12	0.82
219	115	3.24	0.70
229	118	3.16	0.74
239	73	3.10	0.81
249	130	3.15	0.83
259	143	3.24	0.84
269	142	3.15	0.74
279	168	3.21	0.80
289	59	3.16	0.70
299	101	3.17	0.66
309	73	3.11	0.87
329	131	3.26	0.67
339	110	3.20	0.69
349	127	3.24	0.71
359	89	3.15	0.57
369	106	3.22	0.63
379	106	3.16	0.72
389	148	3.20	0.69
409	133	3.15	0.68
419	149	3.23	0.71
429	131	3.23	0.68
439	122	3.26	0.65
449	105	3.26	0.60
459	119	3.32	0.65
469	61	3.41	0.47
479	112	3.31	0.56
489	109	3.26	0.58
499	130	3.40	0.66
509	130	3.33	0.52
519	151	3.43	0.69
529	145	3.43	0.63
539	162	3.56	0.58
549	158	3.59	0.58
559	60	3.72	0.43
579	138	3.93	0.48
589	125	3.96	0.33
599	200	4.04	0.35
609	145	4.01	0.35
619	149	4.11	0.27

629	178	4.09	0.30
639	140	4.06	0.21
649	115	3.97	0.22
669	170	4.16	0.31
679	165	4.15	0.37
689	217	4.15	0.38
699	69	4.19	0.31
709	221	4.29	0.21
719	195	4.17	0.31
729	151	4.20	0.16
739	132	4.30	0.23
749	128	4.31	0.11
759	177	4.34	0.18
769	180	4.48	0.16
779	144	4.62	-0.08
789	133	4.46	0.02
799	139	4.43	0.01
819	132	4.26	0.11
829	160	4.35	0.14
839	195	4.30	0.18
849	188	4.25	0.24
859	180	4.22	0.19
869	195	4.25	0.15
879	147	4.09	0.29
889	143	4.14	0.23
899	190	4.32	0.21
909	167	4.26	0.20
919	168	4.13	0.13
929	196	4.17	0.22
939	150	4.18	0.19
949	175	4.13	0.19

Appendix 3.4

Revised age model tie points used to determine the age model for SO136-111 using the same calibration methods as applied to E27-23. AMS dates were converted to calendar ages using the linear-based CALIB07 (Stuiver and Reimer, 1993) with calibration to the Marine13 dataset (Reimer et al., 2013). $\delta^{18}O$ tuning was determined by calibrating the $\delta^{18}O$ record to the global Pliocene-Pleistocene benthic $\delta^{18}O$ stack (Lisiecki and Raymo, 2005a,b) ($\delta^{18}O$ tuning LR04-Linage) applying Analyseries 2.0.8 (Paillard et al., 1996). Previous calibrated age estimates of this core were derived using CALIB05 and the SPECMAP stack (Crosta et al., 2004).

				CALIB07 Marine13, DeltaR223, 2 sigma			
Depth (cm)	**Pointer Method used**	**Raw ^{14}C age yr BP**	**Corrected raw age (RA=623)**	**lower cal range BP**	**upper cal range BP**	**Median Cal Yr BP (This study)**	**Cal Yr BP in Crosta04 (CALIB05, SPECMAP)**
1	^{14}C AMS CALIB07	3715±50	3092	3070	3641	3360	3163
31	^{14}C AMS CALIB07	10235±60	9612	10684	11221	10950	10414
56	^{14}C AMS CALIB07	16860±100	16237	19214	19980	19600	19045
111	^{14}C AMS CALIB07	43120±1870	42497	42912	49428	46170	43120
161	$\delta^{18}O$ tuning					66000	65220
241	$\delta^{18}O$ tuning					87000	90100
366	$\delta^{18}O$ tuning					109000	110790
416	$\delta^{18}O$ tuning					119000	125000
466	$\delta^{18}O$ tuning					126000	135340
501	$\delta^{18}O$ tuning					135000	141330
536	$\delta^{18}O$ tuning					166000	162790
571	$\delta^{18}O$ tuning					192000	193070
681	$\delta^{18}O$ tuning					217000	215540
756	$\delta^{18}O$ tuning					239000	240190
881	$\delta^{18}O$ tuning					286000	288540

Appendix 3.5

The paleo wSIC estimates for marine sediment core SO136-111 using GAM/WSI/13, GAM/WSI/ETS and the MAT from Crosta et al. (2004).

Calendar ages (kyr BP)	GAM/WSI/13 wSIC (%)	95% LCL	95% UCL	GAM/WSI/ETS wSIC (%)	95% LCL	95% UCL	MAT m/yr sea ice cover (Crosta et al. 2004)	MAT SST °C (Crosta et al. 2004)	Samples with no analogue (NA) or a poor analogue (PA)
3.39	0.15	-0.18	0.83	0.11	-0.21	0.78	0.00	5.03	
3.87	0.33	-0.08	1.14	0.27	-0.13	1.10	0.00	4.65	
4.37	2.34	0.69	6.11	2.45	0.70	6.59	0.00	4.61	
4.88	1.66	0.41	4.54	1.89	0.47	5.26	0.00	5.13	
5.38	0.09	-0.22	0.73	0.06	-0.24	0.72	0.00	5.05	
5.89	0.08	-0.22	0.73	0.06	-0.24	0.74	0.00	5.33	
6.40	0.22	-0.21	1.26	0.25	-0.21	1.43	0.00	5.24	
6.90	5.71	2.02	14.00	6.49	2.23	16.26	0.00	5.44	
7.41	1.66	0.41	4.53	1.88	0.47	5.23	0.00	5.13	
7.91	0.08	-0.22	0.73	0.07	-0.24	0.75	0.00	5	
8.42	1.67	0.41	4.59	1.92	0.48	5.36	0.00	4.55	
8.93	0.12	-0.20	0.77	0.08	-0.23	0.74	0.00	5.19	
9.43	0.71	0.11	1.87	0.67	0.07	1.90	0.00	5.71	
9.94	1.65	0.41	4.48	1.83	0.46	5.07	0.00	5.05	
10.44	0.24	-0.13	0.98	0.18	-0.17	0.93	0.00	5.76	
10.96	1.97	0.55	5.19	2.06	0.55	5.60	0.00	5.79	
11.64	0.28	-0.11	1.06	0.23	-0.15	1.01	0.00	4.63	
12.33	1.66	0.41	4.56	1.90	0.48	5.29	0.00	4.76	
13.03	0.49	0.00	1.45	0.43	-0.05	1.43	0.00	5.54	
13.72	0.09	-0.23	0.78	0.09	-0.24	0.83	0.00	5.28	
14.41	22.03	8.88	44.55	26.20	10.57	51.20	0.00	6.09	
15.10	0.78	0.15	2.00	0.74	0.10	2.04	0.00	4.95	
15.79	1.67	0.43	4.51	1.82	0.46	5.02	0.00	5.23	
16.49	6.19	2.81	12.57	6.80	3.00	14.09	0.40	5.51	
17.18	24.93	10.02	49.33	30.01	12.17	56.71	1.00	4.67	
17.87	3.81	1.60	8.13	3.89	1.55	8.61	0.40	4.97	
18.56	23.15	8.15	49.95	30.47	10.67	61.26	0.40	5.15	
19.25	29.99	12.32	56.33	35.65	14.89	63.49	0.40	6.4	
20.08	3.30	1.34	7.22	3.31	1.26	7.54	0.40	3.87	
21.05	12.90	4.96	28.83	14.04	5.25	31.72	1.00	3.86	
22.02	38.97	20.16	61.65	42.95	22.24	66.39	2.00	2.84	
22.98	47.30	27.15	68.35	50.16	28.65	71.62	1.00	3.41	
23.95	37.38	20.22	58.34	39.78	21.25	61.70	1.40	3.34	
24.91	20.15	8.23	41.02	21.76	8.66	44.45	1.40	3.34	
25.88	29.98	13.18	54.43	33.20	14.45	59.17	1.00	3.36	
26.85	9.18	2.77	24.92	10.44	3.04	28.65	1.60	3.37	
27.81	33.09	14.06	59.68	37.34	15.85	65.16	1.90	1.98	
28.78	22.03	8.88	44.55	26.20	10.57	51.20	1.90	2.82	
29.74	17.92	6.75	39.06	19.95	7.35	43.27	1.30	3.1	
30.71	19.84	7.12	43.74	22.19	7.80	48.36	2.00	3.02	
31.68	18.10	8.43	34.29	19.89	9.03	37.93	1.00	3.36	
32.64	35.94	18.05	58.69	39.10	19.48	62.91	1.70	2.65	
33.61	29.54	12.79	54.25	32.64	13.96	58.89	2.00	2.84	
34.58	22.02	9.92	41.63	24.45	10.82	45.98	1.80	2.29	
35.54	17.06	6.75	36.27	19.11	7.42	40.47	1.30	3.3	
36.51	13.82	6.04	28.05	15.38	6.55	31.50	1.20	2.46	
37.47	48.91	27.41	70.81	53.23	30.11	75.07	1.50	2.34	
38.44	36.76	18.87	59.11	40.34	20.63	63.67	1.00	3.28	
39.41	13.78	4.94	32.11	16.42	5.76	37.86	1.30	2.76	
40.37	29.91	13.99	52.60	33.56	15.62	57.77	1.50	2.97	PA
41.34	19.48	7.94	39.90	21.34	8.49	43.75	1.00	5.51	
43.27	8.98	3.65	19.73	9.88	3.90	22.08	1.00	3.61	
45.69	25.57	11.80	46.58	28.98	13.26	51.87	1.30	2.7	
47.76	4.76	1.80	11.08	5.06	1.85	12.10	1.20	2.8	
49.74	7.67	3.08	17.09	8.48	3.31	19.23	1.30	3.54	
51.72	2.24	0.65	5.86	2.34	0.66	6.31	0.00	2.76	
53.71	7.57	2.65	18.68	8.32	2.81	20.96	1.70	3.26	
55.69	5.70	2.04	13.87	6.33	2.19	15.76	1.00	3.62	
57.67	9.44	3.84	20.67	10.41	4.12	23.15	1.40	2.2	
59.65	7.25	3.30	14.65	8.16	3.64	16.75	0.90	3.38	
61.64	27.87	12.89	49.95	31.85	14.69	55.69	1.40	3.31	
63.62	13.92	5.57	30.06	15.68	6.15	33.89	0.44	3.89	
65.60	5.73	1.82	15.20	6.25	1.92	16.97	1.50	2.19	
67.05	24.53	12.28	42.77	26.62	13.08	46.41	1.20	3.34	
68.36	22.18	9.73	42.59	24.10	10.34	46.27	0.84	3.31	
69.41	31.17	14.46	54.59	35.97	16.78	60.86	0.80	2.65	
70.99	9.17	3.58	20.77	9.89	3.74	22.81	0.80	3.36	
72.04	15.27	5.98	33.15	16.91	6.47	36.79	0.44	3.92	

73.61	12.22	5.49	24.51	13.19	5.77	26.87	0.70	3.37	
74.66	19.40	8.88	36.91	21.41	9.60	40.75	0.80	2.61	
76.24	4.01	1.26	10.57	4.38	1.34	11.83	0.80	2.24	
77.29	1.38	0.31	3.78	1.30	0.24	3.80	0.00	5.7	
78.86	0.49	0.00	1.45	0.43	-0.05	1.43	0.04	4.23	
80.18	0.20	-0.21	1.19	0.24	-0.21	1.35	0.10	4	
81.49	1.79	0.54	4.49	1.68	0.44	4.48	0.00	4.87	
82.80	1.68	0.43	4.53	1.82	0.46	5.02	0.00	4.96	
84.11	1.80	0.44	5.01	2.15	0.55	6.05	0.00	5.71	
85.43	11.99	4.76	26.36	13.28	5.15	29.44	0.04	3.73	
86.74	5.99	2.19	14.34	6.48	2.29	15.89	0.40	3.46	
87.70	15.99	7.28	31.14	17.36	7.71	34.13	0.40	3.23	
88.58	7.23	2.89	16.21	8.06	3.12	18.41	0.90	2.42	
89.46	3.50	1.30	8.15	3.93	1.43	9.35	0.50	2.8	
90.34	7.86	3.02	18.10	8.39	3.12	19.74	0.40	3.38	
91.22	1.25	0.24	3.60	1.21	0.18	3.72	0.00	4.28	
92.10	1.26	0.25	3.61	1.22	0.19	3.71	0.00	4.89	
92.98	1.37	0.31	3.76	1.29	0.23	3.78	0.00	3.5	
93.86	0.21	-0.15	0.93	0.16	-0.19	0.88	0.00	4.1	
94.74	0.14	-0.19	0.80	0.09	-0.22	0.76	0.04	3.21	
95.62	0.16	-0.18	0.84	0.11	-0.21	0.79	0.04	3.43	
96.50	2.30	0.68	6.03	2.41	0.68	6.50	0.34	3.9	
97.38	3.06	1.05	7.47	2.95	0.93	7.60	0.00	4.22	
98.26	0.26	-0.12	1.01	0.20	-0.17	0.96	0.04	3.58	
99.14	8.41	3.25	19.23	9.01	3.38	21.02	0.04	3.23	
100.02	1.53	0.40	4.02	1.43	0.31	4.01	0.04	4.19	
100.90	0.15	-0.18	0.83	0.11	-0.21	0.78	0.04	4.3	
101.78	0.28	-0.11	1.06	0.23	-0.15	1.01	0.04	4.13	
102.66	1.33	0.24	3.94	1.41	0.24	4.37	0.00	4.09	
104.42	2.01	0.57	5.31	2.11	0.57	5.71	0.04	4.21	
105.30	1.51	0.39	3.99	1.41	0.30	3.98	0.04	4.54	
106.18	6.19	2.28	14.72	6.65	2.37	16.20	0.04	4.78	
107.06	1.27	0.25	3.62	1.22	0.19	3.71	0.14	3.34	
107.94	0.08	-0.23	0.74	0.07	-0.24	0.76	0.00	3.58	
108.82	1.68	0.43	4.52	1.82	0.46	5.02	0.00	4.28	
109.80	4.20	1.36	10.85	4.62	1.45	12.27	0.04	3.7	
110.80	28.51	15.08	47.06	30.31	15.75	50.13	0.40	2.88	
111.80	5.86	2.39	12.92	6.31	2.50	14.21	0.40	3.46	
112.80	3.94	1.49	9.11	4.20	1.54	9.97	0.00	3.82	
113.80	3.53	1.32	8.19	3.90	1.42	9.26	0.10	3.12	
114.80	6.10	2.14	15.10	7.25	2.49	18.13	0.20	3.31	
116.20	0.26	-0.22	1.53	0.29	-0.22	1.72	0.00	5.46	
117.00	0.14	-0.21	0.93	0.16	-0.22	1.04	0.00	5.03	
117.80	1.76	0.43	4.86	2.08	0.53	5.82	0.00	5.7	
118.60	2.37	0.44	7.87	2.75	0.51	9.51	0.00	5.24	
119.56	0.25	-0.21	1.45	0.28	-0.22	1.64	0.00	5.01	
120.12	2.32	0.46	7.52	2.74	0.54	9.19	0.00	5.13	
120.96	2.36	0.45	7.79	2.75	0.51	9.44	0.00	5.55	
121.52	0.16	-0.21	0.99	0.18	-0.21	1.11	0.00	5.17	
122.36	0.28	-0.22	1.67	0.29	-0.23	1.84	0.00	4.87	
122.92	1.87	0.46	5.25	2.25	0.57	6.39	0.00	5.24	
123.76	0.23	-0.21	1.35	0.27	-0.21	1.53	0.00	4.98	
124.32	0.22	-0.21	1.26	0.25	-0.21	1.43	0.00	4.4	
125.16	2.13	0.18	9.11	1.66	0.01	8.13	0.00	4.25	
125.72	0.27	-0.22	1.61	0.29	-0.23	1.79	0.00	6.07	
127.03	0.28	-0.22	1.69	0.29	-0.24	1.86	0.00	5.36	PA
128.06	0.27	-0.22	1.61	0.29	-0.23	1.79	0.00	5.84	PA
129.60	0.17	-0.17	0.86	0.12	-0.21	0.81	0.04	5.81	
130.63	9.67	3.37	23.65	10.36	3.49	25.86	0.40	3.84	
132.17	17.83	7.61	35.86	19.25	8.01	39.02	1.20	3.34	
133.20	9.26	3.20	22.86	9.95	3.32	25.08	0.80	2.78	
134.74	8.29	2.75	21.17	9.31	2.99	24.18	0.80	3.62	
137.66	7.51	2.64	18.47	8.75	3.01	21.72	1.08	1.76	
142.97	15.65	6.30	33.24	17.47	6.84	37.27	1.20	3.34	
146.51	16.41	7.26	32.53	17.70	7.63	35.44	0.74	3.91	PA
151.83	16.72	6.74	35.25	19.26	7.66	40.15	0.84	3.52	
155.37	8.89	3.25	21.14	9.50	3.35	23.07	1.50	3.08	
160.69	19.92	6.63	45.79	25.20	8.48	54.46	0.84	3.25	PA
164.23	5.85	2.20	13.71	6.29	2.28	15.15	1.74	2.24	PA
168.97	33.10	16.55	55.08	36.78	18.31	60.04	0.80	3.46	
171.94	59.15	34.64	79.89	64.82	39.22	84.13	0.80	2.61	
176.40	44.13	23.27	67.24	49.03	26.17	72.29	0.80	3.3	
179.37	39.60	21.93	60.40	41.85	22.89	63.49	0.80	2.78	
183.83	6.86	2.26	17.72	8.06	2.59	21.05	0.34	2.6	
187.54	2.86	0.76	8.15	3.17	0.82	9.31	0.00	2.88	
191.26	43.15	17.78	72.60	52.17	22.77	80.17	0.74	2.57	
192.91	3.89	1.25	10.05	4.24	1.32	11.28	0.00	4.77	
194.05	0.71	0.11	1.87	0.67	0.07	1.90	0.04	4.66	
195.18	2.94	0.91	7.65	3.12	0.93	8.36	0.44	2.62	
196.32	0.61	0.06	1.68	0.56	0.01	1.68	0.04	3.58	
197.45	0.23	-0.14	0.96	0.17	-0.18	0.91	0.00	4.3	
198.59	0.12	-0.22	0.86	0.13	-0.22	0.95	0.10	5.28	
199.73	0.08	-0.23	0.74	0.07	-0.24	0.77	0.00	4.65	
200.86	4.43	0.80	16.46	3.79	0.56	15.31	0.20	4.07	NA
202.00	0.16	-0.18	0.84	0.11	-0.21	0.79	0.04	3.48	
203.14	0.12	-0.20	0.77	0.08	-0.23	0.73	0.00	4.25	
204.27	0.09	-0.22	0.73	0.06	-0.24	0.72	0.14	3.47	PF
205.41	1.67	0.41	4.59	1.92	0.48	5.36	0.10	4.51	
206.55	2.56	0.94	5.87	2.47	0.84	5.98	0.04	3.81	

207.68	12.54	3.02	37.73	18.05	4.19	50.96	0.42	3.2	
208.82	0.14	-0.18	0.81	0.10	-0.22	0.77	0.04	4.97	
209.95	0.10	-0.21	0.73	0.06	-0.24	0.72	0.00	5.44	
211.09	0.44	-0.02	1.36	0.39	-0.07	1.33	0.04	3.58	
212.23	0.13	-0.19	0.78	0.08	-0.23	0.74	0.04	5.4	
213.36	0.49	0.00	1.45	0.43	-0.05	1.43	0.04	4.94	
214.50	0.11	-0.20	0.76	0.08	-0.23	0.73	0.34	3.53	

Appendix 3.6

The paleo wSIC estimates for marine sediment core E27-23 using GAM/WSI/ETS.

Calendar ages (kyr BP)	GAM/WSI/ETS wSIC (%)	95% LCL	95% UCL	Samples with no analogue (NA) or a poor analogue (PA)
1.54	35.31	14.72	63.11	PA
1.70	4.31	1.18	12.56	PA
1.80	13.96	4.33	35.59	PA
1.95	33.49	13.14	62.35	PA
2.05	16.08	6.46	34.13	PA
2.15	6.42	2.13	16.52	
2.19	17.49	7.53	35.07	
2.44	4.41	0.68	17.85	
2.61	29.98	14.05	52.63	NA
2.86	39.89	16.79	68.44	
3.28	6.79	1.52	22.61	NA
3.70	6.08	1.10	22.94	
3.87	10.17	2.68	29.84	NA
4.13	16.71	6.47	36.11	PA
4.29	10.99	3.49	28.41	
4.55	11.69	3.56	30.82	
4.63	12.17	4.66	27.44	
4.72	13.42	3.60	37.57	PA
4.97	10.24	4.43	21.34	
5.13	8.79	2.66	23.86	
5.19	15.11	5.56	34.19	PA
5.29	12.45	4.35	29.80	PA
5.38	5.82	1.91	15.05	
5.47	10.38	4.03	23.43	PA
5.56	37.98	18.41	62.31	PA
5.66	3.52	0.64	12.73	PA
5.75	12.80	4.63	29.85	
5.84	8.18	2.57	21.70	PA
5.94	2.84	0.80	7.82	
6.03	4.53	1.33	12.56	PA
6.11	2.70	0.70	7.75	
6.18	3.93	1.05	11.49	PA
6.26	1.78	0.23	6.40	
6.33	7.81	1.51	28.15	PA
6.41	2.06	0.29	7.53	
6.48	28.04	12.96	50.21	
6.56	43.92	25.19	64.51	
6.64	50.22	25.39	74.95	PA
6.79	10.05	3.17	26.26	
6.88	12.48	4.15	30.89	
6.97	9.19	1.90	31.43	
7.06	8.33	3.35	18.52	
7.15	25.07	8.16	55.09	PA
7.24	25.54	11.89	46.29	
7.33	18.66	7.51	38.79	
7.42	5.81	1.25	19.85	
7.51	3.84	0.67	14.35	
7.60	5.79	1.42	18.26	
7.70	9.20	3.66	20.50	
7.79	1.25	0.05	4.93	
7.89	20.37	7.72	43.29	PA
7.98	12.33	4.09	30.58	
8.11	17.26	6.92	36.35	
8.38	13.10	5.73	26.70	PA
8.68	1.98	0.49	5.53	
8.99	1.63	0.19	5.94	
9.29	27.41	9.74	56.45	PA

9.59	6.72	2.61	15.39	
9.90	1.96	0.39	6.18	
10.21	1.45	0.29	4.24	
10.57	25.88	10.72	50.01	
11.29	2.16	0.34	7.63	
11.64	2.87	0.90	7.37	
11.99	47.80	28.16	68.13	PA
12.33	54.73	34.14	73.85	PA
12.68	5.65	1.97	13.98	
13.00	4.05	1.24	10.86	
13.23	30.71	15.18	52.13	PA
13.41	8.65	3.33	19.81	PA
13.72	3.39	1.12	8.55	
14.59	2.03	0.38	6.59	
15.46	11.19	4.56	24.27	
15.74	7.38	2.30	19.77	
15.89	21.60	10.32	39.42	PA
16.04	42.61	24.20	63.27	PA
16.19	11.51	4.59	25.33	
16.34	27.53	13.07	48.74	NA
16.49	15.57	6.34	32.84	
16.64	63.22	42.47	80.07	PA
16.78	67.24	45.27	83.68	NA
16.87	51.17	25.36	76.38	NA
16.96	72.70	53.41	86.19	NA
17.04	53.16	30.06	75.01	NA
17.13	47.08	23.10	72.45	NA
17.23	29.71	11.26	58.10	NA
19.28	55.54	30.58	78.04	PA
24.17	21.45	7.11	48.60	PA
27.44	41.19	14.20	74.61	PA
29.26	28.29	9.40	59.50	NA
30.76	39.11	15.40	69.20	NA
32.27	38.64	16.82	66.09	PA
33.77	56.99	26.74	82.87	NA
35.55	57.61	29.17	81.84	PA
38.55	13.54	4.14	34.95	PA
41.82	60.85	33.14	83.07	NA
44.89	47.87	23.72	73.04	NA
47.04	4.69	1.78	10.91	NA
48.76	36.84	19.51	58.27	PA
49.56	16.28	6.05	36.30	
50.15	23.96	10.33	45.91	
50.74	15.01	5.32	34.81	
51.33	29.30	14.28	50.55	
51.68	12.47	4.88	27.64	PA

Appendix 4.1

The age model formulation for marine sediment core MD88-787, and associated data.

MD88-787	Analyseries						AVERAGED data				
Depth cm	Age kyr	Depth cm	Age Kyr	del18O 787	Depth 787	Age Kyr	del18O 787	Depth cm	Pointers (Age tie to E27-23)	Depth cm	Pointers (Age tie to LR04)
0	4.66	0	4.66	2.88	0	4.66	2.88	0	4.62	580	74.99
10	4.92	10	4.92	3.20	10	4.92	3.20	19	5.19	680	108.93
20	5.21	20	5.21	3.41	20	5.21	3.41	30	5.47	700	125.05
30	5.48	30	5.48	2.99	30	5.48	2.99	160	9.60	760	129.00
40	5.78	40	5.78	3.13	40	5.78	3.13	170	13.73	780	130.01
50	6.10	60	6.42	3.37	60	6.42	3.37	190	15.74	860	139.99
60	6.42	70	6.74	3.22	70	6.74	3.22	210	16.04	960	174.05
70	6.74	80	7.06	3.18	80	7.06	3.18	220	16.17	980	185.03
80	7.06	90	7.37	3.56	90	7.37	3.56	240	17.97	1030	191.63
90	7.37	100	7.69	3.47	100	7.69	3.47	260	19.29		
100	7.69	110	8.01	3.38	110	8.01	3.38	300	24.23		
110	8.01	120	8.33	3.11	120	8.33	3.32	320	30.77		
120	8.33	120	8.33	3.54	130	8.65	3.68	340	32.24		
130	8.65	130	8.65	3.68	140	8.96	3.51	540	48.76		
140	8.96	140	8.96	3.51	150	9.28	3.95				
150	9.28	150	9.28	4.00	160	10.08	3.31				
160	10.08	150	9.28	3.91	170	13.34	4.13				
170	13.34	160	10.08	3.37	180	14.73	4.13				
180	14.73	160	10.08	3.34	190	15.63	3.78				
190	15.63	160	10.08	3.24	200	15.89	4.05				
200	15.89	170	13.34	4.13	210	16.04	4.27				
210	16.04	180	14.73	4.13	230	17.07	4.51				
220	16.27	190	15.63	3.78	240	17.94	4.81				
230	17.07	200	15.89	4.05	250	18.63	4.72				
240	17.94	210	16.04	4.27	260	19.36	4.83				
250	18.63	230	17.07	4.51	270	20.52	4.77				
260	19.36	240	17.94	4.81	280	21.76	4.68				
270	20.52	250	18.63	4.72	300	24.48	4.44				
280	21.76	260	19.36	4.83	320	30.45	3.70				
290	22.99	270	20.52	4.77	340	32.25	3.82				
300	24.48	280	21.76	4.68	380	35.55	3.35				
310	27.50	300	24.48	4.44	480	43.81	3.58				
320	30.45	320	30.45	3.70	500	45.46	3.61				
330	31.51	340	32.25	3.82	520	47.11	4.10				
340	32.25	380	35.55	3.35	540	49.48	4.38				
350	33.07	480	43.81	3.58	580	74.60	3.21				
360	33.89	500	45.46	3.61	600	81.78	3.17				
370	34.72	520	47.11	4.10	620	88.57	3.13				
380	35.55	540	49.48	4.38	640	95.36	3.06				
390	36.37	580	74.60	3.21	660	102.14	3.02				
400	37.20	600	81.78	3.17	680	109.52	3.22				
410	38.02	620	88.57	3.13	700	124.13	2.97				
420	38.85	640	95.36	3.06	720	126.37	3.55				
430	39.68	660	102.14	3.02	740	127.69	4.10				
440	40.50	680	109.52	3.22	760	128.98	4.18				
450	41.33	700	124.13	2.97	780	130.10	3.62				
460	42.16	720	126.37	3.55	860	140.26	4.01				
470	42.98	740	127.69	4.10	880	146.80	3.98				
480	43.81	760	128.98	4.18	920	160.43	3.72				
490	44.63	780	130.10	3.62	960	174.31	3.50				
500	45.46	860	140.26	4.01	980	184.51	3.78				
510	46.29	880	146.80	3.98	1000	187.67	3.59				
520	47.11	920	160.43	3.72	1020	190.31	3.18				

530	47.94	960	174.31	3.50	1030	191.47	2.88				
540	49.48	980	184.51	3.78							

Appendix 4.2

The age model formulation for marine sediment core MD88-784, and associated data.

MD88-784	Analyseries					
Depth cm	**Age kyr**	**Depth 784**	**Age Kyr**	**del18O 784**	**Depth 784**	**Pointers (Age tie to E27-23)**
0	5.31	0	5.31	3.06	0	5.31
10	5.56	20	5.82	3.02	40	6.32
20	5.82	40	6.32	2.92	80	9.01
30	6.07	60	7.67	3.1	160	14.86
40	6.32	80	9.01	3.37	180	16.35
50	7.00	100	10.47	3.26	200	17.91
60	7.67	120	11.93	3.39	260	28.30
70	8.34	140	13.39	3.78	460	47.03
80	9.01	160	14.86	4.24	480	48.18
90	9.74	180	16.35	4.41		
100	10.47	200	17.91	4.74		
110	11.20	220	21.37	4.23		
120	11.93	240	24.84	4.13		
130	12.66	260	28.30	4.33		
140	13.39	280	30.17	4.09		
150	14.13	300	32.05	3.79		
160	14.86	320	33.92	3.77		
170	15.60	360	37.67	3.76		
180	16.35	380	39.54	3.91		
190	17.13	420	43.29	3.87		
200	17.91	440	45.16	3.7		
210	19.64	460	47.03	3.61		
220	21.37	480	48.18	3.74		
230	23.11					
240	24.84					
250	26.57					
260	28.30					
270	29.24					
280	30.17					
290	31.11					
300	32.05					
310	32.98					
320	33.92					
330	34.86					
340	35.79					
350	36.73					
360	37.67					
370	38.60					
380	39.54					
390	40.48					
400	41.41					
410	42.35					

420	43.29					
430	44.22					
440	45.16					
450	46.10					
460	47.03					
470	47.61					
480	48.18					
490	48.76					

Appendix 4.3

The partitions of the Crosta et al. (2004) database that were used for our two spatially independent hold out validations. The open triangles illustrate those samples that were used to train each model, whilst the solid black dots illustrate those samples used to test each model. Both plots were produced in R, with the relevant R scripts provided.

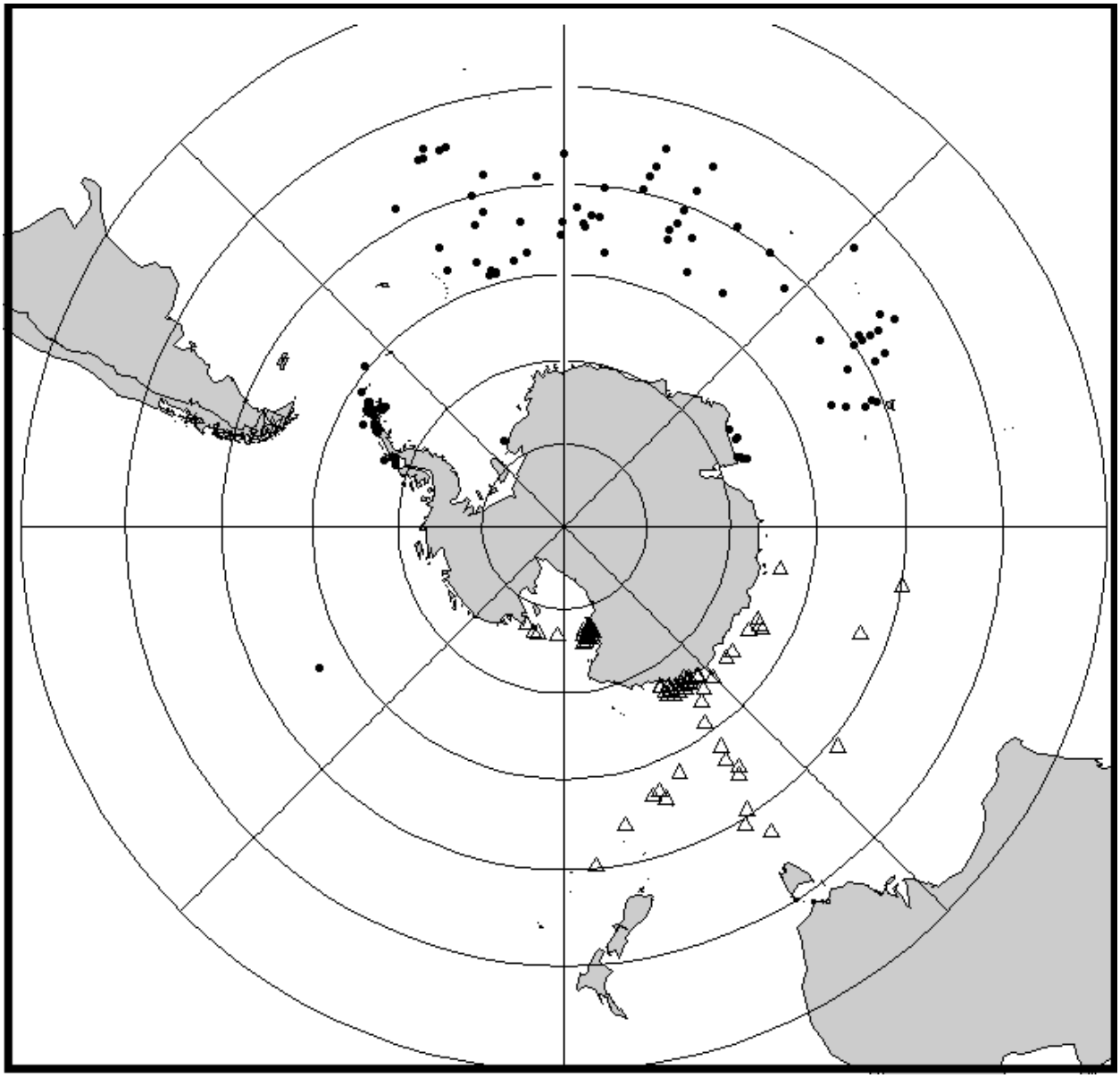

```
map('world',proj='stereographic',orient=c(-90,0,0),ylim=c(-90,-35), col="grey80", fill=T)
map.grid(lim=c(-180,180,-90,-30), nx=9, ny=7, labels=F, pretty=FALSE, lty=1, col='black', cex=0.8)
points(mapproject(list(y= P3CV1$Latitude, x= P3CV1$Longitude, poection='stereographic')), pch=20, col=1,
cex=1)
points(mapproject(list(y= P3CV2$Latitude, x= P3CV2$Longitude, poection='stereographic')), pch=2, col=1, cex=1)
```

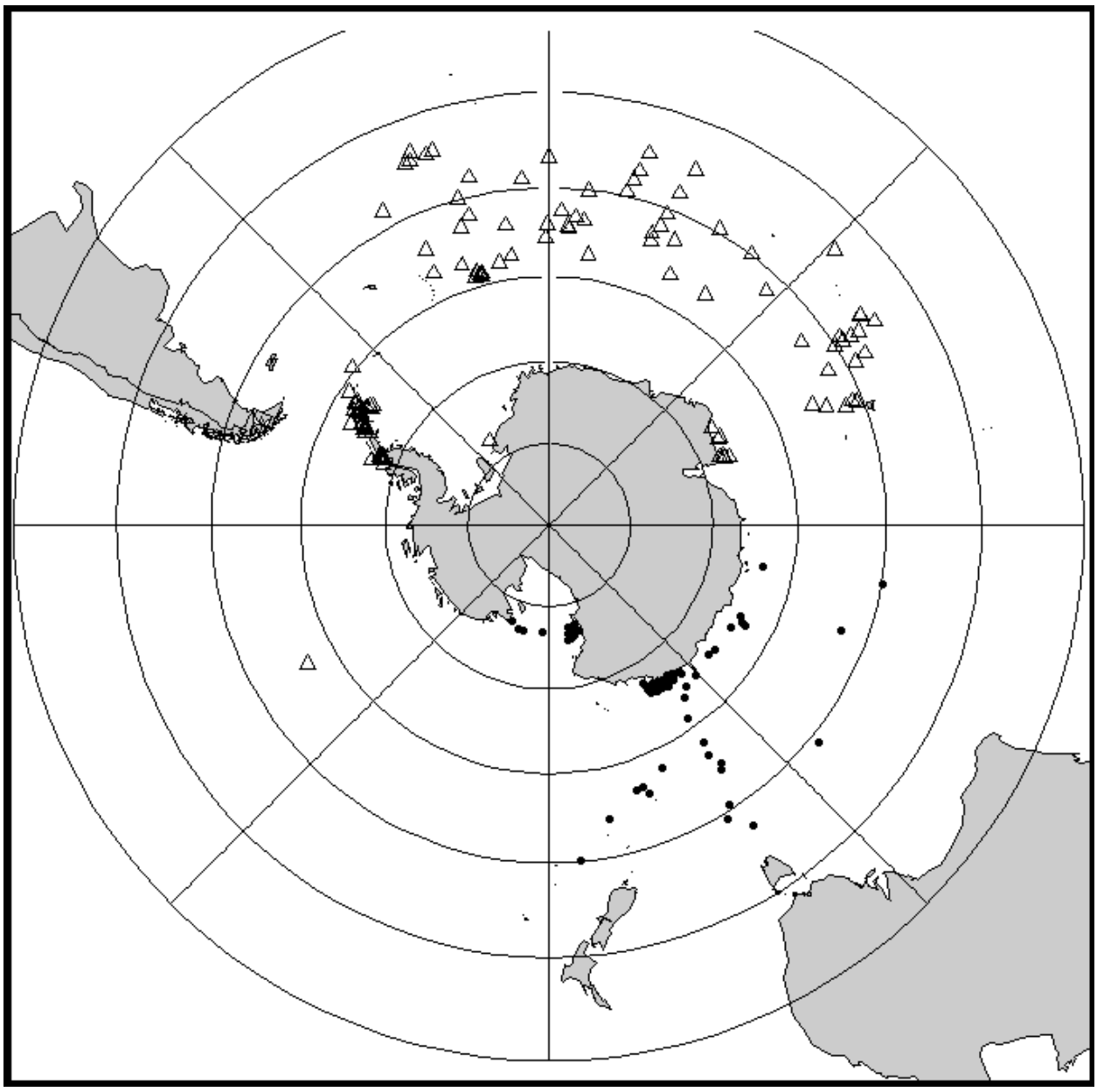

```
map('world',proj='stereographic',orient=c(-90,0,0),ylim=c(-90,-35), col="grey80", fill=T)
map.grid(lim=c(-180,180,-90,-30), nx=9, ny=7, labels=F, pretty=FALSE, lty=1, col='black', cex=0.8)
points(mapproject(list(y= P3CV1$Latitude, x= P3CV1$Longitude, poection='stereographic')), pch=2, col=1, cex=1)
points(mapproject(list(y= P3CV2$Latitude, x= P3CV2$Longitude, poection='stereographic')), pch=20, col=1,
cex=1)
```

Appendix 4.4

Application of the Imbrie and Kipp Transfer Function (IKTF) to our February sea-surface temperature training dataset. Note, we apply IKTF on the log transformed diatom abundances and to untransformed diatom data. Output from the normality and constant variance tests are also included, as are all plots from the PCA procedure. The application of IKTF was carried out using R, hence all of the R scripts used are included as well. The shapiro-wilk and KS normality tests were used to test the assumption that model errors are normally distributed. This test was applied at the 5% significance level, with p-values below 0.05 indicating that the normality assumption does not hold. The normal probability plot (labelled as a normal Q-Q plot in R) provides a visual assessment of model residuals, allowing one to assess if model residuals (and thus model errors) are normal. Normally distributed residuals will fall along the 1:1 line. The Bartels test, NCV test and runs test can be used to assess the assumption that model errors have a constant variance. Similarly, a plot of residuals versus model fitted values should show a random scatter if the assumption of constant variance holds. One cannot properly assess the significance of each predictor within a model, nor can confidence intervals be computed, if the assumption that model errors are normal and have a constant variance, does not hold. The linear regression model using observed data as the response and fitted values as the predictor (mod <- lm(fit ~ SSTfeb$SSTFeb)) would reveal an unbiased model as having a zero intercept and a 1:1 slope.

Application of IKTF to the log transformed diatom abundance data.

```
pca <- princomp(LnAbunBYtenplsONE, score=T)
 plot(pca)
```

A scree plot from the application of PCA to the log transformed diatom abundance data of Crosta et al. (2004).

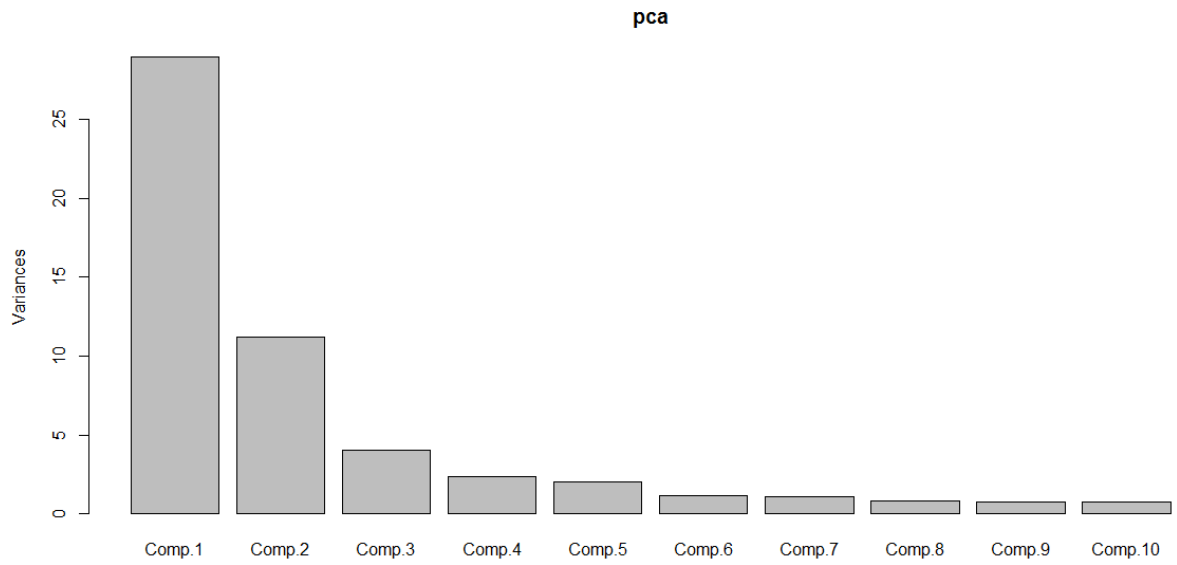


```
lines(bstick(pca))
```

A scree plot from the application of PCA to the log transformed diatom abundance data of Crosta et al. (2004), with a broken stick model plotted over the scree plot.

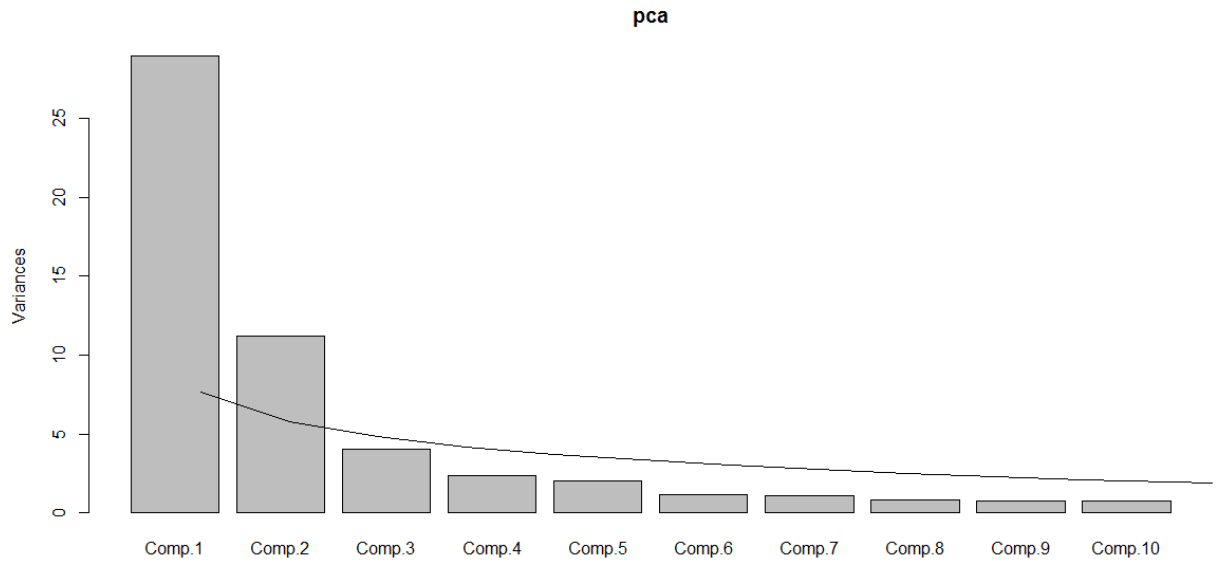


```
trainscore <- pca$score
regCOMPone <- trainscore[,1]
```

```
regCOMPtwo <- trainscore[,2]
regCOMPoneQD <- (trainscore[,1])^2
regCOMPtwoQD <- (trainscore[,2])^2
model <- lm(SSTfeb$SSTFeb ~ regCOMPone + regCOMPtwo + regCOMPoneQD + regCOMPtwoQD)
 summary(model)

Call:
lm(formula = SSTfeb$SSTFeb ~ regCOMPone + regCOMPtwo + regCOMPoneQD +
    regCOMPtwoQD)

Residuals:
   Min     1Q Median     3Q    Max
-5.052 -1.279  0.096  1.085  9.092

Coefficients:
             Estimate Std. Error t value Pr(>|t|)
(Intercept)   1.429847   0.367578   3.890  0.00013 ***
regCOMPone   -0.658188   0.028751 -22.893  < 2e-16 ***
regCOMPtwo    0.587147   0.065964   8.901  < 2e-16 ***
regCOMPoneQD  0.051019   0.009475   5.385 1.74e-07 ***
regCOMPtwoQD  0.055363   0.011740   4.716 4.10e-06 ***
---
Signif. codes:  0 ‘***’ 0.001 ‘**’ 0.01 ‘*’ 0.05 ‘.’ 0.1 ‘ ’ 1

Residual standard error: 2.172 on 238 degrees of freedom
Multiple R-squared:  0.8338,        Adjusted R-squared:  0.831
F-statistic: 298.4 on 4 and 238 DF,  p-value: < 2.2e-16


res <- residuals(model)
fit <- fitted(model)
plot(fit, res)
```

A plot of the residual values from the application of IKTF versus the fitted values from IKTF.

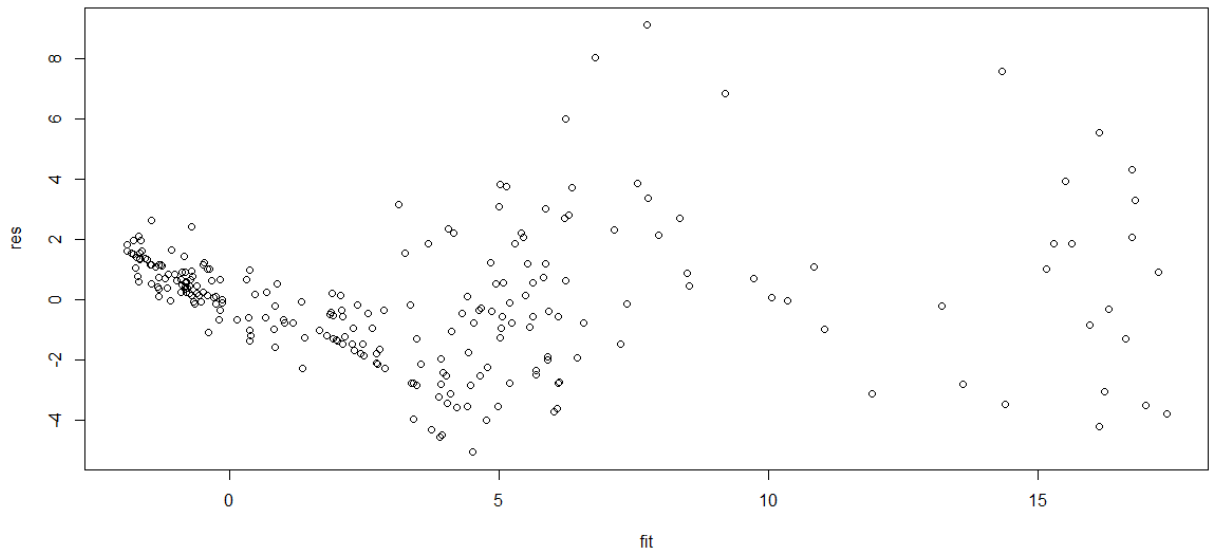


```
qqnorm(res)
```

A normal probability plot for the residuals of the IKTF model.

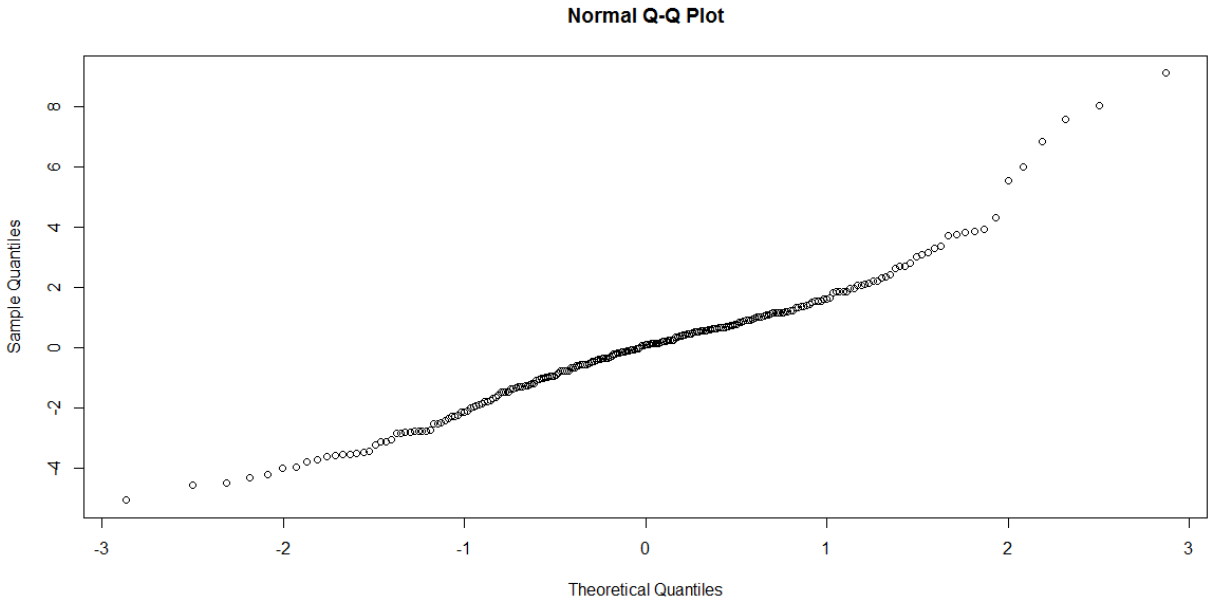

Output for the statistical tests used to assess the normality of the IKTF model residuals.

```
ksnormTest(res)

Title:
 One-sample Kolmogorov-Smirnov test

Test Results:
  STATISTIC:
    D: 0.1577
  P VALUE:
    Alternative Two-Sided: 1.135e-05
    Alternative      Less: 0.0009909
    Alternative   Greater: 5.673e-06
 shapiroTest(res)
Title:
 Shapiro - Wilk Normality Test

Test Results:
  STATISTIC:
    W: 0.959
  P VALUE:
    2.085e-06
 adTest(res)
 lillieTest(res)
Title:
 Lilliefors (KS) Normality Test
Test Results:
  STATISTIC:
    D: 0.0762
```

```
 P VALUE:
   0.001614
ncvTest(model)
Non-constant Variance Score Test
Variance formula: ~ fitted.values
Chisquare = 64.05931    Df = 1     p = 1.207297e-15
plot(SSTfeb$SSTFeb, fit)
```

A plot of the fitted values from IKTF versus the observed wSIC data.

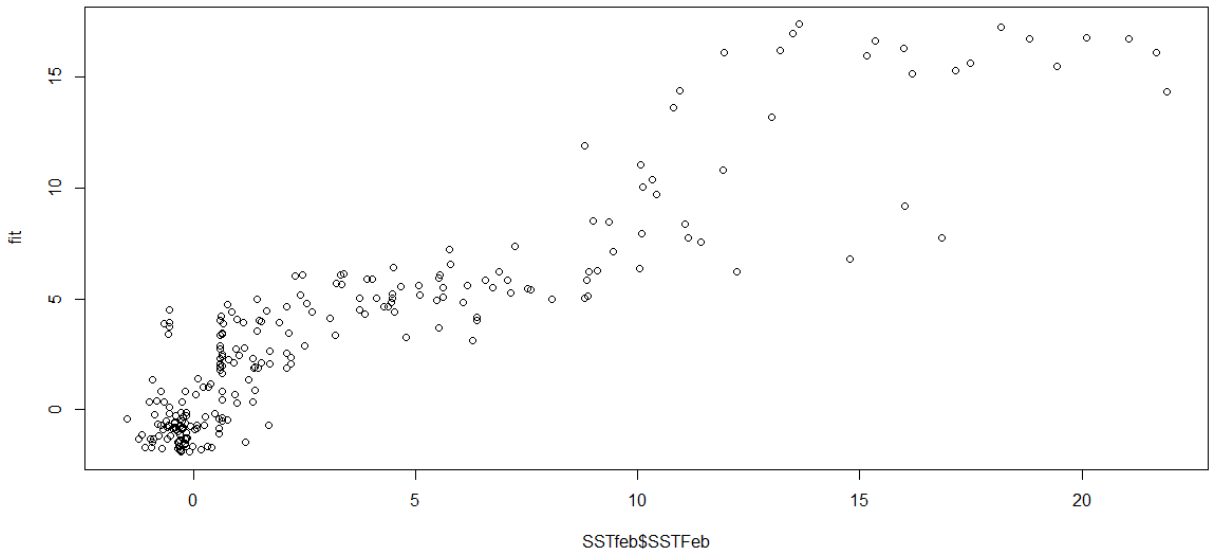


```
mod <- lm(fit ~ SSTfeb$SSTFeb)
summary(mod)

Call:
lm(formula = fit ~ SSTfeb$SSTFeb)

Residuals:
    Min      1Q  Median      3Q     Max
-6.8791 -1.3587 -0.0882  1.0831  5.5844

Coefficients:
             Estimate Std. Error t value Pr(>|t|)
(Intercept)    0.58634    0.15210   3.855 0.000149 ***
SSTfeb$SSTFeb  0.83376    0.02398  34.767  < 2e-16 ***
---
Signif. codes:  0 ‘***’ 0.001 ‘**’ 0.01 ‘*’ 0.05 ‘.’ 0.1 ‘ ’ 1

Residual standard error: 1.971 on 241 degrees of freedom
Multiple R-squared:  0.8338,        Adjusted R-squared:  0.8331
F-statistic:  1209 on 1 and 241 DF,  p-value: < 2.2e-16
RMSE <- sqrt(sum(res^2)/243)
RMSE
[1] 2.149157
mean(res)
[1] -1.277096e-16
```

Application of IKTF to the untransformed diatom abundance data.

```
pca <- princomp(REALabun, score=T)
plot(pca)
```

A scree plot from the application of PCA to the untransformed diatom abundance data of Crosta et al. (2004).

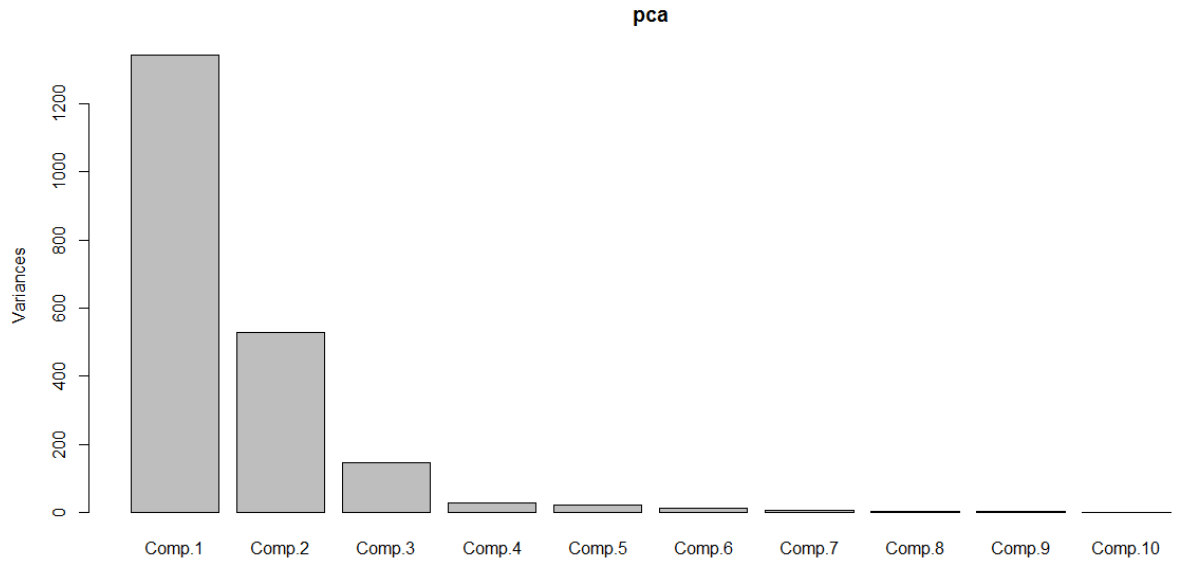


```
lines(bstick(pca))
```

A scree plot from the application of PCA to the untransformed diatom abundance data of Crosta et al. (2004), with a broken stick model plotted over the scree plot.

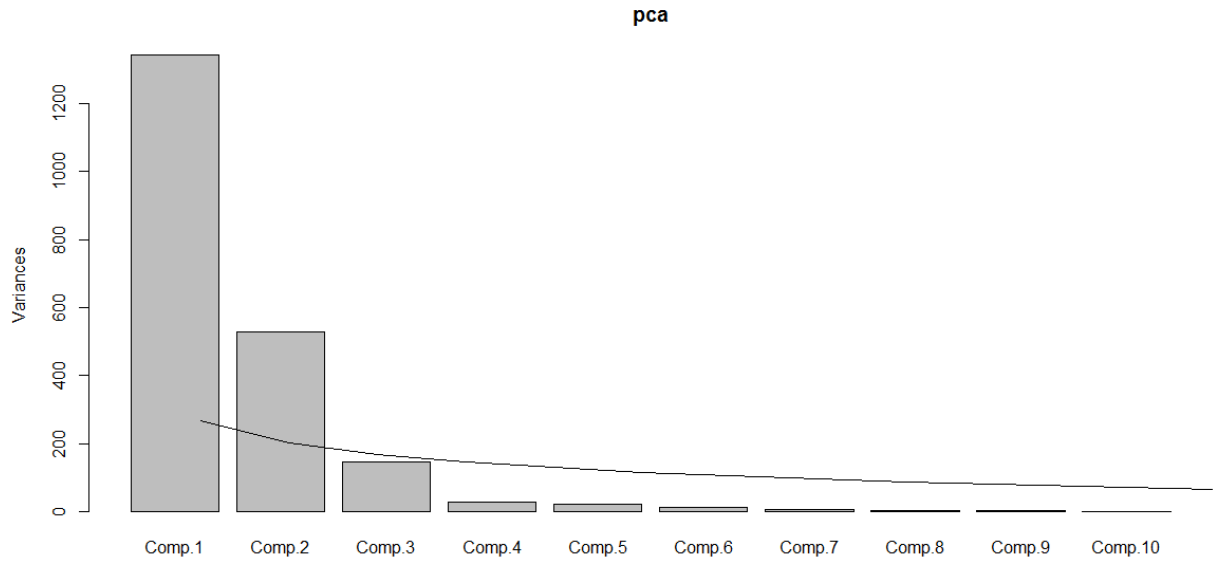


```
trainscore <- pca$score
```

```
regCOMPone <- trainscore[,1]
regCOMPtwo <- trainscore[,2]
regCOMPoneQD <- (trainscore[,1])^2
regCOMPtwoQD <- (trainscore[,2])^2

model <- lm(SSTfeb$SSTFeb ~ regCOMPone + regCOMPtwo + regCOMPoneQD + regCOMPtwoQD)

 summary(model)

Call:
lm(formula = SSTfeb$SSTFeb ~ regCOMPone + regCOMPtwo + regCOMPoneQD +
    regCOMPtwoQD)

Residuals:
    Min      1Q  Median      3Q     Max
-9.4466 -2.7082 -0.0108  1.3950 15.5481

Coefficients:
             Estimate Std. Error t value Pr(>|t|)
(Intercept)   9.0099254  0.6605905  13.639  < 2e-16 ***
regCOMPone   -0.0303356  0.0111223  -2.727  0.00686 **
regCOMPtwo   -0.1661377  0.0238121  -6.977 2.97e-11 ***
regCOMPoneQD -0.0045306  0.0005646  -8.024 4.66e-14 ***
regCOMPtwoQD  0.0011282  0.0007025   1.606  0.10959
---
Signif. codes:  0 ‘***’ 0.001 ‘**’ 0.01 ‘*’ 0.05 ‘.’ 0.1 ‘ ’ 1

Residual standard error: 4.332 on 238 degrees of freedom
Multiple R-squared:  0.3385,        Adjusted R-squared:  0.3274
F-statistic: 30.45 on 4 and 238 DF,  p-value: < 2.2e-16

model <- lm(SSTfeb$SSTFeb ~ regCOMPone + regCOMPtwo + regCOMPoneQD)
summary(model)

Call:
lm(formula = SSTfeb$SSTFeb ~ regCOMPone + regCOMPtwo + regCOMPoneQD)

Residuals:
    Min      1Q  Median      3Q     Max
-9.2153 -2.8020 -0.0796  1.6863 15.3843

Coefficients:
             Estimate Std. Error t value Pr(>|t|)
(Intercept)   8.8427644  0.6544913  13.511  < 2e-16 ***
regCOMPone   -0.0182873  0.0082386  -2.220   0.0274 *
regCOMPtwo   -0.1439108  0.0194414  -7.402 2.27e-12 ***
regCOMPoneQD -0.0039621  0.0004414  -8.977  < 2e-16 ***
---
Signif. codes:  0 ‘***’ 0.001 ‘**’ 0.01 ‘*’ 0.05 ‘.’ 0.1 ‘ ’ 1

Residual standard error: 4.346 on 239 degrees of freedom
Multiple R-squared:  0.3313,        Adjusted R-squared:  0.3229
F-statistic: 39.47 on 3 and 239 DF,  p-value: < 2.2e-16

res <- residuals(model)
fit <- fitted(model)
plot(fit, res)
```

A plot of the residual values from the application of IKTF versus the fitted values from IKTF.

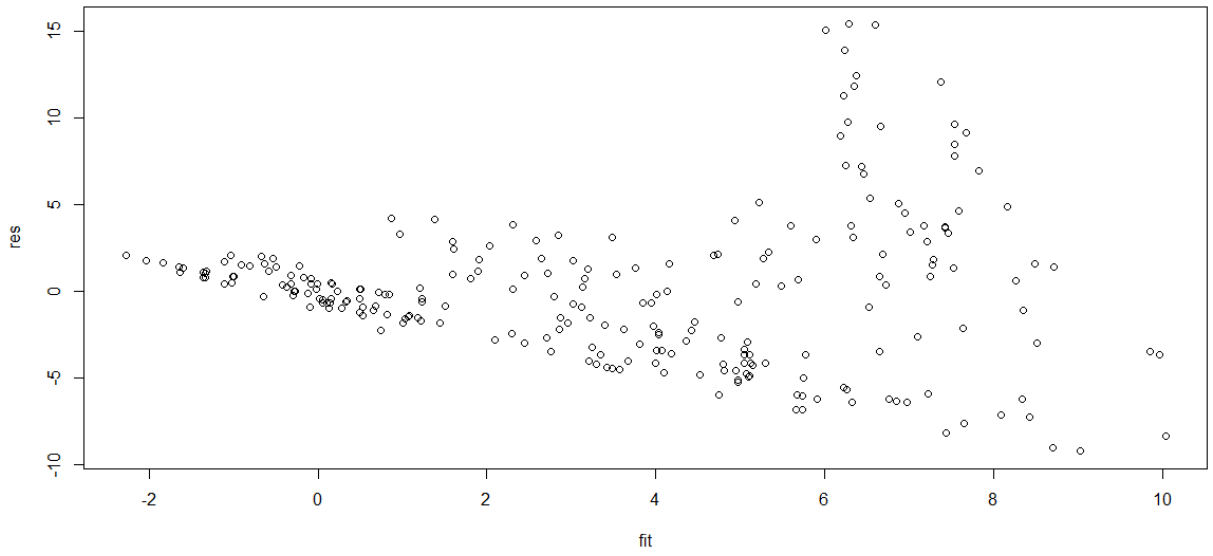


```
qqnorm(res)
```

A normal probability plot for the residuals of the IKTF model.

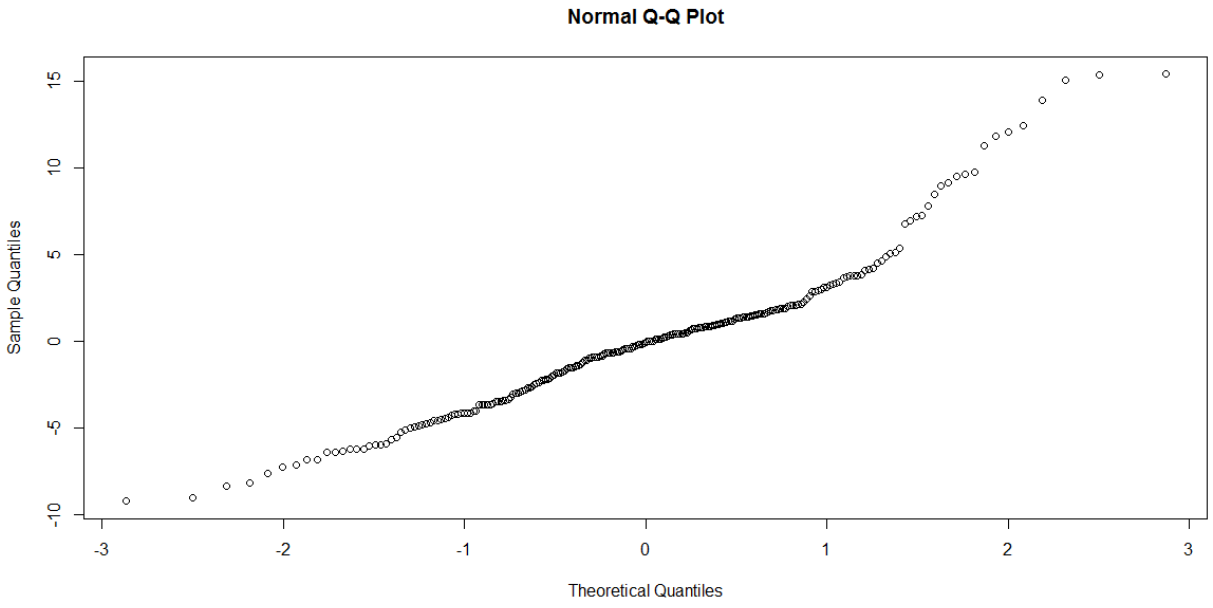

Output for the statistical tests used to assess the normality of the IKTF model residuals.

```
ksnormTest(res)


Title:
 One-sample Kolmogorov-Smirnov test

Test Results:
  STATISTIC:
    D: 0.2878
  P VALUE:
    Alternative Two-Sided: < 2.2e-16
    Alternative      Less: 1.423e-10
    Alternative   Greater: < 2.2e-16

Description:
 Wed Oct 23 14:04:47 2013 by user: aferry

shapiroTest(res)

Title:
 Shapiro - Wilk Normality Test

Test Results:
  STATISTIC:
    W: 0.9398
  P VALUE:
    1.941e-08

Description:
 Wed Oct 23 14:04:47 2013 by user: aferry

lillieTest(res)

Title:
 Lilliefors (KS) Normality Test

Test Results:
  STATISTIC:
    D: 0.1161
  P VALUE:
    1.963e-08

Description:
 Wed Oct 23 14:04:47 2013 by user: aferry

ncvTest(model)
Non-constant Variance Score Test
Variance formula: ~ fitted.values
Chisquare = 92.82072    Df = 1     p = 5.725248e-22
```

The output from the regression between the IKTF fitted values and observed wSIC data.

```
mod <- lm(fit ~ SSTfeb$SSTFeb)
summary(mod)

Call:
lm(formula = fit ~ SSTfeb$SSTFeb)

Residuals:
    Min      1Q  Median      3Q     Max
-4.5616 -2.0448 -0.1049  1.5716  7.1179

Coefficients:
             Estimate Std. Error t value Pr(>|t|)
(Intercept)    2.35847    0.19230   12.27   <2e-16 ***
SSTfeb$SSTFeb  0.33133    0.03032   10.93   <2e-16 ***
---
Signif. codes:  0 ‘***’ 0.001 ‘**’ 0.01 ‘*’ 0.05 ‘.’ 0.1 ‘ ’ 1

Residual standard error: 2.491 on 241 degrees of freedom
Multiple R-squared:  0.3313,        Adjusted R-squared:  0.3286
F-statistic: 119.4 on 1 and 241 DF,  p-value: < 2.2e-16


RMSE <- sqrt(sum(res^2)/243)
RMSE
[1] 4.31032


mean(res)
[1] 5.737339e-16
```

Appendix 4.5

The results from the 10 fold and spatially independent hold out validations using the log transformed diatom relative abundance data. The root mean squared error of prediction (RMSEP) and root mean squared errors (RMSE) for WA PLS, WA (with and without tolerance down weighting) and MAT. Also shown are the RMSE and RMSEP of WA PLS and MAT using untransformed diatom relative abundances. The lowest average values for RMSE and RMSEP, under our 10 fold and hold out validation, are highlighted in red.

	WA PLS (on ln(abun*10+1)		**WA PLS (untransformed data)**		**MAT (abunds*10, as per Crosta et al. 2004)**		**MAT (on ln(abun*10+1)**	
10 fold CV sub set	**RMSE**	**RMSEP**	**RMSE**	**RMSEP**	**RMSE**	**RMSEP**	**RMSE**	**RMSEP**
1	2.13	1.47	4.22	1.37	1.13	1.23	1.187	1.12
2	2.01	1.69	4.32	2.37	1.17	1.42	1.14	1.32
3	2.03	2.08	4.3	2.03	1.11	1.82	1.14	1.52
4	1.89	2.39	4.2	2.71	1.15	1.52	1.16	1.57
5	2.14	1.2	4.5	1.245	1.17	1.29	1.18	0.86
6	1.62	0.94	4.62	1.37	1.16	0.63	1.2	0.76
7	2.15	0.98	4.51	1.535	1.22	0.57	1.26	0.85
8	2.12	1.08	4.54	1.46	1.14	1.07	1.13	1.28
9	2.12	1.34	4.42	2.15	1.18	0.99	1.25	0.89
10	2.16	1.01	4.49	1.68	1.16	0.79	1.18	1.13
Average	**2.04**	**1.42**	**4.41**	**1.79**	**1.16**	**1.13**	**1.18**	**1.13**
Average Under Spatially independent CV	0.71	1.086	2.33	2.02	3.595	1.59	1.005	1.525

Appendix 4.6

A summary of the linear regression models that were fitted between each models predicted values versus the observed data. An unbiased model will have a zero intercept and 1:1 slope. Shown are the slopes for each of the regression models and a 95% confidence intervals for each of the fitted regression model slopes (m). LCL (m) corresponds to the lower bound of the confidence interval, whilst UCL (m) corresponds to the upper bound of the confidence interval.

	WA PLS			**WA PLS ln(abun*10+1)**			**MAT**			**MAT ln(abun*10+1)**		
	m	**LCL (m)**	**UCL (m)**	**m**	**LCL (m)**	**UCL (m)**	**m**	**LCL (m)**	**UCL (m)**	**m**	**LCL (m)**	**UCL (m)**
10 fold CV sub set												
1	1.02	0.92	1.13	0.99	0.95	1.03	1.03	1.00	1.06	1.03	1.00	1.06
2	1.00	0.83	1.18	1.00	0.96	1.03	1.04	1.01	1.07	1.03	1.00	1.06
3	0.97	0.81	1.13	1.00	0.96	1.03	1.02	0.99	1.05	1.04	1.01	1.07
4	0.89	0.72	1.06	0.99	0.96	1.03	1.01	0.98	1.05	1.03	0.99	1.06
5	0.99	0.81	1.17	0.99	0.96	1.03	1.02	0.99	1.05	1.02	0.99	1.05
6	0.90	0.81	0.99	0.99	0.95	1.04	1.02	0.99	1.05	1.02	0.99	1.05
7	0.81	0.65	0.97	0.99	0.96	1.03	1.02	0.99	1.05	1.01	0.98	1.04
8	0.82	0.68	0.97	0.99	0.96	1.03	1.02	0.99	1.05	1.02	0.99	1.05
9	1.13	0.98	1.28	1.09	1.05	1.13	1.04	1.01	1.07	1.04	1.01	1.08
10	1.05	0.90	1.21	0.99	0.95	1.03	1.04	1.01	1.07	1.03	1.00	1.06

Appendix 4.7

The maximum recorded abundance for each diatom species documented within the sea-surface temperature training set is compared with a diatoms maximum recorded fossilized abundance within each marine sediment core. The Hills N2 diversity measure is used to identify diatom species that may have a poorly defined optima. In each plot, the maximum abundance of each diatom within a marine sediment core is plotted against the same diatoms maximum abundance within the sea-surface temperature training data set. Taxa with a greater abundance within the core data in comparison with the training data set can introduce a source of error when used to produce paleo estimates. Any diatom species with a low Hills N2, which are therefore likely to have a poorly defined optima, are coloured red. All of the R scripts used to run the analyses are also included.

E27-23

```
sppmax<-sapply(SSTtrain2723abun,max)
fosmax<-sapply(core2723,max)
n2<-Hill.N2(SSTtrain2723abun)
n2[is.infinite(n2)]<-0
x11(4.5,4.5);par(mar=c(3,3,1,1), mgp=c(1.5,.5, 0))
plot(sppmax,fosmax, xlab="Calibration set maximum", ylab="Fossil data maximum", col=ifelse(n2<=5, 2,1), pch=if
else(n2<=5, 16,1))
abline(0,1, col=2)
identify(sppmax,fosmax, labels=names(sppmax), cex=0.7)
```

The maximum recorded abundance for each diatom species documented within the sea-surface temperature training set is compared with a diatoms maximum recorded fossilized abundance within marine sediment core E27-23.

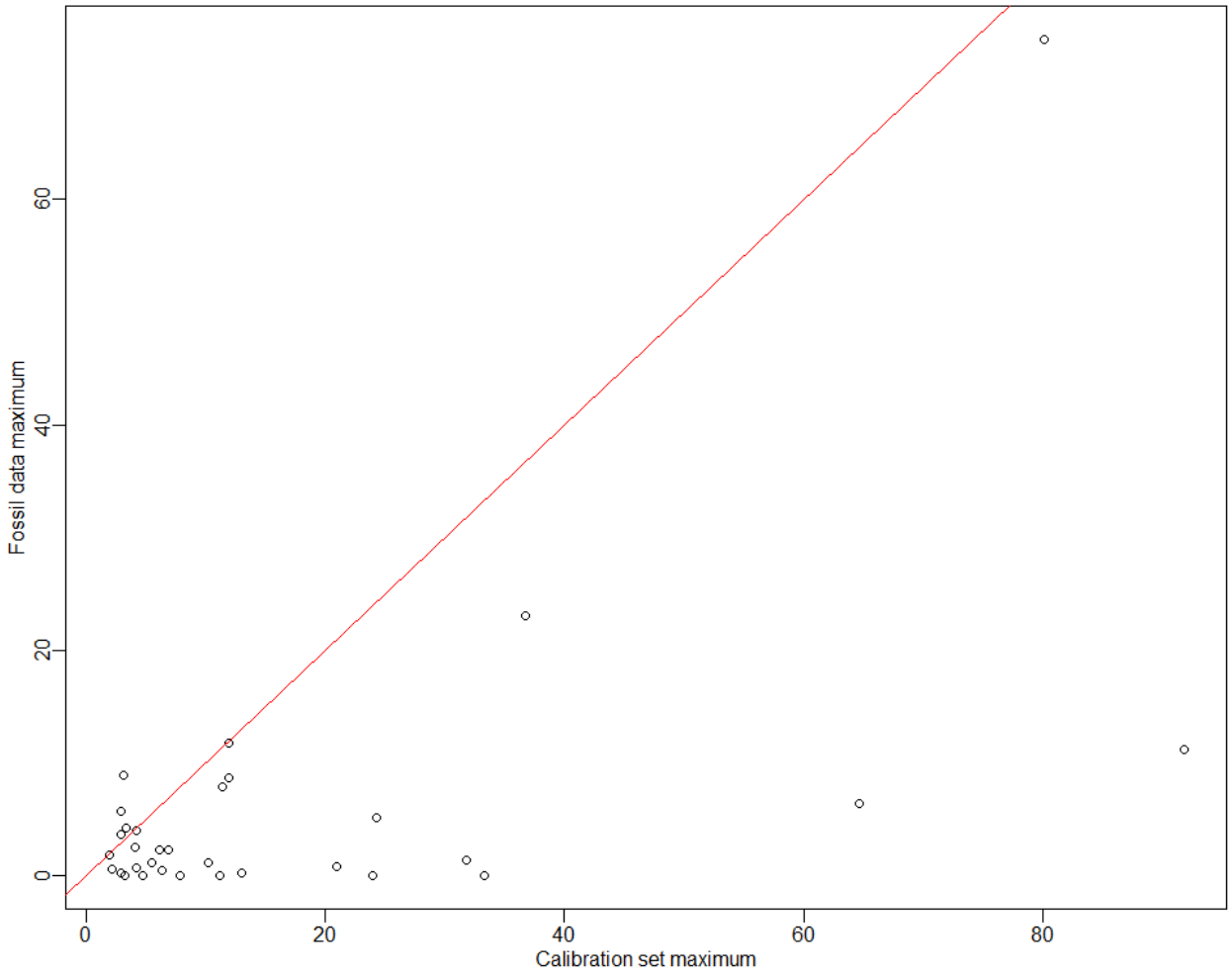

MD88-787

```
sppmax<-sapply(SSTtrain88787abun,max)
fosmax<-sapply(core787,max)
n2<-Hill.N2(SSTtrain88787abun)
n2[is.infinite(n2)]<-0
x11(4.5,4.5);par(mar=c(3,3,1,1), mgp=c(1.5,.5, 0))
plot(sppmax,fosmax, xlab="Calibration set maximum", ylab="Fossil data maximum", col=ifelse(n2<=5, 2,1), pch=if
else(n2<=5, 16,1))
abline(0,1, col=2)
identify(sppmax,fosmax, labels=names(sppmax), cex=0.7)
```

The maximum recorded abundance for each diatom species documented within the sea-surface temperature training set is compared with a diatoms maximum recorded fossilized abundance within marine sediment core MD88-787.

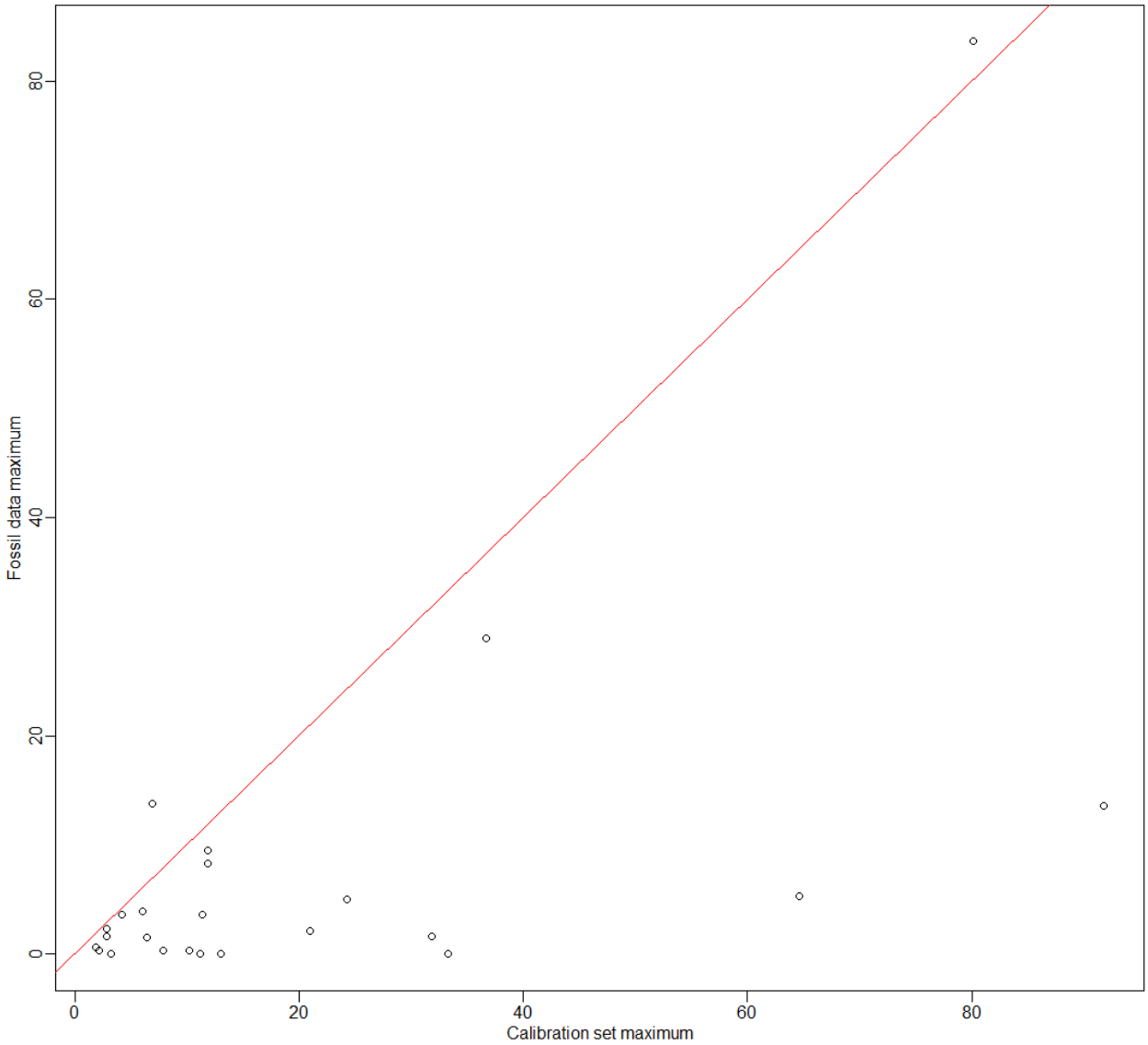

SO136-111

```
sppmax<-sapply(SSTtrain136111abunACTUAL,max)
fosmax<-sapply(core136,max)
n2<-Hill.N2(SSTtrain136111abunACTUAL)
n2[is.infinite(n2)]<-0
x11(4.5,4.5);par(mar=c(3,3,1,1), mgp=c(1.5,.5, 0))
plot(sppmax,fosmax, xlab="Calibration set maximum", ylab="Fossil data maximum", col=ifelse(n2<=5, 2,1), pch=if
else(n2<=5, 16,1))
abline(0,1, col=2)
identify(sppmax,fosmax, labels=names(sppmax), cex=0.7)
```

The maximum recorded abundance for each diatom species documented within the sea-surface temperature training set is compared with a diatoms maximum recorded fossilized abundance within marine sediment core SO136-111.

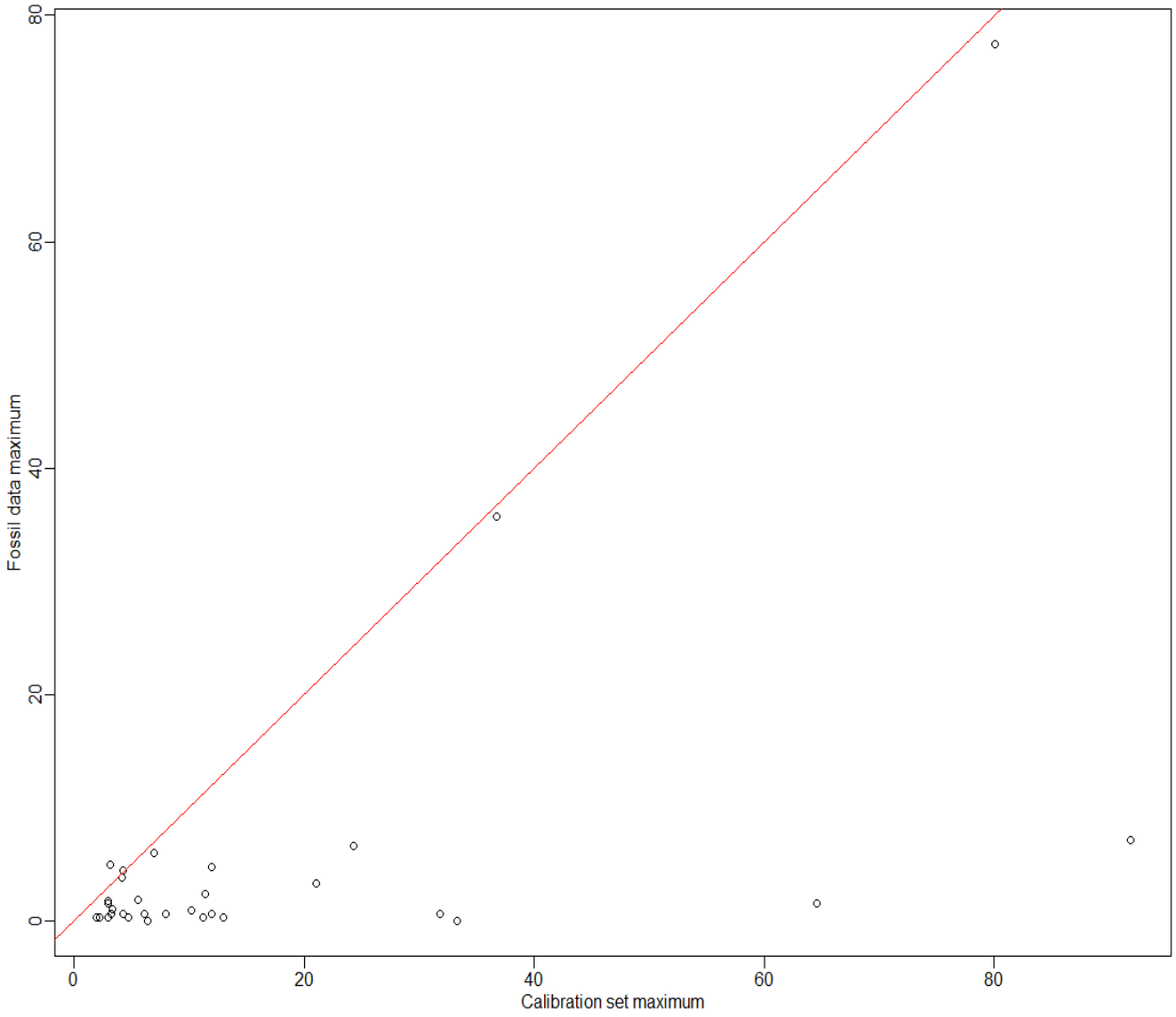

MD88-784

```
sppmax<-sapply(SSTtrain88784abun,max)
fosmax<-sapply(core784,max)
n2<-Hill.N2(SSTtrain88784abun)
n2[is.infinite(n2)]<-0
x11(4.5,4.5);par(mar=c(3,3,1,1), mgp=c(1.5,.5, 0))
plot(sppmax,fosmax, xlab="Calibration set maximum", ylab="Fossil data maximum", col=ifelse(n2<=5, 2,1), pch=if
else(n2<=5, 16,1))
abline(0,1, col=2)
identify(sppmax,fosmax, labels=names(sppmax), cex=0.7)
```

The maximum recorded abundance for each diatom species documented within the sea-surface temperature training set is compared with a diatoms maximum recorded fossilized abundance within marine sediment core MD88-784.

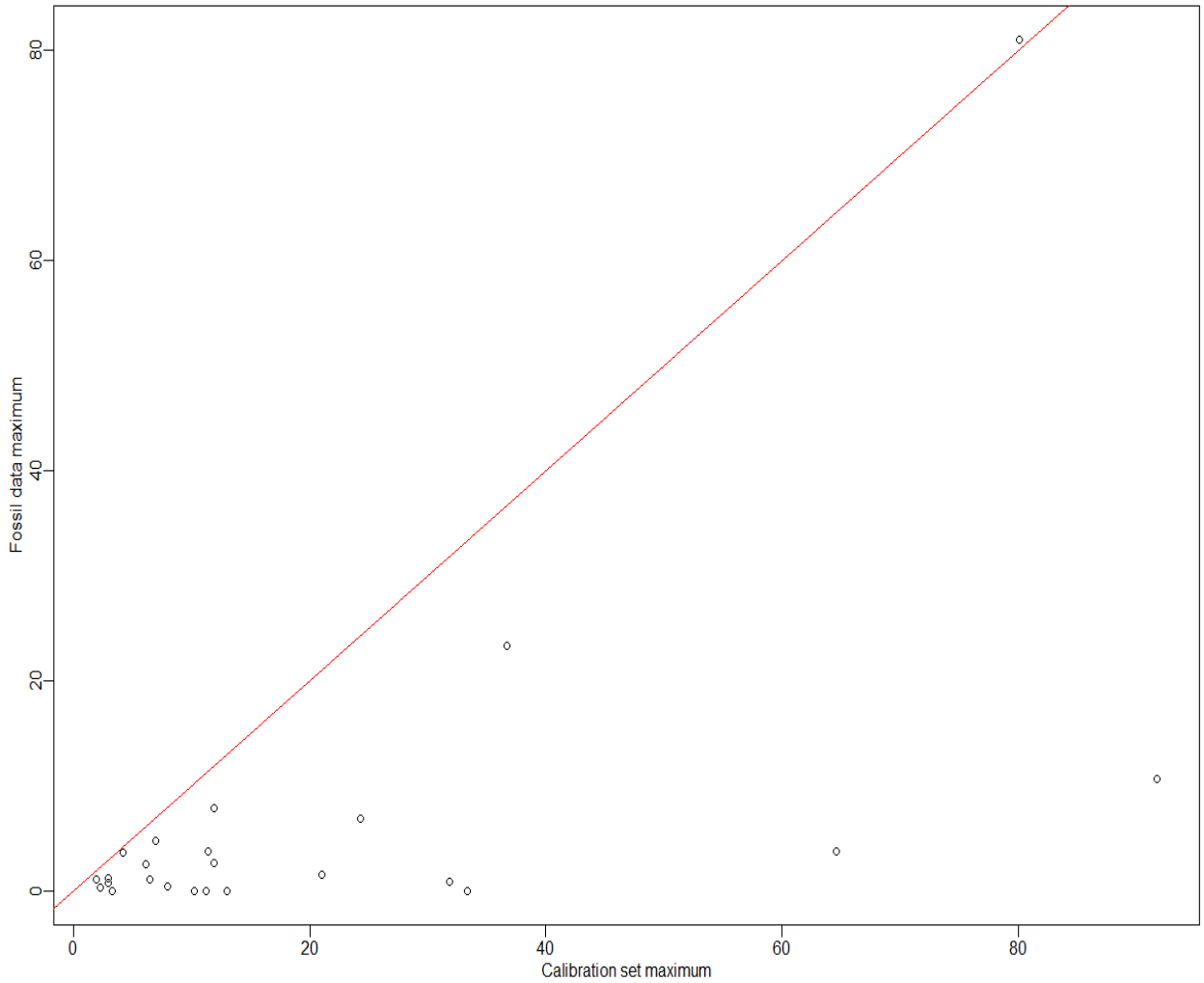

PS58/271-1

```
sppmax<-sapply(SSTtrainPS582711,max)
fosmax<-sapply(PS582711,max)
n2<-Hill.N2(SSTtrainPS582711)
n2[is.infinite(n2)]<-0
x11(4.5,4.5);par(mar=c(3,3,1,1), mgp=c(1.5,.5, 0))
plot(sppmax,fosmax, xlab="Calibration set maximum", ylab="Fossil data maximum", col=ifelse(n2<=5, 2,1), pch=if
else(n2<=5, 16,1))
abline(0,1, col=2)
identify(sppmax,fosmax, labels=names(sppmax), cex=0.7)
```

The maximum recorded abundance for each diatom species documented within the sea-surface temperature training set is compared with a diatoms maximum recorded fossilized abundance within marine sediment core PS58/271-1.

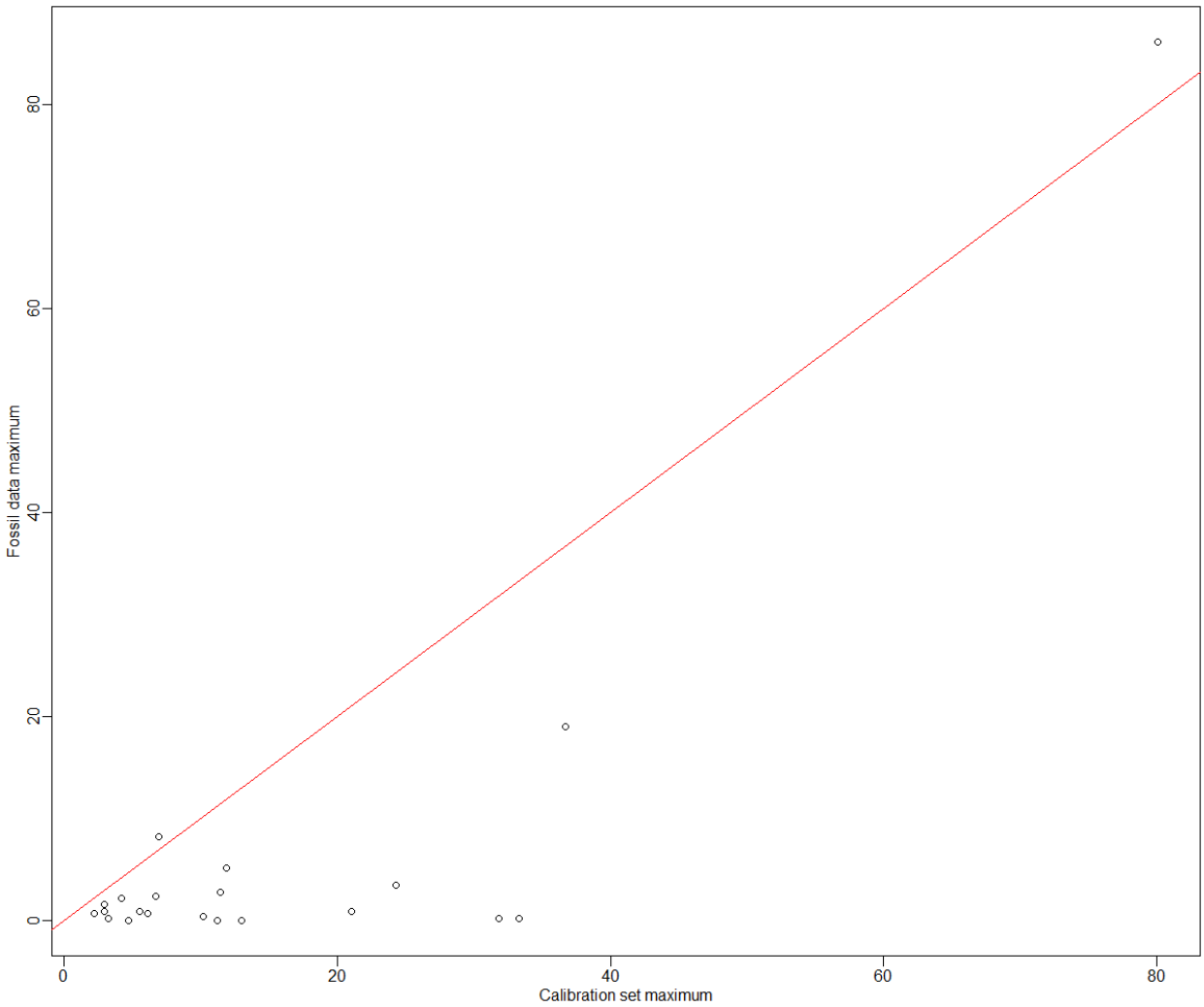

PS1768-8

```
sppmax<-sapply(SSTtrainPS582711,max)
fosmax<-sapply(PS1768,max)
n2<-Hill.N2(SSTtrainPS582711)
n2[is.infinite(n2)]<-0
x11(4.5,4.5);par(mar=c(3,3,1,1), mgp=c(1.5,.5, 0))
plot(sppmax,fosmax, xlab="Calibration set maximum", ylab="Fossil data maximum", col=ifelse(n2<=5, 2,1), pch=if
else(n2<=5, 16,1))
abline(0,1, col=2)
identify(sppmax,fosmax, labels=names(sppmax), cex=0.7)
```

The maximum recorded abundance for each diatom species documented within the sea-surface temperature training set is compared with a diatoms maximum recorded fossilized abundance within marine sediment core PS1768-8.

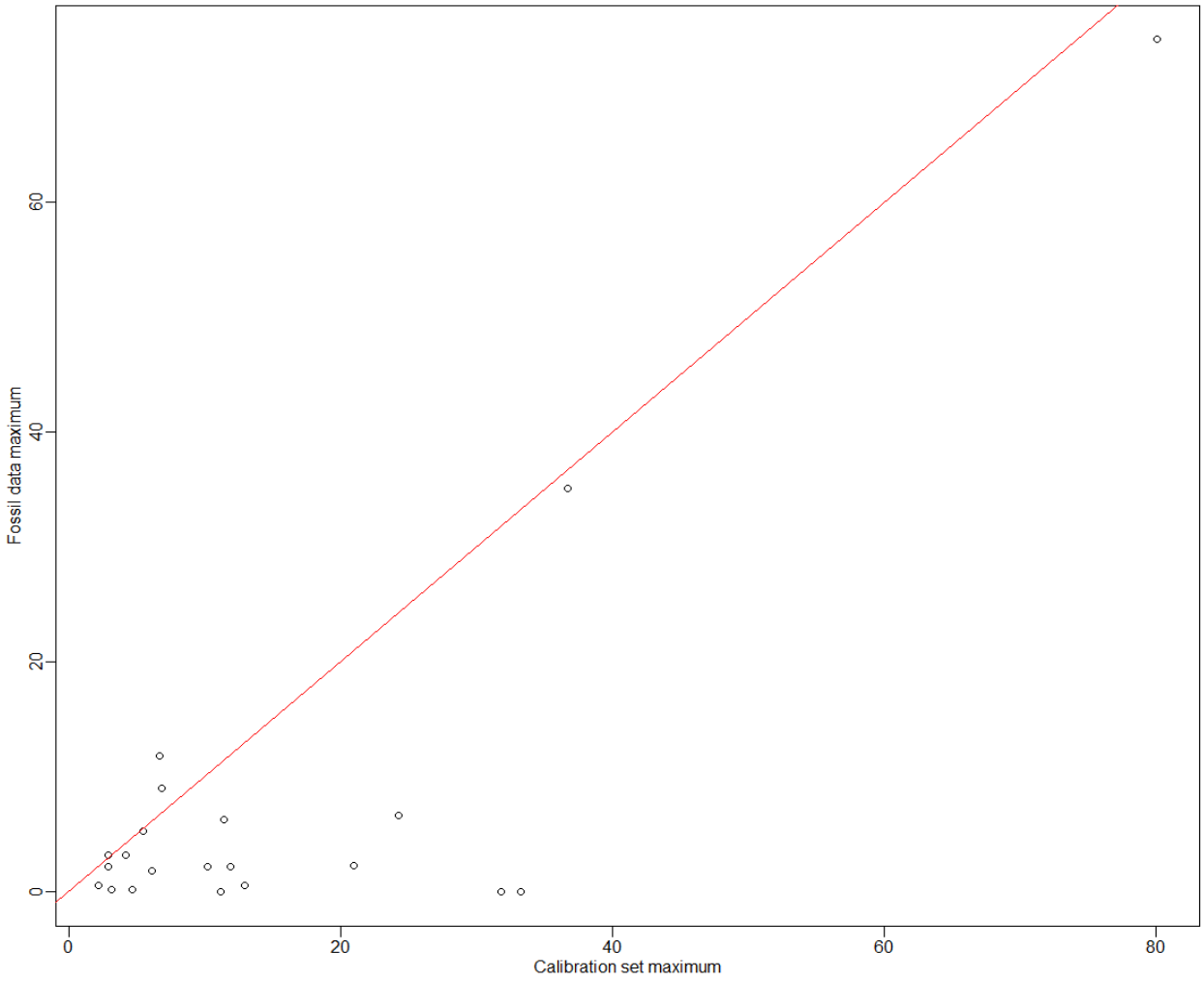

Appendix 4.8

The paleo wSIC estimates for marine sediment core MD88-784 using GAM/WSI/13 from Chapter 3. The associated 95% confidence intervals lower (LCL) and upper (UCL) bounds for each wSIC estimate are included. Also provided are the paleo SST estimates from WA PLS and an indication for those core samples that have no (NA), or poor (PA), analogues.

Kyr_BP784	wSIC	LCL	UCL	SST	Samples with no analogue (NA) or poor analogues (PA)
5.31	0.332523	-0.26004	2.346996	3.350017	
5.56	0.324984	-0.25404	2.230218	2.86409	
5.82	0.17582	-0.20936	1.063527	3.023436	
6.07	0.134222	-0.21608	0.91066	4.746684	
6.32	0.27869	-0.22133	1.656713	3.873681	
7.00	0.326345	-0.25527	2.252453	3.567816	
7.67	0.165316	-0.1722	0.845707	4.440474	
8.34	0.282118	-0.22273	1.686228	2.918971	
9.01	0.239093	-0.21085	1.376119	3.80629	
9.74	0.256954	-0.21447	1.491321	2.591496	
10.47	0.14933	-0.21309	0.962896	3.945722	
11.20	0.261952	-0.21578	1.526542	3.623564	
11.93	0.282275	-0.2228	1.687603	2.661368	
12.66	1.377846	0.255395	4.091763	3.364274	
13.39	0.091565	-0.2256	0.770694	3.813856	
14.13	1.787321	0.476266	4.766331	2.944867	
14.86	0.14165	-0.18553	0.804824	3.037792	
15.60	2.275314	0.56675	6.527958	3.18798	
16.35	3.106064	1.010472	7.864593	3.166948	
17.13	18.9081	8.552336	36.36138	3.222579	
17.91	22.05435	8.782743	44.9067	2.531739	
19.64	15.18217	5.5368	34.55043	1.603396	
21.37	26.7677	11.91539	49.38252	1.599308	
23.11	3.40118	0.84859	10.26342	1.846776	
24.84	0.781117	-0.02194	2.887736	2.359606	
26.57	0.827826	-0.03466	3.229558	2.977282	
28.30	27.25997	11.73348	51.04871	2.640848	
29.24	5.249863	1.831194	12.99622	1.935395	
30.17	14.02866	5.472423	30.80468	2.351715	
31.11	25.5481	10.61976	49.39279	3.146251	
32.05	3.891161	1.087892	11.06748	1.471491	
32.98	5.261526	1.61047	14.2845	2.806386	
33.92	0.268681	-0.21779	1.576409	3.657575	
34.86	0.087649	-0.22602	0.755933	4.407621	
35.79	7.605509	2.14223	21.80354	1.789274	
36.73	1.938806	0.457917	5.570163	1.916072	
37.67	0.315715	-0.24495	2.077334	3.453073	
38.60	0.118476	-0.21965	0.858913	4.373651	
39.54	1.174983	0.162859	3.668321	3.07511	

40.48	23.63049	10.24121	45.25009	3.281773	
41.41	22.6633	10.56691	41.76735	2.666343	
42.35	55.33211	34.49152	74.48477	2.876764	
43.29	9.055584	2.90006	23.60306	2.514985	
44.22	25.24565	10.64941	48.52444	2.63442	
45.16	2.686002	0.359242	10.61415	2.788663	
46.10	4.381711	1.066714	13.70859	3.42335	
47.03	-0.0296	-0.33581	0.840039	3.018478	
47.61	1.789782	0.394112	5.239137	2.829503	
48.18	7.060751	2.734281	16.18688	1.917037	
48.76	1.863715	0.508797	4.939428	1.675467	

Appendix 4.9

The paleo wSIC estimates for marine sediment core MD88-787 using GAM/WSI/13 from Chapter 3. The associated 95% confidence intervals lower (LCL) and upper (UCL) bounds for each wSIC estimate are included. Also provided are the paleo SST estimates from WA PLS and an indication for those core samples that have no (NA), or poor (PA), analogues.

Kyr_BP787	wSIC	LCL	UCL	fSST	Samples with no analogue (NA) or poor analogues (PA)
4.66	0.261039	-0.28236	2.125839	3.426178	
4.92	-0.00082	-0.35614	1.21715	2.406323	
5.21	0.271648	-0.31496	2.659687	2.346163	
5.48	0.265104	-0.20958	1.500237	2.417225	
5.78	0.290067	-0.24964	1.964772	2.636402	
6.10	0.089005	-0.23784	0.818024	2.333175	
6.42	0.260192	-0.28309	2.128687	2.540925	
6.74	0.293124	-0.23283	1.830515	2.967777	
7.06	0.241365	-0.29839	2.187696	2.192713	
7.37	0.070527	-0.24295	0.761521	4.12042	
7.69	3.015575	0.685252	9.469912	2.001986	
8.01	0.087326	-0.23835	0.813105	3.51889	
8.33	2.857751	0.472063	10.45716	2.370976	
8.65	8.482389	2.882122	21.28625	2.970817	
8.96	2.806294	0.385203	11.08311	1.519756	PA
9.28	7.405928	2.692627	17.77722	2.721178	
10.08	3.55693	1.078168	9.535976	2.842772	
13.34	0.086015	-0.23875	0.809248	2.231215	
14.73	1.29646	0.198703	4.040862	2.806526	
15.63	26.44437	12.87843	46.4029	2.559126	
15.89	29.17434	13.53842	51.75974	2.07874	
16.04	48.89758	29.01277	69.13039	3.096133	PA
16.27	17.09715	6.7167	36.51556	1.691379	
17.07	31.08954	12.98755	57.4098	2.318722	
17.94	49.96469	28.69399	71.24793	2.832464	
18.63	35.52749	13.07291	66.61344	2.133544	
19.36	28.58735	12.71302	52.10495	1.037232	
20.52	59.40895	35.72584	79.46173	1.879899	PA
21.76	28.57766	12.38912	52.79934	1.479895	PA
22.99	30.20539	15.18121	50.9447	2.206379	
24.48	12.29599	2.442713	41.1336	2.228941	NA
27.50	17.41417	7.159783	36.0246	2.162322	
30.45	4.836141	1.620791	12.29548	2.747774	PA
31.51	0.129277	-0.22512	0.934098	2.165033	
32.25	5.789596	1.573624	17.05606	3.159036	PA
33.07	2.606744	0.619979	7.824163	1.75481	
33.89	0.220907	-0.20569	1.255075	1.962369	PA
34.72	0.099738	-0.23449	0.849049	2.312294	
35.55	0.623286	-0.13224	2.878836	2.634835	

36.37	5.182474	1.935631	12.19987	1.70796	
37.20	11.90479	4.191146	28.48476	1.539877	PA
38.02	11.00294	3.964049	26.08429	1.825286	
38.85	13.06963	5.286483	28.16933	1.387529	
39.68	28.73263	14.84485	48.06329	1.335242	
40.50	1.754124	0.275768	5.870657	1.378561	PA
41.33	24.24117	11.20464	44.48315	1.153937	
42.16	19.34478	7.304627	41.57373	1.239569	PA
42.98	7.183713	2.820727	16.29353	2.237075	
43.81	4.104657	1.306133	10.74769	2.299653	
44.63	4.123421	1.524036	9.716506	1.589575	
45.46	46.85975	26.71469	68.06069	1.957849	
46.29	15.24006	5.157062	36.34888	2.202774	
47.11	7.392867	2.62641	18.04895	1.776822	
47.94	4.350662	1.626716	10.18641	2.525593	
49.48	6.45011	1.578105	20.33816	1.509431	

Appendix 4.10

The paleo wSIC estimates for marine sediment core PS58/271-1 using GAM/WSI/13 from Chapter 3. The associated 95% confidence intervals lower (LCL) and upper (UCL) bounds for each wSIC estimate are included. Also provided are the paleo SST estimates from WA PLS and an indication for those core samples that have no (NA), or poor (PA), analogues.

PS58/271-1 Depth	wSIC	LCL	UCL	SST	Samples with no analogue (NA) or poor analogues (PA)
6	2.73	0.391401497	10.54078658	2.624665809	PA
12	2.9	0.52337336	10.1762751	2.755288206	NA
23	2.48	0.218306944	11.06827741	2.329589938	NA
33	4.35	0.727936553	16.8098586	3.496417989	NA
43	11.7	3.46002838	31.36603055	2.379080864	
52	2.35	0.16672292	10.88747882	2.23802215	NA
62	8.62	2.357199122	25.0318987	2.818780298	PA
72	0.98	-0.273802676	8.522932555	2.546885111	NA
82	2.68	0.144066387	13.77604867	2.950836381	NA
92	4.58	0.62335158	19.68070028	2.865244698	PA
102	0.17	-0.271688798	1.446051069	3.447541838	NA
112	0.1	-0.361077092	2.011366205	3.136488783	NA
122	0.11	-0.338134409	1.801672733	3.233354689	NA
132	0.14	-0.311966127	1.679850607	3.004779959	NA
142	0.13	-0.321264893	1.722962472	3.66733915	NA
152	0.8	-0.30408239	7.655807764	2.689744682	NA
162	1.1	-0.168748225	6.829919338	3.699322463	NA
172	2.97	0.56971417	10.17924871	3.706082922	PA
182	7.71	2.415900666	20.54366442	3.614883311	
192	6.92	1.760822846	21.26342962	2.724235872	PA
202	4.82	0.528371881	22.85230524	2.73638639	NA
212	13.8	5.047758239	31.83770425	2.083042817	PA
222	7.59	1.960988662	23.01576814	2.755244119	PA
232	9.49	2.806776681	25.99343222	2.187836948	
242	20.1	7.097890959	44.71552323	1.761708261	NA
252	7.09	1.010600661	30.10394675	2.34616472	NA
262	18.4	6.302200402	42.2842653	2.723146314	PA
272	30.5	10.67554922	61.38637056	1.796674485	PA
282	6.71	0.894242489	29.46635372	2.459559343	NA
292	13.1	3.439218964	37.17502654	2.267397069	PA
302	19.4	7.165568638	42.31937046	1.626220912	NA
312	8.66	2.413860211	24.85194955	2.140871253	PA
322	5.93	1.477380897	18.47936093	2.77358915	PA
332	9.65	2.483827479	28.85857496	2.378518674	PA
342	0.97	0.095703445	3.075025947	2.014760486	NA
354	9.99	2.908913598	27.55661972	2.789111578	PA
362	31	13.78386224	55.6116322	2.065272751	
372	34.5	15.82894122	59.32301304	2.30250969	
382	20	8.582033408	39.61650866	2.129179221	PA

392	9.37	2.672065561	26.34127499	2.747339188	PA
402	22.7	10.09953264	43.02028474	2.692148084	
412	5.65	1.47636781	17.0866875	2.796487057	PA
422	7.15	2.035184629	20.39806934	2.578113291	PA
432	20.4	8.697743639	40.46256429	2.094490249	
442	15.1	5.485981744	34.52568484	2.403143685	PA
452	23	10.14578319	43.79071269	2.20491737	
462	29.9	13.85674411	52.87299408	2.634350194	
472	12.2	3.491566435	33.39548744	2.121938206	PA
482	36.2	13.33137207	67.3704664	1.893126325	NA
492	7.99	1.987770271	24.74471193	2.20887772	NA
502	5.89	0.509274779	30.96032642	1.994895282	NA
512	24.8	10.34981786	48.08712663	2.639705067	PA
522	6.31	0.821449323	28.08917491	2.255048023	NA
532	18.1	6.526673765	40.49374441	1.977612448	
542	4.49	1.297404033	12.58920544	3.058847559	PA
552	5	1.355854439	14.69871565	2.914309854	PA
562	5.09	1.524233384	14.02903724	2.711777232	PA
572	4.6	0.610706135	19.95046918	2.515187619	PA
582	7.35	2.031566579	21.3732228	3.237130549	PA
592	12.9	4.660390828	30.12926999	2.440241642	PA
602	19.5	7.334375919	42.08248268	2.587392517	
612	10.8	3.778736783	26.25956601	2.415773212	PA
622	9.49	2.80236937	26.04463685	2.156629919	PA
632	17.9	7.40648419	36.68716644	3.00192397	
642	12.2	4.291636521	29.14264724	2.355709156	PA
652	4.69	1.37012101	13.10694894	2.819436612	PA
662	3.2	0.526422014	11.94595038	3.251609877	PA
672	3.3	0.156485476	18.58845792	3.218123025	NA
682	16.8	5.297762902	41.27532714	3.602808958	PA
692	1.83	0.352291299	5.733013352	2.271110917	NA
702	7.21	2.128640175	20.04756334	2.668914755	PA
712	22.8	10.16394882	43.12970172	2.92341337	
722	3.23	0.272514249	15.68563106	2.793398253	NA
732	23.7	7.223742829	54.49776408	1.87374443	PA
742	28.8	10.01386698	58.98194612	2.980319116	PA
753	9.32	2.626193899	26.38598912	2.150761413	PA
762	21.2	7.310049304	47.26265393	2.866724447	NA
772	20.8	7.789386269	44.32180501	1.653740163	PA
782	28.3	12.95677888	50.81782908	2.558058358	PA
792	33.8	15.00606727	59.41247956	1.438490214	NA
802	22.9	10.16499769	43.3140433	1.683738213	
812	11.6	4.123824407	27.55237328	2.934537074	PA
822	19.1	5.698915503	46.86506858	2.009073335	PA
832	26.5	10.37776679	52.59851244	2.131230396	PA
842	2.73	0.487076751	9.558278671	2.99986399	PA
852	22.1	9.844990919	42.08158212	2.253240684	PA
862	33.2	15.73401506	56.71221369	2.282270013	
872	24.2	10.2768168	46.77669798	2.316098064	PA
882	21.7	8.663439374	44.19317277	2.186369591	PA
892	24.1	10.38156108	46.28572313	2.209423737	
902	8.13	1.974934839	25.56273167	2.51029368	PA
912	2.43	0.422009617	8.419251971	2.550422977	PA
922	10.2	2.366986418	32.34700728	3.217233644	PA
932	14.4	4.648371264	35.68728967	1.877720919	PA

942	19.4	7.717793728	40.41773233	2.375011202	
952	5.27	1.50615181	14.98520541	2.561036213	PA
962	22.4	9.950068766	42.70371019	1.870866733	
972	30.2	13.86716172	53.49346344	2.274613058	
982	20.8	7.412763655	45.71561614	1.878425092	PA
992	30.9	13.00999155	56.96614294	1.839310293	PA
1002	29.2	13.43227199	52.01098975	1.889694202	PA
1012	14.7	4.958451497	35.34194191	2.142509316	NA
1022	18.1	6.700143389	39.76870338	2.276336498	
1032	20.7	6.759142488	47.5921031	2.172557912	PA
1042	4.56	1.284835787	13.00913869	2.2006315	PA
1052	3.2	0.54667561	11.75080727	3.654108733	PA
1062	22.3	9.794398582	42.77346632	2.486461882	
1072	11.2	2.950202698	32.39529054	2.438510965	PA
1082	13.9	4.297665708	35.70478016	2.666657669	PA
1092	6.01	1.04119656	23.18323656	2.521551856	PA
1102	7.58	2.089249834	22.06377197	3.196995264	PA
1112	14.4	4.706895446	35.46627609	2.62105837	PA
1122	10.3	2.911355648	28.94880732	3.653938602	PA
1132	21.1	7.150580981	47.44548672	2.23172454	PA
1142	0.11	-0.342273597	1.822409431	2.974387779	NA
1152	3.82	0.499320032	16.29994185	3.290621903	PA
1162	18.1	4.651859171	48.55289889	2.491844934	PA
1172	4.33	0.433922216	20.99553426	2.860794514	NA
1182	6.77	1.930400259	19.28886544	4.041695226	PA
1192	1.08	-0.214525737	7.798287277	3.19899038	NA
1202	0.11	-0.343750861	1.830074323	2.609104784	NA
1212	14	5.159546918	31.87231782	2.795091882	PA
1222	20.1	6.972539497	44.92999619	2.411815994	PA
1232	7.88	2.196324387	22.70577903	3.081697906	
1242	10.8	3.491629327	27.60332914	3.552182731	PA
1252	23.1	9.679778452	45.35577356	2.686974382	
1262	20	7.722171871	42.03995998	1.885921124	PA
1272	22.8	10.12775845	43.38209614	2.40854383	
1282	17.3	5.216618214	43.04902893	2.049335282	PA
1292	21.9	7.186908381	49.64574532	1.783230121	PA
1302	27	11.96529694	49.88554316	1.66689169	PA
1312	28.6	13.16311942	51.0668847	2.043880019	
1322	24.3	10.17151489	47.36462038	2.476377971	
1331	23.4	8.32383251	50.03430163	2.739406219	
1342	23.1	10.1796372	43.99167403	2.708160754	
1352	28.7	13.09146801	51.4825014	1.594566897	PA
1362	3.31	0.19732331	17.81521323	1.97610197	PA
1372	11.6	3.33616545	31.65473934	3.374758625	
1382	25.8	10.89920342	49.30208601	2.505161467	PA
1392	20.8	7.607057167	44.94627667	1.932003813	
1402	12.2	3.711532295	31.94535599	2.094276457	PA
1412	3.15	0.287307815	14.84424161	2.358192823	NA
1422	21	8.938154376	41.3305987	2.590811166	
1432	25.1	9.94006542	50.10005192	2.106605435	PA
1442	5.04	1.280380026	15.48206757	2.955998964	PA
1452	23.9	9.449392919	48.105819	2.192412727	
1462	2.97	0.426507937	11.62137755	2.618747079	PA
1472	6.86	1.823208583	20.50810583	4.065221022	PA
1482	5.44	1.246723726	17.81824323	3.246783229	PA

1492	1.12	-0.156631776	6.812534225	2.685032145	PA
1502	1.03	-0.236721135	7.834346736	4.264589046	PA
1512	0.96	0.0298484	3.449654019	2.558153193	NA
1522	13.3	3.472179053	37.64331013	2.47809885	PA
1532	2.25	0.046504249	12.21632898	3.649811943	PA
1542	2.91	0.330586663	12.47949548	4.283132203	PA
1552	1.01	-0.234968597	7.655001938	2.989558995	NA
1562	9.54	2.453912555	28.59371336	2.230587375	PA
1572	3.57	0.278214882	18.15751493	2.307497075	PA
1582	0.95	-0.042861859	3.975518313	2.560032574	NA
1592	3.02	0.238735656	14.70158086	3.840645928	NA
1602	0.88	-0.293249775	8.184437297	2.365898222	NA
1612	19.8	6.803736372	44.89847344	2.437226331	PA
1622	1.16	-0.205211855	8.26132497	2.78449607	NA
1632	6.56	1.684563172	20.05989282	2.5580267	PA
1642	21.9	8.61368437	45.08100777	3.131058485	PA
1652	6.27	1.624313979	19.07273864	3.809875898	PA
1662	25.3	8.051165804	55.97361816	2.378995666	PA
1672	7.15	1.850442162	21.69583954	3.294790156	PA
1682	21.4	9.383952136	41.45950366	2.996442851	
1692	18.9	5.917463879	45.40543685	2.01007857	PA
1702	6.59	1.428227576	22.35446246	3.255359648	PA
1712	6	1.208162724	21.28292532	3.420320631	PA
1722	6.98	1.446274933	24.28882986	2.756509467	PA
1732	2.75	0.281349158	12.0138604	3.279879276	PA
1742	14.3	3.67358652	40.40926152	2.637368697	PA
1752	5.24	0.689899338	23.08220222	2.626271641	NA
1762	1.04	-0.159623513	6.199514338	2.823481695	NA
1772	4.99	0.872935206	19.04146837	3.145878092	PA
1782	1.01	0.007321632	3.904286038	2.743047832	NA
1792	19.4	6.602162722	44.30538873	2.749849961	PA
1802	6.33	1.419271688	21.09271438	2.319635289	PA
1812	10.2	2.470537304	31.66800782	2.898535806	PA
1822	11.7	3.381393812	32.06263089	2.676250325	
1832	10.5	2.949157377	29.46283899	2.74623822	PA
1842	9.99	2.612388284	29.48617142	3.517545713	
1852	7.14	1.771210021	22.25209379	3.195198096	PA
1862	20.2	5.494624683	51.28475178	2.830427673	PA
1872	8.94	2.063772929	28.7879976	2.444481485	PA
1882	0.16	-0.238001217	1.142234571	3.355971831	NA
1892	2.96	0.114069426	16.77040371	2.744944518	NA
1902	13.7	4.960071502	31.64548488	2.888498981	PA
1912	6.52	1.298691735	23.28082973	3.39767551	PA
1922	4.64	0.92134087	16.40854068	3.167718302	PA
1932	6.04	0.940022269	24.61938808	3.140828331	NA
1942	2.62	0.357074872	10.2305732	2.55055475	PA
1952	2.63	0.318557851	10.70676271	2.681806058	PA
1962	0.16	-0.284983	1.535262565	2.996484118	NA
1972	0.96	-0.026201561	3.922466248	3.095520039	NA
1982	0.14	-0.310953142	1.675043605	3.646251466	NA
1992	3.25	0.212584893	16.97560555	3.407135042	PA
2002	5.45	1.069210831	19.61785401	2.396721372	NA
2012	1.09	-0.219997749	7.965902517	4.422985755	NA
2022	1.05	-0.254974207	8.659075872	4.327329521	NA
2032	0.1	-0.348120959	1.853864974	3.133385987	NA

2050	0.15	-0.306447744	1.653256451	2.429904584	NA
2060	0.97	-0.284201948	8.890760783	3.038932177	NA
2070	0.99	-0.277471182	8.850259801	2.652472807	NA
2080	2.57	0.137904485	13.00339352	3.450595761	NA
2090	1.07	-0.254191022	8.878574464	3.317755604	NA
2100	1.12	-0.206486621	7.9431071	2.814657733	PA
2110	0.1	-0.350245695	1.866241276	2.441741214	NA
2120	1.39	-0.214068222	10.95351454	3.344923324	NA
2130	1.06	-0.250642512	8.601725012	3.150146693	NA
2140	4.47	0.739785659	17.4089759	3.070617017	PA
2150	0.15	-0.302792957	1.634993423	3.246382385	
2160	3.01	0.038282307	19.21529121	3.424960443	NA
2170	1.31	-0.226436285	10.50266949	2.288083276	NA
2180	0.1	-0.350477573	1.867633959	2.674859243	NA
2190	1.07	-0.257912098	9.042637801	4.494802169	NA
2200	0.1	-0.345942647	1.84177102	2.814027087	NA
2210	1.1	-0.252480291	9.106831346	3.145248377	NA
2220	0.16	-0.242540844	1.194336713	3.465221376	NA
2230	1.09	-0.242948378	8.680654631	4.248984066	PA
2240	0.09	-0.361165356	1.963442937	4.19561194	PA
2250	1	-0.271346211	8.660767803	4.001288248	NA
2260	3.08	0.166033986	16.61306857	2.363769055	NA
2270	0.35	-0.285690115	2.790946914	2.096353235	NA
2280	0.1	-0.358883648	2.046778704	3.167393508	NA
2290	0.17	-0.253539831	1.300751922	3.179502262	NA
2300	2.68	-0.029246704	18.06694148	3.336366899	NA
2310	0.93	-0.018038112	3.667588129	2.067069273	NA
2320	7.51	1.67482006	24.99101909	2.185904105	NA
2330	4.43	0.523169175	20.13945462	2.632629026	NA
2340	6.26	0.669076415	30.31994346	2.841894994	NA
2350	5.16	0.542974856	24.98677052	1.974613736	NA
2360	4.65	0.364977442	24.810365	1.342498987	NA
2370	6.53	1.1664859	24.75260796	1.205455667	NA
2380	3.72	0.339308915	18.21609303	2.040919488	NA
2390	3.49	0.295856357	17.21705855	1.6904281	NA
2400	1.21	-0.168548205	7.818043626	2.51019756	NA
2410	5.27	0.692114655	23.27709606	2.152593431	NA
2420	19.6	8.432111195	38.74736579	2.933464811	
2430	8.13	1.313518371	32.15802189	2.067765099	NA
2440	12.1	4.163143313	29.18689585	2.866031915	

Appendix 4.11

The paleo wSIC estimates for marine sediment core PS1768-8 using GAM/WSI/13 from Chapter 3. The associated 95% confidence intervals lower (LCL) and upper (UCL) bounds for each wSIC estimate are included. Also provided are the paleo SST estimates from WA PLS and an indication for those core samples that have no (NA), or poor (PA), analogues.

PS1768-8 Depth	wSIC	LCL	UCL	SST	Samples with no analogue (NA) or poor analogues (PA)
2	3.462286232	0.39007672	15.449193	1.71851	NA
10	29.37920796	9.689690904	61.245681	2.37105	
20	15.24991059	4.985309128	37.150936	2.36553	PA
30	35.08020465	11.9598527	67.940013	3.34845	PA
40	4.225744057	1.205702749	11.92389	2.9539	PA
46	10.8711802	3.434883377	28.204894	3.32631	PA
50	1.487826985	0.001447628	7.0491404	3.85559	NA
60	2.896763449	1.062450454	6.7280211	3.8763	NA
65	0.977189782	-0.208310602	6.6393023	1.96747	NA
70	3.981480811	1.762835681	8.1841202	2.97983	NA
80	0.407593399	-0.065332746	1.3854251	5.45004	NA
90	0.127841537	-0.224502341	0.924438	1.86528	NA
100	5.355145906	1.517138495	15.327998	4.37979	PA
104	11.36716786	4.109719072	26.812955	4.82479	PA
110	10.81229593	3.104543147	29.863574	4.30909	PA
120	11.5211951	3.294342712	31.680291	3.26732	
130	9.84773056	3.485203506	23.821653	2.73403	PA
140	10.80289944	2.640067251	32.935481	2.2777	NA
150	11.86144744	3.576521744	31.43619	0.68141	NA
160	55.13402215	33.70141599	74.847693	0.33855	NA
170	85.64210089	68.83034954	94.324334	0.45024	NA
180	62.17892809	40.19751674	80.15356	0.61395	NA
190	72.50835037	47.4706076	88.645821	0.11041	NA
200	71.54278813	49.3412354	86.764655	0.24206	NA
204	89.22366652	73.92309469	96.221909	0.39033	NA
210	67.85168126	37.97987771	88.063658	0.48478	NA
220	83.75432912	66.52140465	93.199291	0.37232	NA
230	87.29854647	68.76535622	95.750433	0.02846	NA
240	74.50678499	52.23151844	88.785912	0.41092	NA
250	69.31899725	48.1889947	84.686087	0.34695	NA
260	80.37775071	62.08725686	91.246713	0.14064	NA
270	81.03912151	58.6935232	92.961962	0.99619	NA
280	69.93440987	48.17889842	85.442064	0.52541	NA
290	93.41853406	80.18344215	98.270009	0.96027	NA
300	83.00172952	62.56963562	93.626993	1.39539	NA
304	85.04438857	64.04205425	94.982243	1.79077	NA
310	90.77689439	75.05757713	97.207427	1.80352	NA
320	49.61885152	21.96999904	77.498126	1.1012	PA
330	82.80813411	62.50402488	93.472454	0.61772	PA

340	84.98388743	64.13998618	94.911743	0.49285	PA
350	84.38082502	61.18539322	95.091061	0.98793	PA
360	85.58073886	66.15005672	94.937425	1.85488	PA
370	84.50914459	58.65495683	95.68848	2.33102	PA
380	64.24753157	28.46786603	89.192304	2.08981	PA
390	82.97972584	57.40930096	94.855441	0.89145	NA
400	90.81511313	74.75313133	97.285034	1.62501	PA
404	92.88170957	77.43879761	98.278103	1.78805	NA
410	80.37316238	60.18464339	91.886874	1.68349	NA
420	87.32143356	68.91160293	95.738032	0.89771	NA
430	89.0108443	70.83157999	96.651753	1.15764	NA
440	74.5792631	46.79258555	90.90623	2.04341	NA
450	88.92896253	63.97621658	97.600759	2.14464	PA
460	88.24193733	68.86686367	96.443833	1.24196	NA
470	71.61126941	41.83969493	90.014867	2.15242	NA
480	87.20587085	66.51952999	96.121665	1.97082	NA
490	83.1986467	61.71022673	94.022561	1.29191	NA
500	92.02777568	74.50542854	98.114382	0.92647	NA
510	82.67896812	60.17976365	93.973653	0.77486	NA
520	81.41864407	61.57534955	92.456805	0.30013	NA
530	88.15384964	70.41198423	96.085263	1.50846	NA
540	89.27347045	71.53724308	96.718525	1.06469	
550	81.27383259	57.51120183	93.488844	0.48186	
560	69.4776202	40.81734405	88.404106	2.5518	NA
570	23.51714553	6.240691328	57.72245	2.66486	NA
580	84.54399085	58.37155499	95.764586	2.62332	PA
590	68.49003123	37.84392509	88.742788	1.8547	NA
600	53.25246162	27.95583841	77.00978	2.67693	
610	93.45636466	68.7397707	99.277508	2.65376	PA
620	38.97277863	18.03665522	64.823668	2.83466	NA
630	81.14713007	53.88078992	94.287847	2.14257	PA
640	78.81970465	53.63224159	92.477191	2.30091	
650	84.62827493	57.69503131	95.942158	4.07631	PA
660	58.45988544	28.24773774	83.506604	2.01704	
670	42.63891986	19.98015646	68.793045	3.50119	
680	30.08572021	12.48374892	56.182784	2.54672	PA
690	69.39859198	30.04012395	92.517874	1.5327	NA
700	56.61037788	29.97137404	79.967541	2.93555	PA
710	66.26508093	34.66776052	88.060925	3.3201	
720	63.84989712	38.59448946	83.3277	2.00192	
730	9.711467173	3.240772511	24.498155	3.17567	
740	13.47206759	4.862902593	31.305492	2.71045	
750	5.622945589	1.531859504	16.533575	2.15487	NA
760	6.495097934	1.991906126	17.637755	2.13228	NA
770	8.122611516	1.257776761	32.801207	3.07188	
780	2.11009327	0.214287462	8.5819251	3.01133	
790	0.158420541	-0.294981955	1.5937057	2.43254	NA
800	0.837165057	-0.235038549	5.9695372	3.60423	NA
810	0.112481264	-0.339528873	1.8085517	3.11038	NA
820	2.927434614	0.644530361	9.3162355	2.24399	NA
830	29.81464996	12.27505813	56.010681	0.66268	NA
840	88.51932668	73.5474072	95.712228	0.18938	NA
850	81.29811455	57.65284354	93.471747	-0.1491	NA
860	65.56062871	42.93432556	82.897737	0.67268	NA
870	80.0905204	60.44662485	91.519767	0.3713	NA

880	50.44118442	28.87829726	71.844379	-0.0035	NA
890	77.78710329	54.87924538	91.136902	-0.261	NA
894	81.53744357	58.85609206	93.352882	1.13818	NA

Appendix 4.12

The paleo fSST estimates for marine sediment cores SO136-111 and E27-23. The paleo fSST estimated wee estimated using WA-PLS and log transformed data, as described in sections 2.3 and 3.1.1.

Kyr_BPSO136111	SO136-111 fSST	Kyr_BPE2723	E27-23 fSST
3.39	4.09	1.54	0.95
3.87	4.58	1.70	2.83
4.37	4.50	1.80	2.23
4.88	3.97	1.95	2.66
5.38	3.33	2.05	0.99
5.89	3.67	2.15	2.99
6.40	4.81	2.19	0.65
6.90	4.51	2.44	2.74
7.41	4.15	2.61	3.09
7.91	5.11	2.86	2.23
8.42	3.26	3.28	2.61
8.93	3.91	3.70	0.78
9.43	4.73	3.87	1.30
9.94	3.08	4.13	2.87
10.44	4.60	4.29	1.08
10.96	4.99	4.55	0.87
11.64	5.10	4.63	2.39
12.33	3.89	4.72	3.47
13.03	4.46	4.97	2.58
13.72	3.48	5.13	0.93
14.41	4.69	5.19	3.24
15.10	4.04	5.29	4.53
15.79	4.29	5.38	3.45
16.49	4.51	5.47	3.53
17.18	4.14	5.56	2.73
17.87	3.85	5.66	4.12
18.56	3.38	5.75	2.38
19.25	3.04	5.84	2.45
20.08	3.39	5.94	3.75
21.05	2.57	6.03	4.01
22.02	2.19	6.11	3.67
22.98	2.59	6.18	2.68
23.95	2.31	6.26	0.81
24.91	1.82	6.33	1.16
25.88	1.32	6.41	0.89
26.85	1.63	6.48	0.54
27.81	1.57	6.56	1.75
28.78	1.42	6.64	-0.15
29.74	1.64	6.79	2.65
30.71	1.87	6.88	0.79
31.68	1.45	6.97	0.39
32.64	3.06	7.06	1.48

33.61	3.22	7.15	1.16
34.58	2.86	7.24	0.42
35.54	2.24	7.33	0.85
36.51	2.16	7.42	1.25
37.47	3.38	7.51	1.11
38.44	2.84	7.60	1.12
39.41	3.25	7.70	0.86
40.37	2.82	7.79	1.59
41.34	3.07	7.89	0.79
43.27	2.98	7.98	1.54
45.69	2.45	8.11	0.95
47.76	2.26	8.38	0.25
49.74	3.12	8.68	1.09
51.72	1.90	8.99	1.35
53.71	2.79	9.29	0.74
55.69	2.21	9.59	1.98
57.67	1.86	9.90	1.72
59.65	3.36	10.21	2.08
61.64	2.70	10.57	1.56
63.62	3.12	11.29	1.71
65.60	2.94	11.64	4.75
67.05	1.87	11.99	0.54
68.36	2.25	12.33	-0.25
69.41	1.91	12.68	0.61
70.99	2.04	13.00	1.41
72.04	2.52	13.23	0.71
73.61	3.27	13.41	0.93
74.66	2.87	13.72	0.96
76.24	3.20	14.59	1.59
77.29	3.96	15.46	1.07
78.86	3.50	15.74	1.48
80.18	3.68	15.89	1.12
81.49	3.50	16.04	0.84
82.80	4.80	16.19	1.67
84.11	4.53	16.34	1.16
85.43	3.98	16.49	1.31
86.74	3.24	16.64	0.86
87.70	3.11	16.78	0.79
88.58	2.25	16.87	2.49
89.46	2.45	16.96	0.61
90.34	1.99	17.04	1.22
91.22	3.86	17.13	2.18
92.10	4.82	17.23	2.30
92.98	3.88	19.28	1.09
93.86	4.72	24.17	-0.08
94.74	4.10	27.44	0.40
95.62	3.61	29.26	1.18
96.50	3.93	30.76	1.63
97.38	4.05	32.27	1.02
98.26	5.05	33.77	0.56
99.14	3.33	35.55	0.27
100.02	4.63	38.55	1.87
100.90	4.26	41.82	1.19
101.78	5.07	44.89	0.62
102.66	4.17	47.04	2.31

104.42	4.73	48.76	1.87
105.30	4.35	49.56	1.78
106.18	4.53	50.15	2.68
107.06	2.88	50.74	1.70
107.94	3.94	51.33	2.64
108.82	3.14	51.68	1.50
109.80	3.42		
110.80	3.11		
111.80	3.98		
112.80	3.48		
113.80	3.13		
114.80	3.50		
116.20	4.10		
117.00	3.79		
117.80	3.75		
118.60	4.51		
119.56	5.09		
120.12	3.12		
120.96	4.64		
121.52	4.21		
122.36	5.62		
122.92	5.17		
123.76	5.14		
124.32	4.60		
125.16	5.59		
125.72	6.55		
127.03	7.36		
128.06	5.86		
129.60	5.35		
130.63	3.49		
132.17	2.17		
133.20	1.53		
134.74	2.15		
137.66	1.97		
142.97	2.54		
146.51	3.93		
151.83	2.59		
155.37	2.83		
160.69	1.61		
164.23	3.26		
168.97	1.35		
171.94	2.69		
176.40	2.78		
179.37	1.74		
183.83	4.00		
187.54	3.03		
191.26	3.64		
192.91	4.32		
194.05	5.74		
195.18	3.37		
196.32	4.76		
197.45	3.44		
198.59	4.17		
199.73	4.01		
200.86	3.23		

202.00	4.14		
203.14	4.46		
204.27	4.40		
205.41	4.68		
206.55	4.21		
207.68	3.52		
208.82	4.92		
209.95	4.80		
211.09	4.30		
212.23	5.90		
213.36	5.00		
214.50	4.82		

Appendix 5.1

Those samples from the Crosta et al. (2004) Southern Ocean diatom database that were sampled from areas that are currently covered by Southern Ocean fronts.

	Southern Ocean Front								
	SAF-N	**SAF-M**	**SAF-S**	**PF-N**	**PF-M**	**PF-S**	**SACFF-N**	**SACCF-S**	**SB**
Crosta et al. (2004) samples located under modern position of each front	4501	4345	4934	5000	5624		5314	5258	6440
	4604			5043	5746		5900	5430	6545
				5305					6550
									6606
									6609
									6659
									6731
									6828
									6855
									6857
									6858
									6914

Appendix 5.2

The down core records of fossilised diatom relative abundances for marine sediment core MD88-784. Also provided is the depth and age (in calendar years before present) for each of the cores samples.

Depth	Kyr_BP784	Actinocyclus actinochilus	Azpeitia tabularis var. tabularis	Chactoceras resting spores	Fragilariopsis curta	Fragilariopsis cylindrus	Fragilariopsis doliolus	Fragilariopsis kerguelensis	Fraglariopsis obliquecostata	Fragilariopsis rhombica	Fragilariopsis ritscheri	Fragilariopsis separanda	Fragilariopsis sublinearis
0	5.31	0.00	2.69	0.00	0.00	0.00	0.00	78.32	0.00	0.34	0.00	0.67	0.00
10	5.56	0.00	1.47	0.29	0.00	0.00	0.00	77.17	0.00	1.77	0.00	1.77	0.00
20	5.82	0.00	2.16	0.00	0.00	0.00	0.00	72.64	0.00	0.00	0.00	0.31	0.31
30	6.07	0.00	2.88	0.00	0.00	0.00	0.00	72.52	0.00	0.00	0.00	1.92	0.00
40	6.32	0.00	3.78	1.37	0.00	0.00	0.00	73.88	0.00	0.00	0.00	1.37	0.00
50	7.00	0.00	4.15	0.00	0.00	0.00	0.00	77.83	0.00	0.00	0.00	0.32	0.32
60	7.67	0.00	1.73	0.00	0.00	0.00	0.00	71.63	0.00	0.00	0.00	0.35	0.35
70	8.34	0.00	0.98	0.00	0.00	0.00	0.00	81.05	0.00	0.33	0.00	3.27	0.00
80	9.01	0.00	2.67	0.00	0.00	0.00	0.00	75.67	0.00	0.33	0.00	2.33	0.67
90	9.74	0.00	2.31	0.33	0.00	0.00	0.00	74.14	0.00	0.66	0.00	1.98	1.32
100	10.47	0.00	2.19	0.00	0.00	0.00	0.00	67.28	0.00	0.00	0.00	1.46	0.73
110	11.20	0.00	2.43	0.00	0.00	0.00	0.00	68.39	0.00	1.22	0.00	3.04	0.30
120	11.93	0.00	2.12	0.35	0.00	0.00	0.00	72.66	0.00	0.71	0.00	1.76	0.71
130	12.66	0.31	3.43	0.62	0.00	0.00	0.00	67.39	0.00	0.31	0.31	2.18	0.31
140	13.39	0.00	3.34	0.33	0.00	0.00	0.00	67.89	0.00	0.00	0.00	3.34	0.67
150	14.13	0.00	4.54	4.21	0.32	0.00	0.00	62.56	0.00	0.65	0.00	0.65	0.32
160	14.86	0.00	2.75	0.34	0.00	0.00	0.00	60.59	0.00	0.34	0.00	0.69	0.34
170	15.60	0.00	4.96	5.29	0.33	0.00	0.00	63.80	0.00	1.65	0.66	1.98	0.33
180	16.35	0.00	6.82	1.80	0.36	0.00	0.00	48.11	0.00	0.72	0.00	0.72	0.72
190	17.13	0.66	4.95	6.27	0.66	0.00	0.00	43.23	0.00	0.99	0.00	0.99	0.00
200	17.91	0.33	0.65	6.54	2.61	2.61	0.00	49.02	0.00	0.98	0.33	0.98	0.00
210	19.64	0.00	0.67	2.33	2.00	0.33	0.00	51.25	0.00	1.66	0.33	1.66	0.67
220	21.37	0.71	0.71	1.41	2.12	1.41	0.00	53.00	0.00	0.00	0.00	3.53	1.06
230	23.11	0.00	1.92	7.68	0.64	0.96	0.00	47.68	0.00	2.24	0.32	3.52	0.96
240	24.84	0.00	2.95	3.27	0.33	0.65	0.00	57.28	0.00	0.98	0.00	3.93	0.65
250	26.57	0.00	1.66	10.63	0.33	1.00	0.00	40.86	0.00	2.33	0.66	2.33	0.00
260	28.30	0.68	1.35	1.02	1.02	0.68	0.00	52.12	0.00	0.68	0.00	1.35	1.35
270	29.24	0.00	0.95	1.58	0.95	0.32	0.00	54.52	0.00	2.54	0.32	1.58	0.00
280	30.17	0.00	0.99	0.00	2.65	0.33	0.00	61.92	0.00	0.33	0.00	4.30	1.99
290	31.11	0.00	1.26	1.26	2.83	0.00	0.00	52.28	0.00	1.57	0.31	4.41	0.00
300	32.05	0.00	0.63	0.32	1.27	1.27	0.00	65.93	0.00	0.32	0.00	4.12	1.27
310	32.98	0.00	0.31	0.63	1.25	0.63	0.00	73.35	0.00	1.88	0.31	0.31	0.00
320	33.92	0.00	3.50	0.00	0.00	0.00	0.00	77.39	0.00	0.32	0.00	1.59	0.96
330	34.86	0.00	1.25	0.93	0.00	0.00	0.00	71.34	0.00	0.93	0.00	0.00	0.31
340	35.79	0.00	0.68	0.68	1.36	0.34	0.00	71.99	0.00	0.34	0.00	4.75	0.34
350	36.73	0.00	2.06	0.88	0.29	0.00	0.00	67.85	0.00	3.24	0.88	1.47	0.88
360	37.67	0.00	1.59	0.32	0.00	0.00	0.00	76.75	0.00	0.00	0.00	1.91	1.91
370	38.60	0.00	3.08	0.92	0.00	0.00	0.00	66.46	0.00	1.23	0.00	0.92	0.00
380	39.54	0.00	2.39	0.00	0.34	0.34	0.00	61.67	0.00	0.34	0.00	2.04	0.68
390	40.48	0.00	1.25	2.18	3.12	0.00	0.00	55.14	0.00	3.74	0.31	2.49	0.00
400	41.41	0.64	1.91	1.28	1.59	0.64	0.00	62.84	0.00	0.32	0.00	4.15	1.59
410	42.35	0.29	1.44	0.86	3.75	0.00	0.00	64.55	0.00	0.86	0.00	0.86	0.29
420	43.29	0.00	0.62	1.24	2.16	0.93	0.00	67.70	0.00	0.00	0.00	0.62	1.85
430	44.22	0.00	0.92	1.54	3.07	0.00	0.00	64.82	0.00	0.92	1.23	0.61	0.00
440	45.16	0.00	0.62	0.31	0.31	0.00	0.00	78.00	0.00	0.00	0.00	1.87	2.50
450	46.10	0.34	1.70	1.70	0.34	0.68	0.00	71.31	0.00	0.00	0.34	0.68	0.00
460	47.03	0.00	1.33	0.66	0.00	0.33	0.00	71.76	0.00	0.33	0.00	1.66	1.00
470	47.61	0.00	0.61	1.21	0.61	0.61	0.00	71.52	0.00	0.00	0.91	2.12	0.00
480	48.18	0.00	0.32	0.32	0.96	0.00	0.00	71.38	0.00	0.00	0.00	1.93	1.93
490	48.76	0.00	0.34	0.00	0.34	0.00	0.00	71.50	0.00	0.34	0.00	1.69	1.01

Depth	Kyr_BP784	Hemidiscus cuneiformis	Porosira glacialis	Porosira pseudodenticulata	Roperia tesselata	Stellarima microtrias	Thalassiosira Antarctica Group	Thalassiosira oestrupii including the varieties oestrupii and venrickae	Thalassiosira gracilis	Thalassiosira lentiginosa	Thalassiosira oestrupii including the varieties oestrupii and venrickae	Thalassiosira oliverana	Thalassiosira tumida
0	5.31	0.00	0.00	0.00	0.00	0.00	0.00	0.00	3.36	6.39	0.00	1.01	0.00
10	5.56	0.00	0.00	0.00	0.00	0.00	0.00	0.00	2.65	6.77	0.00	0.29	0.00
20	5.82	0.00	0.00	0.00	0.00	0.00	0.00	0.00	4.33	11.44	0.00	0.93	0.31
30	6.07	0.00	0.00	0.00	0.00	0.00	0.00	0.00	1.28	12.46	0.32	0.32	0.00
40	6.32	0.00	0.00	0.00	0.00	0.00	0.00	0.00	2.06	8.93	0.00	0.00	0.00
50	7.00	0.00	0.00	0.00	0.00	0.00	0.00	0.00	3.83	6.70	0.00	0.00	0.00
60	7.67	0.00	0.00	0.00	0.00	0.00	0.00	0.00	2.42	17.99	0.35	0.00	0.00
70	8.34	0.00	0.00	0.00	0.00	0.00	0.00	0.00	1.96	8.82	0.00	0.65	0.00
80	9.01	0.00	0.00	0.00	0.00	0.00	0.00	0.00	1.33	10.00	0.33	0.33	0.00
90	9.74	0.00	0.00	0.00	0.00	0.00	0.00	0.00	3.29	9.56	0.00	0.33	0.00
100	10.47	0.00	1.10	0.00	0.00	0.00	0.00	0.37	0.00	12.07	0.00	0.37	0.00
110	11.20	0.00	0.00	0.00	0.00	0.00	0.00	0.00	1.52	9.42	0.30	0.30	0.00
120	11.93	0.00	0.00	0.00	0.00	0.00	0.00	0.00	3.88	8.82	0.00	0.35	0.00
130	12.66	0.00	0.00	0.00	0.00	0.00	0.00	0.00	1.56	12.79	0.31	0.62	0.00
140	13.39	0.00	0.00	0.00	0.00	0.00	0.00	0.00	1.67	14.05	0.33	0.33	0.33
150	14.13	0.00	0.00	0.00	0.00	0.00	0.00	0.00	2.92	15.24	0.00	0.97	0.00

160	14.86	0.00	0.00	0.00	0.00	0.00	0.00	0.00	3.79	17.56	0.00	2.07	0.00
170	15.60	0.00	0.00	0.00	0.00	0.00	0.00	0.00	1.32	10.91	0.33	0.99	0.00
180	16.35	0.00	0.00	0.36	0.00	0.00	0.00	0.00	1.44	20.11	0.36	1.80	1.08
190	17.13	0.00	0.00	0.00	0.00	0.00	0.00	0.00	4.29	19.14	0.33	2.64	0.33
200	17.91	0.00	0.00	0.00	0.00	0.00	0.00	0.00	3.59	18.63	0.65	1.63	0.00
210	19.64	0.00	0.00	0.00	0.00	0.00	0.00	0.00	3.33	21.63	0.00	2.33	0.00
220	21.37	0.00	0.00	0.00	0.00	0.00	0.00	0.00	3.53	19.08	0.00	2.12	0.00
230	23.11	0.00	0.00	0.00	0.00	0.00	0.00	0.00	1.28	22.08	0.00	0.64	0.00
240	24.84	0.00	0.00	0.00	0.00	0.00	0.00	0.00	1.31	17.35	0.00	2.95	0.00
250	26.57	0.00	0.00	0.00	0.00	0.00	0.33	0.00	2.99	18.94	0.66	2.99	0.00
260	28.30	0.00	0.00	0.00	0.00	0.00	0.68	0.00	3.05	23.35	1.02	2.03	0.34
270	29.24	0.00	0.00	0.00	0.00	0.00	0.32	0.00	3.80	19.97	0.00	2.22	0.00
280	30.17	0.00	0.00	0.00	0.00	0.00	0.33	0.00	4.30	11.26	0.33	3.64	0.00
290	31.11	0.00	0.00	0.00	0.00	0.00	0.00	0.00	7.87	19.53	0.94	0.94	0.00
300	32.05	0.00	0.00	0.00	0.00	0.00	0.63	0.00	4.12	11.41	0.00	1.27	0.32
310	32.98	0.00	0.00	0.31	0.00	0.00	0.00	0.00	1.57	10.03	0.94	0.94	0.00
320	33.92	0.00	0.00	0.00	0.00	0.00	0.32	0.00	1.59	9.24	0.32	1.59	0.00
330	34.86	0.00	0.00	0.00	0.00	0.00	0.00	0.00	2.80	14.33	0.93	1.25	0.00
340	35.79	0.00	0.00	0.00	0.00	0.00	0.34	0.00	3.74	7.13	0.00	0.00	0.00
350	36.73	0.00	0.00	0.00	0.00	0.00	0.00	0.00	3.54	11.50	0.00	1.18	0.00
360	37.67	0.00	0.00	0.00	0.00	0.00	0.00	0.00	2.23	7.32	0.32	0.32	0.32
370	38.60	0.00	0.00	0.00	0.00	0.00	0.31	0.00	3.69	12.92	0.92	1.23	0.00
380	39.54	0.00	0.00	0.00	0.00	0.00	0.34	0.00	2.04	18.06	0.34	0.68	0.00
390	40.48	0.00	0.00	0.00	0.00	0.00	0.31	0.00	3.43	12.77	1.56	1.87	0.00
400	41.41	0.00	0.00	0.00	0.00	0.00	0.00	0.00	3.83	11.16	0.64	3.19	0.00
410	42.35	0.00	0.00	0.00	0.00	0.00	0.86	0.00	5.48	12.39	0.58	1.44	0.00
420	43.29	0.00	0.00	0.00	0.00	0.00	0.31	0.00	6.80	9.89	0.31	1.24	0.00
430	44.22	0.00	0.00	0.00	0.00	0.00	0.00	0.00	6.14	11.06	0.31	1.23	0.00
440	45.16	0.00	0.00	0.00	0.00	0.00	0.31	0.00	3.74	5.93	0.31	1.56	0.31
450	46.10	0.00	0.00	0.00	0.00	0.00	0.00	0.00	4.75	9.17	0.68	1.02	0.00
460	47.03	0.00	0.00	0.00	0.00	0.00	0.00	0.00	4.32	9.30	0.33	2.33	0.33
470	47.61	0.00	0.00	0.00	0.00	0.00	0.00	0.00	2.42	12.73	0.30	1.82	0.00
480	48.18	0.00	0.00	0.00	0.00	0.00	0.00	0.00	3.54	11.25	0.00	1.29	0.00
490	48.76	0.00	0.34	0.00	0.00	0.00	0.34	0.00	4.05	14.84	0.00	1.01	0.00

Appendix 5.3

The down core records of fossilised diatom relative abundances for marine sediment core MD88-787. Also provided is the depth and age (in calendar years before present) for each of the cores samples.

Depth	Kyr_BP 787	Actinocyclus actinochilus	Azpeitia tabularis var. tabularis	Chactoceras resting spores	Fragilariopsis curta	Fragilariopsis cylindrus	Fragilariopsis doliolus	Fragilariopsis kerguelensis	Fraglariopsis obliquecostata	Fragilariopsis rhombica	Fragilariopsis ritscheri	Fragilariopsis separanda	Fragilariopsis sublinearis
0	4.66	0.00	2.28	0.00	0.00	0.00	0.00	77.00	0.00	0.00	0.00	1.96	0.00
10	4.92	0.00	2.97	0.30	0.00	0.30	0.00	74.78	0.00	0.59	0.30	3.26	0.30
20	5.21	0.00	0.62	0.31	0.00	0.00	0.00	78.45	0.00	0.31	0.00	3.10	0.62
30	5.48	0.00	1.17	0.00	0.00	0.00	0.00	77.66	0.00	0.29	0.00	1.46	0.58
40	5.78	0.00	0.96	0.00	0.00	0.00	0.00	77.19	0.00	1.28	0.00	4.47	0.00
50	6.10	0.00	1.53	0.00	0.00	0.00	0.00	69.31	0.00	0.31	0.31	2.14	0.61
60	6.42	0.00	1.56	0.00	0.00	0.00	0.00	80.25	0.00	0.62	0.00	2.80	0.62
70	6.74	0.00	1.92	0.64	0.00	0.00	0.00	75.08	0.00	0.00	0.00	3.19	0.64
80	7.06	0.00	0.95	0.63	0.00	0.00	0.00	77.22	0.00	0.95	0.32	3.80	0.32
90	7.37	0.00	2.57	0.32	0.00	0.00	0.00	71.70	0.00	0.64	0.00	2.89	0.32
100	7.69	0.00	1.01	0.00	0.34	0.00	0.00	73.70	0.00	2.35	0.00	5.70	0.34
110	8.01	0.00	2.01	0.58	0.00	0.00	0.00	67.91	0.00	1.15	0.00	2.88	0.58
120	8.33	0.00	1.90	0.00	0.32	0.00	0.00	74.37	0.00	1.27	0.00	4.43	0.00
130	8.65	0.31	2.17	0.31	0.31	0.00	0.00	65.53	0.00	1.24	1.55	4.66	0.00
140	8.96	0.00	0.65	1.63	0.33	0.00	0.00	73.53	0.00	1.96	1.63	4.25	0.65
150	9.28	0.00	1.56	1.56	0.62	0.00	0.00	60.75	0.00	1.25	0.00	0.62	0.00
160	10.08	0.00	2.28	1.14	0.29	0.00	0.00	62.48	0.00	0.00	0.57	2.28	0.00
170	13.34	0.00	1.32	0.66	0.00	0.00	0.00	70.72	0.00	0.99	0.99	2.63	0.00
180	14.73	0.31	2.20	1.57	0.00	0.00	0.00	69.07	0.00	1.57	0.00	2.51	0.00
190	15.63	0.31	4.97	4.04	0.93	0.00	0.00	53.73	0.00	1.55	0.00	0.93	0.31
200	15.89	0.63	4.10	2.84	0.95	0.00	0.00	69.72	0.00	0.95	0.00	1.26	1.26
210	16.04	0.96	3.83	7.66	2.23	0.00	0.00	49.76	0.00	2.87	0.00	0.32	0.00
220	16.27	0.80	1.07	13.60	0.53	0.00	0.00	57.87	0.00	3.20	0.27	2.13	1.60
230	17.07	1.68	1.34	3.03	1.68	0.67	0.00	55.13	0.00	1.68	0.34	1.01	1.01
240	17.94	1.27	1.27	3.49	2.86	0.32	0.00	52.70	0.00	0.32	0.00	1.27	0.00
250	18.63	2.32	1.32	0.99	1.32	0.66	0.00	52.65	0.00	0.66	0.66	0.33	0.33
260	19.36	1.14	0.00	1.99	0.85	0.00	0.00	69.80	0.00	0.85	0.00	2.56	0.57
270	20.52	1.24	0.62	1.24	5.27	1.24	0.00	53.33	0.00	1.86	0.31	1.86	1.55
280	21.76	0.60	0.60	6.31	0.90	0.00	0.00	64.26	0.30	1.50	0.00	6.61	1.20
290	22.99	0.31	1.56	1.88	2.19	0.31	0.00	51.88	0.00	1.56	0.00	3.75	1.25
300	24.48	0.00	0.92	4.31	4.00	8.31	0.00	46.15	0.00	1.54	0.00	7.08	3.38
310	27.50	0.92	1.22	0.31	0.92	0.31	0.00	60.86	0.00	0.92	0.31	3.67	0.92
320	30.45	0.00	1.20	3.30	0.90	0.30	0.00	59.07	0.00	0.90	0.00	6.30	1.80
330	31.51	0.00	1.24	0.00	0.00	0.00	0.00	73.07	0.00	1.24	0.00	3.10	0.62
340	32.25	0.00	1.23	2.16	0.62	0.00	0.00	70.99	0.00	0.00	0.31	2.47	2.78
350	33.07	0.00	0.91	0.30	0.30	0.00	0.00	72.56	0.00	0.91	0.91	1.22	0.91
360	33.89	0.00	0.66	1.32	0.00	0.00	0.00	68.53	0.00	0.33	0.00	5.27	2.64
370	34.72	0.00	2.29	0.98	0.00	0.00	0.00	70.26	0.00	1.96	0.33	0.33	0.33
380	35.55	0.00	4.92	0.35	0.35	1.41	0.00	54.83	0.00	1.41	0.00	4.57	1.05
390	36.37	0.00	1.65	0.33	0.66	0.00	0.00	58.65	0.00	2.97	0.99	1.98	0.33
400	37.20	0.00	1.65	0.99	2.64	0.66	0.00	48.26	0.00	3.64	0.00	4.96	2.64
410	38.02	0.00	0.32	0.00	0.64	0.00	0.00	60.26	0.00	0.64	0.00	1.60	0.64
420	38.85	0.33	0.33	0.65	0.98	0.65	0.00	62.64	0.00	0.00	0.00	1.96	3.92
430	39.68	0.31	0.31	0.31	1.55	0.00	0.00	62.44	0.00	0.62	0.93	2.78	0.31
440	40.50	0.00	0.32	1.90	0.63	1.27	0.00	52.93	0.00	0.63	0.00	5.07	2.54
450	41.33	0.62	0.62	0.31	1.56	0.62	0.00	61.15	0.00	0.62	0.62	6.55	0.62
460	42.16	0.32	0.32	1.27	1.27	0.64	0.00	65.92	0.00	0.64	0.00	3.18	1.91
470	42.98	0.00	0.91	1.21	0.91	0.00	0.00	58.57	0.00	0.30	0.61	1.52	0.00
480	43.81	0.00	1.39	1.04	0.35	0.00	0.00	57.89	0.00	0.00	0.00	2.08	1.73
490	44.63	0.00	0.31	0.31	0.62	0.00	0.00	65.52	0.00	0.31	0.62	2.18	0.00
500	45.46	0.29	0.29	0.58	2.89	0.00	0.00	53.47	0.00	0.87	0.00	3.76	1.73
510	46.29	0.00	2.25	1.12	2.25	0.56	0.00	57.58	0.00	0.56	0.00	0.84	0.28
520	47.11	0.00	0.65	0.65	1.31	0.33	0.00	70.59	0.00	1.31	0.00	3.59	0.33
530	47.94	0.00	0.98	0.98	0.65	0.00	0.00	66.88	0.00	0.98	0.00	3.92	0.00
540	49.48	0.00	0.36	0.36	0.71	0.00	0.00	75.44	0.00	2.49	0.36	3.20	0.36
550	55.32	0.00	0.00	0.00	0.33	0.00	0.00	81.97	0.00	0.00	0.00	1.31	0.00
560	61.88	0.00	1.74	0.69	0.35	0.00	0.00	70.14	0.00	1.04	0.00	2.78	0.35
570	68.44	0.00	2.29	0.00	0.33	0.00	0.00	72.88	0.00	0.98	0.00	2.94	0.00
580	74.60	0.00	1.88	0.00	0.00	0.00	0.00	77.24	0.00	0.63	0.00	1.88	0.31
590	78.39	0.00	1.54	0.00	0.00	0.00	0.00	79.57	0.00	0.61	0.00	2.46	0.00
600	81.78	0.00	0.95	0.32	0.00	0.00	0.00	83.62	0.00	1.59	0.00	1.59	0.00
610	85.17	0.00	2.91	0.00	0.00	0.00	0.00	80.58	0.00	0.00	0.00	0.97	0.00
620	88.57	0.00	1.68	0.00	0.34	0.00	0.00	74.83	0.00	0.34	0.00	0.34	0.00
630	91.96	0.30	0.90	0.00	0.00	0.00	0.00	80.36	0.00	1.50	0.00	1.20	0.30
640	95.36	0.00	1.35	0.34	0.34	0.00	0.00	71.62	0.00	0.68	0.34	3.72	0.34
650	98.75	0.00	1.94	0.55	0.55	0.00	0.00	74.79	0.00	0.83	0.00	1.39	0.00

660	102.14	0.00	3.02	0.00	0.30	0.00	0.00	78.85	0.00	0.91	0.60	2.11	0.30
670	105.54	0.31	2.79	0.00	0.31	0.00	0.00	76.59	0.00	0.31	0.31	1.55	0.00
680	109.52	0.00	1.61	0.00	0.00	0.00	0.00	71.06	0.00	0.00	0.00	0.96	0.00
690	116.99	0.00	2.54	0.32	0.00	0.00	0.00	72.70	0.00	1.90	0.00	7.94	0.32
700	124.13	0.00	2.50	0.00	0.00	0.00	0.00	75.43	0.00	0.63	0.00	4.69	0.31
710	125.71	0.00	1.44	1.15	0.29	0.00	0.00	64.94	0.00	2.59	0.00	4.60	0.00
720	126.37	0.00	1.57	0.63	0.00	0.00	0.00	64.58	0.00	1.57	0.00	2.19	0.00
730	127.03	0.31	2.45	2.45	0.00	0.00	0.00	67.99	0.00	2.14	0.61	2.14	0.61
740	127.69	0.34	1.01	5.72	0.34	0.00	0.00	52.53	0.00	1.01	0.00	1.01	0.00
750	128.34	0.00	0.59	4.70	0.00	0.29	0.00	59.62	0.00	2.06	0.00	1.17	0.00
760	128.98	0.00	0.58	6.64	0.87	0.00	0.00	49.06	0.00	1.15	0.58	0.00	0.00
770	129.50	0.98	0.33	2.62	0.00	0.00	0.00	58.69	0.00	0.33	0.00	0.98	1.64
780	130.10	1.80	0.00	3.31	1.50	1.20	0.00	49.32	0.00	0.30	0.00	3.01	1.50
790	131.25	0.90	0.00	0.00	0.30	0.00	0.00	56.07	0.00	0.30	0.00	1.20	0.90
800	132.50	0.00	0.00	1.00	1.34	2.00	0.00	40.73	0.00	2.00	0.33	2.00	1.34
810	133.75	0.97	0.00	0.00	0.32	0.32	0.00	48.95	0.00	2.25	0.64	2.25	1.61
820	135.00	0.65	0.98	0.33	1.96	0.33	0.00	53.03	0.00	0.98	0.00	4.91	2.95
830	136.24	0.33	0.00	0.99	1.64	0.33	0.00	47.29	0.00	1.64	0.00	5.25	0.99
840	137.49	0.33	0.00	3.33	3.00	0.00	0.00	54.58	0.00	0.33	0.00	10.65	2.00
850	138.74	0.00	0.00	0.30	1.20	0.00	0.00	67.86	0.00	1.49	0.00	5.68	0.90
860	140.26	0.33	0.00	0.00	0.98	0.33	0.00	69.17	0.00	1.96	0.00	5.22	2.61
870	143.39	0.00	0.33	0.00	0.00	0.00	0.00	65.79	0.00	0.00	0.00	4.28	0.00
880	146.80	0.31	0.31	0.31	0.92	0.00	0.00	64.31	0.00	0.62	0.00	6.77	0.92
890	150.21	0.00	0.00	0.28	0.83	0.00	0.00	47.50	0.00	1.11	0.00	11.39	0.28
900	153.61	0.00	0.00	0.65	0.33	0.33	0.00	71.69	0.00	0.33	0.00	6.55	1.96
910	157.02	0.00	0.30	0.30	0.30	0.00	0.00	58.79	0.00	0.61	0.00	7.88	0.91
920	160.43	0.00	0.32	0.00	0.32	0.00	0.00	63.43	0.00	0.65	0.00	11.65	2.27
930	163.83	0.00	0.62	0.31	0.31	0.00	0.00	57.19	0.00	0.93	0.00	11.75	0.31
940	167.24	0.32	0.32	1.30	0.32	0.00	0.00	59.32	0.00	0.32	0.00	11.99	0.65
950	170.65	0.58	1.73	2.02	0.58	0.00	0.00	45.66	0.00	0.00	0.29	3.47	0.87
960	174.31	0.00	0.98	2.62	1.64	0.33	0.00	46.23	0.00	0.66	0.00	11.15	1.97
970	179.54	0.61	0.00	2.13	1.83	0.00	0.00	46.58	0.00	1.22	0.00	7.31	0.91
980	184.51	0.30	0.00	1.52	4.24	0.30	0.00	55.76	0.00	1.82	0.00	11.82	0.30
990	186.35	0.30	0.59	0.89	1.18	0.00	0.00	52.58	0.00	0.59	0.00	7.98	0.59
1000	187.67	0.00	0.63	0.63	0.63	0.00	0.00	55.80	0.00	0.94	0.00	7.84	0.94
1010	188.99	0.00	2.42	0.30	0.60	0.00	0.00	59.21	0.00	0.60	0.00	3.63	1.21
1020	190.31	0.34	0.34	0.00	0.00	0.00	0.00	66.90	0.00	0.00	0.00	13.79	0.00
1030	191.47	0.00	0.74	3.35	0.00	0.00	0.00	51.67	0.00	0.00	0.00	9.67	0.37

Depth	Kyr_BP787	Hemidiscus cuneiformis	Porosira glacialis	Porosira pseudodenticulata	Roperia tesselata	Stellarima microtrias	Thalassiosira Antarctica Group	Thalassiosira oestrupii including the varieties oestrupii and venrickae	Thalassiosira gracilis	Thalassiosira lentiginosa	Thalassiosira oestrupii including the varieties oestrupii and venrickae	Thalassiosira oliverana	Thalassiosira tumida
0	4.66	0.00	0.00	0.00	0.00	0.00	0.00	0.00	4.89	7.18	0.00	1.31	0.00
10	4.92	0.00	0.00	0.00	0.00	0.00	0.00	0.00	2.67	7.72	0.00	1.19	0.00
20	5.21	0.00	0.00	0.00	0.00	0.00	0.00	0.00	6.20	4.03	0.00	0.93	0.00
30	5.48	0.00	0.00	0.00	0.00	0.00	0.00	0.00	2.92	10.22	0.00	1.46	0.29
40	5.78	0.00	0.00	0.00	0.00	0.00	0.00	0.00	2.55	8.29	0.00	0.64	0.00
50	6.10	0.00	0.00	0.00	0.00	0.00	0.00	0.00	3.66	14.05	0.00	1.22	0.00
60	6.42	0.00	0.00	0.00	0.00	0.00	0.00	0.00	2.18	7.15	0.00	0.62	0.00
70	6.74	0.00	0.00	0.00	0.00	0.00	0.00	0.00	3.51	8.95	0.00	0.96	0.00
80	7.06	0.00	0.00	0.00	0.00	0.00	0.00	0.00	3.80	6.65	0.00	0.32	0.00
90	7.37	0.00	0.00	0.00	0.00	0.00	0.00	0.00	1.29	14.79	0.64	0.32	0.00
100	7.69	0.00	0.00	0.00	0.00	0.00	0.00	0.00	2.68	9.72	0.00	0.34	0.00
110	8.01	0.00	0.00	0.00	0.00	0.00	0.00	0.00	2.30	14.10	0.58	0.86	0.29
120	8.33	0.00	0.00	0.00	0.00	0.00	0.00	0.00	2.22	7.91	0.00	0.32	0.32
130	8.65	0.00	0.00	0.00	0.00	0.00	0.00	0.00	3.73	11.18	0.62	0.93	0.00
140	8.96	0.00	0.00	0.00	0.00	0.00	0.00	0.00	1.96	6.86	0.00	0.00	0.00
150	9.28	0.00	0.00	0.00	0.00	0.00	0.00	0.00	2.80	21.50	0.00	0.62	0.00
160	10.08	0.00	0.00	0.00	0.00	0.00	0.00	0.00	2.00	21.68	0.00	0.86	0.00
170	13.34	0.00	0.00	0.33	0.00	0.00	0.00	0.00	2.30	14.14	0.00	0.66	0.00
180	14.73	0.00	0.00	0.00	0.00	0.00	0.00	0.00	1.57	14.44	0.00	0.31	0.00
190	15.63	0.00	0.00	0.00	0.00	0.00	0.00	0.00	0.93	20.81	0.00	0.93	0.00
200	15.89	0.00	1.58	0.00	0.00	0.00	0.00	0.00	0.00	10.41	0.00	0.63	0.00
210	16.04	0.00	0.00	0.00	0.00	0.00	0.32	0.00	1.28	14.67	0.32	2.23	0.00
220	16.27	0.00	0.00	0.00	0.00	0.00	0.00	0.00	1.07	12.27	0.00	0.53	0.00
230	17.07	0.00	0.00	0.00	0.00	0.00	0.34	0.00	2.02	18.82	0.67	3.03	0.00
240	17.94	0.00	0.00	0.00	0.00	0.00	0.32	0.00	1.90	18.41	0.63	2.54	0.32
250	18.63	0.00	0.00	0.00	0.00	0.00	0.66	0.00	3.97	21.52	0.33	2.65	0.00
260	19.36	0.00	0.00	0.00	0.00	0.00	0.00	0.00	5.13	11.40	0.00	0.00	0.00
270	20.52	0.00	0.00	0.00	0.00	0.00	0.00	0.00	4.65	16.12	0.62	1.24	0.00
280	21.76	0.00	0.60	0.00	0.00	0.00	0.00	0.00	0.00	9.31	0.00	0.90	0.00
290	22.99	0.00	0.00	0.31	0.00	0.00	0.31	0.00	3.75	18.13	0.31	2.19	0.00
300	24.48	0.00	0.00	0.00	0.00	0.00	0.31	0.00	9.54	6.46	0.92	0.31	0.00
310	27.50	0.00	0.00	0.00	0.00	0.00	0.00	0.00	1.53	14.37	0.31	2.14	0.00
320	30.45	0.00	0.00	0.00	0.00	0.00	1.20	0.00	4.20	11.69	0.90	0.00	0.30
330	31.51	0.00	0.00	0.31	0.00	0.00	0.00	0.00	2.17	13.00	0.00	0.31	0.00
340	32.25	0.00	0.00	0.00	0.00	0.00	0.00	0.00	3.09	8.64	0.62	0.31	0.00
350	33.07	0.00	0.00	0.00	0.00	0.00	0.91	0.00	1.83	10.67	0.00	0.61	0.00
360	33.89	0.00	0.00	0.00	0.00	0.00	0.66	0.00	3.29	11.20	0.00	0.00	0.33
370	34.72	0.00	0.00	0.00	0.00	0.00	0.65	0.00	2.94	13.73	0.00	0.33	0.33
380	35.55	0.00	0.35	0.00	0.00	0.00	1.41	0.00	1.76	16.17	0.35	0.70	0.00
390	36.37	0.00	0.00	0.00	0.00	0.00	0.00	0.00	2.97	18.78	0.00	1.32	0.33
400	37.20	0.00	0.00	0.00	0.00	0.00	1.32	0.00	5.62	17.52	0.00	0.66	0.00

410	38.02	0.00	0.00	0.00	0.00	0.00	0.00	0.00	3.53	23.40	0.00	2.24	0.00
420	38.85	0.00	0.00	0.00	0.00	0.00	1.63	0.00	7.83	12.07	0.00	0.65	0.00
430	39.68	0.00	0.00	0.00	0.00	0.00	0.93	0.00	2.47	16.07	0.00	1.85	0.00
440	40.50	0.00	0.00	0.00	0.00	0.00	0.63	0.00	7.29	18.07	0.00	1.58	0.32
450	41.33	0.00	0.00	0.00	0.00	0.00	0.31	0.00	3.12	12.79	0.00	0.62	0.00
460	42.16	0.00	0.32	0.00	0.00	0.00	0.64	0.00	5.41	8.60	0.00	2.23	0.00
470	42.98	0.00	0.00	0.00	0.00	0.00	0.30	0.00	2.12	18.51	0.00	2.43	0.00
480	43.81	0.00	0.35	0.00	0.00	0.00	0.35	0.00	2.77	21.49	0.00	2.43	0.00
490	44.63	0.00	0.00	0.31	0.00	0.00	0.00	0.00	2.81	16.54	0.00	0.62	0.31
500	45.46	0.00	0.00	0.00	0.00	0.00	0.00	0.00	4.91	16.47	0.29	1.45	0.29
510	46.29	0.00	0.00	0.00	0.00	0.00	0.28	0.00	2.25	21.07	0.00	1.40	0.00
520	47.11	0.00	0.00	0.00	0.00	0.00	0.00	0.00	2.94	11.44	0.00	0.33	0.00
530	47.94	0.00	0.00	0.00	0.00	0.00	0.00	0.00	1.31	16.64	0.00	1.63	0.00
540	49.48	0.00	0.00	0.00	0.00	0.00	0.00	0.00	2.14	7.12	0.00	0.36	0.00
550	55.32	0.00	0.00	0.00	0.00	0.00	0.00	0.00	1.64	7.21	0.00	0.33	0.33
560	61.88	0.00	0.00	0.00	0.00	0.00	0.35	0.00	1.74	12.15	0.00	0.00	0.00
570	68.44	0.00	0.00	0.00	0.00	0.00	0.33	0.00	1.31	11.76	0.00	1.31	0.00
580	74.60	0.00	0.00	0.00	0.00	0.00	0.00	0.00	0.31	9.73	0.31	0.00	0.00
590	78.39	0.00	0.00	0.00	0.00	0.00	0.00	0.00	1.23	8.91	0.00	0.31	0.00
600	81.78	0.00	0.00	0.00	0.00	0.00	0.00	0.00	2.23	5.41	0.00	0.64	0.00
610	85.17	0.00	0.00	0.00	0.00	0.00	0.00	0.00	1.62	9.39	0.00	0.00	0.00
620	88.57	0.00	0.00	0.00	0.00	0.00	0.67	0.00	4.03	8.05	0.00	0.34	0.00
630	91.96	0.00	0.00	0.00	0.00	0.00	0.00	0.00	2.40	7.80	0.30	0.30	0.00
640	95.36	0.00	0.00	0.00	0.00	0.00	0.00	0.00	3.38	6.42	0.00	0.68	0.00
650	98.75	0.00	0.00	0.00	0.00	0.00	0.00	0.00	1.66	11.63	0.00	0.28	0.00
660	102.14	0.00	0.00	0.00	0.00	0.00	0.30	0.00	3.02	4.83	0.00	0.30	0.30
670	105.54	0.00	0.00	0.00	0.00	0.00	0.00	0.00	1.86	11.47	0.31	0.31	0.00
680	109.52	0.00	0.00	0.00	0.00	0.00	0.00	0.00	1.29	17.04	0.32	1.61	0.00
690	116.99	0.00	0.00	0.00	0.00	0.00	0.00	0.00	2.54	6.35	0.00	0.63	0.00
700	124.13	0.00	0.00	0.00	0.00	0.00	0.31	0.00	1.88	6.89	0.63	0.94	0.00
710	125.71	0.00	0.00	0.00	0.00	0.00	0.00	0.00	5.17	8.91	1.72	0.29	0.29
720	126.37	0.00	0.00	0.00	0.00	0.00	0.00	0.00	3.76	15.05	0.63	0.94	0.31
730	127.03	0.00	0.00	0.00	0.00	0.00	0.00	0.00	1.23	9.49	0.31	0.00	0.31
740	127.69	0.00	0.00	0.34	0.00	0.00	0.34	0.00	2.69	14.81	1.01	0.00	0.34
750	128.34	0.00	0.00	0.00	0.00	0.00	0.29	0.00	1.47	10.87	0.59	0.00	0.00
760	128.98	0.00	0.00	0.00	0.00	0.00	0.58	0.00	1.15	12.41	0.87	0.58	0.00
770	129.50	0.00	0.00	0.00	0.00	0.00	0.00	0.00	1.97	16.39	0.66	0.98	0.00
780	130.10	0.00	0.00	0.00	0.00	0.00	0.00	0.00	2.11	17.44	0.60	2.11	0.00
790	131.25	0.00	0.00	0.00	0.00	0.00	0.00	0.00	1.20	22.79	0.00	3.00	0.30
800	132.50	0.00	0.00	0.00	0.00	0.00	0.33	0.00	4.01	27.38	0.33	3.01	0.00
810	133.75	0.00	0.00	0.00	0.00	0.00	0.32	0.00	0.97	24.48	0.64	3.22	0.00
820	135.00	0.00	0.00	0.00	0.00	0.00	0.65	0.00	0.98	19.97	0.33	2.29	0.33
830	136.24	0.00	0.00	0.00	0.00	0.00	0.00	0.00	3.94	25.94	0.99	1.64	0.00
840	137.49	0.00	1.33	0.00	0.00	0.00	0.00	0.00	0.00	13.31	0.33	0.67	0.67
850	138.74	0.00	0.00	0.00	0.00	0.00	0.30	0.00	1.49	14.95	0.30	0.30	0.00
860	140.26	0.00	0.00	0.00	0.00	0.00	0.65	0.00	1.63	9.79	0.00	0.33	0.00
870	143.39	0.00	0.00	0.00	0.00	0.00	0.00	0.00	1.32	17.11	0.00	0.33	0.00
880	146.80	0.00	0.00	0.00	0.00	0.00	0.31	0.31	1.54	16.62	0.31	1.23	0.00
890	150.21	0.00	0.00	0.00	0.00	0.00	0.28	0.00	0.83	25.83	0.83	3.61	0.00
900	153.61	0.00	0.00	0.00	0.00	0.00	0.33	0.00	1.64	11.78	0.00	0.33	0.00
910	157.02	0.00	0.00	0.00	0.00	0.00	0.30	0.00	0.61	23.03	0.00	1.82	0.00
920	160.43	0.00	0.00	0.00	0.00	0.00	0.00	0.00	0.65	12.30	0.65	0.65	0.00
930	163.83	0.00	0.00	0.00	0.00	0.00	0.31	0.00	1.55	17.31	1.24	1.55	0.00
940	167.24	0.00	0.00	0.00	0.00	0.00	0.65	0.00	0.32	13.94	1.94	0.32	0.00
950	170.65	0.00	0.00	0.00	0.00	0.00	0.29	0.00	1.45	28.90	0.58	3.18	0.00
960	174.31	0.00	0.00	0.00	0.00	0.00	0.00	0.00	1.64	14.43	0.33	0.66	0.00
970	179.54	0.00	0.00	0.00	0.00	0.00	0.30	0.00	1.83	17.96	0.30	2.44	0.00
980	184.51	0.00	0.00	0.00	0.00	0.00	0.00	0.00	2.42	11.52	0.30	1.21	0.30
990	186.35	0.00	0.00	0.00	0.00	0.00	0.00	0.00	1.77	20.97	0.59	1.48	0.30
1000	187.67	0.00	0.00	0.00	0.00	0.00	0.00	0.00	2.51	16.61	0.94	1.88	0.00
1010	188.99	0.00	0.00	0.00	0.00	0.00	0.30	0.00	1.51	16.62	2.11	1.21	0.00
1020	190.31	0.00	0.00	0.00	0.00	0.00	0.00	0.00	1.72	4.14	1.03	0.00	0.00
1030	191.47	0.00	0.00	0.00	0.00	0.00	0.00	0.00	1.86	9.67	1.12	1.49	0.00

Appendix 5.4

Those samples from the Abbott southeast Indian Ocean diatom database that were sampled from areas that are currently covered by Southern Ocean Polar Frontal branches. Also provided are the computed presence of the PF-S, PF-M and PF-N (mpa) over each of the Abbott database samples.

Abbott database sample	**PF-S mpa**	**Abbott database sample**	**PF-M mpa**	**Abbott database sample**	**PF-N mpa**
E34-17	3.75	E34-17	0.2	E35-5	1.3
E36-14*	2.65	E35-5	0.25	E36-6	1.15
E34-16	2.9	E36-6	0.1	E36-14*	0.05
E44-21	0.5	E36-14*	0.2	E44-21	0.25
E44-22*	0.6	E34-16	0.25	E44-22*	0.2
E44-23*	0.6	E44-21	1.25	E44-23*	0.2
E44-27*	0.1	E44-22*	1.3	E44-27*	1.15
E45-42*	1.1	E44-23*	1.45	E44-26	0.95
E45-44	2.65	E44-27*	0.5	E34-19*	1.2
E44-26	0.1	E45-42*	1.15	E35-4	0.7
E35-4	0.1	E45-44	0.35	E36-8	0.85
E36-11*	3.45	E44-26	0.45	E37-19*	0.15
E37-19*	0.3	E34-19*	0.05	E39-35*	0.85
E45-33	0.3	E35-4	1.2	E44-13	0.05
E45-35	0.65	E36-8	0.9	E44-15	0.9
E45-39*	0.55	E36-11*	0.55	E44-16	0.55
E45-60*	0.3	E37-19*	1.9	E45-33	0.7
E45-58	0.95	E39-35*	0.6	E45-35	0.2
E35-16	0.15	E44-13	1.9	E45-39*	0.45
E44-24	0.25	E44-15	0.7	E45-60*	0.55
E45-37	0.35	E44-16	0.8	V16-115	1.2
E45-63	0.25	E45-33	1.1	E45-58	0.45
E35-15	0.15	E45-35	1.75	E35-16	0.8
E45-64	0.2	E45-39*	1.2	E44-24	0.2
		E45-60*	0.85	E45-37	0.2
		V16-115	0.35	E45-63	0.25
		E45-58	1.05	E35-15	0.85
		E35-16	1.1	E45-64	0.15
		E44-24	1.75		
		E45-37	1.8		
		E45-63	1.15		
		E35-15	0.7		
		E45-64	1.15		

Appendix 5.5

Those samples from the Abbott southeast Indian Ocean diatom database that were sampled from areas that are currently covered by the SACCF-S and SASCCF-N. Also provided is the mpa for the SACCF-N and SACCF-N over each of the Abbott database samples.

Abbott database sample	SACCF-N mpa	Abbott database sample	SACCF-S mpa
E36-14*	0.95	E38-4	1.55
E34-16	0.85	E36-12	0.15
E36-34	3.5		
E44-21	0.05		
E44-22*	0.05		
E44-23*	0.05		
E45-42*	0.1		
E45-44	0.4		
E38-4	1.3		
E36-12	4.35		

Appendix 5.6

The R scripts used to fit the Huisman Olff-Fresco (HOF) models described in sections 2.2.1 and 3.2. Also shown is the raw output from R for each of the HOF models fitted to describe the associations between diatom relative abundances and anuual average monthly presence (mpa) of the PF-S, PF-M and PF-N. The final HOF models were chosen via bootstrapping, with the most frequently fitted model selected. Additionally, models were compared using the Alike Information Criterion. As all models were compared with a model that has no optima (which, if selected, would imply that diatom species have no response to the presence of the Polar Front), it was possible to infer that a chosen HOF model, with a given response, is significant. Importantly, GAM's were also considered in the HOF modelling used for this thesis. By including GAM within the suite of HOF models fitted, it is possible to also identify linear relationships between diatoms and the presence of the Polar Front.

The final HOF models used to explain the association between diatom relative abundances and PF-N m/ps (PF4).

```
PFfourVECTOR <- as.vector(PFfourVECT$PFfourVECT)
> PFfourVECTOR <- as.vector(PFfourVECT$PFfourVECT)
> HOFmod <- HOF(PFdiaABUN, PFfourVECTOR, family=gaussian, lim=100, bootstrap=100, test='AIC')
> pick.model(HOFmod, level=0.95, test=("AIC"), gam=T, selectMethod=('IC.weight'))
          F.kerguelens
                 "III"
         Thalassiothrix
                 "GAM"
          T.lentiginosa
                  "II"
              Az.tab.gp
                  "II"
           F.separanda
                  "II"
               Th.nitz
                 "VII"
```

The final HOF models used to explain the association between diatom relative abundances and PF-M m/ps (PF5)

```
PFfiveVECTOR <- as.vector(PFfiveVECT$PFfiveVECT)
> HOFmod <- HOF(PFdiaABUN, PFfiveVECTOR, family=gaussian, lim=100, bootstrap=100, test='AIC')
> pick.model(HOFmod, level=0.95, test=("AIC"), gam=T, selectMethod=('IC.weight'))
          F.kerguelens
                 "VII"
         Thalassiothrix
                 "GAM"
```

```
T.lentiginosa
"GAM"
```

The final HOF models used to explain the association between diatom relative abundances and PF-S mpa (PF6)

```
PFsixVECTOR <- as.vector(PFsixVECT$PFsix)
HOFmod <- HOF(PFdiaABUN, PFsixVECTOR, family=gaussian, lim=100, bootstrap=100, test='AIC')
pick.model(HOFmod, level=0.95, test=("AIC"), gam=T, selectMethod=('IC.weight'))
F.kerguelens
"GAM"
Thalassiothrix
"GAM"
T.lentiginosa
"VII"
F.separanda
"VII"
Th.nitz
"VI"
```

Appendix 5.7

A list of the 60 samples taken from the Abbott database that were used in this thesis. Included are the sample codes, as well as the latitude and longitude for each sample. The relative percentage abundance of the 7 diatom species that have a significant species response relationship with the average annual monthly presence of the PF-S, PF-M and PF-N are listed. The full list of diatom species that were counted within the Abbott database are provided in Appendix 2.5 of Armand (1997, unpublished thesis).

Abbott database Core Name	**Latitude**	**Longitude**	***Azpeitia tabularis***	***Fragilariopsis kerguelensis***	***Fragilariopsis separanda***	***Thalassiosthrix antarctica***	***Thalassiosira lentiginosa***	***Thalassiosnema nitzschioides***	***Thalassiosira oliverana***
E34-17	60°17.1'S	144°58.3'E	0.99	59.93	2.32	26.49	4.64	0.00	0.66
E34-19	56°40.0'S	135°13.1'E	0.66	59.08	2.31	18.81	3.30	0.00	0.00
E34-20	54°10.2'S	135°12.7'E	5.10	37.26	1.27	35.99	7.01	3.50	0.64
E35-3	48°16.0'S	131°51.0'E	1.32	59.60	1.66	21.85	5.30	0.66	0.33
E35-4	56°52.1'S	129°38.1'E	1.95	52.34	1.56	24.22	8.59	0.39	0.78
E35-5	56°03.0'S	128°10.8'E	1.63	44.44	0.65	37.58	7.19	1.96	0.65
E35-6	53°12.1'S	128°05.8'E	1.63	58.17	0.00	21.24	6.21	0.33	0.00
E35-7	49°58.1'S	128°04.4'E	1.65	58.09	1.65	25.08	6.93	0.00	0.33
E36-5	53°01.6'S	139°59.2'E	2.94	59.15	0.65	22.22	4.90	1.31	0.00
E36-6	54°32.4'S	140°03.1'E	2.27	65.58	1.30	14.61	6.17	0.00	0.32
E36-8	58°05.5'S	139°54.6E	1.64	65.13	0.00	21.38	6.91	0.33	0.66
E36-11	60°37.4'S	142°04.7'E	1.01	62.63	9.76	14.48	4.38	3.03	0.34
E36-14	58°05.6'S	150°14.4'E	0.50	39.30	1.49	34.83	10.95	0.00	1.00
E34-16	58°08.2'S	149°59.5'E	0.66	63.28	0.33	20.66	8.20	0.00	0.33
E36-34	60°00.0'S	155°02.5'E	0.33	54.10	4.59	21.97	8.52	0.00	0.00
E37-19	56°05.6'S	124°53.3'E	1.44	67.15	0.00	15.88	8.30	0.72	0.00
E37-20	50°53.5'S	125°10.3'E	2.61	36.16	1.30	32.90	12.05	4.56	0.33
E39-13	45°00.7'S	125°58.9'E	0.50	60.00	2.50	26.50	4.00	0.50	0.00
E39-17	47°01.6'S	125°56.8'E	1.49	66.17	0.50	23.88	3.48	0.00	0.00
E39-18	48°00.5'S	126°05.5'E	2.65	56.62	0.66	25.17	6.29	0.66	0.00
E39-23	51°07.3'S	126°10.6'E	0.98	45.57	1.31	27.21	10.82	2.95	0.00
E39-26	52°58.5'S	126°08.2'E	0.00	61.38	0.00	18.97	6.21	3.45	1.03
E39-35	57°30.6'S	133°58.5'E	1.63	49.19	0.98	26.71	5.54	0.33	0.98
E39-38	53°S	133.5°E	1.32	48.03	0.33	39.47	2.30	3.29	0.33
E39-39	52°05.1'S	133°56.3'E	1.94	61.24	1.16	18.60	3.88	0.00	0.39
E39-53	48°49.0'S	144°32.4'E	4.88	49.76	0.00	27.32	9.76	1.46	0.49
E39-55	49°56.9'S	145°55.8'E	2.64	40.92	0.33	39.93	7.92	0.66	0.00
E44-13	58°01.1'S	142°27.0'E	0.66	65.25	0.98	22.62	3.28	0.00	0.66
E44-15	57°59.6'S	137°26.6'E	1.32	55.63	1.32	29.14	4.30	1.32	0.33
E44-16	57°59.2'S	134°58.2'E	1.97	57.24	0.99	28.95	5.26	0.00	0.33
E44-21	58°03.6'S	130°06.5'E	0.32	61.49	2.59	18.12	2.91	1.62	0.00
E44-22	58°05.3'S	130°0.8.2'E	0.33	54.58	3.59	27.12	4.25	0.00	0.00
E44-23	58°06.2'S	130°11.0'E	0.99	52.81	1.65	29.70	6.93	0.00	0.33
E44-27	53°02.3'S	119°44.1'E	1.65	51.16	0.66	28.38	5.28	3.96	0.33
E45-33	51°58.7'S	110°28.4'E	0.34	64.04	1.37	20.89	7.53	1.37	0.00
E45-35	53°29.7'S	111°20.0'E	1.98	56.77	2.97	20.79	7.92	0.33	0.00
E45-39	56°00.4'S	112°42.9'E	2.00	66.67	2.33	14.00	8.00	0.33	1.00
E45-42	57°12.7'S	113°20.2'E	0.33	53.64	1.99	23.84	9.93	0.00	0.33
E45-60	55°03.7'S	114°09.1'E	0.66	72.94	1.32	11.55	5.61	0.99	0.33
E45-69	48°50.9'S	114°37.0'E	5.54	26.71	0.00	36.16	19.54	1.95	0.33
E45-71	48°01.5'S	114°29.2'E	1.63	27.12	0.65	35.95	22.55	0.65	0.33
E45-77	46°26.9'S	114°25.0'E	2.96	40.89	0.00	17.73	19.70	0.00	0.99
E45-79	45°03.4'S	114°22.0'E	4.89	48.86	0.65	19.87	10.75	2.93	0.65
Conrad 8-63	51°05.0'S	129°58.0'E	6.88	39.07	0.98	23.59	15.48	0.49	0.49
Conrad 8-64	51°30'S	135°51'E	0.50	55.00	1.00	20.00	4.00	0.00	4.00
Vema 16-115	55°41'S	141°17'E	2.63	69.74	0.00	16.78	4.93	0.66	0.99

E45-44	58°28.5'S	114°07.3'E	1.32	60.07	3.30	19.80	8.58	0.00	0.00
E38-4	64°13.9'S	150°03.8'E	0.99	47.68	1.99	22.52	6.29	0.00	0.00
E36-12	61°45.1'S	149°33.1'E	0.00	65.23	3.97	17.88	6.62	0.00	0.00
E45-58	56°35.0'S	114°06.9'E	2.73	65.01	1.99	15.38	7.20	1.74	0.00
E35-16	53°11.6'S	116°57.5'E	2.70	54.66	0.74	26.23	6.13	1.23	0.25
E44-24	56°02.4'S	119°54.0'E	2.30	64.80	0.33	18.42	2.96	3.29	0.66
E45-37	54°41.8'S	111°57.9'E	1.32	62.25	5.96	18.21	3.97	1.66	0.00
E44-26	54°01.1'S	119°46.4'E	1.63	61.11	1.31	13.73	4.25	5.88	0.65
E45-63	53°26.2'S	114°15.4'E	2.64	58.42	2.31	18.48	5.61	1.98	0.66
E35-15	52°56.4'S	116°59.5'E	1.00	54.15	0.33	29.90	5.98	1.00	0.33
E45-64	52°29.0'S	114°05.4'E	1.00	60.67	0.33	23.33	8.33	0.67	0.67
E39-21	48°51.7'S	126°01.0'E	2.54	52.28	1.52	26.40	9.64	2.03	0.00
E45-31	46°04.2'S	107°13.5'E	0.00	43.38	0.66	32.12	9.93	0.33	0.66
E45-29	44°52.6'S	106°31.1'E	5.94	38.28	0.00	23.43	16.50	1.98	0.00

Appendix 5.8

The MAT derived down core paleo record for PF-S, PF-M and PF-N mpa for marine sediment core MD88-784. Also provided is the age of each core sample in calendar years before the resent day.

Kyr_BP784	PF-S mpa	PF-M mpa	PF-N mpa
5.31	0.1375	0.7625	0.775
5.56	0.08	0.45	0.82
5.82	1.55	0.725	0.075
6.07	0.4	0.725	0.6667
6.32	0.11	1.01	0.93
7.00	0.15	0.8	0.85
7.67	0	0.2	1.3
8.34	0.6	0.87	0.31
9.01	0.5	1.3	0.5
9.74	0.48	1.19	0.53
10.47	0.4	1.15	0.6667
11.20	1.112	0.99	0.2125
11.93	0.48	1.112	0.53
12.66	0.6	1.15	0.35
13.39	1.1	1.15	0
14.13	0	0.2	1.3
14.86	2.65	0.2	0.05
15.60	0.6	0.725	0.3
16.35	2.65	0.2	0.05
17.13	2.65	0.2	0.05
17.91	2.65	0.2	0.05
19.64	2.65	0.2	0.05
21.37	2.65	0.2	0.05
23.11	2.65	0.2	0.05
24.84	2.65	0.2	0.05
26.57	2.65	0.2	0.05
28.30	2.65	0.2	0.05
29.24	2.65	0.2	0.05
30.17	2.65	1.15	0
31.11	2.65	0.2	0.05
32.05	1.65	1.2	0.1
32.98	1.083	0.99	0.3333
33.92	0.4	1.18	0.6
34.86	0.3	1.15	0.15
35.79	0.6	0.69	0.2
36.73	0.4	0.725	0.6667
37.67	0.19	0.6375	0.78
38.60	0	1.15	1.3
39.54	2.65	0.2	0.05
40.48	1.875	0.2	0.025
41.41	2.65	1.15	0
42.35	0	1.15	1.3
43.29	1.033	1.083	0.4833
44.22	0.1	0.725	0.725
45.16	0.08	0.68	0.82
46.10	0.7	1.19	0.59
47.03	0.48	1.188	0.53
47.61	0.6	1.15	0.35
48.18	0.45	0.725	0.55
48.76	1.1	1.15	0

Appendix 5.9

The MAT derived down core paleo record for PF-S, PF-M and PF-N mpa for marine sediment core MD88-787. Also provided is the age of each core sample in calendar years before the resent day.

Kyr_BP787	PF-S mpa	PF-M mpa	PF-N mpa
4.66	0.19	0.6833	0.78
4.92	1.375	0.86	0.2875
5.21	0.25	1.067	0.725
5.48	0.21	1.3	0.77
5.78	1.183	0.85	0.15
6.10	0.6	1.15	0.35
6.42	1.1	0.6833	0.41
6.74	0.6	1.18	0.31
7.06	1.533	0.8	0.15
7.37	1.1	1.15	0
7.69	2.65	1.3	0
8.01	1.1	1.15	0
8.33	0.5	0.85	0.2167
8.65	1.65	0.725	0.1
8.96	0.425	0.6833	0.225
9.28	2.65	0.2	0.05
10.08	2.65	0.2	0.05
13.34	0.6	1.15	0.35
14.73	0.6	1.15	0.35
15.63	2.65	0.2	0.05
15.89	0.25	1.05	0.725
16.04	2.65	0.2	0.05
16.27	1.1	1.15	0
17.07	2.65	0.2	0.05
17.94	2.65	0.2	0.05
18.63	2.65	0.2	0.05
19.36	0.6125	0.725	0.275
20.52	2.65	0.2	0.05
21.76	2.65	1.083	0
22.99	2.65	0.2	0.05
24.48	3.45	1.175	0
27.50	2.65	0.2	0.05
30.45	2.65	1.15	0
31.51	0.6	1.15	0.35
32.25	0.53	1.112	0.41
33.07	0.11	1.083	0.87
33.89	2.65	0.725	0
34.72	0	1.15	1.3
35.55	2.65	0.2	0.05
36.37	2.65	0.2	0.05
37.20	2.65	0.2	0.05
38.02	2.65	0.2	0.05
38.85	0.6	1.15	0.35
39.68	2.65	0.2	0.05
40.50	2.65	0.2	0.05
41.33	2.65	1.15	0
42.16	1.112	1.3	0.2125
42.98	2.65	0.2	0.05
43.81	2.65	0.2	0.05
44.63	2.65	0.2	0.05
45.46	2.65	0.2	0.05
46.29	2.65	0.2	0.05
47.11	1.467	0.725	0.06667
47.94	2.65	0.2	0.05

49.48	1.375	0.6833	0.2875
55.32	0.08	0.45	0.86
61.88	0.6	1.2	0.35
68.44	1.02	0.725	0.22
74.60	0.48	1.18	0.53
78.39	0.53	0.91	0.41
81.78	0.1	0.7875	0.6125
85.17	0.14	1.01	0.87
88.57	0.8375	0.85	0.5375
91.96	0.05	0.6375	0.9
95.36	1.533	0.6833	0.15
98.75	0.05	0.725	1
102.14	0.83	0.925	0.72
105.54	0.2	0.35	0.75
109.52	2.65	0.2	0.05
116.99	0.35	0.45	0.2
124.13	0.6	0.6833	0.2
125.71	1.65	0.99	0.1
126.37	1.875	0.2	0.025
127.03	0.5	1.175	0.5
127.69	2.65	0.2	0.05
128.34	0.05	1.15	1
128.98	0.3	0.2	0.15
129.50	2.65	0.2	0.05
130.10	2.65	0.2	0.05
131.25	2.65	0.2	0.05
132.50	2.65	0.2	0.05
133.75	2.65	0.2	0.05
135.00	2.65	0.2	0.05
136.24	2.65	0.2	0.05
137.49	2.65	0.2	0
138.74	2.65	1.15	0
140.26	1.65	1.083	0.1
143.39	2.65	0.2	0.05
146.80	2.65	0.2	0.05
150.21	2.65	0.2	0.05
153.61	2.65	0.725	0
157.02	2.65	0.2	0.05
160.43	3.45	1.15	0
163.83	2.65	0.2	0.05
167.24	3.45	0.2	0
170.65	2.65	0.2	0.05
174.31	2.65	0.2	0.05
179.54	2.65	0.2	0.05
184.51	3.45	1.15	0
186.35	2.65	0.2	0.05
187.67	2.65	0.2	0.05
188.99	2.65	0.2	0.05
190.31	3.45	1.8	0
191.47	3.45	1.15	0

Appendix 5.10

All of the R output for the GAM models that show a statistically significant association between diatoms and the mean annual monthly presence of the PF-S, PF-M and PF-N

PF-N

```
model <- gam(PFfour ~ s(F.separanda),  data=PFfour)
summary(model)

Family: gaussian
Link function: identity

Formula:
PFfour ~ s(F.separanda)

Parametric coefficients:
            Estimate Std. Error t value Pr(>|t|)
(Intercept)  0.50000    0.06981   7.162 4.74e-08 ***
---
Signif. codes:  0 ‘***’ 0.001 ‘**’ 0.01 ‘*’ 0.05 ‘.’ 0.1 ‘ ’ 1

Approximate significance of smooth terms:
               edf Ref.df     F p-value
s(F.separanda)   1      1 5.374  0.0271 *
---
Signif. codes:  0 ‘***’ 0.001 ‘**’ 0.01 ‘*’ 0.05 ‘.’ 0.1 ‘ ’ 1

R-sq.(adj) =    0.12   Deviance explained = 14.8%
GCV score = 0.1712  Scale est. = 0.16083   n = 33


model <- gam(PFfour ~ s(Az.tab.gp),  data=PFfour)
summary(model)

Family: gaussian
Link function: identity

Formula:
PFfour ~ s(Az.tab.gp)

Parametric coefficients:
            Estimate Std. Error t value Pr(>|t|)
(Intercept)  0.50000    0.07046   7.096 5.68e-08 ***
---
Signif. codes:  0 ‘***’ 0.001 ‘**’ 0.01 ‘*’ 0.05 ‘.’ 0.1 ‘ ’ 1

Approximate significance of smooth terms:
              edf Ref.df     F p-value
s(Az.tab.gp)   1      1 4.704  0.0377 *
---
Signif. codes:  0 ‘***’ 0.001 ‘**’ 0.01 ‘*’ 0.05 ‘.’ 0.1 ‘ ’ 1

R-sq.(adj) =  0.104   Deviance explained = 13.2%
```

```
GCV score = 0.17442  Scale est. = 0.16385   n = 33
```

```
model <- gam(PFfour ~s(F.separanda) + s(T.lentiginosa),  data=PFfour)
summary(model)

Family: gaussian
Link function: identity

Formula:
PFfour ~ s(F.separanda) + s(T.lentiginosa)

Parametric coefficients:
            Estimate Std. Error t value Pr(>|t|)
(Intercept)  0.50000    0.06186   8.083 7.06e-09 ***
---
Signif. codes:  0 ‘***’ 0.001 ‘**’ 0.01 ‘*’ 0.05 ‘.’ 0.1 ‘ ’ 1

Approximate significance of smooth terms:
                edf Ref.df     F p-value
s(F.separanda)   1.000  1.000 7.127  0.0122 *
s(T.lentiginosa) 2.318  2.903 3.419  0.0315 *
---
Signif. codes:  0 ‘***’ 0.001 ‘**’ 0.01 ‘*’ 0.05 ‘.’ 0.1 ‘ ’ 1

R-sq.(adj) =  0.309   Deviance explained = 38.1%
GCV score = 0.1453  Scale est. = 0.12629   n = 33
```

PF-S

```
model <- gam(PFsix ~ s(F.separanda) +s(T.lentiginosa), data=PFsix)
summary(model)

Family: gaussian
Link function: identity

Formula:
PFsix ~ s(F.separanda) + s(T.lentiginosa)

Parametric coefficients:
            Estimate Std. Error t value Pr(>|t|)
(Intercept)   0.6939     0.1550   4.478 0.000103 ***
---
Signif. codes:  0 ‘***’ 0.001 ‘**’ 0.01 ‘*’ 0.05 ‘.’ 0.1 ‘ ’ 1

Approximate significance of smooth terms:
                edf Ref.df      F p-value
s(F.separanda)   1.000  1.000 13.047 0.00106 **
s(T.lentiginosa) 1.252  1.464  3.377 0.06004 .
---
Signif. codes:  0 ‘***’ 0.001 ‘**’ 0.01 ‘*’ 0.05 ‘.’ 0.1 ‘ ’ 1

R-sq.(adj) =  0.314   Deviance explained = 36.2%
GCV score = 0.87925  Scale est. = 0.79261   n = 33
```

ksnormTest(res)

Title:
One-sample Kolmogorov-Smirnov test

Test Results:
STATISTIC:
D: 0.2729
P VALUE:
Alternative Two-Sided: 0.0116
Alternative Less: 0.09345
Alternative Greater: 0.005799

Description:
Thu Mar 06 14:57:34 2014 by user: aferry

shapiroTest(res)

Title:
Shapiro - Wilk Normality Test

Test Results:
STATISTIC:
W: 0.7698
P VALUE:
9.004e-06

Description:
Thu Mar 06 14:57:40 2014 by user: aferry

lillieTest(res)

Title:
Lilliefors (KS) Normality Test

Test Results:
STATISTIC:
D: 0.2654
P VALUE:
2.697e-06

Appendix 5.11

The paleo winter sea-ice concentration (wSIC) record for cores MD88-787 and MD88-784 from Chapter 4.

Kyr_BP784	wSIC MD88-784	LCL (wSIC MD88-784)	UCL (wSIC MD88-784)	Kyr_BP787	wSIC MD88-787	LCL (wSIC MD88-787)	UCL (wSIC MD88-787)
5.31	0.33	-0.26	2.35	4.66	0.26	-0.28	2.13
5.56	0.32	-0.25	2.23	4.92	0.00	-0.36	1.22
5.82	0.18	-0.21	1.06	5.21	0.27	-0.31	2.66
6.07	0.13	-0.22	0.91	5.48	0.27	-0.21	1.50
6.32	0.28	-0.22	1.66	5.78	0.29	-0.25	1.96
7.00	0.33	-0.26	2.25	6.10	0.09	-0.24	0.82
7.67	0.17	-0.17	0.85	6.42	0.26	-0.28	2.13
8.34	0.28	-0.22	1.69	6.74	0.29	-0.23	1.83
9.01	0.24	-0.21	1.38	7.06	0.24	-0.30	2.19
9.74	0.26	-0.21	1.49	7.37	0.07	-0.24	0.76
10.47	0.15	-0.21	0.96	7.69	3.02	0.69	9.47
11.20	0.26	-0.22	1.53	8.01	0.09	-0.24	0.81
11.93	0.28	-0.22	1.69	8.33	2.86	0.47	10.46
12.66	1.38	0.26	4.09	8.65	8.48	2.88	21.29
13.39	0.09	-0.23	0.77	8.96	2.81	0.39	11.08
14.13	1.79	0.48	4.77	9.28	7.41	2.69	17.78
14.86	0.14	-0.19	0.80	10.08	3.56	1.08	9.54
15.60	2.28	0.57	6.53	13.34	0.09	-0.24	0.81
16.35	3.11	1.01	7.86	14.73	1.30	0.20	4.04
17.13	18.91	8.55	36.36	15.63	26.44	12.88	46.40
17.91	22.05	8.78	44.91	15.89	29.17	13.54	51.76
19.64	15.18	5.54	34.55	16.04	48.90	29.01	69.13
21.37	26.77	11.92	49.38	16.27	17.10	6.72	36.52
23.11	3.40	0.85	10.26	17.07	31.09	12.99	57.41
24.84	0.78	-0.02	2.89	17.94	49.96	28.69	71.25
26.57	0.83	-0.03	3.23	18.63	35.53	13.07	66.61
28.30	27.26	11.73	51.05	19.36	28.59	12.71	52.10
29.24	5.25	1.83	13.00	20.52	59.41	35.73	79.46
30.17	14.03	5.47	30.80	21.76	28.58	12.39	52.80
31.11	25.55	10.62	49.39	22.99	30.21	15.18	50.94
32.05	3.89	1.09	11.07	24.48	12.30	2.44	41.13
32.98	5.26	1.61	14.28	27.50	17.41	7.16	36.02
33.92	0.27	-0.22	1.58	30.45	4.84	1.62	12.30
34.86	0.09	-0.23	0.76	31.51	0.13	-0.23	0.93
35.79	7.61	2.14	21.80	32.25	5.79	1.57	17.06
36.73	1.94	0.46	5.57	33.07	2.61	0.62	7.82
37.67	0.32	-0.24	2.08	33.89	0.22	-0.21	1.26
38.60	0.12	-0.22	0.86	34.72	0.10	-0.23	0.85
39.54	1.17	0.16	3.67	35.55	0.62	-0.13	2.88
40.48	23.63	10.24	45.25	36.37	5.18	1.94	12.20
41.41	22.66	10.57	41.77	37.20	11.90	4.19	28.48
42.35	55.33	34.49	74.48	38.02	11.00	3.96	26.08
43.29	9.06	2.90	23.60	38.85	13.07	5.29	28.17
44.22	25.25	10.65	48.52	39.68	28.73	14.84	48.06
45.16	2.69	0.36	10.61	40.50	1.75	0.28	5.87
46.10	4.38	1.07	13.71	41.33	24.24	11.20	44.48
47.03	-0.03	-0.34	0.84	42.16	19.34	7.30	41.57
47.61	1.79	0.39	5.24	42.98	7.18	2.82	16.29
48.18	7.06	2.73	16.19	43.81	4.10	1.31	10.75
48.76	1.86	0.51	4.94	44.63	4.12	1.52	9.72
				45.46	46.86	26.71	68.06
				46.29	15.24	5.16	36.35
				47.11	7.39	2.63	18.05
				47.94	4.35	1.63	10.19
				49.48	6.45	1.58	20.34

				55.32	2.87	0.43	11.01
				61.88	2.63	0.73	7.23
				68.44	2.56	0.68	7.20
				74.60	0.28	-0.22	1.63
				78.39	0.29	-0.23	1.84
				81.78	0.21	-0.33	2.34
				85.17	0.29	-0.22	1.72
				88.57	3.04	0.54	10.86
				91.96	1.87	0.21	7.12
				95.36	2.83	0.36	11.49
				98.75	4.51	1.53	11.35
				102.14	2.46	0.20	11.18
				105.54	8.29	2.84	20.72
				109.52	0.08	-0.23	0.74
				116.99	0.23	-0.31	2.22
				124.13	0.25	-0.29	2.16
				125.71	2.64	0.48	9.13
				126.37	0.07	-0.24	0.75
				127.03	1.91	0.32	6.36
				127.69	7.47	2.66	18.21
				128.34	-0.03	-0.32	0.76
				128.98	6.92	2.68	15.88
				129.50	2.07	0.40	6.64
				130.10	22.94	8.11	49.47
				131.25	19.51	7.27	42.18
				132.50	20.82	5.41	53.57
				133.75	19.16	6.52	43.84
				135.00	38.37	20.03	60.66
				136.24	56.75	30.34	79.87
				137.49	51.88	31.15	71.99
				138.74	8.52	3.48	18.68
				140.26	17.41	7.07	36.29
				143.39	0.08	-0.23	0.74
				146.80	18.33	8.72	34.18
				150.21	22.52	8.20	48.04
				153.61	1.43	0.20	4.72
				157.02	5.01	1.59	13.27
				160.43	2.41	0.64	6.72
				163.83	1.98	0.53	5.38
				167.24	7.38	2.59	18.19
				170.65	62.15	32.51	84.96
				174.31	7.81	2.93	18.29
				179.54	41.38	23.10	62.33
				184.51	55.76	34.49	75.15
				186.35	32.16	16.29	53.43
				187.67	4.16	1.54	9.79
				188.99	3.99	1.46	9.44
				190.31	1.95	0.07	9.37
				191.47	0.28	-0.22	1.65

This page is intentionally left blank.